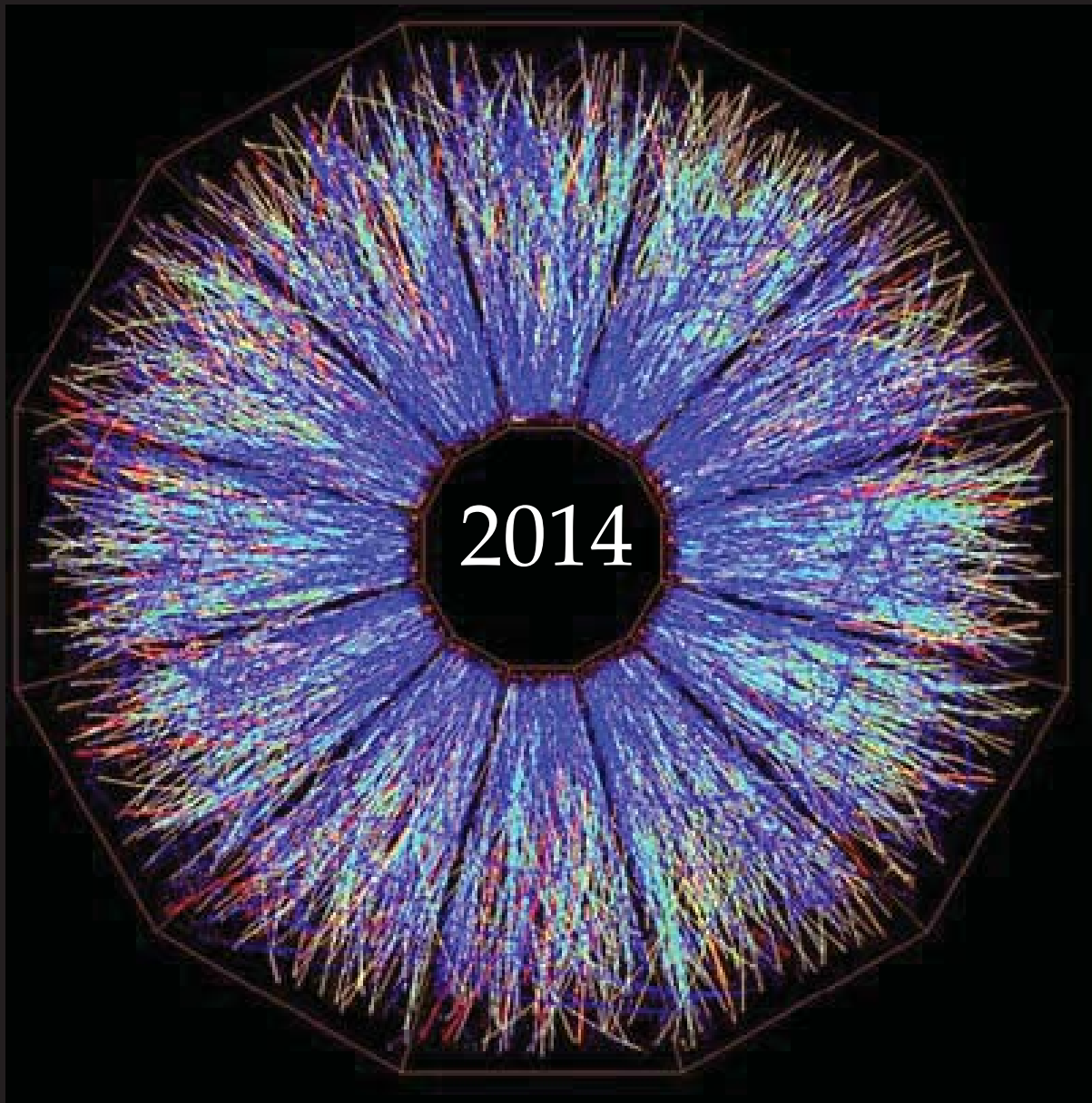


A Compilation of Internship Reports



Prepared for The Office of Educational Programs
Brookhaven National Laboratory
Office of Educational Programs

DISCLAIMER

This work was prepared as an account of work sponsored by an agency of the United States Government. Neither the United States Government nor any agency thereof, nor any of their employees, nor any of their contractors, subcontractors or their employees, makes any warranty, express or implied, or assumes any legal liability or responsibility for the accuracy, completeness, or any third party's use or the results of such use of any information, apparatus, product, or process disclosed, or represents that its use would not infringe privately owned rights. Reference herein to any specific commercial product, process, or service by trade name, trademark, manufacturer, or otherwise, does not necessarily constitute or imply its endorsement, recommendation, or favoring by the United States Government or any agency thereof or its contractors or subcontractors. The views and opinions of authors expressed herein do not necessarily state or reflect those of the United States Government or any agency thereof.



BROOKHAVEN
NATIONAL LABORATORY

Table of Contents

Examining the Water Gas Shift Reaction using a Au-CeO ₂ nanorod Catalyst	7
<i>Stefani Ahsanov</i>	
Harmonic flow in the quark-gluon plasma: insights from particle correlation spectra in heavy ion collisions.	12
<i>Mamoudou Ba</i>	
<i>Paul Glenn</i>	
An intercomparison of Vaisala RS92 and RS41 radiosondes	16
<i>Shannon Baxter</i>	
Testing of a prototype high energy efficient CdTe pixel array x-ray detector (ImXPAD) . . .	20
<i>Elizabeth Berg</i>	
Investigating the electrical properties of doped graphene	24
<i>Keturah Bethel</i>	
<i>Darnel Allen</i>	
<i>Sharadha Sambasivan</i>	
<i>David Paulius and Phil Smith</i>	
Variability in cloud cover at Brookhaven National Laboratory: Impacts on now-casting solar power	31
<i>Ricky Bhola</i>	
Determination of Equilibrium constant for cation-paired anions using the Laser-Electron Accelerator Facility	36
<i>Kierra Brown</i>	
Optimization of beam-line control for the energy recovery linac project.	41
<i>Taylor Campbell</i>	
Planning the decommissioning procedure for the PHENIX collaboration	44
<i>Matthew Chiulli</i>	
Utilization of 3D modeling in the construction of beamlines	49
<i>Luke Chu</i>	
Laser ablation of gold film on plastic and aluminum substrates	51
<i>David Cinquegrani</i>	
Radiolabelled sugars via chemoenzymatic synthesis	54
<i>Mark Cinquegrani</i>	
Using open source information to visualize safeguards data	57
<i>Daniel Cisek</i>	
<i>Dominick Raimondi</i>	
Assembly, calibration, test, and remote control of two extreme temperature sample environments for an x-ray powder diffraction beamline.	61
<i>A. Samuel Conroy</i>	
Automating processes for the production of strontium-82 in an effort to reduce dose and improve reliability	65
<i>Kayle Corneill</i>	

Precision manipulation of samples in a macromolecular crystallography endstation at the National Synchrotron Light Source-II.	68
<i>Tabatha Felter</i>	
A study of neutral pion events in a liquid Argon detector	74
<i>Samantha Fortuna</i>	
Computational optimization of light trapping for ultrathin solar cells	77
<i>Nathan Frey</i>	
Genetic approach to constrain conformation of bioactive peptides.	80
<i>Khalid Habib, Chandra Gadsden, and Abdelaziz Bior</i>	
Targeting lipid abundant mutants of <i>Arabidopsis thaliana</i>	83
<i>Kimberly Giacalone</i>	
<i>Kimberly Okoli</i>	
Reducing hazardous waste at Brookhaven National Laboratory.	87
<i>Kenneth Goodman</i>	
Studies for and development of a preshower detector in the STAR experiment.	91
<i>David Hamilton</i>	
Charge transfer dynamic studies of a series of organic polymer donor-bridge-acceptor multi-interface systems for high efficiency photoelectric energy conversions	95
<i>Muhammad Hasib</i>	
Accelerating computational software through parallelism	99
<i>Ryan Hilbert</i>	
Revealing Traps in Charged Couple Devices using Pocket Pumping Technique	102
<i>Jeremy Hyde</i>	
Design development for Coherent Electron Cooling Proof of Principal and Low Energy RHIC electron Cooling project	105
<i>Robert Jacoby</i>	
Dynamic ATLAS load balancing in the HTCondor workload management system	108
<i>Mark Jensen</i>	
Linear accelerator computer modeling and stress analysis for a proposed electron accelerator	112
<i>Joseph Karp</i>	
Assessment of 5-hydroxymethylcytosine in the DNA of human skin fibroblasts exposed to ionizing radiation.	115
<i>Lucia Kolodiuk and Katherine Z. Sanidad</i>	
<i>Benjamin Daniels</i>	
Integration and automation of computer facility power supply monitoring	119
<i>Christopher Lee</i>	
Monte Carlo simulations of a Cherenkov detector using a water-based liquid scintillator. . .	122
<i>Timothy Leeney</i>	
Improvement of a diffraction-limited, hyperspectral laser beam induced current probe station for thin-film photovoltaics	124
<i>Vittorio Loprinzo</i>	

3D modelling and structural analysis of eRHIC’s low and high energy beamline magnets . . .	126
<i>Sarja Lowe</i>	
Upgrading a 15000 amp power supply for testing new magnets to be used at The Large Hadron Collider	128
<i>Thomas Marone</i>	
Updating the spin program for RHIC	130
<i>Eric McCafferty</i>	
Semi-automatic pre-processing of raw 2-dimensional diffraction images	132
<i>James McClintock</i>	
Analysis of mass concentration time series and coating thickness of black carbon containing particles	135
<i>Kristina Michta</i>	
Chemo-enzymatic development of novel sugar precursors for F-18 labelled Positron Emission Tomography imaging probes	139
<i>Monique Mohammed</i>	
Electrical characterization of silicon photo-multipliers	143
<i>J. Mwathi</i>	
The careful puppet master: using continuous integration to prevent errors in Puppet Configurations	147
<i>Gabriel Richman</i>	
Designing radioanalytical methods for the characterization of Strontium-82 produced at Brookhaven Linac Isotope Producer	149
<i>Valerie Sabatasso</i>	
Evaluation of survival and DNA double-strand break repair kinetics in cells exposed to low dose charged particle irradiation and HDACi treatment	152
<i>Katherine Z. Sanidad</i>	
Infra-red absorptions from charges on conjugated polymers in films and solutions	156
<i>Sabrina Santiago</i>	
Design and modification of a Halbach permanent quadrupole magnet	159
<i>Michael Severance, Physics Department, Stony Brook University, Stony Brook, NY 11790</i>	
Standardization and optimization of training requirements in the Standards-Based Management System (SBMS)	162
<i>Claire Shanklin</i>	
<i>Lauren Lavelle</i>	
Charge coupled device characterization techniques and analysis enhancement	164
<i>Thomas Smit</i>	
Troubleshooting, project management, and asset tracking of HVAC systems	167
<i>Derek Squires</i>	
Evaluating the effect of oxygenated compounds on the long-term stability of home heating oil	170
<i>Andrew Sung</i>	

High throughput screening using acoustic droplet ejection to combine protein crystals and chemical libraries on crystallization plates at high density	175
<i>Ella Teplitsky</i>	
Growth of tropical cumulus congestus clouds	184
<i>Katherine Towey</i>	
Analysis of laser ablation plasma formed from an anisotropic graphite target	188
<i>Christine Truong</i>	
Programmable coil winder for superconducting magnets	192
<i>Nicholas Tsirakis</i>	
Preliminary documentation and specifications for the infrastructure of the sPHENIX detector proposal	196
<i>Nicholas Tully</i>	
Design and optimization of vacuum chambers for eRHIC	201
<i>Benjamin Tuttle, Engineering Department, Cedarville University, Cedarville, Ohio 45314</i>	
Analysis of Temperature Gradient on Polycrystalline Silicon Cells.	203
<i>Ilia Vardishvili</i>	
Determining nanostructure quality via ultrafast emission spectroscopy for enhanced water- splitting photocatalysis	207
<i>Zoey Warecki</i>	
Analysis of cadmium zinc telluride crystals to determine the effects of material defects on detector response capabilities	210
<i>Megan Wart</i>	
Searching for high temperature superconductors	214
<i>Claire Weaver</i>	
Combustion analysis of upgraded pyrolysis oil with regard to efficiency and emissions . . .	230
<i>Michael Worek</i>	
Processing and analysis of weather prediction model data for the Atmospheric Radiation Measurement External Data Center	234
<i>James Young</i>	
Time lag analysis of paleoclimate data from Vostok, Antarctica.	241
<i>Scott Zhang</i>	

Examining the Water Gas Shift Reaction using a Au-CeO₂ nanorod Catalyst

Stefani Ahsanov

Stony Brook University, Stony Brook, NY 11790

Dimitriy Vovchok, Si Luo, and Zongyuan Liu

Stony Brook University and Brookhaven National Laboratory, Upton, NY 11973

Sanjaya D. Senanayake, Wenqian Xu, Kumudu Mudiyansele, and Jose Rodriguez

Chemistry Department, Brookhaven National Laboratory, Upton, NY 11973

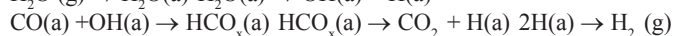
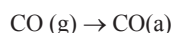
Abstract

The water-gas shift reaction ($\text{CO} + \text{H}_2\text{O} \rightarrow \text{CO}_2 + \text{H}_2$) was studied using a novel gold on ceria oxide nanorod catalyst to further understand the active ingredients critical for the production of clean H₂ as a potential sustainable fuel. In this study we used state of the art *in situ* characterization techniques to determine the bulk structure, intermediates and surface states of the catalyst that prevail during the reaction. These techniques include Diffuse Reflectance Infrared Fourier Transforms Spectroscopy (DRIFTS) and X-Ray Diffraction (XRD). The information we obtained was able to elucidate the surface interactions between adsorbates and the active catalyst sites, the oxidation state of gold and ceria and the relative changes in the structure of the catalyst during the reaction. We also compared the role of Au on the CeO₂ nanorod catalyst with with CeO₂ nanorods without Au, to determine if the presence of Au increased the amount of active sites or changed the reaction intermediates under reaction conditions. Our results show that the gold on ceria oxide nanorods is active for the WGSR but needs modification to enhance the activity further. Furthermore, we have discovered that the Au-CeO₂ catalyst has potential for being an active catalyst for the CO oxidation reaction ($\text{CO} + \frac{1}{2}\text{O}_2 \rightarrow \text{CO}_2$).

I. Introduction

Hydrogen producing reactions are essential for making fine chemicals, fuels, fertilizers, and food through chemical processes.¹ In recent years, there has been a push to examine the use of hydrogen for novel energy applications in fuel cells and automotive fuel. According to the Annual Energy Outlook for 2014, published by the US Energy Information Administration, projections for US production of renewable fuels will increase by 2% while petroleum and other liquids will decrease by 5% in the next 30 years. Though these numbers are low considerable focus will be placed on increasing the supply of sustainable sources of energy while decreasing the reliance on fossil fuels. A precedent has been set for current and future research in the field of renewable energy to look for processes that target not only the most sustainable applications but also those that can be environmental benign. In industry most of the hydrogen supply is derived from the steam reforming hydrocarbons ($\text{C}_n\text{H}_m + n\text{H}_2\text{O} \rightarrow n\text{CO} + (n -)\text{H}_2$) to synthesis gas (CO+H₂); this process produces a gas feed that contains a 1-10% CO impurity that can poison or degrade many chemical processes.² To get cleaner hydrogen, the catalyzed Water Gas Shift Reaction (WGSR)

the CO impurities.¹ The study of nanocatalysts for the WSGR is important for understanding how to efficiently and effectively produce/purify hydrogen. There have been many studies that propose the following mechanism for the WGS:¹



It is suggested that a stable HCO_x intermediate has to precede the formation of CO₂ and H₂.¹ The most commonly observed intermediates are formates (HCOO), carbonates (CO₃) and possibly carboxylates (HOCO).¹ However, intense debate as to which of these is involved in the main mechanism for the reaction is taking place.

The industrial WGSR process is a two step operation: the high temperature shift (HTS) and the low temperature shift (LTS).^{1,3} For the HTS, FeO_x-CrO_x oxide mixtures are typically used at 350-500 °C and for the LTS, Cu/ZnO/Al₂O₃ at 190-250 °C.^{1,3} The standard commercial catalysts for this reaction are not ideal because they are very sensitive to temperature deactivation, are pyrophoric when exposed to air, have an affinity to sinter and require tedious preactivation.^{3,4} For these reasons, we strive in active research pursuit for a new catalyst associated with the low temperature WGSR.

Nanoparticles of gold on oxide supports were first found by Haruta, et al. to be extremely active for the CO oxidation reaction because of their very strong interactions between the metal and support.⁵ Numerous studies were conducted and it was discovered that gold on oxide supports can also be very active for other reactions, such as the WGS. In ongoing research, there has been a lot of interest in the Au-CeO₂ system.¹ Remarkably, neither bulk ceria nor gold display any catalytic activity for the WGS and are both relatively inert.¹ Gold displays different properties in the nanoscale and becomes a very effective catalyst when combined with the ceria oxide support. Ceria oxide on its own is very dynamic material that has a large oxygen storage capacity (OSC) and is able to go through fast reduction/oxidation cycles because of its intrinsic redox character (i. e., interchangeable Ce⁴⁺/Ce³⁺ oxidation states).^{3,6} Ceria can also be synthesized into different architected morphologies that exhibit different chemical activity. These different morphologies can improve the number of active sites, increase the mobility of oxygen and strengthen metal-support interactions.³ In recent years, ceria nanospheres, nanocubes and nanorods have been successfully synthesized and studied extensively, as displayed in Transmission Electron Microscopy (TEM) images in Figure 1.³

$\text{CO} + \text{H}_2\text{O} \rightarrow \text{CO}_2 + \text{H}_2$ is critical to remove a vast amount of

The aim of my project is to determine whether Au-CeO₂ nanorods are active for the Water Gas Shift reaction and what active component of these materials are critical for this reaction. The first technique used in this study was *in situ* X-Ray Diffraction (XRD), which determines the crystalline structure of a powder catalyst by measuring the intensities and angles of the diffracted x-rays. The second technique was *in operando* Diffuse Reflectance Infrared Spectroscopy Fourier Transform Spectroscopy (DRIFTS), which is a method used to observe chemical species on the surface of powder catalysts by collecting and analyzing scattered infrared radiation. Both DRIFTS and XRD also had a mass spectrometer Residual Gas Analyzer (RGA) to determine what products were produced.

II. Experimental

A. Synthesis of the Catalyst

The ceria nanorods were synthesized by the hydrothermal method. The cerium (III) nitrate precursor was dissolved in NaOH aqueous solution with stirring. The sample was then autoclaved and left in at 100°C for 24 hours.³ The precipitates were separated, washed and dried overnight at 60°C. Then, the support was calcined in air at 500°C for two hours after which it had dried.³ Then, the CeO₂ was impregnated with a solution of a Au chloride precursor dissolved in 1 M HCl.⁷ Impregnation was conducted at about 60°C for 10 hours until a homogenous paste was formed.⁷ This was followed by drying in an oven at 100°C overnight. Then the catalyst was calcined at 350°C for 5 hours in air.⁷

Images of the sample were obtained by Transmission electron microscopy (TEM), as shown in Figure 2. The images show the face of ceria oxide [110] and the gold [111]. The representative images show a monolayer of gold present on the surface of the ceria support together with some larger particles. The nanorod morphology of the ceria is also illustrated (2b.). The nanorods are uniform and about 10 nm in diameter and upto 1 μm in length as determined by the HR-TEM.

B. In situ X-Ray Diffraction

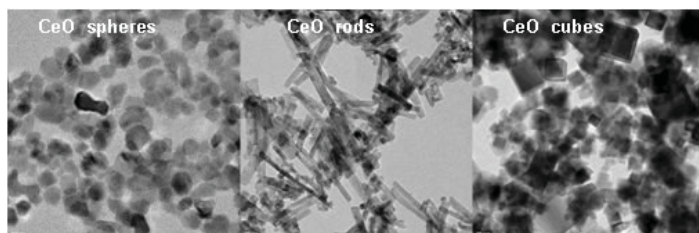


Figure 1. TEM images of CeO₂ nanospheres, nanorods and nanocubes morphologies.³

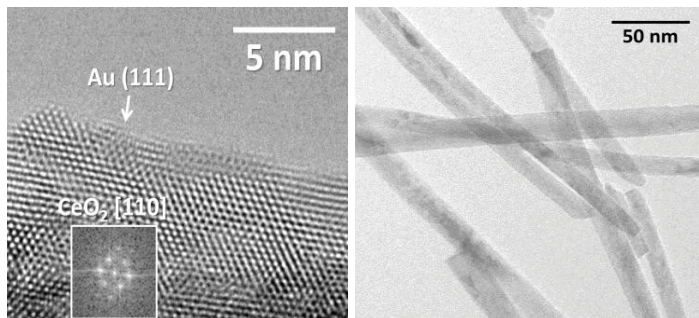


Figure 2. (a) The face of ceria oxide [110] and the monolayer gold [111]. (b) Ceria oxide nanorods

The XRD data were collected from beamline X7B ($\lambda = 0.3196 \text{ \AA}$) at the National Synchrotron Light Source (NSLS) at Brookhaven National Laboratory (BNL). Approximately 2-3 mg of the sample were loaded into a 1.0 mm diameter silica capillary between two pieces of glass wool. It was then mounted into a Klausen cell with a resistance heater directly underneath the capillary for heating. The temperature was monitored by a thermocouple (C-type) 1 mm away from the sample and the heating was regulated by a Eurotherm controller. The gaseous products were analyzed by the mass spectrometer (MS) residual gas analyzer (RGA). The reaction conditions utilized for all experiments were 5% CO and 3% steam (H₂O) from a bubbler, both with He as the carrier gas and a flow rate of 10 cc/min. Before starting the *in situ* measurements, He was pushed through the lines at 40 cc/min for 15 min. Stepwise heating and cooling was used with an increase of 50°C per step between 100°C to 400°C and a time span of 20 minutes. Two-dimensional XRD patterns were obtained from the Perkin-Elmer amorphous silica detector and the diffraction rings were integrated using the Fit2d code

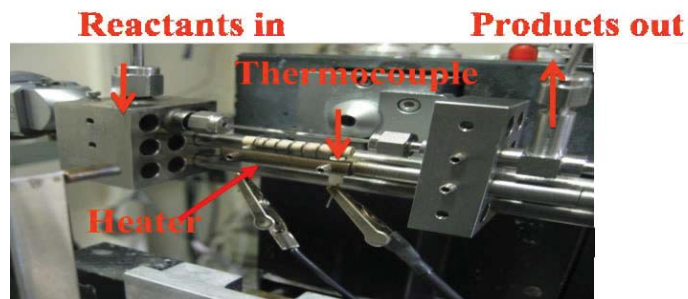
(Intensity versus 2 Theta).¹ The lattice parameters, phase composition and particle size were determined with the GSAS software package using the Rietveld method.

C. In operando DRIFTS

In operando Diffuse Reflectance Infrared Fourier Transform Spectroscopy was used to study the Au-CeO₂ nanorods and the CeO₂ nanorods under WGS conditions using a Burkert Equinox 55 FTIR spectrometer equipped with a modified Harrick Praying Mantis DRIFT cell connected to a gas flow system and mass spectrometer RGA.⁷ The device was used to collect infrared spectra of the powder during stepwise heating under WGS conditions (1% CO, 3% steam from bubbler, He carrier gas). The cell was heated to 100°C and then increased stepwise by 50°C every 20 minutes until 400°C. The composition of the exit feed was analyzed by the RGA.



Figure 3. (a) DRIFTS setup (b) XRD Klausen cell



III. Results

A. *In Situ* XRD

In situ XRD is an exceptional tool for determining the structural and phase transformations in catalysts under reaction conditions. The first *in situ* XRD pattern at 25°C under WGS conditions is shown in Figure 3. The XRD pattern exhibits the typical diffraction peaks for both ceria and gold, except for two peaks located at 3.5θ and 8θ. These small peaks correspond to minor impurities or defects and potential precursor that are still present on the catalyst. The intensities of the ceria peaks are higher than the gold peaks, meaning that the ceria phase is predominant in the sample.

The time resolved set of *in situ* measurements for Au-CeO₂ is shown in Figure 4. The fluctuations in the intensities are due to change in relative ordering of the catalyst at 120°C and subsequently intensifying. This data also show a disappearance of the unknown peaks located at 3.5θ and 8θ at 160°C which can be explained as the removal of impurities in the sample that are burned off, evaporated or cured during the commencement of the reaction.

We were also able to refine the *in situ* data using the Rietveld method to allow us to determine the lattice parameter and particle size of both gold and ceria, as shown in figure

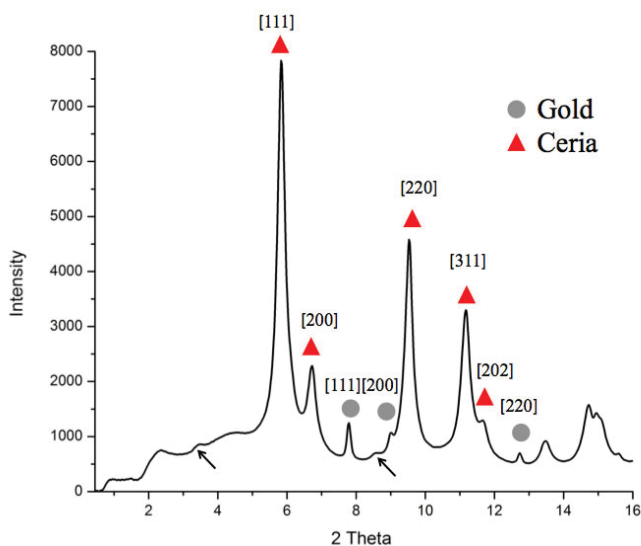


Figure 4. XRD Spectra Au-CeO₂

5. It is clear from this data that the structure of the catalyst is very dynamic and changes with both temperature and activity. This implies further that the *in situ* method of experimentation is critical for the study of catalytic processes.

For both data sets, we see that there is a stepwise pattern in the change to the lattice parameters. The gold exhibits a constant expansion until 400°C and constant contractions with cooling, except for a minority peak at 150°C. The ceria lattice parameter first contracts up to 150°C and then expands until the maximum temperature, which may correspond to the curing of the unknown species. Since this irregularity is present in the gold and ceria parameter at 150°C, we can assume that the defects in the sample are present and heal with continued annealing. Information about the oxidation state of ceria may also be inferred from this data. The growth of the ceria lattice parameter implies reduction is taking place because at 150°C, the lattice expands. This is very typical for an expanded lattice for Ce³⁺ vs that of Ce⁴⁺. The refined data in conjunction with the Scherrer equation was also used to determine the average particle size of the gold to be between 28 nm and 30 nm. This relatively large size of gold could correspond to the weak activity of the catalyst. This result is consistent with the TEM data, where both small and large particles of Au were observed.

The lattice parameter also proves that the Au remains in the metallic state throughout the reaction. The typical lattice parameter for metallic gold is 4.080 Å.¹³

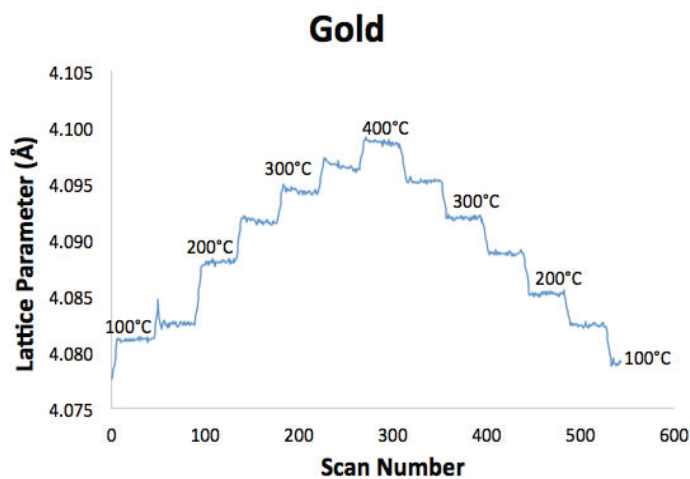


Figure 5. Time resolved *in situ* XRD of Au-CeO₂ (nr) under WGSR.

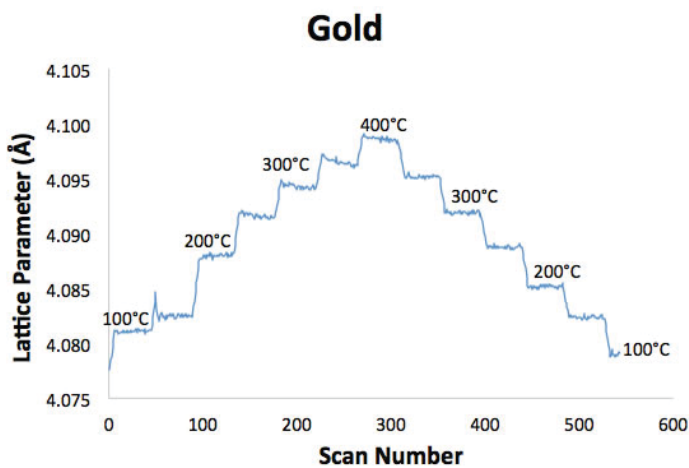
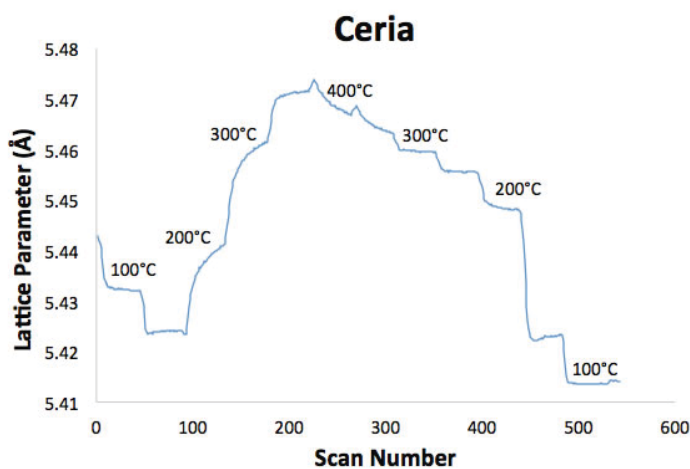


Figure 6. Lattice parameters from refined XRD data: Gold, Ceria



The DRIFTS data for Au-CeO₂ (nr) and CeO₂ (nr) are presented in Figures 6-9. The samples were under WGSR conditions and under a stepwise heating profile. The catalyst with and without Au were compared to determine if the presence of Au played a major role in the reaction mechanism, formation of intermediates and in the evolution of products in the reaction.

The sample at room temperature showed a major peak at 3400 cm⁻¹, which relates to the stretching of -OH of water on the surface.⁸ This peak later disappears as the temperature increases, signifying the loss of water. The peak at 3691 cm⁻¹ becomes sharper as the temperature increases and corresponds to the free hydroxyl species (OH).⁸ The peaks located at 2971 cm⁻¹ and 2922 cm⁻¹ are both assigned to bidentate formates (HCOO), leading us to believe that they may be active surface species. The main peaks where we anticipated seeing formations of CO₂ are at 2362 cm⁻¹ and 2339 cm⁻¹. From Figure 6, we can observe some CO₂ produced from this reaction. Figure 7 (8??) displays the enlarged section of the Au-CeO₂ spectra from 1700 cm⁻¹ to 1200 cm⁻¹.

Once again at 25°C, we see a peak at 1635 cm⁻¹ that corresponds to the bending of the surface absorbed water, which later disappears with the increase of temperature.⁸ The 1549 cm⁻¹, 1371 cm⁻¹ and 1356 cm⁻¹ are all peaks that are identified

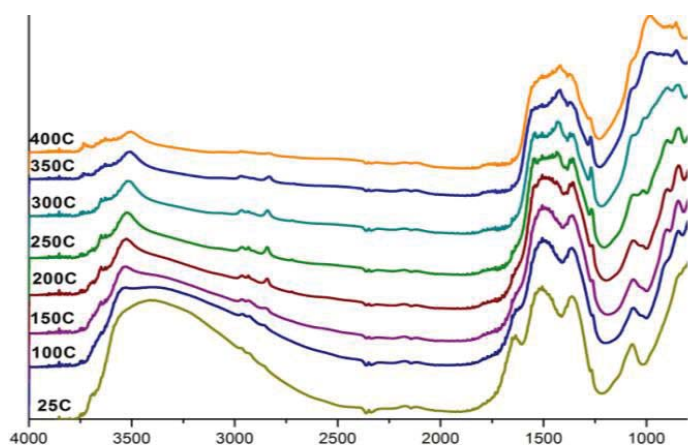


Figure 7. DRIFTS for Au-CeO₂ (nr) while under WGSR 1% CO, 3% H₂O under He

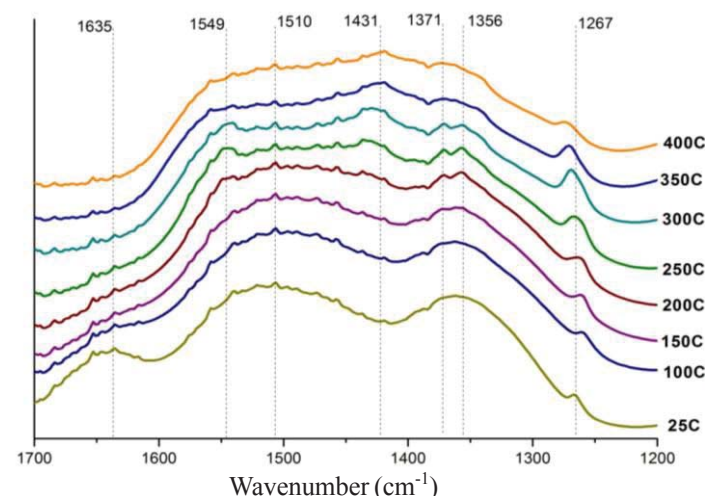


Figure 8. DRIFTS Au-CeO₂ (nr) spectra 1700 cm⁻¹ to 1200 cm⁻¹ under WSG 1% CO, 3% H₂O under He

as bidentate formate.^{10, 11} Other potential species found on the surface are shown in Figure 9.

This is once again an indication of the surface species found on the surface of the catalyst. The remaining peaks, 1510 and 1267 are characteristic of inorganic carboxylate and monodentate formate, respectively.¹² To compare these data we conducted DRIFTS experiment on a metal free CeO₂ (nr) sample under WGS conditions, shown in Figure 8. The peaks are very similar to those in the Au-CeO₂ (nr) spectra. There is a -OH bending peak at 3400 cm⁻¹ and bidentate formates peaks at 2971 cm⁻¹, 2922 cm⁻¹.^{8, 9, 10} There is once again very slight activity of the WGS since we do not see any major increase in the area of the CO₂ peaks (2300 cm⁻¹ to 2200 cm⁻¹).

The major differences lay in the 1700 cm⁻¹ to 1200 cm⁻¹ region, as shown in Figure 10. The major peak that is present in the CeO₂ sample and not on the Au-CeO₂ sample at 300°C - 400°C is located at 1267 cm⁻¹. This peak is characteristic of the monodentate formate and disappears faster on the CeO₂ sample leading us to believe that the Au plays an important role in the surface chemistry of the catalyst. Also the 1637 cm⁻¹ peaks are present at higher temperatures for the CeO₂ (nr), which relate to the -OH bending. This could mean that the gold inhibits the stability of -OH on the surface since it only appears on the CeO₂ spectra, allowing for the liberation of O to CO₂ and H to recombine as H₂.

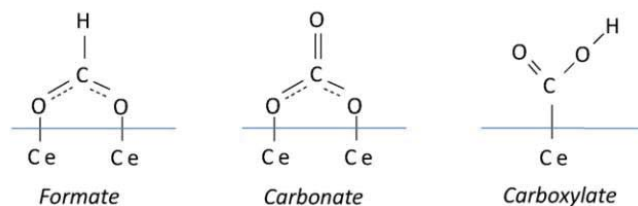


Figure 9. Different coordination modes for formate (HCOO), carbonate (CO₃) and carboxylate (HOCO).²

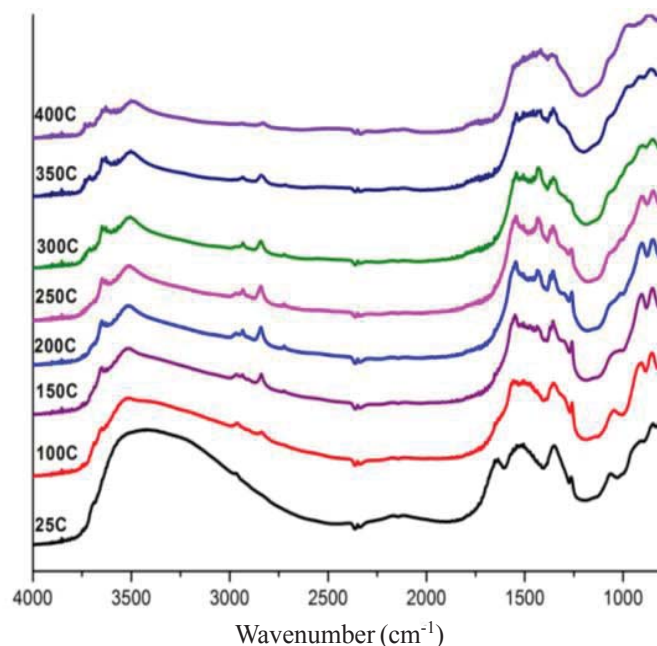


Figure 10. DRIFTS CeO₂ under WSG 1% CO, 3% H₂O under He.

IV. Conclusion

Au-CeO₂ (nr) and CeO₂ (nr) nanocatalysts were studied to determine their activity under water gas shift-reaction conditions. Partially reduced ceria and metallic gold were found to be the critical components of the Au-CeO₂ catalyst for this reaction. The *in situ* X-ray diffraction experiment showed that the Au-CeO₂ sample has a dynamic structure that was highly sensitive to temperature and reaction conditions. The dynamic nature involved an increase in the size of both the CeO₂ lattice and Au lattice. The XRD refinement data established that the Au particle size is 28-30 nm, while TEM identified small particles of Au (1-3nm). The large particle size correlates with the weak activity of the catalyst, while the small particles were more essential to the reaction. The DRIFTS data enabled us to probe the surface chemistry of the reaction. From these measurements we identified that the Au on CeO₂ plays a role in liberating the strongly adsorbed-OH from the surface; a pathway that leads directly to the formation of H₂. The peaks at 1267 cm⁻¹ and 1261 cm⁻¹ for the Au-CeO₂ (nr) and CeO₂, respectively, appear with different intensities on the spectrum. The CeO₂ does not have a peak at 400°C leading us to believe that the Au might increase the oxygen mobility across the surface, since the monodentate formate peak appears on Au-CeO₂ spectrum at 400 °C. Au-CeO₂ is active under water gas shift reaction conditions but needs further modifications such as the removal of the larger particles of Au. The gold particle size is critical for this process and may inhibit the reaction steps which take place on the surface. For future experiments, this catalyst will be studied for the activity in CO oxidation.

V. Acknowledgements

This project was supported in part by the U.S. Department of Energy, Office of Science, Office of Workforce Development

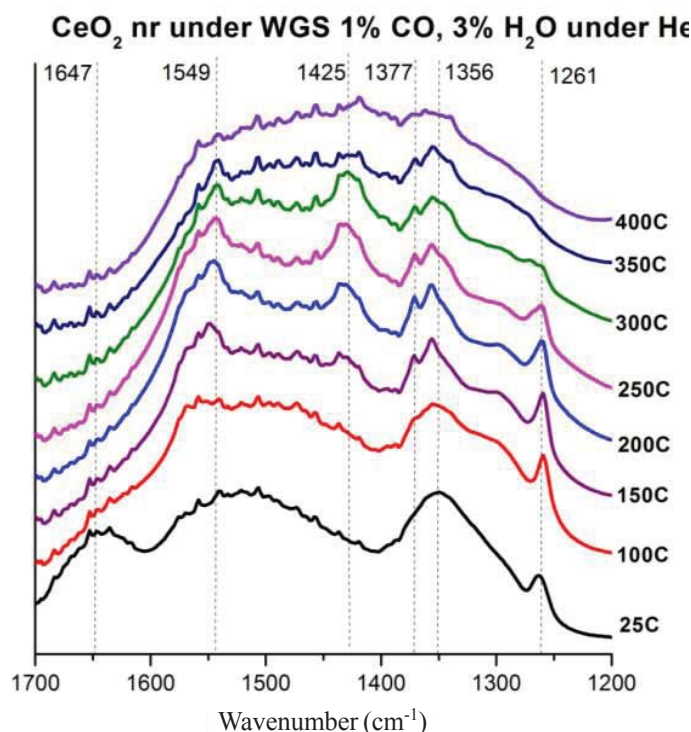


Figure 11. DRIFTS CeO₂ under WGS 1% CO, 3% H₂O under He 1700 cm⁻¹ to 1200 cm⁻¹.

for Teachers and Scientists (WDTS) under the Science Undergraduate Laboratory Internships Program (SULI). Use of the National Synchrotron Light Source, Center for Functional Nanomaterials at Brookhaven National Laboratory, was supported by the U.S Department of Energy, Office of Science, Office of Basic Energy Sciences, under Contract No. DE-AC02-98CH10886.

VI. References

- [1] Rodriguez, José A., Jonathan C. Hanson, Dario Stacchiola, and Sanjaya D. Senanayake. "In Situ/operando Studies for the Production of Hydrogen through the Water-gas Shift on Metal Oxide Catalysts." *Physical Chemistry Chemical Physics* 15.29 (2013): 12004-2025. Web.
- [2] Rodriguez, José A. "Gold-based Catalysts for the Water-gas Shift Reaction: Active Sites and Reaction Mechanism." *Catalysis Today* 160.1 (2011): 3-10. Web.
- [3] Yao, S.Y., Q. XU, A.C. Johnston-Peck, F.Z. Zhao, Z.Y. Liu, S. Luo, S.D. Senanayake, A. Martinez-Arias, W.J. Liu, and J.A. Rodriguez. "Morphological effects of the nanostructured ceria support on the activity and stability of CuO/CeO₂ catalysts for the water-gas shift reaction." *Physical Chemistry Chemical Physics* 16 (2014):17183- 17194
- [4] Fu, Q. "Active Nonmetallic Au and Pt Species on Ceria-Based Water-Gas Shift Catalysts." *Science* 301.5635 (2003): 935-38. Web.
- [5] Haruta, M. "Gold Catalysts Prepared by Coprecipitation for Low-temperature Oxidation of Hydrogen and of Carbon Monoxide." *Journal of Catalysis* 115.2 (1989): 301-09. Web.
- [6] Reina, Tomás Ramírez, Wenqian Xu, Svetlana Ivanova, Miguel Ángel Centeno, Jonathan Hanson, José A. Rodriguez, and José Antonio Odriozola. "In Situ Characterization of Iron-promoted Ceria-alumina Gold Catalysts during the Water-gas Shift Reaction." *Catalysis Today* 205 (2013): 41-48. Web.
- [7] Xu, Wenqian, Rui Si, Sanjaya D. Senanayake, Jordi Llorca, Hicham Idriss, Dario Stacchiola, Jonathan C. Hanson, and José A. Rodriguez. "In Situ Studies of CeO₂- supported Pt, Ru, and Pt-Ru Alloy Catalysts for the Water-gas Shift Reaction: Active Phases and Reaction Intermediates." *Journal of Catalysis* 291 (2012): 117-26. Web.
- [8] Du, Xuezhong, Lin Dong, Chun Li, Yingqiu Liang, and Yi Chen. "Diffuse Reflectance Infrared Fourier Transform and Raman Spectroscopic Studies of MoODispersed on CeOSupport." *Langmuir* 15.5 (1999): 1693-697. Web.
- [9] Vignatti, Ch., M.s. Avila, C.r. Apesteguía, and T.f. Garretto. "Catalytic and DRIFTS Study of the WGS Reaction on Pt-based Catalysts." *International Journal of Hydrogen Energy* 35.14 (2010): 7302-312. Web.
- [10] Binet, Claude, Marco Daturi, and Jean-Claude Lavalley. "IR Study of Polycrystalline Ceria Properties in Oxidised and Reduced States." *Catalysis Today* 50.2 (1999): 207-25. Web.
- [11] Kubacka, Anna, Rui Si, Piotr Michorczyk, Arturo Martínez-Arias, Wenqian Xu, Jonathan C. Hanson, José A. Rodriguez, and Marcos Fernández-García. "Tungsten as an Interface Agent Leading to Highly Active and Stable Copper-ceria Water Gas Shift Catalyst." *Applied Catalysis B: Environmental* 132-133 (2013): 423-32.
- [12] Tao, Franklin (Feng), and Zhen Ma. "Water-gas Shift on Gold Catalysts: Catalyst Systems and Fundamental Studies." *Physical Chemistry Chemical Physics* 15.37 (2013): 15260.
- [13] <http://www.infoplease.com/periodictable.php?id=79>

Harmonic flow in the quark-gluon plasma: insights from particle correlation spectra in heavy ion collisions

Mamoudou Ba

Department of Physics and Astronomy, SUNY at New Paltz, New Paltz, New York, 12561

Paul Glenn

Department of Physics, University at Buffalo, Buffalo, NY 10466

Paul Sorensen

Department of Physics, Brookhaven National Laboratory, Upton NY 11973

Abstract

It is believed that a state of matter called the Quark-Gluon Plasma (QGP) has been found at the Relativistic Heavy Ion Collider (RHIC) at Brookhaven National Laboratory. This state, in which the constituents of protons and neutrons are no longer confined to hadronic states, is thought to have existed one microsecond after the Big Bang. Interactions within the QGP cause spatial anisotropies in heavy ion collisions to manifest in the momentum-space distribution of produced hadrons. In this study we used data from Au+Au and U+U collisions to study the correlations of particles produced in the hadronic freeze-out, comparing this data with physical predictions and several models. These comparisons help us to understand more about interactions within the QGP and its viscosity, which has been measured to be close to the theoretical minimum. We also try to understand whether symmetries are broken within the QGP and suggest a way to study its phase diagram. Future studies motivated by this work should help us understand the phenomenology of the QGP.

I. Introduction

Heavy ion collisions at RHIC involve highly Lorentz-contracted nuclei traveling asymptotically close to the speed of light. The energies at which they collide give the system an effective temperature of a few trillion Kelvin. At these temperatures, quantum chromodynamics (QCD) predicts a phase transition where instead of protons and neutrons (examples of particles called *hadrons*) being the relevant degrees of freedom of the system, quarks and gluons, which constitute hadrons, exist in free states. Quarks and gluons are elementary particles that possess a property called a *color charge* as well as an electrical charge. At normal temperatures, the hadrons contain combinations of quarks and gluons such that they are color-neutral. In the state that results from collisions, however, color charges exist freely; this is analogous to ions in electrical plasma. This new state has properly been called the Quark-Gluon Plasma (QGP). Due to the high temperature of the phase transition, the properties of the QGP cannot be easily characterized using QCD theory or measurement devices; another limiting feature is the fact that rapid cooling results in a lifetime of only $\sim 10^{-23}$ seconds. Instead of observing the QGP itself, we can only measure properties of the hadrons produced in the “kinetic freeze-out” – that is, when the temperature decreases enough that the quarks and gluons are bound together into color-neutral particles once again. From these measurements we try to infer the conditions of the QGP.

In this work we analyze the correlations of the particles pro-

duced in the freeze-out. These correlations can give us information about the initial conditions of the collision via Fourier expansion of the triple differential particle distribution,

$$E \frac{d^3 N}{d^3 p} = \frac{1}{2\pi} \frac{d^2 N}{p_t dp_t dy} \left(1 + 2 \sum_{n=1}^{\infty} v_n \cos[n(\varphi - \Psi_{RP})] \right) \quad (1)$$

Here E is the energy of the particle, p and p_t are the total and transverse momenta, φ is the azimuthal angle of the particle trajectory as defined by the detector, y is the rapidity (a measure of the speed) and Ψ_{RP} denotes the angle of the reaction plane. The coefficients in the expansion denote different types of anisotropic flow: v_1 is called “directed flow”, v_2 is called the “elliptic flow,” and v_3 is the “triangular flow.” Since the matter in the QGP is strongly interacting, one expects these coefficients to reflect spatial anisotropies in the initial distribution of matter in the collision. We can therefore use the flow coefficients to make inferences and test theories³.

II. Conversion of the anisotropy from the initial conditions into momentum-space

In Figure 1 we show a cartoon picture of a spherical nuclear collision. The almond-shaped overlap region of the two nuclei causes particles to feel different pressure gradients with respect to the reaction plane. This causes preferential particle flow in the reaction plane, which breaks the isotropy that would be expected in a more central collision.

The spatial anisotropy in the initial conditions can be theoretically quantified by defining the spatial eccentricity

$$\varepsilon_n = \frac{\sqrt{\langle r^n \cos n\theta \rangle^2 + \langle r^n \sin n\theta \rangle^2}}{\langle r^n \rangle} \quad (2)$$

Unfortunately this parameter cannot be measured in an actual collision; it can only be estimated from models. Looking at the elliptic shape in Figure 1, then, it becomes interesting to compare the ellipticity ε_2 to the elliptic flow v_2 . By taking the ratio

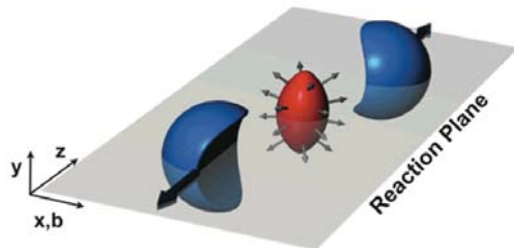


Figure 1. Typical collision geometry in a non-central nuclear collision.²

v_2/ε_2 one is effectively probing the efficiency of conversion for the anisotropy into momentum space. In particular, we compare this quantity to the multiplicity of particles produced during the kinetic freeze-out. In experiments where the eccentricity is estimated, linear behavior is observed for these conversions.⁴ We use eccentricity values from the Impact Parameter dependent Glasma model and Monte-Carlo based Glauber model, mapping from their results for multiplicity to ours by fitting the ellipticity using a generalized form of power series expansion called the Padé approximant,

$$f_{fit}(x) = \frac{A + Bx + Cx^2}{1 + Dx + Ex^3}. \quad (3)$$

Figure (2) helps motivate the exact form of Equation (3); in particular, the eccentricity is expected to decrease with the multiplicity since a more central collision will have a less pronounced almond-shape. Then we can take the ratio v_2/ε_2 at the points for which we have STAR data, resulting in Figure 3; unfortunately, we see that neither of the models reproduce the predictions.

The MC-Glauber model is built on the two-component model in Equation (4) for taking the number of nucleons that collide and the number of binary collisions in a collision for which the nuclei are randomly oriented to the number of produced particles:

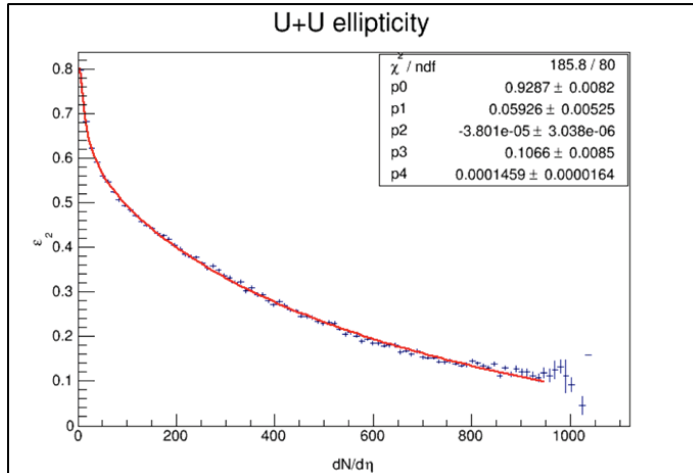


Figure 2. Fit of the ellipticity from the MC-Glauber model, with fit parameters and resulting statistics.

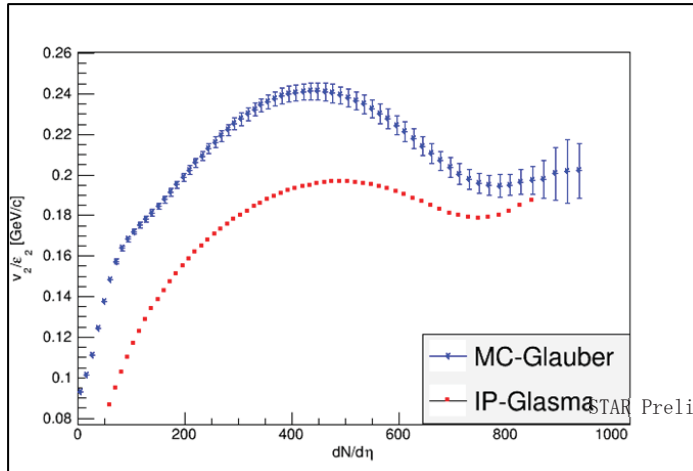


Figure 3. Comparison of the elliptic flow to ellipticity for two different models (STAR Preliminary).

$$\frac{dN}{d\eta} = n_{pp} \left[(1-x) N_{part} + x N_{coll} \right] \quad (4)$$

In this equation, $dN/d\eta$ represents the multiplicity per unit pseudo-rapidity (a measure of the speed and relative angles of the particles), x is a tunable parameter, and n_{pp} should be a conversion factor for the number of equivalent proton-proton collisions for a given number of nucleons. For the number of colliding participants N_{part} and the number of binary collisions N_{coll} , the Glauber model relies on a single sample from the negative binomial distribution. We tried to fix the model by recognizing that the two random variables N_{coll} and N_{part} should be independent, meaning we should use two samples instead of one for the negative binomial distribution. We also tried a different value for a parameter that controls the shape of the uranium nucleus (its deviation from a spherical distribution of nucleons). Although these patches to the model did seem to affect the behavior of the ratio v_2/ε_2 , neither was sufficient to reproduce the linear behavior.

III. Local parity violation (LPV) in heavy ion collisions

In non-central heavy ion collisions, the positively charged spectator nucleons contribute to circular currents, which create large magnetic fields along their angular momentum vector. It is predicted that these fields, along with an asymmetric distribution of quark chirality, will cause more positive charges to be emitted in one direction and more negative in the other along the field vector.⁴ Parity conservation in physics demands that odd functions or observables average to zero over the whole domain of a system at any given time. The electric dipole moment created by preferential particle production as mentioned above violates this parity. To study this in an experiment we can look at the correlations between particles of the same charge (p-p and/or n-n) as opposed to particles of different charges (p-n). If p-p and n-n correlations were large compared to p-n, this would be evidence for this “Chiral Magnetic Effect.” Observations consistent with the chiral magnetic effect have been made for Au+Au collisions.⁵

The picture above relies on the non-centrality of the collision to create the current of charged spectators. It is interesting, then, to look at central collisions where this effect should in principle be severely attenuated. An alternate explanation for the observed preferential flow has been presented which depends on the elliptic flow;⁶ it also becomes interesting to look at dependence on v_2 as well.

For central U+U collisions there is already very small magnetic field, and by fine-graining the most central collisions based on multiplicity we can infer the collision geometry. The prolate shape of uranium gives us a nice advantage here: we can select the

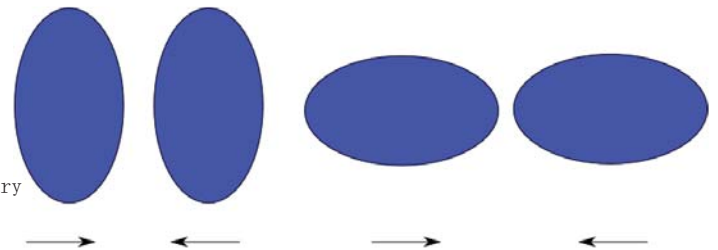


Figure 4. Two orientations for central U+U collisions. The first should have high elliptic flow v_2 , while the second should have very small value of v_2 .

strength of v_2 based on this geometry (see Figure 4).

Taking the angles at which particles come out with respect to the reaction plane and averaging the relative differences for a given pair of charges would be ideal; the reaction plane itself, however, cannot be measured. An equivalent method, however, is to look at the quantity

$$C^{q_1 q_2} = \langle \cos(\phi_1 + \phi_2 - 2\phi_3) \rangle / v_2. \quad (5)$$

By varying the charges q_1 , and q_2 of particles 1 and 2, we can look at charge-dependent correlations. To give an example of how this quantity is utilized: if particles 1 and 2 come out at similar angles on average (expected for p-p), the argument of the cosine will be close to π and so $C^{q_1 q_2}$ will be negative. On the other hand, if the particles (p-n) are observed at largely opposite angles, then the angles will be nearly supplementary and so $C^{q_1 q_2}$ will be positive. An example of this is shown in Figure 5 for Au+Au collisions – the ordinate contains an equivalent formula for Equation (5). Figure 5 was also used to verify the correctness of our code by comparison to the data from the STAR Collaboration.⁷

The result of our calculation comparing the Eq. 5 for p-p, n-n and p-n pairs is shown in Figure 6; it does seem to indicate that

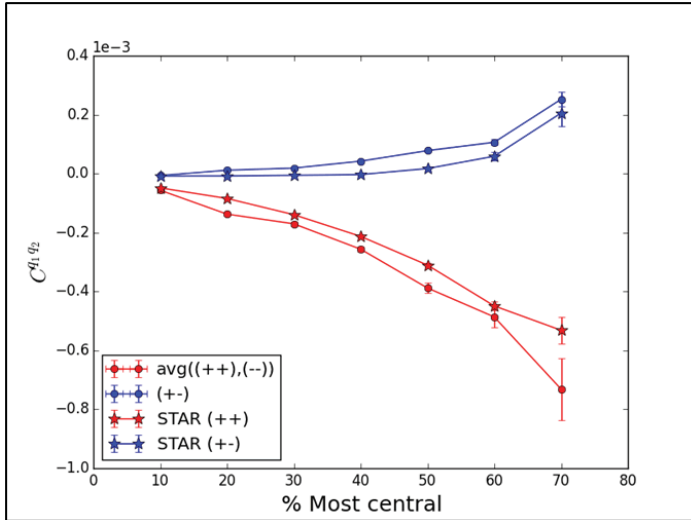


Figure 5. Charge-dependent correlations for Au+Au collisions.

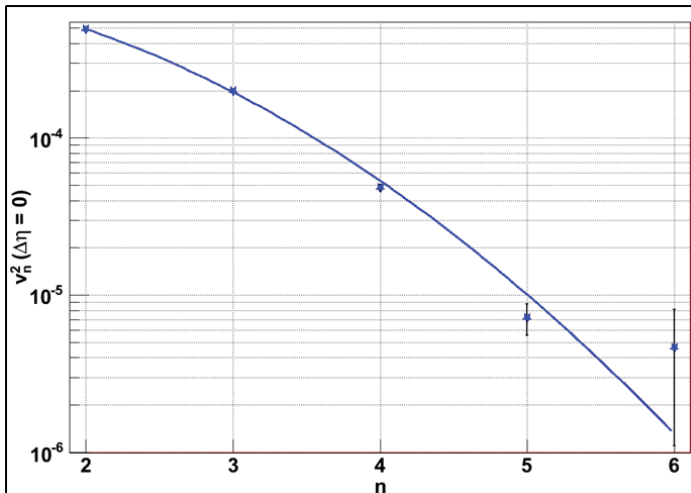


Figure 7. Power spectrum of Equation (1) for 0.25% ZDC centrality of Au+Au collisions (STAR Preliminary)

the relationship between the correlations does not depend strongly on the elliptic flow; in particular, there is no strong evidence that it goes to zero with the flow. We also note that the signal is smaller in less central Au+Au collisions (reference line in black on Figure 6). These features are consistent with local parity violation due to the chiral magnetic effect.

IV. Viscosity of the QGP

Scientists are greatly interested in the viscosity of the QGP since it seems to be close to a universal lower bound $\eta/s = \hbar/4\pi k_B$, where s is the entropy density, \hbar is the reduced Planck's constant and k_B is Boltzmann's constant.³ This has led to it being referred to as a nearly perfect liquid, which means that the liquid particles have very little flow other than the hydrodynamic velocity. We studied the viscosity by looking at the flow harmonics $\{v_n\}$. As the QGP thermalizes, anisotropies in the flow must be washed out. The rate at which peculiar momenta are brought to zero is related directly to the viscosity of the liquid. The width of the curve in

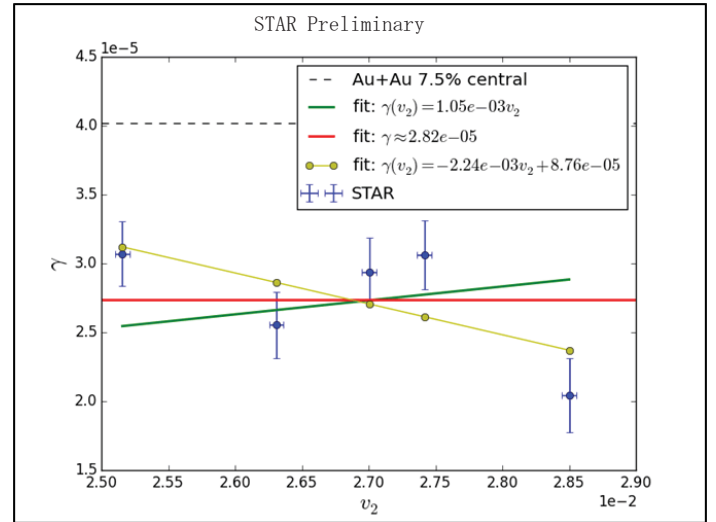


Figure 6. Difference γ for same-charge and opposite-charge pairs vs. elliptic flow for central U+U collisions. A goodness-of-fit test (chi-square) gives the constant function 10x higher probability than the increasing linear behavior.

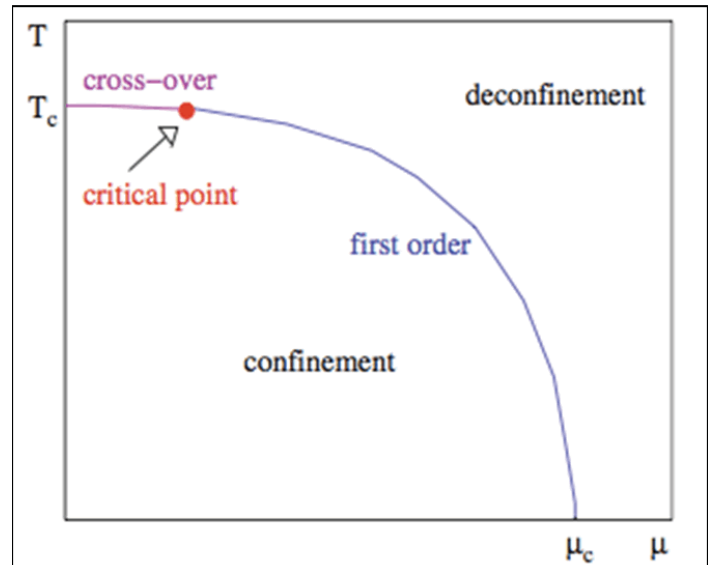


Figure 8. QCD phase diagram (temperature vs. baryon chemical potential) for massive quarks.⁶

the power spectrum of Equation (1), that is, $\{v_n^2\}$ vs n , tells us how effectively the momentum space anisotropies are attenuated. A wider curve means that any lumpiness in the initial distribution is not immediately smoothed out by non-hydrodynamic flow, for example, and so indicates a low viscosity.

We used code written by P. Sorensen to obtain profiles of each of the v_n^2 vs. the particles pseudo-rapidity difference $\Delta\eta$. Using some of the most central events, we fit Gaussian curves to each of the $\{v_n^2\}$ curves and extracted the amplitudes. This yields the plot of v_n^2 vs. shown in Figure (7). The elliptic flow, v_2 is very sensitive to β_2 because of the oblate shape of the gold nucleus. So we had to take into account the eccentricity, ε_2^2 . We accomplished this by running the MC-Glauber model for $\beta_2=0$ and then $\beta_2=-0.13$. We extracted mean ε_2^2 and then scaled by the ratio of the eccentricities. We plotted vs. and fitted with a Gaussian in Figure 7. Then we extracted the width and using the hydrodynamic calculations in [9]. Comparing our width to Figure 4(c) in [9], we obtained with our analysis. We note that this value is three times the lower bound, reinforcing the ‘perfect liquid’-like behavior of the QGP.

V. Discussion and Future Work

Another interesting question about the QGP is to the existence of a critical point in its phase diagram (shown below). Phase transitions are usually designated by some singularity in the free energy function of a physical system. For low baryon chemical potential, however, the crossover between hadronic matter and QGP is a continuous one, meaning that the free energy is regular for all temperatures. It is predicted that at some value of the transition becomes first-order, which means that the first derivatives of the free energy experience discontinuities. For example, in a liquid the entropy and volume experience jump discontinuities.

The triangular flow, which is sensitive to the equation of state of the QGP,⁶ may be promising in helping to find the QCD critical point. We plan to do so in the framework of the VISHNU model, a hydrodynamic model which uses a Cooper-Frye freeze-out algorithm to calculate the properties of the produced particles based on the hydrodynamic properties.³ Using different equations of state while calculating may help to find this point, or it may verify the transition temperature T_c of the QGP.

We calculated the correlations between particles produced during the freeze-out due to the rapidly decreasing temperature of the QGP. By calculating the flow coefficients we were able to gain insight into the conversion of spatial eccentricities into anisotropic flow, and the decay of this flow with harmonic number. In comparing with two models we exemplified just how little is known about the behavior of the QGP. We created further evidence for the chiral magnetic effect in heavy ion collisions by comparing its predictions with those of a competing theory. More data to reduce the statistical error could rule out dependence of the signal in Figure 6 on the elliptic flow. We would also like to know why the decreasing line in Figure 6 gives the best fit; the physical implications there are unclear. Finally, for the viscosity calculation, hydrodynamic calculations need to be done for ultra-central Au+Au at 200 GeV. We hope that our work will have been useful in bringing particle physicists’ thinking a bit closer to reality.

VI. References

- [1] Snellings R. *Elliptic flow: a brief review*. New Journal of Physics 2011; 13:0555008.
- [2] Sorensen P. *Higher Flow Harmonics in Heavy Ion Collisions from STAR*. ArXiv nucl-ex 2011; 1110.737v1.
- [3] Sarkar S, Satz M, Sinha B ; *The Physics of the Quark-Gluon Plasma: Introductory Lectures*. Springer-Verlag Berlin Heidelberg 2010.
- [4] Kharzeev D. *Parity violation in hot QCD: Why it can happen, and how to look for it*. Phys Lett B 2006; 633:260-264.
- [5] STAR Collaboration. *Observation of charge-dependent azimuthal correlations and possible local strong parity violation in heavy-ion collisions*. ArXiv nucl-ex 2010; 0909.1717v2.
- [6] Discussion with P. Sorensen.
- [7] STAR Collaboration. *Azimuthal Charged-Particle Correlations and Possible Local Strong Parity Violation*. ArXiv nucl-ex 2010; 0909.1739v3.
- [8] Song H. *VISHNU hybrid model for the viscous QCD matter at RHIC and LHC energies*. Central European Journal of Physics 2012; 10(6):1242-1244.
- [9] Lacey R, Gu Y, Reynolds D, Ajitanand N, Alexander J M, Mway M, Taranenko A. *Is anisotropic flow really acoustic?* ArXiv nucl-ex 2013; 1301.0165v4.

An intercomparison of Vaisala RS92 and RS41 radiosondes

Shannon Baxter

Department of Mathematics, SUNY Geneseo, Geneseo, NY 14454

Michael Jensen

Environmental Sciences, Brookhaven National Laboratory, Upton, NY 11973

Abstract

The Department of Energy's Atmospheric Radiation Measurement (ARM) Climate Research Facility launches thousands of weather balloons each year. These large helium balloons carry a small instrument package, known as a radiosonde, high into the atmosphere. The radiosonde measures important atmospheric parameters such as temperature, pressure, humidity and wind speed. Vaisala, the company that designs and manufactures the radiosondes that ARM uses, recently released a new type of radiosonde, RS41, that is supposed to have a simpler launch preparation procedure and produce more accurate temperature and humidity measurements. In June of 2014, a series of weather balloon launches at the ARM Southern Great Plains (SGP) site, in Oklahoma, were conducted to evaluate these new radiosondes. Using data from these launches, this project analyzed and compared the performance of the two Vaisala radiosondes, RS92 and RS41. Using MATLAB, plots for comparing the pressure, temperature and relative humidity against height were created for the two radiosonde types for each balloon launch. These plots show that the average measurements from the two radiosonde types for temperature generally agree within 1°C, relative humidity (RH) measurements agree within 10%, and the pressure measurements agree within 0.5 hectopascals (hPa). We also investigated the difference in temperature between the

radiosondes for varying humidity conditions; from dry (RH <20%) to moist (RH >80%). This analysis indicates minimal dependence of radiosonde performance on humidity conditions. Finally, we partitioned our analysis by cloud and meteorological conditions using complementary instruments at the ARM site. This analysis will help the ARM facility decide whether to use the new radiosondes. Participating in this research project has enhanced my knowledge of programming with MATLAB and has educated me on the usefulness of programming in the scientific world.

I. Introduction

Thousands of weather balloons are launched each year with weather recording instruments attached called radiosondes. These radiosondes measure important meteorological variables such as pressure, relative humidity, temperature and wind speed which are used to report current weather conditions and as input to weather forecast models. The accuracy of these measurements are important, thus the manufacturers produce new models of the radiosondes redesigned with the intention of increasing the accuracy of the measurements.

II. Scope and Objectives

In June 2014, a series of 20 weather balloon launches at the ARM Southern Great Plains (SGP) site, in Oklahoma, were

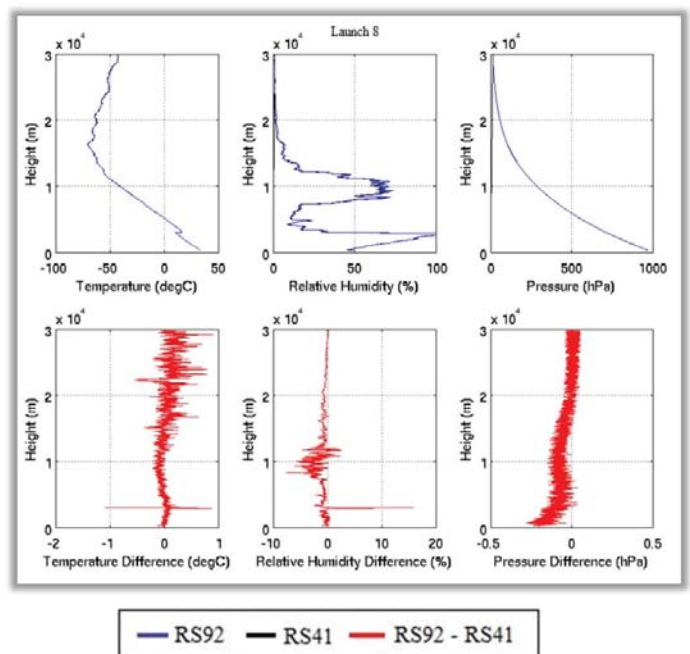
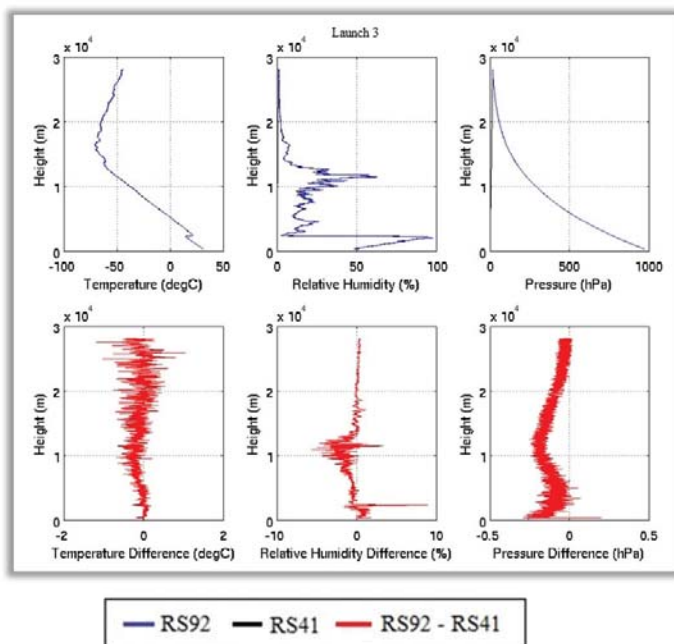


Figure 1. Height vs. Temperature, Height vs. Relative Humidity, Height vs. Pressure (top) and Height vs. Temperature Difference, Height vs. Relative Humidity Difference, Height vs. Pressure Difference (bottom) for a single launch.

Figure 2. Height vs. Temperature, Height vs. Relative Humidity, Height vs. Pressure (top) and Height vs. Temperature Difference, Height vs. Relative Humidity Difference, Height vs. Pressure Difference (bottom) for a single launch.

conducted to evaluate the new Vaisala radiosondes (RS41). Using the data from these launches, our goal was to analyze and compare the performance of the two Vaisala radiosondes, RS41 and RS92.

III. Methods

Using MATLAB, the data for the RS41 and RS92 radiosondes was interpolated in order to create two arrays of the same size to ensure an accurate analysis and comparison of the data. Using the interpolated data, plots were created for each launch. These plots show the measurements of temperature, relative humidity and pressure for both RS41 and RS92 each plotted against height as well as the difference between the two radiosondes for each measurement. Corrupted data was identified and removed using these plots. The mean relative humidity, pressure and temperature over the 20 radiosonde launches for RS41 and RS92 at each height level was calculated and plotted. The difference was

then taken of the averages for RS41 and RS92. Then, in order to determine if one radiosonde behaves differently than the other in varying weather conditions, the data was broken in to five intervals of 20% relative humidity from 0% to 100% and within each of these intervals, broken into nine intervals of 10°C from -80°C to 10°C. The data values that satisfied these constraints from both the RS41 and RS92 data were then plotted on the same plots and the difference between the means was then calculated. Time series plots of precipitable water vapor, relative humidity, temperature and sky cover were created with the time for each launch plotted to see the weather conditions for each launch.

IV. Discussion and Results

Figures 1 and 2 each show plots for a single launch. These plots were created in order to find corrupted data and to see if there were any extraneous values within the data for each launch. The bottom row of plots show the difference in the measurement between the RS92 and RS41 radiosondes at each height level for temperature, relative humidity and pressure. These plots show that the largest difference between the two radiosondes for temperature is less than 2°C. Aside from the two large spikes in the differences for relative humidity, the difference in relative humidity is less than 5% and the difference between the two radiosonde measurements for pressure is less than 1 hPa.

Figures 3, 4 and 5 show plots for the mean temperature, pressure and relative humidity for the two radiosondes and the difference of the mean between the two radiosondes for each measurement. It can be seen that from these plots the greatest difference of the mean temperature, mean pressure and mean relative humidity is less than 0.8°C, 0.2hPa and 4%, respectively.

Figure 6 is a plot the difference of the mean relative humidity for the RS41 and RS92 radiosondes for the weather balloon launches that occurred during the day and night. The weather balloon launches were split into day and night groups to see if the radiosondes differed more during the day or at night. The day launches are represented by the red line and the night launches by the blue line. It is easy to see that the radiosondes differ more at night as there are larger differences.

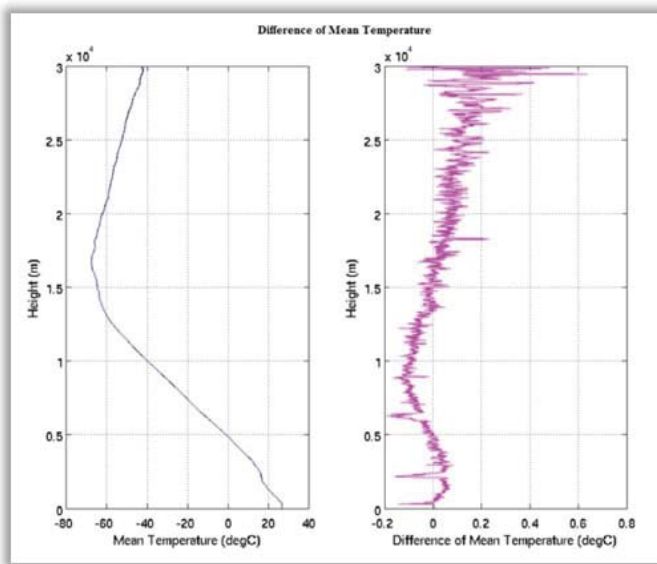


Figure 3. Height vs. Mean Temperature (left), Height vs. Difference of Mean Temperature for all 20 weather balloon launches (right)

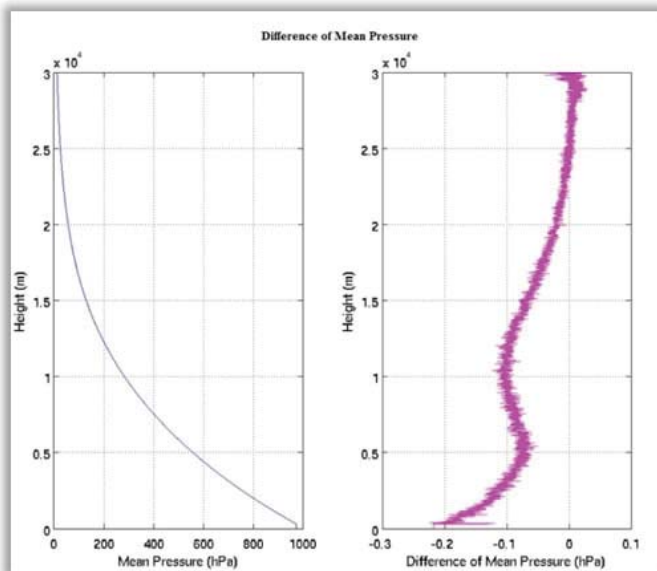


Figure 4. Height vs. Mean Pressure (left), Height vs. Difference of Mean Pressure for all 20 weather balloon launches (right)

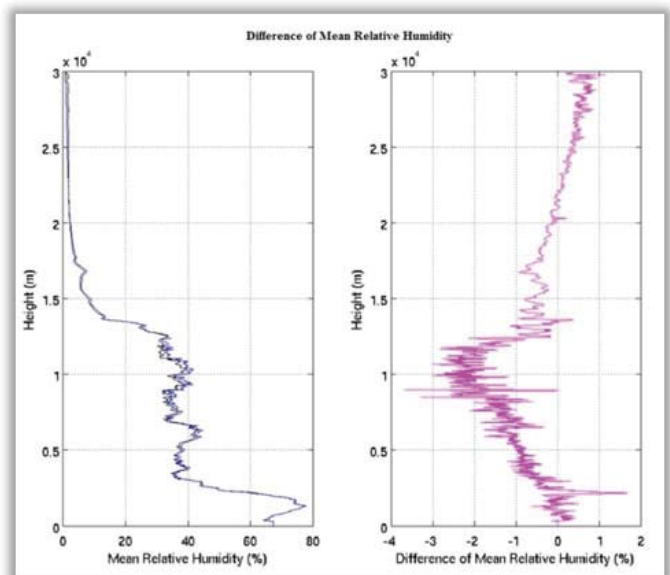


Figure 5. Height vs. Mean Relative Humidity (left), Height vs. Difference of Mean Relative Humidity for all 20 weather balloon launches (right)

Figure 7 contains three time series plots of meteorological variables for the duration of the twenty radiosonde launches. These plots were created to see the weather conditions at the time of each launch. Each of the twenty black vertical lines on the three plots represents a weather balloon launch.

In order to see if the two radiosondes differ more when the atmosphere is very moist vs. dry, or on cloudy vs. clear days, the 20 weather balloon launches were divided into the bottom 50% and top 50% precipitable water vapor measurements and bottom 50% and top 50% sky cover measurements. The sensors on the radiosondes have different responses to wetting as they go through clouds or to heating by the sun. So by looking at the difference between cloudy and clear days, we could possibly see if the radiosondes' sensors are affected. The mean relative humidity for the RS41 and RS92 radiosondes in top 50% and bottom 50% was found and the difference between the means calculated and plotted. Figure 8 shows these plots. The left plot is of the launches with top 50% precipitable water vapor measurements represented as the blue line and the launches with bottom 50% precipitable water vapor measurements represented as the red line. The left plot is of the launches with top 50% sky cover measurements represented as the blue line and the launches with bottom 50% sky cover measurements represented as the red line..

In order to determine whether the two radiosonde types differ more in varying weather conditions, the data for the 20 weather balloon launches was divided into five intervals of 20% relative humidity from 0% to 100% relative humidity and within each of these intervals, the data was further divided into nine intervals of 10°C from -80°C to 10°C. Figure 9 shows that the greatest difference of mean relative humidity is in the 60%-80% relative humidity interval and the difference is less than 2%.

V. Future Work and Conclusion

This project compared and analyzed the RS41 and RS92 Vaisala radiosondes through various types of plots that represent the data in different ways. Overall, this analysis found little difference between RS41 and RS92. Relative humidity varied more than either temperature or pressure. It is ideal that there be a small difference between the two radiosondes because if ARM were to

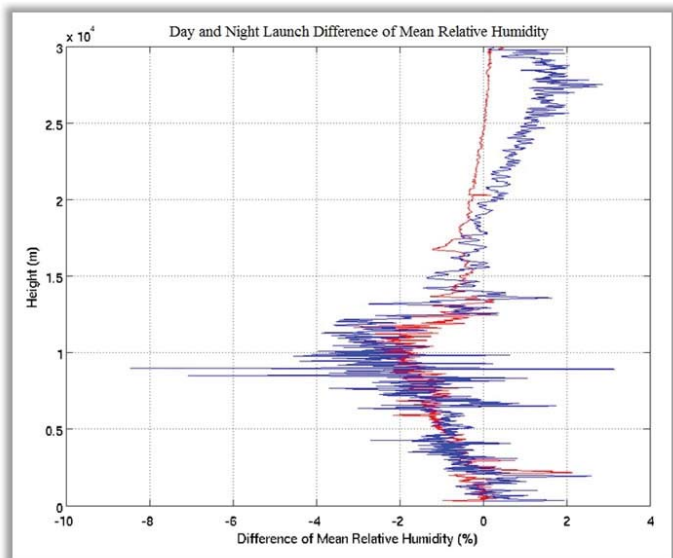


Figure 6. Height vs. Difference of Mean Relative Humidity for Day (red) and Night (blue) Weather Balloon Launches

switch to the RS41 radiosonde, and the two radiosonde measurements were very similar, there would not be a great difference between the old data sets and the new data. This would make it very easy to compare the current data to past data.

There is much more analysis to be done with these data sets. The following are possible methods of future analysis; a partition comparison by meteorological factors (e.g. cloud cover), a comparison of precipitable water vapor to Microwave Radiometer measurements and a comparison of relative humidity with respect to cloud-top (wet-bulb effect).

VI. Acknowledgments

This project was supported in part by the U.S. Department of Energy, Office of Science, Office of Workforce Development for Teachers and Scientists (WDTS) under the Science Undergraduate Laboratory Internships Program (SULI). I would like to thank Brookhaven National Laboratory, the Office of Educational Programs and my mentor Michael Jensen for the opportunity to take part in the SULI program. Thank you!

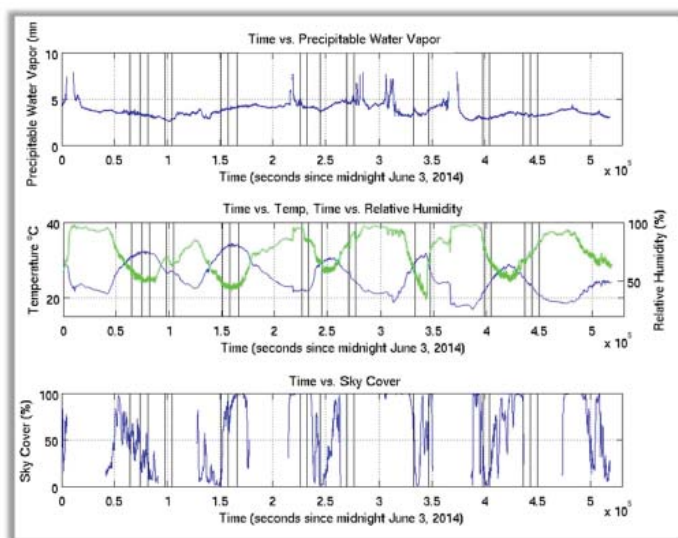


Figure 7. Precipitable Water Vapor vs. Time (top), Temperature (blue) vs. Time and Relative Humidity (green) vs. Time (middle), Sky Cover vs. Time (bottom). The black vertical lines represent a weather balloon launch.

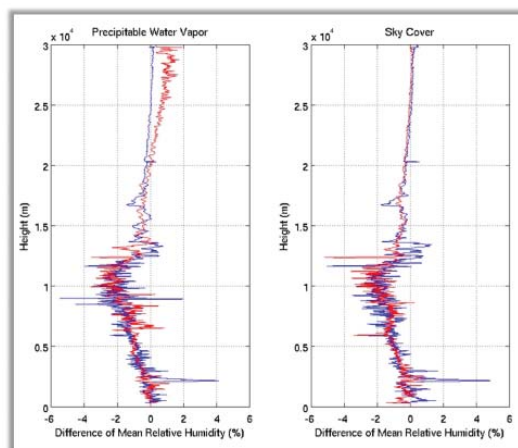


Figure 8. Height vs. Difference of Mean Relative Humidity for Precipitable Water Vapor and Sky Cover

VII. References

“ARM Climate Research Facility.” *ARM Climate Research Facility*. N.p., n.d. Web. 01 Aug. 2014.

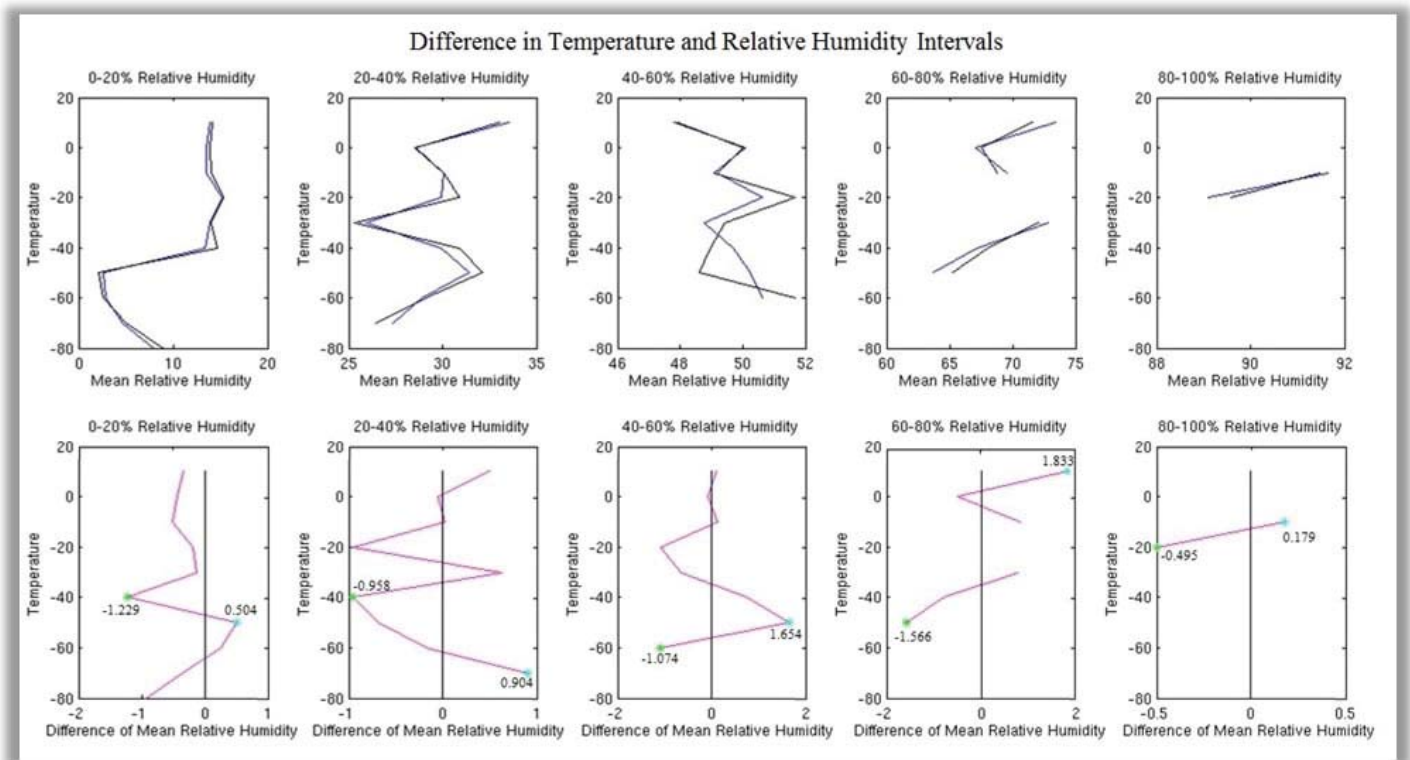


Figure 9

Testing of a prototype high energy efficient CdTe pixel array x-ray detector (ImXPAD)

Elizabeth Berg

Department of Earth, Atmospheric and Planetary Sciences, Massachusetts Institute of Technology, Cambridge, MA 02139

Sanjit Ghose

Photon Sciences, Brookhaven National Laboratory, Upton, NY 11973

Abstract

The C10 ImXPAD detector is a single photon counting CdTe detector designed to collect data from x-rays with energies over 25 keV. Compared to other area detectors, it covers less area (80x118 pixels) and has smaller pixels (130x130 μm), offering high resolution and a quick data collection period. The goal of our project has been to evaluate the performance of this detector at high energies (nearly 67 keV) at the National Synchrotron Light Source X17A beamline as a prototype high-energy pixel array detector. A full stripe larger version of C10 will be used at the X-ray Powder Diffraction beamline at the National Synchrotron Light Source II beginning in October, 2014, in research with applications in condensed matter physics, nanomaterials and new materials for energy research. Three different standard powder samples were used to determine the efficiency and resolution of the ImXPAD C10. We placed the detector approximately 800 mm away from the sample on a stand connected to a motor. This motor was used to drive the detector up to 200 mm vertically from the beam center, collecting images over a wide range of diffraction angles. For each sample, we collected 17 images with a 60 second exposure time. Each image was spaced 13 mm apart with two mm of overlap. A python script was developed to read these images, convert them to pixel arrays, normalize the overlapping regions, and stitch everything together into a complete

2D diffraction pattern from the sample. We integrated this calibration pattern to calculate the resolution of the detector, ultimately confirming that the CdTe sensor and small pixels offer better resolution than the large Si sensor in use that the X17A beamline. This project has not only helped me learn python programming, but also introduced me to experimental x-ray powder diffraction techniques.

I. Background

A. Synchrotrons and x-ray powder diffraction

X-ray powder diffraction (XPD) is the technique of shooting x-ray beams at powder samples to study the samples' structures. Because these powders contain a full range of crystalline orientations, the resulting diffraction pattern is a series of rings, each corresponding to a single diffraction angle. By integrating over these rings, one can determine the various d-spacings of the sample.

High-energy x-ray beams are necessary for collecting high-resolution data [1]. For this reason, many XPD experiments are performed at synchrotron light sources, large machines that use magnets to accelerate electrons in order to generate a range of electromagnetic radiation. Brookhaven National Laboratory (BNL) contains two such facilities: the National Synchrotron Light Source (NSLS), which currently contains 65 running beamlines but is slated to shut down in the fall of 2014, and the National Synchrotron Light Source II (NSLS-II), which will begin

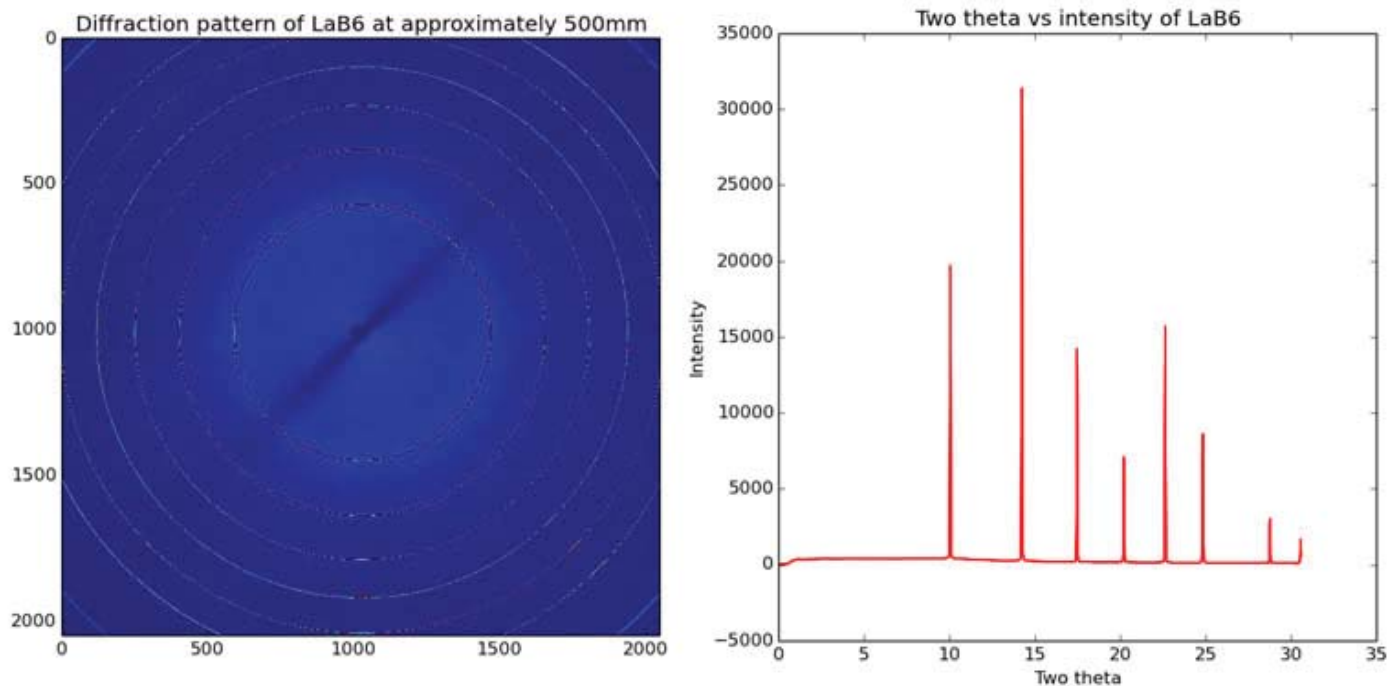


Figure 1. Full diffraction pattern of LaB₆ (left), and the resulting plot of intensities vs. two-theta angle (right)

operation in August 2014 and produce x-rays up to 10,000 times brighter than those currently generated at NSLS [2,3].

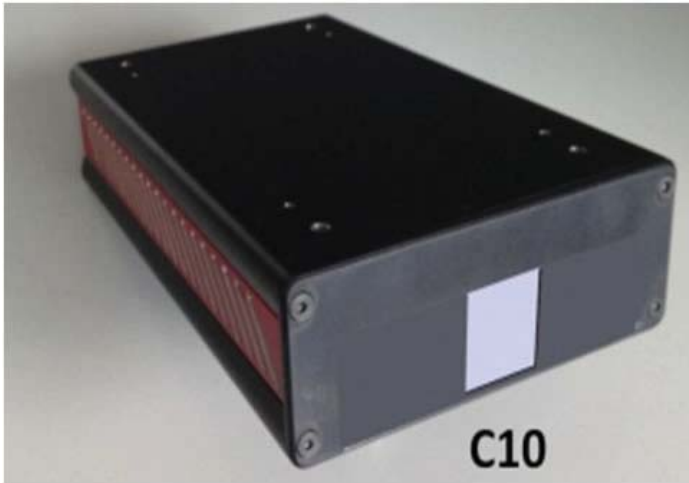


Figure 2. C10 ImXPAD detector.
Source: http://www.imxpad.com/5-xpad_c10-3.html



Figure 3. ImXPAD detector mounted at the X17A beamline.

B. X-ray detectors

X-ray detectors are a vital component of x-ray diffraction (XRD) experiments. At their most basic, these detectors count photons as they hit the detectors' surface. The most important characteristics of XRD detectors are their counting efficiency, point spreading, dynamic range, and noise level. These factors depend on the detector's materials, pixel size, and design. Large area detectors are used to collect data over a full 2θ range and large portion of reciprocal space in a single image, but their materials and design sacrifice peak resolution and efficiency [4]. At the opposite end of the spectrum, point detectors are used with slit or analyzer crystals for better resolution but perform poorly with regards to efficiency, scanning time, and background noise level [4]. The C10 ImXPAD detector ideally offers a compromise between these two extremes. The 80×118 pixel array covers a larger area than point detectors, but the small pixel size should still offer a better resolution than large area detectors. Additionally, the use of a CdTe sensor in the C10 detector offers much higher efficiency than conventional Si sensors at x-ray energies greater than 25 keV [5,6]. In this work, we have tested the performance of a prototype C10 detector using 67 keV x-rays at NSLS.

II. Methods

The detector was tested at the X17A beamline of NSLS, where it was mounted on a stand driven by a motor. Three NIST standard powders (LaB_6 , Ni, and CeO_2) were imaged, and the same procedure, sample-detector distance, and x-ray wavelength were used for each sample. The detector was initially set up just below the beam center before being driven up to 200 mm vertically, recording images over 2θ angles from 0° to 13° .

For each sample, 17 images were collected with a 60 second exposure time each. Every frame was spaced 13 mm apart with two mm of overlap. A python script was developed to read these images, convert them to pixel arrays, normalize the overlapping regions, and stitch all the frames together into a complete 2D diffraction pattern.

III. Data and Results

To determine the resolution of the detector, we integrated the stitched images, generating plots of the two-theta angles against intensity. These plots contain peaks at the two-theta angles of

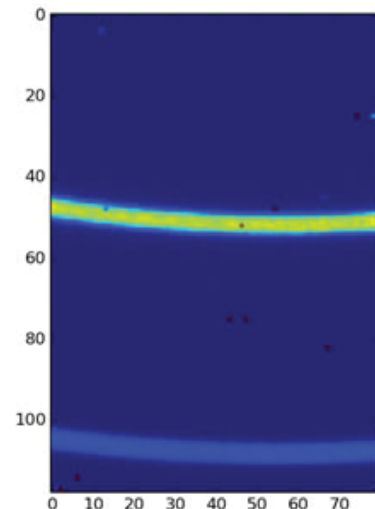


Figure 4. A single frame showing the first two rings of CeO_2 .

each diffraction ring. By fitting these peaks to Gaussian profiles (figure 6), we could plot the ratio of each peak's width to the corresponding location. An ideal detector, with maximum resolution, would have peaks with infinitesimal width.

We knew that there wasn't enough precision in our data to assign exact numbers to the detector's precision. Therefore, we additionally performed the same calculations for similar data collected by a different detector, a PerkinElmer with 200x200 μm pixels. Both images were taken with an LaB_6 powder sample at the X17A beamline. In the figure below, you can see the precision of the ImXPAD detector, represented by a plot of $\Delta Q/Q$ vs. Q , plotted on the same scale as the PerkinElmer detector. Both plots follow a similar curve, but the systematically lower values of the ImXPAD should suggest that this detector has better resolution. Unfortunately, later analysis suggested that there were many other factors at play.

IV. Conclusions

Unfortunately, we faced a number of difficulties in completing the data reduction. Most 2D diffraction data reduction software, notably Fit2d and pyFAI, are designed for conversions from XY coordinates to scattering angle or reciprocal coordinates for images that span large portions of reciprocal space. These programs were unable to convert the diffraction rings in the final stitched images collected with the C10 detector (Figure 5) or perform geometric corrections. This prevented us from calibrating the diffraction patterns or determining the sample-detector distance or location of the beam center to the desired level of precision. Consequently, we could not integrate the intensities over 2θ angles. Instead, we integrated over the vertical distance between

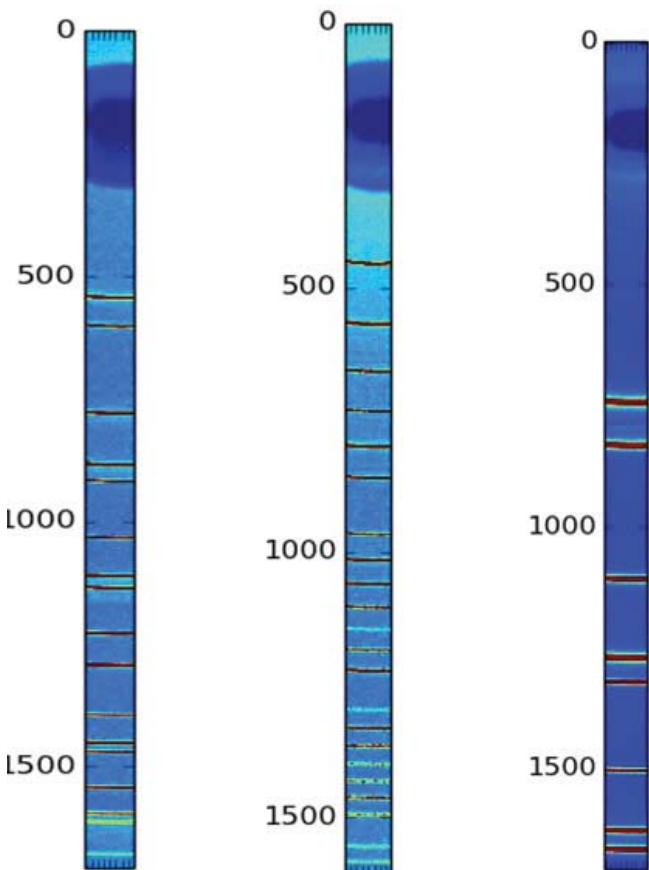


Figure 5. The final stitched images. In order, from left: CeO_2 , LaB_6 , Ni

each pixel and the beam center, approximating a negligible $\Delta 2\theta$ over each 80-pixel row. As shown by figure 8, these approximations were generally accurate to $.1^\circ$, with larger errors found on the inner rings.

While there was a surprisingly high degree of accuracy in the calculated angles, figure 8 also shows a large difference in the intensities collected by the two detectors, both in terms of overall magnitude and relative intensities. There are number of factors that may have led to this result. Because the PerkinElmer is a Si CMOS detector while the ImXPAD uses a CdTe sensor, they measure intensities on entirely different scales. However, this should lead us to expect consistent proportionality between the peaks, which is not the case. Unfortunately, the variance in relative peak heights is probably the result of errors propagated by the horizontal integration of the ImXPAD data. In particular, we couldn't completely mask all the bad pixels, which are pixels

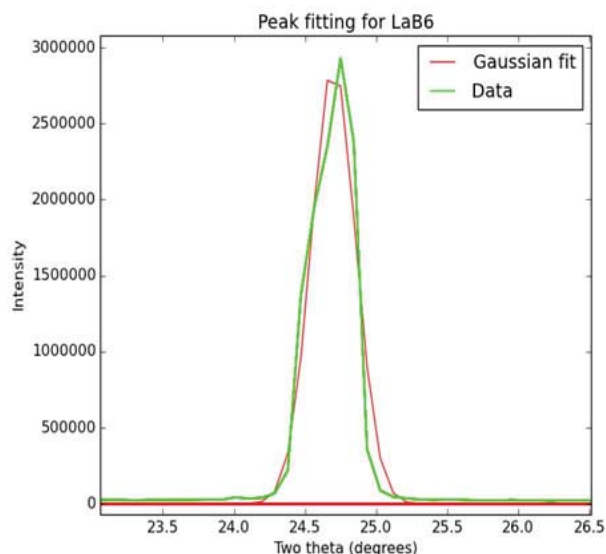


Figure 6. A single peak from the LaB_6 diffraction pattern plotted with the Gaussian fit.

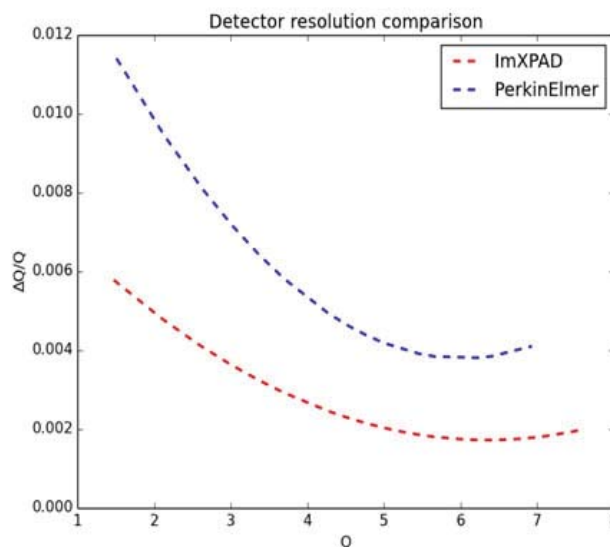


Figure 7. The resolution of the ImXPAD detector plotted against the resolution of the 2048x2048 PerkinElmer detector, both calculated from LaB_6 diffraction data.

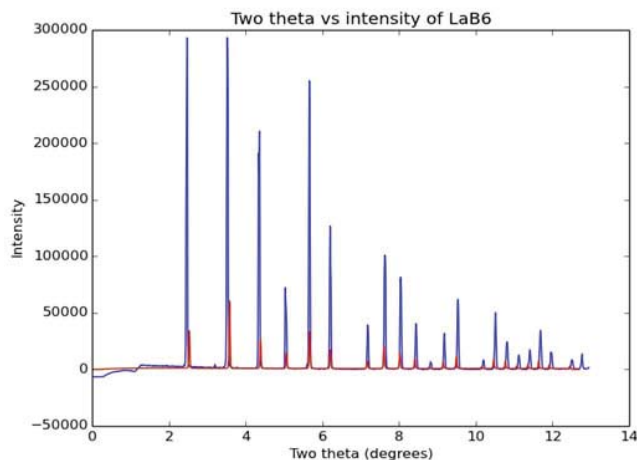


Figure 8. LaB6 diffraction peaks. The blue curve was collected by a PerkinElmer detector and generated by azimuthal integration. The red curve was collect by the C10 ImXPAD detector through vertical integration.

in the detector that register orders of magnitude higher than the actual measurements, and these had a much larger effect on the ImXPAD data because of our method of integration. Additionally, there were only around 1500 data points, one for each row, in the ImXPAD data set, which does not offer enough precision for accurate peak fitting when spread over 15 peaks. Lastly, the reason we integrated over horizontal rows instead of over two theta angles is because we did not have enough azimuthal resolution to generate a calibration file. This means that we had very rough measurements for the beam center and sample-detector distance, and no measurements at all of the degree of detector tilt. This imprecision, along with the approximation that the image was narrow enough to neglect all horizontal contributions to two theta measurements, also contributed to errors and inaccuracy in the integrated intensity.

With only one day of beamtime, we unfortunately were unable to correct any of our initial mistakes with the data collection. However, we now understand that data reduction programs like pyFAI and fit2d only work when there is symmetry. In the future, we would image the samples with the detector both above and below the beam center. It seems likely that we would be able to calibrate the data if the final image contained thin slices of the same diffraction rings on both sides of the beam center.

V. References

[1] B. B. He, U. Preckwinkel, K. L. Smith. “Fundamentals of Two-Dimensional X-Ray Diffraction (XRD²).” *Advances in X-ray Analysis*, Vol 43.

[2] “About the National Synchrotron Light Source” <<http://www.bnl.gov/ps/nsls/about-NSLS.asp>>

[3] “About the National Synchrotron Light Source” <<http://www.bnl.gov/ps/nsls2/about-NSLS-II.asp>>

[4] B. H. Toby, T. J. Madden, et al. “A scanning CCD detector for powder diffraction measurements.” *Journal of Applied Crystallography* (2013).

[5] P. M. Abdala, H. Mauroy, W. van Beek. “A large-area CMOS detector for high-energy synchrotron powder diffraction and total scattering experiments.” *Journal of Applied Crystallography* (2013).

[6] S. Basolo, J.F. Bélar, et al. “A 20 kpixels CdTe photon-counting imager using XPAD chip.” *Nuclear Instruments and Methods in Physics Research A* 589 (2008): 268-274.

VI. Acknowledgments

This project was supported in part by the U.S. Department of Energy, Office of Science, Office of Workforce Development for Teachers and Scientists (WDTS) under the Science Undergraduate Laboratory Internships Program (SULI). I am also grateful for the guidance from my mentor, Sanjit Ghose, and want to thank all the members of the XPD beamline group at NSLS-II for their immense help and support during this project.

Investigating the electrical properties of doped graphene

Keturah Bethel

College of Science and Mathematics, University of the Virgin Islands, St Thomas, United States Virgin Islands 00802

Darnel Allen

Materials Science, University of Florida, Gainesville, Florida 32605

Sharadha Sambasivan

Chemistry, Suffolk County Community College, Selden, New York 11784

David Paulius and Phil Smith

College of Science and Mathematics, University of the Virgin Islands, St Thomas, United States Virgin Islands 00802

Wayne Archibald

College of Science and Mathematics, University of the Virgin Islands, St Thomas, United States Virgin Islands 00802

Fernando Camino

Center for Functional Nanomaterials, Brookhaven National Laboratory, Upton, New York 11973

Abstract

This project sought to explore the electronic properties of doped chemical vapor deposition (CVD) graphene. Single layer CVD graphene samples were doped with 0.5Å of gold, 1Å of silver and 1Å of titanium via thermal/e-beam evaporation. Compared to our pristine graphene sample, the titanium doped, gold doped and silver doped samples exhibited an increase in hall mobility of ~19%, a decrease of ~24% and a decrease of ~8% respectively. Near-edge X-ray Absorption Fine Structure (NEXAFS) Spectroscopy of the pristine graphene sample and the doped samples illustrated that there was a slight shift in the position of the π^* resonance peak in the doped samples when compared to that of the pristine graphene sample. Differences were also noticed in the inter-layer states of all the samples.

I. Introduction

To keep pace with the demand for ever-faster and smarter computing devices, the size of transistors is continually shrinking, allowing increasing numbers of them to be squeezed onto microchips. The more transistors you can pack on a chip, the more powerful the chip is going to be, and the more functions the chip is going to perform. In the semiconductor industry, silicon is widely used; but as silicon transistors are reduced to the nanometer scale, the amount of current that can be produced by the devices is also shrinking, limiting their speed of operation. The field of nanomaterials deals with the study of materials on the nanoscale. A 2D material can be viewed as individual planes of atomic-scale thickness pulled out of bulk crystals. The strength along two dimensions would be similar and much stronger than that of the 3rd dimension¹. These 2D materials have very different properties and applications compared to the 3D bulk material from which they originate. Going from a bulk material to one that is one atomic layer thick, gives rise to novel properties due to the fact that all atoms are very close to the surface and charge and heat transport are confined to a single plane. Some of these properties include high thermal conductivity, high carrier mobility, exceptional optical properties and flexibility.

One of the first 2D materials to be discovered is graphene. It is comprised of a single layer of carbon atoms packed tightly into a two-dimensional honeycomb (hexagonal) arrangement (as

shown in figure 1)². Graphene is particularly interesting because the electronic band structure has a Dirac cone, the consequence of linear dispersion in its electronic band diagram, which makes graphene a high-mobility conductor³. Graphene can be synthesized by mechanical exfoliation from graphite, grown by chemical vapor deposition (CVD) of hydrocarbons on metal substrates such as Cu and Ni and epitaxially grown by thermal decomposition of SiC⁴. The only problem is that high-quality graphene is a great conductor that does not have a band gap. A band gap is the minimum energy required to excite an electron from the valence band to the conduction band which makes it possible for a material to act as a semiconductor. This is important in devices such as transistors because it allows for an on and off state in these devices. Therefore to use graphene in the creation of future nano-electronic devices, a band gap will need to be engineered into it so that these devices can be turned off when not in use. One way to engineer a band gap into graphene is by doping. Since graphene has ultra-high conductivity which changes rapidly when gas molecules are adsorbed on the surface, it makes it very sensitive to surface transfer doping⁵.

Doping is the addition of impurities into an extremely pure (intrinsic) semiconductor for the purpose of modulating its electrical properties. Chemical doping is an effective method to tailor

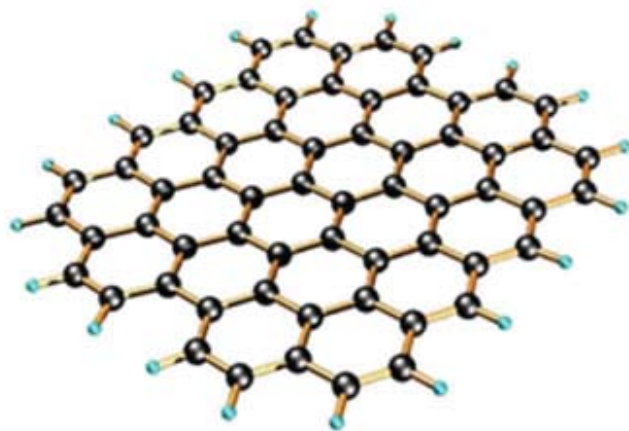


Figure 1: Structure of graphene

the electrical properties of graphene. Two types of chemical doping are surface transfer doping and substitutional doping. Most cases of surface transfer doping are reversible compared to substitutional doping. Surface Transfer Doping is achieved by electron exchange between a semiconductor and dopants which adsorb on the surface of a semiconductor. Graphene can be p-type or n-type doped via chemical doping. For this experiment the graphene samples were doped with 0.5Å of gold, 1Å of silver and 1Å of titanium via thermal/e-beam evaporation. Graphene has a work function of $\sim 4.6\text{eV}$ and will be doped with holes (p-doped) if the metal work function is higher than the graphene's work function and doped with electrons (n-doped) if the metal work function is less than that of graphene. The work function of gold, silver and titanium are $\sim 5.1\text{eV}$, $\sim 4.26\text{eV}$ and ~ 4.33 respectively.

VASP (Vienna Ab-Initio Simulation Package) has been selected for investigating doping in graphene via computational means⁶. VASP is a software package (named for its origin from the University of Vienna in Austria) that draws from the basis of the density functional theory to solve the complex problem that is the Schrödinger's Equation. Although a solution to a single system has been attained (one hydrogen atom), solving the wave function for a many body system is virtually impossible; therefore, the idea behind the density functional theory is to find an approximate solution through the use of self-consistent calculations. VASP can be used for many problems, but special attention will be made on calculating the density of states (DOS) as well as the band structures of graphene structures. These diagrams help in identifying the nature of doping within graphene⁷.

NEXAFS involves the use of low energy X-ray to excite electrons from core levels (K or L shell) to partially filled and unoccupied molecular orbitals of σ or π symmetry, σ^* and π^* , respectively. Element identification is gained from the initial-state of the K or L shell excitation, whilst the final state with the unoccupied states provides NEXAFS with bonding or chemical information. In addition, the intensity of the peaks in the NEXAFS spectrum allows chemical bond determination and their relative population density in the sample. The instrument has a fixed sample geometry relative to the incident X-ray beam. Since the $1s \rightarrow \sigma^*$ and $1s \rightarrow \pi^*$ excitations are governed by dipole selection rules. Thus, the resonance intensities change as with the direction of the field

vector E of the incident polarized x-ray beam relative to the axis of the σ^* and π^* orbitals. This technique enables the study of the molecular bond chemistry and orientation of chemisorbed since sharp core level excitations for C, N, O and F occur in the soft x-ray region. NEXAFS has ability to analyze the electronic structure, which is good for investigating graphene's electronic properties. Moreover, there is no damage done to the sample when using NEXAFS

II. Experimental Procedures

A. Graphene growth

The single layer of graphene was grown via chemical vapor deposition (CVD). A copper foil is placed into a furnace and heated under low vacuum to around 1000°C . The heat anneals the copper, increasing its domain size. Methane and hydrogen gases are then flowed through the furnace. The hydrogen catalyzes a reaction between methane and the surface of the metal substrate, causing carbon atoms from the methane to be deposited onto the surface of the metal through chemical adsorption. After the graphene was removed and cooled, polymethyl methacrylate (PMMA) was spin coated onto the graphene as a support, and then the copper foil was etched away in ferric chloride (FeCl_3). The remaining PMMA and graphene film was then cleaned in de-ionized water and further deposited on top of a 285nm SiO_2/Si wafer substrate. The sample is then immersed for 2 hours in warm acetone (around 60°C) to gradually get rid of the PMMA. Finally the sample was gently dried under a nitrogen blow.

B. Raman spectroscopy

Raman spectroscopy is used extensively to characterize graphene. This technique provides information on vibrational states of a bulk sample. This is the easiest and best method to use in analyzing graphene. The advantages of using Raman Spectroscopy is that it is insensitive to the substrate, there is minimum sample preparation required, it provides high accuracy information, has a fast testing speed and large detection area⁸. A great deal of information on graphene can be extracted from the Raman spectrum. The Raman spectrum consists of two main peaks and few small peaks. The two main bands in the spectrum are known as the G-band at 1582 cm^{-1} and the 2D-band at 2685 cm^{-1} . A third band known as the D-band at 1350 cm^{-1} is also present as shown in figure 2.

When light is scattered from a molecule or crystal, most photons are elastically scattered. The scattered photons have the same frequency and wavelength, as the incident photons. However, a small fraction of light is scattered at optical frequencies different from, and usually lower than, the frequency of the incident photons. The process leading to this inelastic scatter is called the Raman Effect. From figure 3 it can be seen that the majority of scattered light is elastically scattered, meaning it is the same wavelength as the excitation source. A notch filter is used to block elastically scattered light which would otherwise overwhelm the weak signal from the Raman or in elastically scattered photons. The Raman scattered light is dispersed according to wavelength by a grating and detected by a Charge Coupled Device (CCD) detector. A Raman spectrum is then plotting on the computer.

Our Raman experiments were conducted at room temperature and pressure. A 100x objective lens was used with the Alpha 300 WiTEC Microscope. The laser's power was set to 514nm at low power. The parameters used were an integration time of 2.5s

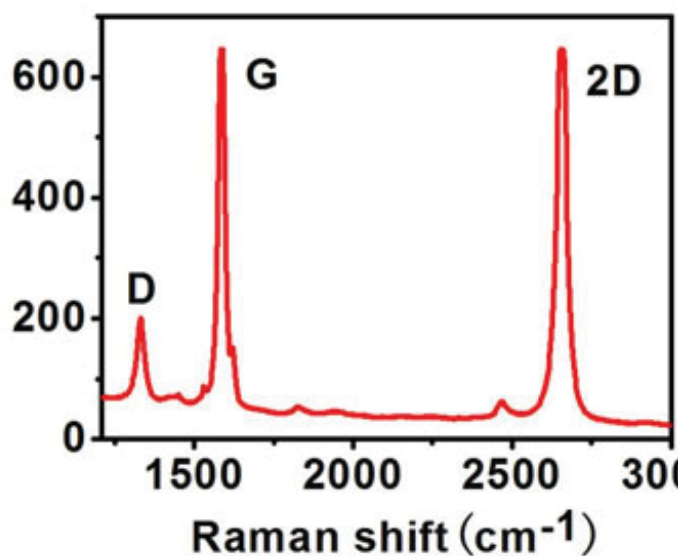


Figure 2: Raman Spectrum of graphene

and accumulation of 25. Our graphene samples were 1cm x 1cm with a p-type doped substrate and a n-type doped substrate. We obtained Raman single spectrums and image mappings of each of the graphene peaks.

C. Hall Effect Measurements

Hall Effect measurements can be used to determine many properties of a material such as the mobility of charged carriers within a material and the carrier density. When a current is passed through a conductor/semiconductor electrons flow from one end to the other but when a magnetic field is introduced perpendicular to it, this creates a force called Lorentz force. Electrons subject to the Lorentz force initially drifts away from the current direction toward the edges. The Hall Voltage (V_H) of this rod is the potential difference between the edges of the material (as shown in figure 7).

$$V_H = \frac{IB}{end}$$

Here e is the charge of an electron, n is the carrier density, d is the thickness, I is the current and B is the magnetic field. The Hall mobility (μ_H) is defined as

$$\mu_H = \frac{|R_H|}{\rho}$$

where ρ is the electrical resistivity at zero magnetic flux density and R_H is the Hall coefficient. Instead of using traditional method of finding resistivity where the geometry of the sample needs to be known, the van der Pauw method was used instead. Figure 8 shows our graphene sample mounting to undergo mobility measurements. The main result of the van der Pauw method is that the resistivity of the sample can be calculated from two resistance measurements using this equation:

$$\rho = \frac{\pi t F}{\ln(2)(R_{12,43} + R_{23,14})}$$

The notation used for resistance measurement ($R_{ij,kl}$) is defined as V_{kl}/I_{ij} , where V_{kl} is the voltage measured between positive contact k and negative contact l and I_{ij} means the current source is connected with positive source on contact i and negative source on contact j . The quantity F is a transcendental function of the two measured resistances ($R_{12,43}$ and $R_{23,14}$). Let R_r be the greater

of the ratios $R_{12,43}/R_{23,14}$ and $R_{23,14}/R_{12,43}$. The quantity F can be found by:

$$\frac{R_r - 1}{R_r + 1} = \frac{F}{\ln(2)} \cosh^{-1} \left(\frac{e^{\frac{\ln(2)}{F}}}{2} \right)$$

The system used for this measurement is a lake shore 8404 AC/DC Hall Effect Measurement System. Either AC field hall effect measurements or DC field hall effect measurements can be done. AC field hall effect measurements are preferred over DC field for samples with low mobility. DC field Hall Effect measurements are able to measure mobility down to 1 cm²/Vs which means that it would be hard to distinguish between the actual measurement and background noise in low mobility samples. On the other hand AC field hall effect measurements can measure mobility down to 0.001 cm²/Vs. This system is also capable of field reversal and current reversal. With a zero field, the hall voltage ideally should be zero; however misalignment voltage arises due to the contacts not being perfectly symmetric on the hall bar. As a result field reversal is needed to counteract this effect. Thermoelectric voltage is generated any time there is a thermal gradient across dissimilar metals which is counteracted with current reversal.

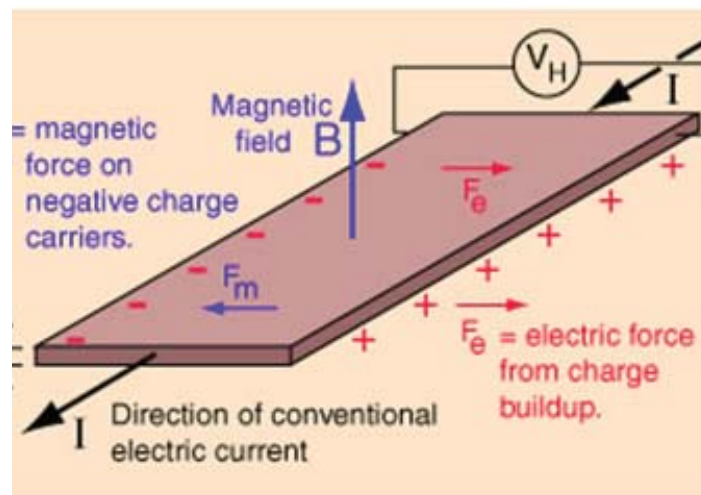


Figure 7: Hall Effect

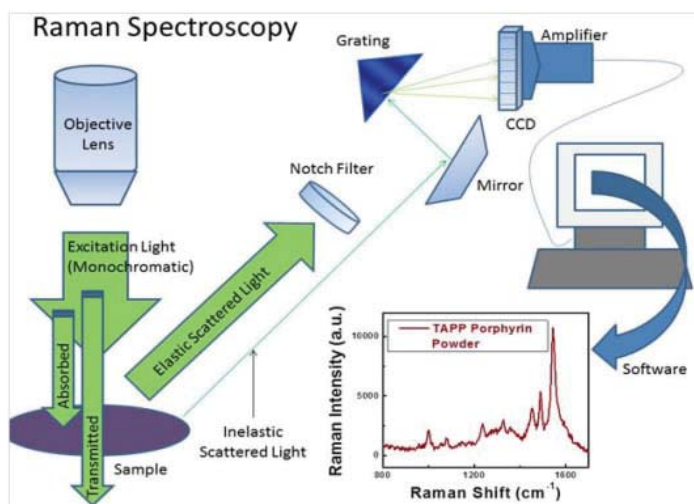


Figure 3: Schematic for Raman Spectroscopy

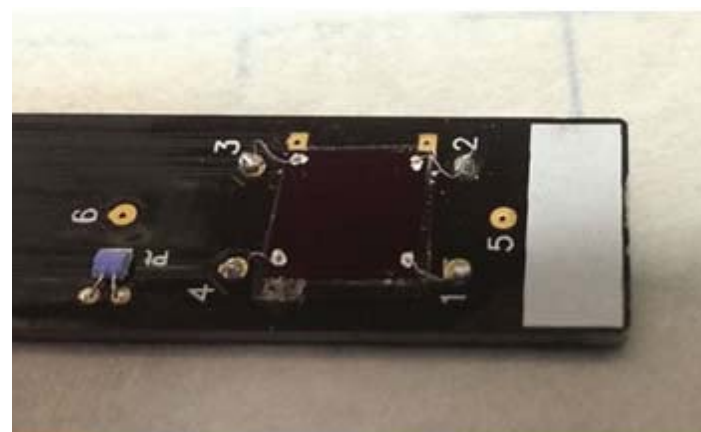


Figure 8: Graphene sample mounted on lake shore 8404 AC/DC Hall Effect Measurement System chip using silver paste to contact.

D. Computational Method

Firstly, the necessary files required by VASP (the INCAR, POSCAR, POTCAR, and KPOINTS files) were prepared for each structure being studied: pristine graphene, Ag-, Au- and Ti-doped graphene. For each structure, the ideal atomic position for the metal atom was found by positioning the atom at varying distances between 1.5 to 4.0 angstroms in length and finding the structure with lowest total energy. VASP requires that a set of self-consistent calculations are run in order to get the density of states as well as the band structure. Therefore, each graphene structure was adjusted accordingly to get both sets of data. Also the CHGCAR file was used for better approximations for DOS

Graphene supercell structures were designed and created using CrystalMaker as well as VESTA (Visualization for Electronic and Structural Analysis) to produce necessary information for density functional theory computations using VASP. The graphene crystal structures were exported to VESTA to create the corresponding POSCAR files needed by VASP; these files are crucial as they contain the atomic coordinates for all species present in the structure as well as the lattice vectors which identify graphene as a hexagonal structure. To demonstrate the effects of doping with the transition metals, it was necessary to perform two basic sets of calculations involving graphene supercells with and without the metals present present in the structure (shown in figures 9 and 10).

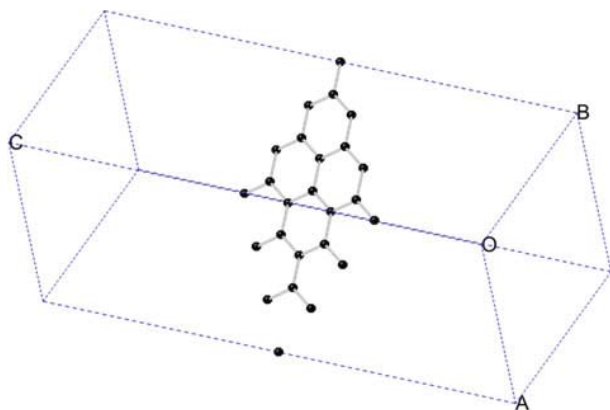


Figure 9: Visualization of 3x3 pristine graphene supercell structure using CrystalMaker.

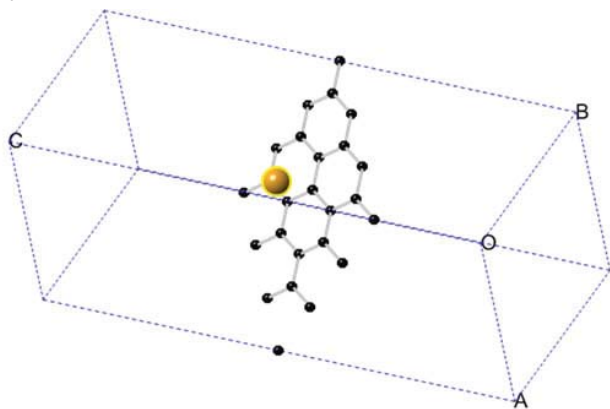


Figure 10: Visualization of 3x3 graphene supercell doped with 1 atom Au using CrystalMaker.

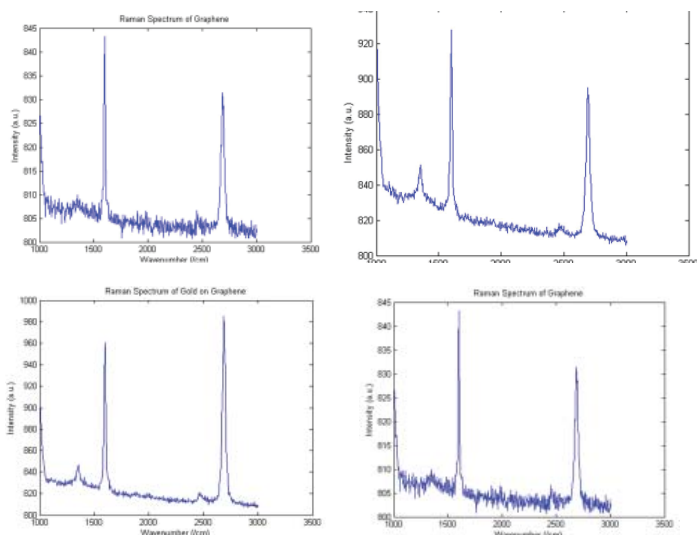
E. NEXAFS

Molecular order characterization at the SAMS surface (top 3-5 nm) was performed using x-ray absorption technique of NEXAFS details reported elsewhere. NEXAFS at the carbon K-edge was carried out at U7A NIST beamline of the National Synchrotron Light source at Brookhaven National Laboratory. The incident soft x-rays are linearly polarized and monochromatic with an energy resolution of 0.2 eV at 300 eV. Multiple samples approximately 1 cm by 1 cm on the Si wafer were freshly prepared with SAMs of different chain lengths and were loaded on a stainless-steel bar and introduced into the vacuum chamber through a sample load-lock system. Samples were precisely aligned with the aid of a fully automated computerized sample manipulator stage. Energy resolution and photon energy calibration of the monochromator were performed by comparing gas-phase carbon monoxide with electron energy loss reference data. The partial-electron-yield (PEY) NEXAFS measurements at carbon K-edge from 270 eV to 330 eV were obtained with a channeltron at a negative 150 volt bias on the entrance grid to enhance surface sensitivity (probe depth of approximately 3 to 5 nm).¹⁷ Under these bias conditions, the partial electron-yield measurement is dominated by the Auger yield from the sample, low energy electrons and other background photoelectrons are rejected by bias electric field. The sample was charge neutralized using a low energy electron flood gun, which added no noticeable background to the NEXAFS spectrum. Electron-yield data are subject to incident beam intensity fluctuations and monochromator absorption features. The spectra are normalized to the incident beam intensity, I_0 , by collecting the total electron yield intensity from a clean gold-coated 90 % transmitting grid placed in the incoming x-ray beam path.

III. Results and Discussion

A. Raman Results

All of the doped graphene samples showed a slight shift in the 2D and G band to the right compared to the pristine graphene. P-type doping causes this to occur and thus it may be related to the position of the Fermi level in the sample. Also there were changes in the Full Width Half Maximum of the 2D peak for each of the different samples. Notably, there was little or no defect peaks in the Raman spectrum.



B. Hall Effect Measurement Results

System	Mobility (m ² /Vs)	Carrier Type
Ti doped	1.02E-01	P-Type
Pristine	8.56E-02	P-Type
Ag doped	8.18E-02	P-Type
Au doped	6.50E-02	P-Type

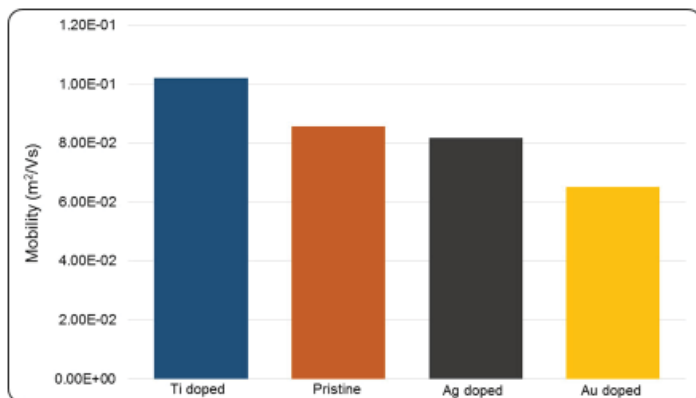


Figure 11: Hall mobility of pristine graphene, Ti-doped, Ag-doped and Au doped graphene

From figure 11, it can be seen that the mobility of the Ti-doped sample increased by ~19% however the mobility of the Ag-doped sample and the Au-doped sample decreased by ~8% and ~24% respectively. The carrier type of all the samples were found to be p-type. Since the work function of Ag and Ti are less than that of graphene we were expecting the samples doped with these metals to be n-type but that wasn't the case.

C. NEXAFS Results

Figure 1 depicts the NEXAFS spectra of Graphene on Si/SiO₂ at the Carbon K-edge measured at magic angle. The salient features in the spectra has been previously analyzed via various citations in the literature.¹¹⁻¹⁶

NEXAFS spectra as shown in figure 2 at the π^* region centered around 285.15 eV for the graphene on Si/SiO₂ but shifted to 285.5 eV in the case of metal doped graphene. This shift may be attributed to the changes in oxidation state and the possible charge transfer effects seen in the presence of a dopant transition metal.¹⁴ In addition careful examination of the peak shape of π^* resonance peak of the metal doped graphene in comparison to the Graphene indicated a higher energy broadening/shoulder around 286 eV. This feature could be attributed to ionization energy shifts and core-hole perturbations due p-doping in graphene.¹⁵ Another possible explanation suggested by Banerjee et. al , is that doping shifts the Dirac point in graphene and uncovers features of the occupied density of states that are then visualized as shoulders to the π^* feature.

Fig. 3 shows two new feature that appears at 287.7 and 288.8 eV between the π^* and σ^* resonances upon transition metal deposition, which appears as a weak shoulder for the graphene on SiO₂ sample. In the literature the assignment of the interlayer state (287–289 eV) in graphite and other carbon systems has been attributed to functionalization, typically C–O or C–H bonding surface contamination or as a dispersion of three-dimensional unoccupied bands¹⁵. Graphite itself has a prominent interlayer state that has been observed using NEXAFS spectroscopy.¹⁵ But Raman spectrum of the metal doped graphene did not indicate the

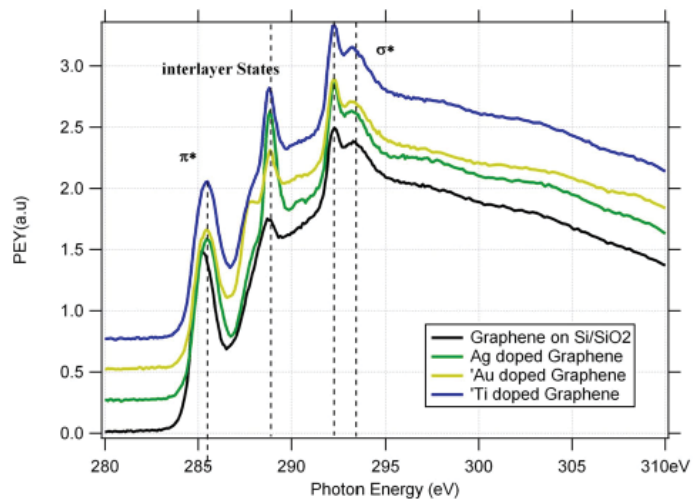


Figure 1.

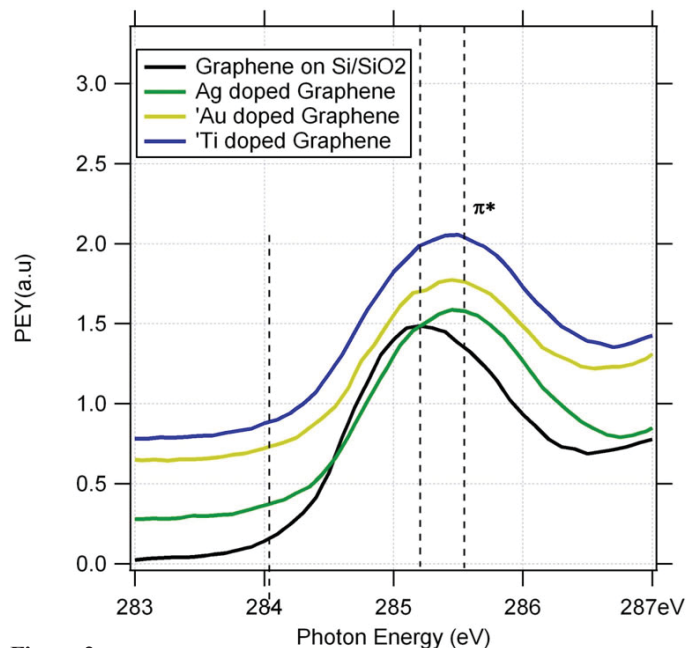


Figure 2.

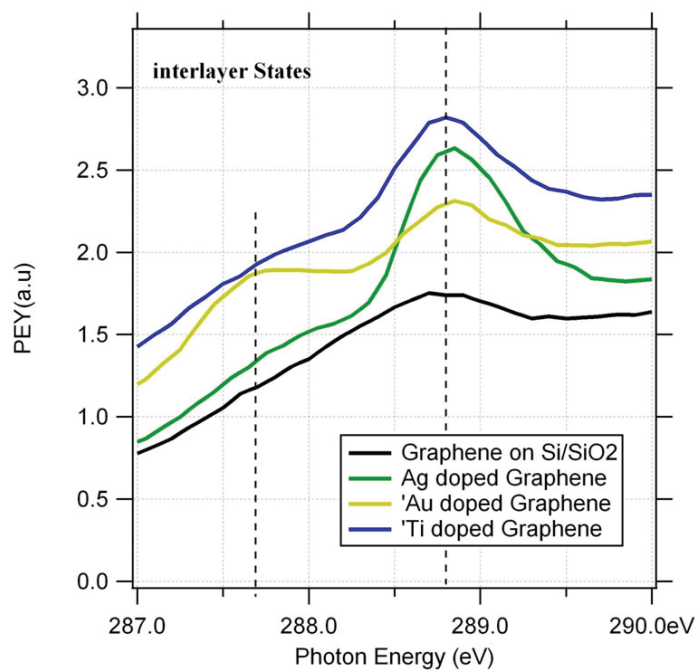


Figure 3.

presence of these CO or CO₂ or aliphatic alcohol or PMMA used in processing graphene samples. Banerjee et. al attributed similar features on Ni or Co monolayer deposited on graphene.¹² to transitions from 1s states to the anti-bonding orbitals of incipient carbonate linkages. Notably, the carbonates are not adsorbed impurities but originate specifically from oxidized carbide type linkages, which have been noted in XPS studies for graphene grown on Ni and upon deposition of Ti contacts.¹⁵ Carbide formation (and subsequent oxidation to the carbonate) has been particularly seen at the edges of the graphene islands as a result of the reaction between under-coordinated C and transition metal atoms.

To provide further insight into the nature of the transition metal-graphene interlayer chemistry, the angular dependent (polarization) NEXAFS spectra were measured at 85°, 54.7 ° (magic angle, polarization independent angle) and 20°. Figure 4 shows the NEXAFS difference spectra for all the four systems which enhanced spectral features sensitive to polarization of the electric field vector of the incident photons. It was noted that Ti-Graphene system showed stronger angular dependence of the interlayer peak a spectroscopy data in Fig. 3 Additionally, it is notable to point out that higher energy shoulder near π^* peak is more pronounced for Ag and Au doped systems. Further studies involving annealing and measuring NEXAFs spectroscopic changes will provide meaningful insights to the molecular species involved contributing to the interlayer states.

D. Computational Results

Doping can be identified through density of states (DOS) and band structure diagrams; VASP produces these sets of information through self-consistent calculations.

As suggested by the density of states diagram, the doped structures show signs of a band gap due to the fact that there are now states present at the Fermi level of 0 eV. The density of states has also shifted slightly for each extrinsic structure of graphene as a result from the metal atom's influence on the graphene. The results also suggest that gold doping has produced a p-type structure due to the shift upwards, while Ti and Ag produced n-type structures from the shift downward. The results of Ag-doping and Ti-doping contradicts what was found experimentally where they both resulted in p-type semi-conductors.

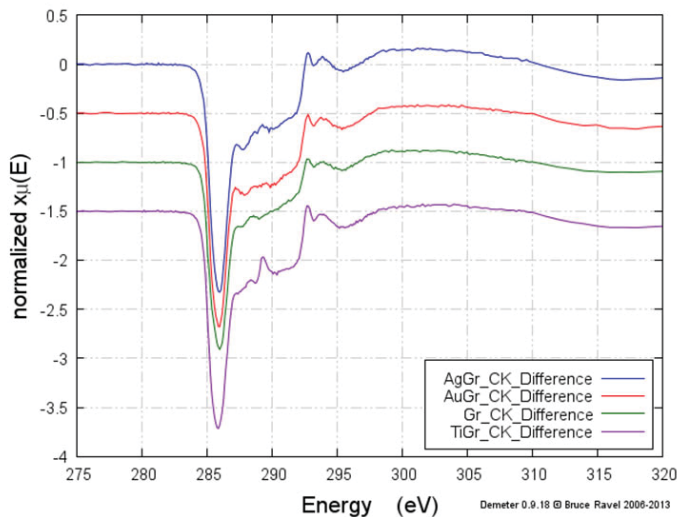


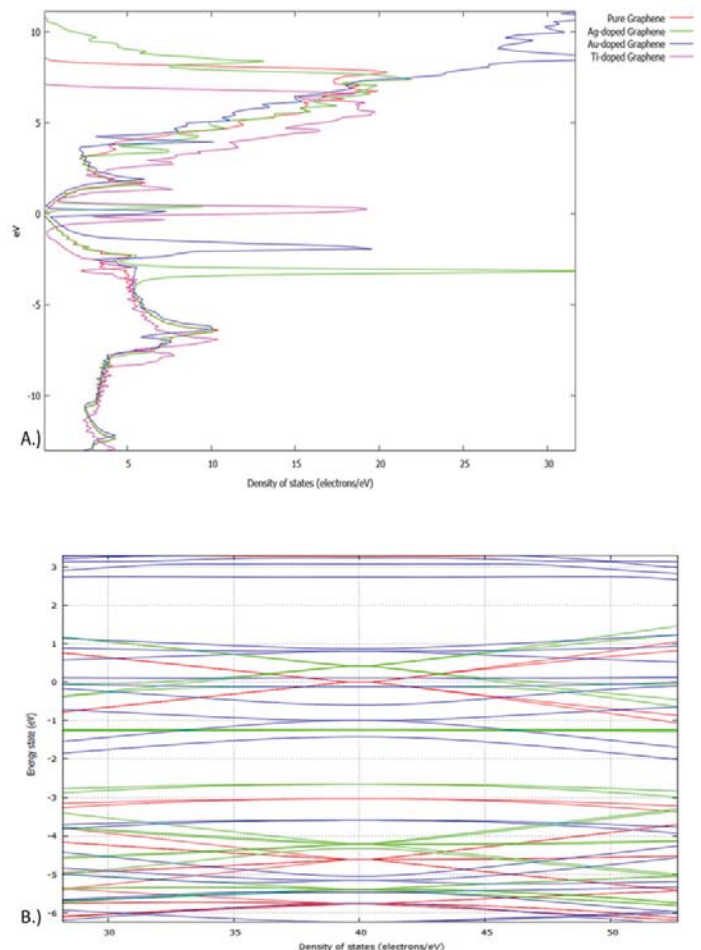
Figure 4.

IV. Conclusion

Based on the results from all the experiments, we conclude that the dopants has created some sort of band gap in the CVD graphene sample but in order to be certain and to know the size of this band gap other more experiments need to be done.

V. Acknowledgement

This project was supported in part by the U.S. Department of Energy, Office of Science, Office of Workforce Development for Teachers and Scientists (WDTS) under the Visiting Faculty Program (VFP). We would also like to acknowledge Fernando Camino, Mark Hybertsen and Sharadha Sambasivan for their continued assistance throughout the summer.



Figures 12 (A) & (B) : Density of states and band structure diagrams showing the effects of doping from adding single atom of different transition metals with the shift of the Dirac points. Band structure diagram contains only three structures, pure, Au-doped and Ti-doped graphene, to show differences in semi-conductor type.

VI. References

1. BUTLER ET AL; "Progress, Challenges, and Opportunities in Two-Dimensional Materials Beyond Graphene" ACS NANO; VOL. 7 NO. 4 2898–2926 2013
2. <http://cnx.org/content/m29187/1.4/>
3. Kristie J. Koski and Yi Cui; "The New Skinny in Two-Dimensional Nanomaterials" ACS Nano VOL. 7 NO. 5 3739–3743 2013
4. Phaedon Avouris and Christos Dimitrakopoulos; "Graphene: synthesis and applications" Materials Today VOL 15, Number 3 March 2012
5. Hongtao Liu, Yunqi Liu and Daoben Zhua; H. Pinto, R. Jones, J. P. Goss and P. R. Briddon, J. Phys: Condens. Matter, 2009, 21, 402001
6. <http://cms.mpi.univie.ac.at/vasp/guide/vasp.html>
7. G. Giovannetti, P. A. Khomyakov, G. Brocks, V. M. Karpán, J. van den Brink, and P. J. Kelly, 2008, Phys. Rev. Lett. 101 026803.
8. Y. H. Wu, T. Yu, and Z. X. Shen JOURNAL OF APPLIED PHYSICS 108, 071301 (2010)
9. <http://www.acsmaterial.com/product.asp?cid=93&id=111>
10. http://www3.nd.edu/~kamatlab/facilities_spectroscopy.html
11. D. A. Fischer, S. Sambasivan, Z. Fu., D. Yoder, J. Genzer, K. Effimenko, A. R. Moodenbaugh, G. M. Mitchell, and B. M. DeKoven, 8th International Conference on Synchrotron Radiation Instrumentation, San Francisco, 2003.
12. D. A. Fischer and B. M. DeKoven Dow National Synchrotron Light Source Newsletter, November 1996, 10.
13. A. P. Hitchcock and C.E. Brion, J Electron Spectrosc. 18, 1(1980).
14. Sapre, V. B. & Mande, C. Chemical shifts in the K X-Ray absorption discontinuity of arsenic. J. Phys. C: Solid State Phys. 5, 793–797 (1972).
15. J. Schultz, C. J. Patridge, V. Lee, C. Jaye, P. S. Lysaght, C. Smith, J. Barnett, D. A. Fischer, D. Prendergast and S. Banerjee, Nat. Commun., 2011, 2, 372.

Variability in cloud cover at Brookhaven National Laboratory: Impacts on now-casting solar power

Ricky Bhola

Department of Civil Engineering, The City College of New York, New York NY 10031

John Heiser

Environmental Sciences Department, Brookhaven National Laboratory, Upton NY 11973

Abstract

Clouds over a solar plant can result in dramatic fluctuations in power output. In regions such as the Northeastern U.S., where this phenomenon is common, now-casting of clouds is beneficial to promote optimal grid integration of solar power. Using data collected at Brookhaven National Laboratory (BNL) for 2012 and 2013, a normalized clearness index (ϕ) was defined and used to classify the sky condition into five categories. It was determined that the dataset consisted of 9.2% cloudy days, 15% mostly cloudy days, 13.9% partly cloudy/partly sunny days, 26.3% mostly sunny days, and 35.6% sunny days. Of these days 75.8 % of the days have the potential to benefit from now-casting.

I. Introduction

Over the last decade the push for renewable energy has gained support across the globe as a response to mitigate the dependency on fossil fuels. In the United States alone, solar capacity increased from 2,326 MW in 2010 to 12,057 MW as of February 2014; an increase of 418%¹. While solar energy from photovoltaic (PV) arrays is a solution to fossil fuels, its full potential is hindered by irradiance fluctuations which have a direct effect on the output current, the plant efficiency, and the voltage level^{2,3}. Rapid fluctuations in the solar irradiance are caused by passing clouds, which shade PV modules. Depending on how the PV modules are connected, irradiance fluctuations at a single location can force other modules to operate at below-optimal conditions. Lobera and Valkealahti determined that modules connected in a parallel circuit are less prone to losses from irradiance fluctuations than series connected modules⁴. To control the power output of PV during irradiance fluctuations, short term forecasting and response is necessary. Alam et al. proposed a method that employs energy storage to control the rate of change in power output⁵. Huang et al. proposed an algorithm to estimate cloud motion using sky images in order to make short-term irradiation prediction with good accuracy in short time windows⁶.



Figure 1: BNL's meteorological services Solar Base Station located on the roof of Bldg. 490D

In this paper we illustrate the impact clouds have on power output by investigating a day where cloud cover resulted in rapid power fluctuations. In order to present a case for cloud forecasting we will determine if the BNL location exhibits a considerable amount of days in the year that will benefit from cloud forecasting. Using data collected for 2012 and 2013, the days will be categorized based on the sky condition to show days where cloud variability will be a factor in power generation.

II. Data Acquisition

Global horizontal irradiance measurements were collected using a Kipp & Zonen CMP22 pyranometer, which is located at Brookhaven National Laboratory's (BNL) Solar Base Station on the roof of Bldg. 490D (see Figures 1-3). Measurements were recorded at 1-minute resolution by a Campbell Scientific CR3000 datalogger. Irradiance measurements on the Long Island Solar Farm (LISF), also located at Brookhaven National Laboratory, were made using Kipp & Zonen SP Lite2 silicon pyranometers and recorded with the CR3000 at 1-minute resolution. All datasets were checked for outliers and missing information.



Figure 2: Kipp & Zonen SP Lite2 pyranometers at the Solar Base Station in LISF arrangement



Figure 3: Kipp & Zonen SOLYS-2 sun tracker with mounted CMP22 pyranometer and CGR 4 pyrgometer at the Solar Base Station

A. Northeastern U.S.- BNL

The Northeastern U.S. does not exhibit predominant clear sunny days year round. The annual average radiation for the Northeast ranges from 3-4 kWh/m²/day while the Southwest average approximately 6-7 kWh/m²/day. For this reason the Northeast presents a challenge for large PV plants and PV integration. LISF is the largest generator in the Northeastern region with a capacity of 32MW; a fraction compared to the largest plant in the Southwest.

In order to integrate larger PV plants to the region, the issue of irradiance fluctuations has to be addressed. The power generated by LISF is a small amount compared to the power provided by the grid, therefore power fluctuations at the LISF does not have an impact on consumers. On the other hand, a larger plant will generate a significant amount of power and will result in larger fluctuations and more impact on the grid. The severity of this issue is illustrated in Figure 4 using data from LISF and the Solar Base Station from June 23, 2014. A zoomed view is presented in Figure 5, which shows the drastic drop in irradiance over a very short time frame. Within the first minute irradiance level drops by 60% and an additional 20% within the second minute at the Solar Base Station, similar values are reported for LISF Powerblock 5.

Over the duration of the first clouds, all 25 powerblocks, spanning 200 acres, reported a drastic drop in irradiance within 1-2 minutes. Figure 6 shows an irradiance plot of eight (8) locations at the LISF reporting rapid fluctuations. A Total Sky Imager (TSI) at Powerblock 5 captures the cloud image at 10:54 AM as illustrated in Figure 7.

PV plant size and capacity will influence how the plant deals with fluctuations. As with the LISF, fluctuations are insignificant, as the grid compensates loss. Integration of larger PV plants requires backup generators or external power input to compensate

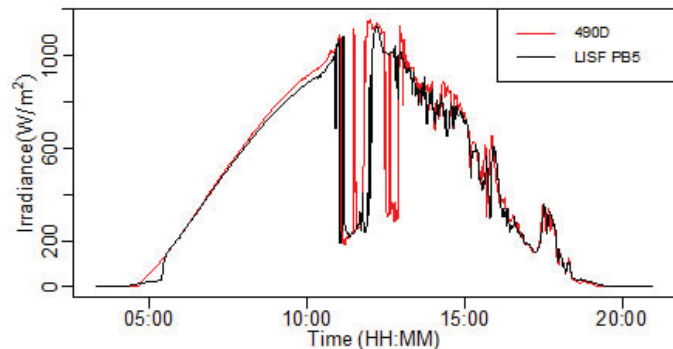


Figure 4: Irradiance plot at the Solar Base Station and LISF on June 23, 2014.

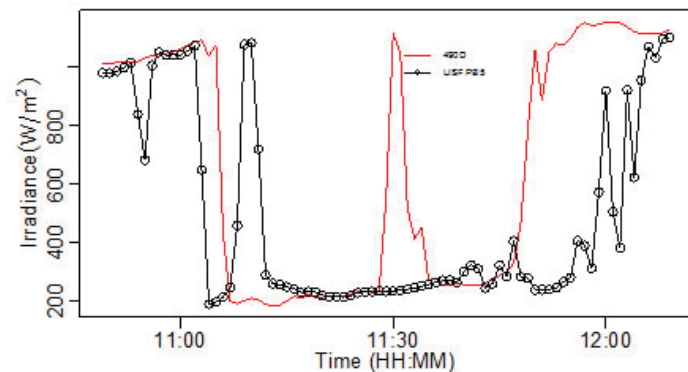


Figure 5: Irradiance plot showing time window from 10:50 AM – 12:10 PM

the grid when sky conditions are poor. These generators need to be online and operational at a moment's notice. Operating a PV plant with a backup generator running full time is not economical therefore forecasting poor sky condition is needed. This can be accomplished using cloud now-casting. The critical component for now-casting is the prediction window which should optimally be longer than the time required to get the generator online. Algorithms that can make accurate predictions for 10-15 minutes into the future are generally preferred over 1-2 minute prediction windows.

Solar energy, as the major power producer for a region, is only a feasible option if the region contains a significant number of sunny days in the year and grid stability can be maintained. The following section detail the solar instabilities associated with the Northeast, specifically, Long Island, NY.

III. Analysis

A. Solar Constant

In order to determine the radiation received by the earth at specific latitudes and longitudes, the incoming radiation normal to the outer atmosphere must be known. This radiation density varies during the year as the distance between the earth and sun changes. The current accepted value is 1367 W/m² with an error of 1% [8].

B. Sun Angle

The sun's elevation angle during the day is a function of the time, location, and elevation at which it is to be determined. Dr.

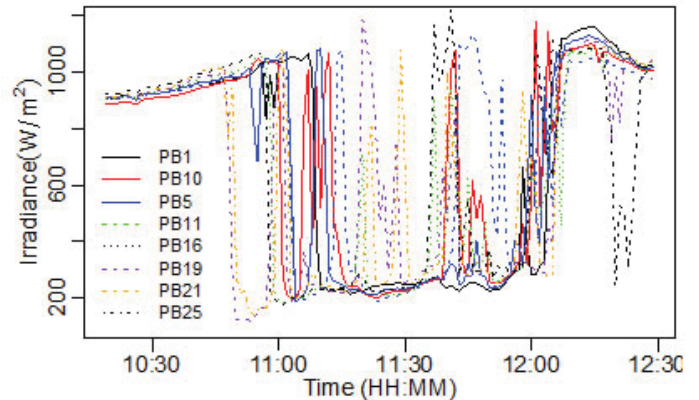


Figure 6: Eight locations on the LISF spanning 200 acres reporting irradiance fluctuations.



Figure 7: TSI image of first clouds covering the sun at LISF Powerblock 5.

Alessandra Colli (BNL) and Dr. Dong Huang (BNL) provided these values (private correspondence). Location parameters used for the BNL location were 40°52'N, 72°53'W, 26.5 meters above sea level, and UTC -5.

C. Extraterrestrial Irradiance

The extraterrestrial irradiance normal to the surface can be calculated using the solar constant and the elevation angle of the sun in the form of equation 1.

$$I = 1367 \left[\text{W} / \text{m}^2 \right] \sin(\theta_e) \tag{1}$$

Where I is the extraterrestrial irradiance and θ_e is the sun's elevation angle.

D. Sky Condition

As the solar radiation travels through the atmosphere, it's power intensity decreases. This is due to scattering and absorption by air molecules, ozone, mixed gases, water vapor, and clouds 9. Of these mechanisms, cloud cover presence is the major factor in decreasing irradiance to the surface. For this analysis we will associate losses in irradiance with cloud presence. The sky condition for a day will be determined using a daily clearness index, which is described by equation 2.

$$k_t = \sum_{j=1}^{1440} I_{[j]} / \sum_{j=1}^{1440} I_{e[j]} \tag{2}$$

Where k_t is the daily clearness index, I is the measured irradiance, and I_e is the extraterrestrial irradiance, both at 1-minute resolution.

The value of the clearness index has an upper limit due to atmospheric loss. Colli et al. also reported this in a similar study 10. As a result, the values obtained for k_t will be normalized by equation 3.

$$\phi = k_t / \max(k_t) \tag{3}$$

Where ϕ is the normalized value.

Normalized clearness index will be grouped into five categories ranging from cloudy to sunny. The categories and parameters are presented in table 1.

Table 1: Sky condition classification

Category	
Cloudy	0 – 0.20
Mostly Cloudy	0.20 – 0.40
Partly Cloudy/Sunny	0.40 – 0.60
Mostly Sunny	0.60 – 0.80
Sunny	0.80 – 1.0

IV. Results

The normalized value for ϕ as it varies during the course of two years is illustrated in Figure 8. The time series plot shows a dense band between $\phi = 0.6-1.0$ which indicates that most of the values fall in the sunny and mostly sunny categories. However the plot shows large variations between categories, which indicated that the day-to-day sky conditions were highly variable. On the yearly scale, the time plot displays a periodic trend that indicates that sky cover is also dependent on the time of the year. In Figure 9 both years are overlaid to illustrate this trend. Winter and spring exhibits days with high values, followed by a dip in the summer before increasing in the fall.

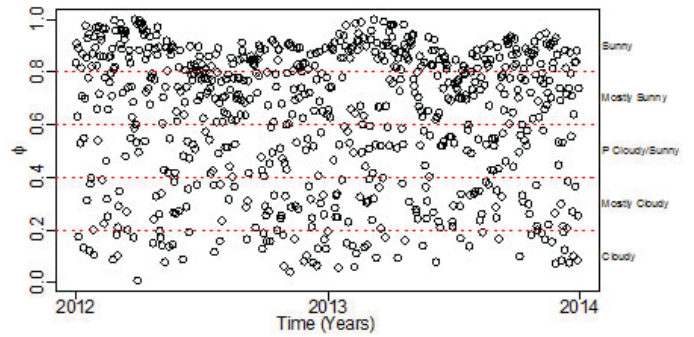


Figure 8: Normalized clearness index for 2012 and 2013

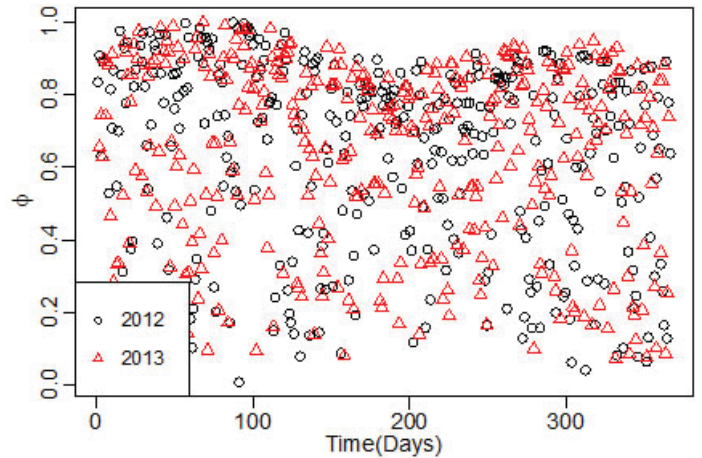


Figure 9: Yearly normalized clearness index for 2012 and 2013 data sets.

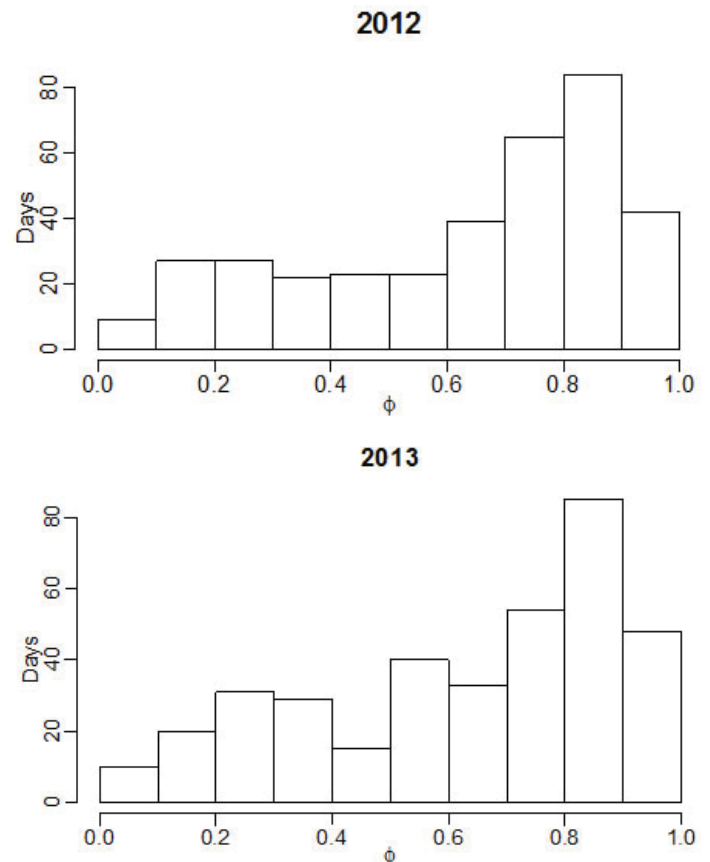


Figure 10: Histogram of normalized clearness index for 2012 (top) and 2013 (bottom)

Histograms in Figure 10-11 illustrates that each year has a large number days with high values. The mean and standard deviation for 2012 are 0.630 and 0.266, while for 2013 the mean is 0.630 and standard deviation is 0.262. Variation between the days of each year is almost consistent with the other year. From Figure 10, both histograms exhibit similar profiles. The variation as calculated by the standard deviation only distinguishes them by 0.04 difference. Since this is a small sample (2 years) a conclusion cannot be reached in terms of annual variability.

Monthly and seasonal variations are illustrated by the bar plots in Figure 12-13. The plot shows that as the number of days categorized as sunny are minimum during the months July and August, however the number of mostly sunny days is maximum.

V. Discussion

During a cloudy day or mostly cloudy day utilities will need to supplement the loss of PV power with an on-site backup plant (e.g., propane powered generating facility) or from an external source (e.g., purchased power). This type of event is illustrated in the discussion on Northeastern U.S. (see figures 4-7). In terms of now-casting, partly sunny/partly cloudy, mostly sunny, and sunny days are of interest because they represent days where significant fluctuations can occur and will benefit from cloud now-casting. Cloudy and partly cloudy dates are not as significant since the backup power to compensate for PV generation loss will be required continuously and grid instability is minimal.

The analysis reveals that there is a large number of days in the year that fall into the ‘partly sunny/partly cloudy’ and ‘sunny days’. The mean standard deviation of 0.264 is greater than the normalized clearness index increment; this illustrates how variable day-to-day conditions can be. Never the less, it was determined that the sample dataset contained 9% cloudy days, 15% mostly cloudy days, 13.9% partly cloudy/partly sunny days, 26.3% mostly sunny days, and 35.6% sunny days. These results indicate that approximately 76% of the days have the potential to benefit from now-casting.

VI. Conclusions

Irradiance data from BNL for 2012 and 2013 were analyzed to describe the daily condition of the sky. Using the daily clearness index, sky conditions were grouped into 5 categories ranging from cloudy to sunny. It was determined that approximately 76%

of the days have the potential to generate significant amounts of solar power. These days are also significant because they also represent the days when the potential for power fluctuations due to clouds is high. Now-casting models, which exhibit larger prediction windows, would allow compensation of these fluctuations in power production.

VII. Acknowledgments

The author would like to thank the following persons for their assistance:

Paul Kalb, Terrence Sullivan, Alessandra Colli, Dong Huang, and Scott Smith

This project was supported in part by the U.S. Department of Energy, Office of Science, Office of Workforce Development for Teachers and Scientists (WDTS) under the Science Undergraduate Laboratory Internships Program (SULI).

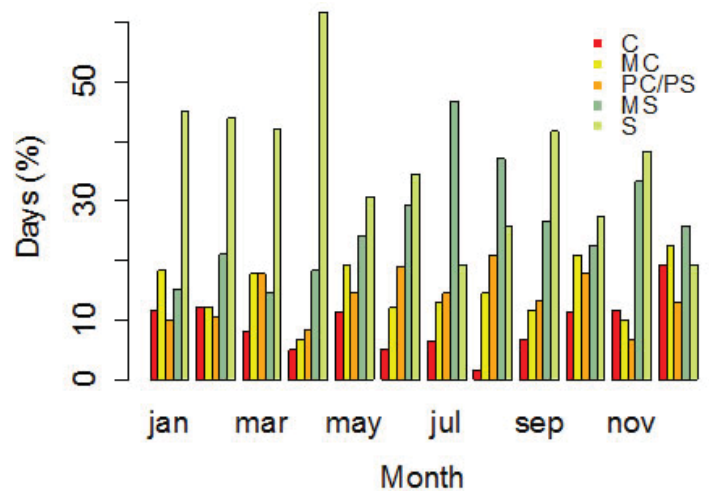


Figure 12: Monthly bar plot indicating percentage days for each sky condition category. C = cloudy; MC = mostly cloudy; PC/PS = partly cloudy/partly sunny; MS = mostly sunny; S = sunny.

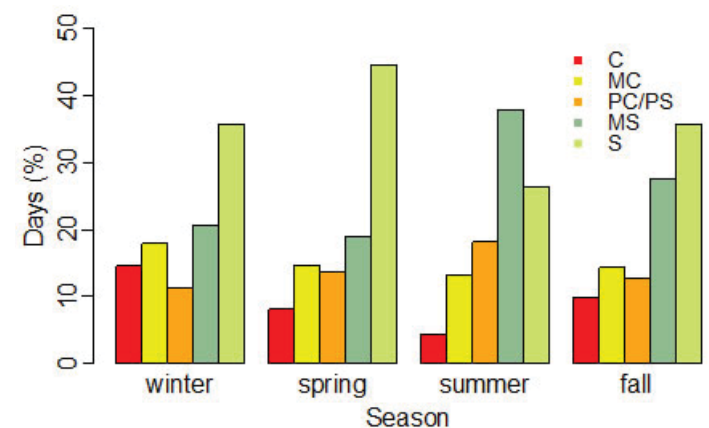


Figure 13: Seasonal bar plot indicating percentage days for each sky condition category. C = cloudy; MC = mostly cloudy; PC/PS = partly cloudy/partly sunny; MS = mostly sunny; S = sunny.

2012 & 2013

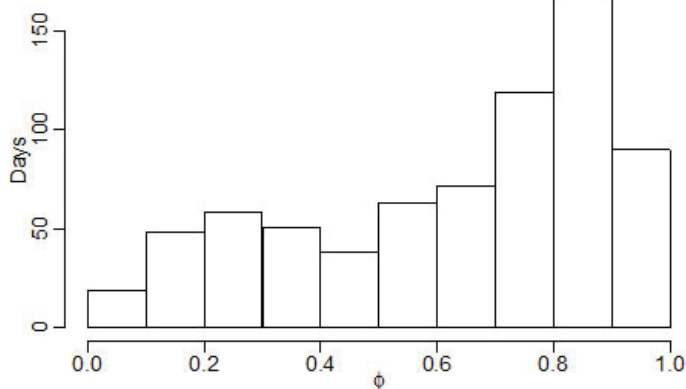


Figure 11: Cumulative histogram for 2012 and 2013

VIII. References

- 1 U.S. Energy Information Administration, "April Electricity Monthly Update," 2014 (July), (2014).
- 2 L. El Chaar and N. El Zein, "Review of photovoltaic technologies," *Renewable and Sustainable Energy Reviews* 15 (5), 2165-2175 (2011).
- 3 J. Samimi, E. A. Soleimani and M. S. Zabihi, "Optimal sizing of photovoltaic systems in varied climates," *Solar Energy* 60 (2), 97-107 (1997).
- 4 D. T. Lobera and S. Valkealahti, in 4th IEEE International Symposium on Power Electronics for Distributed Generation Systems, (IEEE, Rogers, Arkansas, 2013) pp. 1-7.
- 5 M. J. E. Alam, K. M. Muttaqi and D. Sutanto, "A Novel Approach for Ramp-Rate Control of Solar PV Using Energy Storage to Mitigate Output Fluctuations Caused by Cloud Passing," *Energy Conversion, IEEE Transactions on* 29 (2), 507-518 (2014).
- 6 Hao Huang et al., in Smart Grid Communications (SmartGridComm), 2013 IEEE International Conference on, (IEEE,2013) pp. 696-701.
- 7 National Renewable Energy Laboratory, "Global Horizontal Solar Radiation- Annual," 2014 (July), (2005).
- 8 Zekai Sen, *Solar energy fundamentals and modeling techniques*, (Springer, 2008), pp. 66-67.
- 9 Marius Paulescu et al., *Weather modeling and forecasting of PV systems operation*, (Springer, 2013), pp. 32-33.
- 10 A. Colli et al., in Photovoltaic Specialists Conference (PVSC), 2013 IEEE 39th, (IEEE, 2013) pp. 2295-2300.

Determination of Equilibrium constant for cation-paired anions using the Laser-Electron Accelerator Facility

Kierra Brown

Chemistry, Spelman College, Atlanta, GA 30312

John Miller

Chemistry Department, Brookhaven National Lab, Upton, NY 11973

Abstract

The Laser-Electron Accelerator Facility (LEAF) at Brookhaven National Laboratory utilizes a laser to determine the charge transport of polymer electronic materials. These materials have properties which make them a possible source for solar products. The motivation for this experiment is understanding the difference in electrochemical redox properties of conjugated polymers and molecules. The molecule fluorene (FLA) and a conjugated polymer poly (3-decylthiophene) (p3DT) are chemicals with very similar reduction potentials resulting in either being able to gain or lose electrons in solution. Conjugated polymers display charge transport and potential for conduction. The purpose of this experiment is to determine the equilibrium constant of the reaction between FLA and p3DT in the presence of a given concentration of an electrolyte Tetrabutylammonium hexafluorophosphate (TBAPF₆). The results indicate that the equilibrium constant increases linearly with concentration increases of the electrolyte. I obtained an understanding of the instrumentation used in electrochemistry, such as the glove box, LEAF, and titration experiments and how to conduct myself in a laboratory environment.

I. Background

A. Polymeric Electronic Materials

Organic electronic materials are small organic molecules or polymers that display electronic properties such as conductivity. Semiconducting polymer materials have disordered systems with both essential and nonessential parameters. Semiconducting polymers are conjugated polymers composed of alternating pi bonds, π bonds, which enable charge transfer to occur. These polymers are characterized by a succession of conjugated alternating single and double bonds.¹ Electrical and optical properties of the materials depend on parameters such as π -electron delocalization, processing of materials, band gap, inter-chain interaction, morphology, and carrier density. These conjugated polymers electrical properties can be analyzed using dispersion techniques and organic synthesis. The benefits of organic electronics are their low cost compared to traditional inorganic electronics.

Our experiment uses the π -electron delocalization to analyze the charge transfer and determine the equilibrium constant in a system with constant concentration of polymer and molecule with similar reduction potentials while varying the amount of electrolyte. Delocalization results in greater stability for the molecule due to the distribution of electrons which creates charge distribution. In addition, while doing spectroscopy experiments delocalization of electrons results in conductivity. The reduction potential is the propensity of a chemical species to be reduced.

The presence of an energy gap between the filled and empty bands results in a semiconducting nature to the polymer. The separation between highest occupied molecular orbital (HOMO) and lowest occupied molecular orbital (LUMO) is considered the band gap of organic electronic materials. The band gap is typically in the range of 1–4 eV.² The delocalized π -electrons are primarily responsible for the electrical and optical properties in these systems enabling the polymer to have organic solar cell characteristics.

B. Organic Solar cells and Photovoltaic cells

An organic solar cell uses organic electronics that deals with conductive organic polymers or small organic molecules for light absorption and charge transport to attain electricity from sunlight by the photovoltaic effect.³ Conductive organic polymer p3DT is analyzed during the experiment. Due to the optical absorption coefficient of organic molecules being high, a large amount of light can be absorbed with a small amount of materials. A photovoltaic cell is a specialized semiconductor diode that converts visible light into direct current (DC) electricity. Some photovoltaic cells can also convert infrared (IR) or ultraviolet (UV) radiation into DC. A common characteristic of both the small molecules and polymers (Fig. 1) used in photovoltaics is that they all have large conjugated systems.⁵ In these conjugated systems are composed of hydrocarbon electrons.

These hydrocarbons' electrons pz orbitals delocalize and form a delocalized bonding π orbital with a π^* anti-bonding orbital. The delocalized π orbital is the highest occupied molecular orbital HOMO, and the π^* orbital is the lowest unoccupied molecular orbital LUMO.⁴ Upon absorption of a photon, an excited state is created and confined to a molecule or a region of a polymer chain.

Operation of Organic Solar Cell

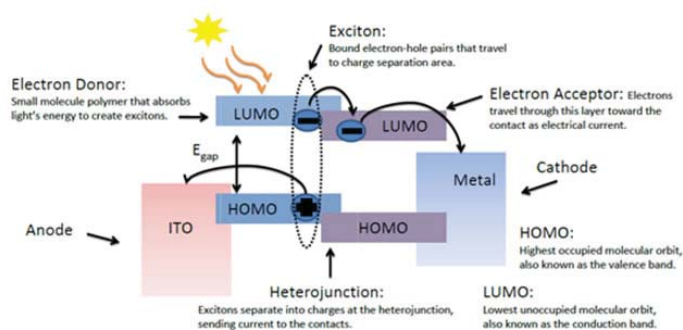
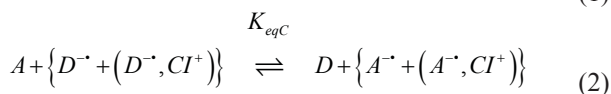


Figure 1

C. Dissociation and Equilibrium Constants

The equilibrium constant (Keq) in chemistry is calculated by taking the value of the reaction quotient when the reaction has reached a state of equilibrium. Specifically in polymeric electron material experiments Keq is shown in Equation (1) with the standard reaction of an electron donor (D), acceptor (A), and cation (CI⁺). Secondly, the addition of the electrolyte or cation results in a more specific Keq equation in reference to the cation in Equation (2). The resulting equilibrium constant derivative in Equation (3) is used to calculate the final Keq. The dissociation constant (Kd) a quantity expressing the extent to which a particular substance in solution is dissociated into ions, equal to the product of the concentrations of the respective ions divided by the concentration of the undissociated molecule.⁷ The general equations for determining Kd for the D and A are illustrated in Equation (4) and (5).



$$K_{eqC} = \frac{[A^{\cdot-} + (A^{\cdot-}, CI^+)] [D]}{[A] [D^{\cdot-} + (D^{\cdot-}, CI^+)]} = \frac{([A^{\cdot-}] + [(A^{\cdot-}, CI^+)]) [D]}{[A] ([D^{\cdot-}] + [(D^{\cdot-}, CI^+)])} \quad (3)$$

$$K_{dd} = \frac{[D^{\cdot-}] [CI^+]}{[(D^{\cdot-}, CI^+)]} \quad (4)$$

$$K_{da} = \frac{[A^{\cdot-}] [CI^+]}{[(A^{\cdot-}, CI^+)]} \quad (5)$$

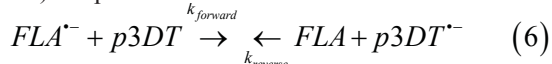
D. LEAF Radiolysis

The instrumentation used to evaluate the polymeric materials is LEAF. The purpose of the laser system in LEAF is to provide a 3-20 picoseconds-long pulse of 266 nm light to excite photoelectrons off of the magnesium metal photocathode inside the radio-frequency electron gun.⁶ Temporal and spatial profiles of the accelerated electron pulse are determined by the characteristics of the excitation laser pulse. A mechanical shutter is used to select pulses for transmission to the photocathode electron gun. Key features of LEAF are the one-thousand-times shorter electron pulse width, the increased electron energy, and the picoseconds synchronization of the laser and electron pulses.

II. Methods

A. Overview of Study

Radiolysis of the solvent used Tetrahydrofuran (THF) produces a high yield of electrons that can react at a bimolecular rate with solutes FLA and p3DT in solution. By preparing THF solutions with the concentration of FLA being significantly greater than the concentration of p3DT, guarantees that most of the electrons will be captured by FLA and basically none by the p3DT. The Keq shown in Equation (6) is the resulting reaction that follows. With the presence of electrolyte cation ions FLA anions (FLA⁻) produced in the reverse reaction while p3DT anions (p3DT⁻) are produced in the forward direction.



In this LEAF experiment, several solutions were prepared such that the concentration of TBAPF₆ was varied in solution by titration with 0.78 mM TBAPF₆ solution. The concentration of

p3DT was fixed at 20 μM and FLA concentration at 1 mM respectively. A wavelength of 1629 nm was selected to analyze the p3DT⁻ due to FLA⁻ not absorbing at this wavelength. The determination of the fraction of p3DT⁻ relative to the total yield of p3DT⁻ when electrolyte is not present in solution. The expected Keq distribution is shown in Graph (1).

B. Real-world Experiment

A titration experiment involving the TBA⁺ solution as titrant into 1.3 mL of a 20 μM p3DT solution in THF, was carried out to determine the equilibrium and dissociation constant. The concentration of TBA⁺ in each titration step was calculated based on the known initial concentration and volume dispersed into the p3DT and FLA solution in Table (1)(see appendix). Using LEAF radiolysis absorption data was compiled at various concentrations until 100 μL of TBAPF₆ was added to the p3DT and FLA solution. Once the data for the respective titrations was collected the absorbance of the p3DT⁻ was measured at 20 milliseconds.

III. Data and Results

The data was compiled into Table (2) from the radiolysis absorbance transients in Graph (2) for trial 1. The range of the concentration used in reference to TBAPF₆ concentration were 0 μM, 5.95 μM, 8.90 μM, 14.72 μM, 20.45 μM, 28.89 μM, 39.85 μM, and 50.50 μM. The correlating concentration for TBA⁺ for each TBAPF₆ concentration was calculated by using Equation (7). Kd for TBAPF₆ was assumed to be 7.8 × 10⁵ due to the solvent THF having a similar dielectric constant of ε (THF) = 7.58 to ε (DME) = 7.2.⁸ The maximum absorbance of the p3DT⁻ was assumed to be at 18 mAbs. The constant fraction of the concentration of FLA/p3DT was 25. The fraction of p3DT⁻ to FLA⁻ fraction was calculated by using Equation (7). Keq was then calculated by using Equation (3).

In trial 2 the polymer was measured with and without the molecule with varied concentrations of electrolyte. The range of the concentration used in reference to TBAPF₆ concentration were 0 μM, 5.95 μM, 11.82 μM, 17.59 μM, 39.85 μM, 50.50 μM, and 55.71 μM. The goal for this trial was to accurately determine the fraction of p3DT⁻ to FLA⁻ by observing the effect on absorbance with and without the presence of FLA. The absorbance spectra in Graph (4) and Graph (5) display the results. To find the fraction of to p3DT⁻ to FLA⁻ at each concentration both absorbance spectra were plotted then corrected so that they overlap using IGOR pro software. The percentage of correction correlated to the percentage of p3DT⁻ in solution. To determine the amount of FLA⁻ the percentage of p3DT⁻ was subtracted by one.

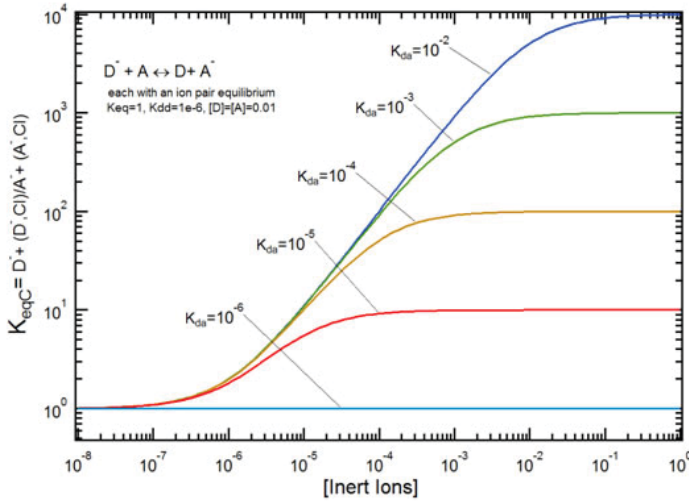
The results indicate that the equilibrium constant increases linearly with concentration increases of the electrolyte. As the concentration of electrolyte was added the rate of decay of the p3DT decreases meaning that reaction favors the formation of p3DT⁻ in the forward direction shown in Graph (2), Graph (4), and Graph (5). Graph (3) displays the Keq as a function of time in μs for trial on and Graph (6) for trial 2. The shape of the result has a similar curvature and orientation in Graph (1) suggesting that the experiment supports the Keq assumption for the effect of polymeric materials with the addition of an electrolyte. In both experiments exposure to oxygen was observed, but we assumed that there was minimal contamination due to the data being reproducible.

IV. Conclusion and Recommendations

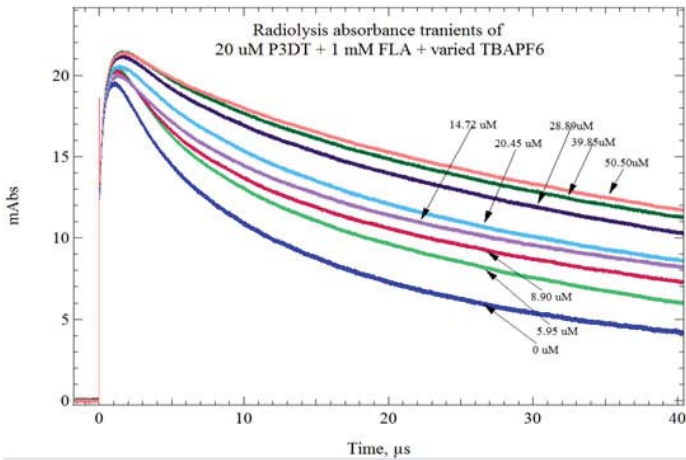
When compared to the general model the experiment supports the linearity of the Keq model in Graph (1). As the concentration of electrolyte increases the formation of polymer anions is favored and the exponential decay rate decreases. Further studies are needed to ensure the precision and accuracy of the data collected during these trials. In the future, additional experiments will need to be conducted to determine Kd. Possibly one way to

interpret the data with further experimentation may include analyzing the rates of exponential decay at each concentration then determining the Keq and Kd using that information.

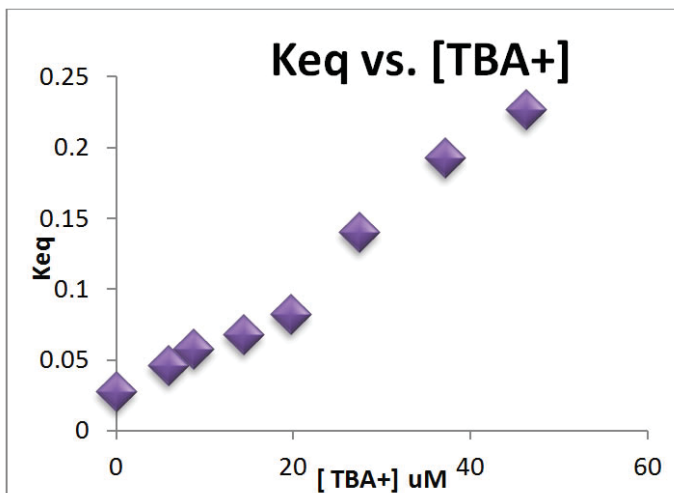
Graph 1.



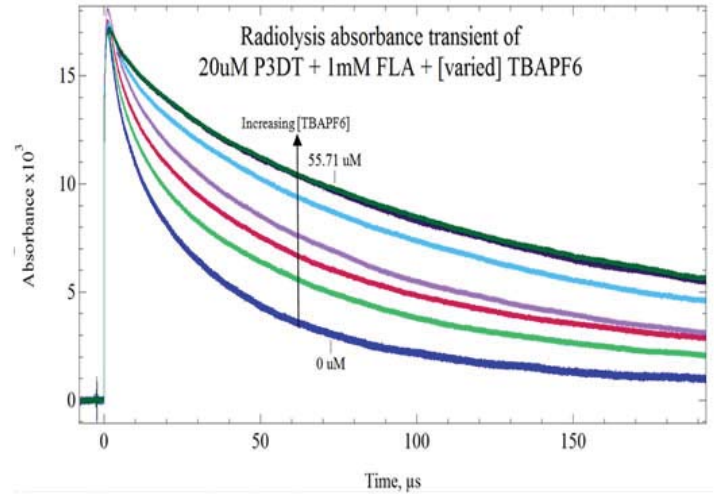
Graph 2.



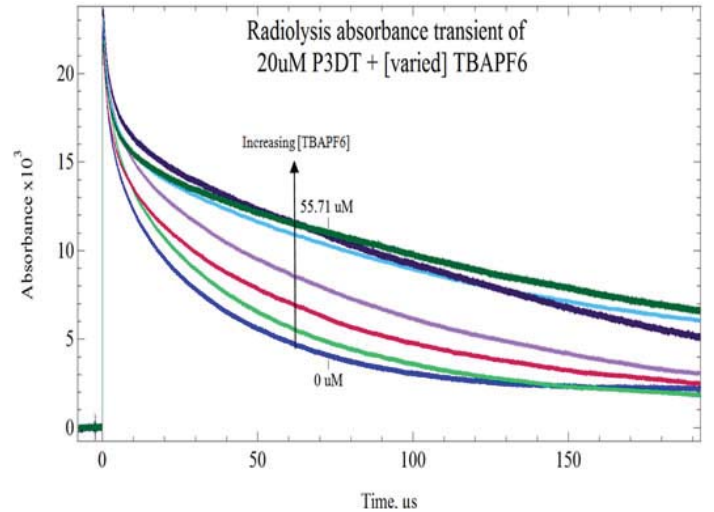
Graph 3.



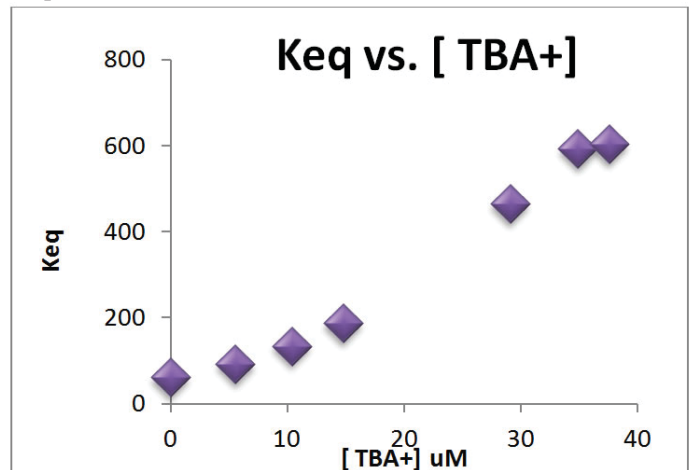
Graph 4.



Graph 5.



Graph 6.



VII. Appendix

Table (1)

starting conc of salt in syringe (M)	7.80E-04	[FLA] (mM)	1
Starting volume of THF in cell (μl)	1300	[p3DT] (uM)	20
Kd salt (M)	7.80E-05		
Amt of dispersed salt soln (μl)	0	Total soln volume (μl)	[salt] (M)
			[TBA ⁺](M)
	0	1300	0.000E+00
	5	1305	2.989E-06
	10	1310	5.954E-06
	15	1315	8.897E-06
	20	1320	1.182E-05
	25	1325	1.472E-05
	30	1330	1.759E-05
	35	1335	2.045E-05
	40	1340	2.328E-05
	45	1345	2.610E-05
	50	1350	2.889E-05
	55	1355	3.166E-05
	60	1360	3.441E-05
	65	1365	3.714E-05
	70	1370	3.985E-05
	75	1375	4.255E-05
	80	1380	4.522E-05
	85	1385	4.787E-05
	90	1390	5.050E-05
	95	1395	5.312E-05
	100	1400	5.571E-05

Excel calculations for trial 1 of the concentration of TBA⁺ during the titration calculated from the starting concentration of TBAPF₆.

Table 2.

[TBAPF ₆] μM	[TBA ⁺] uM	Abs [p3DT ^{•-}]	[p3DT ^{•-}]/[FLA ^{•-}]	[FLA]/[P3DT]	K _{eq} calculated
0	0	0.0073	0.682242991	25	0.02728972
5.95	5.88	0.0096	1.142857143	25	0.045714286
8.9	8.75	0.0106	1.432432432	25	0.057297297
14.72	14.31	0.0113	1.686567164	25	0.067462687
20.45	19.68	0.0121	2.050847458	25	0.082033898
28.89	27.39	0.014	3.5	25	0.14
39.85	37.10	0.0149	4.806451613	25	0.192258065
50.5	46.23	0.0153	5.666666667	25	0.226666667

V. References

¹ Jaiswal, Manu, and Reghu Menon. "Polymer electronic materials: a review of charge transport." *Polymer International* 55, no. 12 (2006).

² Che, Yanke, Aniket Datar, Xiaomei Yang, Tammene Naddo, Jincal Zhao, and Ling Zang. "Enhancing one-dimensional charge transport through intermolecular π -electron delocalization: conductivity improvement for organic nanobelts." *Journal of the American Chemical Society* 129, no. 20 (2007).

³ Wöhrle, Dieter, and Dieter Meissner. "Organic solar cells." *Advanced Materials* 3, no. 3 (1991).

⁴ Günes, Serap, Helmut Neugebauer, and Niyazi Serdar Sariciftci. "Conjugated polymer-based organic solar cells." *Chemical reviews* 107, no. 4 (2007).

⁵ Hoppe, Harald, and Niyazi Serdar Sariciftci. "Organic solar cells: An overview." *Journal of Materials Research* 19, no. 07 (2004).

⁶ Wishart, James F., Andrew R. Cook, and John R. Miller. "The LEAF picosecond pulse radiolysis facility at Brookhaven National Laboratory." *Review of scientific instruments* 75, no. 11 (2004).

⁷ Smith, Joseph Mauk. "Introduction to chemical engineering thermodynamics." PhD diss., Rensselaer Polytechnic Institute, 1975.

⁸ K. Murakoshi, G. Kano, Y. Wada, S. Yanagida, H. Miyazaki, M. Matsumoto, and S. Murasawa, *Journal of Electroanalytical Chemistry*, 396,27 (1995).

VI. Acknowledgements

This project was supported in part by the U.S. Department of Energy, Office of Science, Office of Workforce Development for Teachers and Scientists (WDTS) under the Science Undergraduate Laboratory Internships Program (SULI).

Optimization of beam-line control for the energy recovery linac project

Taylor Campbell

College of Engineering and Applied Sciences, Stony Brook University, Stony Brook, 11790

George Mahler

Collider Accelerator Department, Brookhaven National Laboratory, Upton NY 11973

Abstract

Brookhaven National Laboratory is currently working to transform the Relativistic Heavy Ion Collider (RHIC) into an electron-ion colliding ring titled eRHIC. Now undergoing its early stages of development, the engineers and physicists in charge of eRHIC are building the Energy Recovery Linac (ERL), a scaled-down prototype of the ring for design and testing purposes. ERL uses a polarized e-gun to inject beams of electrons into its ring shaped pipeline while high-powered, super-conducting magnets accelerate, steer, and focus the beams. Our task has been to provide engineering support to optimize this beam control by updating and maintaining ERL's complex system of magnets. Therefore, as the project has developed we have investigated several problematic magnetic components and performed proper reinstallations to restore the ring to full capacity. Additionally, I was personally tasked with creating a new component to solve an issue with insufficient magnetic field near the beam injection site. After diagnosing the problem, I chose to construct a solenoid generating the amount of magnetic field necessary to enhance the focus of our electron beams. Using computer design software and finite element analysis, I have been able to create a solenoid which, when installed, generates a magnetic field of 63.79 Gauss/centimeter to help improve the quality of our beams and collisions. Through my work here at BNL I have become familiar with the design and administrative processes associated with the field of mechanical engineering. The experience of independently creating a component for the particle accelerator has exposed me to not only the common engineering texts, but also numerous brands of design and analysis software, including Creo Parametric, AutoCad, Mechanical, and Finite Element Method Magnetics (FEMM). All of this widespread training which I have received will help prepare me for a future in Mechanical Engineering.

I. Background

The Relativistic Heavy Ion Collider at Brookhaven National Laboratory is a machine which accelerates and collides beams of particles, specifically ions, at near light speed. These particle beams travel around the 2.5 mile RHIC ring maintained in shape and path by strategically placed magnetic components and their induced fields. To deter the particles from natural scattering tendencies, magnets known as solenoids, quadrupoles and sextupoles are used to refocus the beam while dipole magnets steer it along the necessary path. This beam-controlling system of magnets is vital to the proper functioning of such a precise machine as RHIC; that is why as RHIC transitions into its new role as an electron-ion collider, the construction and configuration of magnetic components is a high priority.¹

II. II. Assignment

Still in its early stages of development, the electron-ion collider "eRHIC" is being designed and tested in the form of a small prototype called Energy Recovery Linac. Our task in this process has been to maintain and update the vital system of magnets used to control the ERL's particle beams during experimentation. To maintain existing hardware, we have performed systematic checks of the various ring components; this process has involved the comparison of Gauss-meter field readings with preliminary calculations. Any unexpected readings of magnetic properties resulted in further investigation of problem areas where construction and installation needed to be correctly reconfigured.

Aside from maintaining the current field-producing magnetic components, I was also tasked with the creation of a new device to increase magnetic field in an area where physicists found the need for more beam control. Once the challenge and possible solutions were contemplated I chose to design a solenoid which would induce a centrifugal force toward the central axis of the beam line to enhance the focus of our electron beams.²

III. Design and Placement

In terms of placement, physicists had requested that the field-inducing component be placed in close proximity to the beam injection site, which left only two eligible placement options to consider. The two locations being considered for solenoid placement both possessed positive and negative aspects which had to be considered as I decided which would be optimal. Option one, the location furthest from the beam ejection site, was advantageous because it had limited physical interference by surrounding equipment. However, it was determined that option two, the nearer location, would give physicists the best ability to utilize the solenoid's magnetic field to manipulate beams near their site of origin. The disadvantage of choosing placement nearer the beam injection site was the presence of multiple pieces of equipment which would limit the possible solenoid dimensions; this meant that my design could not solely rely on increasing coil size to optimize field strength. Keeping this limitation in mind, I designed my solenoid with the goal of optimizing field strength through alternative methods.

Central to my solenoid design was a main cylinder, supporting the wound coil through which current is to be run. This hollow cylinder was constructed of Aluminum 6061-T6 material and separated into two halves joined together by mating holes and spring pins. Shelled at different thicknesses, the component could accommodate the need to surround three different widths on the beam pipe; a deeper shell near the right end of the cylinder would help stabilize the piece by allowing for a solid grip on both the wide flange to the right and more narrow bellows to the left. As for length, the cylinder was designed to be as long as possible while still maintaining the ability to fit within the designated

A. Structural analysis:

For my main structural analysis, the computer software Mechanica was used to test how well the solenoid walls could support a multi-layered coil. Results of the testing showed that our walls made of steel material would remain structurally sound even under an obscene coil weight of 200 pounds. The negligible stress values produced by the program proved the structure's excellent strength.

B. Magnetic field analysis:

Additional testing was done using a program called Finite Element Method Magnetics (FEMM), to determine the amount of magnetic field that the solenoid could produce. Once it was determined that the solenoid was capable of producing 63.79 Gauss/centimeter of magnetic field, physicists were called upon to review and approve the design. Upon approval, drawings were sent to the machine shop and the process of fabrication began.

It will now be some time before the product is fully fabricated, implemented and tested, but sadly my internship will end before the process is complete. Nevertheless, the magnetic field results we expect to obtain will surely help improve focus in the beam line and positively impact the ERL project as a whole.

V. References

¹McNulty-Walsh, K. (2012, June 12). eRHIC: Colliding Electrons with Ions at RHIC. . Retrieved June 26, 2014, from <http://www.bnl.gov/rhic/news2/news.asp?a=3145&t=today>

²Kumar V., "Understanding the focusing of charged particle beams in a solenoid magnetic field," *American Journal of Physics* 77(8), 737-741 (2009).

VI. Acknowledgements

This project was supported in part by the Brookhaven National Laboratory (BNL), Collider Accelerator Department under the BNL Supplemental Undergraduate Research Program (SURP).

Planning the decommissioning procedure for the PHENIX collaboration

Matthew Chiulli

Physics, Binghamton University, Binghamton, NY 13902

Don Lynch

Physics, Brookhaven National Laboratory, Upton, NY 11793

Rich Ruggiero

Physics, Brookhaven National Laboratory, Upton, NY 11793

Abstract

The PHENIX detector at the Relativistic Heavy Ion Collider (RHIC) is undergoing a major upgrade known as sPHENIX which enables a compelling jet physics program to address fundamental questions about the nature of the strongly coupled quark-gluon plasma. sPHENIX also provides the foundation for a future detector able to exploit the novel physics opportunities of a planned electron-ion collider at RHIC. In order for the PHENIX detector to undergo the upgrade for sPHENIX, it must first be decommissioned in an organized and engineered manner. The PHENIX detector is to be shut down for this upgrade, leaving the Interaction Region accessible for any decommissioning purposes. The records of installation procedures, decommissioning procedures, time of decommissioning, work permits, and drawings must all be organized but most importantly the lifting fixtures must all be located to make a more efficient decommissioning process. Once identified, the hand drawings of the lifting fixtures are to be converted into electronic form using AutoCAD for an improved archive. Organization of the records of the current PHENIX detector and drawings of lifting fixtures that may be used will be continued, along with physically locating the lifting fixtures that have the potential of aiding in the decommissioning procedure. Planning the decommissioning procedures for the PHENIX detector will help improve my capabilities in engineering planning which entails determining the best possible method and sequence for performing any decommissioning project. My work on this project is an important aspect to the Brookhaven National Laboratory community and will aid in the future development of sPHENIX.

I. Introduction

The PHENIX detector is the largest of the four experiments that have taken data at the Relativistic Heavy Ion Collider. The main objective of the PHENIX detector is to investigate high energy collisions of heavy ions and protons, such as the probes of the products of the collisions: electrons, muons, and photons. The overall main object of the PHENIX detector is to collect data, discover and study a new state of matter known as the Quark-Gluon Plasma. The PHENIX detector is composed of multiple different sections which perform a specific role in the measurement of the results of a heavy ion collision. These sections are the East Carriage, Beam pipe, Muon Magnet South, West Carriage, Central Magnet, and the Muon Magnet North. Each section contains several different central arm detectors. The upgrade from PHENIX to sPHENIX plans to address many fundamental questions about the nature of the coupled quark-gluon plasma. Questions such as, what are the minimum size, shape, and temperature requirements

for the formation of droplets of quark-gluon plasma. Most importantly, sPHENIX provides the foundation for a future detector able to exploit the novel physics opportunities of an electron-ion collider at RHIC. The key design parameters for sPHENIX are the introduction of a superconducting magnetic solenoid, electromagnetic calorimeter, hadronic calorimeter, and readout electronics. With the major upgrade to sPHENIX, the main sections of the PHENIX detector must be decommissioned in a structural and organized manner.

II. Methods/Results

With the PHENIX detector decommissioning coming, there will be many different procedures required to structurally disassemble the PHENIX detector. In order to decommission, we need to know how the detectors were installed, what work permits are required, how long it will take, drawings of detectors/lifting fixtures, and most importantly which lifting fixtures were used for each detector. With this being said, a record of the installation procedures, decommissioning procedures, time of disassembly, work permits, and drawings were to be organized and converted from paper file form into electronic form and most importantly, the lifting fixtures that will be needed for decommissioning must be located. These records are to be developed for each of the six different main sections of the PHENIX detector. With the knowledge of how each detector was installed, the decommissioning procedure will be much easier to undertake. Time of disassembly gives a detailed layout of how long each decommissioning procedure will take, giving a structured schedule for required deadlines.

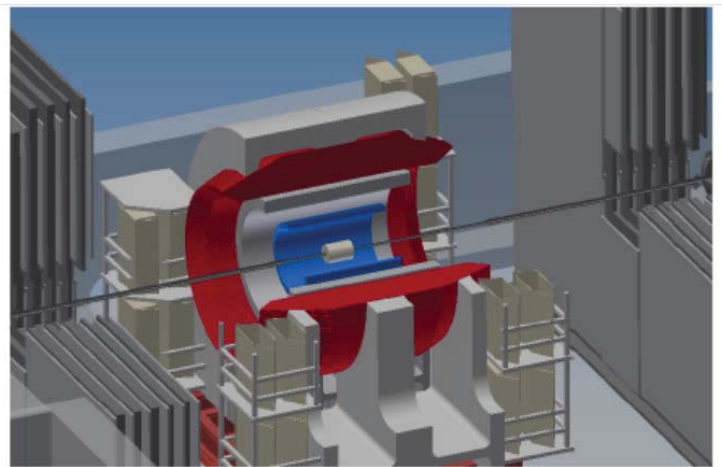


Figure 1: Engineering renderings showing sPHENIX detector concepts. This figure shows the reconfigured VTX tracker, the electromagnetic calorimeter, the superconducting solenoid, and the hadronic calorimeter.

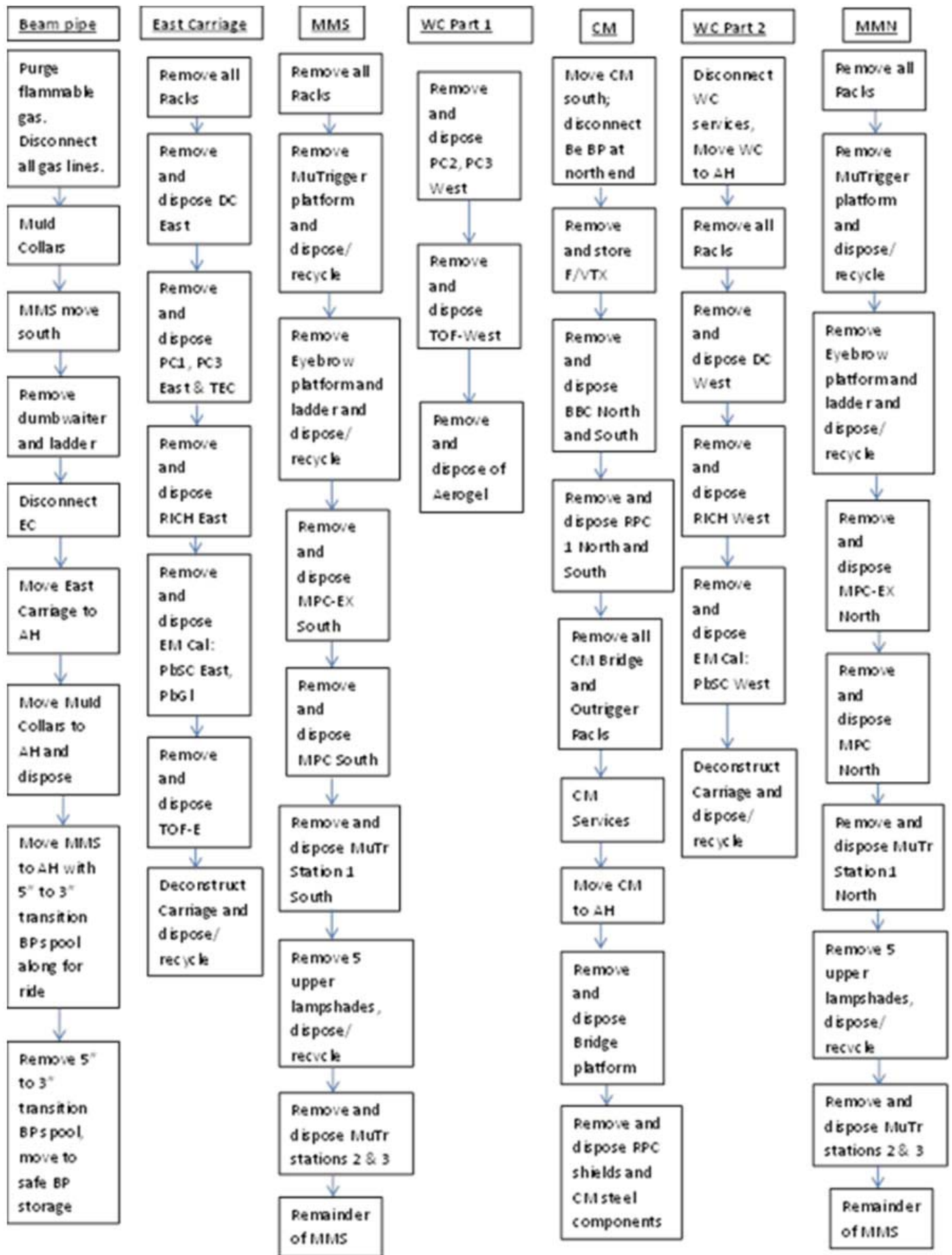


Figure 2: PHENIX Decommissioning Flow Chart

Organization of the correlated work permits will distinguish what work permits will be required for decommissioning. Locating and organizing the drawings of the lifting fixtures that were used for installation will help aid in locating which lifting fixtures will be used for decommissioning the PHENIX detector.

The spreadsheet found in (Appendix Figure 7) is an example of the organized data for the decommissioning procedure. This spreadsheet shows the installation procedures, decommissioning procedures, time of disassembly, work permits, drawings, and list of lifting fixtures for the East Carriage. The East Carriage is the first carriage of the PHENIX detector to be taken out into the assembly hall and disassembled. There are many other spreadsheets that represent the remaining sections of the PHENIX detector that are to be disassembled, which are the beam pipe, MMS, West Carriage, Central Magnet, and MMN.

The following figure is an organized flow chart of the decommissioning procedures for each section of the PHENIX detector. Within this flow chart, each section of the PHENIX detector has a specific order of disassembly. This flow chart helps organize the decommissioning procedures for easier viewing purposes and separates the procedures in an organized manner. As the decommissioning procedure begins, the separated procedures for each section can individually be crossed out to decrease the risk of confusion and ensure accuracy.

The next step in the decommissioning procedure for the PHENIX detector was to turn drawings of the lifting fixtures into electrical copies for an improved archive. The advantage of having electronic copies and drawing numbers listed is that if a lifting fixture cannot be located or used, another one can easily be reconstructed. Alongside of this, the lifting fixtures that are listed must also be physically found in the “boneyard.” The “boneyard” is where the previously used lifting fixtures and equipment are stored for later use. The following photographs are some of the lifting fixtures that were identified in the “boneyard” which can be used to disassemble the central arm detectors after recertification. For example, it was clearly identified that the Caldwell model number 20S-30-14 was previously used for the Time Expansion Chamber and can possibly be used to disassemble it as well.

III. Conclusion and Recommendations

With the upcoming upgrade from PHENIX to sPHENIX, it is necessary to decommission the existing PHENIX detector in order for the intended upgrades to take place. When planning the

decommissioning procedure for the PHENIX collaboration it is important to do so in a structured and engineered manner. A structured and engineered manner entails determining the best possible method and sequence for performing any decommissioning project. The best possible method and sequence for the PHENIX detector decommissioning project was to collect and organize everything that was involved with the installation and everything that will be used for detector disassembling purposes. This included gathering the installation procedures, time of disassembly, work permits that already exist, drawings of existing lifting fixtures, and a list of lifting fixtures used for installation for each detector. Alongside of this, the decommissioning procedures were developed and organized, drawings of lifting fixtures were copied to electronic form for an improved archive and some lifting fixtures were identified and located. With all of this information collected and organized, the PHENIX collaboration can begin to estimate the costs that the decommissioning procedures will entail and create the exact schedules that it will occur. This sequence for the PHENIX detector decommissioning procedure will help organize the flow of decommissioning for the PHENIX collaboration and help prepare for the development of sPHENIX.

IV. References

The PHENIX Collaboration. An Upgrade Proposal from the PHENIX Collaboration. 2013. PDF file.

Mitchell, Jeffery. “PHENIX front page.” PHENIX front page. N.p., n.d. Web. 29 July 2014. <<http://www.phenix.bnl.gov/>>.

V. Acknowledgements

I wish to thank my mentor, Don Lynch, for his professionalism and guidance throughout the SULI program and for giving me a perspective on engineering. I would also like to thank Dave Phillips, Rich Ruggiero, and everyone else in the PHENIX collaboration for their time and effort in making my experience worthwhile. Lastly I would like to thank the Brookhaven National Laboratory and the Department of Energy for giving me this opportunity to expand my research and engineering capabilities.



Figure 3: Lifting Fixtures used for RICH

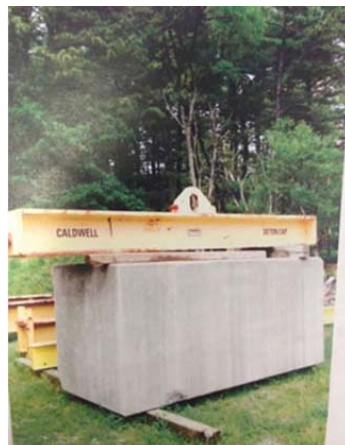


Figure 4: Caldwell 30-Ton Lift Beam

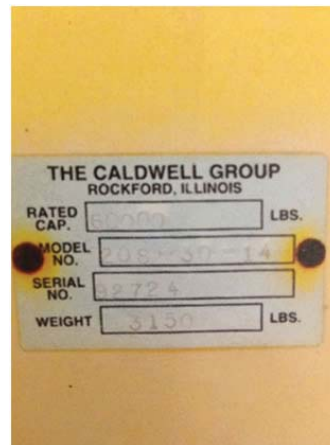


Figure 5: Caldwell #20S-30-14 used for TEC



Figure 6: P/N 12010006 Lift Fixture

VI. Appendix

Figure 7: Example of spreadsheet used for decommissioning procedure for some of the East Carriage detectors. The proposed spreadsheets are far too large to fit; however, there are records of them for the beam pipe, MMS, West Carriage, MMN and Central Magnet.

Detectors	Procedures	Estimated Time of Disassembly
Drift Chamber	<p>Installation Procedure: Attach two 20-Ft slings from the crane to the Drift Chamber's rear mount holes. Adjust one chain fall to 20-Ft length and attach this chain fall between the front central lift point and the crane. Lift crane to tension slings and remove mount pins holding the DC to rolling table. Lift detector and place on PHENIX cart, remove rigging gear and transfer it to the 12-Ton crane in the collision hall. Re-attach rigging gear and lift the detector from the cart in the collision hall using the 12-Ton crane. Place detector in park position on the south tracks. Move the PHENIX central magnet east to allow clear access for the second part of the lift and to allow the magnet to serve as a secure point during the DC/PC lift. Attach the two 20-Ft slings to the DC rear mount holes, adjust one chain fall to 20-Ft length, attach this chain fall to front central lift point and crane hook, attach second chain fall to the front lift point of the DC, position DC so front mounting pins may be inserted. Raise the front chain fall so the front edge of the DC is lifted vertically, adjust crane to keep drum directly above the hook, adjust vertical to bring the DC back to horizontal, continue until rear slings fall slack. Remove rear slings from rear detector mount points. Attach the free end of the second chain fall to the central magnet or tracks for support. Rotate DC/PC about the front mounting pins by raising the crane or the first chain (crane hook) and slackening the second chain fall (central magnet) to bring the chamber to its upright position. Once rear detector mount points align, insert mount pins. Use the manlift to gain access, remove all slings and chain falls from the crane and DC. (PP-2.5.5.4-09)</p> <p>Decommissioning Procedure: Cut all wires and gas lines, move forward on rails, lift off with crane, lay flat on cart, dismantle, outside firm to take structural titanium, rest in dumpster.</p>	4 Days, 8 CAD Tech Days
Pad Chamber 1/Pad Chamber 3	<p>Installation Procedure: PC-1 installed with Drift Chamber, PC-3 installed with TEC.</p> <p>Decommissioning Procedure: Remove PC-1 from the back of DC, throw in dumpster. Disconnect PC-3 by cutting all services, unbolt and slide out the bottom, toss in dumpster.</p>	4 Days, 8 CAD Tech Days
Ring Imaging Cherenkov Detector	<p>Installation Procedure: Raise spreader bar above the RICH vessel and attach chain falls connected to double slings to the lifting frame's swivel shackles nearest the vessel's top, attach other two chain falls to lifting frame's swivel shackles nearest the vessel's bottom. Adjust chain falls to proper length to position spreader bar over vessel's CG. Lift vessel, move it to PHENIX detector carriage, align holes of vessel and carriage pivot mounts. Install pivot pins and one insulating washer. Lock each pivot pin in place. While maintaining vessel's position with crane, relieve tension on the chain falls nearest the pivots transferring the full load to the chain falls nearest the vessel top. Remove chain falls nearest the pivots from the lifting frame and spreader bar and secure the long slings from dangling freely. Relocate chain falls to have one end attached to slings looped around the upper transition plates and one end anchored to the bottom of the carriage tracks or swivel shackle (2.5 ton) bolted to the floor. Slowly raise the vessel with the crane while, simultaneously lengthening the chain falls until vessel rests upon the rear mounts. Do not allow chain falls to become slack. Stabilize the vessel with two come-alongs each having one end anchored to the vessel and one to the carriage crossbar. Remove chain falls from transition plates and floor anchor. Reinstall chain falls to original position from spreader bar to lifting frame's lower swivel shackles. Position spreader bar over lifting frame CG. Tighten chain falls to assume load. Attach tag lines to lower end of lifting frame. Remove bolts attaching upper transition plates to vessel. Remove bolts attaching lower transition plates to vessel pivot. Remove come-alongs, install stabilizing bars to top of vessel. (PP-2.5.5.4-01)</p> <p>Decommissioning Procedure: Cut service lines, unbolt RICH north and south, attach to crane at vessel's center of gravity, move to truck, move to staging area, salvage all PMT modules, dispose of all remaining parts.</p>	<p>(4 Days, 8 PHENIX Tech Days to strip out modules from RICH and dispose of remainder at staging area)</p> <p>(4 Days, 8 CAD Tech Days)</p> <p>Total = 8 days, 8 PHENIX Tech Days, 8 CAD Tech Days</p>

<p>2003-003/SS2003-0026 (Drift Chamber Repair cm Lift Table)(1/17/2003-1/23/2003)</p> <p>na-2003-007 (Replace Drift Chamber power supplies)(11/19/2003-11/21/2003)</p> <p>2004-001/TS04-1 (Troubleshoot & Repair DC Electronics)(2/17/2004-3/31/2004)</p> <p>2004-006/SS-2004-075 (DC Power supply Repair)(5/25/2004-8/15/2004)</p> <p>2004-008/SS-2004-107 (Erect DC Repair Tent)(6/29/2004-8/10/2004)</p> <p>2005-001/SS-2005-054 (DC Repairs)(2/14/2005-4/1/2005)</p> <p>2005-003/SS-2005-090 (DC Cable Repairs)(6/6/2005-6/25/2005)</p> <p>2005-006/SS-2005-098 (DC Repairs)(6/24/2005-8/31/2005)</p> <p>07-006/DRL-2007-006 (DC East & West repairs)(2/9/2007-2/15/2007)</p> <p>07-024/DRL-2007-023 (DC East & West repairs)(10/5/2007-12/31/2007)</p> <p>08-001/SS-2008-113 (Tap into DC supply in a way to flow either 50/50 Ar/Ethane or 50/50 Ar//Ethane +1%alcohol)(1/22/2008-1/29/2008)</p> <p>DRL-2009-3 (DC Repairs)(1/8/2009-2/4/2009)</p> <p>DRL-2009-15 (DC East Repair)(9/24/2009-10/12/2009)</p>	<p>✓</p> <p>(Carriage FAB Folder)</p> <p>(DC Cable Routing)</p> <p>(DC/PC Installation Procedure)</p>	<p>Slings (2): 20-ft, 6200-lb capacity in vertical configuration</p> <p>40-Ton Assembly Hall Crane</p> <p>12-Ton Collision Hall Crane</p> <p>2 Chain Falls rated at or above 3000-Lb each</p>
<p>na-20002-006 (Replace regulator on DC/PC gas rack in mixing house)(12/18/2002-12/18/2002)</p> <p>07-011/DRL-2007-011 (PC Electronics Repair work permit)(5/23/2007-6/30/2007)</p> <p>DRL-2009-10 (PC1 Repair)(6/29/2009-9/24/2009)</p> <p>DRL-2010-1 (PC1EN2 Troubleshooting)(1/21/2010-1/28/2010)</p> <p>DRL-2010-22 (PC1 East and West Troubleshooting & Repairs)(7/20/2010-11/24/2010)</p> <p>DRL-2011-014 (PC1 Repairs)(6/29/2011-12/15/2011)</p>	<p>✓</p> <p>(PC-1 Cable Routing)</p> <p>(PC-3 Cable Routing)</p> <p>((PP-2.5.5.4-09, DC/PC Installation Procedure)</p> <p>(PP-2.5.5.4-06, TEC/PC3 Installation Procedure)</p>	<p>PC-1: Since installed with the Drift Chamber, requires the same lifting fixtures.</p> <p>PC-3: Requires same lifting fixtures as TEC.</p>
<p>98-008 (Rotate RICH Detection)</p> <p>98-009 (Remove Top of Tent)</p> <p>98-011 (Remove Gas Vessel and Transport)</p> <p>98-012 (Replace transition plated & pivots on RICH Vessel)</p> <p>na-1999-005 (Welding repair leaks in RICH vessel)(8/9/1999-8/9/1999)</p>	<p>✓</p> <p>(Lifting I-Beam # 002-0207-033)</p> <p>(Pivot Pin dwg # 002-0501-303)</p> <p>(Insulating Washer dw # 002-0501-304)</p> <p>(Lifting Frame # 002-0207-019)</p> <p>(Upper Transition Plate dwg # 002-0207-018 Part 2)</p> <p>(Lower Transition Plate dwg # 002-0207-081)</p> <p>(Vessel Pivot dwg # 002-0501-300)</p> <p>(Vessel Stabilizing Bar dwg # 002-0207-082)</p> <p>(Detector Carriage Assembly dwg # 002-0501-001 & 001-0501-002)</p> <p>(Carraige Pivot dwg # 002-0501-301)</p> <p>(RICH Installation Procedure, PP-2.5.5.4-01)</p>	<p>(2) Pivot Pins, P/N 002-0501-303</p> <p>Spreader Bar</p> <p>Chain Falls</p> <p>Doubled Slings</p> <p>Lifting I-Beam</p> <p>Swivel Shackles</p> <p>Load Cell</p> <p>Crane</p>

Utilization of 3D modeling in the construction of beamlines

Luke Chu

College of Engineering, Georgia Institute of Technology, Atlanta GA 30332

Dr. Klaus Attenkofer

Photon Sciences, Brookhaven National Laboratory, Upton NY 11973

Brookhaven National Laboratory's (BNL) National Synchrotron Light Source II (NSLS-II), is set to be one of the most powerful synchrotron when running. Currently under construction NSLS-II requires a massive amount of collaboration between scientists, engineers and designers to efficiently design equipment to be utilized in these state-of-the-art facilities. Being on the forefront of technology, means that our equipment must be custom made and designed. Scientists and engineers create ideas and plans for the design and placement of equipment and it is the job of the designer to translate these ideas into 3-dimensional (3D) models. 3D models are quite useful as they provide a visual aspect to a person's design. This aids in the communication of proposed designs. They are also necessary to build designs of entire hutches so scientists and engineers can properly lay-out their equipment and identify problems before they arise in real life. Identifying possible interferences between equipment in the design stage is an incredible advantage. This will streamline the entire process and will help save money. Many times beamlines will discover that equipment ordered does not properly work in their design, this wastes both money and more importantly time. 3D modeling cuts down on all of the aforementioned problems.

My design portfolio at NSLS-II was mostly comprised of proposed designs. The first project I received was to design an Electronics Protection System (EPS) Box for Inner-Shell Spectroscopy's (ISS) beamline. The EPS box housed Programmable Logic Controllers (PLC) which properly routed large amounts of data from the beamline to a computer. The major constraint placed on me for this project was space. Space was limited and made it difficult to fit all the necessary thermocouple inputs, power supply, test points, sink inputs, relay inputs and the PLC. Typically EPS boxes utilize commercial boxes to cut down on cost and also simplify the process of creating a custom box. A popular company at BNL for commercial enclosures is Hoffman Enclosures. Utilizing their customer support, I received a STEP file

of the enclosure that fit our space constraints. Using this as my base, I designed the entire layout of necessary components. It was necessary for me to leave adequate clearance space for people to operate screwdrivers and wrenches to properly maintain the box. I also needed to leave space for wiring and future expansions. According to BNL's safety rules, this box must have sufficient radiological safety precautions. This box is going to be exposed to x-ray radiation and requires an adequate lead-lining to protect the internal components from being damaged. For this design we determined that lead would be applied to the exterior of the box and will not be necessary in the design of the EPS box.

The second design of my internship was the proposed design of a modular solar panel tester. This was an interesting project as it was contracted from another BNL group. BNL was interested in the degradation and lifetime of solar panels. They needed a piece of equipment that could focus set intensities of light toward the single cells of each panel. Over a period of time they would test the solar panels and would record the power created from the same intensity of light. It is expected that over time, solar panels will deteriorate and by recording the degradation of the solar panel, lifetime can be extrapolated. This would allow BNL to efficiently identify when to replace solar panels located throughout the laboratory.

The constraints for the solar panel tester were that it had to be modular and easy to use. The result was a piece of equipment that held 100 plastic lenses that focused light from an LED upon a single cell of a panel. The modular aspect of this design came from its block shape and jigsaw puzzle design. From each side there exists an extruded piece of metal or plastic that serves as a locking mechanism. Each solar panel consists of 72 smaller panels, thus to properly test a solar panel 72 modular solar panel testers are required. They are arranged in a grid with female connectors for the extruded metal or plastic. As such it would be simple to insert each tester with the handle into the grid and connect cables. If



Figure 1. Electronic Protection Box for Programmable Logic Controllers.

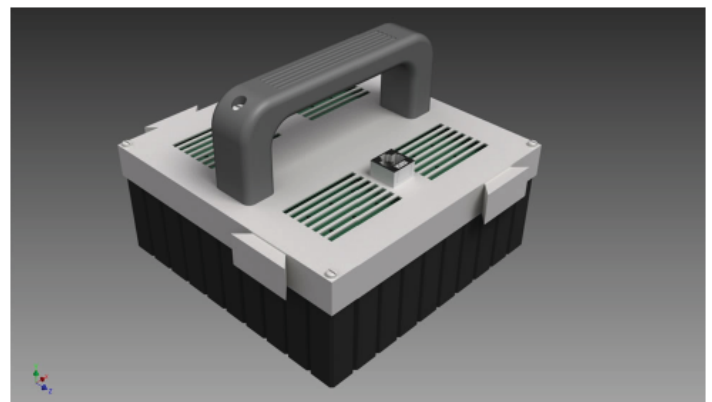


Figure 2. Modular Solar Panel Tester

there were defects with a box, it was meant to be easy to replace. Whether a single lens is broken or the circuitry is broken, it's a matter of either replacing the single defective lens or replacing the box in the grid.

The most difficult design I created was an X-ray Emission Spectrometer (XES). The XES is a critical component to the ISS beamline. It measures various properties of x-rays that are released when the experiment takes place. The chamber where the experiment is conducted is surrounded by a large amount of XES's. Each XES is comprised of a lens that focuses x-rays to a Mythen detector. However the difficulty of this project lies with the necessity for the XES lens and detector to have movement freedom in one plane. The distance between the lens and the x-ray source, and the lens and the detector was about 1:1. Thus I utilized commercial piezo motors to move both the detectors and lens. Another very difficult aspect of this project was creating methods to reduce ambient noise in the chamber. To reduce the amount of unwanted photons, we utilize a series of bevells to block unnecessary sources of noise. This was difficult to employ because the lens and detector were able to move. This degree of freedom made it difficult to devise a simple way to block efficient amounts of outside noise. Because of this our design is not ideal, but is the most cost efficient and within the tolerance of the ISS beamline.

The only actual design of my internship was an EPS box for transmitters for the HXN beamline. This was the most technical design I have created for BNL. Each aspect of the design had to be incredibly detailed and precise. This was by far the most time-consuming project as scientists and engineers were always creating better ways to implement certain designs into the 3D model. The 3D model was necessary because each part file would go to different commercial vendors and our machining shop to be created. The most difficult aspect of this project was managing the lead-lining. It had to encompass the majority of the box, but could not be exposed as it runs the risk of being chipped. It is also a health hazard for workers making changes to the box. Thus we decided to employ a thing PET plastic cover that would go above the lead-lining. Space was another major constraint to this project. At one point I had to redo the entire design because the beamline had ordered the incorrect box, and I had to adapt my design to the new box. There were many more challenges that arose with actual designs as opposed to designs for proposal. The box is to be constructed and implemented in late August and early September.

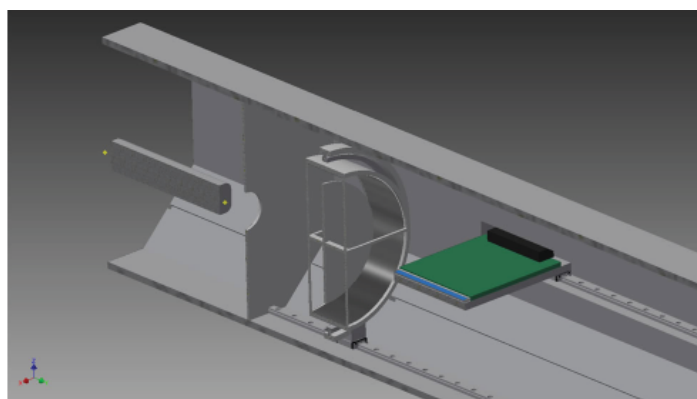


Figure 3. Half Section View of X-ray Emission Spectrometer. Features include Lens and Mythen Detector

My design portfolio for NSLS-II was varied and extensive. Among the two EPS boxes, modular solar panel tester and x-ray emission spectrometer, I designed an ionization chamber, crystal mount and mirror translation system. Each design had a series of constraints that made each project unique and difficult. A challenge that I encountered along the way that was found in all designs was the difficulty of editing cully created designs. This is a flaw with Autodesk Inventor, editing a foundational sketch, would change everything else dependent on it. Sometimes even a miniscule edit could completely destroy an entire design. It was time consuming to go and make proper edits to a design. Another challenge I faced was deciphering the quickly and sometimes poorly drawn hand sketches of scientists and engineers. These sketches usually lacked proper detail and dimensions. Many times I found myself interpreting their diagrams in completely different ways than intended. This sometimes meant I had to redo the entire design. Communicating to scientists and engineers in technical terms was a daunting task, but ultimately quite rewarding as it taught me to be more meaningful with my word choice. My proposed designs will most likely be a foundation for other designers to comb through with a more technical touch to make it more feasible for actual construction. My actual design is already in the process of being implemented.

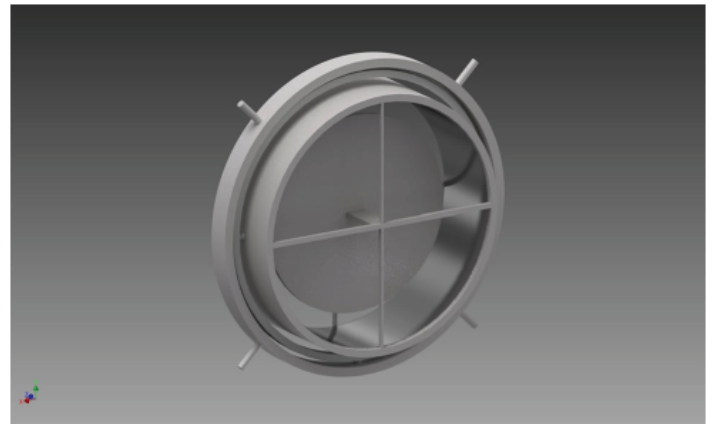


Figure 4. X-ray Emission Spectrometer Lens

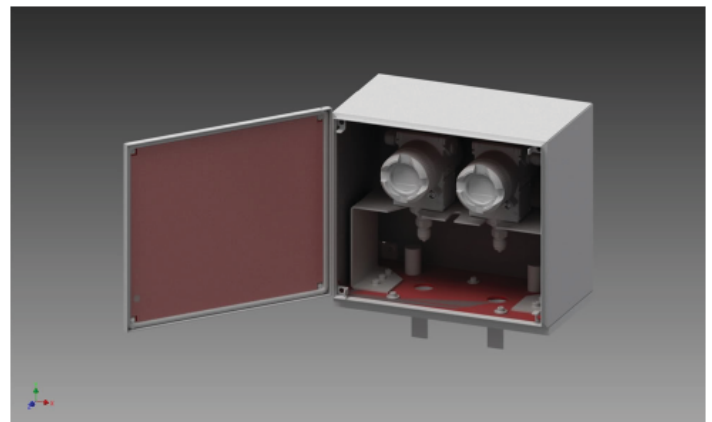


Figure 5. Electronics Protection Box for Transmitters

Laser ablation of gold film on plastic and aluminum substrates

David Cinquegrani

University of Michigan, Ann Arbor, MI 48109

Masafumi Kumaki

Waseda University, Shinjuku, Tokyo, Japan

Masahiro Okamura

Collider–Accelerator Department, Brookhaven National Lab, Upton, NY 11973

ABSTRACT

The Laser Ion Source (LIS) group in Brookhaven National Lab's (BNL) Collider–Accelerator Department focuses mainly on the production and analysis of plasmas and ions created from matter interactions with lasers. A 1064 Nd:YAG laser is used to irradiate a solid target and produce a plasma by laser mass ablation. Two targets were created for this experiment: a polycarbonate (PC) plate coated with a 125 nm gold film and an aluminum plate coated with 125 nm gold. Each target was only half coated so as to use the other half as a target of the just the substrate. The purpose of irradiating these targets was to analyze the ion composition of the resulting plasma to determine if gold was a viable film to produce a higher charge state ratio of protons i.e. higher number of protons than pure plastic. The aluminum target was used to investigate how the substrates were heated comparatively between an organic material and a metal.

I. INTRODUCTION

When a laser with high power irradiates a target, it produces a plasma consisting of ions of the target species. These ions have many applications ranging from use in an accelerator, cancer therapy or use in experiments for NASA. The focus of ion production by the LIS is in high charge state ions. These are ions that have a higher charge than found naturally. The experiments performed in the relativistic heavy ion collider (RHIC) at BNL also require protons that can be polarized. A technique to generate these protons was proposed in which a hydrocarbon, such as PC, is irradiated and the H⁺ ion is used.

The problem with this idea is that many plastics are clear and the laser energy will not be transferred efficiently to the target. A proposed solution to this problem was to coat the plastic target with a film of gold. Gold has a low absorption coefficient at 1064 nm, is generally unreactive and very easy to evaporate onto a target. The goal was to have the gold more efficiently transfer the laser energy to the plastic substrate. The heating of the gold by laser energy occurs in two stages. The electrons in the solid layer will be heated by the laser energy directly and then will transfer the energy to the gold atom lattice¹. The gold then undergoes the phase changes to end up as a plasma on the picosecond timescale.

This paper focuses on the results from the irradiation of two targets and their associated control cases. One target was a transparent polycarbonate plate that was half coated with a 125 nm thickness of gold and the other target was a plate of pure aluminum once again half coated with a layer of 125 nm gold film.

The hypothesis for the first target was that the in the ion charge state signals there would be an increased ratio of H⁺ ions compared to the ions of carbon, oxygen and gold. A higher ratio

would imply that more H⁺ ion were produced compared to a case where the gold film was not irradiated. The aluminum target was constructed to verify results regarding the other ions present in plastic. The carbon ions behaved in a way that was never seen before and needed to be investigated further with a different element target.

II. EXPERIMENTAL SETUP

The creation of the targets for this experiment was made by a process called physical vapor deposition. The process involve heating an element to high enough temperatures that the sample sublimates and is turned into a vapor. This vapor is then deposited onto the target in a relatively even coating. For the deposition of gold onto both the polycarbonate and the aluminum plate we used an electron gun. The plastic target was slightly more difficult to coat as it has a much lower melting point than the aluminum so certain precautions were taken. The thickness of gold that was used was 125 nm. This was chosen because it was an adequate amount to transfer energy and also would not be too thick that the substrate would not be irradiated at all. The size of the target used was 100 x 100 mm and about 1.0 mm thick. This was placed in a target holder that securely fastened the plate to have the most surface area visible. The plate was then attached to a two axis linear stage. A two–axis controller was used to move the target each time it was shot with the laser. A fresh target surface was needed for each shot to be sure that there was a layer of gold that would be shot. The target chamber is completely enclosed and at a pressure very close to vacuum. Then the signal from the Faraday Cup (FC) was taken to determine the total current produced by the plasma. This was used to determine the optimal lens position to produce the highest number of ions in plasma. The next step was to start detecting the ions from the plasma. The ion charge states are separated and detected using an electrostatic ion analyzer (EIA) and secondary electron multiplier (SEM). The target was shot three times at voltages between 1 and 80 V. These voltages determine the electric field for the EIA. The laser used was a Quantel 1064 nm Nb:YAG. The laser power used for both experiments was 208.7 mJ. Two pulse lengths were used for the experiments, 500 picoseconds and 6 nanoseconds. The experiments also involved data taken with the focusing lens in different positions to explore the dependence of power density on the ions produced.

III. RESULTS AND DISCUSSION

The first set of experiments involved both short pulse (6 ns) and a long pulse (500 ps) laser irradiation. The target irradiated was the plastic target that was partially coated with gold.

Measurements taken first were Faraday cup measurements for total plasma current. The measurements were used to deter-

mine the optimal position of the lens for focusing the laser energy. Figure 1 shows the data for both short and long pulse irradiation and coated and pure targets. As seen in the gold-coated graphs, the gold ions can be seen as parts of the total current depending on the lens position. In the picosecond case the ions are seen to appear after the carbon and hydrogen ions but from the same shot.

This is different than the nanosecond case because it appears that there is a point where only one type of ion is present. This is the basis for the third experiment performed which will be discussed later in the paper.

The next set of data was the signal voltage that was measured from the different charge states present in the plasma. The data here is all from nanosecond irradiation, the focus of the following experiment at well. Figure 2 shows the charge states present for two lens position configurations for each target, pure and coated. The lens positions were at the focal point (2.5 mm) and 1.25 mm.

In this case there were a few differences between the irradiated targets used to support our hypotheses. One such is that the ratio of hydrogen compared to the other charge states was higher in the targets that were gold coated. This means that a gold film would help to produce a larger number of protons for use in RHIC. This was only the case for the well focused gold coated target though.

Another observation from this data is that the carbon ions produced from the plastic are delayed when the target is coated with gold. This meant that the ions showed up in the plasma but

only at electric fields that were higher than those that showed the same ions in the pure plastic target. Something that we did not expect to happen was in the well focused laser case and gold coated target, no gold ions were produced. This means that all the laser energy that hit the target went to the plastic substrate that was behind the gold.

The next experiment that was performed had a gold coated aluminum substrate. The data obtained from this experiment is shown in Figure 3. The experiment was done with the 6 ns laser pulse and at the same lens positions as the plastic target.

Expected results for the aluminum target included some sort of delay in the aluminum ions similar to that which was seen with the carbon ions in the plastic target. However this was not observed in the data. The aluminum ions were seemingly unaffected by the gold coating. In this case the charge ratios seem to stay the same between the gold coated case and the pure case. There is one case where the Al^{3+} charge state has an increase in ratio but the reason why is unclear. The ions appeared at the same voltage and in the same ratios as the pure cases. The last difference is that in both the unfocused and well focused gold coated cases there were no observable gold ions. This is different from the plastic target and from the picosecond laser cases (see Appendix).

To further investigate the reason why the gold ions were not present at certain lens positions we re-examined the Faraday Cup data in Figure 1. It seemed that in the nanosecond cases the total current was indicative of the ions present in the plasma. When

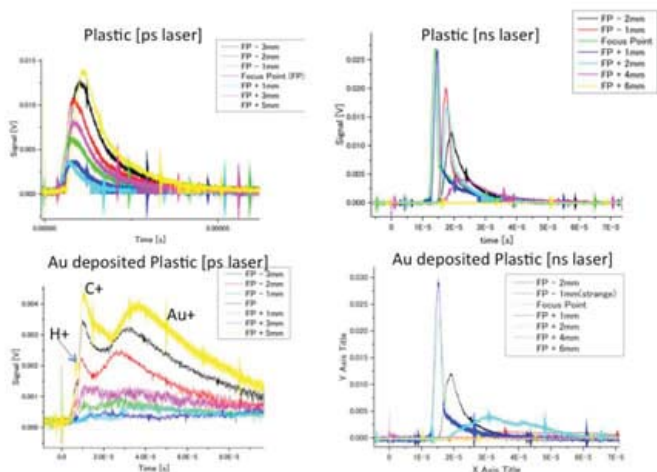


Figure 1: Faraday cup measurements for plastic target at various lens positions for each laser pulse length

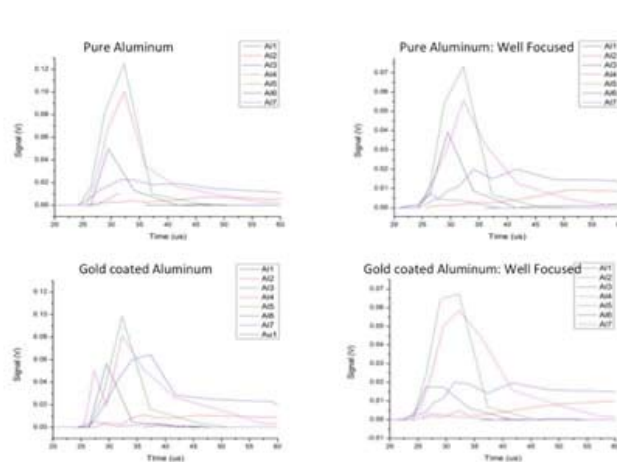


Figure 3: Plasma charge state voltage signal from nanosecond laser irradiation of aluminum target

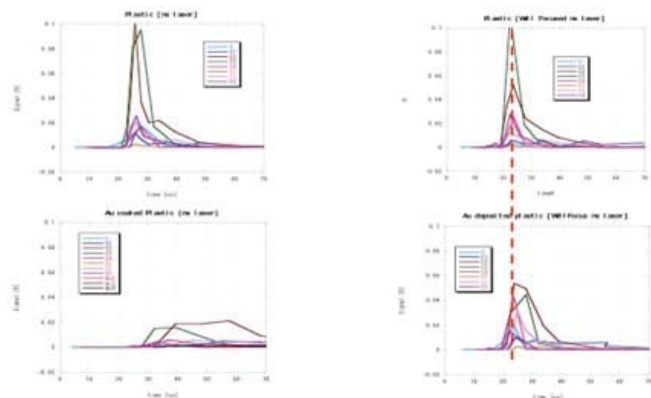


Figure 2: Plasma charge state voltage signal from nanosecond laser irradiation of plastic target

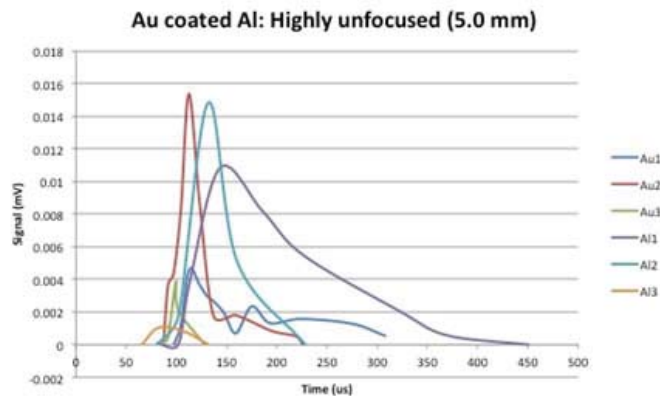


Figure 4: Plasma charge state signals from irradiation of gold-coated aluminum target at lens position of 5 mm

substrate ions were present the typical peak was present. In the case of the pure substrate the peak simply got smaller as the lens was moved further way. However, as the lens was moved away in the gold-coated case, the peak began to flatten. This was hypothesized to be a plasma generated of all gold ions. Figure 4 shows the data obtained from an experiment in which the lens was moved considerably far away from the target, 5 mm. The target used was the gold-coated aluminum plate.

The results seem to only be more confusing than before. Not only were aluminum ions present in the plasma, they were delayed in appearance in a similar way as the carbon ions in the plastic substrate cases. There was an increased amount of gold ions than there were with the prior aluminum target experiments. However, the appearance of aluminum does not support our hypothesis.

IV. CONCLUSION

This series of experiments solved some problems but also created many more questions. The hypothesis was that it would be possible to generate a higher ratio of protons by coating a plastic substrate with gold film. This was supported through the experiments with the picosecond and nanosecond laser irradiation. This will be crucial for later studies of plasmas generated by the Laser Ion Source and use in RHIC for future experiments. Though more questions came from irradiating the aluminum target, further work will be done including repeating the experiment with the picosecond laser and using a pure gold target to investigate lens position scenarios.

V. ACKNOWLEDGEMENTS

This project was supported in part by the U.S. Department of Energy, Office of Science, Office of Workforce Development for Teachers and Scientists (WDTS) under the Science Undergraduate Laboratory Internships Program (SULI). Along with my mentor Masahiro Okamura and graduate student advisor Masafumi Kumaki, I would like to thank Takeshi Kanesue, Shunsuke Ikeda, Yasuhiro Fuwa, and Christine Truong for their work on the project. I would also like to acknowledge Dannie Steski for help in production of our targets.

VI. REFERENCES

¹Jing Huang, Yuwen Zhang, J.K. Chen, "Ultrafast solid-liquid-vapor phase change of a gold film induced by pico- to femtosecond lasers" Applied Physics A, June 2009, Volume 95, Issue 3, pg. 643-653

VII. APPENDIX

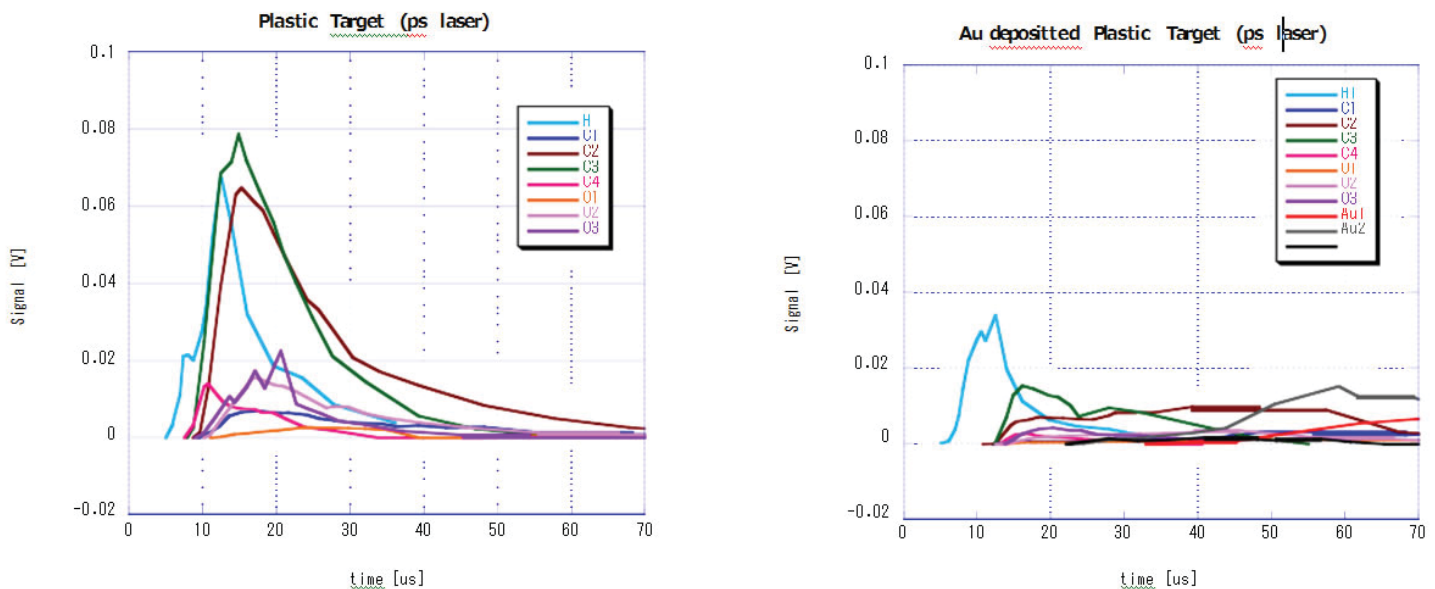


Figure A1: Plasma charge state signal voltage from picosecond laser irradiation of plastic target

Radiolabelled sugars via chemoenzymatic synthesis

Mark Cinquegrani

Department of Biological Sciences, University of Pittsburgh, Pittsburgh, Pennsylvania 15213

Andrew Gifford

Biosciences Department, Brookhaven National Laboratory, Upton, New York 11973

Abstract

The effective goal of this project is to make radiotraced carbohydrate molecules to be used in imaging and plant studies involving the uptake of sucrose for ethanol production. This study exemplifies the use of a novel and simple approach to radiosynthesize (F-18) analog carbohydrates. We have previously found a process that leads to one specific deacylation of sucrose octaacetate (SOA) but would like to find more.¹ My work now uses a different substrate, sucrose octabutyrate (SOB), that we hope is more compatible with the enzymes and their natural substrates. I also participated in studies of novel solvent systems and enzymes using sucrose octaacetate as a starting material. This part of the project aimed to optimize an existing protocol by determining other enzymes and solvents that successfully aid in the conversion of sucrose octaacetate to sucrose heptaacetate. Following thin layer chromatography and liquid chromatography-mass spectroscopy analysis, it was determined that something in the sucrose octabutyrate sample was interfering with the enzyme and was not producing results. Conversely, several enzymes successfully converted the octaacetate starting material to the heptaacetate product in a solvent of 50% dimethyl sulfoxide and 50% water. From initial tests, the process was scaled to a larger volume and will be used for triflation and radiofluorination. These products can then go on to plant and imaging tests.

I. Introduction

Nuclear medicine and biological imaging are increasingly relying on radiofluorinated sugars for varying applications. While the most common of these radiofluorinated sugars is fluorodeoxyglucose, which has been used for PET imaging in medicine, expanding the variety of radiofluorinated sugars would allow for a wider range of studies involving disease and metabolic processes in both humans and plants. Some of these metabolic pathways in plants are especially important for producing ethanol, one option for a renewable fuel source. Radiofluorinated sugars can be easily tracked through the plant using a Positron Emission Tomography (PET) scan to determine location and speed of movement.

Radiofluorinated sugars have previously been made through multiple step chemical synthesis methods but this method is time consuming, costly, and lacks specificity of fluorination. We would like to be able to fluorinate at a specific point on the sugar, but this is made difficult by similar reactivities of the hydroxyl groups. Industrial enzymes have offered a solution that has eliminated the need for multistep chemical synthesis by decreasing time requirements and increasing specificity because they act at a specific point on a specific substrate in order to create a more pure and well-defined product.

Another problem arose when determining a solvent in which to perform the reaction. The protected sugar is hydrophobic and

thus dissolves best in organic solvents, while the enzymes have hydrophilic exteriors and are most soluble in aqueous solvents. These differences in solubility affect the efficiency of the reaction by hindering an interaction between substrate and active site. Most early work was made up of trying varying solvent systems with several enzymes to determine which is best for deacylation. This study offers one possible solution to the solvent problem.

After the initial step of preparing the heptaacetate product, the missing acetate group is to be replaced by a triflate. Triflate is a protecting group that is more reactive than acetate and thus facilitates a reaction at that position rather than any of the others. This is how the radioactive fluorine is placed on to that specific point on the sucrose molecule. The remaining seven acetates can then be stripped away and replaced with the typical hydroxyl groups, allowing the molecule to function normally in further studies.

II. Materials and Methods

For the study of sucrose octabutyrate, the unprotected sugar, sucrose, was chemically altered to place butyrate groups on to each hydroxyl available on the molecule (eight total). This was done using pyridine, butyric anhydride and dimethylaminopyridine (DMAP). The reaction took place overnight and was followed by liquid-liquid extraction to purify the product and remove the chemicals used in the reaction. Following the purification, approximately 100 μ l of product was used in each vial of enzyme tests containing varying lipases and a solvent made up of 50% dimethylsulfoxide and 50% distilled water. After incubation for 48 hours, about 0.5ml was taken from each sample and mixed with 0.5ml diisopropyl ether to examine reaction progress via thin layer chromatography. Samples that would have converted sucrose octabutyrate to sucrose heptabutyrate would have been used for further study.

Sucrose Octaacetate was incubated with enzymes such as lipases from *Candida antarctica*, wheat germ, *Candida* sp, and *Aspergillus niger*, as well as a protease from *Bacillus licheniformis*. These enzymes were reported to preferentially remove acetate groups from the 1' position in sucrose octaacetate.^{2,3} After incubation for at least 48 hours, approximately 0.5ml of the liquid sample was extracted with 0.5ml diisopropyl ether. This separated into layers and purified the sugars away from the enzyme used. About 4 μ l of sample was taken from the very top of this liquid extraction and plated on a silica plate for thin layer chromatography. The TLC plate was then placed in to a chamber containing a mixture of 60% ethyl acetate to 40% hexanes. After the solvent front had moved appropriately far for separation (about ten to fifteen minutes) the plate was removed and allowed to dry. The spots were then developed using a naphthol and sulfuric acid solution to soak and then dry and heat the plate. Samples that showed spots only where SOA would migrate did not work, while those that had a spot below this SOA spot were successful in deacylating the

SOA. Approximately 10ul of these samples were dissolved in 1ml of acetonitrile and examined using liquid chromatography-mass spectroscopy for identification. After determining that the correctly monoacylated product was present, the sample trials were repeated on a larger scale and tested again.

After second verification, the products still in solution would be purified away from the enzymes used to make them using a combination of liquid-liquid extraction and flash chromatography. The pure product would then have a triflate group added on to it, and then this triflate replaced with an 18-F radiolabel.

III. Results

Deacylation of SOB was unsuccessful perhaps due to the presence of a large amount of pyridine present in the reaction conditions. This chemical harms the enzymes and halts the reaction.

Enzyme screening for hydrolysis of acetylated derivatives (SOA) showed that the lipase *Candida rugosa* had the highest yield in producing regioselectively deacylated product in the chosen solvent system. *Bacillus licheniformis* protease also showed a large decrease in starting material and produced a deacylated product. Other results are shown in the supplemental figures (S3) LC-MS analysis of reaction of mixture indicated that the enzyme initially yielded just a single mono deacylation product. We have currently optimized heptaacetate and are currently under the process of radio-fluorinating.

IV. Conclusions

Sucrose octabutyrate may be a better substrate than sucrose octaacetate, but until an effective way to remove pyridine is found, sucrose octaacetate will need to be used for enzyme tests. The process to remove the pyridine was too time consuming and resulted in too great a loss of product to be a worthwhile method in the case of these experiments. It is also possible that there may be another way to make sucrose octabutyrate that does not involve pyridine but we did not have a chance to explore this option.

These sucrose octaacetate enzyme studies have shown that there are a number of enzymes that perform the desired reaction in a solvent system containing 50% dimethyl sulfoxide and 50% water. Enzymes such as lipase from *Candida rugosa*, protease from *Bacillus licheniformis*, and lipase from *Candida antarctica* have shown promise in effectively creating precursors for radiofluori-

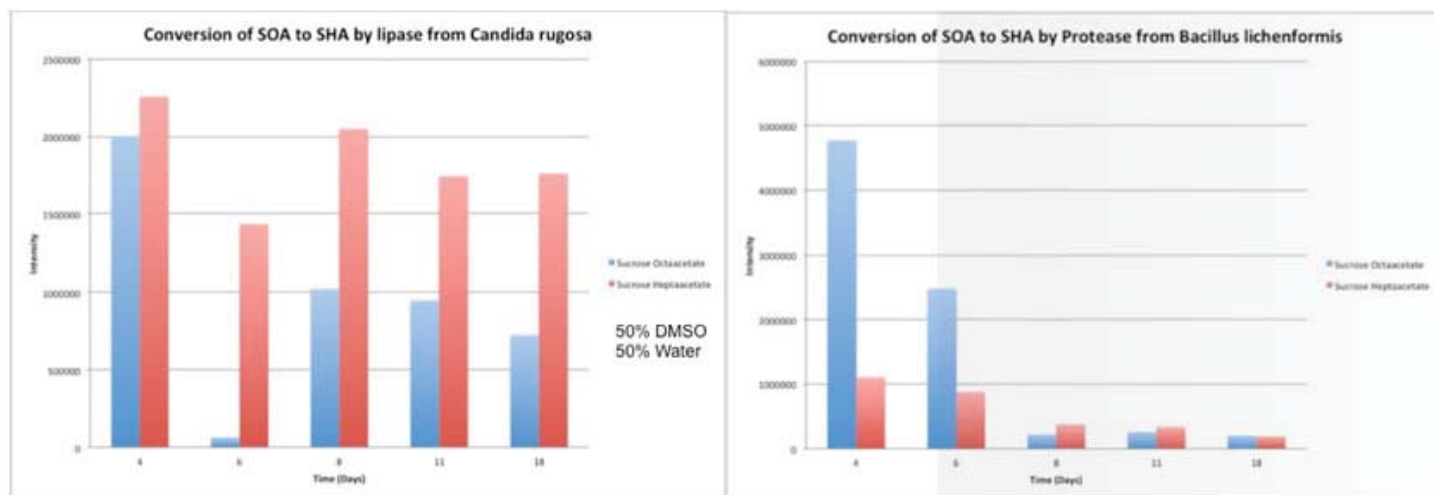
nation. They have also shown that there are other conditions, such as pH, that will affect the ability for the enzyme to perform the desired reaction such as the case with *Candida antarctica*. Why this is so is not entirely clear, but the process is better than the previous chemical pathways and effective for the tests that use these precursors.

V. Future Studies

Once an effective and efficient way of producing radiolabelled sugars is found these molecules can be used to study metabolic pathways in plants. By studying these pathways, we can find available sucrose in plants that can be extracted for ethanol production and other industrial uses. These radioisotopes can also be used to monitor cancers and other health risks due to the specificity of the disease metabolisms.

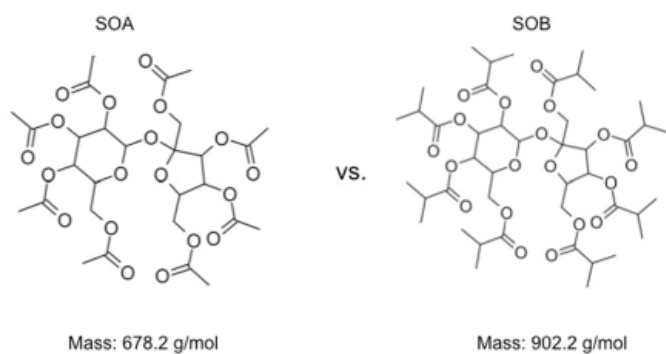
VI. References

- Gifford AN, Bennett CV, Fowler JS. Radiosynthesis of the fluorinated sucrose analogue, 1'-[18F]fluoro-1'-deoxysucrose. *J. Label Compd. Radiopharm* 2012; 55, 441-446
- Bornemann S, Cassells JM, et al. The use of enzymes to regioselectively deacylate sucrose esters. *Biocatalysis and Biotransformation* 1992; 7(1): 1-12
- Chang KY, Wu SH, Wang KT. Regioselective Enzymatic Deacetylation of Octa-O- Acetylsucrose- Preparation of Hepta-O-Acetylsucrose. *Carbohydr Res* 1991; 222, 121- 129



Figures 1 and 2: Enzymes in 50% DMSO/50% Water, Time v. LC-MS Intensity

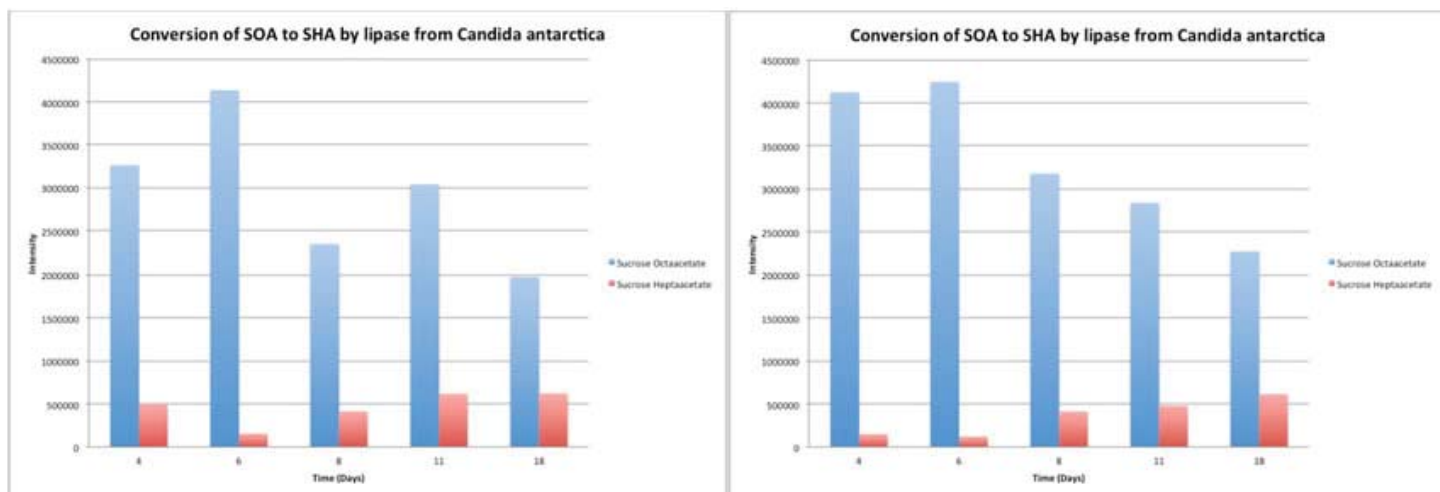
VII. Supplemental Figures



S1. Structure comparison of Sucrose Octaacetate and Sucrose Octabutyrate



S2. Example of TLC



S3. Lipase from *Candida antarctica* at pH 6 (left) and 8 (right), 50% DMSO/50% Water

Using open source information to visualize safeguards data

Daniel Cisek
St. Joseph's College
Dominick Raimondi
Farmingdale State College
Susan Pepper and Nicolas Gallucci
Brookhaven National Laboratory

Notice: This manuscript has been authored by employees of Brookhaven Science Associates, LLC under Contract No. DE-AC02-98CH10886 with the U.S. Department of Energy. The publisher by accepting the manuscript for publication acknowledges that the United States Government retains a non-exclusive, paid-up, irrevocable, world-wide license to publish or reproduce the published form of this manuscript, or allow others to do so, for United States Government purposes.

DISCLAIMER

This report was prepared as an account of work sponsored by an agency of the United States Government. Neither the United States Government nor any agency thereof, nor any of their employees, nor any of their contractors, subcontractors, or their employees, makes any warranty, express or implied, or assumes any legal liability or responsibility for the accuracy, completeness, or any third party's use or the results of such use of any information, apparatus, product, or process disclosed, or represents that its use would not infringe privately owned rights. Reference herein to any specific commercial product, process, or service by trade name, trademark, manufacturer, or otherwise, does not necessarily constitute or imply its endorsement, recommendation, or favoring by the United States Government or any agency thereof or its contractors or subcontractors. The views and opinions of authors expressed herein do not necessarily state or reflect those of the United States Government or any agency thereof.

Abstract

The Nonproliferation and National Security Department at Brookhaven National Laboratory works alongside several other agencies to create policy, procedures, and instruments to help combat the threat of nuclear proliferation worldwide. The International Atomic Energy Agency (IAEA) conducts inspections to ensure that countries are meeting their safeguards agreements under the Nonproliferation Treaty (NPT). Our project seeks to assist IAEA inspectors in their assessment of a country by providing them with a comprehensive visual depiction of a country's safeguards history. These graphics present a timeline of the country's nuclear facilities, their construction dates, operational history, and any proliferation significant events. This information would help inspectors quickly gain a basic understanding of the country's history of cooperation under the NPT, as well as more specific information relating to individual sites. Also, by using the proliferation significant events, users can identify trends and hopefully predict future proliferation issues. A large part of our data was garnered from open-source information, including IAEA reports, The Nuclear Threat Initiative, and The Institute for Science and International Security. From this project we have gained an understanding of public relations, safeguards implementation, nuclear policy worldwide, and the nuclear fuel cycle.

I. Introduction

One-hundred and ninety countries are parties to the Treaty on the Non-Proliferation of Nuclear Weapons (NPT). Of these 190 countries, only five are recognized as nuclear weapon states. These five countries include the United States, United Kingdom, Russia, France, and China. Outside the NPT, only four countries

remain. These include India, Israel, Pakistan, and the Democratic People's Republic of Korea (DPRK). These countries in particular are watched very intently. The purpose of the treaty is to ensure that nuclear material is being used for peaceful purposes, through the application of comprehensive safeguards. These safeguards are carried out by an international agency known as the International Atomic Energy Agency (IAEA) (Rosenthal, et al., 2013).

The NPT plays a key role in the safeguard system. It helps international efforts to stem the proliferation of nuclear weapons. The NPT is a complex verification system built on states reporting their nuclear material accounts and on-site inspection by the IAEA. The goal of the IAEA is to verify that what the states report is true, much like the IRS auditing an individual's taxes. The IAEA can then confirm that all the accounts are "correct" when everything has been reported "correctly" and "completely". From this all nuclear material can be present and accounted for by the IAEA (Rosenthal, et al., 2013).

"An intrinsic tension exists between the pursuit of nuclear energy and the effort to prevent the illicit development of nuclear weapons- [a]fter all, certain elements of the nuclear fuel cycle and nuclear material used to produce energy can also be used to produce nuclear weapons" (Rosenthal, et al., 2013). One prime example of this is that many nuclear reactors use uranium as fuel. Not only is uranium a fuel, but if it is enriched to a high enough level, it can be used for nuclear weapons. Because of this, any facilities known as "reprocessing" or "enrichment" plants used to make fuel for reactors are also regarded as sensitive facilities and fall under comprehensive safeguards (Rosenthal, et al., 2013).

This tension between peaceful use and proliferation use is unescapable due to two factors. The first was the development of nuclear weapons and their subsequent use during World War II, as well as the use of these weapons in countries national security

programs. The second is the development of nuclear power reactors to take advantage of the clean energy produced for peaceful purposes, by splitting the atom (Rosenthal, et al., 2013).

The comprehensive safeguard system upheld by the IAEA is continually changing and has to respond to real world events. For instance, in the early 1990's Iraq, the DPRK, and South Africa played important roles in forcing the IAEA safeguard system to adapt its legal authorities and to change how the role of safeguards is conceptualized. In 2012 the IAEA was confronted with non-compliance with its safeguards agreements by both Iran and Syria (Rosenthal, et al., 2013).

The fact that many countries have vastly different sets of comprehensive safeguards can be daunting for inspectors looking to verify the correctness and completeness of countries nuclear materials. A graphical representation of the history of specific country's nuclear facilities can help to get a rough overview. With this overview inferences can be made based on events about what may happen in the future. For instance Iran is normally viewed as being "non-compliant", by hiding programs. This is actually not so true, when one examines the details. Besides a few specific incidents in their nuclear history, Iran has been compliant and allowed inspections into their nuclear facilities. A graphical representation of the country's entire nuclear program along with specific events and periods where there was proliferation significant events or non-compliance can display this in detail.

II. Methods

In order to represent the operational history of each nuclear

fuel cycle relevant site we used a combination of open source and restricted access data. This information was gleaned from a combination of books, websites, and official documents. When possible, information was cross-checked between different sources to ensure accuracy. When using websites as a source, precaution was taken to ensure that only the most reliable websites were referenced. Given the highly selective nature of these sources, only a few websites met the standard. These include The Nuclear Threat Initiative, The Institute for Science and National Security, The Center for Nonproliferation Studies, and The Center for Strategic & International Studies, among others. To catalog the data that was gathered on these sites, the use of an Excel spreadsheet was employed. Here, dates essential to the sites operation were recorded, such as initial time of construction, proliferation significant events, and current status. Once we finished compiling the needed information, it was then taken to be turned into a visual format. The graphic shown below is a portion of the spreadsheet used to organize the relevant information.

The Excel spreadsheet consists of seven columns to organize the data. Most of the columns are self-explanatory, though some points need be made. First the name of the facility is listed. Occasionally several names are listed, as some sites have multiple names. Issues with this also come up with different spellings of certain regions or towns. For example, the Isfahan Nuclear Technology Center (INTC) occasionally is listed in reports as the Esfahan Nuclear Technology Center (ENTC). In this example the spelling difference comes from its history; Esfahan is the traditional Persian spelling, while Isfahan is its more modern spelling.

Facility	Construction Date	Operational History	Proliferation Significant	Current Status	Additional Information	Sources
Natanz Fuel Enrichment Plant (FEP)	The Natanz facility was first publicly identified by NCFI in August 2002. They identified the facility as a nuclear fuel fabrication plant. In December 2002, ISIS released satellite photos of the facility for the first time and correctly identified the site as a gas centrifuge enrichment facility. [2] Construction started in 2000[3] or in early 2000's (NITI)	The FEP began operating in February 2007, and construction on centrifuge cascades is ongoing. The FEP ostensibly exists to produce enriched uranium for light water reactors in Iran, including the Bushehr facility and others that Iran has not yet built. [2]		Operational	between 16 October and 11 November 2011, the Agency conducted a physical inventory verification (PIV) at FEP. The nuclear material at FEP (including the feed, product and tails), as well as all installed cascades and the feed and withdrawal stations, are subject to Agency containment and surveillance. The consequences for safeguards of the seal breakage in the feed and withdrawal area will be evaluated by the Agency upon completion of its assessment of the PIV. Based on the results of the analysis of environmental samples taken at FEP since February 2007 and other verification activities, the Agency has concluded that the facility has operated as declared by Iran in the Design Information Questionnaire (DIQ). (1)	1. Implementation of NPT Safeguards in Iran 2011 (N/N/2012/2011) (Visual/IR Documents) 2. http://www.isisnuclear.org/site/default.asp? [3] publicintelligence.net, "Iran Nuclear Site: Natanz Uranium Enrichment Site"
Natanz Pilot Fuel Enrichment Plant (PFEP)	2001 Iran began the construction of Pilot Fuel Enrichment Plant in Natanz. Planned to have some 1000 centrifuges for enrichment up to 5% U-235. [2]	2002-2003 Small testing. Facility still under construction. [2] June 25 2003 Introduced UF6 into first centrifuge [2] August 19 2003 Began testing of small ten-machine cascade [2] October 2003 Single machine testing using UF6 carried out. Installation of a 64 machine cascade finalized. [2] 21 October 2003 Suspended all uranium enrichment [2] 29 June 2004 Iran resumes testing of Gas Centrifuges [2] 14 November 2004 Iran suspends enrichment [2]	18 Dec 2000 Iran Signs AP August 1 2005 Iran notifies IAEA that it has decided to resume uranium conversion activities to produce UF6 Esfahan Uranium Conversion Facility for feed for Natanz [2] 10-11 January Iran resumes uranium enrichment at PFEP [2] 5 Feb 2006 Iran withdraws from IAEA AP [2] 15 Iran begins testing of a 10 machine centrifuge [2] 22 Iran begins testing of a 20-machine centrifuge [2] March 2006 Iran completes installation of 64-machine cascade and initiated to introduce UF6. Also began construction of a second centrifuge cascade [2]	Operational	First brought into operation in October 2003. In the production area, Iran first began feeding low enriched UF6 into Cascade 1 on 9 February 2010, for the stated purpose of producing UF6 enriched up to 20% U-235 for use in the manufacture of fuel for the Tehran Research Reactor (TRR). Between 13 and 29 September 2011, the Agency conducted a PIV at PFEP and verified that, as of 13 September 2011, 720.8 kg of low enriched UF6 had been fed into the cascade(s) in the production area since the process began on 9 February 2010, and that a total of 73.7 kg of UF6 enriched up to 20% U-235 had been produced. Based on the results of the analysis of the environmental samples taken at PFEP and other verification activities, the Agency has concluded that the facility has operated as declared by Iran in the DIQ. (1 Implementation)	1. Implementation of NPT Safeguards in Iran 2011 (N/N/2012/2011) (Visual/IR Documents) 2. Global security: Iran, fifth report of session 2007-08, report, together with formal minutes, oral and written evidence. ISBN 0215513051, 9780215513054
Fordow Fuel Enrichment Plant	Due to its late discovery, an exact construction date is unknown. However, some construction was noted around 2004. [4] This started again in 2007 and continued again until the report (2009)	[5] Operating since 2011	[3] Site not reported to IAEA until 2009, though construction was already started by this point	Operational	In September 2009, Iran informed the Agency that it was constructing the Fordow Fuel Enrichment Plant (FFEP), located near the city of Qom. In its DIQ of 19 October 2009, Iran stated that the purpose of the facility was the production of UF6 enriched up to 5% U-235, and that the facility was being built to contain 16 cascades, with a total of approximately 3000 centrifuges. In September 2010, Iran provided the Agency with a revised DIQ in which it stated that the purpose of FFEP was to include R&D as well as the production of UF6 enriched up to 5% U-235. As previously reported, Iran provided the Agency with another revised DIQ in June 2011 in which the stated purpose of FFEP was the production of UF6 enriched up to 20% U-235, as well as R&D. The Agency continues to verify that FFEP is being constructed according to the latest DIQ provided by Iran. The results of the analysis of the environmental samples taken at FFEP up to 27 April 2011 did not indicate the presence of enriched uranium. (1 Implementation)	1. Implementation of NPT Safeguards in Iran 2011 (N/N/2012/2011) (Visual/IR Documents) 2. International Atomic Energy Agency (IAEA), "Implementation of the NPT Safeguards Agreement and relevant provisions of Security Council resolutions in the Islamic Republic of Iran," Report by Director General, 22 May 2013, www.iaea.org 3. http://www.niti.org/iaesites/IR51 [4] iaea.org/Publications/IDocuments/Board/2009/igov20-09-74.pdf [5] Assessment of the Nuclear Programs of Iran and North Korea By Jungmin Kang, pg. 104

Figure 1: Facilities Overview Chart

Although issues like this may seem small, when collecting data it is important to also look into the history of the surrounding area to ensure that you are not missing any information. The third column is for information pertinent to when the site began operating. In the case of Iran this information can sometimes be difficult, if not impossible, to dig up. Although for most of their history Iran was compliant under the Nonproliferation Treaty, there were several undeclared facilities that they attempted to keep secret due to their role in Iran's nuclear weapons program. Facilities like the Fordow Fuel Enrichment Plant, Natanz Fuel Enrichment Plant (FEP), and Lashkar Ab'ad Laser Enrichment Plant are examples of this, as knowledge of their existence was obtained often long after construction began.

III. Data and Results

The end product of this project was a complete visualization of the DPRK's fuel cycle, as well as a partial one for Iran. The slide shown below is a finished copy of the overarching view of the DPRK's nuclear fuel cycle. This perspective allows for the user to quickly and concisely gain a broad understanding of the state's history – both in terms of construction chronology and

safeguards implementation. The visualization utilizes a simple yet powerful means of communicating operational status and safeguards coverage, by means of a color and shape coding guide.

The second view, shown below, is more facility specific. Here, information pertinent to one specific facility is displayed, accompanied by detailed information about any proliferation significant events that happened at that site. As can be seen in the bottom half of the slide, this is the view where additional information, media, and sources will be displayed. These can be anything from articles, videos, or even pictures, though special emphasis is placed upon official IAEA reports.

IV. Conclusions and Recommendations

Many states have extensive nuclear programs that are often complex and varied. In order for IAEA inspectors and country officers to make informed decisions they need to be able to obtain and remember large quantities of relevant technical and safeguards information. Here, a graphical approach to a state's nuclear facilities and history of safeguards compliance can be a huge advantage when making critical decisions. This global perspective also allows users to directly see how the implementation

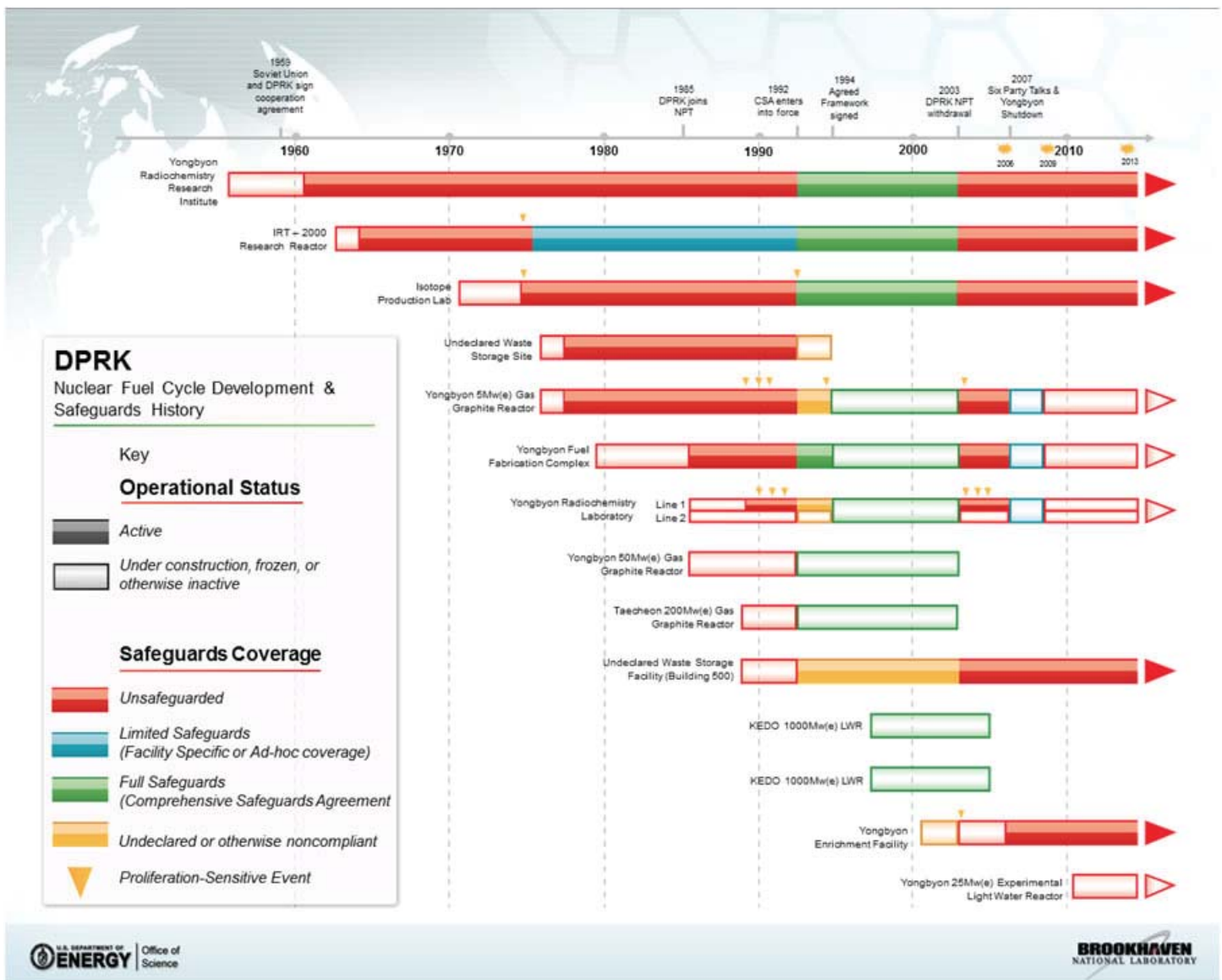


Figure 2: DPRK Visualization

of specific policies affects the operation of certain facilities.

Given the limited amount of time given to accomplish this project we were only able to completely finish the visualization for Iran. The continuation of this project rests in the hands of the IAEA if they see a benefit in the implementation of such a project. Should they decide to back this project, then further effort will be taken to develop visualizations for additional countries. Whether this would take the form of assembling a graphic for every country immediately or simply those that require attention would of course be decided by the budget for the project. Given the amount of time needed to research and construct an accurate visualization for a given country, the later approach would seem more of a realistic undertaking. If further visualizations are made, certain additions could be made to the process that would increase the depth of the graphics and delve into the how different fuel cycle facilities are connected. Facility operational history and safeguards information are certainly important on their own, but the importance of these pieces of information is more graspable when shown in the larger context of the fuel cycle as a whole. For example, an additional view could be provided that would show the

movement of the fuel both between facilities and through the fuel cycle. Additionally, the possibility of making this visualization into an interactive system has been considered. This would allow the user to quickly switch between the global and facility specific views, and give them access to even more information through pop-ups. For example, clicking on a particular proliferation significant event would display a variety of hyperlinked resources, including relevant media files, supporting documents, and IAEA reports concerning the facility. Although upgrading the visualization to this format would make the system much more intuitive, implementing it would require a lot of research and time. Several possibilities exist for the platform this system would be based on, but finding one that has the right combination of features is a difficult task. Preliminary research found the program ChronoZoom to be the most likely candidate for this project, though given the very specific needs of the project, building a platform from the ground up might prove to be the best choice.

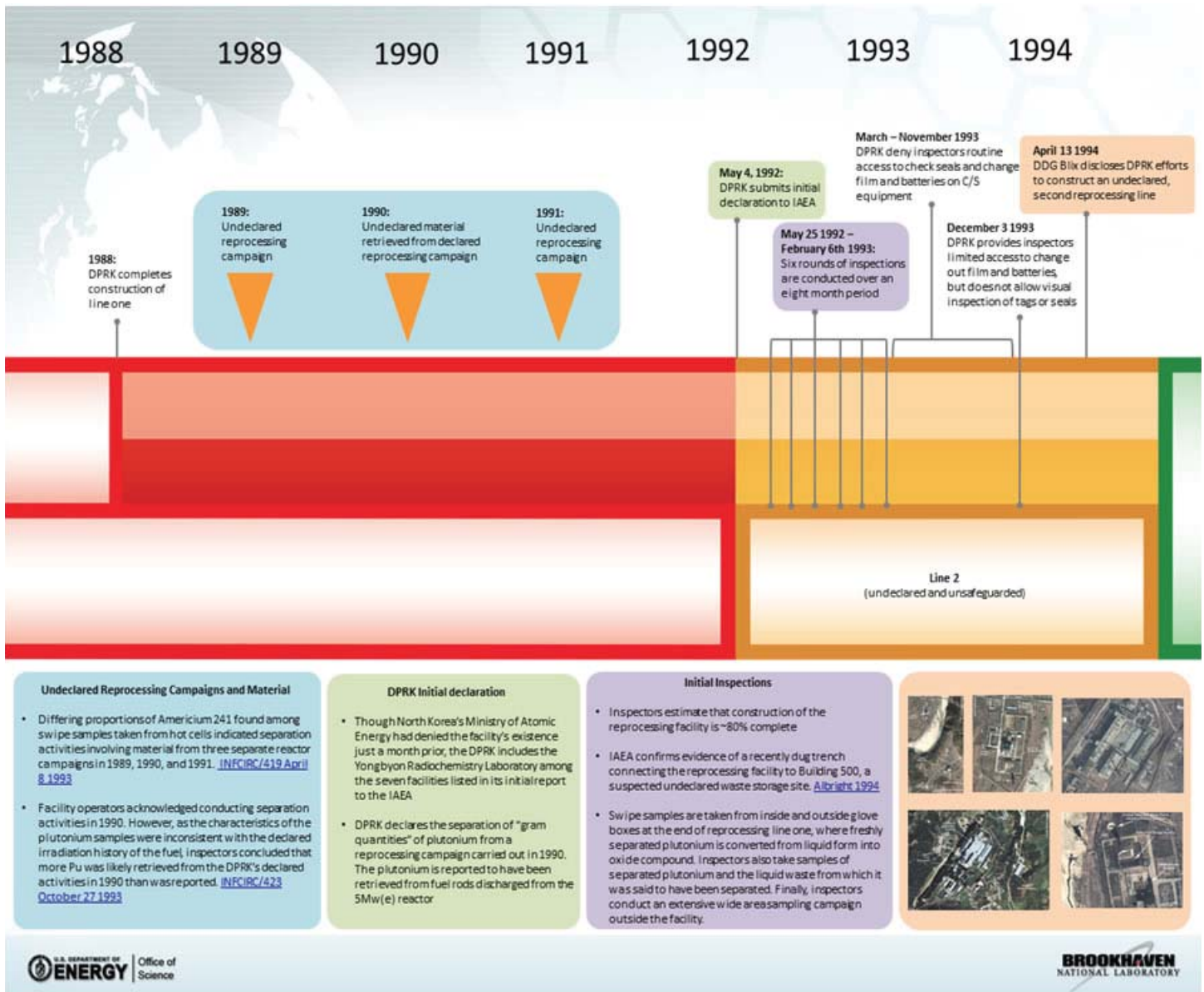


Figure 3: DPRK Facility Specific View

Assembly, calibration, test, and remote control of two extreme temperature sample environments for an x-ray powder diffraction beamline.

A. Samuel Conroy

School of Physics, University of Bristol, Bristol, UK, BS8 1TH

E. Dooryhee

Photon Sciences Department, Brookhaven National Lab, Upton, NY 11973

S. Ghose

Photon Sciences Department, Brookhaven National Lab, Upton, NY 11973

ABSTRACT

The National Synchrotron Light Source II (NSLS-II) at Brookhaven National Laboratory (BNL) is a medium energy x-ray synchrotron proposed to begin operation in 2015, replacing and outperforming the existing NSLS. At start-up the facility will contain seven x-ray beamlines designed for experimental research. Two extreme temperature sample environments at the X-ray Powder Diffraction (XPD) Beamline of NSLS-II will help users to perform in situ measurements of materials used in energy research, nanomaterial science, and condensed matter physics. They are a liquid nitrogen Cryostream capable of a temperature range of 80 K to 500 K and a TS1500 heater capable of heating to 1773 K. Temperature calibration is verified using a k-type thermocouple on both devices. Performance issues are identified in both devices in advance of their installation at the beamline. An interface program is written in Python Scripting Language to drive the Cryostream controller under Experimental Physics and Industrial Control System (EPICS) environment.

I. INTRODUCTION

A synchrotron is a facility in which particles can be maintained at a high energy, confined to travel in a ring by a combination of magnetic and electric fields. At the National Synchrotron Light Source (NSLS) at Brookhaven National Lab (BNL), electrons stored in the ring are used to produce x-ray radiation with exceptional brightness and brilliance. The unique nature of these

x-ray beams is invaluable for scientific research across many disciplines as it allows for the study of structure down to the atomic level. An example is research into Alzheimer's disease where the metal content in the brains of mice was measured by X-ray Fluorescence Microprobe (XFM) using the X26A x-ray beamline at NSLS. The quantity and distribution of metal irons in the brain is linked to Alzheimer's development and potentially lead to identifying an early marker for the disease [1]. However the resolution achievable through x-ray imaging is limited by the quality of the x-ray source, and this is one example of research that would benefit from access to an x-ray synchrotron of even greater brilliance.

The NSLS-II is a synchrotron facility under construction at BNL due to be commissioned in October 2014 that promises to be the world's brightest light source, with x-ray intensities 10,000 times that of NSLS. Approaching operation, the NSLS-II consists of a half mile synchrotron ring with seven tangential beamlines. X-rays produced by high energy electrons in the ring are directed along the beamlines, filtered and focused through samples onto detectors in order to shed light on the properties of the sample. Each beamline contains many constructions and devices to manipulate the properties of the beam and sample as the same beamline may be used for research across scientific disciplines. This includes systems that can control the temperature of a sample placed in the beamline.

The X-ray Powder Diffraction (XPD) beamline at NSLS-II will have two such extreme temperature sample environments: an Oxford Cryostream Cooler liquid nitrogen (LN2) based jet nozzle with an 80 K to 500 K temperature range; and a Linkam TS1500 furnace with a room temperature to 1773 K range. They are tested to ensure their performance meets specifications and problems are identified with both devices. Software controls are written for the Cryostream in order for it to be remote controlled alongside the other components of the beamline through a centralized control



Figure 1 – Cryostream in the lab

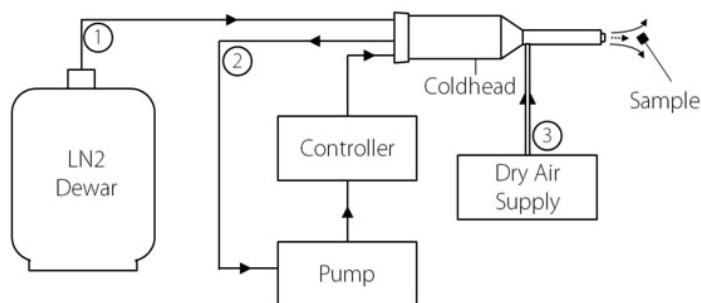


Figure 2 - Diagram of Cryostream

interface utilizing the Experimental Physics and Industrial Controls System (EPICS) software.

II. METHOD

A. Oxford Cryostream Cooler

The Cryostream liquid nitrogen cooler works by projecting a flow of supercooled nitrogen onto the sample. Figure 1 shows the Cryostream set up in the lab, and Figure 2 shows a schematic of the system. Arrows show the flow of liquid or gaseous nitrogen through connecting tubes.

Liquid nitrogen is drawn from the Dewar along channel (1) to the Coldhead. Within the Coldhead it passes through a heat exchanger, is evaporated, and exits at room temperature. This means that the Coldhead is maintained at 80 K, just above the boiling point of nitrogen [2], while the nitrogen can pass through the pump and controller via channel (2) as a gas – avoiding icing problems in the pump. Upon reentering the Coldhead the gas is cooled back down to 80 K by the heat exchanger. It finally exits through the nozzle and is projected onto the sample. A heater in the nozzle controls the final temperature of the gas - between 80 K and 500K.

Dry air is supplied through channel (3) as the Cryostream uses a laminar flow to prevent icing on the sample. The jet of cold nitrogen is encased in a surrounding jet of dry air, shown the curved arrows in Figure 2. This prevents water vapor in the atmosphere condensing onto the sample while it is cooled.

Initially the Cryostream was set up to check basic functionality in the Cryostream and its accompanying Dewar refill system. The Cryostream uses a heat map to calculate the temperature at sample point. To verify that the Cryostream's displayed temperature corresponded to the sample temperature a k-type thermocouple was placed at the intended sample position as shown in Figure 3. The tip of the thermocouple was positioned using the provided Nozzle Alignment Tool supplied with the Cryostream. The wire of the thermocouple was aligned along the axis of the nozzle and gas flow in order to minimize the steep temperature gradient along the wire, a possible source of error. Temperature was set and then recorded across the range 80 K to 500 K, with results shown in Figure 6.

An attempt was made to test the Cryostream's temperature calibration more precisely and accurately using a sample. Using

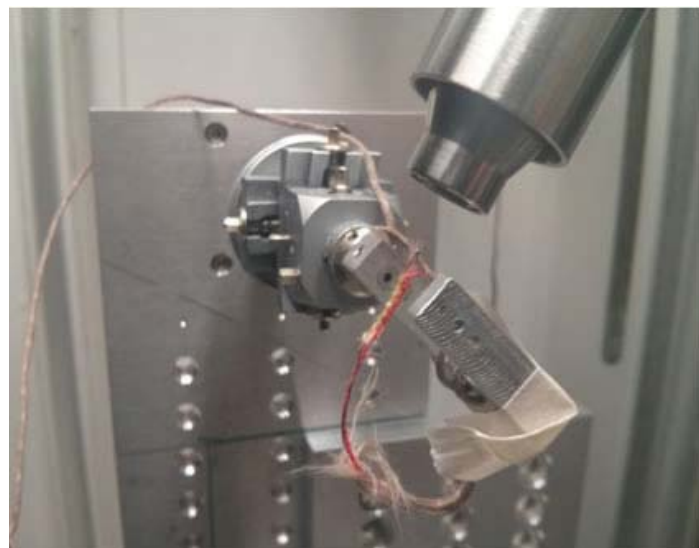


Figure 3 – Arrangement of thermocouple in Cryostream testing

the X17A beamline the lattice spacing of a sample could have been measured – allowing the sample's temperature to be calculated and compared to the Cryostream's displayed temperature. Unfortunately this was not possible due to problems running with the X17A beamline.

The Cryostream was supplied with a control box allowing manual control and ramping of temperature. However remote control is desirable as the Cryostream may have to be operated from outside the beamline due to safety restrictions around high energy x-rays. Furthermore controlling the Cryostream through the same interface as other beamline devices reduces difficulty of experiments for users of the beamline. This requires an EPICS compatible driver allowing Python code to be written to interface the driver with the central beamline controls.

B. Linkam TS1500 heater

The Linkam TS1500 heater, pictured in Figures 4 and 5 is a stage containing an electrical heating element capable of being loaded with a ~200 mg sample. Windows in the base and lid allow viewing and x-ray diffraction of the sample as it is heated. The stage is water cooled and is also capable of maintaining a vacuum or inert gas atmosphere around the sample.



Figure 4 – Linkam with control panel reading 1400oC

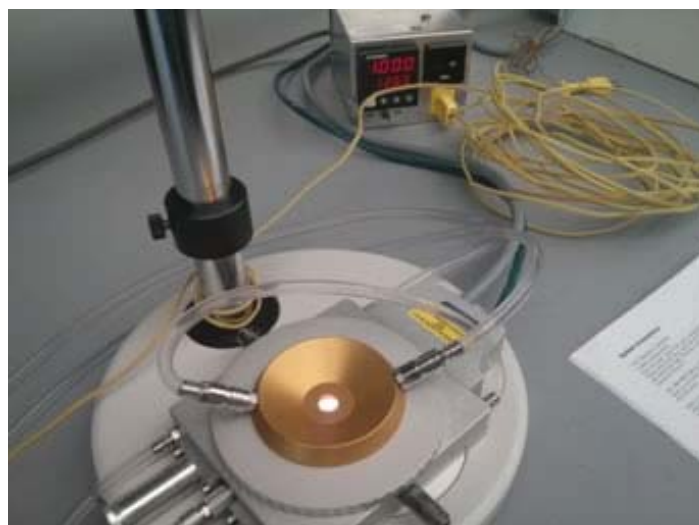


Figure 5 – Linkam with thermocouple display reading 1000oC

A thermocouple was positioned before the initial test of the heater, the end of the thermocouple being placed in the heating element sample cup. The heater was taken up to 100 degrees below the maximum of 1500 °C Results of the first run are shown in Figure 7. Further results were not taken as the Linkam failed during this first run.

An attempt was also made to test the Linkam’s temperature calibration more precisely and accurately using a sample. A known phase change, identified under a microscope, would allow comparison of the sample’s temperature with the Linkam’s displayed temperature. Unfortunately the Linkam failed before this could be implemented.

III. DATA AND RESULTS

A. Oxford Cryostream Cooler

Upon setting up the Cryostream the automatic Dewar refill system was found to be non-functional. Provided the Dewar is full the Cryostream was still functional so a preexisting Dewar refill system was used in place while a recalibration of the new refill system was arranged. Initial runs of the Cryostream found no faults beyond this.

Figure 6 shows the results of testing the Cryostream with a thermocouple. The y-axis shows the difference between the temperature displayed by the device and that recorded by the thermocouple, divided by the displayed temperature to give a percentage. It should be noted that in cooling only a very small volume to cryogenic temperatures the Cryostream necessarily induces a sharp temperature gradient along the thermocouple wire that can cause EMFs potentially affected the recorded temperature. Furthermore the thermocouple wire can act as a thermal conductor, meaning the thermocouple tip may reach a greater temperature that would be the case with an isolated sample. With these errors in mind it is unsurprising that the thermocouple results display higher temperatures that those of the Cryostream controller at low temperatures. It should also be noted that at lower temperatures the same discrepancy will be a higher percentage.

The code written for the Cryostream allows for the ramp-

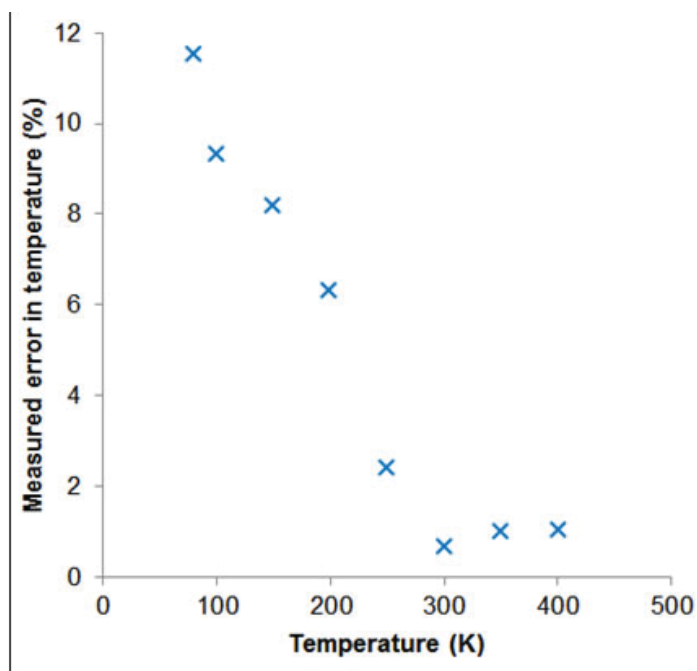


Figure 6 – Results for Cryostream test.

ing of temperature to anywhere within the physically achievable range and any specified rate remotely, and for macroinstructions to be written for the Cryostream to follow a temperature profile of several different stages.

B. Linkam TS1500 heater

The Linkam heater was set up in the lab. It was tested with the water cooling system running and with room atmosphere (the Linkam also has options to heat in an inert gas flow or a vacuum). A k-type thermocouple was fed in through one of the unused vacuum ports into the sample cup/heater. Upon the first run the Linkam successfully reached 1400 °C but failed on cooling and the heating element became unresponsive. Using a multimeter the resistance across the heating element was found to be infinite, suggesting the element was damaged. Further investigation and repair necessitated returning the heater to manufacturer.

Data recorded during the first run of the Linkam before failure are displayed in Figure 7. There is a higher discrepancy at high temperatures and this is most likely due to the difficulty in positioning the end of the thermocouple in the heating cup, and the fact that the sample would be enclosed within a sapphire plate and lid whereas this was not possible with the thermocouple, requiring a wire to access the sample heating cup, meaning greater heat loss that would be the case with a sample.

IV. CONCLUSIONS

Both devices were found to have defective components. The Cryostream was delivered with a faulty refill system and while it could be tested with a refill system from a Cryostream from another beamline, this was a very short term fix and the Cryostream has been inoperable for two months while waiting for a recalibration of the refill system. The Linkam heater failed on the first use and had to be sent for repairs. In both cases large delays were caused by these problems and so the importance of testing the devices well in advance before installation at the beamline is highlighted. A couple of months of delay at an operational beamline could have been very costly.

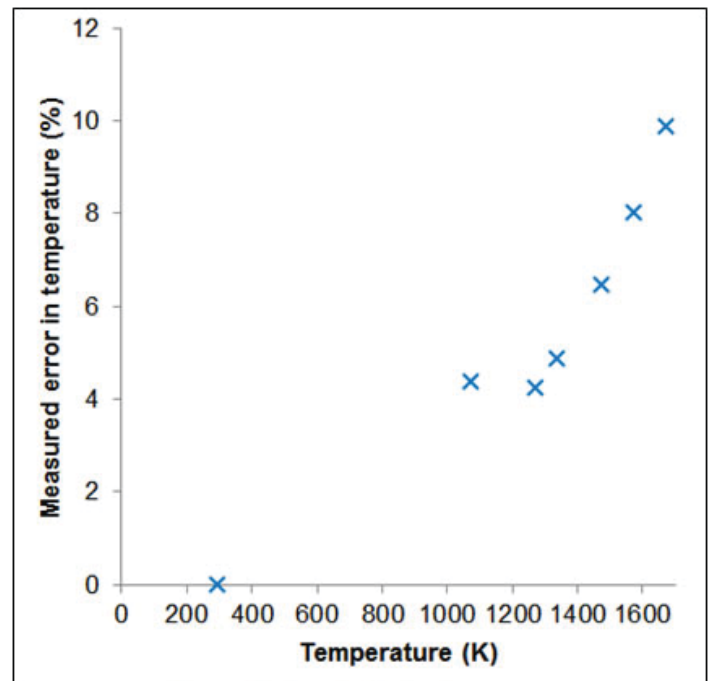


Figure 7 – Results for Linkam test.

The results from the tests with a thermocouple were as expected but would not have identified smaller problems such as discrepancies of 2%. This is why tests using samples and phase changes should be performed again when the devices are repaired. Furthermore, for the Cryostream the temperature was only measured at one point (the sample position) using the thermocouple. It would be useful to measure the temperature around this point and produce a heat map. This would give valuable information on how large an area around the sample is cooled to the desired temperature and help in the future with positioning samples.

V. ACKNOWLEDGEMENTS

This project was supported in part by the Brookhaven National Laboratory, Photon Sciences, under the BNL Supplemental Undergraduate Research Program (SURP). I would like to thank the XPD team as well as Andrew Broadbent for their guidance and support during my internship.

VI. BIBLIOGRAPHY // REFERENCES

[1] A. C. Leskovjan, A. Kretlow, A. Lanzirotti, R. Barrea, S. Vogt and L. M. Miller, "Increased brain iron coincides with early plaque formation in a mouse model of Alzheimer's disease", *Neuroimage* 55(1), 32-38, (2011)

[2] N. Wiberg, A. F. Holleman and E. Wiberg, *Inorganic Chemistry*, (Academic Press, San Diego, CA, 2001), p14

Automating processes for the production of strontium-82 in an effort to reduce dose and improve reliability

Kayle Corneill

Computer Systems Technology Department, New York City College of Technology, Brooklyn, NY 11201

Suzanne V. Smith

Collider-Accelerator Department, Brookhaven National Laboratory (BNL), Upton, NY 11973

Lisa Muench

Collider-Accelerator Department, Brookhaven National Laboratory (BNL), Upton, NY 11973

Abstract

The separation and dispensing of high levels of radioactive solutions for commercial applications can be a daunting task because the requirements for accuracy and reliability are very high. At the same time, production managers have to ensure that their staff members are not exposed to high radiation dose levels. The current procedure used at the Medical Isotope Research Program (MIRP), involves heating and dispensing radioactive solutions behind a thick lead shielded glass window using manipulators (large mechanical hands over 10 feet long) to move materials around. This research project has identified a couple tasks that are dependent on the operator and seeks to automate them in order to mitigate the dependency on human input for error. Automated control of the operation of a syringe pump system and an in-house custom built brass hot plate was tested for accuracy and precision. Results indicated that the instruments are very accurate and precise for use in their specified areas. The validation of these operations is complete however the next test is to assess their performance and use in the hot-cell.

I. Background

This study focused on some mechanical processes used in the production of the radioisotope ^{82}Sr . Strontium-82 (^{82}Sr) is a radioactive nuclide used to generate Rb-82, which is used in PET scan imaging. ^{82}Sr is produced through the bombardment of stable RbCl salt with a proton beam. These processes are done in the hot cell where accuracy and precision suffer due to the use of mechanical arms (manipulators). Being that each staff members skills in operating the manipulators vary, the production process's level of precision changes. Presently radioactive solutions are transferred by adding drops of a solution using a plastic pipet, to an open vial positioned on a balance in the hot-cell environment. In any case this is very bad practice due to the possibility of cross contamination from the pipet. This makes the process of dispensing solution even more challenging as the manipulators are difficult to maneuver. Also using instruments such as a commercial hot plate or balance can be costly, since long term exposure to radiation can cause the equipment to malfunction. Since the equipment cannot withstand prolonged exposure to radiation, the alternative is to use an automated system comprising basic mechanical parts with the electronic component controls outside the hot-cell. The implementation of the syringe pump system for dispensing and a custom-built program logix controlled hot-plate

for evaporating solution should provide greater precision and accuracy in the respective tasks while reducing does rates to staff and possibly spillage.

II. Methods & Materials

A. Overview of the study

The production of (^{82}Sr) is challenging requiring a high level of skill in order to operate the hot-cell manipulators. To improve the accuracy and precision of various processes, such as evaporation and dispensing, the Medical Isotopes Research Program at Brookhaven National Laboratory designed a number of automated systems. The first is a Program Logix Controlled hot plate designed to replace commercial plates that malfunction due to high radiation exposure. Another piece of equipment identified was the acid scrubber system used to evaporate small to large concentrations of acid solutions. Its purpose also serves to replace the industrial acid scrubber system due to its size. The third piece of equipment identified was a syringe pump system used to dispense solution mechanically into vials to reduce pipetting errors and stress on the operators' hands from dispensing with the manipulators.

B. Program Logix Control

The Program Logix Control software is a computer application that was designed and built in the Collider Accelerator Department at Brookhaven National Laboratory. It was used to regulate the rate at which a custom-built hot plate's temperature fluctuated. This study involved, testing the PLC's ability to heat and control the temperature of the hot-plate. The plate was turned on and allowed to heat up to 50 ($^{\circ}\text{C}$) then measured. After taking readings with an Infrared Laser Gun and a Thermocouple to determine the temperature, the hot plate setting was then raised. The temperature was then increased in 50 ($^{\circ}\text{C}$) intervals, up to 400 ($^{\circ}\text{C}$) and measured. Another test involving acid evaporations was conducted in order to find the optimal time taken for the solution to evaporate. These evaporations were done on an open beaker placed in the fume hood and then with the PLC hot plate.

C. Acid Scrubber System

This glassware system along with Program Logix Control Homemade Hotplate, were set up in a fume hood in order to evaporate various concentrations of HCL solutions. The Acid Scrubber is portable glassware system that consists of an evaporation flask, two connected reservoirs to neutralize acidic fumes from

the evaporated solutions. There were two versions of this system Marc I and Marc II. Marc I consisted of common glassware from the laboratory while Marc II was a custom ordered glassware. Experiments done on this system included evaporating various solutions of acids from 0.1 M to 6 M HCl and the radioactive isotope ⁵⁷Co in a 0.1 M solution.

D. Syringe Pump System

The Syringe Pump is a software program coupled with a pump hardware component, used to dispense various volumes depending on the type of syringe used. Since pipetting is currently done using the manipulators in the hot cell, this system can save time, increase precision and reduce human error due to variations in skill. Various tests were conducted to measure the amount of solution dispensed into vials using the syringe pump. Also with the implementation of this system operators will have less exposure to radioactive materials and an even lesser chance of causing the spillage of a radioactive solution.

III. Data and Results

A. Logix Control Data

The PLC hot plate was calibrated using a thermocouple and an infrared laser gun. After testing the set point verse the actual temperature, it was indicative that the infrared laser gun began with an accurate measurement but strayed as the temperature rose. The thermocouple however remained constant and was able to read accurate temperature values as the plate's temperature rose in increments of 50 (°C). The two instruments were compared resulting in the plot below.

B. Acid Scrubber Data

The commercial hot plate as per the plot, indicates that it takes about 50 minutes to evaporate an acid concentration of 0.1M HCl. The time increases significantly as the acid concentration increases to 6 M. The same experiment conducted using the PLC hot plate indicated that the time taken to evaporate the same acid solutions resulted in a time reduction. This indicated that the PLC hot plate was very efficient at evaporating solutions. It was also noted that the time taken to evaporate various acid concentrations to dryness was cut by half. The glassware system attached to the evaporating flask functioned properly as it carried the acidic fumes created over to the base reservoirs. A pH indicator placed into the base solution revealed a color change in the solution as

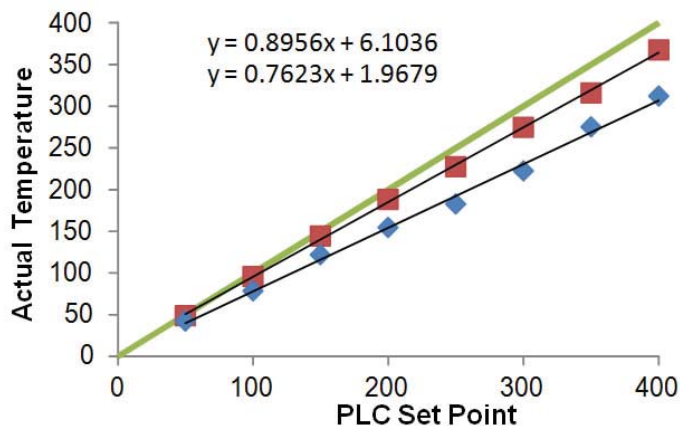


Figure 1: Actual Thermocouple and Infrared Laser Gun Readings vs. Plot of PLC Set Temperature.

the condensed acidic solution fell into the base reservoir. This was a positive indicator that the system is air tight and there was sufficient air flow.

C. Syringe Pump Data

The weight differences between an empty and filled vial enabled the detection of how much volume was placed into a vial. Of the 8 mL dispensed, an average amount of activity was measured per mL, enabling the detection of the total amount of activity per vial. These two measurements were useful as they indicated the amount of solution being placed into a vial relative to the estimated amount of activity in each vial.

Table 1: Accuracy & Precision of Syringe Pump.

Radioactive Dispensing Test Co-57			
	(Avg) Activity/ mL	Amount Dispensed (Total)	Activity/vial
	20556	8083	166154
	20101	8080	162416
	20336	7979	162261
	20584	8097	166669
Average	20394	8060	164375
STDev	225	54	2362

IV. Conclusion and Recommendations

The results from these experiments indicated that the Program Logix Controlled hot plate, acid scrubber glassware and syringe pump systems were all reliable and precise. The Program Logix Control system turned out to be very efficient in raising and maintaining the temperature set point values on the hot plate. Also the rate at which the hot plate temperature escalated was impressive, due to the heating cartridges being near the surface of the brass plate. This allows for the heat transferred from the plate's surface to contact the medium and solution being heated quickly. On the other hand the evaporations done on the Program Logix Controlled hot plate attached to the portable acid scrubber system also saw an improvement in the amount of time taken to evaporate solutions. The time taken to evaporate various acid concentrations was cut by half. Also the glassware for the miniature acid scrubber system worked well in carrying acidic fumes

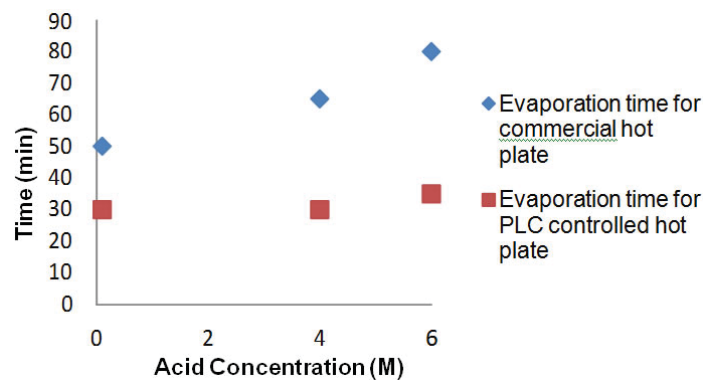


Figure 2: Plot of time to evaporate acid solution using Commercial vs. Program Logix Controlled Hot Plates.

from the evaporation flask over to the base reservoirs where they were neutralized. This closed vacuum system will replace that of the industrial acid scrubber system because of its efficiency and portability. The syringe pump system was accurate and precise in dispensing solutions into vials. This system is considerably easier to use compared to the manipulators. The goal achieved through this experiment is that the operator can now dispense accurate amounts of solution in vials while limiting their exposure to radiation. These experiments were all very successful and once applied to the production of Strontium-82, will save time and money.

V. Acknowledgements

This project was supported in part by the U.S. Department of Energy, Office of Science, Office of Workforce Development for Teachers and Scientists (WDTS) under the Science Undergraduate Laboratory Internships Program (SULI). The authors wish to thank their colleagues John Ponaro, Steve Pontieri and Pablo Rosas.

Precision manipulation of samples in a macromolecular crystallography endstation at the National Synchrotron Light Source-II

Tabatha Felter

Engineering Physics, Cornell University, Ithaca NY 14853

Richard Jackimowicz, Jean Jakoncic, Stuart Myers, and Martin Fuchs

Photon Sciences Division, Brookhaven National Laboratory, Upton NY 11973

I. Introduction

The Advanced Beamlines for Biological Investigations with X-rays (ABBIX) are a suite of beamlines being developed at the National Synchrotron Light Source-II (NSLS-II) capable of micron resolution to be used for macromolecular crystallography. Because ABBIX users must manipulate their samples with a high degree of precision, they need a high resolution microscope capable of resolution on the order of 1 micrometer, and a high precision rotational motor, also called a goniometer. To test the resolution of potential microscopes, I developed a Kohler lamp used to test a Questar QM-100 microscope and derived the formulas necessary to adjust the lamp for other microscopes. As a result of the Kohler illumination, the quality of images taken by the Questar microscope dramatically improved, performing well enough that it may be a viable candidate for use in the ABBIX endstations. I also used a combination of MATLAB and Control Screen Studio (CSS) to analyze measurement data from a goniometer to measure the sphere of confusion. In addition to developing data processing programs, I also built graphical user interfaces (GUIs) that beamline scientists and users can use to easily control the goniometer and process the data.

II. Köhler Lamp

The Köhler lamp is designed to illuminate samples without focusing an image of the light source itself onto the sample. The lamp is composed of five main elements: two lenses (a collector and a condenser), two irises (one associated with each lens), and a light source.

For optimal lighting, the spacing between these elements needs to be calculated (or at least estimated) beforehand based on the focal length and sizes of the lenses and the numerical aperture of the microscope being used. I performed two types of calculations to design Köhler lamps: the first used the specifications of the lenses we had in the lab to determine the rest of the characteristics of the lamp, and the other used the specification of our final endstation and the desired characteristics of the lamp to determine the specifications of the lenses.

III. Design calculations

In an ideal Köhler system, the numerical aperture of the lamp ought to match the numerical aperture of the microscope. The

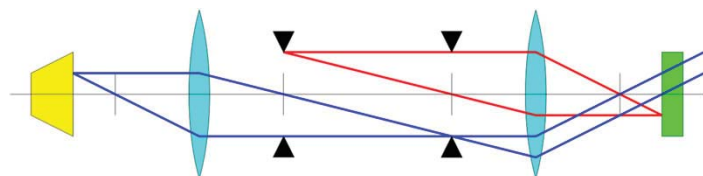


Figure 1: Basic Köhler lamp

numerical aperture of a system can be calculated by

$$fNA = n \sin \mu$$

Where n is the index of refraction of the medium and μ is an angle determining the divergence (or convergence) of the light from the source. We can calculate the NA in the case of a Köhler lamp by assuming the light focuses at a point on the sample.

This is illustrated for the case of determining the numerical aperture of a Köhler lamp in figure 2.

In this case, because the medium is air, $n \approx 1$, so the equation is simplified to $NA = \sin \mu$. From this, we can derive:

$$NA = \sin \mu = \frac{D/2}{\sqrt{(D/2)^2 + L^2}} = \frac{D}{2\sqrt{D^2/4 + L^2}}$$

Where D is the diameter of the last lens in the Köhler and L is the distance between the lens and the sample. In cases where the NA is small enough, we can use the small angle approximation that the sine of μ will equal its tangent. This simplifies the calculation to

$$NA = \frac{D/2}{L} = \frac{D}{2L}$$

When using a microscope with a larger numerical aperture, though, we must assume a larger angle, making this approximation invalid.

Because the numerical aperture should be given in the microscope specs, and the diameter of the lenses in the Köhler are known, we are attempting to solve for L , the ideal distance between the sample and the lens. For large angles, this comes out to:

$$L = \frac{D}{2} \sqrt{\frac{1}{(NA)^2} - 1}$$

It is clear that as the numerical aperture becomes smaller and smaller, the term containing the numerical aperture comes to dominate the expression under the radical. If we take the limit as NA goes to zero, we find

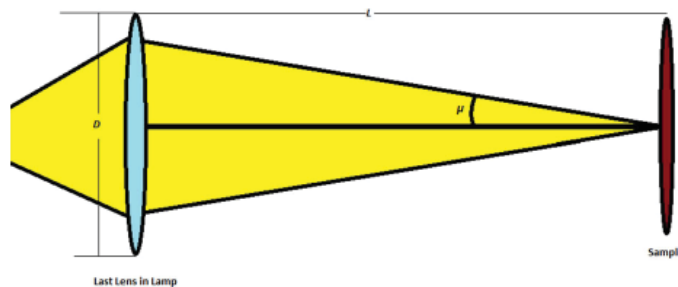


Figure 2: NA calculation

$$L = \frac{D}{2NA}$$

which is simply another expression of the formula given by the small angle approximation earlier.

It should be born in mind that while constructing Köhler lamps for microscope testing, it was found that optimal lighting was found using a numerical aperture somewhat larger (0.21) than the given aperture of the microscope (0.18). This is most likely due to the fact that the light does not converge to a point on the sample, which means the actual numerical aperture of the lamp is smaller than the calculated value. Thus, the calculations should be taken to be an estimate of the ideal distance, rather than the exact value.

The length of the lamp and the spacing of the lenses are determined by the extremely familiar lensmaker's equation:

$$\frac{1}{f} = \frac{1}{s} + \frac{1}{s'}$$

Where f is the focal length, s is the distance of the object from the lens, and s' is the distance of the image from the lens.

The Köhler lamp is designed so that the image of the lamp filament appears on a different image plane than the image of the sample. To do this, the lamp ought to be set up so that the image of the lamp is focused on the second (condenser) iris, while the image of the first (field) iris is projected onto the sample.

Working from our calculation of L in the previous section, then, we begin with calculating the distance from the condenser lens to the collector iris.

The focal length of the lens should be known from the specifications from the manufacturer, and $s^{\wedge}=L$. Using the small angle approximation and solving for s , the formula becomes:

$$s_1 = \frac{s_1' f_1}{s_1' - f_1} = \frac{L f_1}{L - f_1}$$

Now we must relate s_1 - the distance between the condenser lens and the iris nearest the collector lens - and s_2' the distance between the collector lens and the iris nearest the condenser lens. This would be difficult if it were not for the fact that the spacing between each iris and its nearest lens are determined by the focal lengths of the lenses. In the diagram in figure 1, the leftmost iris must be placed one collector focal length (f_2) away from the lens. This is to ensure that any parallel light emitted from the light source will focus at the iris, narrowing the beam so that minimal light is lost at this iris. The rightmost iris must likewise be one condenser focal length (f_1) from the condenser lens. This is an even more crucial point because this is where the image of the light source is projected. If that image is projected onto a position one focal length away from the condenser lens, when the rays of light pass through the condenser lens, they will emerge parallel to one another, providing a maximally even illumination. This leads to the relationship that:

$$s_2' + f_1 = f_2 + s_1$$

$$s_2' = f_2 + s_1 - f_1$$

and we can work backwards to find s_2 .

$$s_2 = \frac{s_2' f_2}{s_2' - f_2} = \frac{(f_2 + s_1 - f_1) f_2}{f_2 + s_1 - f_1 - f_2} = \frac{\left(f_2 + \frac{L f_1}{L - f_1} - f_1\right) f_2}{\frac{L f_1}{L - f_1} - f_1} = \frac{(f_2 (L - f_1) + f_1^2) f_2}{f_1^2}$$

Because the image of the collector iris is projected onto the sample, adjusting the width of the collector iris will change the size of the spot projected onto the sample. This is essential to avoid illuminating areas outside the area of interest and thereby minimizing stray light. As a result, if an L is chosen that results in a slightly larger than optimal NA , adjusting the collector iris can be used for fine adjustments of the lamp's NA .

IV. Application and Results

Once I designed and built this lighting system, I applied it to testing a Questar QM-100 microscope. Because the Questar was a candidate for use in the endstations, we had to be certain that we could reliably achieve resolution on the order of 1 micron with the Questar. To do this, we took several test images with the Questar, adjusting the camera and the lighting to achieve optimal conditions.

In this Köhler lamp, we had the following design parameters:

$$f = 30\text{mm}$$

$$NA = 0.18$$

$$D = 30\text{mm}$$

This gave us a lamp of the following specifications:

$$L = 83.3\text{mm}$$

$$s = 46.875\text{mm}$$

Due to the symmetry of the lamp, the distance between the light source and the collector lens is also equal to L . This gives a proposed lamp with a total size of about 120mm.

This was not the value for L ultimately used in the lab. These calculations make a few key assumptions for the sake of simplification that are not true. For example, this calculation assumes that the light spot on the sample is a point, which is certainly untrue. As a result, smaller L values resulting in larger NA values were found to produce better images. It is important to note, though, that when changing L , one must also change s so that the

relationship $s = \frac{L f}{L - f}$ holds true.

When we had the flexibility of trying different lenses, we solved the first equation differently:

$$NA = \frac{D}{2L}$$

One might ask why we did not solve for the characteristics of the lenses (D and f) and find the optimal lenses that way. If we could order custom lenses to our exact specifications, that would indeed be the best course of action. We are ordering lenses out of a catalog, however, meaning that the optimal lenses might not exist.

Instead of trying to solve for the optimal focal length and diameter, we take a list of possible lenses and calculate what the characteristics of a lamp using those lenses would be. Because that would take an enormous amount of time and tedious calculations, I wrote a MATLAB script that would perform these calculations on two different lens combinations and then prompt the user to choose which combination produced the better lamp. This script will be updated with more precise formulas for calculating the numerical aperture of the lamp and amount of light loss, so as to make the final numbers more reliable for final lamp design.

The final images taken with the Questar were taken by Jean Jaconcic. The image featured here has a field of view of 300 microns x 225 microns.

A. Goniometer

Because the proposed beamspot at the ABBIX beamlines is going to be as small as one micron, it is crucial that the goniometer used to rotate the crystal during crystallography be able to move very precisely without deviating significantly in space from its initial position, lest the crystal move out of the beam. To confirm that the proposed goniometer can meet this requirement, I was tasked with developing a workflow and system to measure the sphere of confusion of a goniometer. The measurements were taken using capacitive sensors manufactured by Lion Precision, which are able to calculate the distance between a sensor and a measurement ball by the voltage between these two elements. Data was then collected via an oscilloscope and processed using a set of data processing algorithms and tools.

B. Triggering

Because we are only interested in data gathered while the goniometer is rotating, we needed a triggering device. To this end, Stuart Myers programmed the Delta Tau controller that commands the goniometer to trigger high voltage pulses as the goniometer begins and ends its rotation. This can either be used to

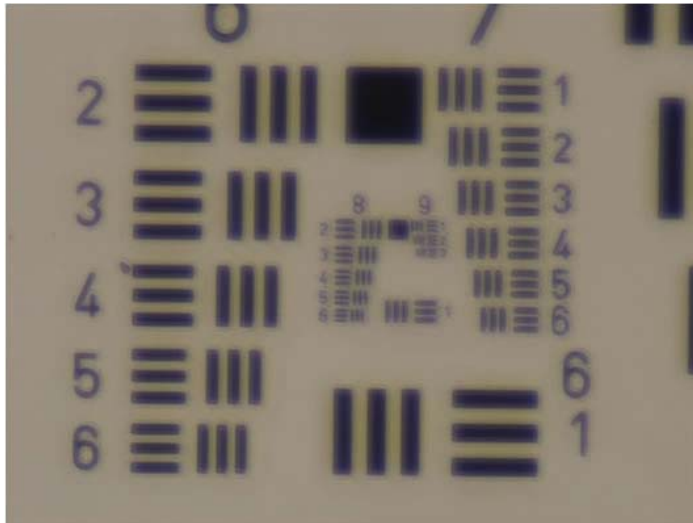


Figure 3: Image taken of USAF target with Questar QM-100. Field of View is 300 microns x 225 microns.

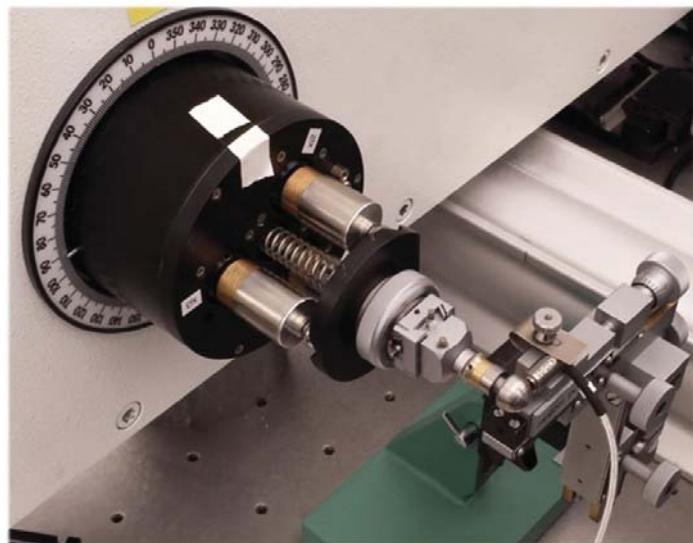


Figure 4: The Goniometer, Measurement Ball, and Capacitive Sensor

trigger the oscilloscope to begin and end recording the signal, or, if the user manually triggers the data, to determine where the data processing program should cut off irrelevant data.

C. Data Processing Interface

I designed two Graphical User Interfaces (GUIs) in Matlab for the purpose of data analysis, of which only one will be used in measurement. Because the majority of the development of the data processing tools had already been finished at a similar project at the Swiss Light Source, I had access to a number of tools that had a number of capabilities and functionalities. My first GUI was built around these programs, attempting to make it as easy as possible for users to access the tools. Within the span of a day of programming, I was able to develop a GUI that could partially progress test data taken from the Swiss Light Source project.

While developing this GUI was very useful for me to understand the steps involved in processing the data, its usefulness in dealing with actual collected data was extremely limited. Building the GUI around existing programs rather than on the workflow meant that while it could do many different things, it was not very good at combining those things into what a user actually needed to do with the data. Furthermore, the oscilloscope in our lab saved the data differently from the oscilloscope used at Swiss Light Source, so the program could not process the data.

Deciding that starting again from scratch would be quicker than trying to fix these problems in the existing program, I built a new GUI, focusing this time on what a user would need the GUI to do instead of on what existing functions could enable it to do. As a result, I was able to eliminate redundant features and greatly simplify the computational side of the program to the point that the GUI only called functions defined within its own code file, instead of relying on external functions as it had previously.

We can divide the GUI's abilities according to whether they are part of the preprocessing steps, or the processing steps.

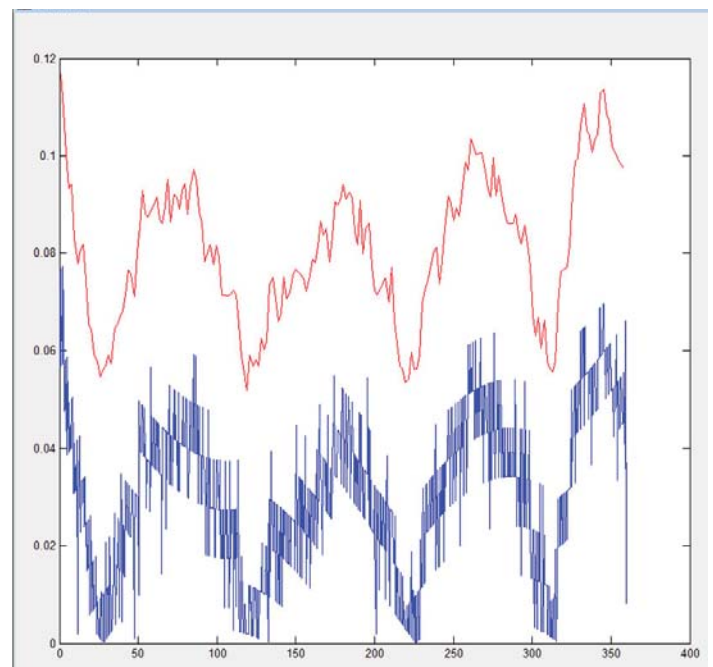


Figure 5: The Matlab GUI with raw and binned data plots. The aliasing artefact in the unbinned trace was due to a large trace offset. In later measurements, this offset was subtracted during data collection, to yield un-aliased traces.

V. Pre-Processing

The oscilloscope saves data in CSV format, but Matlab works with arrays. The pre-processing button “convert” and “Cut Data” both save data as .mat files, converting CSV lists into arrays. The difference between the two buttons is the degree to which they modify the contents of the CSV file identified as the dataset. “Cut Data” is designed for use when the oscilloscope is started manually and the collected data needs to be cut after the fact. “Convert,” on the other hand, assumes that the only data in the file is relevant data, so it only converts the CSV to arrays.

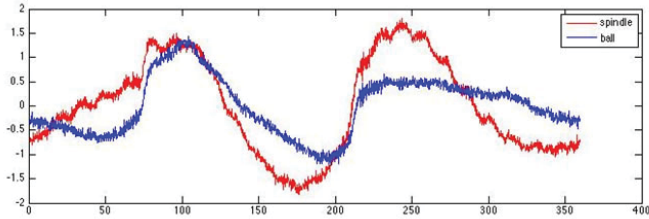


Figure 6: Error due to ball imperfections and spindle error separated via Donaldson Ball Reversal.

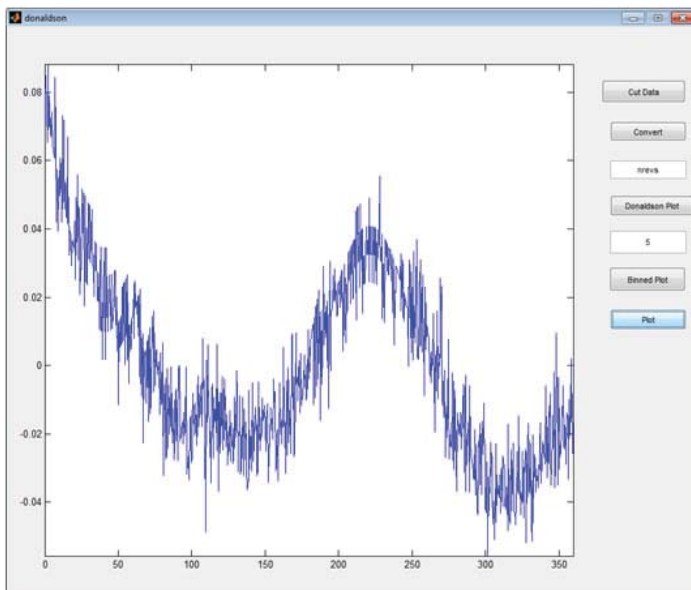
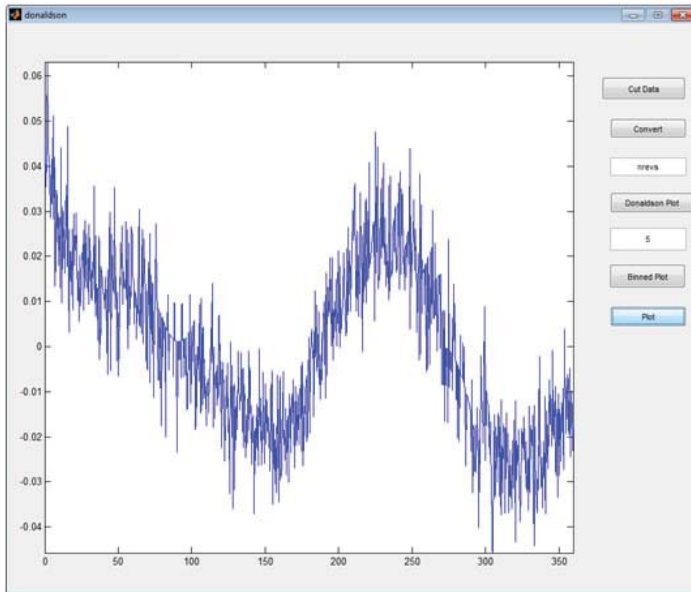


Figure 7. TOP: Ungrounded Measurement Ball.
BOTTOM: Grounded Measurement Ball.

VI. Processing

Once the data is saved as a .mat file, we can begin filtering out irrelevant signals. As of this writing, “Donaldson Plot” is the only button that can take .mat files and turn them directly into a data plot. “Donaldson Plot” prompts the user for two .mat files: the two Donaldson trace data files.

The Donaldson ball reversal technique involves taking two traces under the same conditions except that the ball is rotated 180°, and the sensor is moved to the opposite side of the ball. Variations in the signal caused by imperfections in the surface of the ball will then be the same in both traces, but signals resulting from goniometer error (the signals we are interested in) will be 180° phase shifted from one another. As a result, one can eliminate error due to the surface of the ball by dividing the difference in the traces by 2. Mathematically, we can represent it like this:

$$T_1(\theta) = B(\theta) + S(\theta)$$

$$T_2(\theta) = B(\theta) + S(\theta + 180^\circ) = B(\theta) - S(\theta)$$

$$T_1(\theta) - T_2(\theta) = B(\theta) + S(\theta) - B(\theta) + S(\theta) = 2S(\theta)$$

$$S(\theta) = \frac{T_1(\theta) - T_2(\theta)}{2}$$

Where $T_1(\theta)$ is the first trace, $T_2(\theta)$ is the trace taken with the reversed ball, $B(\theta)$ is the error due to the surface of the ball, and $S(\theta)$ is the spindle error (what we actually want to measure). It is very important that the user does not haphazardly place the sensor after the reversal. If the sensor is moved 180° to the opposite side of the ball, then $T_2(\theta) = B(\theta) + S(\theta + 180^\circ)$. If the user does not move the sensor after rotating the ball, then $T_2(\theta) = B(\theta + 180^\circ) + S(\theta)$. This makes $S(\theta) = (T_1(\theta) + T_2(\theta))/2$. The GUI is programmed with the assumption that the user will move the sensor to the opposite side of the rotated ball. If this is not the case, the data will not be processed correctly.

Once the user has selected the two traces (it does not matter what order they are chosen in), the traces are filtered using fCut (Adrian Curtin, 2010), a function that eliminates the error due to incomplete centering of the ball on the goniometer by removing first order sinusoids from the Fourier transform of the signal.

It should be noted that this step could be done either before or after the application of the Donaldson Ball Reversal to the two traces because the addition of integrals and sums is a linear operation.

Once fCut and the combination have been applied, the GUI displays the data as a plot in the main figure window. Finding the peak-to-peak deviation of the signal in one dimension is the very simple matter of finding the maximum and minimum values of the trace, which gives us the sphere of confusion for a one dimensional measurement (a line of confusion, if you will). Finding the sphere of confusion in three dimensions is a somewhat more complicated matter. Using the peak-to-peak values calculated in each dimension as the parameters is problematic as the maximum value in the x-axis might not correspond to the maximum value in the y- or z-axes. As a result, combining the one-dimensional peak-to-peak values can result in an overestimation of the sphere of confusion.

A. Grounding

The first dataset collected during this process of measurement, testing, and analysis revealed a pervasive high frequency signal that made it very difficult to identify the goniometer’s over-

all pattern of motion. At first I dealt with this using code provided to me from the previous project at the Swiss Light Source; the code in question would bin the data, reducing the number of data-points by combining several points into an average data-point, but this did not address the root cause of the noise: bad grounding. Because the ball on the goniometer was constantly rotating, attaching a grounding wire to it was out of the question, and any electrical contact between it and ground had to be made through the spindle itself. “Beep tests” – testing the resistance between two points to see if they were electrically connected – revealed that the ball was electrically isolated from its mount, and thus was unconnected to ground.

Because the ball was poorly grounded, changes in its position relative to ground (the surface of the optical table) would cause the amount of voltage of the ball relative to ground to change, which would in turn change the voltage difference between the ball and the capacitive sensor, giving the (false) impression that the ball was rapidly changing position relative to the sensor. This was confirmed by a simple test: by waving one’s hand near the ball, if the ball is not well connected to ground, the capacitance between the ball and a hand can change the amount of charge on the ball, resulting in a sharp change in the measured voltage between the ball and the capacitive sensor. When I waved my hand near the measurement ball, the voltage output on the oscilloscope was observed to spike suddenly, confirming that the ball was inadequately grounded.

There is a relatively quick way of fixing this problem. The capacitive sensors work by way of a sensing current. The current is AC, and controlled by drivers in the controller. If two sensors with frequencies phase shifted by 180o are placed next to the same target, then the current would be moving towards the ball in one probe and away from it in the other, allowing one probe to serve as a path to ground. The manufacturer set up the controller so that odd and even channel current drivers are phase shifted from each other in this manner, allowing users to ground the measurement ball using the probe.

After applying this technique, there was an appreciable reduction in signal noise. In my setup in the lab, however, the sensitivity of the system was reduced because we were limited by the precision of our sensor holder. Because this was only a proof of concept measurement, our holders were rather crude, and I could not manipulate them with enough precision to use the high precision setting.

A longer-term (and easier to work with) solution would be to find a way to ground the target ball through the spindle itself. This would be difficult, as there are at least three electrically isolated areas between the target ball and the back of the goniometer, but if these regions could be connected via slip rings or some other technique, grounding the ball would be much simpler for the user.

VII. Conclusions

Over the course of this internship, I have developed a method for determining the optimal configuration of a Köhler lamp given its desired characteristics, as well as a user interface and data processing program to analyze goniometer measurements. The Köhler lamp I designed for testing purposes was used to test microscope candidates. The data processing GUI for the capacitive sensor traces can be used to calculate the sphere of confusion based on filtered measurement traces.

Both tools can be applied to future work at the FMX/AMX

endstations. The selection algorithm I wrote can be modified and used again in the future to design a light source for use in the endstation itself. Furthermore, now that a CSS screen has been developed by Stuart Myers and Annie Heroux to control the goniometer, the GUI can be installed on a laptop with the CSS screens as part of a mobile metrology station that can be used to align goniometers in the endstations.

VIII. Acknowledgements

This project was supported in part by the U.S. Department of Energy, Office of Science, Office of Workforce Development for Teachers and Scientists (WDTS) under the Science Undergraduate Laboratory Internship Program (SULI). I would also like to thank Annie Heroux and Dieter Schneider for their assistance and advice through this project.

IX. Bibliography

Curtin, Adrian. “fCut.” Code Report. Paul Scherrer Institute, 2010.

Davidson, Michael W. Configuring a Microscope for Köhler illumination: Introduction. Zeiss. 6 August 2014 <<http://zeiss-campus.magnet.fsu.edu/articles/basics/kohler.html>>.

Donaldson, R.R. “A Simple Method for Separating Spindle Error from Test Ball Roundness.” *Annals of the CIRP* 21.1 (1972): 125-126.

Fuchs, M R, et al. “NSLS-II Biomedical Beamlines for Macromolecular Crystallography, FMX, and AMX, and for X-ray Scattering, LIX: Current Developments.” 17th Pan-American Synchrotron Radiation Instrumentation Conference (SRI2013). *Journal of Physics: Conference Series*, 2014.

Lion Precision. “Capacitive Sensors - Ungrounded Target.” Vols. LT03-0022. March 2013.

Rottenfusser, Rudi, Stephen P Price and Michael W Davidson. Microscope Alignment for Köhler Illumination. 6 August 2014 <<http://zeiss-campus.magnet.fsu.edu/tutorials/basics/microscopealignment/indexflash.html>>.

Salathe, Marco. “Evaluation of the Sphere of Confusion of Goniometer Devices and Analysis of the SmarAct Linear Positioners.” Internship Report. Paul Scherrer Institut, Ecole Polytechnique Fédérale, 2010.

X. APPENDIX: DERIVATION OF FCUT LINEARITY

fCut is a function which filters out the centering error by taking the Fast Fourier Transform (FFT) of a signal and subtracting the first order signal. We can represent this process mathematically thus:

$$fCut(f(x)) = \int_{-\infty}^{\infty} \left(\int_{-\infty}^{\infty} f(x) e^{-2\pi i x \xi} dx - K(\xi) \right) e^{2\pi i x \xi} d\xi$$

Where f(x) is your original data, ξ is your frequency parameter, and $K(\xi)$ is the first order signal we are subtracting to eliminate centering error.

An important question arose while designing the GUI as to the order of procedure for data processing. The dilemma is best explained by example: the GUI is designed to be able to plot signals that have been cleaned up via Donaldson reversal (explained in more detail earlier in the report) and raw signals without a second Donaldson trace for filtering. When dealing with raw signals, it is clear that one can apply fCut at the very last stage before plotting the signal because that is the only processing of the data

that takes place. When dealing with Donaldson reversed data, it is unclear as to whether or not fCut should always be applied before combining the signals or if it is acceptable to apply the function afterwards. Determining the linearity of fCut helps to determine the restrictions (if any) we should place on how to order the data processing within the GUI. It is for this reason that this derivation was performed. Replacing $f(x)$ with $f(x)-g(x)$, we find:

$$\begin{aligned} fCut(f(x)-g(x)) &= \int_{-\infty}^{\infty} \left(\int_{-\infty}^{\infty} (f(x)-g(x))e^{-2\pi ix\xi} dx - K(\xi) \right) e^{2\pi ix\xi} d\xi \\ &= \int_{-\infty}^{\infty} \left(\int_{-\infty}^{\infty} f(x)e^{-2\pi ix\xi} dx - \int_{-\infty}^{\infty} g(x)e^{-2\pi ix\xi} dx - K(\xi) \right) e^{2\pi ix\xi} d\xi \end{aligned}$$

At this point, we have almost managed to separate the two functions from each other, with only $K(\xi)$ still holding them together. We can write $K(\xi)$ as the difference between two functions:

$$K_f(\xi) - K_g(\xi)$$

And we assign each function to either $f(x)$ or $g(x)$. This is a reasonable enough assumption, as each trace will have its own centering error.

Now that we have separated the centering errors, we can group them with their respective functions. From there, the rest of the derivation is almost trivial.

$$\begin{aligned} &= \int_{-\infty}^{\infty} \left(\int_{-\infty}^{\infty} f(x)e^{-2\pi ix\xi} dx - K_f(\xi) - \int_{-\infty}^{\infty} g(x)e^{-2\pi ix\xi} dx + K_g(\xi) \right) e^{2\pi ix\xi} d\xi = \\ &= \int_{-\infty}^{\infty} \left(\int_{-\infty}^{\infty} f(x)e^{-2\pi ix\xi} dx - K_f(\xi) \right) e^{2\pi ix\xi} d\xi \\ &\quad - \int_{-\infty}^{\infty} \left(\int_{-\infty}^{\infty} g(x)e^{-2\pi ix\xi} dx + K_g(\xi) \right) e^{2\pi ix\xi} d\xi = fCut(f(x)) - fCut(g(x)) \\ fCut(f(x)-g(x)) &= fCut(f(x)) - fCut(g(x)) \end{aligned}$$

This gives us some more freedom in how to apply fCut in the GUI. It is possible to refrain from removing the centering error until the very last step, even building it into the plotting function, or we can make it the very first step. Based on this derivation, it does not matter when in the process we apply it, as long as we do not forget to do so.

A study of neutral pion events in a liquid Argon detector

Samantha Fortuna

Department of Physics, University of Virginia, 583 Brandon Avenue, Charlottesville, VA, 22903

Mary Bishai

Department of Physics, Brookhaven National Laboratory, Upton, NY, 11973

Abstract

MicroBooNE and the Long Baseline Neutrino Experiment (LBNE) are both neutrino experiments targeted at discovering the remaining mysteries of charge parity violation and neutrino mass hierarchy. To do so, particles such as muons, electrons, and pions are shot in a beam toward a Liquid Argon Time Projection Chamber (LArTPC), from which researchers can observe their interactions and how the neutrinos oscillate over short and long distances, which can lead our study to determining these conditions. One important feature of each experiment is to be able to identify, reconstruct, and analyze the different reactions recorded by three sets of wires in the LArTPC. Therefore, our study created simulation software that would simulate electrons, muons, and neutral pions, and record the data of their interactions in the liquid Argon detector. The study compiled and ran this software, and produced hundreds of event displays of different pions, electrons, and muons, in order to see and understand their path throughout the detector. Then, our study reconstructed the data; one approach was to study the charge deposition of electrons as a function of parent energy and of distance from the detector. We examined the ways in which the reactions compared across 4000 events, created histograms of the data, fitted the data to a curve, and then plotted the results of this fit data. Next, we examined the effect that different fiducial cuts to the volume of the detector will have on different particles, and if such fiducial cuts are practical. When the experiment is running, researchers will be able to use the techniques used in our simulations to analyze and understand the data from the detector, and answer the questions of mass and charge parity that neutrinos still pose.

I. Introduction

In this study, we examined simulations of photons, electrons, muons and neutral pions in a Liquid Argon Time Projection Chamber (LArTPC), in order to further understand the charged particle interactions that will occur in the upcoming short baseline neutrino experiment MicroBooNE. MicroBooNE will use the LArTPC to re-examine the evidence provided by earlier short baseline neutrino experiments of the possibility of a fourth type of neutrino, sterile neutrinos. This hypothesis arose from the detection of an excess of an electron neutrino-like signal in previous short baseline neutrino experiments.² However, previous detectors have failed in determining whether this signal is due to an excess of electron neutrinos or if the detector was mistaking photons for electrons. If such an excess of electron neutrinos is present, it would imply that muon neutrinos are changing flavors over a much shorter distance than previously imagined. If they are mixing over such a short distance, it points to the need for a fourth flavor of neutrino, the sterile neutrino. This would prove physics

beyond the Standard Model, which predicts three massless flavors of neutrino. Therefore, electron and photon separation is of utmost importance. The methods used and data taken from MicroBooNE will also serve as research and development work for larger neutrino experiments, most notably the Long Baseline Neutrino Experiment (LBNE). These longer baseline projects seek to find the remaining unknown parameters of neutrinos, such as their mass differences, the charge parity (CP) phase, and their mixing angles. Finding these parameters will further confirm physics beyond the Standard Model, such as the fact that neutrinos do have mass,

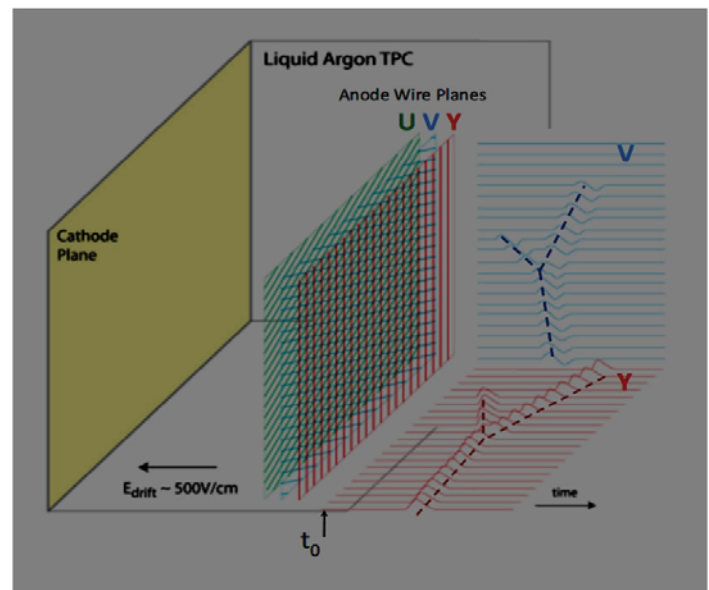


Fig. 1 Detector geometry (taken from reference 1)

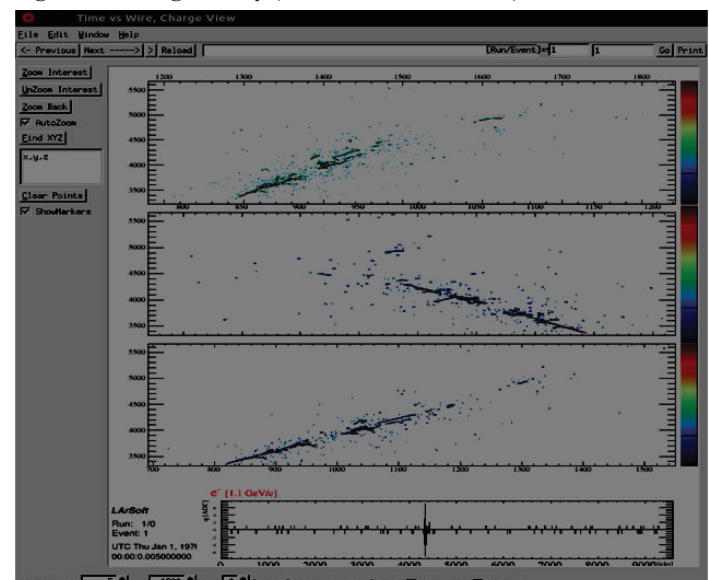


Figure 2 Electron Simulation

albeit a minuscule one. Also, the discovery of the CP phase could prove further CP violation, which would explain why there is an imbalance of matter and antimatter in the universe.

The LArTPC provides a more in-depth look at the interactions that will help answer these questions; it creates a three dimensional reconstruction of the interactions within the detector. Interactions in Liquid Argon produce an ionization charge and scintillation light. Photomultiplier tubes within the detector see the scintillation light, while the ionization charge drifts into the uniform electric field created in the detector. This ionization signals the beginning of the time calculation. The ionization charge is deposited on anode wire planes (delineated as the u, v, and y axis) placed at 60 degree angles to one another. From the data collected from the photomultiplier tubes and the wire planes, we can calculate the time and the drift velocity to predict where and how particles decay and travel. The charge deposited on the wire and the time at which it does so allows a three dimensional reconstruction of the particle interactions.^{1,3} This detector geometry is displayed in the figure below.

Liquid Argon was selected to fill the detector for several reasons. It is inexpensive, which is important when filling kilotons of detector volume. It has a high density, and the ionization can be tracked over long distances, as long as there is not interference.³ This study focuses on comparing the various decay of neutral pions into two photons, and comparing these reactions to electron scattering. By studying the data produced from simulations of these particles, we could begin to differentiate between the two particle reactions and get a better understanding of the reactions occurring in the LArTPC.

II. Body

In order to examine the different reactions in the LArTPC, we ran FhiCL files that simulated a set number of particle events. We then looked at them in a standard viewer and in a three dimensional viewer that reconstructed their path. At first we focused on visually comparing the neutral pion and the electron scattering, to see if they were at points indistinguishable. For example, in the standard viewer, there were many cases in which it was difficult to discern whether the neutral pion decayed into two photons, or appeared as an electron scattering. Figures 2 and 3 below demonstrate this.

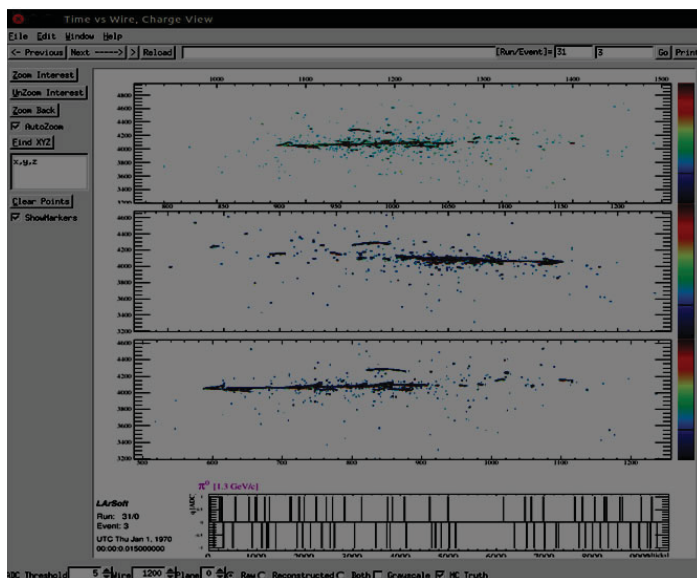


Figure 3 Neutral Pion Simulation

Although the neutral pion particle decays into two photons with individual paths, at points two distinct branches are difficult to discern. The figures above demonstrate that further analysis would be necessary in order to understand and differentiate between different reactions. After simply simulating the data, it became necessary to begin various methods of reconstruction.

To do so, we looked at the charge deposition as a function of several different parameters; first, as a function of parent energy, then as a function of distance from the detector. To do so, our study created histograms for each cut of parent energy, and then for x, y, and z cuts of electrons and photons. Also, to get a more accurate picture of the data, we made fiducial cuts to the data, so only reactions contained within the volume 20 cm from the edge of the detector was recorded. This prevented a “tail” of energy in the histograms; that is, an unusual amount of lower level charge deposited. Next, we fitted a Gaussian curve to the histograms, calculated its mean and sigma, and created graphs for the x, y, and z dimensions that plotted position, Gaussian mean, and Gaussian sigma. The results of these plots are in Figures 4-9.

These graphs demonstrate a relatively constant Gaussian mean and sigma throughout y and z cuts, and a mean and sigma that steadily decreases for electrons and photons in the x dimension. The green error bars represent the sigma on the mean, and the black error bars represent the error calculation of the mean. These calculations represent that there is a decrease in the average charge deposition (here represented in ADC counts/MeV) as the particle moves farther and farther away from the detector. The decrease in mean and sigma as a function of x distance from the detector is vital for the calibration of the energy calculation. As the particle moves farther from the wire and deposits charge,

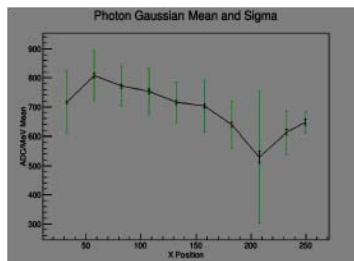


Fig. 4 Electron X Cuts

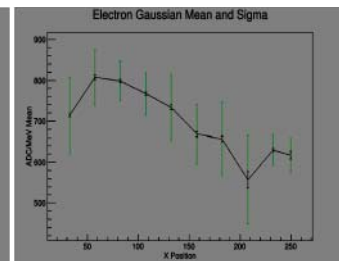


Fig. 5 Photon X Cuts

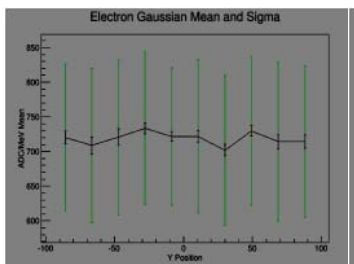


Fig. 6 Electron Y Cuts

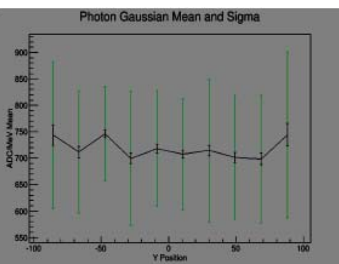


Fig. 7 Photon Y Cuts

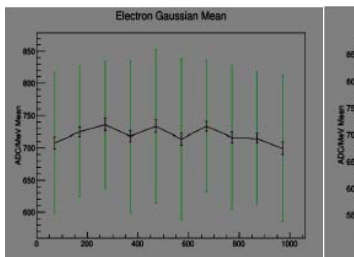


Fig. 8 Electron Z Cuts

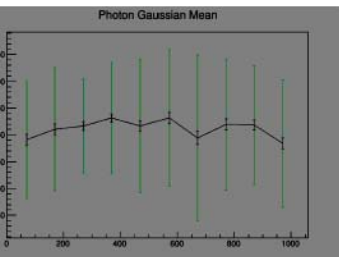


Fig. 9 Photon Z Cuts

the amount of charge deposited per wire proportionally decreases; this must be accounted for when solving for dE/dx . These graphs give the first experimental confirmation that such a calibration is necessary; it confirms the theory of the physics of the detector.

Next, we examined the efficacy of various cuts to the fiducial volume of the detector. Particles that passed fiducial cuts were events which all tracks were contained within a certain distance from the edge of the detector, known as the width of the fiducial cut. A strange phenomenon had been occurring when examining the neutral pion particles with 20 cm fiducial cuts. Unlike photons and electrons, in which the majority of particles passed through the fiducial cuts, only about 2.54% of π^0 particles were passing. This is important to note, too, because $98.823 \pm .034\%$ of neutral pion particles decay into two photons, and $1.174 \pm .035\%$ decay into an electron-positron pair and a photon. The relativistic mean lifetime of a 1 GeV neutral pion is $6.11 * 10^{-16}$ s. This leads to an average mean distance to be 183.2 nm before decay. This demonstrates that the parent particle should not be traveling outside of the fiducial volume of the detector. To explore further, we first examined the fiducial efficiency (that is, the ratio of particles that passed 20 cm fiducial cuts over the total number of particles) as a function of parent energy for neutral pion particles. The results of this calculation are in the figure below.

This graph pointed to a correlation between lower parent energy values and higher fiducial efficiency. However, this graph also points to that the fiducial efficiency of neutral pions is far lower than that of electrons and photons. To further compare and confirm this, our study calculated the ratio of particles that passed 5, 10, 15, 20, and 25 cm fiducial cuts for neutral pions, electrons, and photons, and plotted them all on a graph as a comparison. The results are in the figure below.

In the figure above, the green line represents electrons, the black line photons, and the purple line neutral pion particles. The neutral pion efficiency is clearly much lower; for example, in the 5 cm cut, 75-80% of the photons and electrons pass, whereas only about 6% of the neutral pions pass. This further demonstrates the inefficiency of fiducial cuts in neutral pion particles.

To further determine the cause of the failure of fiducial cuts, our study looped over the parent neutral pion particles and its two daughter particles, the two photons, in thousands of events, and studied the percentage of which these single particles passed the fiducial cuts. We found for the parent neutral pion particle the percentage was 67.9%, and for the two photon particles the percentages were 66.3% and 66.4%. Given the high pass rate, this implied that it was the electron, positron, and photon showers after the first decay that were leaking out of the fiducial volume.

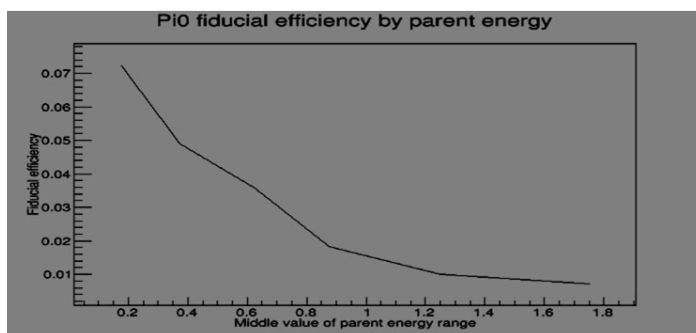


Figure 14 Pi0 fiducial efficiency

III. Conclusion

This experiment resulted in several conclusions that will assist in the understanding of the physics of LArTPC, and providing important research and development work for upcoming short and long baseline neutrino experiments. First, it concluded the visual similarity between neutral pion decays and electron scattering. Next, it confirmed the theory of a decrease in charge deposition as the x detector distance increased. Finally, it calculated the likelihood of a neutral pion passing fiducial cuts of 20 cm to be 2.54% and concluded that fiducial cuts could not be practically made to neutral pion particles. These observations and calculations will assist in the analysis of particle reactions when the detectors begin running.

IV. References

- 1 Lockwitz, Sarah. "The MicroBooNE LArTPC." . FNAL, 13 Aug. 2013. Web. 23 July 2014. <<http://www-microboone.fnal.gov/talks/dpfMicroBooNELArTPC.pdf>>.
- 2 Carls, Ben. "MICROBOONE PHYSICS." . Fermilab, 17 Aug. 2013. Web. 22 Aug. 2014. <<http://www-microboone.fnal.gov/talks/uBDPF.pdf>>.
- 3 Grosso, Ryan. "The MicroBooNE Experiment." . University of Cincinnati, 5 Apr. 2013. Web. 23 July 2014. <http://www-microboone.fnal.gov/talks/APS_April_Grosso.pdf>.

V. Acknowledgements

This project was supported in part by the U.S. Department of Energy, Office of Science Workforce Development for Teachers and Scientists (WDTS) under the Science Undergraduate Laboratory Internships Program (SULI).

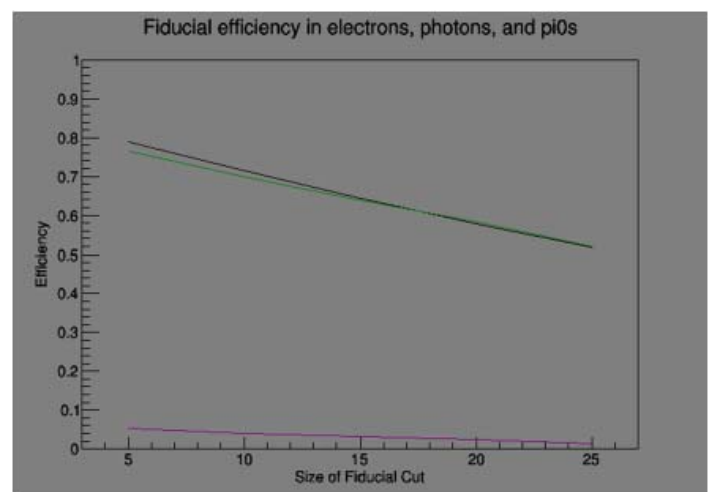


Figure 15 Comparison of fiducial efficiency

Computational optimization of light trapping for ultrathin solar cells

Nathan Frey

Physics and Astronomy, University of Missouri, Columbia, MO 63303

Yutong Pang

Physics, Stony Brook University, Stony Brook, NY, 11790

Matthew Eisaman

Sustainable Energy Technologies Department, Brookhaven National Lab, Upton, NY 11973

Abstract

Organic solar cells with ultrathin (less than 50 nanometer) absorber layers are a promising alternative to stateoftheart photovoltaic devices. Cells with thinner active layers have the potential to benefit from increased conversion efficiency of the incoming solar energy because photogenerated charges are more easily collected from the thinner layers. However, in order to realize this potential, lighttrapping (the redirection of normally incident light to inplane propagation) must be used to enable strong optical absorption in the ultrathin layers. We present a computational optimization of nanostructured surface corrugations (light trapping structures) employed within the cell to scatter incident light in the transverse direction into guided optical modes. Analytical and numerical techniques were applied to calculate the guided modes supported by model waveguide structures, and to determine the fraction of incident light coupled to each mode. Based on these calculations, a computational approach was utilized to design optimized device architectures for light trapping.

I. Introduction

A. Model Waveguides

In this computational study we inspect slab waveguide structures that model photovoltaic cells to varying degrees of approximation. In the simplest case, a dielectric slab (glass) in air was used to test the methods described below. More complicated structures include periodic waveguides, that is, structures with layers of alternating refractive index. Of particular interest is the model slotwaveguide ultrathin organic photovoltaic (OPV) [1]. This structure is comprised of glass, transparent conductive oxide, top, absorber, bottom, and metal layers. A full device simulation includes a periodic surface corrugation in the absorber layer and complex refractive indices to account for optical absorption.

Ultrathin OPVs have been presented as a potential solution to typical problems that limit the efficiency of standard solar cells. The ultrathin absorber layer improves charge extraction, but at the cost of decreased optical absorption. This study presents a computational strategy for investigating light trapping in model waveguide structures of experimental interest.

B. Mathematical Formalism

In order to examine the efficiency with which incident light is absorbed in ultrathin organic photovoltaics, the eigenmode expansion (EME) method was used. Eigenmode expansion is a rigorous analytical formalism that enables calculation of the electric field distribution inside a multilayer slab waveguide structure with complex valued refractive indices. The method is predicated on the orthogonality of modes for the linear operator of the wave

equation. From the proof for the Hermiticity of this operator, it follows that its eigenfunctions form an orthonormal basis. This basis can then be used to decompose any incident electric field into eigenmodes of the structure [2].

An electric field within the structure is split into a summation of xdependent mode fields and zdependent exponential terms that govern propagation in the transverse direction. Mode fields are calculated via the mode equation, and corresponding coupling coefficients are calculated as an overlap integral between the mode field and the incident electric field [3].

It is also possible to solve the eigenvalue problem analytically for specific toy model cases, and this method was implemented to motivate an understanding of the underlying physics of the problem. Using the standard solution of the Helmholtz equation and matching boundary conditions, we obtain a transcendental equation for the propagation constants of the eigenmodes. This equation can be solved graphically or with a numerical root finder in the general case, and for simple cases, an exact solution can be obtained. However, for a perturbed structure, a purely numerical approach is preferable.

A small, periodic dielectric perturbation applied to the structure in the form of a surface corrugation is used to impart transverse momentum to the incident light. The perturbation introduces a slight zdependence to the mode coupling coefficients, as power is exchanged between the modes throughout propagation. If we assume a weak perturbation, the parabolic approximation holds and higher order derivatives of coefficients in the wave equation are ignored. By orthonormality of modes, a relation between the derivative of any coefficient and the functional form of another is obtained. This equation depends upon the amplitude and period of the perturbation, and it incorporates a mode matching condition that describes the allowed propagation constants. The coupled coefficient equation gives new coefficients for two coupled modes,

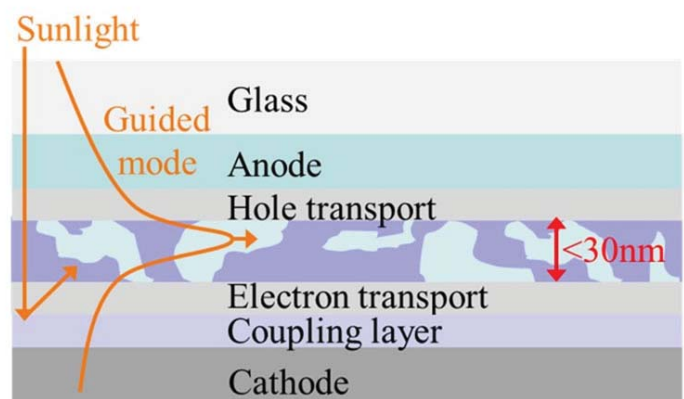


Figure 1. Typical OPV structure

ignoring interactions with other modes, and can be iterated to update any coupling coefficients of interest to a z-dependent form.

II. Methods

A. Incident Light

In the simplest case, the incident electric field profile along the x-axis at $z = 0$ of the structure can be specified by some simple closed form expression, such as that of a Gaussian beam profile. To study a more realistic scenario, it is necessary to construct the initial field within the structure based on a monochromatic plane wave at normal incidence. Angled incidence and broadband spectrum can be accounted for by looping over discretized wavelengths and angles, and integrating over the solar spectrum.

After calculating the wavelength in the absorber layer, Bragg's Law was applied to obtain the diffraction angles based on the light trapping structure, which serves as a diffraction grating. Using these angles and the intensities of the diffraction orders, the transfer matrix method was applied to construct the incident electric field profile.

B. Guided Modes

Guided modes are confined within the structure and evanescent. These modes are characterized by a propagation constant and a corresponding effective index, which is the eigenvalue of the mode. Eigenvalues for guided modes exist within a small window dependent on the refractive indices of the bounding layers, and can therefore be easily filtered out after computing all of the eigenmodes of the structure.

By integrating over the guided modes, absorption in each layer was calculated. It should be noted that all nonguided modes, so called radiation or leaky modes, also contribute to absorption, but because they are not confined in the structure, they were not considered in this analysis.

C. Evolution Strategy Optimization

An evolution strategy was employed in the optimization. The number of variables and complexity of the parameter space suggested the use of a (1+1) evolution strategy algorithm as a starting point for optimizing simple 2D waveguide structures.

In our implementation of a (1+1) evolution strategy, an initial guess at the structure dimensions, optical properties, and light

trapping structure configuration were inputted. The optimization holds all optical properties constant, as well as all layer thicknesses other than that of the absorber layer, to ensure that a realistic (and manufacturable) structure is output. The initial guess serves as the parent. A lognormal selfadaptive method was used to mutate the parent parameters, and to determine mutation strengths at appropriate levels for each step. After each mutation, some fitness value is evaluated. Fitness functions may include overlap between guided modes and incident electric field, absorption in the absorber layer, or coupling into fundamental modes.

The algorithm causes continual mutation and updates with better structures that replace the parent structure. The optimization is typically set to terminate after a specified number of generations, or after a target fitness value has been achieved. Evolution strategies are prone to becoming trapped around a local optimum, but this problem can be circumvented by running multiple parent strains in parallel and introducing a crossover function.

To facilitate ease of use for the optimization and other calculations, a graphical user interface was created. The GUI defaults to a preset slotwaveguide configuration, but the user can input optical constants, incident light wavelength, and a perturbation to generate the geometry for any model slab waveguide. The interface allows for visualizing the structure's geometry and refractive index profile, and returning values for unperturbed coupling coefficients, integrated perturbed coefficients, absorption in each layer, propagation constants for guided modes, and losses due to leaky modes. There are also options for plotting guided modes and, for simple unperturbed structures, visualizing power propagation in the transverse direction with a contour plot.

III. Discussion

The EME approach allowed for a thorough numerical study of the electric field incident within the structure due to an incoming plane wave, and its evolution in the transverse direction due to a periodic perturbation.

To satisfy the "ultrathin" requirement, the absorber layer must have a thickness between 10 and 150nm. The bounds on layer thickness and refractive index (as dictated by realistic, typical OPV materials) are important for performing a computationally efficient optimization, but the thickness in particular is a severe limit. The optimization will seek to increase layer width to the

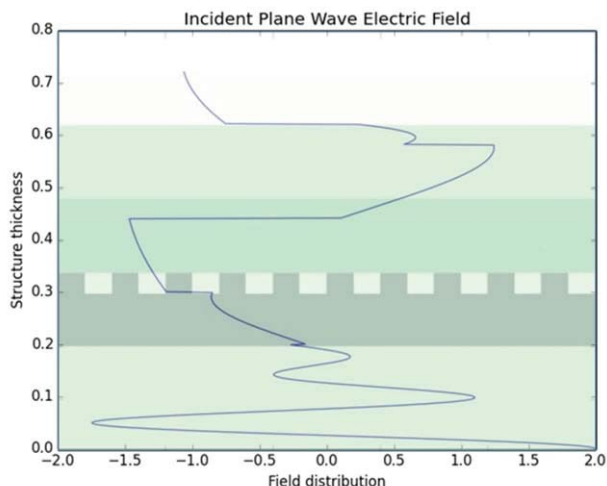


Figure 2. Electric field within an OPV structure calculated via transfer matrix method

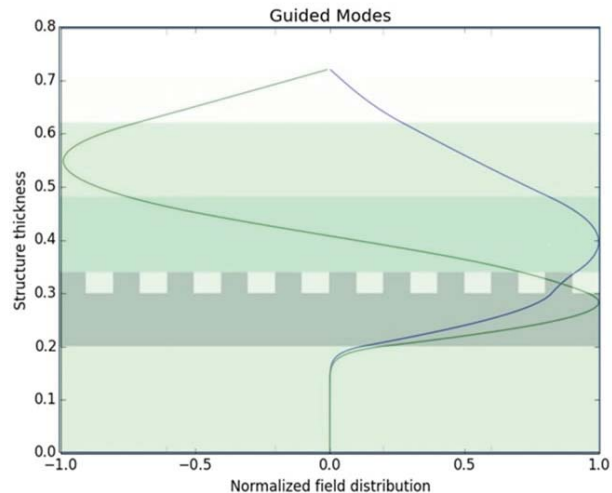


Figure 3. Transverse electric guided modes overlaying a slot-waveguide OPV

upper bound because, regardless of other inputs, absorption scales with absorber layer thickness. Therefore, it is necessary to hold layer thickness constant at some desired value, and focus on other parameters.

Perturbation geometry may be the most useful target for optimization, as it affects the diffraction angles and consequently, the change in initial electric field throughout the structure. Applying the optimization in its current state did routinely result in ten or twenty per cent increases in absorption, but the evolution strategy relies on randomly generated normal variables during the mutation step and is therefore stochastic by nature. The efficacy of the optimization could be improved by devoting more computational resources to the problem and increasing the number of generations to iterate over.

Our work focused on only a few key parameters, but now that the basic formalism and programmatic structure necessary for examining and optimizing structures has been developed, a more complete treatment is possible. A more computationally intensive optimization might attempt to not only modify an existing experimentally verified structure, but also vary the number, thicknesses, and optical constants of the nonabsorber layers to test new structures.

IV. Conclusions and Future Work

The methodology detailed above provides a simple, streamlined approach to treating slab waveguides and performing first order optimization of light trapping structures. The method is general in scope and well suited to handling 2D slices of many realistic structures, including OPVs.

Future work may involve consideration of three dimensional light trapping structures.

Whereas the 2D structures evaluated in this work are useful for understanding the physics of the light trapping problem and for considering surface corrugations within the context of a larger slab waveguide, 3D structures have been shown to provide optimal light trapping across the broadband solar spectrum. A more complex optimization scheme, such as a genetic algorithm, may provide more realistic structures to implement from an engineering perspective [4,5].

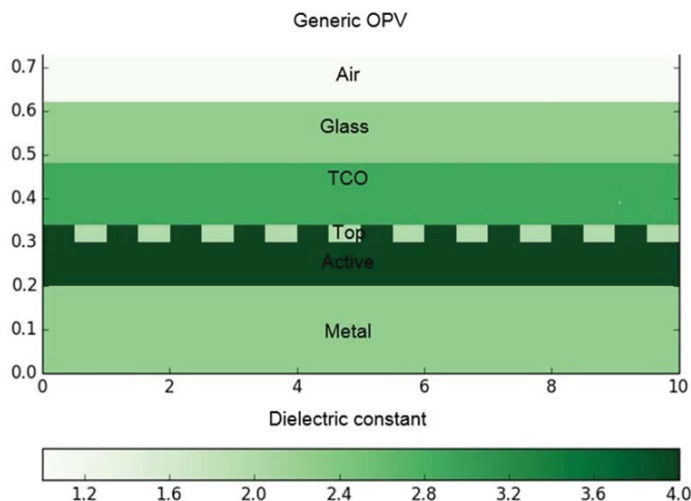


Figure 4. OPV refractive index profile with surface corrugations visualized by modeling program

V. References

[1] Pang, Yutong et al. “Guidedmode absorption in ultrathin organic photovoltaics.” IEEE. 2011.

[2] Yeh, Pochi. Optical Waves in Layered Media. New York: Wiley, 1988. [3] Hertel, Peter. “Mode coupling and propagation.” 2011.

[4] Dobson, David. “Optimal mode coupling in simple planar waveguides.” IUTAM Symposium on Topological Design Optimization of Structures, Machines and Materials: Status and Perspectives, 311–320. 2006.

[5] Yu, Shuangcheng et al. “Topology optimization for highlyefficient lighttrapping structure in solar cells.” Structural and Multidisciplinary Optimization. 2014.

VI. Acknowledgements

This project was supported in part by the U.S. Department of Energy, Office of Science, Office of Workforce Development for Teachers and Scientists (WDTS) under the Science Undergraduate Laboratory Internships Program (SULI).

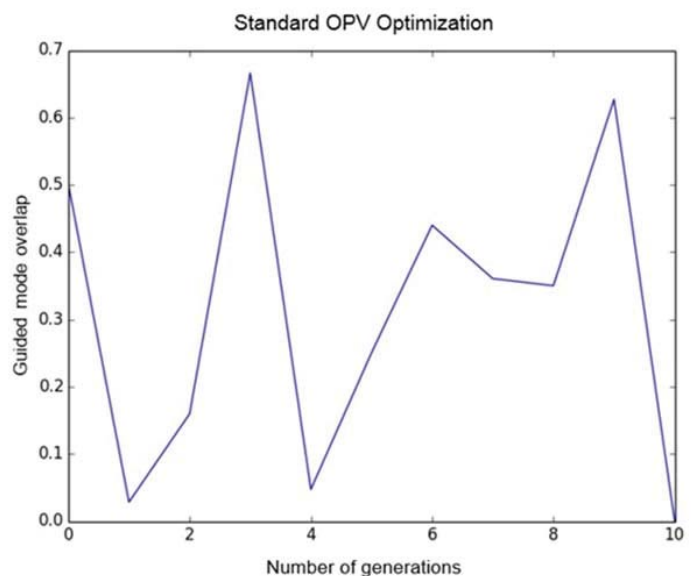


Figure 5. Some typical values for guided mode overlap fitness function

Genetic approach to constrain conformation of bioactive peptides

Khalid Habib, Chandra Gadsden, and Abdelaziz Bior
Cheyney University
Paul Freimuth

Department of Biosciences Brookhaven National Laboratory, Upton, NY 11973

Abstract

Cellular proteins normally fold into their native tertiary or three dimensional structures in order to support specific function (s) in their respective cell types. This native conformation is inherent in the primary sequence of those proteins and supported by protein helpers known as chaperons. Protein misfolding on the other hand is considered abnormal although it might result in a unique conformation that deviates from the original structure that could lead to toxic phenotype. In the current ongoing research in Dr. Freimuth laboratory it was demonstrated that a piece of a gene name Golgi-localized DOMON (Gld) was inserted into pASK expression plasmid. Expression of this piece of Gld in *E. coli* produced an acute and automatic toxic activity that resulted in immediate stalling of growth and death of the bacterial cells. Investigation of this toxic activity using enzyme assays indicated that the 26-mer peptide possibly inhibited RNA polymerase (RNAP) in the cell by binding specifically to the polymerase. This inhibitory activity was observed and confirmed when a purified RNAP was used in vitro. For further investigation of the 26-mer peptide toxicity, the same piece of DNA was inserted into a specific *E. coli* alkaline phosphatase gene and cloned into pASK plasmid between residues 211-212. Transformation of *E. coli* with the pASK-AP-Gld and induction with anhydrous tetracycline, and analysis of the protein product indicated that the AP-Gld protein was expressed. Nevertheless, the toxic activity was not observed but the recombinant protein remained in the cytoplasm and failed to be exported into the periplasmic space as revealed by the enzyme activity assays of the soluble fractions as being inactive. To investigate the failure of the protein export to the periplasmic space, we cloned six other pieces of Gld gene produced by PCR-based cloning into the same site on AP gene and test for protein expression and enzyme activity. The results showed that the first three peptides produced some support of AP enzyme activities, while the other three were inactive using AP enzyme acting upon its substrate p-nitrophenylphosphate (PNPP). The three active guest peptides were found to be on the disordered side of the RONN algorithm while the other three inactive guest peptides were found on the ordered side similar to the 26-mer peptide. To elucidate the lack of activity of the 26-mer and the other three peptides, we created eight other sites on the host protein AP and inserted the 26-mer gene piece into each of these sites using the same PCR-based cloning technique. This was done to investigate whether the structure of the 26-mer that led to the misfolding of AP-Gld was due to that particular site on AP or merely due to the unique amino acid sequence of the 26-mer guest peptide. The techniques used were bacterial growth in LB and the fragments from Gld were cloned into pASK plasmid using a PCR based cloning. The *E. coli* cells

were induced for the production of recombinant AP, AP-Gld, wild type and AP-SecM. The wt was used as a positive control and SecM protein was used as a negative control. The preliminary results were analyzed by agarose, and polyacrylamide gel electrophoresis. Western blotting using antibody against AP host enzyme was carried as a confirmatory test for the expression of recombinant AP Proteins in *E.coli*. The project is continuous and more investigations are needed to understand the misfolding behavior of the AP recombinant proteins. The ultimate goal of the project is to identify a site on the host cell (*E.coli*) AP that will support the activity of the enzyme, and reveal the reason behind the inability to transport the protein into the periplasmic space of *E.coli*. By working on this experiment, we have learned many techniques that will be helpful in our future profession. Moreover, we understood the importance of doing research and how the possible advances can influence everyday life.

I. Background

A. Toxicity of peptide derived from Golgi-localized DOMON gene on bacterial cells

Cellular proteins fold into their native tertiary or three dimensional structures in order to support specific functions in their respective cell types. This native conformation is inherent in the primary sequence of those proteins and supported by protein helpers known as chaperons. Protein misfolding on the other hand is considered abnormal although it might result in a unique conformation that deviates from the original structure that could lead to a toxic phenotype. In the current ongoing research in Dr. Freimuth's lab, it was demonstrated that a gene named Golgi-localized DOMON (Gld) was inserted into pASK expression plasmid. Gld is a 40 kD type 1 membrane protein localized in the Golgi complex of a plant called *Arabidopsis thaliana*. Expression of this gene produced an acute and automatic toxic activity that resulted in immediate stalling of growth and death of bacterial cells following induction of expression. Western blot analysis showed Gld protein was predominately soluble and was synthesized only during the first 10-15 minutes of induction. Investigation of this toxic activity indicated that the 26mer peptide possibly inhibited RNA polymerase in the cell by binding specifically to the polymerase. This inhibitory activity was observed and confirmed when a purified RNAP was used in vitro.

B. Tolerance of Guest peptide insertion in *E.coli* Alkaline Phosphatase

Insertion of foreign sequences or guest peptides into a single point on the molecular surface of a stable host molecule like AP constrains the guest peptides insert into a hairpin-like structure, and thus is a powerful approach to study structure-activity relationships in our 26-mer peptide. The role of Alkaline phos-

phatase in bacterial cells is to dephosphorylate molecules when the bacteria cells are low in phosphate or experiencing phosphate starvation. When active, alkaline phosphatase is soluble and exported from the cytoplasm into the periplasmic space between the cell wall and cell membrane. It is in the periplasmic space where the enzyme is active in a dimer conformation. The mechanism of AP in *E.coli* cells when in its active state serves as an important indicator for the tolerance of guest peptide at different sites in the AP gene. If a particular site in the gene can tolerate an insert, the enzyme will be active which means we will observe activity of soluble AP during protein analysis as well detection of AP in western blotting by AP specific antibodies and vice versa. Discovering a site that can tolerate the 26mer peptide will give insight on the importance of its conformation in relation to its toxicity.

II. Methods

For further investigation of the 26mer peptide toxicity, the same piece of DNA was inserted into a specific *E.coli* Alkaline phosphatase gene and cloned into pASK plasmid between residues 211-212. Transformation of *E.coli* with the pASK-AP-Gld and induction with anhydrous tetracycline, and analysis of the protein product indicated that the AP-Gld protein was expressed. Nevertheless, the toxic activity was not observed but the recombinant protein remained in the cytoplasm and failed to be exported into the periplasmic space as revealed by the enzyme activity assays of the soluble fractions as being inactive. To investigate the failure of the protein export into the periplasmic space, we cloned six other pieces of Gld gene produced by PCR-based cloning into the same site on AP gene and tested for protein expression and enzyme activity. The results showed that the first three peptides produced some support of AP enzyme activities, while the other three were inactive using AP enzyme acting upon its substrate p-nitrophenylphosphate (PNPP). The three active peptides were found to be on the disordered side of the RONN aphorism while

the other three inactive guest peptides were found on the ordered side similar to the 26mer peptide. To elucidate the lack of activity of the 26mer and the other three peptides, we created eight other sites on the host protein AP and inserted the 26mer gene piece into each of these sites using the same PCR based cloning technique. This was done to investigate whether the structure of the 26mer that led to the misfolding of AP-Gld was due to that particular site on AP or merely due to the unique amino acid sequence of the 26mer guest peptide. The techniques used were bacterial growth in LB and fragments from Gld were cloned into pASK plasmid using a PCR based cloning. The *E.coli* cells were induced for the production of recombinant AP, AP-Gld, wild type and AP-SecM. The wt was used as a positive control and Sec M protein was used as a negative control. The preliminary results were analyzed by agarose and polyacrylamide gel electrophoresis. Western blotting using antibody against AP host enzyme was carried as a confirmatory test for the expression of recombinant AP proteins in *E.coli*.

III. Data and results

Our first insert of the 6 Gld guest peptides showed some activity for the first three inserts. However the last three inserts did not show activity but, none of the inserts were toxic to the cells. When we inserted the 26mer into 8 different sites on AP, we found that the 26mer was toxic at site 7 which of course produced no AP activity. However at sites one and eight, there was more AP activity; more so site 8 than 1. We then tried inserting 6 guest peptides into the same position on site 7. Our finding from this experiment is that guest peptide number 3 out of the six peptides, showed more AP activity and solubility at site 7 than the rest. Most of the proteins were expressed and found in the soluble fractions as precursor proteins. The active portion of peptide three which is named DC 3, was processed and exported to the periplasmic space thus becomes apparently active. Lastly we inserted the sub-

wt Gld 1C 2C 3C 4C
P S P S P S P S P S P S

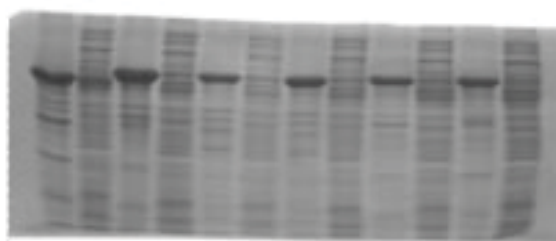


Figure 1. 26-mer Gld guest peptide inserted into 8 positions on alkaline phosphatase

wt Gld 5C 6C 7C 8C
P S P S P S P S P S P S



Figure 2. 26-mer Gld guest peptide inserted into 8 positions on alkaline phosphatase

WT AP-Gld DC
4197 4197 4197 4197
26/7 7 A/7 B/7 DC1 DC2 DC3
A B A B A B

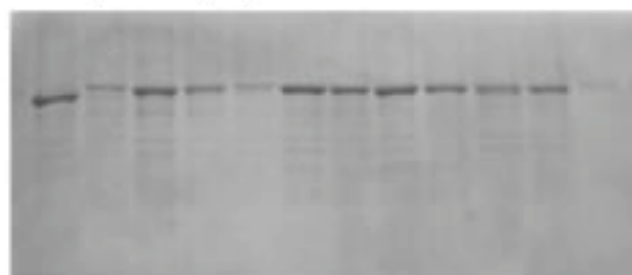


Figure 3. Gel 1: Insertion of DC (Gld-3) into 8 sites of AP

WT AP-Gld DC
4197 4197 4197 4197
26/7 4/7 5/7 6/7 DC1 DC2 DC3 DC4
A B A B A B A B A B

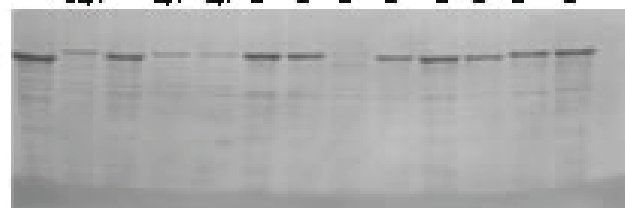


Figure 4. Gel 2: Insertion of DC (Gld-3) into 8 sites of AP

sequent DC3 into all 8 positions on AP as well as a 26mer mutant inserted into only position 7. Our data showed that DC 3 is soluble and active in all sites compared to the toxic peptide and its mutant. Then we inserted Alzheimer disease AB guest peptide into the same eight sites of AP we have inserted the 26mer into. And we have found that AB has act as same as the 26mer, therefore it was active into site 1 and site 8.

The two gels above show the results of a western blot in which antibodies specific for alkaline phosphatase were used. The results show which positions on alkaline phosphatase tolerated the insertion of foreign peptides enough to synthesize and retain the function of active AP. The bands represent the presence of AP that the antibodies acted on. Gel (1) shows that positions 1,2,5,6 and 8 produced the AP enzyme. Cell growth was stunted at position 7 which resulted in no AP enzyme being made. Gel (2) shows that the A-beta peptide produced more AP at sites 1,2 and 8 than any of the other positions.

IV. ACKNOWLEDGMENTS

We would like to thank the National science foundation (NSF), Louis Stokes Alliance for Minority Participation (LSAMP) program, Dr. Paul Ferimuth in the department of biosciences at Brookhaven national lab, for giving us the opportunity to be a part of this research.

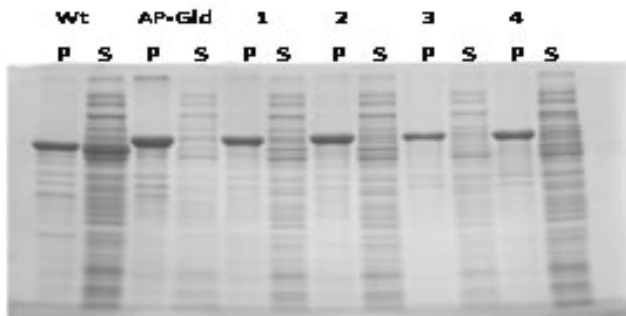


Figure 5. Gel 1: Amyloid ($A\beta$ of Alzheimer's disease into different 8 sites on AP

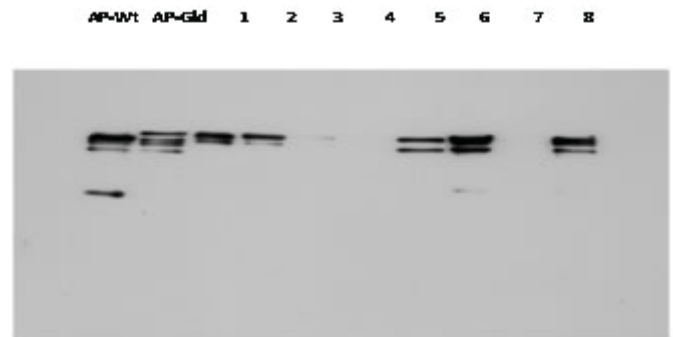


Figure 7. Gel (1): 26mer guest peptide into 8 sites of AP

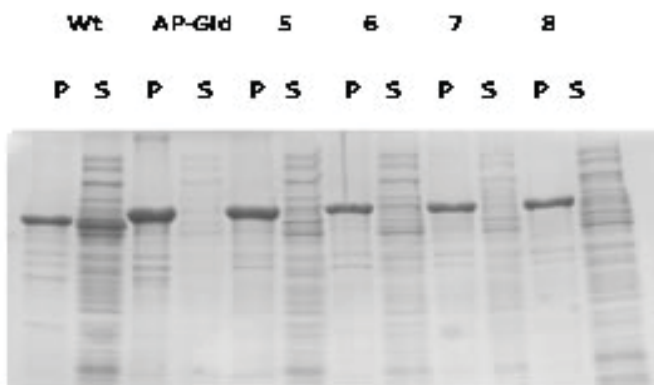


Figure 6. Gel 2: Amyloid ($A\beta$ of Alzheimer's disease into different 8 sites on AP

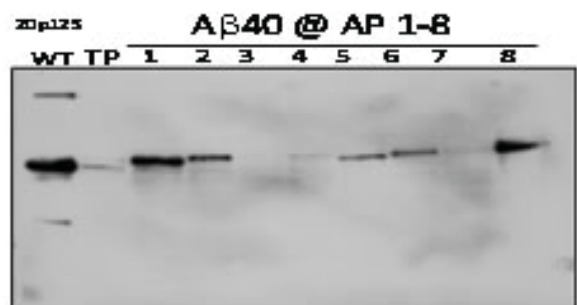


Figure 8. $A\beta$ inserted into 8 sites of AP

Targeting lipid abundant mutants of *Arabidopsis thaliana*

Kimberly Giacalone

Biology, State University of New York at Geneseo, Geneseo, NY 14454

Kimberly Okoli

Biological Sciences, Cornell University, Ithaca, NY 14853

Changcheng Xu

Biosciences Department, Brookhaven National Laboratory, Upton NY 11973

Jilian Fan

Biosciences Department, Brookhaven National Laboratory, Upton NY 11973

Abstract

The field of engineering green biomass for the production of plant oils for biofuel is expanding. Deriving biofuels from sustainable bio-resources is environmentally friendly, has low energy intensive operations, and optimally utilizes our environment. In this study we tried to determine what gene is responsible for the production of lipids in *Arabidopsis thaliana*. By using DNA extraction followed by polymerase chain reaction, we were able to locate mutations on the chromosomes. Several thin-layer chromatography (TLC) tests were also used to ascertain which strain of mutant has the most triacylglycerol (TAG) content. Though this study is not complete, tentative conclusions can be made, specifically that *Arabidopsis* mutants overexpressing phospholipid diallycerol acyltransferase1 (PDAT1) and oleosin (a structural protein found in vascular plant oil bodies) have shown increases in leaf TAG content. Clarification of the role PDAT1 plays in increasing TAG content will be useful in future engineering efforts aimed at enhancing oil accumulation for biofuel production.

I. Background

In recent years, there has been much concern about the state of the planet, the rate at which nonrenewable resources are being consumed, and our dependency on them. To combat this there has been an increased interest in finding more sustainable forms of energy, such as plant oils. Plant oils are an energy-rich source of renewable fuels, most of which occur in the form of triacylglycerols (TAGs), esters derived from a glycerol and three fatty acids. While plants are able to synthesize TAGs naturally, the plant demand for sucrose takes priority for carbon over lipids. Excess carbon is normally stored as starch, while TAGs are thought to serve as a temporary storage form for fatty acids¹. An increase in oil production is necessary to meet growing demand for biofuel. One method to increase oil production is to identify a mutant or strain of a plant that has a high production of TAGs. TAGs do not normally accumulate largely in vegetative tissues, but they are prevalent in the seeds. These TAGs compose oil droplets, which are monolayers of phospholipids with embedded proteins. The most abundant proteins are oleosins, and a possible key role of theirs could be to prevent oil droplets from combining while keeping them small and mobile with freezing tolerance. In conjunction with phospholipid diacylglycerol acyltransferase 1 (PDAT1), oleosin is also responsible for increasing TAG content in the wild-type strains of the plant, *Arabidopsis thaliana*.

So far most research focuses on the TAG accumulated and

synthesized in vegetative tissues like leaves. We developed a strategy to isolate mutations involving accumulating oil in leaves. Oleosin, was fused with GFP (green fluorescent protein), and overexpressed in the wild type. The seeds of the homozygous transgenic line was used for mutagenesis and the leaf tissue of M2 plants was used to screen mutants. The first round screening was conducted last year; this study is to further analyze the candidate mutants we got from the first round screening, using both fluorescent microscope and thin-layer chromatography (TLC). In order to find a strain of *Arabidopsis thaliana* with the highest TAG production, we used seeds that were harvested from a previous study. In this study, the plant genome was manipulated to overexpress the oleosin gene by using a T-DNA insert. This recombinant T-DNA vector was then transformed into agrobacteria to be introduced to the wild types COL2. Genetic selection was used with antibiotic plates to determine the homozygous transgenic plants. In order to measure which strains of mutants produced the most oil, we plated oil droplets on TLC plates.

II. Methods/Materials

A. Thin-Layer Chromatography

- At least 60 mg of leaves from young plants were measured out and placed in individual centrifuge tubes.
- A 1:7 ratio of the fresh weight of the leaves in milligrams to extraction buffer in microliters was added and the tubes were all placed on a vortex on a low setting for 15 minutes or until all the chlorophyll in the leaf samples were gone.
- Half the volume of extraction buffer was calculated and that amount of KCl buffer was added.
- The tubes were placed in a centrifuge for 1 minute at 13,000 rpm. This separates the liquid so the total lipids collected at the bottom of the tubes.
- A pencil line was drawn about half an inch from the bottom of the TLC plate and 60 μ L of lipid from each sample was placed on the plate above the line.
- When the samples dried, the plate was placed in a tank with developing solvent until the solvent traveled almost all the way up the plate.

We also did map-based cloning to identify the gene mutation of one confirmed mutant. The F2 plants of the mutant crossing with lansberger ecotype was used as a mapping population. For rough mapping, the SSLP markers were used and a polymerase chain reaction (PCR) and gel electrophoresis were performed.

B. B. Polymerase-Chain Reaction

- Individual leaves from young separate plants were placed in different centrifuge tubes and 200 μ L of DNA extraction buffer was added.
- Blue pestles were used to ground up the leaves and 400 μ L of 100% ethanol was added in order to make the DNA precipitate.
- The centrifuge tubes were shaken in order to mix completely and then placed in the centrifuge at 13,000 rpm for 5 minutes.
- After the tubes were removed from the centrifuge, the supernatant was discarded and the tubes were left upside down in order to remove all of the liquid.
- Once all the ethanol was removed, 200 μ L of TE buffer was added, the tubes were vortexed and pipetted into PCR tubes along with DNA polymerase, primers, an enzyme and dNTP. Each PCR had a different set of primers from markers on chromosome I (nga63, ciw12, nga111, and nga280) and chromosome II (athBio, ciw2, LPRP and LB2RP). The PCR tubes were then placed in the PCR machine.
- 9 μ L of PCR product for each sample was loaded into the agarose gel for electrophoresis, and then the gel was examined with gel imager.

III. Results

Candidate 16 shows a greater amount of oil while candidate 8 has almost no oil present

IV. Discussion

The main focus of our experiment was mutant screening using Thin Layer Chromatography, the goal of which was to find mutants with an abnormally high or low amount of oils. As the solvent traveled up the silica plate, the different components of the lipid traveled at different speeds due to their sizes. One sample

was a control of either Ler or Col-2 for comparison purposes. A pre-existing knowledge of where the TAGs would fall on the plate for the control was necessary in order to recognize whether the mutants were lipid-deficient or high in lipids. After performing multiple TLC tests, we saw found several candidate mutants (Fig 1). When the young leaves were observed through a microscope, we found that the mutants that showed a higher amount of TAGS, also showed a higher abundance of oil bodies when compared to the control (Fig 2-4).

The samples that showed no TAGs also showed no oil bodies.

Once it is clear which plants hold the mutation for a larger amount of TAGs, the next step is genetic mapping using PCR and gel electrophoresis to find out which ecotype the mutation is found on, and out-cross it to the opposite ecotype as the first step of map based cloning. Map based cloning identifies the genetic cause of mutant phenotypes by looking for links to markers with known physical locations². It is done by locating a mutant and finding the gene responsible for the altered phenotype, as opposed to reverse genotyping approaches, which rely on prior knowledge of gene in the hopes of finding a mutation with a changed phenotype. Map based cloning has no prior assumptions about a gene or genome, making it possible to find mutations anywhere in the entire genome.

V. References

- ¹J. Ohlrogge and K. Chapman Bio.Soc. 34 (2011)
- ²G. Jander et al Plant Phys 129,440 (2002).

VI. Acknowledgements

We would like to thank our mentors Jilian Fan and Changheng Xu for their guidance and support throughout this project. We would also like to thank the Virginia Pond Scholarship Program, the Department of Energy, and the Office of Educational Programs.



Figure 1. TLC Results- Control wild type COL2Ole shows a normal amount of oil.

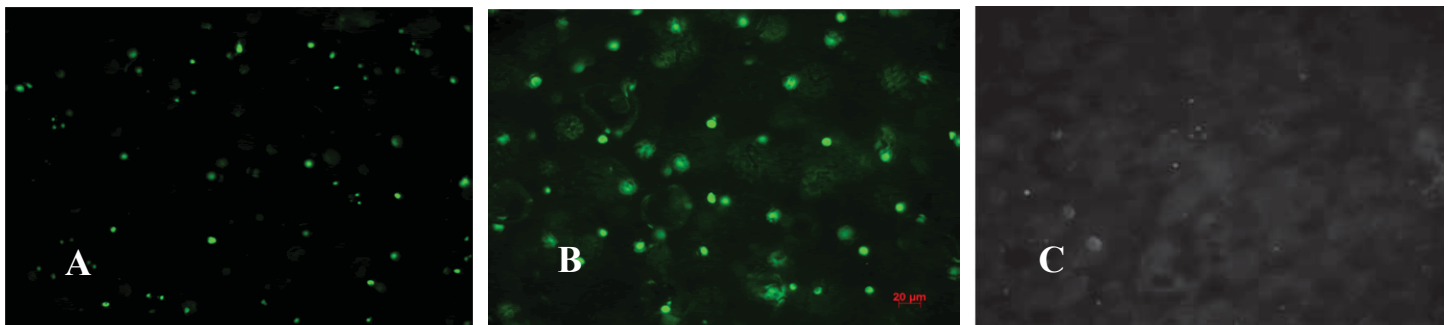


Figure 2. Images of A) control wild type COL2Ole; B) sample 16 mutant M2-63; and C) sample 8 mutant M2-17. (A-C: 20x comparison; scale bar = 20 μ m.)

VII. Appendix

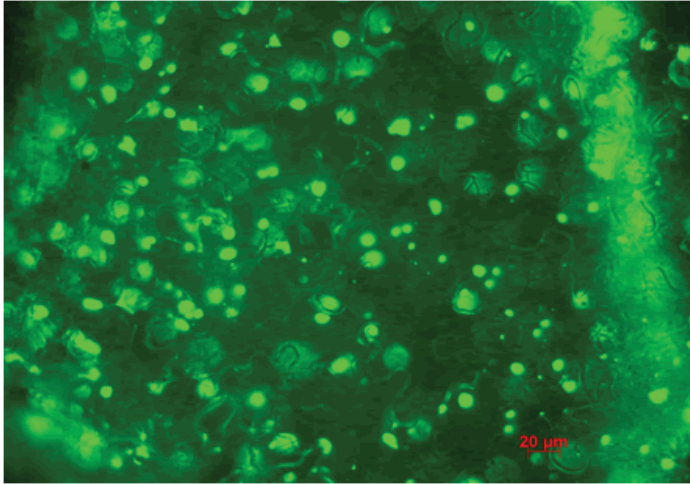


Figure 3. Sample 12: M4-1

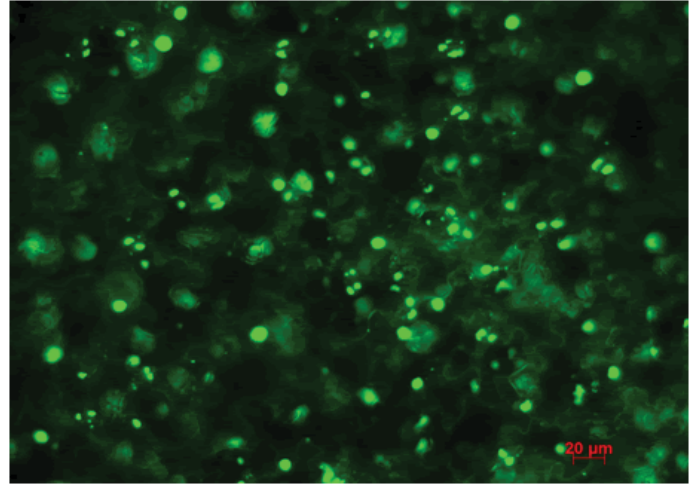


Figure 4. Sample 5: M2-81

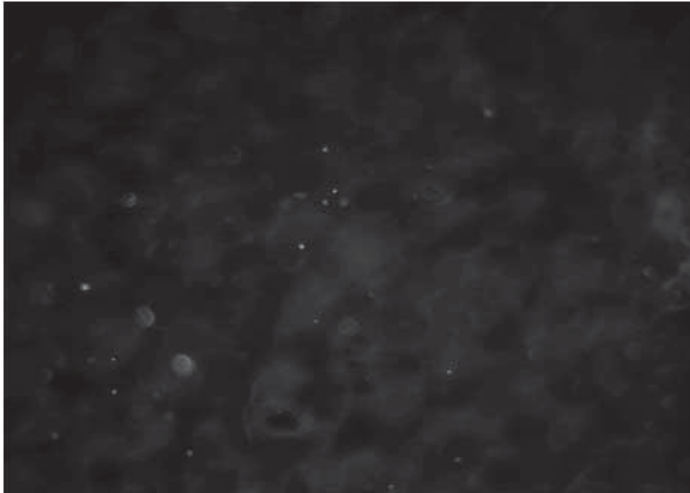


Figure 5. Sample 8: M2-17

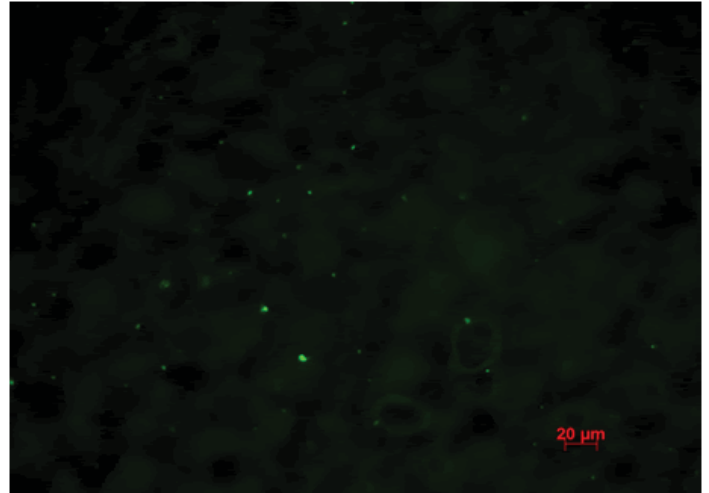


Figure 6. Sample 9: M2-17

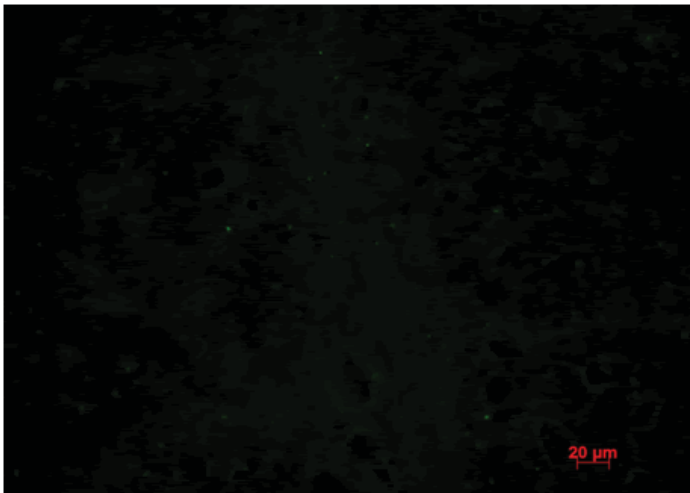


Figure 7. Sample 22: M2-16



Figure 8. Sample 23: M2-16

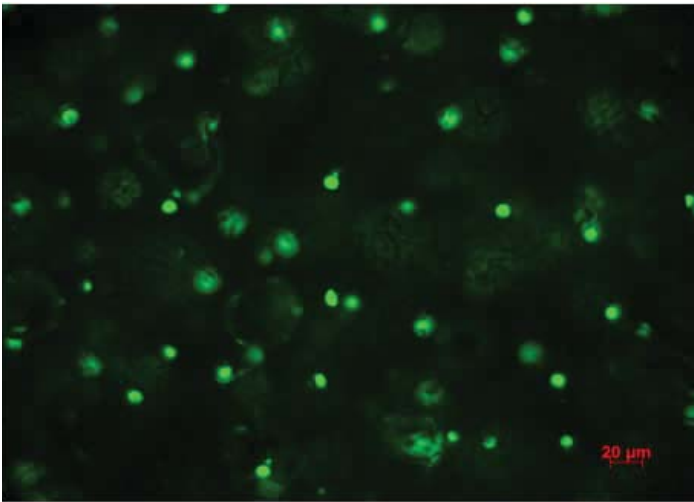


Figure 9. Sample 16: M2-63

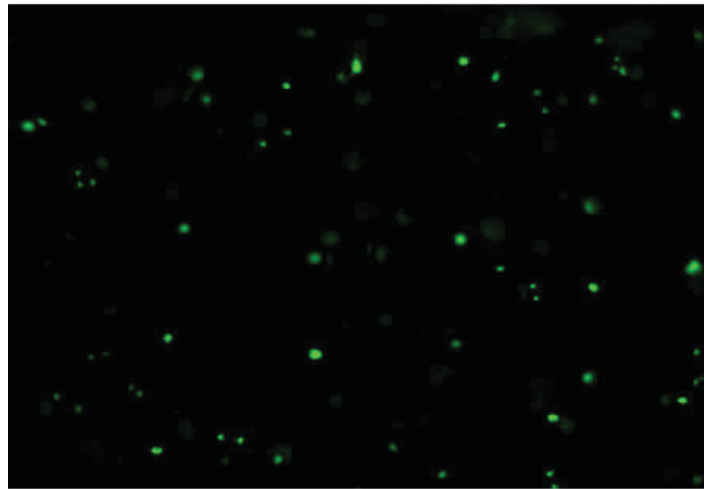


Figure 10. Control: COL2 WT

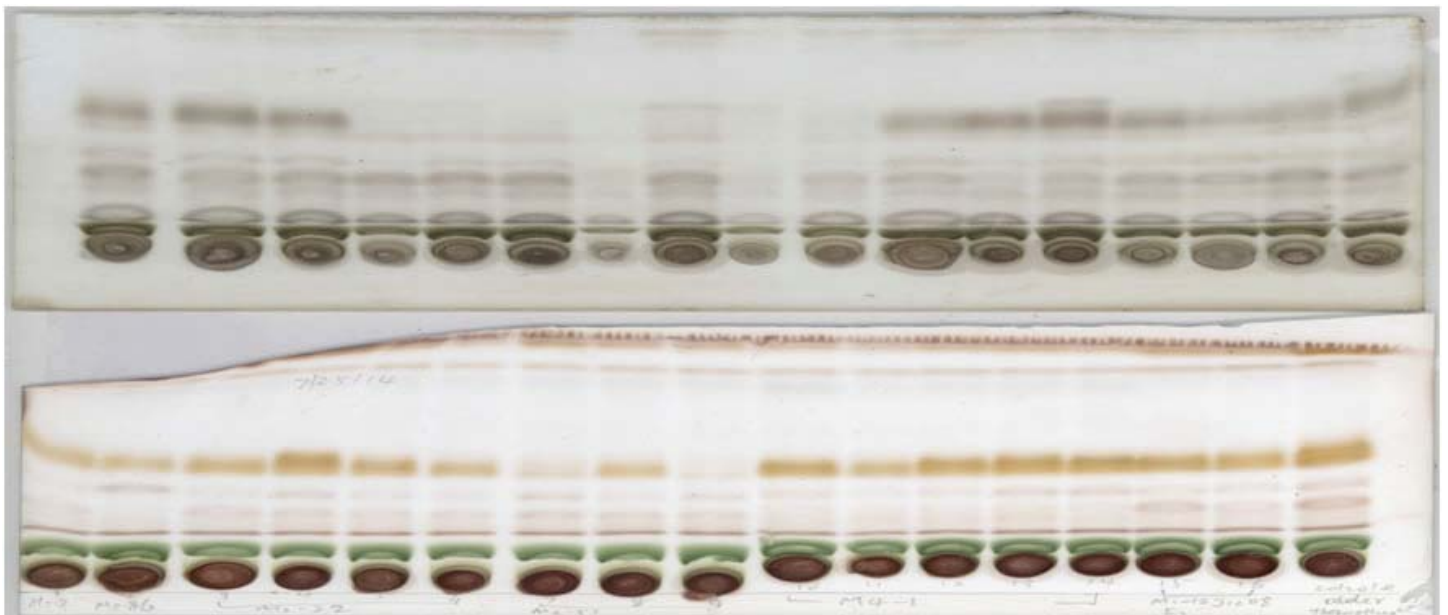


Figure 11. Additional TLC plate from 7/17/14

Reducing hazardous waste at Brookhaven National Laboratory

Kenneth Goodman

Chemistry Department, Long Island University, Brookville, NY 11548

Joe Pavlak

Waste Management Department, Brookhaven National Laboratory, Upton NY 11973

Peter Pohlot

Waste Management Department, Brookhaven National Laboratory, Upton NY 11973

The excess of both chemical and radioactive inventory across the Brookhaven National Laboratory (BNL) site has been an ongoing issue for many years. This chemical accumulation issue has numerous concerns associated with it such as the following: aging chemicals that have gone past their expiration date, especially those in the peroxide forming category; chemicals stored in areas above the area's rated storage capacity such as flammable chemicals; and finally chemical hygiene and chemical compatibility during storage which could provoke very serious consequences including hazardous health situations. The potential hazard of radioactive waste is an even greater risk due to the acute negative side effects that large radiation doses could cause in very short exposure periods. The prevention of extremely dangerous radioactive pollution while strictly monitoring these materials for national security purposes is the most important issue regarding the management of radioactive waste. Participating in this internship has awarded me the opportunity to work in various buildings and work with a countless number of scientists to determine how to effectively and economically reduce BNL's hazardous footprint from chemical and radioactive wastes. Working with and assisting Joe Pavlak (BNL Waste Management Representative) has taught me methods of preventing and minimizing waste through speaking with researchers about the quantity of chemicals they order for their research and trying to reduce the quantity of waste that is produced from experiments. A second method of avoiding waste accumulation is to transfer chemicals or radioactive materials that one person views as waste and give it to someone who will use it. The implementation of hazardous waste reduction methods not only helps BNL scientists, but also the environment. Through this internship I have been put into a position to classify chemical and radioactive waste based on both Department of Transportation and Environmental Protection Agency standards which then gives the waste management technicians information about how to handle, pack, and transport this waste onsite. Working towards responsible waste disposal will not only help reduce the chemical and radiation safety hazard of Brookhaven National Laboratory, but will also benefit the residents that reside around the lab that are at potential risk as well.

I. INTRODUCTION

Responsibly monitoring and disposing of chemical, radiological, and biological waste has become increasingly important to people as the negative effects of pollution can be observed in every corner of the globe. The weight of environmental stewardship has become a greater load for people to bear as fuel efficiency in their cars, organic foods, and their overall carbon footprint has

become intertwined in mainstream thought. Here at Brookhaven National Laboratory, responsible waste management has become crucial to the Department of Energy's mission to ensure America's security and prosperity by addressing its energy, environmental and nuclear challenges through transformative science and technology solutions. Preventing these environmental problems was the challenge proposed to me when beginning this internship. The challenge was attempting to reduce chemical inventory across Brookhaven National Laboratory in every department on site. Working to resolve this issue has shown to be a difficult challenge for both my mentor and I. Using different methods to analyze, reduce and dispose of waste has been the most valuable knowledge learned from this internship. Implementing these methods into action have shown to be incredibly difficult due to the vast amount of hazardous waste encountered and the extensive knowledge and experience required which I have only just begun to develop. Determining how effectively these methods are working is crucial to rate how well the Department of Energy is meeting its mission of tackling tough environmental issues.

II. DISCUSSION

Throughout my time here at Brookhaven I have encountered various types and forms of hazardous waste. The etching solution used in various experiments was one that was particularly hazardous. Piranha solution is the most common etching solution used at the lab and that consists of highly concentrated sulfuric acid and inorganic peroxide, usually hydrogen peroxide. The danger is that the solution has both a Department of Transportation (DOT) class nine substance (corrosive) and a DOT class 5.1 which is an inorganic peroxide, like hydrogen peroxide.¹ Due to the peroxide presence in solution, it may cause many problems in handling, transporting, and treating. The reactive nature of peroxide causes this solution to possibly become explosive if left in the right conditions and could exothermically react with other waste chemicals in the immediate surroundings to form dangerous products. Due to the chemical activity of this solution, it was left to the Waste Management Department to write a treatment procedure to deactivate all the waste Piranha solution. My mentor and I came up with a plan to use ferrous sulfate which will cause the reduction of the hydrogen peroxide in solution by forming ferrous oxide, which is commonly known as rust. The production of non-toxic, non-hazardous rust creates a much safer environment for the technicians to handle. The complete reaction of the peroxide in solution allows for the waste to be handled as a single corrosive hazard once this done. Since the only hazardous material in solution now is the concentrated acid and it can be disposed of as such, rather than as an oxidative waste which takes many more steps and has many more hazards involved.

The proper treatment of chemical waste was the single largest job we performed throughout the summer. Since every department on site produces chemical waste whether it was used refrigeration oil at the maintenance shop or picric acid in the chemistry lab, we were required to be familiar with every type of waste produced. This was a major undertaking to learn in just ten weeks, however I defiantly have a stronger understanding of how waste generated from research labs get handled once it leaves the hands of the researchers. Classifying chemicals according to both the DOT and EPA was essential to preserving the safety of the technicians who actually transport the waste. The DOT classifies chemicals into nine major categories.²

If the waste being handled fits into any of these categories then it become regulated hazardous waste and must be appropriately disposed of by a licensed waste facility. The regulations for the packaging of these hazardous materials are very clear in what is required.³ The hazardous materials that are regulated by both the DOT and EPA required a standard red hazardous waste label with the chemical name clearly written on it with the date it will be put into the 90-day area. The 90 Day Hazardous Waste Storage Facility is an area at which hazardous chemical waste can be accumulated for a limited amount of time without a permit.⁴ All waste containers must have accumulation start date and be labeled as Hazardous Waste. Moreover, no waste container should remain in the storage beyond the 90 days including the first day waste was placed in the container. The satellite accumulation point, on the other hand, is an area at or near the point of generation where waste is initially accumulated and which is under the control of the operator of the process generating the waste; practically every research laboratory where chemical waste is generated. If the bottle is not large enough to place the label on it so it can be easily seen then it must be put into a plastic bag of appropriate size. Then the label can then be placed on the outside of the bag so it can be clearly seen from outside the 90 day area. Once the waste is properly labeled then the chemicals can placed into the 90-day area. The 90-day area requires secondary containment for the potential spills, which means that the waste must be placed into a bin or some type of container that will be able to hold the spill and will not react or corrode due to the hazardous waste.⁵ The most common type of containment is a bin usually made of high density polyethylene due to its stability against corrosives, oxidizers and solvents. After the waste is placed in the 90 day area the EPA representative designated to that area inspects it once a week for leaks and possible spills.⁶ The representative also inspects the labels for proper dates and chemicals names as well.

The handling of radioactive waste is a completely different issue all together from chemical waste. Radioactive waste is comprised of a variety of materials requiring different types of management to protect people and the environment. When processing radioactive waste, the main goal is to classify the waste as either a low-level, medium-level or high-level. The levels are set by both the DOE and the EPA through the Radiation Control Act (RCA) and the Radiation Policy Act (NWPA) according to the amount and types of radioactivity in them. The overwhelming majority of waste generated here on site is considered low-level radioactive waste. Since the shutdown of all of the sites nuclear reactors, the majority of the radioactive was is generated from very limited radioactive experimentation. The large majority of this radioactive waste is paper, rags, tools, clothing, and filter which contain small amounts of mostly short-lived radioactivity. It is not dangerous to

handle, but must be disposed of more carefully than normal garbage. The majority of the waste ultimately ends up being buried at one of the several guarded low-level radiation sites mainly based in Utah and Colorado. Worldwide it comprises 90% of the volume but only 1% of the actual radioactive energy.⁷

Once the radioactive waste has been classified, very strict labeling procedures must be followed to ensure safety for everyone involved. First the generator must attach a yellow radioactive waste tag to each container of radioactive waste. Any material considered radioactive waste must bear a completed radioactive waste tag. The yellow tag must contain the isotopic information on the front of the tag and the chemical form and concentration on the back of the tag.⁸ A complete description of the chemical contents as well as the radioactive content is needed. If the radioactive isotopes are dissolved in mixtures or solutions, the identity and amount (percent, molarity, ppm, etc.) of all constituents must be included. Prior to disposal the total quantity of radioisotope in millicuries (mCu) must be recorded on the tag.⁹ Any radioactive waste that also meets the definition of a hazardous chemical waste must be managed as a mixed waste, according to the requirements of both the radioactive and chemical constituents. This includes labeling the container with the words "Hazardous Waste" and a maximum accumulation time of 90 days. Most radioactive waste does not meet the mixed waste criterion; however, wastes which contain flammables, corrosives, or toxic substances would fall into this category.

Transporting waste on site is another major aspect of the job of the Waste Management Department. Safely transporting waste requires a lot of knowledge about what chemicals are being transported and what sort of characteristics those chemicals have. Since the chemicals have to be safely packed so they cannot be spilt, a lot of the chemicals have to be packed together and knowing what can and cannot be placed together will help prevent any unwanted chemical reactions from occurring. Researching chemical properties such as flashpoint, reactivity in certain conditions and boiling point are all extremely important when moving chemicals in a warmer climate, such as the type encountered this time of year. Knowing everything about a chemical before it is sent out for shipment is the most important part of the whole process. Understanding the risks when shipping many of these chemicals falls into the hands of trained personnel at the Waste Management Department.

After the risks of each chemical being transported are understood the waste must be equipped with labels, at least four inches by four inches in size, are applied to the outside of hazardous materials shipping packages near the shipping name.¹⁰ These labels identify the primary and secondary hazard specific to the material being transported and give warning information about handling precautions in case of an emergency. If the diamond label will not fit on the package, shippers will put the label on a tag. For example, compressed gas cylinders that will not hold a label will have tags or decals.¹¹ After the individual packages are labeled, the outside of the vehicle transporting the waste must be equipped with signs used to warn others of hazardous cargo and its DOT classification.¹² A placarded vehicle must have at least 4 placards representing the applicable hazard. They are attached to each side and each end of the vehicle. Placards must be readable from all four directions. There are 22 DOT specification placards. They are 10 3/4 inches square, turned upright on a point, in a diamond shape. Cargo tanks and other bulk packaging show the ID number

of their contents on placards, orange rectangular panels, or plain white square-on-point configurations having the same dimensions as placards.¹³

Reducing chemical waste can be considered the single most important aspect of the waste management's mission of environmental stewardship. Many methods are put into place to reduce chemical waste, however they all stem from the idea of source reduction.¹⁴ This is defined as, any activity that reduces or eliminates the generation of chemical hazardous waste at the source. This can be accomplished by proper material management, substitution of less hazardous materials, and proactive laboratory procedures. Creating plans to reduce chemical consumption is the biggest portion of the efforts by waste management. Helping scientists order the correct amount of chemicals is another way to reduce the chemical inventory of the site. Creating a plan with the scientists that determine the amount of chemicals they should order is the easiest way to reduce chemical consumption. Many companies will give scientist a discount if they buy the chemicals in bulk, which would be fine if they actually used the amount they ordered. Since the scientists order the chemicals in bulk they are getting a better deal per unit, however if the chemicals sit around and then are disposed of later because of expiration the cost of disposal outweighs the initial savings. Preventing this from happening is both environmentally and economically responsible. Another method of preventing a vast chemical inventory is a simple plan of recycling.¹⁵ Trying to use the waste material for another purpose, treated and reused in the same process, or reclaimed for another process will help ease the burden of hazardous waste accumulation. Many of the chemicals encountered by the waste management division are recycled with both environmental and economic issues in mind. During a short laboratory cleanout period the waste management division transferred about 40 bottles of various porphyrins from a laboratory that was being shut down to another laboratory that was doing research with these porphyrins. These bottles of porphyrins were recycled from a laboratory in the medical research department and given to another research laboratory in the chemistry department, ultimately preventing them from entering a chemical waste facility which is great for the environment. Moreover these porphyrins were valued at over ten thousand dollars which they now saved, could be spent on some other aspect of research in the chemistry department. Recycling these chemicals across departments that normally have limited communication is a great feat that would have not happened if it were not for the Waste Management professionals. The least preferable technique for waste minimization is chemical treatment. The most common treatment is the neutralization of corrosives like acids and bases.¹⁶ Chemical treatment of hazardous waste will help reduce the chance for chemical pollution since the waste has had its harmful characteristics removed.

III. CONCLUSION

The need for a well operated and well trained Waste Management Division is a clear necessity for any large research facility. The fact is having a well trained and well operated Waste Management Division is somewhat a different story. A successful Waste Management Division will help drive the potential of any research facility by preventing federal fines, greatly limiting environmental pollution, and responsibly disposing of chemical, radiological, and biological waste. Luckily Brookhaven National Laboratory has a top tier Waste Management Division that

pride them self on protecting the environment, researchers and residents of Suffolk County from further chemical, radiological and biological pollution. Working alongside these individuals has given many opportunities to understand why they work so hard to abide by and enforce the Department of Energy's mission of environmental protection through innovative solutions and technologies. Learning and implementing these methods procedures, and regulations at Brookhaven National Laboratory has been an incredible experience that has proven and will continue to prove in the future to be a valuable skill set that otherwise might not have been taught to me.

IV. AKNOWLEDGEMENTS

I wish to thank my mentor, Peter Pohlott and Joe Pavlak, for their professionalism and generosity during the SULI program. Further, I would express my gratitude to the Office of Science Education. Finally, I wish to acknowledge the hospitality and kindness of Brookhaven National Laboratory and the Department of Energy. This project was supported in part by the U.S. Department of Energy, Office of Science, Office of Workforce Development for Teachers and Scientists (WDTS) under the Science Undergraduate Laboratory Internships Program (SULI).

V. ENDNOTES

- ¹The Hazardous Materials Regulation, 1 Code of Federal Regulations § 100-185 et seq. (2009). Print.
- ²The Hazardous Materials Regulation, 1 Code of Federal Regulations § 100-185 et seq. (2009). Print.
- ³United States. Environmental Protection Agency. Hazardous Waste Generator Regulations. N.p., Aug. 2012. Web
- ⁴United States. Environmental Protection Agency. Hazardous Waste Generator Regulations. N.p., Aug. 2012. Web
- ⁵United States. Environmental Protection Agency. Hazardous Waste Generator Regulations. N.p., Aug. 2012. Web
- ⁶"Frequent Questions | Waste Minimization." EPA. Environmental Protection Agency, 15 Nov. 2012. Web. 08 Aug. 2013.
- ⁷"New Approach for Selecting UK Repository Site." Waste Management Overview. World Nuclear Organization, Dec. 2012. Web. 30 July 2014.
- ⁸Code of Federal Regulations." Www.gov.gov. Department of Transportation, 21 Dec. 1990. Web. 31 July 2014.
- ⁹Code of Federal Regulations." Www.gov.gov. Department of Transportation, 21 Dec. 1990. Web. 31 July 2014.
- ¹⁰The Hazardous Materials Regulation, 1 Code of Federal Regulations § 100-185 et seq. (2009). Print.
- ¹¹The Hazardous Materials Regulation, 1 Code of Federal Regulations § 100-185 et seq. (2009). Print.
- ¹²The Hazardous Materials Regulation, 1 Code of Federal Regulations § 100-185 et seq. (2009). Print.
- ¹³The Hazardous Materials Regulation, 1 Code of Federal Regulations § 100-185 et seq. (2009). Print.
- ¹⁴"Hazardous Waste Reduction Techniques." Hazardous Waste Reduction Techniques. Idaho State University, n.d. Web. 08 Aug. 2013.
- ¹⁵"Hazardous Waste Reduction Techniques." Hazardous Waste Reduction Techniques. Idaho State University, n.d. Web. 08 Aug. 2013.
- ¹⁶"Hazardous Waste Reduction Techniques." Hazardous Waste Reduction Techniques. Idaho State University, n.d. Web. 08 Aug. 2013.

VI. CITATIONS

“Frequent Questions | Waste Minimization.” EPA. Environmental Protection Agency, 15 Nov. 2012. Web. 08 Aug. 2013.

“Hazardous Waste Reduction Techniques.” Hazardous Waste Reduction Techniques. Idaho State University, n.d. Web. 08 Aug. 2013.

[49 FR 30903, Aug. 1, 1984, as amended at 73 FR 75595, Dec. 12, 2008]

The Hazardous Materials Regulation, 1 Code of Federal Regulations § 100-185 et seq. (2009). Print.

United States. Environmental Protection Agency. Hazardous Waste Generator Regulations. N.p., Aug. 2012. Web.

“FT-IR Spectroscopy—Attenuated Total Reflectance (ATR)”. Perkin Elmer Life and Analytical Sciences. 2005. Archived from the original on 16 February 2007. Retrieved 2007-01-26.

Chhabil Dass (11 May 2007). Fundamentals of Contemporary Mass Spectrometry. John Wiley & Sons. p. 5. ISBN 978-0-470-11848-1.

Studies for and development of a preshower detector in the STAR experiment

David Hamilton

Department of Physics, University of Texas, Austin, TX 78712

K. Oleg Eyser

Department of Physics, Brookhaven National Laboratory, Upton, NY 11973

Abstract

This project was part of the development process of a preshower detector that will be installed in front of an existing calorimeter in the Solenoidal Tracker experiment at the Relativistic Heavy Ion Collider (STAR) for an upcoming proton-proton collision experiment. One of the main goals of the RHIC spin program is to investigate the structure of the proton, since the spin carried by the valence quarks does not add up to the total proton spin of $1/2 \hbar$. In addition to the spin of the quarks, we must also consider the orbital motion of the quarks, as well as the spin contributions from sea quarks and gluons that mediate interactions between them. This remains an unsolved puzzle to which RHIC may contribute in a unique way. The preshower detector will be installed in the winter of 2014 and will help to separate photons from various other background particles that are generated in the collisions. Prior to implementing the detector, event simulations were carried out to specify detector layout, granularity, and efficiency. This requires us to make use of ROOT, a C++ data analysis framework developed by CERN that allows us to study Monte Carlo simulations of full proton-proton collisions or single particles. These simulations served to further develop our skills in programming and data/error analysis. The project also required us to test individual components of the preshower, such as the scintillators and electronic readout parts prior to its assembly. This included cosmic ray measurements and a test stand for radiation damage of silicon photo detectors.

I. Introduction

The proton spin puzzle remains an unsolved problem in physics, as the three valence quarks of the proton do not account for the total proton spin of $1/2 \hbar$. The Relativistic Heavy Ion Collider (RHIC) aims to contribute to solving the spin puzzle in an experiment that will be conducted in late 2014. The experiment will consist of proton-proton collisions at center-of-mass energies of 200 GeV, which will allow us to determine the spin contribution from the orbital motion of the quarks, as well as spin contributions from sea quarks and gluons that mediate the strong interactions between the quarks. The measurements will focus on direct photons made in the collisions.

In order to distinguish the photons from the charged particles that are produced in the collisions, a preshower detector must be placed in front of an existing electromagnetic calorimeter. This will allow us to measure direct photons resulting from the collisions. The measurements will then allow us to investigate the spin contributions due to the partons that make up the proton, thereby helping to piece together the spin puzzle of the proton.

As the experiment is still several months away at the time of this writing, the project focused mainly on modeling the predicted

data of the preshower rather than the assembly of its individual components. This took the form of Monte Carlo simulations within ROOT, which is a C++ programming environment developed by CERN specifically to process data from particle physics experiments. The simulations were used as preparation for the data analysis of silicon photomultipliers (SiPMs) that will be used in the preshower.

II. Setup and Radiation Damage Test

The preshower will be a hodoscope placed in front the electromagnetic calorimeter downstream of the STAR detector. It will be comprised of two perpendicular layers of scintillators, followed by a single layer of lead converters and an additional single layer of scintillators at the rear of the preshower. Each layer will have 76 scintillators with their own channel for data gathering. Two thicknesses of scintillators will be used, with half of them 5.8 cm thick and the other half 4 cm thick. Each layer of scintillators will be made up of four quadrants that contain nine of the 5.8 cm scintillators and twelve of the 4 cm scintillators, which brings the size of the preshower to $2 \text{ m} \times 2 \text{ m}$. The positioning of the preshower may be seen below in Figure 1.

The main components are the plastic scintillators, light guides, and SiPMs, which may be seen in Figure 2. Scintillators produce flashes of light whenever minimum ionizing particles pass through them. The resulting light is reflected on the inside of the scintillator until it eventually reaches the light guides. The light guides are the tapered ends of the scintillators that force the light to converge onto the silicon photomultipliers that are in contact with the flat end of the guide. The ends of the light guides are $3 \text{ mm} \times 3 \text{ mm}$. SiPMs are highly sensitive devices that are capable of detecting single photons. They are comprised of small photodiodes that are as small as $25 \mu\text{m} \times 25 \mu\text{m}$ which generate a signal that is proportional to the light that reaches them.

Before implementing the SiPMs that will be used in the preshower, damage due to radiation must be investigated. SiPMs are very sensitive to radiation damage, mainly from highly energetic neutrons. The SiPMs therefore needed to be tested under radiation conditions that would be similar to the proton-proton collision experiment that will be conducted later this year. The SiPMs were placed near the STAR detector where the preshower will be installed, after which they were subjected to neutron radiation exposure from two heavy ion collision experiments---one Au+Au and the other $3\text{He}+\text{Au}$.

The SiPMs were later retrieved and set up in a small lab that can be seen above in Figure 3, where the reverse bias voltage of the SiPMs was then scanned. This generates a dark current, which is due to the noise present in the diodes and worsens with the

radiation damage. The current itself depends on the value of the reverse bias voltage.

The reverse bias voltage measurements in Figure 4 revealed clear damage to both SiPMs. The first measurement was taken in late May during the Au+Au collision experiment, and shows a minimal dark current at the operating voltage. By the 3He+Au experiment in mid June, the dark current jumps significantly, revealing noise present in the photodiodes. Over time, the damage due to the neutron radiation exposure from the heavy ion collision experiments shifts the threshold for the dark current, making it occur at a lower reverse bias voltage.

From the dark current measurements in Figure 5, we see that the background noise in the SiPM signal does not diminish over time, which means that the SiPMs will continually suffer radiation damage until they are rendered unusable. This in turn puts an upper limit on the lifetime of the SiPMs that will be used in the proton-proton collision experiment. It should however be noted that while the neutron radiation damage from the heavy ion collisions is significant, the SiPMs will be exposed to less radiation in the course of the future proton-proton collision experiment, thereby extending the effective lifetime.

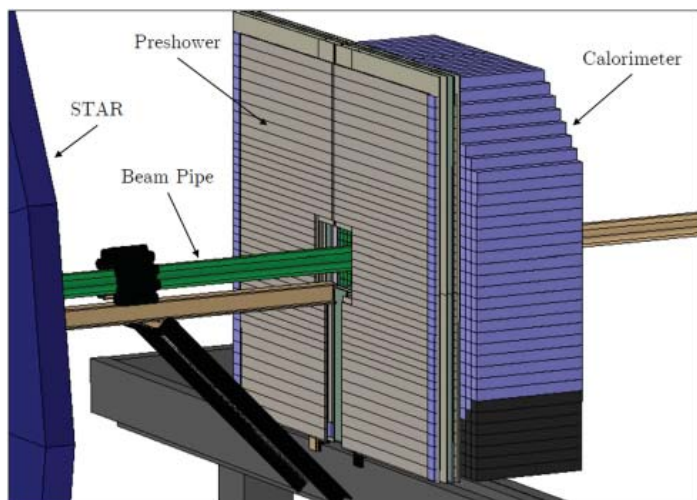


Figure 1: Illustration of installed preshower at the STAR detector.

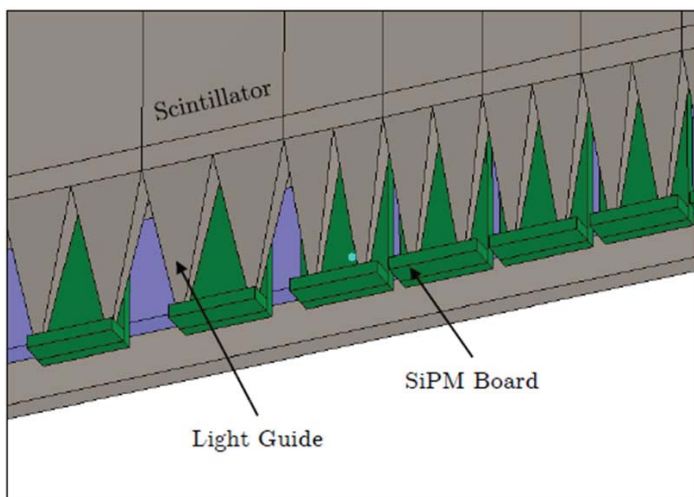


Figure 2: Main preshower components. Two of the 5.8 cm scintillators may be seen to the left while the four remaining scintillators on the right are 4 cm thick.

III. Toy Monte Carlo Simulations

Later on in the course of the experiment, it will be necessary to investigate the transverse asymmetry of the distribution of the detection events for the preshower. In order to do so, we must first determine the proper statistical model for the asymmetry. By modeling the data points with a cosine modulation given by

$$f(x) = \epsilon \cos(x + \varphi)$$

where ϵ is the amplitude of asymmetry and φ is the azimuth angle of a particle incident on the detector about its central axis. An illustration of an incident particle may be seen in Figure 6.



Figure 3: Setup of the 50 μ and 25 μ SiPMs connected to a voltage source and a computer that would record the reverse bias voltage measurements.

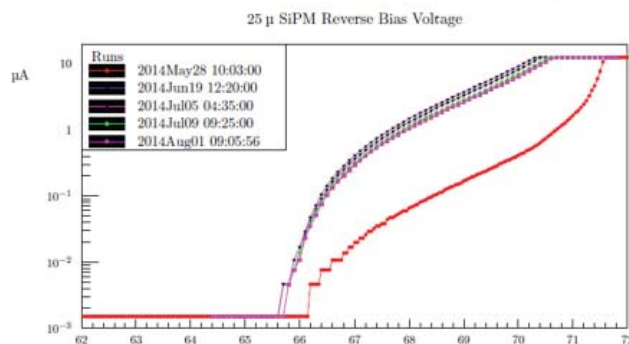
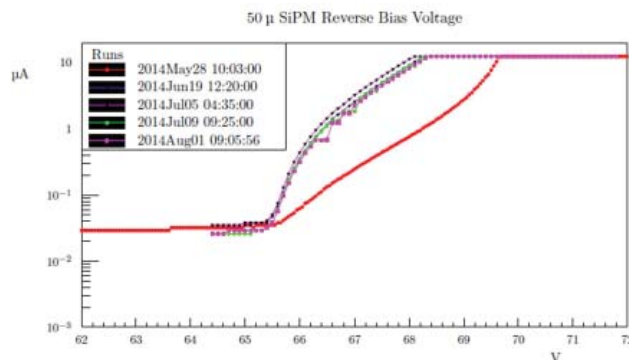


Figure 4: Reverse bias voltage measurements for both the 50 μ A and 25 μ A SiPMs for various dates. The earliest date (red) refers to the first recorded usage of the SiPMs, which corresponds to the least amount of noise. Operating voltages for the 50 μ A and 25 μ A SiPMs are 66.9 V and 68 V, respectively.

The simulations of particles were conducted while assuming the azimuthal acceptance of the experiment to be from 0 to 2π . The simulation generates random data points for the azimuth angle ϕ between 0 and 2π for a particle incident on the preshower.

The data points are generated from a random number generator with a uniform distribution between 0 and 2π . They along with an amplitude ϵ_{input} are used as the input of a sinusoidal model. The data points are later fitted again with a sinusoidal fit, which gives us an amplitude of asymmetry for each set of points. The simulation is repeated thousands of times and bins the amplitudes for each simulation run so that we may obtain the total asymmetry for the data runs. These simulations allow us to investigate the transverse asymmetry of the events, which is a measure of how many more events occur on one side of the preshower detector. More explicitly, the asymmetry is defined as

$$\begin{aligned} \epsilon_{asym} &= \frac{N_L - N_R}{N_L + N_R} \frac{1}{\cos \phi \left[\frac{\pi}{2}, \frac{\pi}{2} \right]} = \\ &= \frac{N_L - N_R}{N_L + N_R} \frac{\int_{-\frac{\pi}{2}}^{\frac{\pi}{2}} d\phi}{\int_{-\frac{\pi}{2}}^{\frac{\pi}{2}} \cos \phi d\phi} \\ &= \frac{\pi}{2} \frac{N_L - N_R}{N_L + N_R}, \end{aligned}$$

where N_L is the number of particles incident to the left and N_R is the number of particles incident to the right.

The sinusoidal input model was given by

$$f_{input}(x) = \epsilon_{input} \cos(x + \phi_{input})$$

where ϕ_{input} in this case is distinguished from ϕ as the phase of the

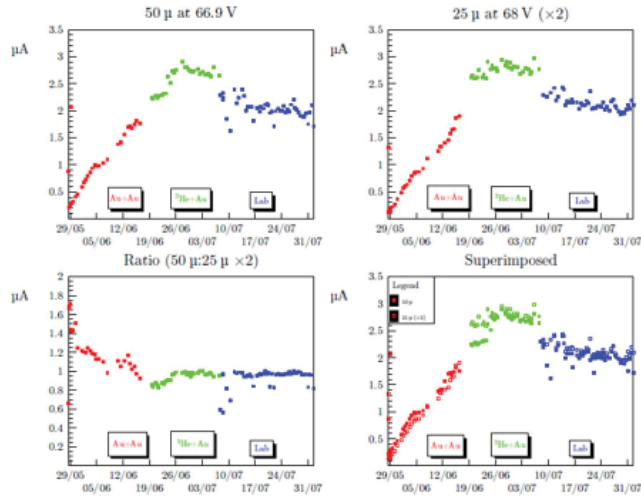


Figure 5: Plots of the dark current for both the 50 μA and 25 μA SiPMs at their operating voltages as a function of measurement date. The measurements are divided into three groups based on experiment: Au+Au (red), 3He+Au (green) and the small laboratory measurements (blue).

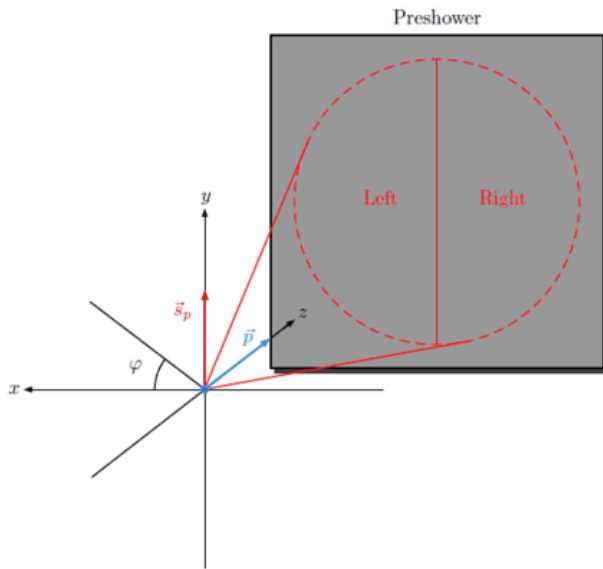


Figure 6: Illustration of a particle incident on the preshower in the z direction with an azimuth angle ϕ relative to the central axis of the detector and its spin component S_p polarized in the y direction.

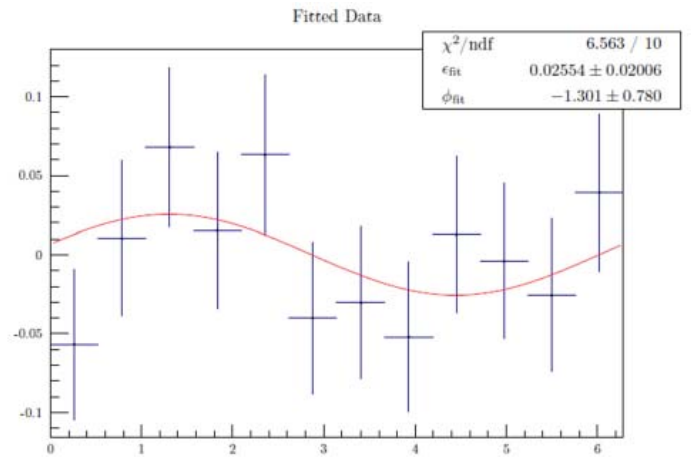


Figure 7: Plot of data points generated by the simulation. Points were fitted with the fit function $f_{input}(x) = \epsilon_{input} \cos(x + \phi_{input})$. The fit parameters may be seen in the top right corner.

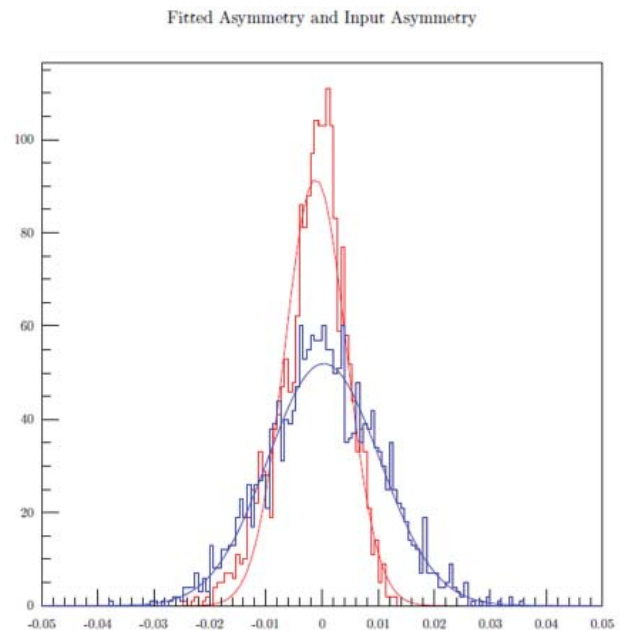


Figure 8: Histograms of ϵ_{input} (red) and ϵ_{fit} (blue) for 200,000 simulated runs.

input model—not the azimuth angle for a simulated particle. In input asymmetry ϵ_{input} was randomly generated from a Gaussian distribution with mean $\mu=0$ and standard deviation $\sigma=0.01$, while ϕ_{input} was held constant at 0.

In order to determine whether or not the fit function is a good model of the data, we must perform basic statistical analysis. Propagation of uncertainties tells us that the standard deviation in the fitted function σ_{fit} is given by

$$\sigma_{\text{fit}} = \sqrt{\sigma_{\text{input}}^2 + \sigma_{\text{event}}^2},$$

and because the event generator follows Poisson counting statistics, the relative error σ_{event} is simply

$$\sigma_{\text{event}} = \frac{1}{\sqrt{N_{\text{event}}}}.$$

The above result is then used to predict the distribution of the fitted asymmetries ϵ_{fit} when fitted with a Gaussian curve: if σ_{fit} is found to be around the value derived above, then the model used for fitting the data is sound.

The data from Figure 8 returned values of $\sigma_{\text{input}}=0.099$ and $\sigma_{\text{fit}}=0.02$. Thus, the model is sound for the purposes of investigating the transverse asymmetry.

IV. Lead Glass Scintillators

On occasion, assistance was needed with gluing photomultiplier tube (PMT) mounts to large blocks of lead glass that will later be used as the scintillation material in the preshower. The blocks were vertically mounted onto a table and the edges of the block were sanded before cleaning the surface with alcohol. The sanding was needed to create a strong seal for the PMT mounts, as it was found that the PMT mounts were easily broken off of scintillators that were not sanded down.

Industrial glue would then be applied to the top surface of the scintillators and the PMT mounts would be carefully placed upon them, while carefully ensuring that the glue was not smeared too close to the center of the plastic. Cinder blocks were placed on the top ends of the PMT mounts, with rubber padding between them to keep dust from entering the PMT cylinder.

V. Results and Future Implementation

The Monte Carlo simulations were found to yield the proper results for the uncertainties in the fitted asymmetry versus the input asymmetry, which tells us that the model is suitable. The radiation damage tests indicated that the SiPMs suffer irreparable damage that accumulates over time, which places an upper limit on their overall lifespan. The preshower itself is scheduled to be implemented in late 2014, and there are still some remaining tests that need to be conducted, such as optical simulations of the photons passing through the scintillators.

VI. Acknowledgments

I would like to thank K. Oleg Eyser for his guidance in the course of the project, as well as fellow intern Joseph Newton for his support and collaboration during the beginning of the project. This project was supported in part by the U.S. Department of Energy, Office of Science, Office of Workforce Development for Teachers and Scientists (WDTS) under the Science Undergraduate Laboratory Internships Program (SULI).

Charge transfer dynamic studies of a series of organic polymer donor-bridge-acceptor multi-interface systems for high efficiency photoelectric energy conversions

Muhammad Hasib

Material Science and Engineering, Norfolk State University, Norfolk VA 23504

Sam-Shajing Sun

Material Science and Engineering, Norfolk State University, Norfolk VA 23504

Abram Ledbetter

Chemistry Department, Brookhaven National Lab, Upton, NY 11973

John Miller

Chemistry Department, Brookhaven National Lab, Upton, NY 11973

Abstract

A series of donor-bridge-acceptor or DBA type block copolymer systems, where D is a donor type conjugated Poly (phenylene vinylene) (PPV) block, B is a non-conjugated and flexible aliphatic hydrocarbon bridge chain, and A is an acceptor type non-fluorinated or fluorinated conjugated PPV block, have been studied for potential high efficiency molecular and polymeric photoelectric energy conversion applications. High efficiency photoelectric conversion requires fast photo induced charge separation, fast charge transport, fast charge collection at the electrodes, and slow charge recombination at interfaces. This project uses ultra-fast dynamic electron pulse radiolysis and/or pulsed laser approaches to study the charge transfer dynamics at the interface of the donor and acceptor via bridge or space, and to investigate critical molecular or materials factors that affecting such charge transfer processes. Preliminary study results revealed that, compared to the pure donor block, the steady state photoluminescence (PL) emission of the donor/acceptor blend and DBA in solution quenched between 10-30% indicating photo generated singlet excitons dissociate at D/A inter-face either via collision or via the bridge unit. Radiolysis studies show donor cation decay in the D/A blend is faster (about 4 μ s initial fast decay) as compared to the pure D (about 6 μ s), and that the donor cation decay in DBA is even faster (2 μ s) than the D/A blend. Similar trend were also observed in fluorinated DBfA system, though in much slower rates. In radiolysis studies, the electron transfer from D to A via the bridge appears to be not much faster than via the collision, and the mechanisms were proposed. One interesting observation is that the donor cation in DBfA with four-methylene unit group (C4) appeared exhibiting slightly faster decay as compared to the DBfA with two (C2) and six (C6) methylene unit bridge. The scientific impact of this study include better understanding of the fundamental mechanisms and critical factors affecting the photo induced charge transfers and transport at molecular interfaces, and better molecular and materials design for higher efficiency photo electric energy conversion materials and devices.

I. Introduction

Future molecular and polymer based solar cells are very attractive for cost effective, renewable, and clean energy applications due to a number of potential advantages compared to current commercially available inorganic ones, such as 'greener' environmental impact, tune ability on materials chemical structures and frontier orbitals, tune ability on materials stability, versatility for room temperature and solution-based large-scale industrial processing and fabrications [1]. The polymer based donor/acceptor blend type bulk hetero-junction (BHJ) solar cells has reported a best power conversion efficiency of about 10% under one Sun intensity at AM 1.5 [2]. However, solid-state morphologies (such as donor/acceptor phase domain size and ordering) that are crucial for efficient exciton dissociation and charge carrier transport are hard to control or reproduce in a simple blend, and there are still plenty of room for improvements.

The overall photoelectric power conversion efficiency of an organic/polymeric solar cell is affected by at least five critical steps [1]: 1) Photon capture or exciton generation; 2) Exciton diffusion to donor/acceptor interface; 3) Exciton dissociation or carrier generation at donor/acceptor interface; 4) Carrier diffusion to respective electrodes; 5) Carrier collection by the respected electrodes.

To address the heavy 'exciton loss' and 'carrier loss' in steps (1-4) above, an organic donor/acceptor nano phase separated and bicontinuously ordered nanostructure, also called BONS type morphology self assembled from a DBA type block copolymer primary structure (Figure 1) appears very promising for improving optoelectronic energy conversion efficiency [3].

Specifically, a conjugated donor block (c-D) covalently linked to a conjugated acceptor block (c-A) via a non-conjugated bridge unit (nc-B), also abbreviated as c-D-nc-B-c-A, or simply DBA type block copolymer as shown in Figure 1 have been designed and developed recently [3e-f]. A best solar cell made of a DBfA/PC70BM exhibits about two orders of magnitude (100 times) better photoelectric power conversion efficiency than a best cell made of D/fA/PC70BM blend [3f], and this could be

attributed to solid state morphological improvement that facilitate the exciton dissociation and charge transports. However, the overall solar cell device photoelectric conversion efficiency is still relatively low (about 0.2%) due to both materials and device fabrications are not yet systematically optimized. In order to further improve or optimize the cell efficiency, understanding and controlling the rates of photo induced exciton diffusion, charge separation, charge recombination, charge transfers at different materials interfaces, charge collections at electrodes, and key influencing factors involved in different steps and interfaces are essential. The main objective of this project is to investigate and understand how molecular structures affect solar cell performance in terms of charge separation and transport at molecular level.

The scheme of frontier orbital levels and key electron transfer steps of the DBA type block copolymers are shown in Figure 2, where step 1 represents the electron or photo generated exciton diffusion in donor block along the donor chain, step 2 reflects a photo excitation (exciton generation), step 3 represents the electron transfer from donor to the acceptor via the bridge unit, and step 4 represents the separated charge recombination. One reason for the use of a non-covalent bridge unit B is due to the fact that, in a previous report where a conjugated donor block was covalently and directly linked to a conjugated acceptor block, no stable charge separated D⁺/A⁻ states were detected, and the hypothesis was that it was possibly due to the ultra-fast e⁻/h⁺ pair charge recombination between the donor and acceptor block [4].

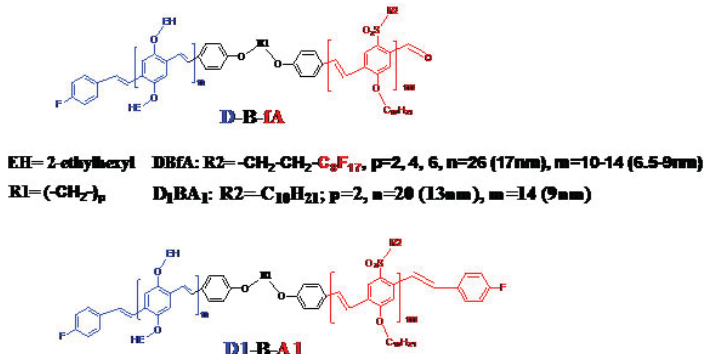


Figure 1. Chemical structures of DBA type block copolymer systems studied.

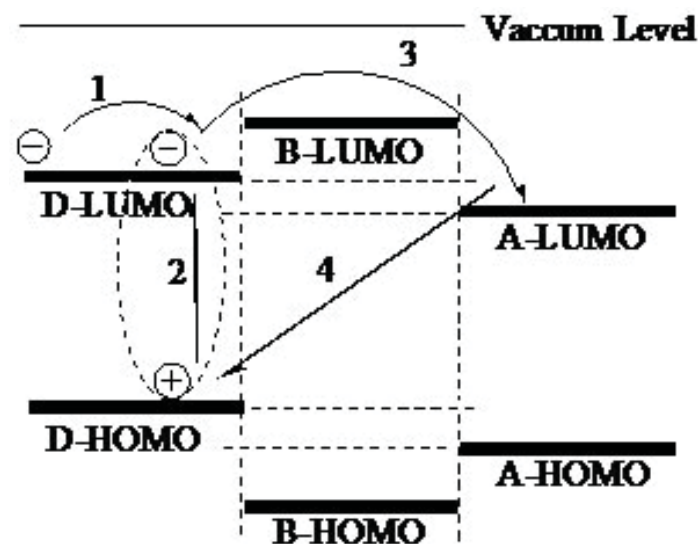


Figure 2. General scheme of the frontier orbital (HOMO/LUMO) levels and electron transfer processes of the DBA type block copolymer.

II. Progress

In this research, pulsed electron radiolysis technique at Laser-Electron Accelerator Facility (LEAF) in BNL are being used first to study the donor anion decay dynamics of DBA type block copolymers and the D/A composites. Several factors could affect charge transfer rates, such as, charge transfer driving and counter-driving forces in energy domain charge transfer associated molecular reorganization energies, distances and molecular shapes [5].

Figure 3 (a) exhibits electron pulse generated donor cation dynamic decays of 50 μM donor block (D1, top blue curve), D1/A1 blend (middle upper purple curve), D1BA1 (middle lower green curve), and the pure A1 block (bottom red curve) in THF. The initial fast decay curve fitting result a 6.0 μs decay constant for the D1 donor block, 3.9 μs for the D1/A1 blend, and 2.2 μs for the D1BA1 block copolymer. The faster decay of donor anions in D1/A1 blend versus pure D1 can be attributed mainly to the electron transfer from D1 to A1 upon collision in solution (a solution diffusion controlled bimolecular collision process). The faster decay of donor anions in D1BA1 versus D1/A1 blend may be attributed to additional electron transfers from the D1 donor block to the A1 acceptor block via the bridge B unit (an intra-molecular or intermolecular process). The similar data trend and explanation may also apply to the fluorinated DBfA system as shown in Figure 3(b). In DBfA case, three different bridge lengths with two, four, and six methylene units were evaluated, and it is interesting that the middle or four methylene unit bridge result a slightly fastest decay. However, it appears the overall intra-molecular electron transfer process via bridge unit (on the micro second time scales) is not significantly faster than the diffusion controlled bimolecular collision process particularly in the DBfA case. The singlet exciton dissociation in DBA is on the order of Nano seconds or faster (from separate steady state PL quenching studies). The overall rate of electron transfer from donor to acceptor via bridge may be considered as the sum of steps 1 and 3 shown in Figure 2. Rate in step 1 is affected critically by the size of the donor block and its distortions/defects; for instance, the exciton diffusion length in solid PPV is typically between 5-20 nm depending on PPV chain environment and interactions. Specifically, the donor size of D1 in D1BA1 is about 20 repeat units (13 nm), while the D block in DBfA has 26 repeat units (about 18 nm). Rate in step 3 is critically affected by both energetic (including driving and counter driving forces) and spatial factors, (i.e., the electronic coupling matrix elements including D-A distance and orientations), and the energy barrier of the bridge unit, etc. For instance, from previous electrochemical and absorption data, the LUMO offset of D1/A1 pair is about 0.6eV, while the LUMO offset of D/fA pair is about 0.3eV. Since the electron or exciton diffusion rate is unlikely orders of magnitude difference, such difference may therefore being attributed mainly to step 3, i.e., the energetic driving/counter-driving forces in exciton dissociation is more optimal then the electron transfer via donor anion, without the exciton binding energy, the D/A pair is in 'inverted' region of Marcus electron transfer model.

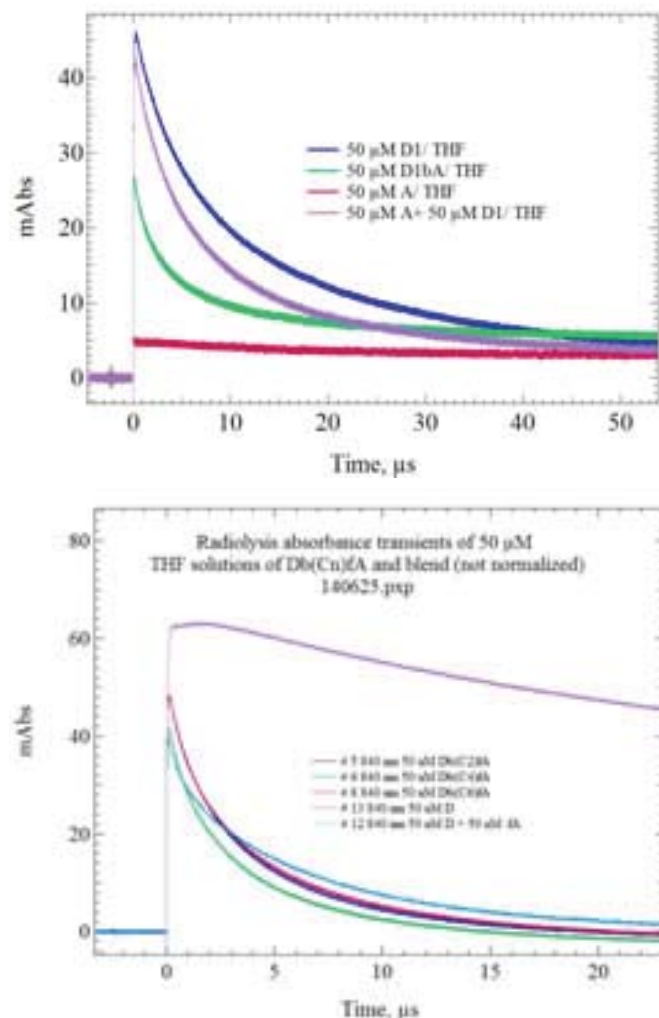
III. Future Work

Bridge units with shorter lengths (such as one methylene unit or no methylene unit, e.g., one ether unit only) need to be synthesized and studied, and this is based on the assumption that current relatively slow intra-molecular electron transfer rate could be due

to too many insulating methylene units resulting in too weak D-A coupling. Different sizes of the donor blocks, particularly as short as five Nano meter sized donor block (7-8 repeat unit) needs to be synthesized and studied using the same dynamic techniques. This is assuming the slow intra-charge transfer rate may be due to slow charge or exciton diffusion on donor block. Different donor/acceptor pairs with evolving LUMO offsets between 0.1-1.0eV needed to be systematically evaluated for both positive (formal) and negative (inverse) regions of the Marcus electron transfer model. Here the hypothesis is that the relative differences of the LUMO offsets are key driving forces contributing critically to the intra-molecular charge transfer rates, and that there may be an optimal LUMO offset exist per Marcus model [5-6].

IV. Impact on Laboratory or National Missions

The science on efficiently converting sunlight into cleans electrical power using inexpensive and renewable materials and processes is a key scientific and research mission of the Department of the Energy and the national labs including BNL. This project and its potential discoveries can further clarify our understanding of the fundamental processes of how sunlight photons are converted into electrons and holes efficiently at molecular level, and what kind of the molecular or solid state structures could lead to high efficiency and cost effective solar cells. Specific-



.Figure 3. (Top) Donor cation decay of 50 μM D1, A1, D1/A1, and D1BA1 in THF, and (Bottom) donor cation decay of 50 μM D, fA, D/fA, and DBfA in THF.

ly, from the preliminary charge transfer dynamic studies of this work, it appears that in a DBA system, the size or energy barrier of the bridge appears playing a critical role. The donor (or acceptor) block size could also be critical, i.e., smaller sized blocks may be favorable than large sized ones for efficient intra-molecular exciton dissociation or charge transfer due to reduced charge or exciton diffusion. For acceptor block side chain fluorination, though fluorination can improve solid-state donor/acceptor Nano phase separation, it may not necessarily improve intra-molecular charge transfer, as it may not necessarily result in optimal driving force for charge transfer. These preliminary results alerted our next researches to carefully design and synthesize new molecules to optimize several parameters (such as donor size, bridge size, LUMO offsets, etc.) at the same time.

V. Conclusions

Electron pulse radiolysis studies revealed that, in either side chain non fluorinated or fluorinated D1BA1 and DBfA, donor cation decay in the D/A blend appears much faster as compared to the pure D due to inter-molecular or bi-molecular collision induced electron transfer from D to A, and that the donor cation decay in DBA is a slightly faster than the D/A blend due to both inter-molecular collisions and intra-molecular electron transfers from D to A via the bridge unit. However, the intra-molecular charge transfer rate appears not significantly faster than the inter-molecular collisions, particularly in the fluorinated DBfA case. The relatively slow intra-molecular charge transfer rate could be due to slow electron diffusion on donor block, or due to slow electron transfer across the bridge unit as a result of weak D/A electronic coupling via the bridge, or due to the non-optimal energetic driving/counter-driving forces for the through-bridge transfer. One preliminary and interesting observation is that the donor cation in DBfA with four methylene units (C4) appeared exhibiting slightly faster decay as compared to the DBfA with two (C2) and six (C6) methylene unit bridge.

VI. Work Cited

- [1] (a) Sun, S. and O'Neill, H., "Sunlight Energy Conversion via Organics", in Handbook of Photovoltaic Science and Engineering, 2nd edition, Luque, A and Hegedus, S., eds., Wiley, the Atrium, England, 2009. (b) Sun, S. and Sariciftci, S., eds., Organic Photovoltaics: Mechanisms, Materials and Devices, CRC Press, Boca Raton, Florida, 2005 (ISBN-13: 978-0824759636).
- [2] Li, G.; Zhu, R.; Yang, Y., Nature Photonics, 2012, 6, 153-161.
- [3] (a) Sun, S., Sol. Ener. Mater. Sol. Cel., 2003, 79(2), 257. (b) Zhang, C.; Choi, S.; Haliburton, J.; Li, R.; Cleveland, T.; Sun, S.; Ledbetter, A.; Bonner, C.; Macromolecules, 2006, 39, 4317-4326. (c) Zhang, C and Sun, S., "Organic and Polymeric Photovoltaic Materials and Devices", in Introduction to Organic Electronic and Optoelectronic Materials and Devices, CRC Press/Taylor & Francis: Boca Raton, Florida, USA, 2008, chapter 14, pp 401-420. (d) Sun, S.; Zhang, C.; Li, R.; Nguyen, T.; David, T.; Brooks, J., Sol. Energy Mater. Sol. Cells, 2012, 97, 150-156. (e) Sun, S.; Brook, J.; Nguyen, T.; Zhang, C., J. Poly. Sci. Poly. Chem., 2014, 52, 1149-1160. (f) Sun, S., "Cost Effective Polymer Solar Cells Research and Education", DE-EE-0004002-RPPR1, October 30, 2013.
- [4] Jenekhe, S. and Chen, L., Macromolecules, 1996, 29, 6189.

[5] (a) Miller, J. R., Calcaterra, L. T., Closs, G. L. J. Am. Chem. Soc. 1984, 106, 3047-9. (b) D. Gosztola, B. Wang and M. R. Wasielewski, J. Photochem. & Photobiol. (A), 1996, 102, 71-80. (c) R. Marcus, et al., J. Phys. Chem., 2003, B, 107, 6668-6697.

[6] Sun, S., Sol. Energy Mater. Sol. Cells, 2005, 85, 261-267.

VII. Acknowledgement

This project was supported in part by the U.S. Department of Energy, Office of Science, and Office of Workforce Development for Teachers and Scientists (WDTS) under the Visiting Faculty Program (VFP).

VIII. Primary DOE funding supports for this project

This material is based upon work supported in part, by the U.S. Department of Energy (DOE), SETP/MURA program grant DE-EE-0004002, and by Office of Science, Office of Basic Energy Sciences through Grant DE-AC02-98-CH10886, including use of the LEAF facility of the BNL Accelerator Center for Energy Research.

Accelerating computational software through parallelism

Ryan Hilbert

Computer Science, Suffolk County Community College, Selden, NY 11784

David Stampf

Computational Science Center, Brookhaven National Laboratory, Upton, NY 11973

Abstract

Modern high-performance computing requires extensive use of parallelism; however, there are many possible approaches to developing parallel software. This study serves to document the process of accelerating computational software through the exploitation of parallelism in order to guide future researchers in their efforts to achieve similar results. To do this, a highly parallelizable serial scientific application, written in the C programming language, was refactored to utilize various parallel computing frameworks, including Compute Unified Device Architecture (CUDA), Open Computing Language (OpenCL), Open Multi-Processing (OpenMP), and Message Passing Interface (MPI), with the goal of increasing computation speed by two orders of magnitude and documenting the benefits and drawbacks of each approach. It was found that the performance increase was most easily obtained using a combination of MPI and CUDA, but because both of these have specific hardware requirements (a cluster and Nvidia GPU (graphics processing unit) respectively), OpenCL is more favorable if a more platform-independent approach is desired. OpenMP can also be used, either separately or alongside these technologies, to exploit smaller amounts of parallelism at the CPU (central processing unit) level with minimal effort. The results of this study serve as a guide for the efficient parallelization of computational applications and should allow future serial programs to be refactored more easily and effectively. Additionally, researching and implementing these frameworks for the first time has made me proficient in parallel programming and given me invaluable experience in high-performance scientific computing.

I. Introduction

Standard serial computer programs are written and executed in a linear fashion; the programmer writes a list of statements and the computer executes them (mostly) in the order they were written, one at a time, and using only a single processor core. For instance, consider this simple C program fragment that squares every number in an array.

```
#define SIZE 1024
for(int i=0;i<SIZE;++i)array[i]*=array[i];
```

Each element of the array is individually loaded, squared, and written back to its original memory location, one at a time. While this works as intended, on modern hardware it could be made to work much faster. Parallel programs accomplish this by specifying statements that should be executed at the same time, allowing them to be spread out among, and thus utilize more of, the available hardware. This concept becomes extraordinarily important in computationally intensive software, where performance is often critical. To demonstrate the effectiveness of software paralleliza-

tion, a serial scientific application, written in the C programming language, was accelerated using the techniques discussed in this paper and the resulting increases in computation speed were recorded.

II. Methods

A. OpenMP

The simplest way to achieve parallelism in a program is to make use of the processor cores that are left idling in a standard serial program. If the problem is small or more powerful hardware isn't available, this can also be the most performant option. OpenMP makes this simple by introducing directives that can be inserted into an existing C program to offload independent tasks to separate processor cores. Referring to the previous example, squaring an individual element of an array is a task independent of squaring every other element in the array. Because of this, squaring the entire array can be easily parallelized using OpenMP.

```
#define SIZE 1024
#pragma omp parallel for
for(int i=0;i<SIZE;++i)array[i]*=array[i];
```

The OpenMP directive before the loop indicates that the loop's iterations should be divided among each of the program's threads. If the number of threads is set to the number of available processor cores, the loop's iterations should be evenly divided among them. Using this method, it is often possible to drastically improve a program's performance by adding just a few lines of code. Additionally, because OpenMP utilizes C's pragma directives, the above OpenMP code is simply ignored if compiling without OpenMP. The framework also defines a preprocessor macro called `_OPENMP` when in use. Together, these features make keeping OpenMP accelerated code backwards-compatible a simple matter.

B. CUDA

Often, exploiting parallelism at the processor level isn't enough. For sizable computations, it may be necessary to offload a portion of the program's work to a device other than the CPU. GPUs in particular excel at performing the same operation on thousands of data elements at once, making them a good fit for many scientific computations. If Nvidia GPUs are available, CUDA is likely the best option for further parallelization. CUDA adds a few extra steps to the flow of the program, so that the order of events becomes initialize data on the CPU, allocate space for the data on the GPU, move the data to the GPU, process the data on the GPU, and finally, move the processed data back to the CPU. This is illustrated by the following expansion of the previous squaring example.

```
#define SIZE 1024; #ifdef __CUDACC__
```

```

void*dptr;
cudaMalloc(&dptr,SIZE*sizeof(*array));
//inner parens optional
cudaMemcpy(dptr,array,SIZE*sizeof*array,cudaMemcpy-
HostToDevice);
square<<<1,SIZE>>>(dptr);
//CUDA function call, must be defined
cudaMemcpy(array,dptr,SIZE*sizeof*array,cudaMemcpy-
DeviceToHost);
#else
#pragma omp parallel for
for(int i=0;i<SIZE;++i)array[i]*=array[i];
#endif

```

CUDA introduces an additional bottleneck, however. The transfer of data between the CPU and GPU can take a significant amount of time. Because of this, use of an external device such as a GPU should be limited to large-scale problems that are arith-

metically intensive. The squaring example above would almost certainly perform worse on the GPU, due to it only performing a single multiplication on a small number of elements. Given a large enough problem, however, CUDA can easily outperform methods such as OpenMP.

C. OpenCL

CUDA is more efficient for Nvidia GPUs, but if the application needs to run on other hardware, such as AMD GPUs, Intel coprocessors, or even IBM accelerators, OpenCL is a viable alternative. OpenCL trades simplicity for portability, and as a result, OpenCL applications are able to run on a wide range of hardware, but are often incredibly verbose. Due to this verbosity, a code example is impractical; however, it's worth noting that some of this burden can be alleviated by using OpenCL bindings in other languages, such as C++.

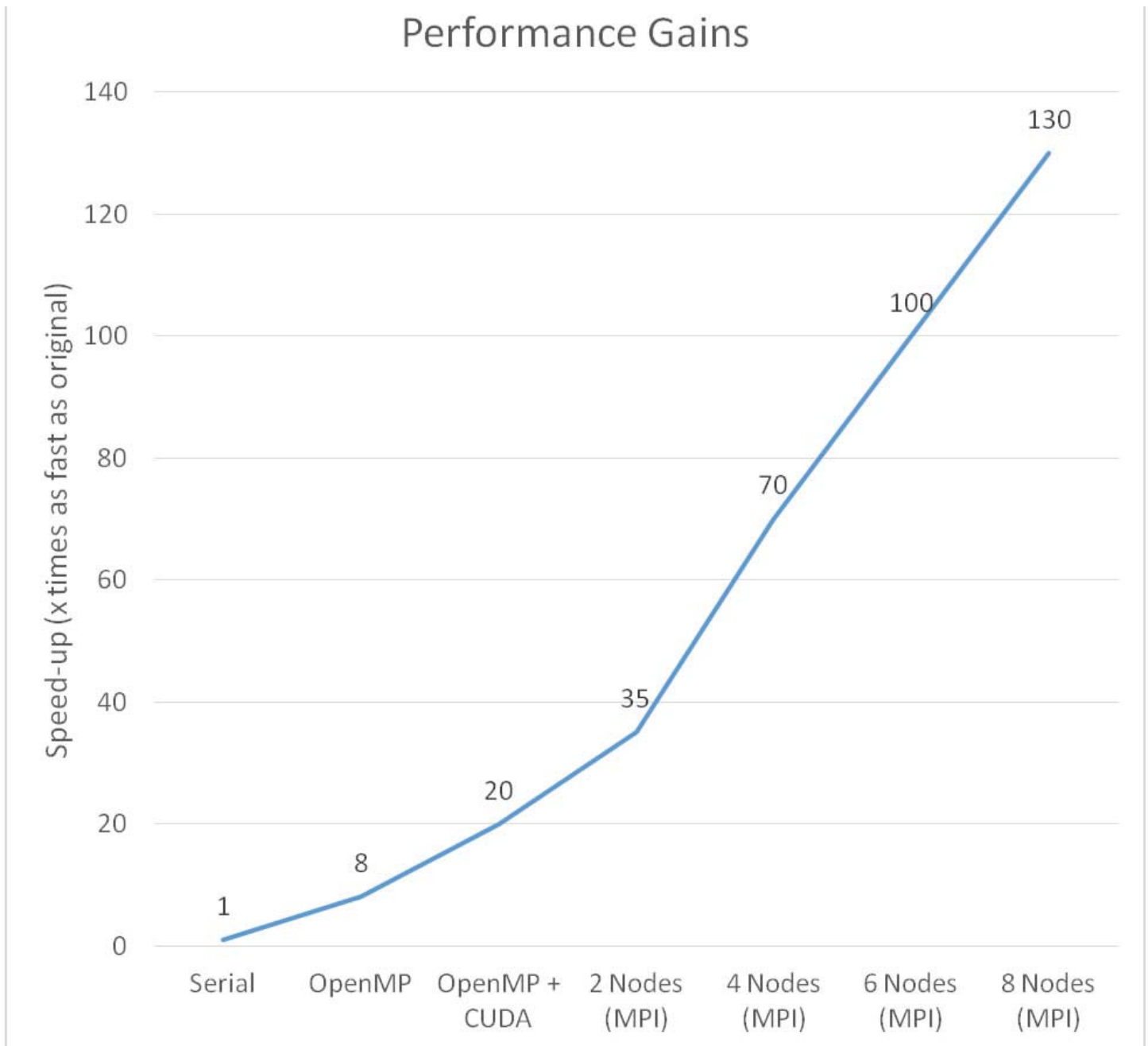


Figure 1.

D. MPI

For truly massive calculations, it can sometimes be necessary to utilize multiple machines, or nodes. This can be done with MPI. MPI allows work to be divided among nodes by assigning each of them a number, or rank, and allowing them to perform different actions or work on different data based on this rank. This can also be combined with frameworks such as OpenMP, OpenCL, and CUDA to utilize more of the hardware available to each node. This, however, often requires modularization to become practical, as discussed below, and communication between nodes can be very time-consuming.

E. Modularization

As demonstrated in previous code samples, parallelizing a program can make it less readable and can obscure its original intent, especially in the case of the extraordinarily verbose OpenCL. Additionally, frameworks such as MPI and CUDA are most easily compiled using their own wrapper compilers, making using them both in the same file difficult. Fortunately, these issues can be mostly resolved by breaking the code into multiple files, or modules. Through modularization, the previous CUDA example can be turned into the following by defining an ‘extern’ function named square in a separate file.

```
#define SIZE 1024;
square(SIZE, array);
```

Now the square function can be written either serially or using any of the previously mentioned frameworks and different implementations can be separated into different files, allowing for multiple frameworks to be used without excessive ifdef statements, as well as certain frameworks to be combined much more easily. This also provides the benefit of the keeping the code easily manageable and readable.

III. Results

Each of the listed methods was applied to an arithmetically intensive scientific application. Each of the nodes used for testing consisted of two Intel Xeon hyper-threaded quad-core CPUs and a single Nvidia K20X GPU. The most time-consuming part of the application was refactored to utilize OpenMP, CUDA, and a combination of CUDA and MPI. Unfortunately, timed results for the OpenCL implementations were unable to be obtained soon enough for inclusion in this paper. The resultant performance gains can be seen in the graph shown in figure 1.

The scaling behaved mostly as expected, as the refactored program contained several levels of parallelism that could be easily exploited. Using CUDA for the primary bottleneck of the program proved more effective than OpenMP, and doubling the amount of nodes with MPI made the computation roughly twice as fast.

IV. Conclusion

Parallelization has proven to be a crucial aspect of scientific computing. By utilizing the techniques and frameworks discussed in this paper, computational software can be made to run several orders of magnitude faster, as has been demonstrated. This can often determine whether or not a solution to a problem is practical and allows a much wider range of problems to be computed as a result.

V. Acknowledgements

This project was supported in part by the U.S. Department of Energy, Office of Science, Office of Workforce Development for Teachers and Scientists (WDTS) under the Science Undergraduate Laboratory Internships Program (SULI).

Revealing Traps in Charged Couple Devices using Pocket Pumping Technique

Jeremy Hyde

Physics Department, Carnegie Mellon University, Pittsburgh, PA, 15289

Ivan Kotov

Instrumentation Division, Brookhaven National Laboratory, Upton, NY, 11973

ABSTRACT

In modern charged couple devices (CCD) there exists small electron trap sites that degrade the overall charge transfer efficiency of a CCD. In order to characterize these CCDs and their we used pocket pumping techniques to produced regions and catalogs for the astronomical analysis software ds9 in order to locate traps in the pixel data from the CCD image files (.fits files). The region and catalog files were then parsed and the traps were analyzed in order to study where the traps were located and how these traps' amplitudes were affected by various amounts of pocket pumping. In order to improve this method, we took several images of the same CCD for the same exposure time and averaged the images together in order to obtain a narrower peak for the trap amplitude. Finally, the CCD was cooled to various temperatures ranging from -140°C to -60°C and the pocket pumping was run at various timing sequences in order to discern the energy levels of the traps and what might be causing them. By analyzing the CCD we hope to optimize the characterization process for CCDs being used in sensors of the LSST. As a result of this project, I have gained greater proficiency in the programming languages, C++, python, and java. I had also worked with CCDs before but this project gave me a chance to great how they function and what problems CCD developers must overcome.

I. INTRODUCTION

Pocket pumping is a method by which electron traps can be found. CCDs are exposed to a flat field and the charge is transferred up and down many times, this causes electrons to be drawn from one pixel and deposited in a neighboring one in the same column, this method is known as pocket pumping. This withdrawal and deposit causes sets of light and dark pixels to appear next to one another due to excess electrons be in one and lack of electrons in the other. By comparing the amplitude of these pixels to the background amplitude it is possible to locate the traps.

To study the amplitude of the traps in the CCD, the CCD was enclosed in a black box to previous extraneous light from reaching it. It was then exposed to a flat field for an exposure time ranging from one-second to ten seconds.

The CCD was then pocket pumped between 1,000 and 20,000 times with a pump depth of one line and read out into a FITS file using code provided by Ivan Kotov on the `ccdtest@lsst2`.

In order to locate traps in the ".fits" file we searched for dipole pairs of pixels that were light and dark. We searched through possible pairs and found the ones that were 3-sigmas from the normal background value and labeled them as traps.

In order to try to improve the data, multiple images were taken in sequences and vaerged together using the `PP_trap_final.cpp` in which each image from a provided directory was base line subtracted and new pixel values averaged together and then treated

like one image.

By varying the timing of the pumps and temperature we hope to be able to determine an approximate value for the energy level of each trap in the CCD. Once its energy level has been determined we will be able to determine the cause for each trap whether it be a foreign particle, valence in the atomic matrix or an extraneous atom. In the timing experiment, we varied the speed of the pocket pumping, this along with the emission time can predict which pixel a trapped electron with me release into to. For a given speed there is a time t_{ph} in which the trapped charge sits under a pixel. The electron is only pumped to the next pixel if it is emitted between $t=t_{ph}$ and $t= 2t_{ph}$. The probability of an electron being pumped is given in equation 1 where t_{ph} can be found from the speed of the pumping.

$$P_p = e^{-\frac{t_{ph}}{\tau_e}} - e^{-\frac{2t_{ph}}{\tau_e}} \quad (1)$$

Therefore the amplitude of the dipole is give by the equation below where N is the number of pumps, P_c is the probability of the electron being captured and assuming the donor pixel has not been depleted.

$$I = NP_c \left[e^{-\frac{t_{ph}}{\tau_e}} - e^{-\frac{2t_{ph}}{\tau_e}} \right] \quad (2)$$

By tracking the I value for various t_{ph} or pumping speeds one can determine the emission time τ_e . Coupling this with variations in temperature we should be able to determine the energy of a trap using the equation below where C is a constant based on various masses, capture cross section and the entropy factor associated with the electron emission.

$$E = kT * \ln(\tau_e * T^2) + C \quad (3)$$

II. DATA PROCESSING

At room temperature a sensor with bad segments was used to gather data with a three second exposure time and the following number of pumps: 1000, 2000, 3000, 4000, 5000, 6000, 7000, 8000, 9000, 10000, 11000, 12000, 15000, and 20000. In order to perform the temperature experiment we used a different, much better, CCD and cooled it down to -140°C and took data at 20°C increments until -60°C . At each temperature the CCD was exposed to it was pumped 1000, 2000, 4000, 8000, and 12000 times with a two second exposure time. In addition to that it was also pumped at similar values with 0.5, 4, 16 and 32 second exposure times as well as with a 0.1 second exposure time for which it was pumped 200, 400, 800, 1600 and 5000 times. The timing experiment was implemented by varying the speed of the pocket pumping between $5\ \mu\text{s}$ and $160\ \mu\text{s}$ and pumping the CCD at -120°C , 8000 times and a one second exposure time.

Once this data was gathered it was run through `PP_trap_and_`

regions.cpp, after first running run_first.cpp. (Note: A similar program was written to use catalog, .xml files, as well). This created a region file, which included data such as the amplitude, above or below background, each pixel, x-coordinate, y-coordinate, and tile number for each trap.

Fig. 1 Pocket pumping regions shown in ds9 with red rectangles around them

This file can be loaded along with the FITS file into ds9 to show the location of the traps on the CCD. This was repeated for several files with the same exposure time but with differing number of pumps.

In PP_trap_analysis.cpp I wrote code that would parse all region files inputted into it by looking for key words and extracting data such as the location of the trap, amplitude of the pixels affected by the trap compared to background and which tile it is in. This information was stored and values such as number of traps per segments and average amplitude were calculated. The data was then graphed using root's TGraph and TMultiGraph.

The next step was to try to improve the signal to noise levels by averaging together multiple exposures of the same image. Multiple exposures were taken one after another and added to a directory. I then manipulated the PP_trap.cpp code provided by Ivan Kotov to be able to take an inputted directory instead of just a single file. The files in the directory were added to a file list. For each file we performed a base line subtraction, which removed the overscan value from the pixels. After this base line subtraction (BaLiS) was performed on each image the pixel values were averaged together into one image and analyzed accordingly. The data taken is saved in the base directory /data2/e2v/112-04 on the lsst2 in the format seen in Table 1.

Table 1 The data is sorted in the directories above

III. POCKET PUMPING DEPENDENCE

The follow data was collected from a CCD exposed for three seconds and pocket pumped 1000, 2000, 3000, 4000, 5000, 6000, 7000, 8000, 9000, 10000, 11000, 12000, 15000, and 20000 times.

In figure 2 it is easy to see which segments are bad by the shape and scale of the graphs. The scale of the segments with low traps go up to around 400 or 800 while the bad segments such as segment 12 (tile 11) goes up to 30000. The shape of the segments with lower number of traps is also much more sigmoidal due to the difficult initially in finding them a low number of pumps and over pumping, producing the inflexion point. The segments with a high concentration of traps tend be much flatter possibly due to the ease of finding traps initially and once again the over pumping at the end.

An interesting thing to note about Fig. 2 is the number of traps found for the 20000 pocket pumping point. We expected it to be on the same level as the 15000 since the pixels with very efficient traps would already have been completely depleted. Instead, we see the number of traps decrease in almost every segment for an unknown reason.

In Fig. 3 we see the graph of the average amplitude of the traps in each segment plotted against number of pocket pumps. The amplitude was calculated by taking the absolute value of the difference between the two pixels and dividing the result by the square root of 2. The bad segments have much high, almost dou-

ble, average amplitude for their traps than do the better segments. However, the most intriguing part of this plot is the shape of the curves and once again, the 20,000 pocket pumping point.

While some of the good segments increase uniformly, others experience a spike at around 2000 or 3000 before also increasing uniformly. The spiking requires further investigation but the uniform increase is to be expected to a certain level as the depletion of the pixels approach 100%. The bad segments on the other hand asymptotically approach a maximum average amplitude due to the fact that these segments are very inefficient and have so many more traps then the good segments whose efficiency approaches 1.

The 20,000 pocket pumping level appears to decrease in all segments once again. This is very noticeable in the bad segments where the 20,000 point jumps down to around a third of the 15000 level instead of staying at the same level as expected. When looking at the region file in ds9 I found that the difference between the background and overscan was around 1,000 at the 20,000 pocket pumping level while it was 3,000 at all other levels. Whether this 1:3 ratio observed again is correlated with the average amplitude difference has yet to be determined.

The plot of each trap is shown in its appropriate tile in Fig. 4/5. Fig. 6 and Fig.7 show zoomed in copies of a relatively good segment (segment 4) and a relatively bad one (segment 12). Most of the traps follow a similar increasing to a certain level and then leveling out when the pixel the trap is in becomes fully depleted. Some of the noted outliers to this pattern are the zigzags appearing in many of the tiles. Even the bad segments follow this pattern if to a higher amplitude as in Fig. 7.

The 20,000 pocket pumping level point is interesting. As can be seen in most tiles and especially in Fig. 7, many of the traps disappear after the 15,000 point. While this was expected due to Fig. 2, I expected that it would be some of the lower amplitude traps if any that would disappear but instead it seems like it is mostly the higher ones that are. Further investigation is required to determine why certain traps are disappearing.

IV. IMAGE AVERAGING

The goal of averaging together images of the same CCD under the same conditions was to decrease the shot noise to signal ratio. The shot noise causes the pixels to fluctuate around a mean value; these fluctuations produce a Poisson distribution and an RMS value associated with the width of the distribution, therefore any decrease in shot noise to signal ratio should be seen in the RMS value. If the images were independent we would expect the RMS value to decrease by a factor of the square root of the number of files so if you inputted a directory with say 100 files it should decrease to around a tenth the original. As can be seen when comparing Fig. 8 to Fig. 9 this is not the case, While it is true that the RMS value of the multiple image graph does decrease compared to the RMS value of the single image this decrease is only around 30% instead of the predicted 10%, this means that there is some issue most probably some innate correlation between pixels in the same rows or columns.

V. TIMING DEPENDENCE

The timing and speed of the pocket pumping affects the amplitude of the traps should allow us to determine the characteristic emission time of the trap, τ_e . As can be seen in Fig. 10, not only has the amplitude of the traps, with an increase in pocket pumping

speed, i.e. a decrease in the time the trap is in each phase, but the number of traps has also grown. As can be seen in Fig. 11 there is an increase in the number of traps until around 40 μ s per step at which point it begins to level out. Unlike the number of traps the amplitude of the traps stays constant. These two facts imply that the best pumping seems to occur when the timing is around 1 μ s or 5 μ s per step.

VI. TEMPERATURE DEPENDENCE

Finally we began to study the temperature dependence of the CCD in hopes of combing what we found with the timing dependence to determine the energy level of the traps. As can be seen in Fig. 12 the number of traps found increases with temperature until -100 °C at which point it drops sharply and then keeps dropping at a more moderate rate. This indicates that the best temperature to run the CCD at seems to be at hotter temperatures, however, one must balance this against the dark current which is least at low temperatures. This means that the optimal temperature for the CCD to function at is about 80 °C.

VII. CONCLUSION

The novel trap identification technique has been developed. This technique has been used to analyze pocket pumped images obtained with CCD 250 at various temperatures, timings and pocket pumping levels. For the 113-03 CCD the optimal temperatures seems to be at -80 °C. In the future by using the timing dependence we can calculate the τ_e , which in turn can be used with the temperature dependence to determine the energy level of the trap, and hint at what imperfection in the crystal structure of the CCD caused it.

VIII. ACKNOWLEDGEMENTS

This project was supported in part by the U.S. Department of Energy, Office of Science, Office of Workforce Development for Teachers and Scientists (WDTS) under the Science Undergraduate Laboratory Internship Program (SULI).

Hall, David J.; Murray, Neil J.; Holland, Andrew D.; Gow, Jason; Clarke, Andrew and Burt, David (2014). Determination of in situ trap properties in CCDs using a “single-trap pumping” technique. IEEE Transactions on Nuclear Science (In press).

Design development for Coherent Electron Cooling Proof of Principal and Low Energy RHIC electron Cooling project

Robert Jacoby

Mechanical/Aeronautical Engineering, Rensselaer Polytechnic Institute, Troy, NY, 12180

Jean Clifford Brutus

Collider Accelerator, Brookhaven National Laboratory, Upton, NY, 11973

ABSTRACT

At Brookhaven National Laboratory's Collider Accelerator Department, mechanical engineers and physicists have been collaborating on the design development of the Coherent Electron Cooling Proof of Principle (CeC PoP) experiment and the Low Energy RHIC electron Cooling Project (LEReC). My two principal contributions involved the engineering and design development of the 2.1 GHz Warm RF Cavity for LEReC, and the design, analysis, and fabrication of components for CeC PoP such as the laser breadboard support, the air flow sensor housing, and the dipole vacuum chamber. Computer Aided Design software such as Creo Parametric 2.0, AUTOCAD, and Inventor were used to create virtual three-dimensional scaled models. The models were based on input from existing AUTOCAD drawings, other existing models, and input from the mechanical engineers and physicist working on the project. I learned how to use ANSYS, a power engineering simulator, and to perform structural and thermal analysis in order to confirm the structural stability of different components. My design for a spacer was fabricated to support the laser breadboard and was attached shortly after. The air flow sensor housing I designed was 3D printed and is making its way through the approval process before being inserted into the system. The dipole vacuum chamber I designed was an upgrade from the old design, and will be fabricated as soon as the idea is approved.

I. Background

Coherent Electron Cooling is a technique that is being used to improve the brightness in high energy hadron-hadron and electron-hadron colliders. The Proof of Principle experiment at BNL is going to demonstrate the CeC technique. Part of the experiment is a short 22MeV superconducting linear accelerator. This accelerator will prove a beam that is capable of cooling only one ion bunch store in RHIC. The accelerator is made up of two SRF systems and one normal conducting RF system. Dipoles are used to bend the electron beam into RHIC. Looking into the future is the Low Energy RHIC electron Cooling Project as seen in figure 1. LEReC will be based on using bunched electron beams produced with the SRF accelerator. This project will incorporate many different Cavities including a 2.1GHZ SRF 7-cell cavity. The 7-cell cavity is designed to correct the energy spread in the beam and is essential for the success of this experiment.

II. Methods

Virtual three-dimensional scaled models are powerful tools that engineers use to make a physicist's idea become reality. These models are generated using ProEngineer Computer Aided

Design (CAD) software like Creo Parametric and Inventor. The models are created using specifications from existing drawings and input from the mechanical engineers and scientists working on the project. After the model is made, simulation software like Ansys is used to analyze the model with different test. These tests will confirm the structural stability of the model in different environments.

III. Individual projects and results

Part of CeC PoP experiment was a laser and the breadboard mount had to be shaped differently to allow more access and clearance for the laser. This task required a virtual three-dimensional model of the mount using Creo parametric. The task demanded specific specifications that would come from measuring the dimensions off the laser breadboard and using other virtual models as references. Originally a long piece of Rexroth was going to be extended behind the laser breadboard but this reduced the access and other parts were in the way. A short piece of Rexroth would be attached from the top of the structure to the laser breadboard to correct the problem. The Rexroth piece was too far away from the laser breadboard and needed an additional piece to make up the empty space. The spacer had to fit in between the Rexroth piece and breadboard but also have holes that lined up with the threaded breadboard holes and line up onto the Rexroth piece using T-screws. After making the spacer model on Creo, the spacer was placed into the assembly containing the laser breadboard structure. There was no way to use the T-screws with the current design since there would be no room for the nuts. To fix this problem, the two holes for the T-screws would have to be counter bored to allow the nuts to sit into the material. A drawing was made after checking all the dimensions and sent to the ma-

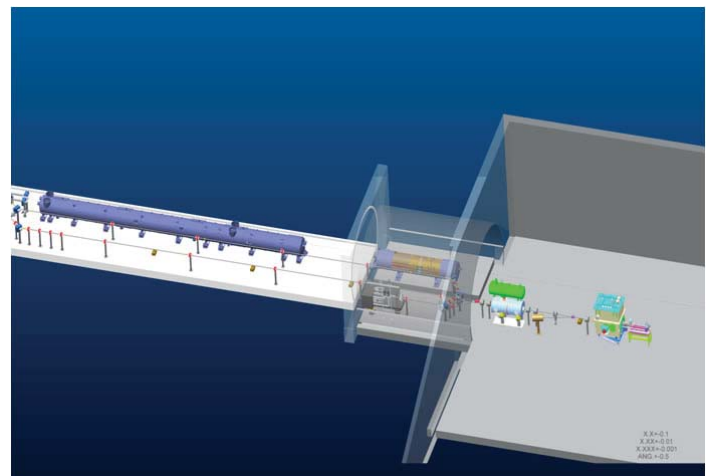


Figure 1. LEReC at 2 O'clock Interaction Region

chine shop to be fabricated. After it was fabricated, it was taken into the tunnels and attached to the laser breadboard.

The second component that I worked on for this experiment was an air flow sensor assembly. The sensor assembly was requested to be a safety check in case a pump decided to stop working correctly. If the pump stopped blowing air, the system could over heat and damage the outer conductor of the fundamental power coupler and the solenoid magnet. To stop this from happening, an air sensor would need to be installed in the pipe lines to detect if there is air flow. The sensor would then shut the system off if it detected no air flow. A simple tube design would hold the air sensor with support around part of the sensor and glue to permanently hold it. The flap on the sensor was designed to be close to the middle of the tube in order to maximize the amount of air to hit the flap. The specification for the tube came from the existing pipe and was 3D-printed after a three-dimensional model was created on Creo. The sensor assembly is waiting to be inserted into the system.

A 7-Cell warm cavity is being designed for the LEReC project. The cavity is being designed from RF models provided by the physicist. In parallel, a stand to support the cavity, two Ion pumps, and a tuner is being designed as well. The cavity design is being optimized by physicists and engineers. Among the few changes that had to be made, the vacuum ports had to be moved by 90 degrees because it was too close to the tuner port. The next modification was reducing the inside diameter for part of the cavity.



Figure 2. Laser Breadboard Mount

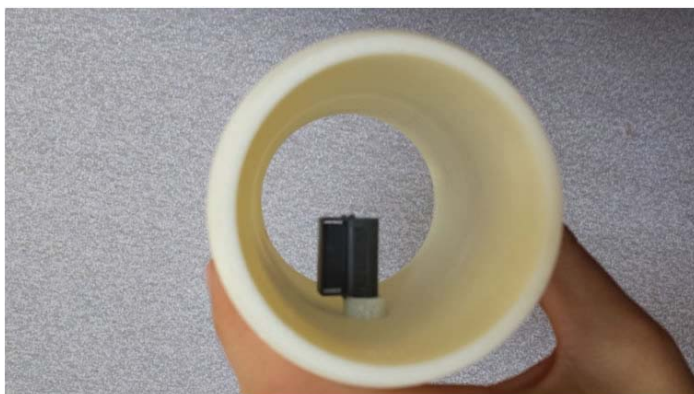


Figure 3. Sensor Assembly

The completed cavity can be seen below in figure 4.

Structural simulation was done on the cavity in order to find out the deformation and stress on the cavity. The simulations were done using Creo and the initial results show that there is high stress on the beam line ports and a bigger radius was needed in order to reduce deformation. The initial results can be seen in figure 5.

Flanges were added to all of the ports and elbows were initially added to the vacuum ports. The 90 degree elbows were removed after discussing with the physicists that it would affect the pump out of the cavity during commissioning. The pump was moved to be directly attached to the vacuum port flanges and on its side to allow clearance for the cables. A fundamental power coupler (FPC) was designed and will be located on the top of the cavity. The FPC included a custom flange at the top to hold the lens and a flange welded to the bottom to attach to the FPC port on the cavity. As mentioned earlier, a stand to support all the parts of the assembly was designed. The stand was built to move in all three-dimensions allowing for the cavity to be precisely located along the beam line. This was possible using threaded rod to move in the x and y direction while having slides to move in the z direction. The completed three-dimensional model can be seen in figure 6.

Figure 6. Master assembly for 2.1GHz 7 Cell warm cavity

A chamber originally designed for a dipole assembly along the CeC beam line had to be redesigned. This original idea needed to be simplified because it was not cost effective and the material needed to be changed from aluminum to stainless steel in order to increase the bake out temperature. The new designed is made of machined plates that would be welded together like a box. The design needed to be as simple as possible but due to different constraints, the plates were more complicated. The gap between the Dipole was 2.375 inches while the beam path clearance needed

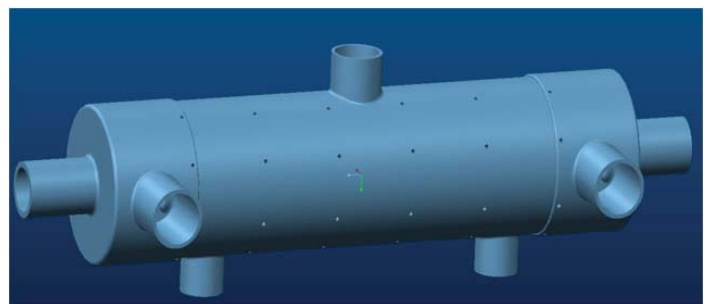


Figure 4. 2.1GHz 7 Cell warm cavity

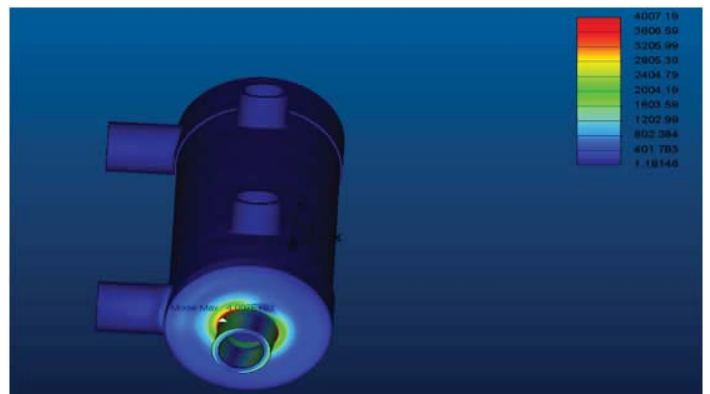


Figure 5. 2.1GHz 7 Cell warm cavity deformation analysis

to be 2.00 inches. A demand for only using 2.25 inches of the 2.375 inches was requested as well. The design had the top and bottom layer being welded to the tops and bottom of each wall. This smaller clearance meant the top and bottom would have to be recessed into the chamber with lips on each wall. This made the plates more complicated but was a necessity and can be seen in figure 7.

The new vacuum chamber design was analyzed using ANSYS. The pressure caused the top and bottom layers to have a large deformation. In order to correct this problem, simulations with one support rod added and two supports rods were done. The simulations proved that adding a support rod would result in a much smaller deformation and adding one support would be effective enough. Using only one support rod would help keep the overall cost of the chamber lower. The next modification resulted after a high stress was seen where the walls would hold the top and bottoms layers. This problem was corrected by making the walls closer and to do this, another wall was introduced making the chamber look more like a Y shape. Simulations confirmed the idea, and would result in an additional wall needing to be manufactured. Once the model is completely finished, drawings are made to be approved by a chain of command.

IV. Conclusion

The assembly process for the 7-cell cavity is still a work in progress with the physicist making changes as more analysis is done. The dipole chamber was recommended and is making its way through the approval process. For both main projects, the final three-dimensional models accurately define the actual hardware. Virtual assemblies and models allow researchers and scientists to verify the accuracy of their measurements and initiate corrections. These assemblies are also great for demonstrating an idea to an investor or sponsor.

V. References

Belomestnykh, S. SRF AND RF SYSTEMS FOR CeC PoP EXPERIMENT. Pasadena: CC-BY-3.0, 2013. PDF.

C-AD Electron Cooling Team. Low-Energy RHIC electron Cooler. New York: Brookhaven National Laboratory, June 11, 2014. Print.

VI. Acknowledgements

This project was supported in part by the U.S. Department of Energy, Office of Science, Office of Workforce Development for Teachers and Scientists (WDTS) under the Science Undergraduate Laboratory Internships Program (SULI). Thank you to my mentor Jean Clifford Brutus, for all of his help and guidance throughout the summer.

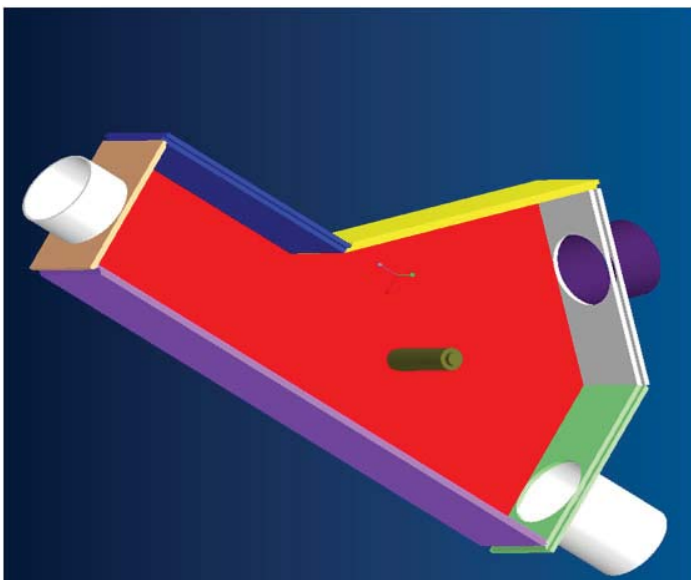


Figure 7. Dipole Chamber

Dynamic ATLAS load balancing in the HTCondor workload management system

Mark Jensen

Stony Brook University, Stony Brook, NY 11794

Antonio Wong

Brookhaven National Laboratory, Upton, NY 11973

I. Background and introduction

The ATLAS program is a particle physics experiment at CERN that is searching for new discoveries through the colliding of protons of extraordinarily high energy. The RACF (RHIC and ATLAS Computing Facility) contains a group of computers all running the HTCondor workload management system, referred to as the “Linux farm”, which is comprised of 12,792 CPU processors reserved for computations relating to the ATLAS program. The overall goal of this project is to develop an intuitive script that will analyze the amount of workload waiting to be processed, as well as heuristics on past behavior in order to dynamically adjust the available resources accordingly to ensure optimization of both CPU usage and work queue wait times.

In 2005 an analysis system named PANDA (Production and Distributed Analysis) was developed by the US ATLAS program as a means to manage and monitor the jobs specifications being run throughout the ATLAS program. It monitors the current workloads for all the facilities involved in the project monitoring both the prod and analysis groups, in order to maintain a database con-

taining all the running, holding, failed, and waiting jobs currently in the system. It is the data obtained from this PANDA database that our load balancing script will use and analyze in order to update the HTCondor manager accordingly.

The HTCondor workload management system is a full-featured batch system, developed at the University of Wisconsin-Madison, which provides a job queueing mechanism, scheduling policy, priority scheme, and resource monitoring and management. It is a program which is used as a means to distribute and maintain the work load for all the incoming resource demands of the ATLAS program. To summarize, the ATLAS program is monitored by the PANDA server, which in turn is monitored by our running scripts, which populate the HTCondor workload management system.

II. Group Layout and tree structure

Our current workload structure is shown in figure 1.

This tree structure represents the work groups that are currently being run in Brookhaven National Laboratory’s ATLAS

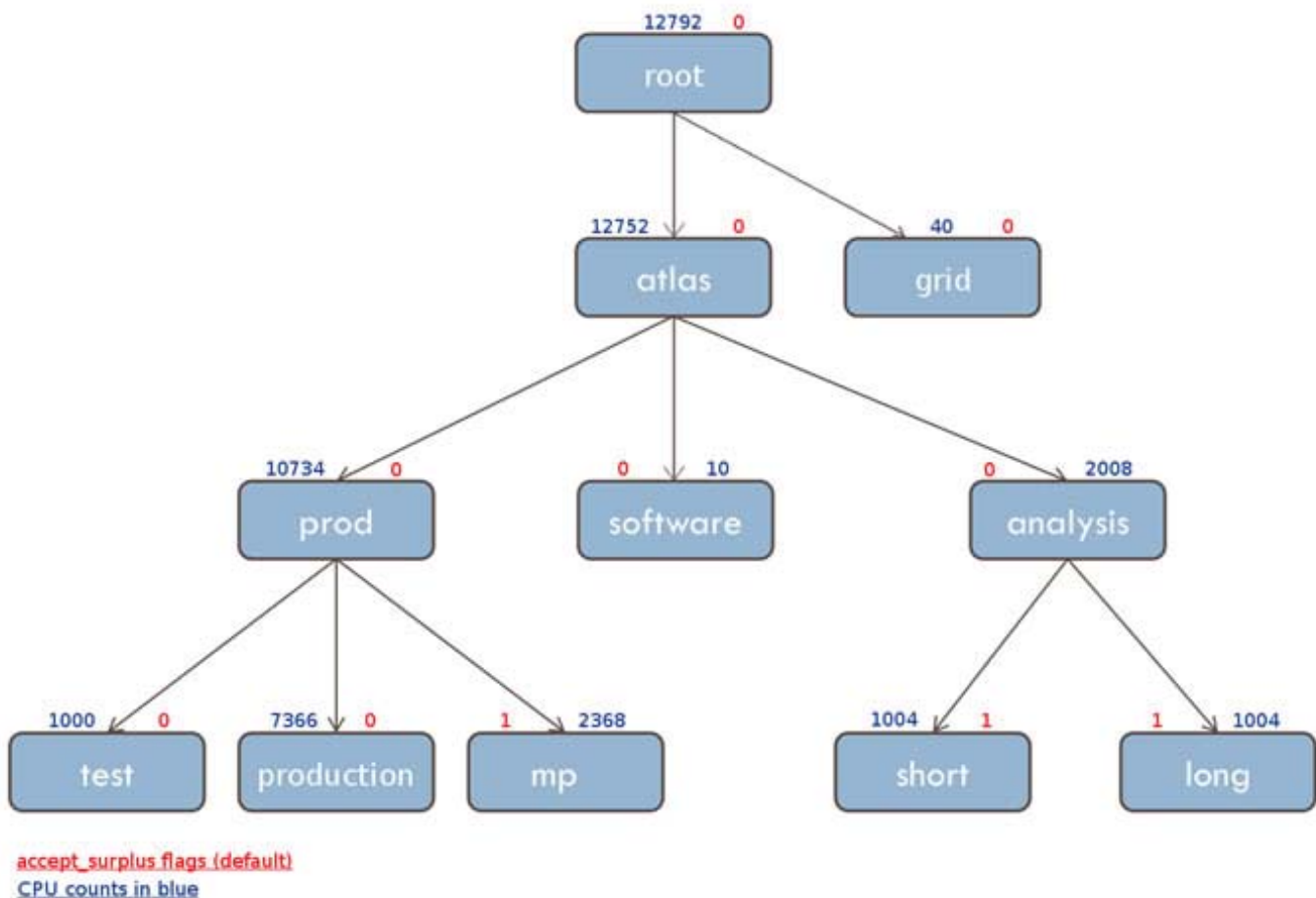


Figure 1. Completed tree structure created using generalized tree creation function

Linux farm. Analysis and Prod run on separate CPU clusters to avoid competition with each other, and have different policies for data-transfers. DDM transfers files for prod, while analysis does not trigger file-transfers since analysis jobs are sent to sites where the input files already exist. The prod cluster contains a much larger proportion of the overall CPU count also due to their greater overall use. The common ratio maintained is approximately 80:20. Jobs are only submitted to the leaf nodes, which will always sum up to the CPU counts of their parents. An important point to note is that the prod cluster contains both single-core jobs (production), and multi-core jobs (mp: 8cores, and test: 2cores). It is for this reason that special care must be taken when distributing CPU surplus in order to avoid greedy single core jobs from blocking any multi-core jobs from being processed, i.e. should the 8-core mp incoming jobs drop to 0 and production is allowed to use their CPUs in order to alleviate production's backed up queue, when the next mp job comes in, it may be unable to find an adequate continuous 8-core CPU block unless accounted for.

The goal is to continually analyze group queues provided by PANDA and allow surplus to be switched on and off for each group depending on the amount waiting to be run, the priority (multi-core before single-core), cross over between analysis and prod jobs if one cluster has a large lull in work, and eventually overall CPU ratio adjustments given long term analysis.

III. Queue Data Logging

The first goal for my internship was to develop a means to monitor the PANDA database and maintain a record for the five leaf nodes being submitted to. The PANDA database, when queried, delivers a large data dump for all the facilities around the world, in which it is up to the individual facility to sort through. An example of the PANDA data can be seen below in figure 2.

The PANDA data shown is just a small portion of several pages of text to be parsed. The highlighted portions are two of the five groups pertaining to our facility and represent the production leaf, and the long leaf. The amounts waiting to be run are denoted by the string "activated:". With this information, we can see that there are 285 analysis-long jobs running, and no jobs waiting to be run. The relevant information is parsed from this data and saved every five minutes to an ever growing MySQL database which logs the name, the amount in the queue, and the time-stamp for the query. Using this information, we are able to begin our analysis. A sample of the queue_log can be seen below in figure 3.

Using this information we can see that the entire prod cluster has developed a lull in queue amounts for the most recent 15 minutes. This is not to say there are no jobs being run, but instead demonstrating that prod is currently below its maximum CPU allotment and no jobs are waiting.

```
182, 'activated': 565, 'holding': 4}}, 'ANALY_IAAS': {'user': {'running': 1, 'activated': 3}},
BNL_PROD_MCORE: {'ptest': {'activated': 2}, 'managed': {'running': 359, 'transferring': 20,
activated': 223, 'holding': 13}}, 'ANALY_INFNO-BOLOGNA-T3': {'rc_test': {'defined': 1, 'activated':
1}, 'user': {'running': 1, 'activated': 1}}, 'ANALY_IN2P3-CC-T3_VM01': {'panda': {'activated': 3},
'install': {'activated': 7}, 'user': {'defined': 3}}, 'TOKYO_HIMEM': {'prod_test': {'running': 5,
'activated': 1, 'holding': 2}, 'managed': {'assigned': 136, 'running': 593, 'transferring': 2092, 'activated':
442, 'holding': 48}}, 'BU_ATLAS_Tier2_LMEM': {'ptest': {'activated': 3}, 'prod_test': {'activated': 4}},
'LRZ-LMU_C2PAP_MCORE': {'prod_test': {'starting': 2}}, 'wuppertalprod_HI': {'managed':
{'transferring': 1, 'activated': 1}}, 'ANALY_BNL_SHORT': {'ptest': {'activated': 1}, 'rc_test':
{'activated': 1}, 'panda': {'activated': 2}, 'user': {'defined': 1001, 'failed': 60, 'running': 948, 'activated':
11658, 'holding': 1}}, 'DCSC': {'prod_test': {'activated': 2, 'transferring': 1, 'starting': 6}, 'managed':
```

Figure 2. Sample PANDA data containing workload information for facilities throughout the world.

IV. Average Queue Check

In order to make decisions and determinations regarding the CPU amounts, and whether a group allows surplus, we first need default settings. At present, our default settings can be seen in figure 4.

The table contains a list of all the groups within the project and their respective default values. The structure is currently set to only check and modify the prod cluster of leaves, and once this is fully functional, we will move on to the analysis cluster. The group tree structure is as follows, the tree begins at the root and its children are those names listed without a "." in their name. From there, the next tree level contains the parent's name followed by the node's name, and likewise for its children. Following this pattern, I was able to create a tree structure in order to facilitate in the traversal and future decision making regarding which groups to set the surplus flag for, and which to turn off.

The priority field will be used to add a weight to the different leaf nodes in order to prioritize by the number of cores. I added this field in order to ensure that the groups would be prioritized such that if a multi-core group is seeking additional resources, the single-core production leaf cannot as well. The accept_surplus field is what determines whether or not a group will seek additional resources. For the prod cluster, the default setting is that the production leaf will always have its accept_surplus set to true, meaning that it will seek out any available CPU space in the rest of the prod tree in order to process any jobs waiting in its queue. This is the most common state as there are commonly very few multi-core jobs waiting to be processed, but should a group of multi-core jobs enter the system, they may have to wait a longer time than usual due to the lack of continuous CPU space.

This scenario is where an analysis of the average amount in the queue over the past hour is beneficial. The script I have created will determine if, over the past hour, the average amount in the queue is larger than the set threshold for that group. The more

group_name	amount_in_queue	query_time
group_atlas.prod.production	0	2014-06-10 14:25:03
group_atlas.analysis.short	259	2014-06-10 14:25:03
group_atlas.prod.mp	0	2014-06-10 14:25:03
group_atlas.prod.test	0	2014-06-10 14:25:03
group_atlas.analysis.long	1422	2014-06-10 14:25:03
group_atlas.prod.production	61	2014-06-10 14:30:03
group_atlas.analysis.short	168	2014-06-10 14:30:03
group_atlas.prod.mp	0	2014-06-10 14:30:03
group_atlas.prod.test	0	2014-06-10 14:30:03
group_atlas.analysis.long	1211	2014-06-10 14:30:03

group_atlas.prod.production	0	2014-06-18 11:20:03
group_atlas.analysis.short	319	2014-06-18 11:20:03
group_atlas.prod.mp	0	2014-06-18 11:20:03
group_atlas.prod.test	0	2014-06-18 11:20:03
group_atlas.analysis.long	127	2014-06-18 11:20:03
group_atlas.prod.production	8	2014-06-18 11:25:02
group_atlas.analysis.short	302	2014-06-18 11:25:02
group_atlas.prod.mp	0	2014-06-18 11:25:02
group_atlas.prod.test	0	2014-06-18 11:25:02
group_atlas.analysis.long	127	2014-06-18 11:25:02
group_atlas.prod.production	0	2014-06-18 11:30:13
group_atlas.analysis.short	301	2014-06-18 11:30:13
group_atlas.prod.mp	0	2014-06-18 11:30:13
group_atlas.prod.test	0	2014-06-18 11:30:13
group_atlas.analysis.long	129	2014-06-18 11:30:13
group_atlas.prod.production	0	2014-06-18 11:35:02
group_atlas.analysis.short	290	2014-06-18 11:35:02
group_atlas.prod.mp	0	2014-06-18 11:35:02
group_atlas.prod.test	0	2014-06-18 11:35:02
group_atlas.analysis.long	129	2014-06-18 11:35:02

Figure 3. Sample queue log. Maintains a record of the amount of jobs waiting to be run (over the current job quota).

cores required, the smaller the threshold. Therefore, in our previous example, should the production flag be set to true, and a substantial amount of multi-core jobs arrive over the course of an hour, which exceeds the given threshold for that multi-core group, then the production `accept_surplus` flag is turned off to allow for the continuous blocks that will be required. This script is functional and is running every ten minutes in a testing capacity.

V. Spike Detection

Having created a script which adjusts the surplus based upon the average amount in the past hour, it was later realized through testing that a false flag may be raised if an excessive spike in activity appears at any point in the previous hour. Such a spike may be able to fool the average queue detection into thinking the queue is too large, when in reality there was simply a spike which has since gone down. The need for a method that could detect a spike in activity and then analyze the activity would be required.

The function which I devised was to take the 12 queue amounts, for each group, sampled over the past hour and create an array of values from which I will be analyzing. The function will first check to see if the average value is above a maximum threshold, if so there is no need to check for a spike. The next decision is to check whether the values are all below the value that is considered a spike, if so there is no need to check for a spike. Finally, if the values are in the spike range the function will search the values for a spike.

The current function goes through the array of values finding the difference between one value and the next determining whether the amount has increased the correct percentage to be considered a spike. Once a value has been found which meets this criteria, a spike flag is set to true. The function searches the entire hour for a spike, but if the spike is found in the first half of the array, then the true analysis begins and we determine whether the spike is reducing normally by the end of the hour or not. If so, then there is no need to change the surplus, the queue is reducing normally, but if the spike is increasing, or not reducing fast enough, then we determine whether the surplus can be enabled or not. The reason we only look at the first half for final analysis is to recognize a last minute spike, and wait enough time until we have sufficient data to determine whether it is rapidly decreasing or not. Using this function, I was able to obtain the correct results through testing in order to determine whether an increased average was steady, or due to a rapid increase in work and sudden decline.

VI. Tree structure creation and traversal

With the demand detection functions completed and functioning correctly, the next step was to implement the functions into the tree structure in as generic a way as possible. The purpose

of such generalization is to allow the script to function correctly, even if the overall structure of the tree is modified in the future. Generalization will ensure the flexibility of the script, with very few modifications required should the ATLAS resources expand in the future.

The script begins by creating the tree structure using the master table of group names, see figure 4, and a backtracking algorithm of my own creation. The script sorts the names alphabetically, and adds the groups to the tree structure beginning at a default root node. As it progresses down the list, it recognizes the “.” delineation of the names and populates the tree accordingly ensuring that the names without a “.” symbol are children of the root, and those groups containing the parent name are its children. Once the algorithm reaches a name which does not contain the previous entry, it backtracks until a correct parent is found. The current tree creation function produces the tree structure seen in figure 1.

Once the tree structure is created, we can begin our traversal functions. Using a depth first search method, we begin traversal of the tree identifying the leaf nodes and, using our demand detection functions, we determine whether the surplus flag should be set to true or false. This first pass is meant to identify the demand of the leaf nodes, and set the parents demand values as the sum of their children’s demand. The demand value is important for future comparisons as it will allow us to compare the demand of siblings with one another.

The next tree traversal is used for comparisons. This second pass is also a depth first pass which will compare the surplus values of the nodes against their siblings in order to determine whether the surplus values will need to be modified based upon sibling demand. This comparison will ensure that multi-core and single core jobs with the same parent can never be both set to true. As I discussed in section 1, greedy single-core jobs can interfere with the incoming demand of multi-core jobs by not allowing them sufficient room to operate. The comparison will also ensure that a parent’s surplus flag can only be set to true if there is no demand in its siblings.

VII. Updating the surplus flags

The final step in the script is to update the surplus flags. Having created the tree structure and modified the surplus values based upon the job group demand, and the demands of each group’s siblings. This final step compares the desired surplus state of each with its current state. If these two values are different, the function will then determine whether the surplus has been changed recently, within the past hour. This final recent change check prevents the surplus from flipping back and forth between true and false. Rapid flipping of the surplus value will lead to an uneven transition, reducing the productivity of the surplus system.

group_name	quota	priority	accept_surplus	surplus_threshold	last_update	last_surplus_update
group_atlas	12752	2	0	0	2014-06-05 11:25:12	2014-07-22 11:06:55
group_atlas.analysis	2008	1	0	0	2014-06-05 11:25:12	2014-07-24 16:17:31
group_atlas.analysis.long	1004	1	1	0	2014-06-05 11:25:12	2014-07-21 14:44:29
group_atlas.analysis.short	1004	1	1	0	2014-06-05 11:25:12	2014-07-21 14:44:29
group_atlas.prod	10734	2	0	0	2014-06-05 11:25:12	2014-07-29 05:30:02
group_atlas.prod.mp	2368	8	1	20	2014-06-05 11:25:12	2014-07-28 08:20:02
group_atlas.prod.production	7366	1	0	160	2014-06-05 11:25:12	2014-07-24 16:17:31
group_atlas.prod.test	1000	2	0	80	2014-06-05 11:25:12	2014-07-24 16:17:31
group_atlas.software	10	0	0	0	2014-06-05 11:25:12	2014-07-17 12:00:00
group_grid	40	1	0	0	2014-06-05 11:25:12	2014-07-28 08:20:02

Figure 4. Master table containing the groups in the data tree structure, along with all relevant group information.

Instead, the transition between sharing and not should be more gradual and less jarring.

Once all the surplus changing criteria have been met, a different value, and a recent change time greater than one hour, the master table will be updated to reflect the new change in surplus. It is this master table which interacts with the HTCondor workload management system in order to schedule the job allotments between all the available resources.

VIII. Summary

During my research at Brookhaven National Laboratory, I was able to create a script which would detect a rapidly growing queue amount in a job group, and determine whether the amount is reducing normally, or whether the extra workload can be sent to other groups in order to hasten the job times and reduce the amount of idle CPUs in the Linux farm. Should the program not detect such a rapid growth, it will then determine if the overall amount waiting to be run exceeds the allotted threshold and from there determine additional resource availability. This script will be automatically run every ten minutes in order to reduce the amount of time before surplus flags are set and eliminating the need for manual adjustments.

My time spent at Brookhaven National Laboratory has given me the opportunity to experience a real world application of my

classroom knowledge. This opportunity has also allowed me to expand my skill set through the use of the Python programming language, Linux operating system, and MySQL on a daily basis. Having previously had limited experience in Python, having the opportunity to explore new libraries and learn new programming techniques has been greatly beneficial in adding to my knowledge base. I have also been able to learn the basics of MySQL which has been eye opening as a means of data storage, sorting and manipulation. This has been a tremendous introduction to the many possibilities available to a computer scientist and has encouraged me to continue down my STEM field career path. This project was supported in part by the U.S. Department of Energy, Office of Science, Office of Workforce Development for Teachers and Scientists (WDTS) under the Science Undergraduate Laboratory Internship (SULI).

IX. References

ATLAS Experiment. (2008). Retrieved July 14, 2014, from <http://atlas.ch/>

What is HTCondor? (2014). Retrieved July 14, 2014, from <http://research.cs.wisc.edu/htcondor/description.html>

The PanDA Production and Distributed Analysis System (06 Jun 2014, TorreWenaus). Retrieved July 14, 2014, from <https://twiki.cern.ch/twiki/bin/view/PanDA/PanDA>

Linear accelerator computer modeling and stress analysis for a proposed electron accelerator

Joseph Karp

Mechanical Engineering, Binghamton University, Binghamton, NY 13902

Joseph Tuozzolo

Collider Accelerator Department, Brookhaven National Laboratory, Upton NY 11973

Abstract:

The Collider Accelerator Department at Brookhaven National Laboratory is currently working on a proposal to add an electron accelerator to the current Relativistic Heavy Ion Collider (RHIC). This project, titled eRHIC, would provide polarized reflection on polarized proton collisions and electron on ion collisions and enable physics experiments which cannot be done on the current system. To accelerate electrons to relativistic speeds, a linear accelerator (LINAC) will be used. LINACs achieve this acceleration using a pulsing electric field to accelerate charged particles. This work is focused on re-modeling an old design for the LINAC to get a sense of possible design concerns such as material behavior in a cryogenic environment, and any physical interference between the new LINAC and the equipment currently in the RHIC tunnel. Using Creo Simulate 2.0, I demonstrated that by using six $\frac{3}{4}$ inch threaded rods the RF cavity and its cryogenics system could be suspended in a vacuum with a maximum displacement of $4.2e-5$ inches. I was also able to demonstrate that in order to mechanically tune the niobium cavity the required 1mm would require approximately 4000N of force. Using Creo Parametric, I was able to demonstrate that there is a possibility of an intersection between the currently planned beam path and the current RHIC cryogenic system. Using Creo Parametric, I was also able to estimate the mass and length of the LINAC to be 86688 lbm and 116 m respectively. This summer I have learned to use Creo Parametric 2.0 to design and model and to use Creo Simulate 2.0 to do thermal, stress, and strain analysis. In addition to this hands on experience with modeling and analysis software, I was able to learn about manufacturing techniques such as brazing and vacuum technologies such as turbomolecular and ion pumps.

I. Introduction

Building a 3D model of a part is an essential part of the design process. A 3D model can serve as a proof of concept as well as provide information vital to the design. In this project I built a 3D model of the LINAC planned for use in eRHIC. The LINAC consists of three main components: the superconducting radio frequency (SRF) cavity, the cryogenics system, and the vacuum system. The SRF cavity is a niobium cavity that creates a pulsing high strength electric field when a RF current is passed through it in order to accelerate electrons. The cryogenics system employs liquid helium to keep the niobium SRF cavity at superconducting temperatures around 2°K. The cavity needs to be kept at superconducting temperatures so that a very high intensity field can be produced without melting the niobium from resistive heating. The vacuum system serves two purposes. The first is to prevent

convection heating from the surrounding environment. This type of vacuum is called an insulating vacuum. The second is to allow the electron bunches to pass through the LINAC without running into other particles which would create dangerous radiation. All three of these systems need to fit into a single package inside of the preexisting RHIC tunnel without physical interference with the current beam path. It is also necessary to prove that the cavity will not move out of position when suspended or tuned.

II. Methods and Materials

Using Creo Parametric I was able to create accurate 3D models of the proposed LINAC. AutoCAD was used to create a piping and instrumentation diagram for the cryogenics system. These models include information on material properties. With these models I was able to use Creo Simulate to calculate displacement of the RF cavity when supported by six $\frac{3}{4}$ ” rods. Using a model of the niobium cavity I was able to calculate the force necessary to compress or expand the niobium cavity by 1mm. In order to check for interference with the equipment already in the RHIC tunnel I inserted my model of the LINAC into an existing model of the RHIC tunnel including the RHIC magnets.

III. Results

As can be seen in figure 1 at the 2 o'clock intersection point in RHIC it is possible to fit the 116m long LINAC (shown in orange) into the tunnel without interfering with the current magnets (shown in red). However in order to prevent interference the LINAC had to be shifted out of line with the RHIC beam. It should be possible to shift the beams back in line at the other intersection points around RHIC. This 116m length includes forty two 5-cell cavities and a cold to warm transition shown in figure 2 on both ends of the LINAC. The cold to warm transition includes several features. The first feature is the bellows. These bellows are to allow for thermal strain without causing excessive stress on the system. The second feature is the heat sink flange. This flange is meant to be attached to the aluminum heat shield inside of the vacuum to act as a heat sink. This works because of aluminum's good thermal conductivity and because the heat shield is kept at 60K by a helium line. This feature reduces the heat differential that the bellows experience which means that there will be less heat transferred from outside to inside the system. The third feature is the vacuum valve at the end of the transition section. This

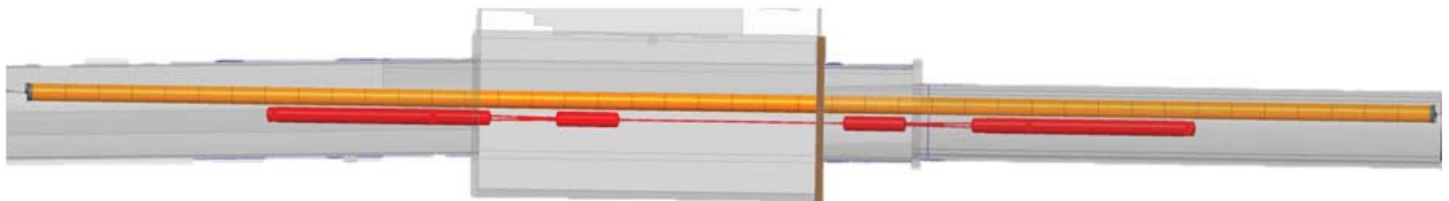


Figure 1.

is an important feature because it allows the LINAC's vacuum to be separated from the rest of RHIC in the case of a leak or the need for a repair. If this part was not implemented it would mean that the entire RHIC vacuum would have to be broken and then re-established in the case of a problem costing time and money.

The three rod support structure is shown in figure 4 and shows that the maximum displacement of the cavity do to gravity is 4.195×10^{-5} inches. This is very minimal and so will not cause the beam line to move significantly out of line with its planned trajectory. In order to tune the cavities frequency it needs to be stretched or compressed as much a 1mm 4000N of force must be applied to the niobium cavity (figure 3). This change in length changes the Niobium cavities natural frequency and so you can change its resonance to match what is needed. In order to accomplish this device is placed on one end of the cavity and it squeezes the cavity with the necessary force with the titanium helium vessel keeping the other side stationary. The effect this would have on the titanium has been calculated with Creo simulate to be less than .002 mm of displacement.

The piping and instrumentation diagram (figure 6) was designed the way it is for several reasons. First is for flux trapping. A fast cool down helps to trap ambient magnetic flux in the Ni-

obium cavity reducing its residual resistance (A. Romanenko, 2014). This is important because it increases the efficiency of the cavity during operation. The fast cool down is accomplished by sectioning the LINAC into 7 discreet sections each containing six cavities and its own bottom fill line. The piping and instrumentation diagram also has a bypass for its heat exchanger because during the cool down process warm vapor is returned to the cryogenic refrigerator through the heat exchanger. This would cause a problem because if the cold liquid nitrogen passed through the heat exchanger with the warm vapor it would gain some of the heat from the vapor slowing down the cool down process and making it less efficient. The third feature of the piping and instrumentation diagram is its liquid supply header. This header allows the cavity to be refilled from the top after the initial cool down is over. This is important because after being pushed through the valve the Joule Thomson effect causes some of the liquid Helium to become a vapor. If this happens when the cavity is already full it will cause bubbles to form inside of the Helium cavity which would decrease the efficiency of the cryogenics system. It also allows for a large surface area where vapor separation can occur and feed directly into the vapor return line.

IV. Conclusion

The models I have made and simulations I have run have enhanced our understanding of the issues and possible solutions that will come up when creating eRHIC. The models also serve as a form of proof that this project can be feasibly done with the current tunnel and equipment available to the lab. This project helped to enhance my understanding of the engineering profession and get hands on experience with powerful 3D modeling software.

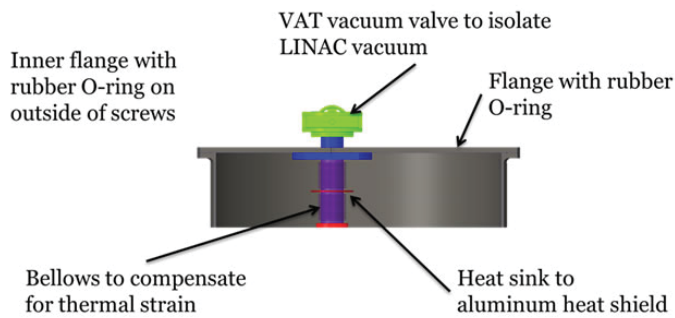


Figure 2.

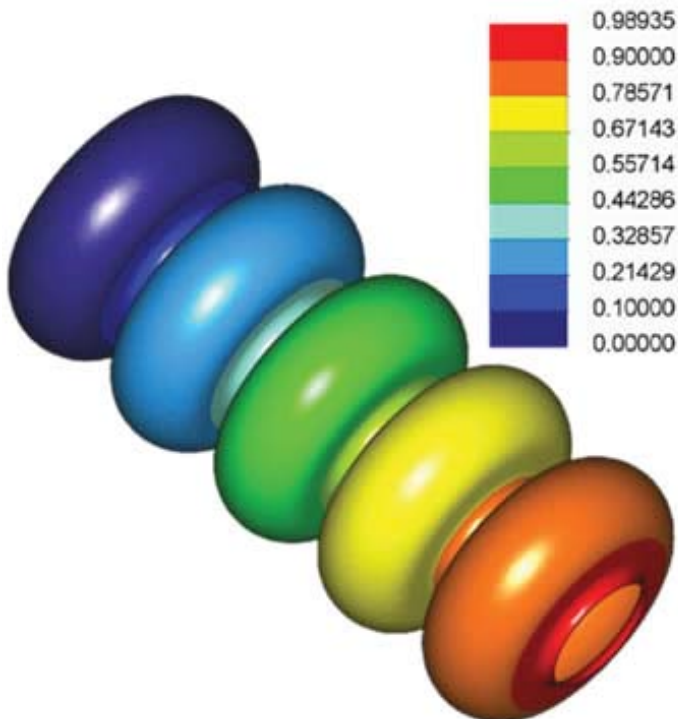


Figure 3.

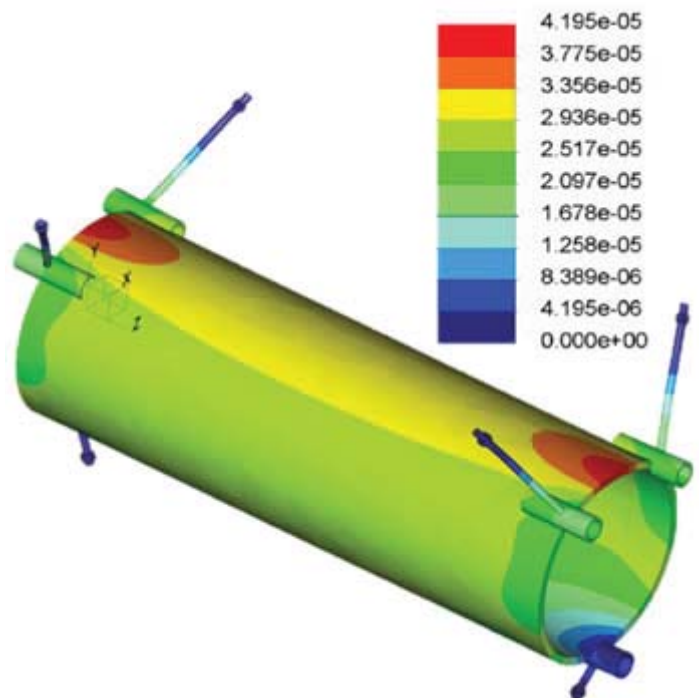


Figure 4.

V. Bibliography

A. Romanenko, *. A. (2014, March 11). Dependence of the residual surface resistance of superconducting RF cavities on the. Retrieved August 1, 2014, from Cornell University Library: <http://arxiv.org/abs/1401.7747v3>



Figure 5.

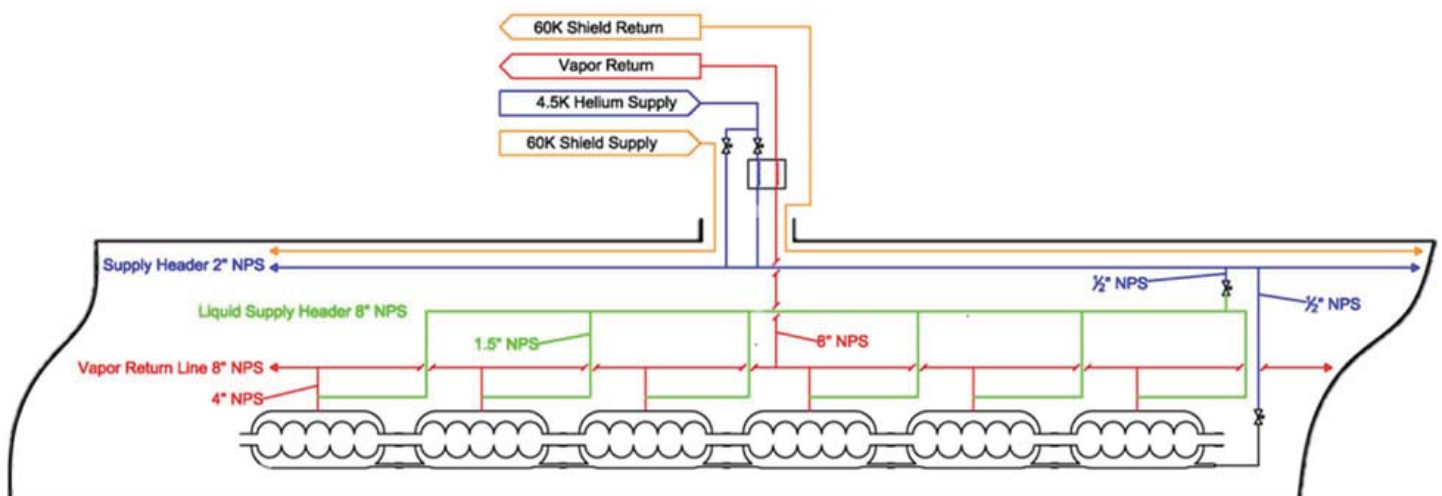


Figure 6.

Assessment of 5-hydroxymethylcytosine in the DNA of human skin fibroblasts exposed to ionizing radiation

Lucia Kolodiuk and Katherine Z. Sanidad

Biology, Stony Brook University, Stony Brook, NY 11790

Benjamin Daniels

Biochemistry, Rensselaer Polytechnic Institute, Troy, NY 12180

Deborah J. Keszenman, Paula V. Bennett, Alicia Johnson, and Paul F. Wilson Jr.

Biosciences, Brookhaven National Laboratory, Upton, NY 11973

Abstract

Epigenetics refers to non-DNA sequence changes that are heritable and modulate gene expression, including DNA methylation and DNA-associated chromatin remodeling through histone post-translational modifications. Improper regulation of epigenetic states may contribute to different disease outcomes including carcinogenesis. Methylation of DNA bases, such as the conversion of cytosine to 5-methylcytosine (5-mC), is known to play a role in controlling transcriptional activities in developing neuronal tissues. Further chemical modification of 5-mC to 5-hydroxymethylcytosine (5-hmC) may occur by exposure to reactive oxygen species generated by ionizing radiation (IR). However, the biological function of 5-hmC in human cells and tissues is still largely unknown. We have recently shown that IR is capable of converting 5-mC to 5-hmC, and we have been developing assays to analyze 5-mC and 5-hmC levels in human cells treated for 18 h with the histone deacetylase inhibitors SAHA (vorinostat; a drug that relaxes chromatin packing), PTACH and M344, and then exposed to gamma rays, protons, oxygen ions, and carbon ions at the NASA Space Radiation Laboratory (NSRL). DNA from human neonatal foreskin fibroblasts (NFF28) and osteosarcoma cells (U20S) was isolated in agarose plugs and treated with the restriction endonuclease PvuRts1L, an enzyme that specifically cleaves DNA sequences containing 5-hmC. Relative levels of 5-hmC were then assessed by pulsed field gel-electrophoresis (PFGE) and gel image analysis. We determined that this enzyme can be used with DNA embedded in agarose plugs and tested the appropriate amounts of enzyme and buffer for optimal reaction conditions. Work is to be done to see a positive correlation between IR dose and 5-hmC occurrence. This project promoted my interest in science by helping develop a new assay to analyze epigenetic changes following different types of IR exposures, which can be utilized to better understand the impact of 5-hmC in irradiated human tissues.

I. Introduction:

Epigenetics refers to non-DNA sequence changes that are heritable and modulate gene expression, including DNA methylation and DNA-associated chromatin remodeling through histone post-translational modifications. Open chromatin is related to active DNA transcription and it is usually characterized by unmethylated cytosines, acetylated histone tails and methylation of histones. Closed chromatin may happen when cytosines become methylated and acetyl groups are removed from histone tails by histone deacetylases (HDAC) (1, 2). Inappropriate regulation of

epigenetic states may contribute to different disease outcomes including carcinogenesis.

Methylation of DNA bases, such as the conversion of cytosine to 5-methylcytosine (5-mC), is known to play a role in controlling transcriptional activities in developing neuronal tissues. Further chemical modification of 5-mC to 5-hydroxymethylcytosine (5-hmC) may occur by exposure to reactive oxygen species generated by ionizing radiation (IR). The figure below displays the pathway in which cytosine is modified into 5-mC and further into 5-hmC.

The creation of 5hmC can lead to demethylation of DNA, which may contribute to a change in the dynamics of DNA methylation (1, 2). However, the biological function of 5-hmC in human cells and tissues is still largely unknown.

There are many techniques to study DNA methylation and methylation patterns including PCR techniques. Nonetheless, most techniques do not distinguish between 5-mC and 5-hmC. One way to differentiate 5-mC from 5-hmC is to use antibodies that recognize the two different modified bases (1). Another approach to determine the cytosine methylation patterns is based on the use of restriction enzymes sensitive to both methylated and hydroxymethylated cytosines cutting DNA if it is methylated (2). Recently, only the restriction endonuclease PvuRts1I has been identified to specifically recognize 5-hmC and cleave DNA sequences containing this modified base (3).

We have recently shown that IR is capable of converting 5-mC to 5-hmC and we hypothesize that the increase in 5-hmC is IR dose dependent. To test this hypothesis we have been developing assays to analyze 5-mC and 5-hmC levels in human cells exposed to photon or charged particle radiation. Using human neonatal foreskin fibroblasts (NFF28) we proposed to study the levels of 5-hmC in cells exposed to increasing doses of IR alone or preceded by radiosensitization treatment. NFF28 cells were treated for 18 h with the HDAC inhibitors SAHA (Vorinostat) PTACH and M344 and then exposed to gamma rays, protons, oxygen ions, or carbon ions at the NASA Space Radiation Laboratory (NSRL).

II. Materials and Methods

A. DNA Substrate:

The unmethylated, 5-methylcytosine and 5-hydroxymethylcytosine double-strand DNA were created by the inclusion of either unmethylated dCTP, 5-methyl dCTP or 5-hydroxymethyl dCTP in the PCR reaction mix of a 338 base pair fragment from the APC (adenomatous polyposis coli) gene promoter (Active Motif, Catalog No. 55008 USA).

B. Cell Culture and Irradiation:

Human neonatal foreskin fibroblasts (NFF28) or osteosarcoma cells (U20S) were cultured in appropriate nutrient medium at 37 °C in 5% CO₂ to confluency in G₀/G₁ phase. Cells were trypsinized and resuspended in 0.5 ml medium at a concentration of 2x10⁶ cells/ml. Cell samples were exposed to gamma rays in doses ranging from 0 to 10 Gy at room temperature using a Shepherd Mark I Cesium137 Source (LET 0.80 keV/μm). Other samples were exposed at room temperature to 200 MeV protons with doses from 0 to 4 Gy (LET 0.45 keV/μm) at the NSRL. Proton irradiated samples were pretreated for 18h with 0.2% DMSO (dimethylsulfoxide), SAHA (Vorinostat), M344, or PTACH. HDAC inhibitors were dissolved in 0.2% DMSO and used at a concentration of 10 mM. After irradiations, cells were immediately placed in dry ice and kept at -80°C until further processing.

C. DNA Agarose Plugs:

Cells or 338-bp DNA were subject embedded in 2% InCert Agarose to form 1% DNA agarose plugs. 338-bp DNA agarose plugs were kept in TE Buffer (10 mM Tris, 1mM EDTA, pH 8) at 4°C.

The preparation of DNA agarose plugs from frozen cells is as follows. The cells were thawed rapidly in a 37°C water bath. Then, 50μl 0.5M EDTA pH 8.0 were added. Rapidly after, 600μl of 2% InCert Agarose (prepared in 50mM EDTA) were added and the mixture was placed in molds. The molds were set to solidify at 4°C for 10 min. Next, the plugs were placed in tubes with Proteinase K Lysis solution (1mg/ml Proteinase K, 2% N-Lauroyl-Sarcosyl in L-buffer: 100mM EDTA, 10mM Tris, 20mM NaCl pH 8.0) and chilled on ice for 15 min followed by incubation at 37°C overnight. On the next day, the Proteinase K Lysis buffer was changed. On ice, the old Lysis solution was removed and L-buffer was added. After 15 min on ice, the L-buffer was removed and new Proteinase K Lysis solution was added. Then, the plugs were incubated at 37°C overnight. For the next 2 days, the Proteinase K Lysis solution was changed using the process described above. On day 5, the plugs were washed with L-buffer and then treated with 0.2mM PMSF twice 30 min at room temperature. Then, the PMSF solution was removed and the plugs were rinsed with cold

TE buffer several times until no traces of Sarcosyl detergent were left. The plugs were soaked in TE buffer overnight and stored at 4°C in the dark until they were to be digested with the enzyme.

The plugs from cells were treated with NotI restriction endonuclease to generate DNA fragments that can be analyzed by pulsed field gel electrophoresis (PFGE). The restriction digestion of the DNA in agarose plugs is as follows. The plugs were equilibrated on ice in 2-3ml restriction enzyme buffer (NEB3: 50 mM Tris-HCl, 100 mM NaCl, 10 mM MgCl₂, pH 7.9) without BSA (Bovine Serum Albumin) or DTT (dithiothreitol) added to the enzyme buffer. The samples were left to soak on ice overnight. The following day, the samples were equilibrated on ice in 2.0ml reaction mix containing 100 μg/ml acetylated BSA and 1 mM Sigma molecular biology grade DTT and soaked for 2h. The reaction mix was replaced with 1.0 ml reaction mix containing 2 to 3 units of restriction enzyme per microgram of DNA and incubated for at least 1h on ice. The estimated concentration of DNA per plug was 1320 ng. Then, the samples were incubated at 37°C for 18h. The following day, the samples were moved samples to ice to stop reaction with a 1 hour soak in Argon treated TE (4).

DNA Digestion with PvuRtsII Restriction Enzyme:

PvuRtsII restriction enzyme specifically cleaves DNA sequences containing 5-hmC. The enzyme recognition site is hmCN11-12/N9-10G.

DNA in solution was digested at room temperature using 2 protocols. One protocol used was according to reaction conditions and reagents following the instructions provided by the vendor of the PvuRtsII enzyme (Active Motif, Catalog No. 55011, USA). The composition of the Reaction Buffer and the preferred reaction conditions were undisclosed. The other protocol used a reaction mixture containing 1X PvuRts Buffer (150 mM NaCl, 20 mM Tris pH 8.0, 5 mM MgCl₂), 1mM DTT, 50 μg/ml BSA, and DNA. The DNA in agarose plugs was digested using the second protocol described.

D. Electrophoresis:

Static field gel electrophoresis was utilized to assay the activity of the enzyme PvuRtsII on the DNA in solution or in agarose

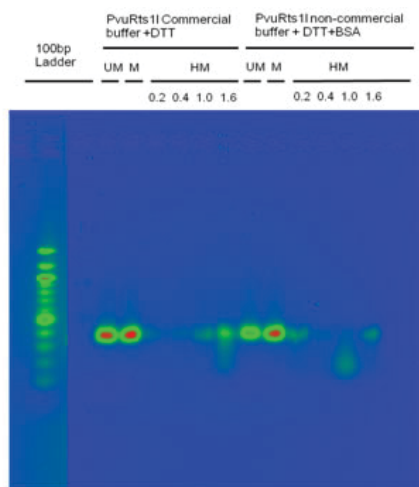


Figure 1. PvuRts1I enzyme activity assay. Samples of unmethylated (UM), methylated (M), or hydroxymethylated (HM) DNA (100 ng) in solution were treated at room temperature for 2 h using protocols a or b with increasing amounts of PvuRts1I enzyme (0.2, 0.4, 1.0, 1.6 U). The UM and M DNA were treated with 1.0 U of enzyme.

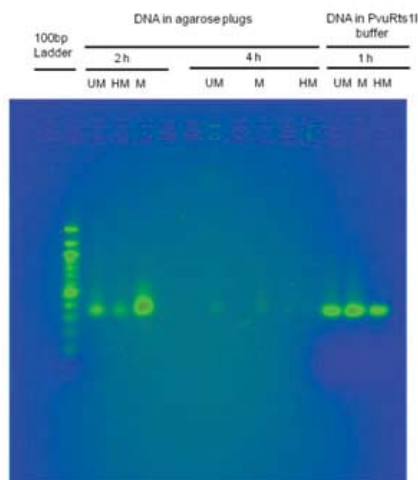


Figure 2. PvuRts1I enzyme DNA cleavage assayed in agarose plugs. Samples of 125 ng of unmethylated (UM), methylated (M), or hydroxymethylated (HM) DNA embedded in agarose plugs were treated at room temperature for 2 or 4 h using protocol a with 0.5 U of PvuRts1I enzyme. 100 ng of UM, M or HM DNA samples in solution were treated at room temperature for 1 h using protocol b with 0.4 U of PvuRts1I enzyme.

plugs. Gels of 1.5% Sea Kem L.E. Agarose in 1X TAE buffer (40 mM Tris, 20 mM acetic acid, 1 mM EDTA, pH 8.0) were run in 1X TAE Running buffer for 2 to 2.5 h or until the loading dye was visible half way down the gel at 30 V at room temperature. The gels were stained with ethidium bromide (0.50 $\mu\text{g}/\text{ml}$) and imaged using the Gel Image System (4, 5). Pulsed Field Gel Electrophoresis was used to detect DNA double-strand breaks (DSB) produced by IR (gamma or protons) and/or restriction digestion by PvuRtsII. DSB levels were determined using gel image analysis (4, 5).

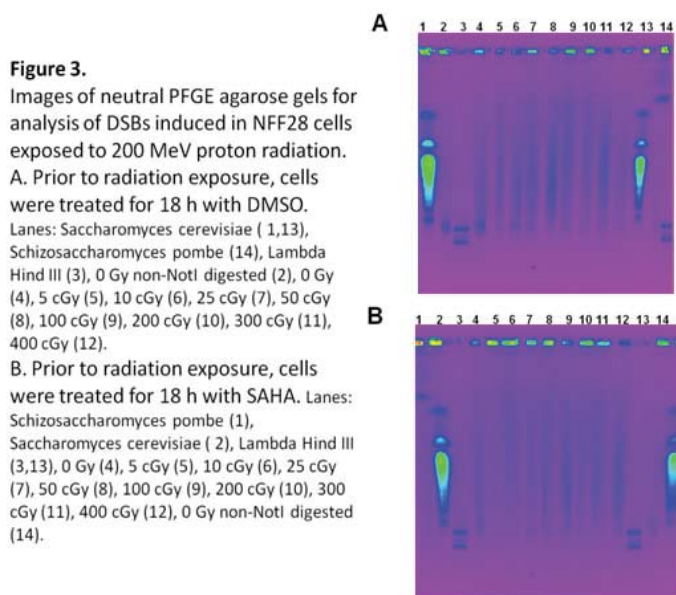
III. Results

To test the hypothesis that 5-hmC levels increase with IR dose, we have been developing assays to specifically determine 5-hmC in irradiated DNA. To test the levels of 5-hmC we used the PvuRtsII enzyme that is commercially available. Since the composition of the commercial buffer supplied with the enzyme or the reaction mixture for optimal enzyme activity are not described by the vendor (Active Motif), we decided to test the PvuRts buffer described in the original article that reported this enzyme (3). Figure 1 shows the PvuRtsII enzyme activity assay. Samples of unmethylated (UM), methylated (M), or hydroxymethylated (HM) DNA (100 ng/sample) in solution were treated at room temperature for 2 h using the commercial buffer with DTT (first 7 lanes after 100-bp ladder) or the non commercial buffer plus DTT and BSA (rightmost 6 lanes). In both treatments the UM and M DNA were treated with 1.0 U of enzyme and increasing amounts of PvuRtsII enzyme (0.2, 0.4, 1.0, 1.6 U) were used for HM DNA. As expected, in both cases we found that the enzyme did not digest the unmethylated or methylated DNA. Both restriction digestion buffers were effective in digesting hydroxymethylated DNA. Also, in both reaction mixtures the DNA was not fully digested at the highest amount of enzyme tested. From Figure 1, the range of optimal amount of enzyme per 100 ng of DNA is from 0.4 to 1.0 U. In order to assess the kinetics of the digestion reaction we tested a shorter incubation period of 1h in non commercial buffer using 0.5 U of enzyme per sample of U, M, and HM DNA in solution (Figure 2, rightmost 3 wells). As seen in Figure 2, the hydroxymethylated DNA was not fully digested with a 1 h incubation.

Since we want to apply this enzyme in DNA isolated from mammalian cells in agarose plugs, we needed to test if the PvuRtsII enzyme was able to cleave HM DNA embedded in agarose plugs. Agarose plugs containing 125 ng of the U, M, or HM DNA were prepared. The plugs were incubated in PvuRts buffer at 4°C overnight to equilibrate. The plugs were incubated in the reaction mixture containing non commercial buffer with 0.5 U of enzyme for 2 or 4 h at room temperature. This is shown in Figure 2, in which the decrease of the band fluorescence displays that the reaction digestion indeed occurred when the HM DNA was embedded in agarose plugs. The action of the PvuRtsII endonuclease was more evident after 4 h of incubation. Also this figure further reinforces that the PvuRtsII enzyme cuts DNA containing 5-hmC and not methylated or unmethylated DNA.

To analyze the levels of 5-hmC induced by IR in human skin fibroblast NFF28 cells we propose to develop an assay based on the recognition and cleavage of 5-hmC sites in DNA by the PvuRtsII restriction endonuclease, leading to double-strand breaks (DSB). As a previous step, the levels of DSBs produced by exposure to increasing doses of IR must be determined. As previously described in the literature (4), we have employed the method of neutral PFGE and number average length analysis to study the levels of DSBs produced by exposure of NFF28 cells to 200 MeV proton radiation. In addition, prior to radiation exposure, cells were treated for 18h with DMSO or SAHA (an HDAC inhibitor). Figure 3A shows the image of PFGE gel of proton irradiated samples pretreated with DMSO and figure 3B shows the gel image for the proton irradiated NFF28 samples pretreated with SAHA. In both gels, a progressive fragmentation of DNA was observed with an increasing radiation dose as seen by the further migration in the gel away from the wells.

Figure 4 shows the frequencies of DNA DSBs obtained by the analysis of the gels shown in Figure 3. The graph represents the DNA DSBs dose response induced by increasing doses of 200 MeV proton radiation. For both DMSO and SAHA pretreatments, the DSB frequencies increased linearly with the radiation dose. In this experiment, the SAHA pretreated samples showed a higher frequency of DSBs as compared to the DMSO pretreated samples. However, more experiments are needed to determine the significance of the difference.



IV. Conclusions and Discussion:

Epigenetic changes such as 5-mC and the chemically modified 5-hmC are known to be important in controlling gene expression and under inappropriate regulation may contribute to cancer and other diseases (1, 2). Nonetheless, the role of 5-hmC is still

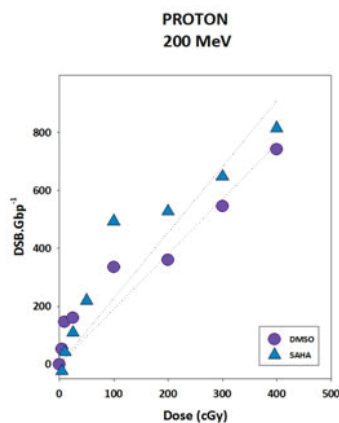


Figure 4. DNA DSBs dose response induced by 200 MeV proton radiation in NFF28 cells pretreated with DMSO (circles) or SAHA (triangles).

largely unknown. We have recently shown that IR is capable of converting 5-mC to 5-hmC and we hypothesize that the increase in 5-hmC is IR dose dependent. To test this hypothesis we have been developing assays to analyze 5-hmC levels in human cells exposed to IR using the PvuRtsII restriction endonuclease commercially available.

Using DNA in solution we determined the reaction mixture for optimal PvuRtsII enzyme activity. As shown in Figure 1, the appropriate PvuRtsII enzyme reaction mix contained 1X PvuRtsII Buffer (150 mM NaCl, 20 mM Tris pH 8.0, 5 mM MgCl₂), 1mM DTT, and 50 µg/ml BSA. Therefore, both the commercial and the non-commercial buffers may be used for the enzyme reaction mixture. In the same assay we studied the amount of PvuRtsII endonuclease to fully digest 5-hydroxymethylated DNA. The range was from 0.4 to 1.0 U per 100 ng of double-strand DNA.

Our results shown in Figure 2 evidenced that hydroxymethylated DNA embedded in agarose plugs was digested significantly by the PvuRtsII restriction enzyme under the tested reaction conditions. Thus, the PvuRtsII enzyme may be applied to the detection of 5-hmC present in DNA isolated in agarose plugs.

Since the PvuRtsII enzyme will recognize and cleave at DNA sites containing 5-hmC, and therefore producing DSBs, we assessed the frequencies of DSBs induced by exposure of NFF28 cells to IR alone or with radiosensitization pretreatment prior to testing the enzyme. As shown in Figure 3, the DNA fragmentation increased with the dose of 200 MeV proton radiation. The analysis of the PFGE gels by number average length analysis demonstrates that the DSB frequencies increased linearly with the radiation dose for both DMSO and the HDAC inhibitor (SAHA) pretreatments (Figure 4). The higher frequencies of DSBs observed with SAHA pretreatment compared to DMSO is probably related to the open state of the chromatin. Work is to be done to see a positive correlation between IR dose and 5-hmC occurrence in DMSO or SAHA pretreated samples.

V. References

- 1-Dahl C., Grønbæk K., Guldborg P. Advances in DNA methylation: 5-hydroxymethylcytosine Revisited. *Clinica Chimica Acta* 412: 831-835, 2011.
- 2-Aypar U., Morgan W.F., Baulch J.E. Radiation-induced genomic instability: Are epigenetic mechanisms the missing link? *Int. J. Radiat. Biol.* 87: 179–191, 2011
- 3-Szwagierczak, A., Brachmann A., Schmidt C.S., Bultmann S., Leonhardt H., Spada F. Characterization of PvuRtsII Endonuclease as a Tool to Investigate Genomic 5-hydroxymethylcytosine. *Nucleic Acids Research* 39: 5149-5156, 2011.
- 4-Keszenman D.J., Sutherland B.M. Yields of clustered DNA damage induced by charged-particle radiations of similar kinetic energy per nucleon: LET dependence in different DNA microenvironments. *Radiat Res.* 174:238-250, 2010.
- 5-Sutherland B.M., Bennett P.V., Sutherland J.C., Laval J. Clustered DNA damages induced by x rays in human cells. *Radiat Res.* 57:611-616, 2002.

VI. Acknowledgments

I would like to thank my mentors Paula Bennett, Deborah Keszenman and Paul F. Wilson for all of their guidance and patience. Special thanks to Paul Wilson for instructing and supporting me in his lab. Thank you to Alicia Johnson for her assistance on this project. My appreciation goes to James Jardine for his laboratory support. Thank you to David Schlyer, Ann Emrick, John Trunk and Denise Monteleone for all of their help. Thank you to my fellow SULI coworkers Katherine Z. Sanidad and Benjamin Daniels for their assistance. This work was supported by the Department of Energy and the Office of Education Programs at Brookhaven National Laboratory. This work was performed under the auspices of the U.S. Department of Energy by Brookhaven National Laboratory and supported by BNL LDRD-12-012 grant to P.F. Wilson.

Integration and automation of computer facility power supply monitoring

Christopher Lee

Computer Science, Marist College, Poughkeepsie, NY 12601

Antonio Wong

Physics Department, Brookhaven National Laboratory, Upton, NY 11973

Abstract

The RHICATLAS Computing Facility (RACF) at Brookhaven National Laboratory contains four rooms of computer servers being monitored at all times for changes in temperature and disruptions in power. Two of the four rooms, Sigma7 and the Computer Data Center Expansion (CDCE), are newer and rely on a monitoring technology known as Sensaphone. The Sensaphone device's primary purpose is to detect disruptions in the power supply of the Sigma7 and CDCE rooms and relay any alarms to system administrators. Currently, the device is only capable of alerting administrators who are currently on site, and is incapable of recording any detailed information on outages. Our task was to write two scripts, both in Python: one script will parse the data from the Sensaphone device every five minutes using Cron, a software designed to automatically run scripts every so often, and write log entries to a database if any disruptions are detected. The second script will begin taking action if alarms are detected by alerting administrators even when they are offsite and if no response is given, begin shutting down the servers as a precautionary measure. This way, the database can store information relating to the power disruption and prevent any damage to the servers in the event of an outage. In order to keep the RACF up and running for researchers around the world to use at all times of the day, these two scripts will allow administrators much greater control and faster reaction time to any power issues that arise. In addition, automating the monitoring of the newer sections of the RACF allows it to be fully integrated with existing monitoring code for the older sections of the RACF.

I. Introduction

A. Data Center Power Monitoring

The data center at the RACF provides the bulk of the computational power needed for the Relativistic Heavy Ion Collider (RHIC) experiments. Data collected from RHIC is processed and analyzed by the computers in the data center. The power required to keep the facility running is not only used to power the servers, but also the air conditioning that keeps the servers from overheating. Any disruption in the power supply at the data center could lead to loss of valuable research data or

hardware damage as a result of the servers shutting down or the facility overheating. To prevent this, the Brookhaven Computer Facility (BCF), the original section of the computer facility built in 19961, is connected to an uninterruptible power supply (UPS) which provides backup power in the event of main power failure from the Long Island Power Authority. The older sections have a dedicated monitoring technology designed around the UPS and existing scripts written for this technology. The newer sections of the facility, Sigma7 (built in 20081) and the Computer Data Center Expansion (CDCE) (built in 20091), contain cooling

equipment that are not connected to the UPS and instead use a monitoring technology known as Sensaphone to track disruptions in the power supply and alert administrators if necessary. This is done in order to prevent damaging expensive computer equipment and to prevent electrical fires. While all computer servers are backed up by the UPS, the cooling system in the newer section is not, due to compatibility issues. As a result, any disruptions in the power supply for the newer sections must be manually attended to until a permanent solution can be found.

B. Project Overview

The main objective is to create two scripts, each performing one half of a process designed to detect any disruptions in the power supply connected to the cooling systems in Sigma7 and CDCE.

The first script's purpose is to gather data from the Sensaphone device and check for the power status of the data center section it is tracking. The script then writes any status update to a MySQL database if necessary. The second script's purpose is to read the most recent entry in the database and take action if necessary. While the device itself is capable of alerting administrators via email or phone in the event of an alarm, it is unable to save any status data for statistical purposes. Both scripts combined will allow administrators to keep accurate data on power disruptions through the database.

II. Methods

As a project designed around technology, my work was done entirely on a computer outfitted with Fedora 20, a Linux operating system. The scripts itself are written entirely in Python on Notepad, with MySQL code embedded using a Python package known as MySQLdb that allows Python to log into MySQL databases and execute MySQL commands. Three methods were suggested as to how the data on the Sensaphone device could be parsed and stored. The first method was to perform a screen scrape on the Sensaphone device website and parse the HTML for the required information. This required use of a program known as Wget, which takes the HTML code of a specified webpage and dumps this raw data into a predetermined location². The second method was to parse the automatic emails sent and use the status updates to update the database. This required use of the sendmail restricted shell, a Unix shell that limits the number of commands that sendmail can use but also allows some extra utility not normally available to sendmail. The third method was to use Simple Network Management Protocol (SNMP), a system that monitors all other systems on a specified network, to read alerts and update the database³. The first and second options were feasible, as the data center already has all the necessary resources. The third option thus resulted in being a fallback option, as the data center does not currently have a system set up with SNMP. The first option was

chosen because it eliminates the short delay between the device picking up an alert and the email being sent to administrators, since it interacts with the Sensaphone device itself. The Sensaphone webpage can also be set up to easily interact with Wget to dump the raw data on the webpage every five minutes to a test host within the data center's firewall.

III. Function

The project comprised of two scripts for each of the two newer sections of the data center. The first script runs every five minutes using Cron, a timebased task scheduler, and parses through the data to read in one of three possible statuses: Normal, Alarm, and Unknown. In this situation, Unknown is the status written to the database in the event that Normal and Alarm are both not found; this could be the result of a bug in the device's programming, or the internal battery of the device needing replacement. The script then writes the status, the timestamp, and the data center section the Sensaphone device is monitoring into the MySQL database.

The second script also runs every five minutes, staggered by thirty seconds to allow the first script to finish. It reads the most recent entry and takes necessary action: if the entry is Alarm, it sends an email to administrators and begins a ten minute countdown. If this countdown ends without a status update or manual override, it begins shutting down the servers in the data center it is responsible for to prevent loss of data in the event of a power disruption. If the entry is Unknown, it sends an email to administrators and begins a twentyfour hour countdown. If this countdown ends without a status update or manual override, it sends the email again. If the entry is Normal, the script runs to completion and does nothing.

To keep accurate records of power disruptions and prevent

an unnecessary overflow of Normal status updates, the first script does not write an entry to the database if the previous entry was Normal and the current status it detects is also Normal. It will continue writing entries if the status it reads is Alarm or Unknown.

IV. Testing and Debugging

A. Wget Screen Scrape with the Sensaphone Webpage

The main issue that arose while writing these scripts was that Wget did not work properly on the Sensaphone website by itself. This is due to the fact that the Sensaphone webpage is not a static webpage; the statuses of the areas the device is monitoring is refreshed every thirty seconds. If the webpage is screen scraped, the status instead comes up as Javascript code, which is used to update the status. To get around this, the Sensaphone website itself has an option that allows Wget to capture a static screenshot of the webpage for parsing purposes. This static screenshot keeps the current status instead of linking to the Javascript code itself, thus allowing it to be parsed and recorded.

B. Differing Status Location

Due to the layout of the Sensaphone webpage, a normal status is located under the "Channels" section while alarms are moved to their own dedicated section. In the raw HTML code, this means when the status changes, so does the location of the status. The script has to account for this by association with the section name: Channels or Alarms.

C. Variable Storage

The script is designed to run every five minutes using Cron, but this prevents any data from being stored by the script itself. The data center shutdown countdown has to rely on system time

```
mysql> select * from Sensaphone_Data;
```

```
+-----+-----+-----+
| Date           | Location | Status      |
+-----+-----+-----+
| 2014-07-03 09:15:02 | Sigma-7 | Power_Normal |
| 2014-07-03 09:46:49 | Sigma-7 | Power_Alarm  |
| 2014-07-03 09:47:01 | Sigma-7 | Power_Alarm  |
| 2014-07-03 09:48:01 | Sigma-7 | Power_Alarm  |
| 2014-07-03 09:49:02 | Sigma-7 | Power_Alarm  |
| 2014-07-03 09:50:01 | Sigma-7 | Power_Alarm  |
| 2014-07-03 09:51:01 | Sigma-7 | Power_Normal |
+-----+-----+-----+
```

```
7 rows in set (0.00 sec)
```

```
mysql> delete from Sensaphone_Data;
Query OK, 7 rows affected (0.01 sec)
```

```
mysql> insert into Sensaphone_Data VALUES(NOW(), 'Sigma-7','Power_Normal');
Query OK, 1 row affected (0.00 sec)
```

```
mysql> exit
```

```
Bye
```

```
aplay8 % crontab -r
```

```
aplay8 % █
```

to keep accurate count, but not within the script itself. The solution was to use the timestamps in the MySQL database to keep track of the current and previous times a status change occurred.

V. Conclusions

Extensive testing was performed on both scripts to ensure both performed properly. Once complete, the script is to be turned over to administrators mainly to insert the data center shutdown statements, as that could not be used during testing of the scripts. After, the scripts will be left on the test host and run indefinitely. The objective of this project is to provide full monitoring coverage over all parts of the data center by creating new scripts to manage the monitoring of the newer sections while running the data collection in conjunction with the old scripts to provide full, integrated and easily accessible monitoring data for administrators to use. Both my department and I greatly benefitted from my project. During my time at Brookhaven National Laboratory, I learned a great deal about programming in Python, using and managing MySQL databases, executing commands in Unix shell script, and using Cron and Wget.

VI. References

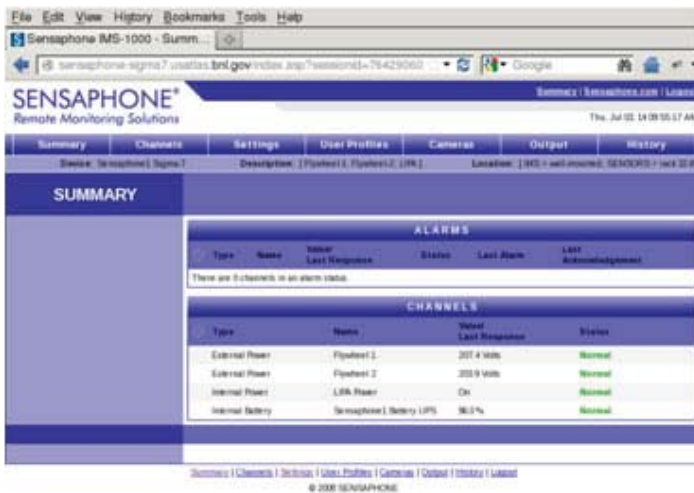
¹Wong, Tony. "Business Continuity Experiences at BNL." Jan 2013. <<https://indico.cern.ch/event/220443/session/1/contribution/37/material/slides/0.pdf>>

²GNU Wget. <<https://www.gnu.org/software/wget/>>

³NetSNMP. <<http://www.netsnmp.org/about/history.html>>

VII. Acknowledgments

This project was supported in part by the U.S. Department of Energy, Office of Science, Office of Workforce Development for Teachers and Scientists (WDTS) under the Science Undergraduate Laboratory Internships Program (SULI).



Monte Carlo simulations of a Cherenkov detector using a water-based liquid scintillator

Timothy Leeney

Physical Sciences, Suffolk County Community College, Selden, NY 11784

Brett Viren

Physics, Brookhaven National Laboratory, Upton, NY 11973

Abstract

Water-based Liquid Scintillator (WbLS), a liquid scintillator developed at Brookhaven National Laboratory, is currently under investigation for future use in neutrino detectors. Its high light output and relatively low cost make it a good candidate for detecting neutrinos at low energies, but its isotropic scintillation light impedes methods of particle and track identification traditionally used for water Cherenkov detectors. Since these are key requirements of a neutrino detector, the usefulness of WbLS in neutrino detection is unconfirmed. Our study made use of an existing Monte Carlo simulation to simulate a Cherenkov detector filled with a range of percentages of WbLS and examined at which percentages particle identification was possible. The simulation was repeatedly run with electrons and muons at energies above 50 MeV created by charged-current interactions. We analyzed the light detected by the simulated photomultiplier tubes in the detector and modified and implemented an existing algorithm to identify electrons and muons from detected Cherenkov radiation. Our algorithm analyzed the intensity slope of detected Cherenkov radiation patterns, and successfully performed particle identification with 1% WbLS. As a result of my work this summer, I am now familiar with the description and analysis of data required for measurements with Cherenkov detectors as well as analysis of data using the ROOT program. I have also gained valuable experience writing and maintaining programs in C++ and running GEANT4 particle simulations.

Neutrinos are fundamental subatomic particles. Like electrons and muons they are leptons and do not interact with the strong nuclear force. Unlike electrons and muons, they have no electric charge and do not interact with electromagnetic fields. This means neutrinos feel only the weak force and gravity, which greatly reduces their interactions with other particles. This makes them extremely difficult to detect directly. Physicists are only beginning to measure the mass of neutrinos, but their mass is known to be less than one-millionth the mass of an electron. Neutrinos come in three flavors, corresponding to the three flavors of charged leptons: electron, muon, and tau. In a charged-current interaction a neutrino collides with another particle and exchanges a W particle (a carrier of the weak force) and converts into the corresponding charged lepton (electron, muon, or tau). The electric charge of the resulting particle makes it easier to detect than its neutrino predecessor.

The detection of this charged lepton is the purpose of Cherenkov detectors. It is a well known principle of relativity that nothing travels faster than light in a vacuum. However, when light travels through matter it is slowed by an amount given by the refractive index of the medium. It is then possible for a particle moving through matter to travel faster than the speed of light

in that medium. The refractive index is a function of the light's wavelength, but for visible light in water the refractive index is approximately 1.33, so light in water travels at 75% its speed in free space. Just as an airplane traveling faster than the speed of sound in air emits a sonic boom, a charged particle traveling faster than the speed of light in a medium emits a cone of electro-magnetic radiation. This is the Cherenkov cone. The photomultiplier tubes inside a Cherenkov detector detect the light cone emitted by such an electron or muon. Because of electromagnetic showers and scattering the cone produced by an electron tends to be fuzzier and not as sharp as the cone produced by a muon at a similar energy.

The GEANT4 WCSIM program was used to simulate muons and electrons at energies from 100MeV to 5Gev within a cylindrical detector with a radius of 31m and height of 80m. The data output by the simulation was analyzed using C++ and ROOT, and the charge collected in the simulated PMTs was used to determine the identity of the particle. Several methods of automated particle identification were tried. The most accurate method was based on the RISPID algorithm developed by Florian Goebel[1]. In this method the charge in the hit PMTs is projected onto the particle track at the Cherenkov angle. This projection is called the charge-track histogram. Because of the sharp outer edge of the muon ring on the detector wall, the rising edge of the charge-track waveform is steeper than the rising edge of the electron waveform. The RISPID algorithm exploits this fact by finding the steepest point on the rising edge and calculating the ratio of charge 5m before to 5m after this point. The steeper curve for muons means that, in theory, the RISPID ratio should be lower for muons than electrons. For each event, the steepest point on the rising edge was determined by evaluating a finite difference derivative along the rising edge. The steepest point, or inflection point, can then be determined by finding the location of the maximum value bin in the first derivative histogram or the location of the zero crossing in the second derivative histogram. The isotropic scintillation light adds scatter to the charge-track histograms, which impedes particle identification. To lessen the scintillation light on the charge-track histogram, PMT hits whose hit times deviated far from their expected hit times relative to the other hits were discarded.

Comparisons were made between RISPID ratios for muons and electrons with different percentages of scintillator in the detector. The RISPID ratio for muons was compared to that of electrons with energies 54MeV lower. This was to correct for the fact that muons slow below the speed of light in water at an energy of 54 MeV, which causes the Cherenkov cone to disappear. Accurate particle identification was made in 99% of events with muon energy at 300MeV and higher when a photon yield of 90 photons/MeV was used, corresponding to approximately 1% WbLS in the tank of the detector. Particle identification in a detector using WbLS was consistent with one using pure wa-

ter. These findings show that a water-based liquid scintillator is a realistic solution to use with Cherenkov detectors since particle identification is possible and serve to justify the continued R&D work on WbLS at Brookhaven National Laboratory.

Attached below is the class definition for the LightTrackAngle class that I wrote in C++ to analyze charged current events. I also wrote the function definitions for the functions in the class and the code for a program that creates multiple objects of the class LightTrackAngle.

```
class LightTrackAngle{
public:
    LightTrackAngle(TTree* theDataTree,TTree* theGeoTree,string theParticleEnergy,string theParticleType,string
thePhotonYield, int nXBins=14000, double xMin=-1.1, double xMax=1.1);
    void Fill(const WCSimRootEvent* event,int eventIndex);
    void Draw() const;
    void DrawChargeTrackHist();
    void DrawChargeTrackHist1Der();
    void DrawRispidHist();
    TH1F* GetHistogram();
    double CalculateRispid();
    TH1F* GetRispidHist();
    void DrawChargeTrackHist1Der();
    void DrawChargeTrackHist2Der();
private:
    TH1F *h;
    TH1F *timeLagHist;
    TH1F *chargeTrackHist;
    TH1F *rispidHist;
    TH1F *chargeTrackHist1Der;
    TH1F *chargeTrackHist2Der;
    string lightAngleHistFileName;
    string rispidFileName;
    string chargeTrackFileName;
    string chargeTrackHist1DerFileName;
    string chargeTrackHist2DerFileName;
    string particleType;
    string particleEnergy;
    string photonYield;
    TTree *dataTree;
    TTree *geoTree;
    WCSimRootGeom *detectorGeo;
    TBranch *geoBranch;
    WCSimRootTrigger *currentTrigger;
    WCSimRootTrack *currentTrack;
    WCSimRootPMT *currentPMT;
    double currentPMTVector[3];
    double vertexVector[3];
    double particleDirVector[3];
    double differenceVector[3];
    double currentAngle;
    double differenceMagnitude;
    void findCurrentAngle();
    bool FillChargeTrackHist(double correctedQ);
    void FillChargeTrackHist1Der();
    void FillChargeTrackHist2Der();
    double expectedHitTime();
    bool keepHit(WCSimRootCherenkovDigiHit *theDigiHit);
    bool checkOrientation();
    int FindSteepest();
    int discardCounter;
};
```

LITERATURE CITED

[1] Goebel, Florian. (1996). A Study of Particle Identification with the Super-Kamiokande Detector. (Master's Thesis).

Improvement of a diffraction-limited, hyperspectral laser beam induced current probe station for thin-film photovoltaics

Vittorio Loprinzo

Department of Physics and Astronomy, Johns Hopkins University, Baltimore MD 21218

Ahsan Ashraf

Department of Physics and Astronomy, Stony Brook University, Stony Brook NY 11794

Matthew D. Eisaman

Sustainable Energy Technologies Department, Brookhaven National Laboratory, Upton NY 11973

Abstract

The efficiency of solar cells is often limited by spatial inhomogeneities that arise during device fabrication. The Laser Beam Induced Current (LBIC) technique can help to qualify the role of such impurities in solar cell operation so that manufacturing and efficiency can be improved. At the Interdisciplinary Science Building at Brookhaven National Laboratory, an LBIC setup was used to characterize the spatial inhomogeneities present in Copper Indium Gallium Diselenide (CIGS) solar cells. Initially, the complex electronics and optical measurement devices comprising the experimental setup were operated manually and individually. However, the automation and aggregation of these processes into generalized interfaces using LabView greatly accelerated the measurement procedure, and allowed data to be taken more rapidly. Using the improved setup, the lateral variation in cell efficiency was quantified and connected to the variation in stoichiometry resulting from cell fabrication. This work directly supports the goals of the DOE SunShot Program to improve solar cell technology. Additionally, the automation and improvement of the LBIC setup offered great insight into both the field of photovoltaic science and the use of modern programming languages, such as Python and LabView, in current scientific research.

I. Background

A. Photovoltaics

Photovoltaics are semiconductor devices designed to trap light and produce photocurrent, for use in energy production in solar cells. The semiconductor materials employed are typically Silicon or Copper Indium Gallium Diselenide (CIGS). A tradeoff exists between device efficiency and amount of light trapped; thinner solar cells tend to be more efficient, but trap less light than thicker counterparts. This group focused on ultra-thin solar cells. The efficiency of such cells is limited by chemical inhomogeneities that arise during device fabrication. Small impurities in cell structure can provide mechanisms for electron-hole recombination, and a loss of photoelectric current that could otherwise be harnessed. Understanding the role such impurities play in device behavior will help improve the efficiency of future solar cells.

B. Laser beam induced current experiments

Many techniques exist to study PV devices. Laser beam induced current (LBIC) experiments are used to examine how small physical details affect cell performance. They are effective for this purpose, as laser light can be focused to extremely small spot sizes, and the spectral response of minute cell areas can be stud-

ied as a result. The effects of chemical inhomogeneities and other impurities can be examined in this way. Types of measurement include simple current-versus-voltage response measurements and measures of quantum efficiency, as well as many more specialized options, such as band-edge scans and CELIV (charge extraction by linearly increasing voltage) studies of charge mobility.

II. Experimental setup

A. Devices employed

At the Interdisciplinary Science Building at Brookhaven National Laboratory, a laser beam induced current probe station was set up to characterize primarily CIGS PV devices. A hyperspectral laser and a Helium-Neon laser were set up to be used interchangeably within the experiment. Devices in the laser path included flip mirrors, polarizers to control power, shutters, lenses configured to adjust beam spot size, a ‘chopper’ used to create a pulsed signal, beam splitting cubes that allowed incident and reflected power to be measured, and an objective lens used to focus the laser beam on samples. Samples were mounted on a stage free to move in three dimensions to an accuracy of two microns for fifteen thousand of motion. An air and water coolant system was affixed to the stage and controlled by a PID temperature controller. A microscope was put in place so probes could be positioned on samples. The probes were connected to a voltage control device and a lock-in amplifier able to read a pulsed signal to measure induced current without background interference.

B. Measurement procedure

Measurements performed on the LBIC station, in the most general sense, involve focusing laser light on different areas of a sample and reading the current output by the cell. Before the new measurement software described below was developed, much of the measurement process occurred manually. Samples were mounted on the stage and set up with probes and aligned by hand. Scans were programmed individually, and code had to be modified if different measurement instruments were to be used. Scans often did not run at maximum resolution because of the slow speed of the program. Scan outputs were formatted as text files for use with external analysis programs.

III. Automation of experiment

A. Initialization

The first component of the developed LabView software was a routine built to assist users with the preparation of samples for scans. The code, when run, first positions the sample stage under the microscope and prompts users to position the probes. It then

returns the sample to its position underneath the objective lens and executes a procedure to align the Z axis of the stage so that the laser spot is focused exactly on the surface of the sample. Since the samples are flat, incident laser light is in part reflected back through the objective lens and travels backwards through the experiment until it reaches a beam splitter cube. There, the reflected laser light is redirected sideways into a photodiode sensor. Due to the geometry of the objective lens, the smaller the laser spot size, the more light will travel back through the beam path to arrive at the photodiode. As such, an alignment for the stage's Z axis can be achieved by optimizing the reflected signal at the photodiode with respect to Z position. The program first locates a reflective contact on the sample, and then varies Z, records the reflected signal, and displays a graph to the user so the optimum value of Z position can be selected.

B. Measurement program

The second piece of the developed program was built to control at once all instruments involved in performing scans on samples. It was designed as a customizable user interface that could perform any type of measurement done at ISB's LBIC probe station. The program's main feature was a stacked loop structure which enabled simultaneous variation of temperature, two dimensional stage position, applied voltage, and laser wavelength. Users specify ranges and step sizes with which to vary each of these parameters. The program adjusts instruments accordingly, ensures they are positioned correctly, and reads and outputs measurements of raw current. The program also included an enableable graph which slowed down the program significantly but displayed real-time updates to relationships between output and other experimental parameters. This program was built to be hardware limited in terms of speed, and all subroutines written in C or Python were required to run more quickly than involved instruments could move. The program was also designed so that it could itself be used as a subroutine in larger programs.

C. Outer shell

The final component of the program was constructed to allow LBIC users to set up and run multiple scans on the same sample over a time period of many hours. It consisted of a programmable outer shell that accepts multiple sets of scan parameters and runs the measurement program once for each set. The outer shell program is intended to be used for overnight scans, so that high-resolution maps of device behavior can be obtained. It is thus designed to run without any interactions from users during measurement.

IV. Results

A. Test measurement: Band edge characterization

To qualify the effectiveness of the newly developed measurement programs, a typical measurement was performed. A standard CIGS sample device previously characterized using the outdated version of the experimental setup was reexamined for this purpose. A simplified band-edge scan was performed. A hyperspectral area scan of the cell was performed while voltage and temperature were held at constant values. The location of the band edge was bounded above and below by looking at such area scans at 1000nm and at 1100. At the shorter wavelength, charge activity was seen to be present all over the cell. At the latter wavelength, however, nearly no photocurrent was observed. It is therefore safe to conclude that the band edge for that sample lies between 1000

and 1100 nanometers.

B. Conclusions about measurement program

Compared to the previously existing programs used to individually control instruments installed in the LBIC station, the developed programs ran quicker, more smoothly, and in a more user-friendly fashion. The test scan described above consisted of 11262 measurements, and was completed in 128 minutes. The scan was able to produce an accurate band-edge characterization for a device whose behavior was already known. The group found the program easy to use and thought it self-explanatory enough to be utilized by visiting scientists and collaborators outside the group.

C. Future work

An attempt was made to write a subroutine in Python for the measurement program what would display to users constantly updating values of efficiency, fill factor, and other parameters often used to talk about PV devices while data is being taken. However, the subroutine required several numerical methods, such as Newton-Raphson root finding, which caused the code to run much too slowly to be used during the measurement procedure. If the subroutine could be sped up, either through elimination of the needs for numerical methods or through improvement of their employment, the measurement program could feasibly be improved so that live updates to solar cell parameter values could happen at least occasionally during long measurement processes.

V. Acknowledgements

This project was supported in part by the Brookhaven National Laboratory (BNL), Sustainable Energy Technologies Department, under the BNL Supplemental Undergraduate Research Program (SURP).

VI. References

1. Gray, Jeffery L. "Physics of the Solar Cell." Handbook of Photovoltaic Science and Engineering. By A. Luque and Steven Hegedus. Chichester, West Sussex, U.K: Wiley, 2011. N. pag. Print.
2. Hegedus, Steven S., and William N. Shafarman. "Thin-film Solar Cells: Device Measurements and Analysis." Progress in Photovoltaics: Research and Applications 12.23 (2004): 155-76. Web.

3D modelling and structural analysis of eRHIC's low and high energy beamline magnets

Sarja Lowe

Bronx Community College, Bronx, NY 10453

Joseph Tuozzolo

Collider-Accelerator Department, Brookhaven National Laboratory, Upton, NY 11973

ABSTRACT

Physicists at Brookhaven National Laboratory believe that an electron Relativistic Heavy Ion Collider (eRHIC) will answer additional questions regarding the characteristics of matter and laws of quantum mechanics. eRHIC will be the first high energy polarized protons/ions and polarized electron collider. Installing a 21 GeV electron accelerator in the RHIC tunnel without major civil construction modifications to control cost is a major challenge. Hence, Computer Aided Design (CAD) software was certainly required to model out the 3D model of the most cost effective magnets conceptualized by the physicists in the Collider-Accelerator Department. The new ring/eRHIC will consist of a low energy section and a high energy section. Thus two different types of magnets are required for the electron circulation in the eRHIC. The “Tchoubar” magnet, a magnet designed for the high energy section of the ring, and the “Wuzheng” magnet, a magnet designed for the low energy section of the ring were the two magnets chosen for the eRHIC system. The “Tchoubar” magnet is composed of a permanent magnet material and steel poles in order to provide the necessary focusing/bending for the electron beams. The “Wuzheng” magnet is composed of Samarium Cobalt and stainless steel. It was actually conceptualized by Dr. Meng Wuzheng of the Collider-Accelerator Department. While the high energy section magnet (“Tchoubar” magnet) was conceptualized by Dr. Oleg Tchoubar and Dr. Stephen Brooks. This new ring/beam line will replace the RHIC's Yellow ring, which was used for the proton-proton collision. Since the eRHIC will collide electrons and protons, the RHIC's Blue ring will still be used to accelerate protons, while the new designed ring (compose of the two magnets mentioned above) will circulate electrons. So no civil construction is required for the eRHIC project.

I. Background

Since eRHIC system composes of the proton/blue and the electrons ring, the “Brooks-Tchoubar” magnet and “Wuzheng” were essential for the new ring (electron ring). Hence, I was assigned to construct the 3D model of these two magnets. During this assignment execution, I used a computer software to build and analyze the structural appearance of the 3D model of these magnets. This process involved calculations and pop-up discussions with scientists. It was my job to accurately build the 3D model of the magnets, assemble them with the accelerator's supporting equipment, including the vacuum chamber and the beam diagnostic equipment, and eventually position them in the tunnel properly. These magnets are actually cheaper than the other two magnets conceptualized by the other two physicists. I eventually built the magnets and embedded a vacuum chamber built by another intern in between the top and down magnets of each magnet

assembly (consist of two identical magnets – facing each other, as shown in Figure 1a and 1b). The magnets were then placed in the beam line “lattice” as to provide the necessary bending/focusing of electrons in the vacuum chamber. This information was provided by Dr. Stephen Brooks, who did series of calculations in order to figure out the accurate points for the coordinate system(x, y, and z).

II. Methods and Materials

Since my project entails designing and structural analysis of eRHIC's magnets, the CREO/ProE software was used as the main tool to accomplish this project. ProE/Creo helps in labeling and differentiating parts to be made up of a different material. As in Figure 2, the color of the vacuum chamber, drift, and the magnet is used to mark difference in material makeup. The “Tchoubar” magnet, a magnet composed of a permanent magnet material and steel poles and the “Wuzheng” magnet, a magnet composed of Samarium Cobalt and steel are the two magnets I worked on, so it's a good idea that I used different colors for each section/part

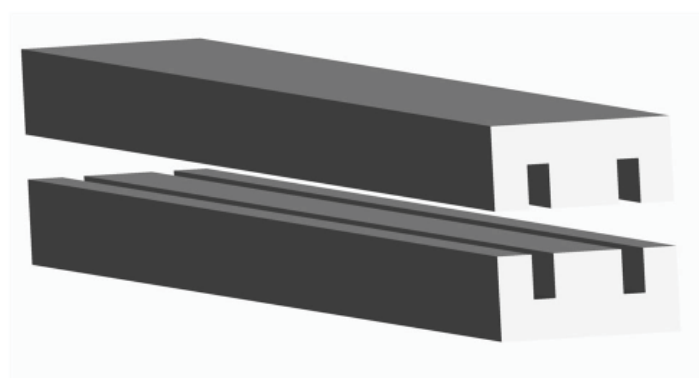


Figure 1a. The “Tchoubar”

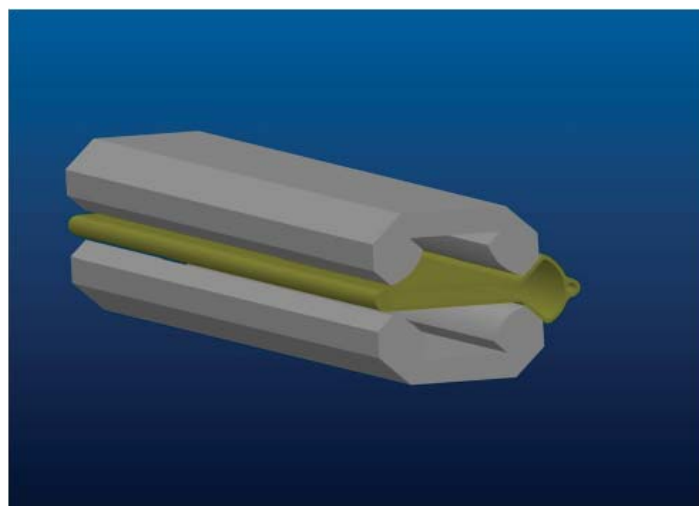


Figure 1b. The “Wuzheng”

made up of a special material as to indicate difference in material makeup.

Figure 2 also shows the magnet layout or “lattice” of the low energy section of the ring. A set of assemblies, as shown in Figure 1b, are combined/assembled together to form the “lattice”. The construction of the “lattice” or magnet layout requires values for each coordinate (x, y, and z). With these values, we can plot points (datum points) as to orient the path/direction of the curve. Basically, the main tool used in this project is Computer Aided Design (CAD) software, which also requires a good knowledge in mathematics and science.

III. Conclusion

Eventually, these magnets were assembled with other eRHIC’s supporting equipment such as the vacuum chamber and the beam diagnostic equipment. As the images below shows, this is the 2 o’clock section of the eRHIC. It’s compose of “Tchoubar” magnets, vacuum chambers, spreader/splitter, combiner, and etc. The magnet assembly is attached to the end of the combiner because the magnets are essential for the bending/focusing of the beams. Beams at the higher energy section of the ring travels close to the speed of light. That’s why the “Tchoubar” magnet is designed for that section of the ring. Eventually, I’m glad that these magnets will be used as the new magnets for the eRHIC.

IV. Acknowledgments

This project was supported in part by the U.S. Department of Energy, Office of Science, Office of Workforce Development for Teachers and Scientists (WDTS) under the Community College Internships Program (CCI). I wish to thank my mentor, Joseph Tuozzolo, for his leadership, magnanimity and professionalism during this project execution. I would also like to thank the Office of Educational Programs (OEP) here at Brookhaven National Laboratory (BNL) for their marvelous support. Finally, I would express my gratitude to all those who assisted me during my time here.

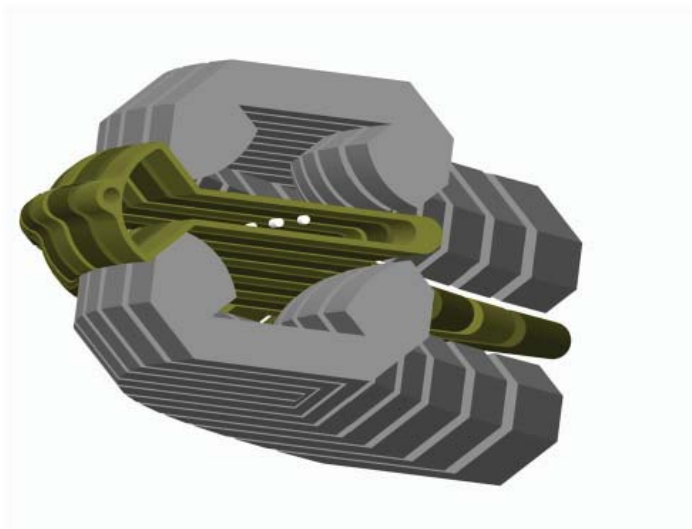


Figure 2. The white colored drifts shows how the beams travels in the Vacuum Chamber

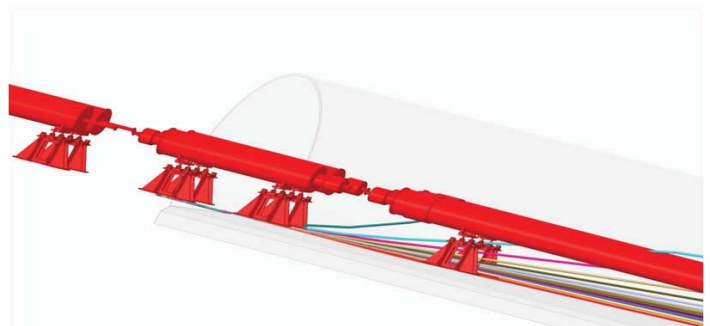


Figure 3. Combiner attached to Linac in the tunnel

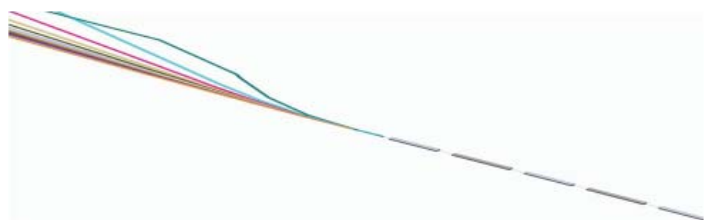


Figure 4. “Tchoubar” Magnet attached to the end of the combiner.

Upgrading a 15000 amp power supply for testing new magnets to be used at The Large Hadron Collider

Thomas Marone

Mechanical Engineering, University of Rochester, Rochester NY, 14627

Paul Kovach

Superconducting Magnet Division, Brookhaven National Laboratory, Upton NY, 11973

Abstract

The main purpose of the Large Hadron Collider Accelerator Research Program (LARP) being conducted at Brookhaven National Laboratory (BNL) is developing new coil patterns that produce a stronger magnetic field, to be used at the Large Hadron Collider (LHC) at CERN in Geneva, Switzerland. These higher magnetic fields will allow for faster particle acceleration and better collisions between particles which will help with the research of how the universe began and the discovery of new particles. In order to produce these stronger magnetic fields the magnets needed a much higher current passing through them. Here at BNL the current power supply for magnet testing has the ability to deliver 15000 amps of direct current but, in order to test these new magnets the output of these power supplies needs to be upgraded to 24000 amps. In order to accomplish this upgrade we had to redesign the power supplies using Pro Engineer in order to fit in double the amount of capacitors and other hardware to produce this current. When the upgrade is complete the new coil patterns will be able to be tested and we can discover if they function better than the old coils. If so they can then be sent to the LHC to be used in their experiments. From this project I have gained valuable experience using Pro Engineer for modeling, creating drawings, and creating plumbing schematics.

I. Background

A. History of Existing Power Supplies

Two current power supplies for testing super conducting magnets at Brookhaven National Laboratory (BNL) were originally built by Rapid Electric Co. Inc. in May of 1978. They each have the ability to deliver 15000 amps of direct current at 0-24 volts. The power supplies were then placed in storage in December of 1978 before being used. Both power supplies eventually arrived at BNL in April of 1984 where they were put into their current location. Upon arrival the supplies had to be cleaned of all dust and rust, then had to be tested to make sure they were correctly operational before use in testing.

B. LARP

The project the power supplies are being upgraded for is called the Large Hadron Collider Accelerator Research Program I (LARP). This is a project done in collaboration with CERN in Geneva, Switzerland with four other U.S. laboratories; BNL, FNAL, LBNL, and SLAC. The main purpose of this program is to improve technology for the Large Hadron Collider (LHC) and improve its performance. One of the improvements being researched is new coil designs using a new Niobium Tin (Nb₃Sn) superconductor for producing higher magnetic fields inside the magnets.

These new coils require a higher current to power them which will allow them to create the stronger magnetic field. A current of 24000 is needed to test and operate these new coil configurations and magnets that they will be inserted into.

I

II. Methods

A. Project Overview

This project was done primarily on a computer using a computer aided design program called Pro Engineer Wildfire 4.0 (Pro E). Initially the existing 15000 amp power supplies had to be modeled and documented using Pro E, which will create a three dimensional model of the power supplies. Then from this three dimensional model twice the amount of capacitors, insulated- gate bipolar transistors (IGBT), and other hardware could be added to upgrade the existing power supplies to 30000 amps of direct current. Other improvements that were deemed necessary, such as increasing water cooling capacity and providing greater monitoring of cooling of components, were implemented at this time as well. Some of these elements required engineering calculations of heat transfer and fluid flow to be completed to validate the designs. Drafting of drawings for required parts and assemblies could then be made and sent out for fabrication after they go through the appropriate approval process.

B. Initial Modeling

Initially the existing 15000 amp power supplies needed to be modeled on the computer to allow for modifications and documentation. The measurements were taken by hand from the power supplies and all parts contained inside of them. These measurements with the aid of 3-D modeling of Pro E allowed for an exact copy of the existing power supply to be made of the computer. This included all thirty capacitors, three IGBTs, all plumbing, and measurement recording equipment such as flow meters and temperature sensors.



Figure 5: Picture of existing power supply with capacitors, IGBTs, and hardware.

C. Modeling the Upgrade

In order to increase the current to 30000 amps the amount of capacitors, IGBTs, and hardware needed to fit into the same amount of available space as the existing. Using the guidelines from the Chief Electrical Engineer and through manipulating the model on Pro E, a new capacitor configuration for the silver capacitors was designed that was also able satisfy the space constraints. The configuration and how they were connected to the IGBT was important because if not done a certain way could create a magnetic field destroying the smaller capacitors, and wire lengths needed to be identical for capacitors to properly function. The plumbing was then redesigned using new custom made manifolds equipped with brass flow regulators to save space and reduce the length of hose that needed to be snaked through the power supply.

D. Creating Drawings

Drawings of the new parts that needed to be fabricated were drafted to be put through the approval process and then sent out for machining. Top assembly drawings were also drafted so technicians could assemble the new power supplies when all the parts are finished being fabricated. These drawing will be stored for reference for repair or other modifications at a later date.

III. Results

At the most recent final design review the proposed upgrade was determined to meet all technical requirements. All of the parts align correctly and were able to fit in the available space with only a small addition of about 8 inches needing to be added to the existing power supplies. We were able to make upgrades to the existing equipment and add new essential equipment to the supplies as well. New pieces of equipment like water flow regulators and more compact manifolds were able to be added without driving the price past the allowed budget for the project. The new supply

will be state of the art and able to successfully deliver the 24000 amps of direct current needed to power the new magnets. The new power supplies will also have more sensors to report back data to make sure the power supply is operating safely which is an important risk reduction feature for the project.

IV. Conclusions

The modifications were successful in allowing the new power supplies to be able to deliver the necessary current to power the magnets. The design was approved and the drawings have been checked are being approved to be sent out for fabrication. Construction of the new power supplies will begin next fiscal year and be completed that same year so testing can begin on the new magnets. Without these new state of the art power supplies testing could not be completed at BNL, research would not be able to continue on these new magnets and thus research at CERN in Geneva, Switzerland would also be unable to continue. The new magnets that these power supplies help to test will be going to CERN to be used in The Large Hadron Collider for particle focusing in their experiments at higher energies.

V. References

¹“LARP.” LARP. U.S. Department of Energy, 21 Nov. 2013. Web. 04 Aug. 2014.

VI. Acknowledgements

This project was supported in part by the U.S. Department of Energy, Office of Science, Office of Workforce Development for Teachers and Scientists (WDTS) under the Science Undergraduate Laboratory Internships Program (SULI).

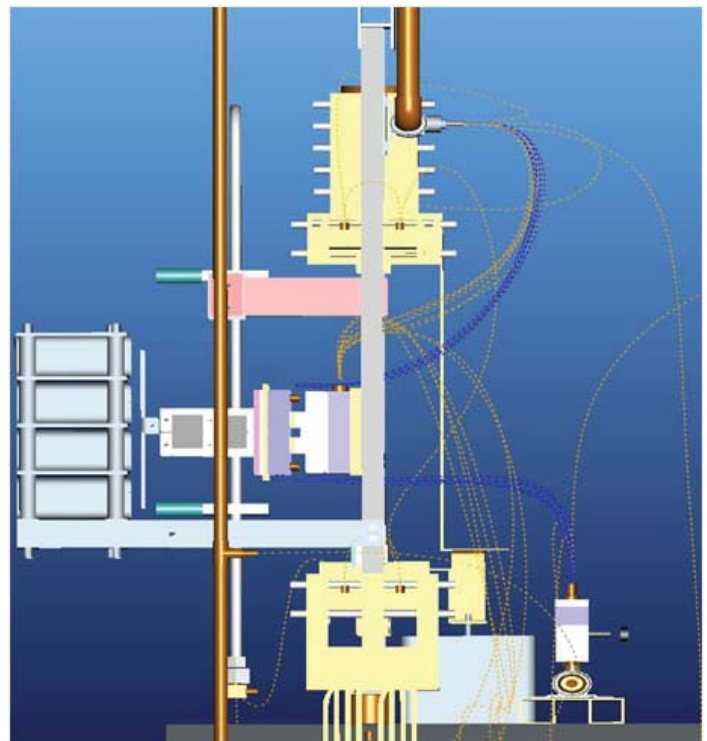
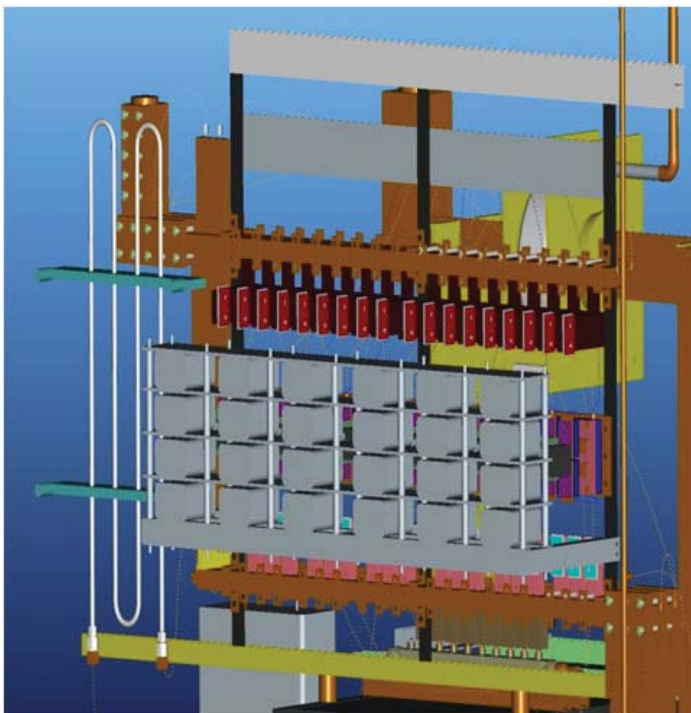


Figure 2 and 3: Views of the model of the new power supplies.

Updating the spin program for RHIC

Eric McCafferty

Collider Accelerator Department, Farmingdale State College, Farmingdale, NY 11735

Jörg Kewisch

Collider Accelerator Department, Brookhaven National Laboratory, Upton, NY 11973

Abstract

One of the programs used by the Relativistic Heavy Ion Collider (RHIC), the spin program, is necessary to ensure that proper polarization of the beam is maintained by determining how the magnets must be adjusted to keep things running correctly. This program, along with numerous others, was written in the Fortran 77 language years ago. Due to the unwieldy nature of the existing spin programs, a new program is being written in the C++ language which, when complete, will be faster and easier to use. The conclusion of this project saw the completion of the tracking, closed orbit, and spin portions of the program.

To keep RHIC running smoothly, Brookhaven National Laboratory makes use of a variety of programs and applications. One of these programs calculates the proton spin polarization by track-

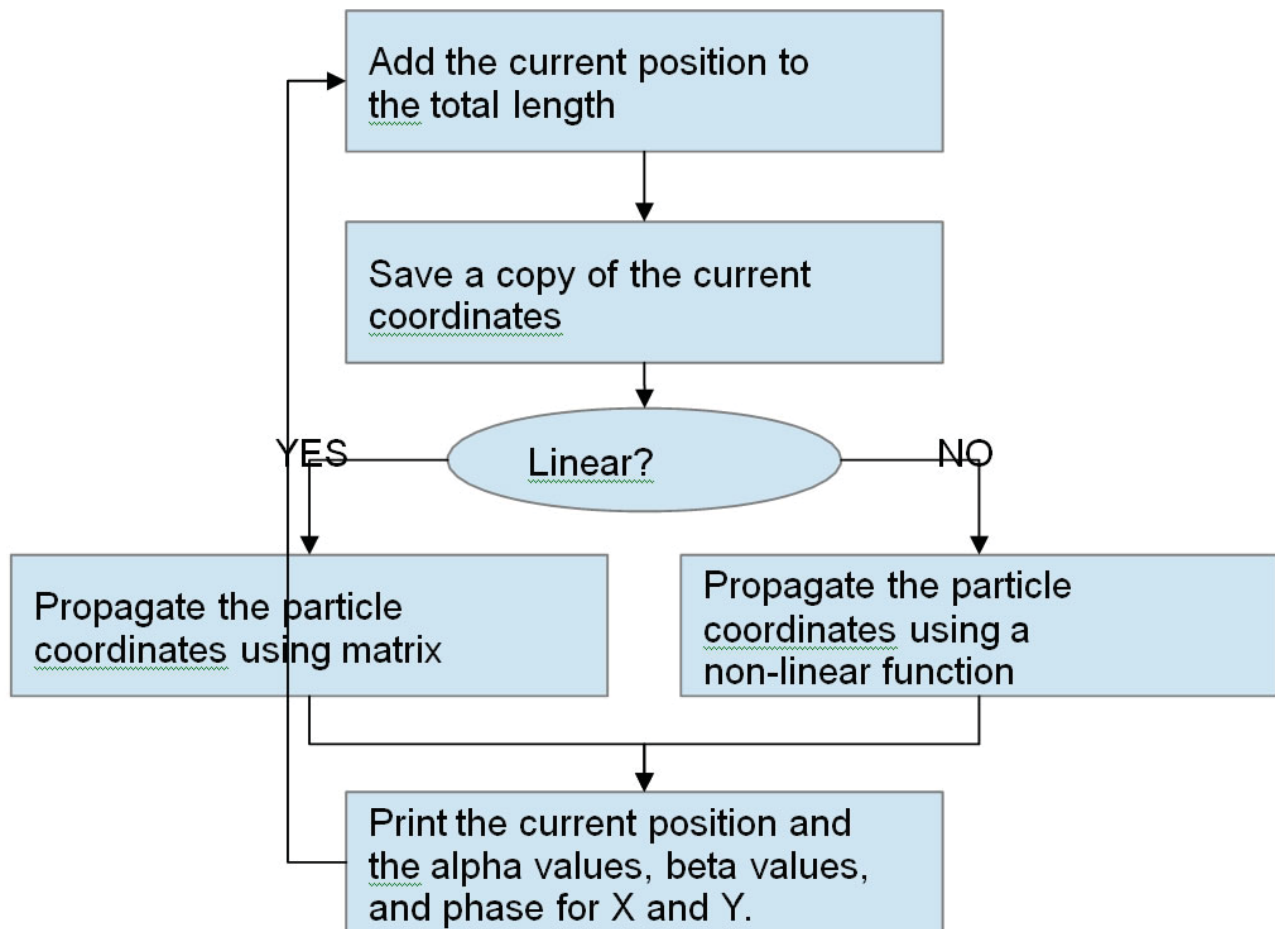
ing particles through the RHIC ring, and calculating how much the polarization decreases along the way. The ultimate goal of the spin program is to determine how the magnets in RHIC must be adjusted to ensure that the beam polarization is maintained. Several spin programs are available and work well; however, they are either slow or complicated to use. A new program must therefore be written which, using reasonable approximations, is fast and integrates into the RHIC control framework.

Starting from a rudimentary program which implements the interface of the MAD8 program, we added functions to track a single particle through the ring. The tracking allows the use of linear elements like dipoles and quadrupoles, as well as nonlinear magnets like sextupoles, octupoles and higher multipoles.

Of special interest in a storage ring is the particle trajectory that returns to the initial position.

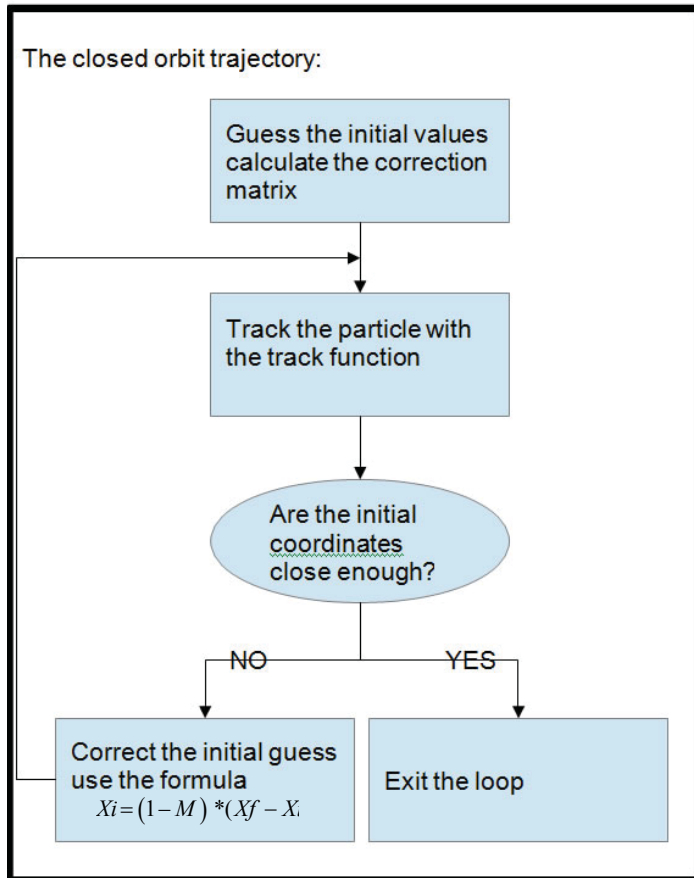
This is called the closed orbit. In an iterative process, using

To track each element:



tracking and correction of then initial coordinates, this trajectory is found.

The spin component of the proton is implemented using the spinor formalism. This method expresses rotations of the spin vector as a vector of four components. The usual 3 by 3 matrix multiplication requires 27 multiplications and 18 additions. By employing spinor algebra, concatenating rotations requires only 16 multiplications and 12 additions.



Computer code similar to the new code exists in many programs. We reused such code, but converted it from Fortran to C++. In doing so, we had to be aware of the differences between the two languages: the numbering of array indices (starting from 1 in Fortran and from 0 in C++) and the mapping of multi-dimensional arrays into memory.

Most programming was done using Vi in the OSX Terminal. Applications such as GDB and gnuplot were used to debug and check the results. Because similar programs already exist in Fortran, we had a proven version of the program to compare results against. Other complications were dealt with through other existing programs. For example, floating point numbers in C++ lack a certain degree of precision, leading to large rounding errors when subtracting numbers of an array of vastly different values. An existing function was available which, with some tweaking, helped resolve this issue.

The creation of a spin program in C++ is an ongoing process. The conclusion of this project saw the program one step closer to completion; however, there remains much work to be done in the future.

References

J. Kewisch, "Spinor Algebra"

Acknowledgments

I would like to thank my mentor, Jörg Kewisch, for making this internship possible and guiding me through the project. I would also like to thank Brookhaven National Laboratory for offering enrollment in the SULI program, and the Department of Energy for funding the program.

Spinor formalism:

Two successive rotations are expressed by multiplying matrices:

$$\begin{aligned}
 & M(k_0, k_1, k_2, k_3) * M(c_0, c_1, c_2, c_3) \\
 & = (k_0 c_0 - k_1 c_1 - k_2 c_2 - k_3 c_3) I \\
 & - i(k_0 c_1 + k_1 c_0 + k_2 c_3 + k_3 c_2) \sigma_1 \\
 & - i(k_0 c_2 - k_1 c_3 + k_2 c_0 + k_3 c_1) \sigma_2 \\
 & - i(k_0 c_3 + k_1 c_2 - k_2 c_1 + k_3 c_0) \sigma_3
 \end{aligned}$$

The coefficients for the product are:

$$\begin{aligned}
 & M(g_0, g_1, g_2, g_3) = M(k_0, k_1, k_2, k_3) * M(c_0, c_1, c_2, c_3) \\
 & g_0 = k_0 c_0 - k_1 c_1 - k_2 c_2 - k_3 c_3 \\
 & g_1 = k_0 c_1 + k_1 c_0 + k_2 c_3 + k_3 c_2 \\
 & g_2 = k_0 c_2 - k_1 c_3 + k_2 c_0 + k_3 c_1 \\
 & g_3 = k_0 c_3 + k_1 c_2 - k_2 c_1 + k_3 c_0
 \end{aligned}$$

Semi-automatic pre-processing of raw 2-dimensional diffraction images

James McClintock

College of Engineering, Cornell University, Ithaca, New York, 14853

Eric Dooryhee

Photon Sciences, Brookhaven National Laboratory, Upton, New York, 11973

Before specific data analysis and interpretation can be done at the X-Ray Powder Diffraction (XPD) beamline, interactive pre-processing of raw data is required for background correction, averaging, extraction of regions of no interest (RONI), and the treatment of statistical distributions of measured events. A RONI is typically due to the presence of a beamstop or a defective or inactive sub-set of the detector, i.e. regions where the scientific diffraction image is altered or corrupted. One-pixel events (like non-responsive pixels or pixels with a count which exceeds the threshold) should also be detected and eliminated. Another case is a beam dump or a detector failure causing a series of images to become “black” (i.e., no signal on the detector). The program I worked on aims to automatically mask these RONIs while filtering noise in order to improve the accuracy of the diffraction analysis through the use of thresholding and convolution while also allowing for the manual manipulation of the mask.

I. Introduction

As the construction of Brookhaven National Laboratory’s National Synchrotron Light Source II (NSLS-II) nears completion, the development of efficient and intuitive software is essential to creating a comfortable work environment for its users. Just as the National Synchrotron Light Source (NSLS) hosted thousands of

scientists every year, the NSLS-II too will eventually be available to a wide range of users with different levels of experience. With the support for rapid data acquisition at the X-ray Powder Diffraction (XPD) beamline comes the need for robust analytical software that can handle the large amount of data. Before specific analysis can be conducted, corrections must be applied to ensure that accurate results are extracted. One such correction is the application of a “mask”. The data collected at XPD comes in the form of two-dimensional images taken by the detector. The purpose of the mask is to cover up the areas of the image where the pixel data is corrupted by either detector malfunctions or by effects of the experimental setup. Previously, these masks would be created manually for each experiment using external software such as FIT2D. The goal of this project was to create an automatic mask-writing program that could easily be incorporated into the workflow of the software suite being developed for XPD while still allowing for the manual manipulation of the mask to account for the difficulty in writing a program that will perfectly mask images taken in any experimental context. Two different approaches were employed for writing the mask. The first, thresholding, is useful for finding single-pixel events and other extremely corrupted data. The second is a gradient-based approach, where the derivative of the pixel intensities in each ring is observed in order to

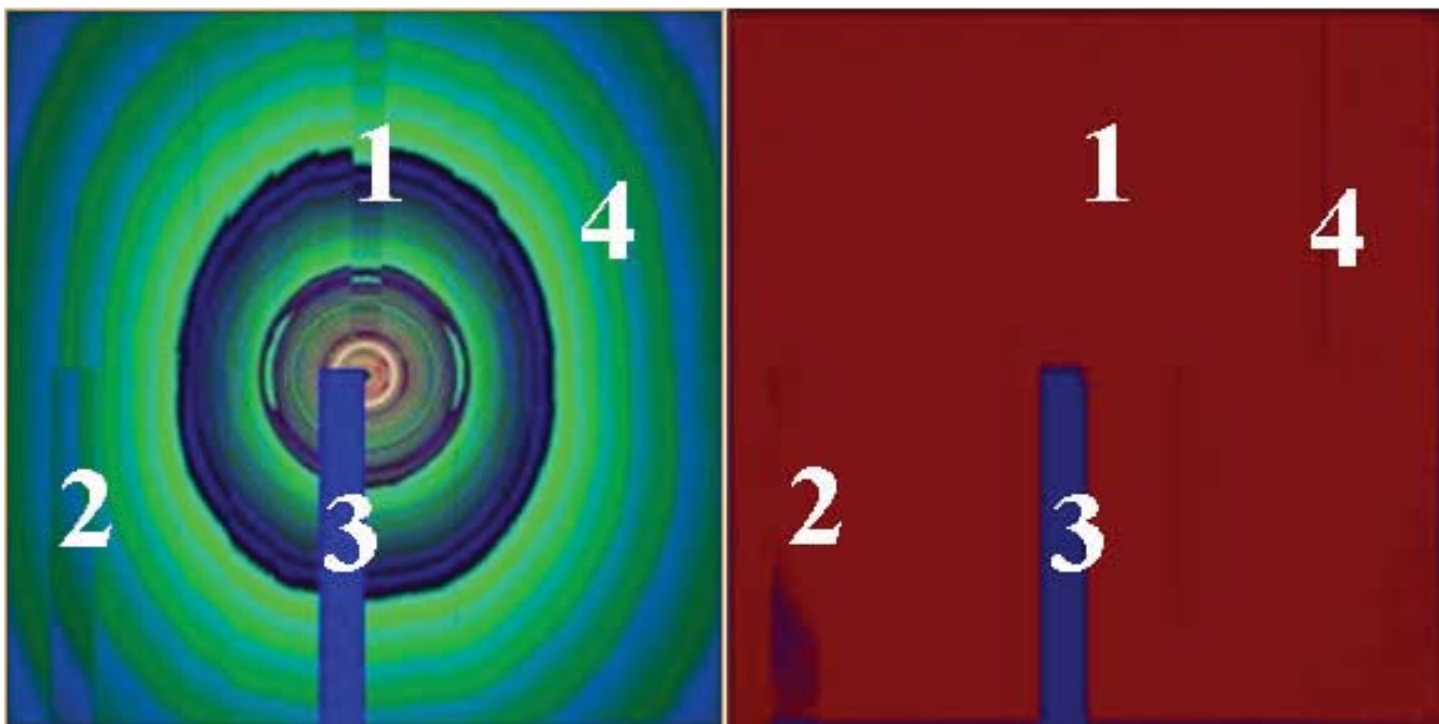


Figure 1. On the left is the diffraction image of a Nickel Palladium sample with the contrast enhanced to make the RONIs easier to see. On the right is a plot of the intensities of the pixels at a distance of ~800 pixels from the center. The large RONIs are labeled.

find the less obvious (yet still inaccurate) portions of data.

II. Thresholding

A simple approach to finding regions of no interest (RONIs) is by using the statistics of the pixel data in order to find the outliers. Damaged pixels that do have zero intensities or saturated pixels that have maxed values are easily found by comparing their values to other pixels. Due to the circular symmetric nature of powder diffraction images, statistics are taken radially across the pixels. In other words, pixels the same distance away from the center of the diffraction pattern should have approximately the same value so the incorrect pixels will be more apparent. By contrast, comparing pixels to those in the same column or row, or to the pixels in a cluster around it does not yield particularly useful information because we can expect there to be a large degree of variance within those groupings.

Through the use of PyFAI, a Python software package used for azimuthal integration, we are able to generate a two-dimensional array containing the radial distances to the center of the diffraction pattern, where each element corresponds to the pixel in the same location within the image array. This allows us to easily bin the pixels into rings containing every other pixel at approximately the same distance from the center. The program calculates the mean pixel intensity and the standard deviation for each ring and masks every pixel beyond the upper or lower thresholds, determined by adding or subtracting a multiple of the standard deviation to the mean. By using statistical tools provided by SciPy, a scientific computing Python library, these calculations are able to be done very quickly allowing the thresholding to be incorporated into the real-time analysis of images during beam time.

As seen in Figure 1, the corrupted data caused by a mostly “dead” region of the detector (3) as well as columns of dead pixels (4) were successfully masked.

However, the damaged region of the detector on the left-hand side of the image (2), which still absorbs light but gives an incor-

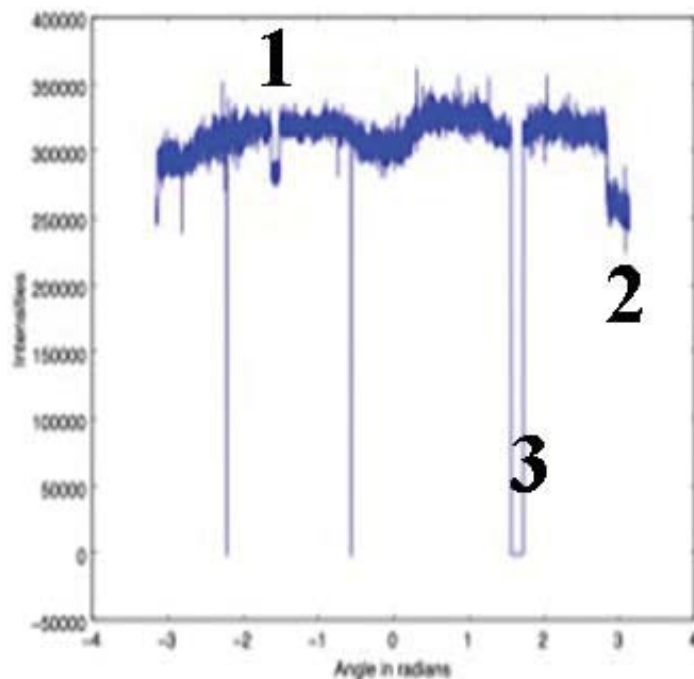


Figure 2. Plot of the intensities of the pixels from the Nickel Palladium sample at a distance of ~800 pixels from the center of the diffraction image.

rect reading, as well as the region at the top caused by the shadow of the beamstop (1) (used for stopping the remaining intense X-rays that were not diffracted by the sample) were largely missed. This encouraged the development of another approach to finding the large RONIs.

III. Gradient Method

The issue with the large RONIs is that they have enough of an impact on the mean of each ring that they are less statistically different from the rest of the image and are missed by thresholds that do not also mask many good pixels. This can be seen in Figure 2 where the pixels along the ring at a radius of 800 pixels from the center are plotted (again, PyFAI was used to generate the two-dimensional array containing the angular data from the center of the diffraction pattern)³, and only (3) sticks out very apparently. While (1) and (2) stand out to the human eye, a stricter threshold that would cut off good pixels would be required to mask them.

In order to address this problem, an algorithm that explicitly searches for the abnormal dips or bumps in intensities (as seen at (1) and (2) in Figure 2) was employed.

The algorithm works by smoothing the pixel data using a moving average, and then inspecting the gradient (essentially the first derivative of the intensity plot) for the RONIs. We must first smooth the data to remove the noise and slight pixel-to-pixel variations in order to make the significant changes in gradient stand out more.

Figure 3 shows the gradient of the smoothed out intensities of the pixels from Figure 2 after being thresholded, hence why there is no sign of (3). Once we have the gradient information, the program finds every local minimum and local maximum and filters out those below a statistical threshold. What remains are the peaks labeled in Figure 3, the peaks that directly correspond to the beginnings and ends of the RONIs. The program then attempts to associate maximums with minimums by checking which of the minimums are within a predetermined angular distance of the

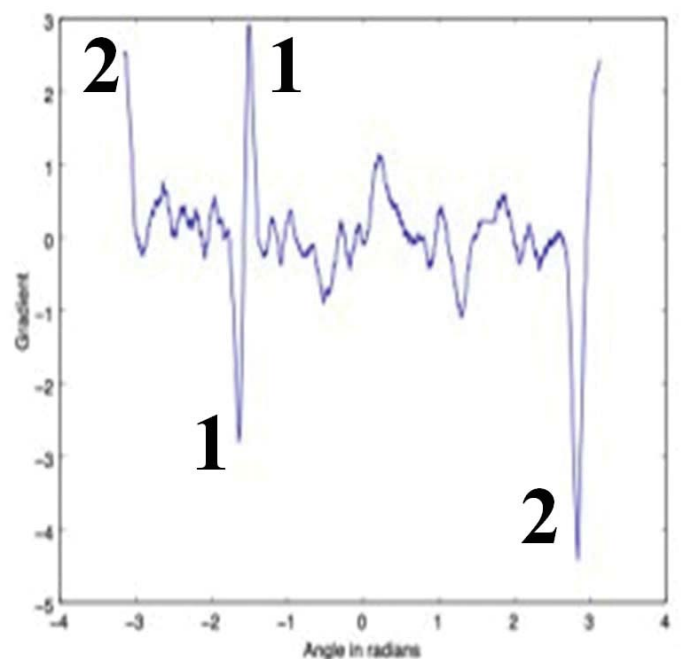


Figure 3. Plot of the gradient of the intensities from Figure 2 after being thresholded and smoothed

maximum. In Figure 3, this leads to the maximum and minimums labeled (1) to be paired up and those labeled (2) to be paired up (with (1) corresponding to (1), the beamstop, from Figures 1 and 2, and (2) corresponding to (2), a damaged region of the detector, from Figures 1 and 2). The program then masks the pixels in-between each pair for each ring, giving an effective mask of these large RONIs, as seen in Figure 4.

Using the gradient method, the entire beamstop (1) is effectively masked and most of the damage region of the detector (2) is covered.

IV. Results

In order to evaluate the effectiveness of the masks, their impact on the analysis must be considered.

Figure 6 shows the integrated intensities of each ring in Q-space, with the pixels binned in rings of width 0.02 Å⁻¹. The plot on the right shows the relative uncertainties of each ring's value, which is the square root of the variance (sigma, or the standard deviation) divided by the mean of the pixels in the bin in order to give a percentage. We can see that the presence of the mask greatly reduces the noise and fuzziness at each peak, which translates to less uncertainty across the integration.

Furthermore, the dip that occurs at ~23 Å⁻¹ is removed by the mask, which leads to a more gradual rise in uncertainty rather than the sudden spike.

V. Conclusion

In its current state, the program does an effective job of masking single-pixel events and large, statistically significant RONIs. Improvements can be made through the tuning of certain parameters, such as the scaling factor of the standard deviation used for the threshold and the window size used for the smoothing before taking the gradients of the rings. Additional work needs to be done to optimize the program's speed and to fit it into the workflow at the XPD beamline. More functions and parameters should be added to the program as well in order to make the mask-writer more flexible for dealing with different detectors and experimental setups.

VI. Acknowledgements

I would like to thank Eric Dooryhee and Sanjit Ghose for their assistance and guidance throughout the Summer. This project was supported in part by the U.S. Department of Energy, Office of Science, Office of Workforce Development for Teachers and Scientists (WDTS) under the Science Undergraduate Laboratory Internships Program (SULI).

VII. References

- Xiaohao Yang, Pavol Juhas, Simon J. L. Billinge, On the estimation of statistical uncertainties on powder diffraction and small angle scattering data from 2-D x-ray detectors, arXiv:1309.3614
- Kieffer, Jérôme, and Dimitrios Karkoulis. "PyFAI, a Versatile Library for Azimuthal Regrouping." Journal of Physics: Conference Series 425.20 (2013): 202012. Web. 23 July 2014.

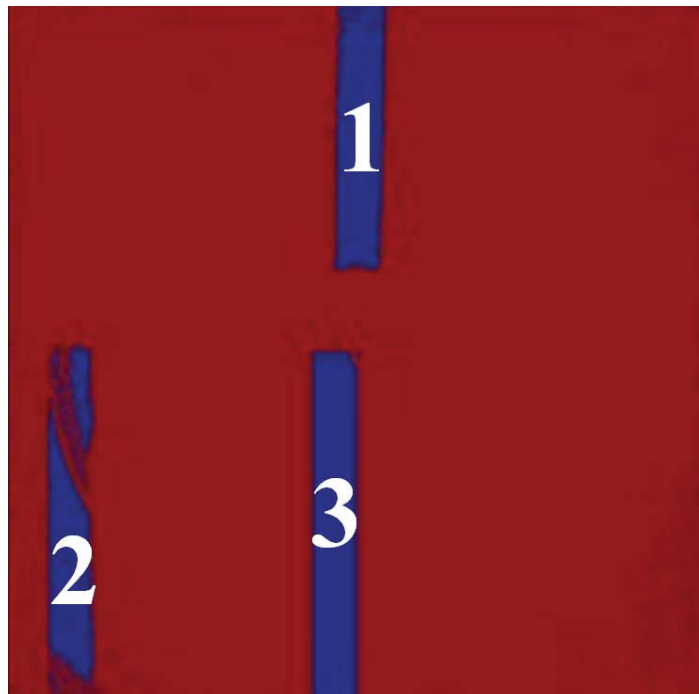


Figure 4. Mask generated by the the gradient method (thresholding already applied) for the Nickel Palladium sample shown above

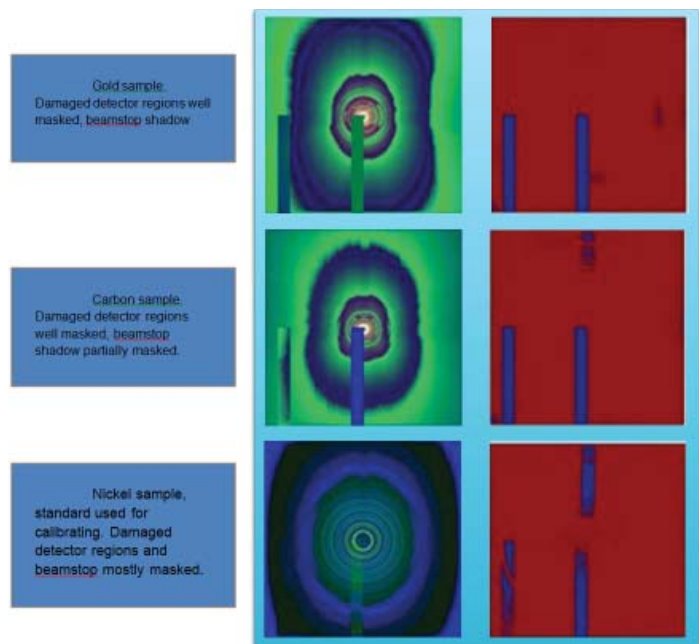


Figure 5. Masks generated for images taken from different samples

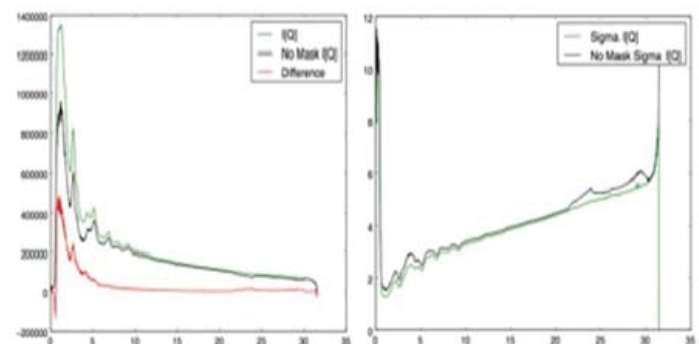


Figure 6. Left: integrated intensities of the gold sample from Figure 5 with and without its mask Right: relative uncertainties of the integrated intensities

Analysis of mass concentration time series and coating thickness of black carbon containing particles

Kristina Michta

Department of Chemistry, University of Massachusetts at Lowell, Lowell, MA 01854

Ernie Lewis and Art Sedlacek

Atmospheric Sciences Department, Brookhaven National Laboratory, Upton, NY 11973

Abstract

Like, greenhouse gases, black carbon (BC)-containing particles play a large role in climate change. BC is formed from incomplete combustion and has the second largest positive direct radiative forcing effect caused by its strong light absorption. A Single-Particle Soot Photometer (SP2) was used to study BC-containing particles in urban and biomass burn plumes during a recent field campaign in Manacapuru, Brazil. Total mass concentrations and coating thickness of BC-containing particles were studied extensively using the SP2. It was found that the mass concentrations of BC-containing particles in the atmosphere drop considerably after about two weeks from about 500 ng/m³ to about 200 ng/m³. Additionally, the longer BC-containing particles stayed in the atmosphere, the thicker a coating they formed. By studying the characteristics and microphysical properties of BC-containing particles and their relation to particle source a better understanding of how BC particle morphology affects radiative forcing can be attained.

I. Background

A. Black Carbon (BC)

Black carbon (BC) is a major component of soot that is formed due to incomplete combustion and can be emitted into the atmosphere as an aerosol through various anthropogenic sources. Most aerosols in the atmosphere are light in color and scatter light creating a cooling effect whereas aerosol particles that contain BC are dark in color and are the strongest light absorbing component of the particle¹. This leads to a strong warming effect in the atmosphere and causes BC to be second in positive direct radiative forcing only to carbon dioxide (CO₂). BC can absorb almost a million times more light than CO₂ but it can only remain in the atmosphere for about two weeks whereas CO₂ stays in the atmosphere for up to 100 years². Additionally, BC can be emitted into the atmosphere with a coating comprised of either organic or inorganic materials or as it stays in the atmosphere it can develop a coating. It is believed that coated BC particles can have an even stronger positive radiative forcing effect on climate change. BC has a strong short term effect on climate change and should be studied extensively to understand how it interacts and behaves in the atmosphere.

B. Sample Sites

According to a study conducted by Lamarque et al.³ in 2010 global emissions of BC came from the following in decreasing quantities; open biomass burnings, domestic/ residential sources, industrial sources, transportation sources, energy/power sources, and other sources. In developing countries, open biomass burning is the primary source of energy and power and techniques such as

slash and burn agriculture are still used. Due to these factors, data collected from Manacapuru, Brazil from the Green Ocean Amazon (GOAmazon) campaign was chosen to be used as the primary data being analyzed and studied. One day of data from the Biomass Burn Observation Project (BBOP) campaign in Memphis, Tennessee was also analyzed extensively in order to develop a baseline to compare known BC properties and characteristics of agriculture burns to BC properties and characteristics of unknown sources from the GOAmazon data.

C. Single Particle Soot Photometer (SP2)

The Single Particle Soot Photometer (SP2) has the ability to detect individual BC particles through laser-induced incandescence while also using scattered light to size any remaining non-BC particles or to size the thickness of BC particle coatings.

According to Figure 1, a YAG crystal diode laser is set up opposite a highly reflective mirror to create a laser beam lasing at 1064 nm. The sample air is lased via inter-cavity, or in the middle of the laser beam, so as to heat the air sample where the laser is most intense. As an uncoated BC particle enters into the laser beam, the particle begins to heat up as it rapidly absorbs light in a Gaussian manner until it eventually incandesces at about 4000K⁵ and is detected by the SP2. For BC particles with coatings, light will first be scattered as the coating evaporates off until the BC core is exposed and can begin to heat until it incandesces. Non-BC particles will enter in the laser beam and purely scatter light. The SP2 can collect hundreds of thousands of particles in a single day of sampling and is an invaluable instrument in studying aerosol particles in the atmosphere.

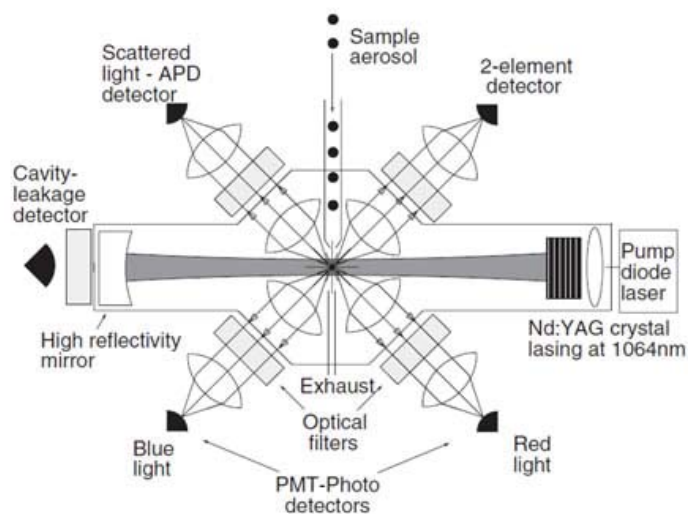


Figure 1. Schematic of SP2⁴

II. Methods

A. Calibration and Comparison of SP2s

During the research conducted this summer the opportunity to calibrate two SP2s and then compare the two instruments presented itself. In order to calibrate each SP2, both the incandescence and scattering channels of the instruments had to be individually calibrated. First the scattering channels for both instruments were calibrated to known particle diameters ranging from 220nm to 400nm with Polystyrene Latex (PSL) spheres. PSL spheres are often used for calibrating instrumentation because they can be set to a known shape, diameter, and refractive index and they are fairly unreactive with other substances. Next, the incandescence channels of the two SP2s were calibrated with Fullerene Soot particles ranging from 60nm to 450nm in diameter using a Differential Mobility Analyzer (DMA). Fullerene Soot particles can be set to a desired shape and will incandesce because they are composed entirely of carbon. With a DMA particles with a desired diameter can be selected for the experiment. Particles with diameters smaller than those used during the calibration were not used because any smaller and the particles will burn up before the SP2 can detect their presence and particles with diameters larger than those used are not likely to appear in nature and were therefore not used in the calibration.

After calibrating the two SP2s, both instruments were set to collect data from ambient air outside the lab for four days, collecting 1 out of every 10 particles. This data was then processed using the analysis software IGOR Pro version 6.20B02 with the PAPI Panel. Each mass concentration in ng/m³ versus time in

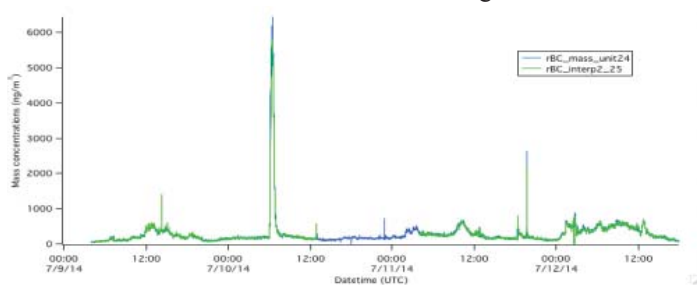


Figure 2: Concatenated mass concentration versus time plots for ambient data collected for Units 24 and 25 overlaid on each other

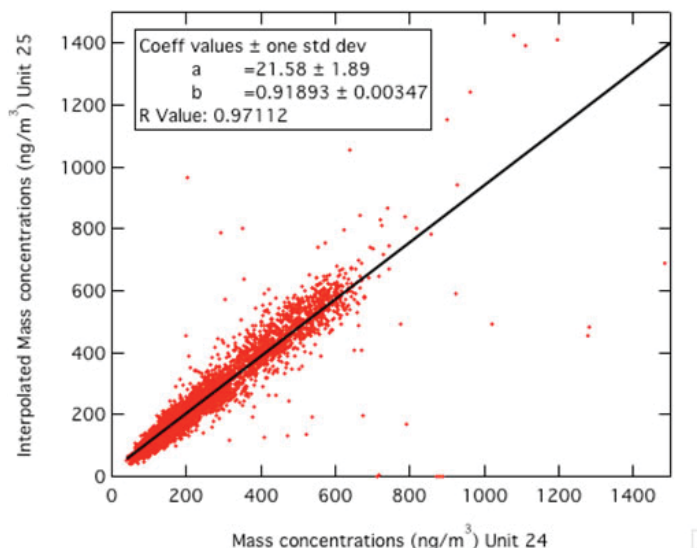


Figure 3: Interpolated mass concentrations for Unit 25 versus mass concentrations for Unit 24

UTC (Coordinated Universal Time) was plotted for each day and then concatenated for each instrument. The concatenated mass concentrations for each SP2 were then plotted against each other to determine how similar the two instruments were to each other.

B. GOAmazon and BBOP Data Analysis

The data from the GOAmazon and BBOP campaigns were both processed and analyzed the same way using the analysis software IGOR Pro version 6.20B02 with the PAPI Panel. The raw data was first converted from .sp2b files to .dat files using the PAPI Panel so that IGOR Pro would be able to read in the files correctly. After the files were converted properly, mass concentration in ng/m³ versus time in UTC plots and coating thickness in nm versus BC mass-equivalent diameter in μm plots were created for each day. A concatenation of the mass concentration plots for the month of April for the GOAmazon data was also created in order to provide an additional perspective in which to view and analyze the data.

III. Results

A. SP2 Comparison

Figure 2 shows the concatenation of the mass concentration versus time plots for SP2 Unit 24 and Unit 25 that were first overlaid to see qualitatively how similar the two units were. It can be seen that the two units agree very closely after Unit 25's data was interpolated to adjust for differences in time between the two units. It can also be seen that for about 12 hours between 7/10/14 and 7/11/14 Unit 25 went down unexpectedly and then came back online without being detected due to the lack of data during this period.

When the concatenated mass concentrations versus time plots

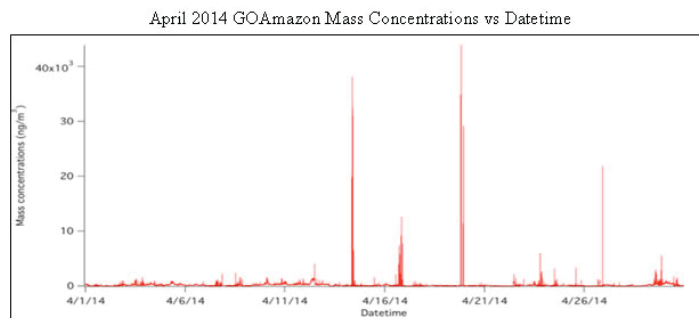


Figure 4: Concatenated mass concentrations versus time for April from the GOAmazon campaign

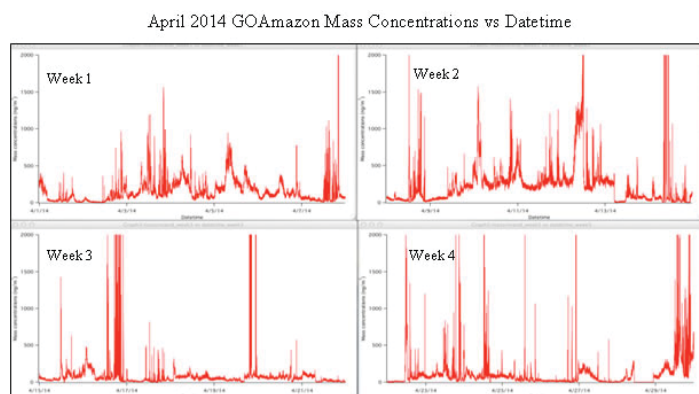


Figure 5: Mass concentrations versus time concatenation for April from GOAmazon on a weekly scale

for Unit 24 and Unit 25 were plotted against each other it can be seen from the resulting R value of 0.97112 that the two units were calibrated very closely to each other.

B. GOAmazon Concatenated Mass Concentration versus Time for April

The concatenated mass concentrations versus time data for April from the GOAmazon campaign is initially difficult to analyze due to sharp and intense peaks occurring throughout the month that is thought to be caused by localized events such as a passing by tractor or nearby generator kicking on.

It is desirable to try and filter out such localized events in order to look for patterns or cycles within the data. Figure 5 shows the concatenated mass concentrations versus time for April broken up into four weeks in order to get a more zoomed in view that ignores the extreme narrow peaks from localized events. This figure shows that for almost the first two weeks of April, the mass concentration is about 500 ng/m³ but for the end of the second week and for the remaining two weeks, the concentrations drops off significantly to about 200 ng/m³.

If one were to zoom in even more looking at only a few days at a time, it could also be seen that around 12:00 UTC or about 8:00 AM local time, there are frequent narrow peaks that almost occur daily.

C. Mass Concentrations versus Time Plots for BBOP and GOAmazon

A single day from the BBOP campaign was selected to analyze in order to develop a baseline of characteristics of BC particles from agricultural burns. In the BBOP campaign, an aircraft was flown over agricultural fields looking for biomass burning events. When a burn was detected, the aircraft was flown through the plume. During this day, five distinct plumes were flown through and the third plume, because it was so large, was pen-

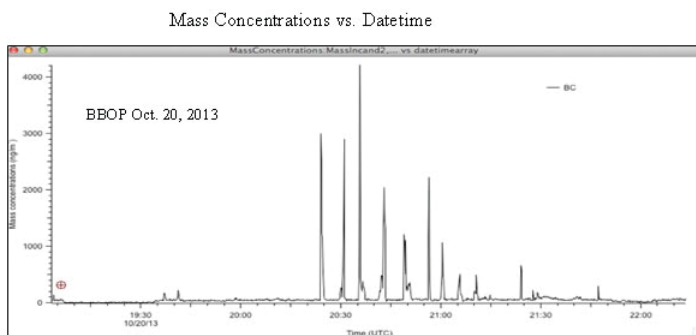


Figure 6: October 20, 2013 mass concentration versus time plot from the BBOP campaign

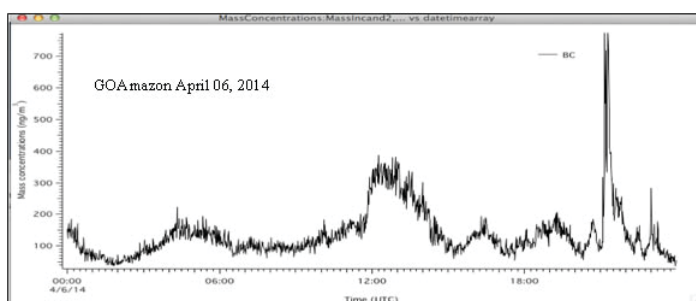


Figure 7: April 6, 2014 mass concentration versus time plot from the GOAmazon campaign

etrated nine different times in the hopes of being able to see BC particles age over time within a single plume. Figure 6 shows the mass concentrations versus time plot for October 20, 2013. It can be seen from this figure that the agricultural burns tend to have very defined and narrow peaks in the mass concentrations. It was also observed that when looking at the different penetrations for the third plume that between the first and last penetrations, the peaks tend to become less intense and a little bit broader.

When looking at a single day from the GOAmazon data, the figure below shows more broad peaks with no clear definition between being inside an advecting plume and outside a plume.

D. Coating Thickness Plots for BBOP and GOAmazon

The following coating thickness versus BC mass-equivalent diameter plots corresponds to the second and fourth penetrations of the third plume from the October 20, 2013 data from the BBOP campaign. Figure 8 shows that qualitatively the BC particles from the fourth penetration have a thicker coating than the particles sampled from the second penetration.

Figure 9 corresponds to the coating thickness versus BC mass-equivalent diameter plots for the April 6, 2014 GOAmazon mass concentration for the broad peak around 12:00 UTC and the narrower peak around 21:00 UTC. It can be observed that the broader peak at about 12:00 UTC has a larger coating thickness on the BC particles than those found in the narrower peak around 21:00 UTC.

IV. Discussion

The research performed this summer provided an opportunity to gain a great deal of information on how BC particles differ from different sources and how they interact with the atmosphere dif-

BBOP Oct. 20, 2013: Coating Thickness vs. BC Mass-equivalent Diameter

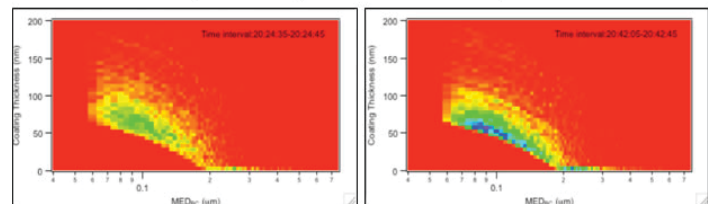


Figure 8: Left: Coating thickness versus BC mass-equivalent diameter plot for the second penetration of the third plume from the corresponding mass concentration versus time plot. Right: Coating thickness versus BC mass-equivalent diameter plot for the fourth penetration of the third plume from the corresponding mass concentration versus time plot.

GOAmazon April 06, 2014: Coating Thickness vs. BC Mass-equivalent Diameter

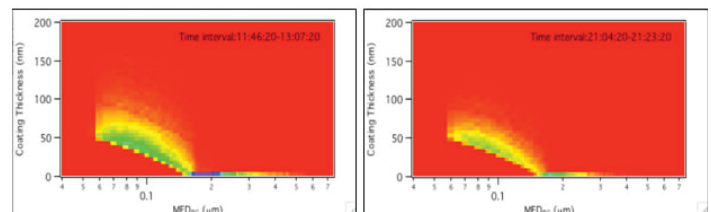


Figure 9: Left: Coating thickness versus BC mass-equivalent diameter plot for the broad peak at about 12:00 UTC from the corresponding mass concentration versus time plot. Right: Coating thickness versus BC mass-equivalent diameter plot for narrow peak at about 21:00 UTC from the corresponding mass concentration versus time plot.

ferently. By being able to compare two different SP2 instruments after calibrating them both helps to validate the data collected at different sites on different field campaigns. By being able to show that the two instruments were very similar it can reassure scientists that if properly calibrated, data collected from campaigns can be compared closely with great confidence and without having to adjust greatly for differences between different units.

When looking at the drastic drop in mass concentration for the GOAmazon April concatenation on the weekly scale it can be concluded that the decrease was due to BC being deposited out of the atmosphere through a rain event. It is known that BC can stay in the atmosphere for up to two weeks which is supported by the mass concentrations dropping off after almost two weeks' time. It is thought that fresh BC with no coating is very hydrophobic allowing it to stay in the atmosphere. However, as it stays in the atmosphere it can develop an organic or inorganic coating around the BC which would be hydrophilic allowing water droplets to condense on the surface to form clouds and eventually be rained out through wet deposition. This theory appears to be supported from the data collected from the GOAmazon campaign.

With regards to the spikes in narrow peaks around 12:00 UTC or about 8:00AM local time, this could be indicating that a more urbanized plume of air with fresher BC particles is potentially advecting over from Manaus, Brazil which could be due to an increase in morning activity with people heading to work and starting off the day.

By comparing the two mass concentrations versus time plots from the BBOP and GOAmazon campaign it can be seen that the air sampling is very different and therefore the type of air sampling must be taken into account before collecting data. For instance, the plumes from BBOP are well defined and last for a very short amount of time; therefore particles should be collected as frequently as possible to assure that enough data is being collected. Compared to the GOAmazon data, particles can be collected at slower rates because air plumes are advecting over the SP2 site much slower and more gradually.

It is thought that when looking at mass concentration versus time plots that sharp narrow peaks indicate fresher BC particles that have little or no coating and broad peaks indicate older BC particles with thicker coatings. This is thought to occur because the longer a BC particle is in the atmosphere, the longer it has to mix with other substances in the atmosphere and develop a coating. This theory is supported by Figures 8 and 9. In Figure 8 the plot on the left indicates BC particles from the second penetration of plume 3 and the plot on the right is from the fourth penetration from the third plume. It is given that the second penetration of a plume will sample fresher particles than those of a fourth penetration on the same plume and it would be expected that particles from the second penetration would have a thinner coating than those of the fourth penetration. This expectation is confirmed when comparing the two plots in Figure 8. Likewise Figure 9 compares the coating thickness from a plume that created a broad peak on the mass concentration plot and a narrower peak on the same plot. It would be expected that the broader peak would have more thickly coated particles than those from the narrower peak and again these expectations we met when comparing the thickness plots.

Being able to understand the characteristics and properties of BC particles in the atmosphere from different sources can greatly aid in scientists' understanding of how these particles interact in

the atmosphere and their effects on climate change more accurately and can aid in the prediction of future effects as well as finding new ways to counteract negative impacts. Like any good research there are always areas that can be improved. In the future it could be beneficial to determine the exact size of particle coatings as well as the composition of these coatings. Thicker coatings can have greater or different impacts on the climate and currently the method used to determine coating thickness is only a place to start due to the fact that when calculating the thickness, BC particles are thought of as perfect spheres with even shell coatings. In reality BC particles tend form wispy, fractal-like aggregates where these structures can be unevenly coated. Additionally, different types of coatings will interact differently in the atmosphere as different side reactions and products are formed with different substances, allowing for different types of impacts on climate. It could also be helpful to specifically track wind directions throughout the day at sample sites to help eliminate speculation of where air plumes are originating from and what their sources are. Having the ability to pinpoint the source of air plumes can aid in the analysis of data greatly and make explanations of data and particle behavior more accurate.

V. References

1. Institute for Governance & Sustainable Development. <http://www.igsd.org/blackcarbon/index.php>. 2009. (accessed July 20, 2014)
2. United States Environmental Protection Agency. <http://www.epa.gov/blackcarbon/basic.html>. (accessed July 20, 2014)
3. Lamarque, J.F.; et al.; US EPA. Historical (1850–2000) gridded anthropogenic and biomass burning emissions of reactive gases and aerosols: methodology and application. *Atmos. Chem. Phys.*, 2010, 10, 7017-7039.
4. Schwarz, J.P.; et al. Single-particle measurements of mid-latitude black carbon and light-scattering aerosols from the boundary layer to the lower stratosphere. *J. Geophys. Res.: Atmos.*, 2004, 111.
5. Huang, X.F.; et al. Black carbon measurements in the Pearl River Delta region of China. *J. Geophys. Res.: Atmos.*, 2011, 116.

VI. Acknowledgements

This project was supported in part by the U.S. Department of Energy, Office of Science, Office of Workforce Development for Teachers and Scientists (WDTS) under the Science Undergraduate Laboratory Internships Program (SULI).

Chemo-enzymatic development of novel sugar precursors for F-18 labelled Positron Emission Tomography imaging probes

Monique Mohammed

Adelphi University, Garden City, NY 11530

Mentor: Andrew Gifford

Brookhaven National Laboratory, Bioscience Department, Upton, NY 11973

I. Preface

Within the bioscience department at Brookhaven National Laboratory the main focus of the research within the subsection of the lab is sucrose fluoridation through a novel chemo-enzymatic reaction. This national laboratory is funded by the Department of Energy, so the main focus of this lab is to understand the biochemical mechanisms of sucrose transportation within the plant so that it can be further studied to allow for the understanding of the disaccharide sugar.

II. Background

Bioethanol is an alcohol made by fermentation. It is part of a worldwide effort in replacing fossil fuels with alternative sources of energy. However, making this fuel choice economically profitable will require engineering biofuel plants to maximize their production of fermentable sugars. Sucrose, the main transported plant sugar is readily fermentable to bioethanol.

Sucrose is synthesized in leaves by photosynthesis and transported to roots, seeds, stems, etc. (sinks). To engineer plants to maximize the sucrose flux and storage into sink regions of the plant, it is important to understand the different biochemical factors controlling sucrose uptake and metabolism in these sink regions. "Sinks" are comprised of non photosynthetic roots, seeds and other carbohydrate storage structures, including those important for biofuels a prime example being sugar cane stems. In sink regions of the plant, sucrose may be unloaded from phloem by several possible routes: (i) a symplastic route via plasmodesmata, (ii) an apoplastic route in which intact sucrose is transported into parenchyma cells, and (iii) an apoplastic route in which hexoses are transported into parenchyma following hydrolysis of sucrose by invertase. Deoxy and florin

Towards this objective, we have been synthesizing novel sucrose analogues as probes to examine the biochemical pathways involved in sucrose storage in sweet Sorghum, a biofuel plant that

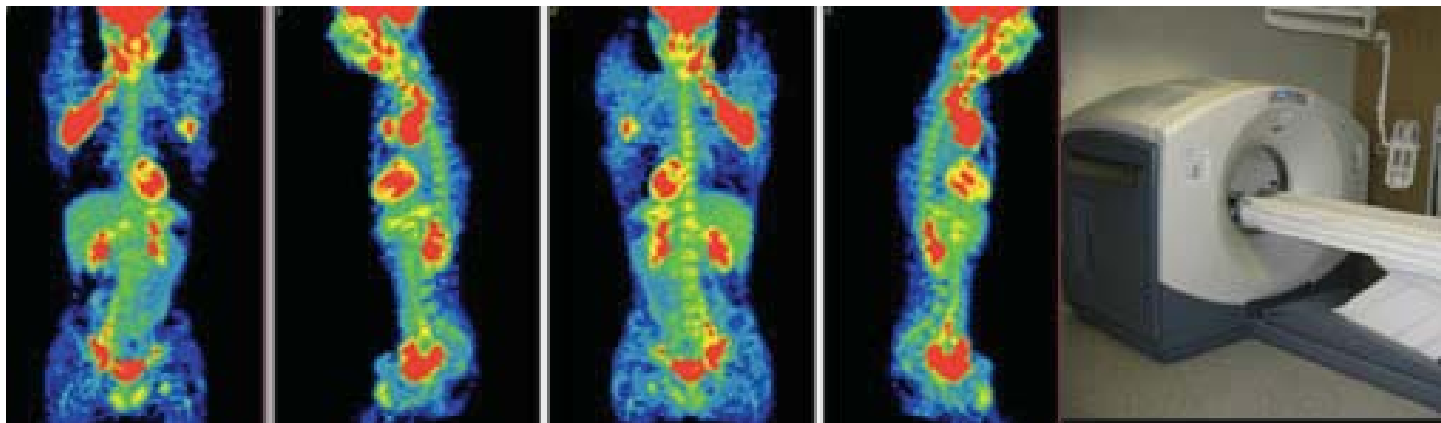
is suitable for temperate climates such as in the US. Novel radiofluorinated sucrose derivatives were synthesized by employing a new chemo-enzymatic synthesis route, starting with readily available naked sucrose. As the first step in the synthesis scheme, several industrially available lipase and protease enzymes were examined for regioselective de-esterification under incubation with sucrose over several days to give sucrose heptaacetate.

Fluorinated and deoxysucrose analogues have been proven useful in probing the substrate specificity and roles of sucrose processing enzymes and transporters in plants. Sucrose is the main transported disaccharide sugar within plants. The sugar is synthesized in the leaves and then transported to sink regions of the plant such as roots and seeds where it is used for either respiration, biosynthesis, or is stored.

III. Basic Science: Medical Diagnostics

Positron emission tomography (P.E.T.) imaging is a functional imaging technique that produces a three-dimensional image of functional processes in the body. P.E.T. is both a medical and research tool. This functional imaging technique is commonly used to detect disease conditions like cancer, neurodegenerative diseases, etc. The system detects pairs of gamma rays emitted indirectly by a positron-emitting radionuclide (tracer), which is introduced into the body on a biologically active molecule. A common biologically active molecule chosen for PET is 2-deoxy-2-[18F] fluoroglucose (FDG), which is an analog of glucose.

To conduct the scan, a short-lived radioactive tracer isotope is injected into the living subject (usually into blood circulation). The tracer is chemically incorporated into a biologically active molecule. FDG, a sugar, typically has a waiting period of an hour before the active molecule becomes concentrated in tissues of interest. 18F-FDG is a good indicator of glucose uptake and cell viability and is of importance in disease conditions like cancer or neurodegenerative conditions where the glucose metabolism in



specific tissues is significantly changes. As the radioisotope undergoes positron emission decay, it emits a positron, an antiparticle of the electron with opposite charge.

IV. Exploration

A. Enzymatic De-acylation of Protected Sucrose

To begin this experiment we started with the deacetylation reaction through starting with the sucrose octaacetate (SOA). Because different isomers of hepta products are inseparable by regular chemical separation techniques hydrolytic enzymes provide a unique advantage because they are known to have regioselective action on their substrates. As the first step in the synthesis scheme, several hydrolytic enzymes were examined for regioselective de-esterification under incubation with SOA over several days to five sucrose heptaacetate.

Figure. Chemo-enzymatic synthetic route. (i) Enzyme, Solvent combination, Overnight incubation at 37°C (ii) (Tf)2O, Py, DCM (iii) K18F, K2CO3, K2.2.2., DMSO (iv) Aq. KOH.

SOA was incubated with the solvent and enzyme overnight. The amount of enzyme that was used depended on various factors: cost and number of lipase units/unit weight of the commercial form of the enzyme. Being that this is an exploratory study the quantities of the enzymes are not strictly enforced. The above solution was placed at 45 degree angle on an incubator at 37 deg C and 150 rpm for a designated amount of days with gentle shaking. Following incubation, the mixture was extracted into ether and washed with water. The method used is liquid-liquid extraction. Water and ether are immiscible, they form two different layers during the recovery of the reaction products. SOA along with its other products are soluble in the ether layer, while the other impurities from the left over enzyme is in the water layer. The two also have very distinctively different densities; the ether layer is lighter and becomes the upper layer in the liquid-liquid extraction, which allows for much easier separation. The organic layer is dried over

sodium sulfate, and the organic solvents are evaporated using the speedvac (for smaller analytical volumes). Finally the remaining product is redissolved in an acetonitrile/water (1:1) mixture, which prepares the product for LC-MS. All reagents and solvents were acquired from Sigma Aldrich.

V. Analytical Studies

In order to determine the success of the above scheme it is important to examine if (i) the mono de-acylated product is present (ii) the position of mono de-acylation in the SOA molecule is unique and novel.

The reaction product after purification from the above scheme contain a mixture of unreacted sucrose octaacetate (SOA), along with possible hepta and hexaacetate products. All of these compounds have different chemical structures and different levels of hydrophobic character. They can easily be separated by liquid chromatography techniques like Thin Layer Chromatography (TLC) and LC-MS (Liquid Chromatography-Mass spectrometry).

VI. Analytical Conditions

A. Thin layer Chromatography (TLC)

Silica gel plates are used. A 10mg/ml solution of sucrose octaacetate is used as a standard. 2µL spots are used for the analysis. The spots are developed in an enclosed saturated solvent chamber of 70% Ethyl Acetate and 30% Hexane with treatment with Sulfuric Acid/Naphthol reagent. TLC was used just for analytical purposes in this part of the lab.

B. High Performance Liquid Chromatography/ Mass Spectrometry (HPLC-MS)

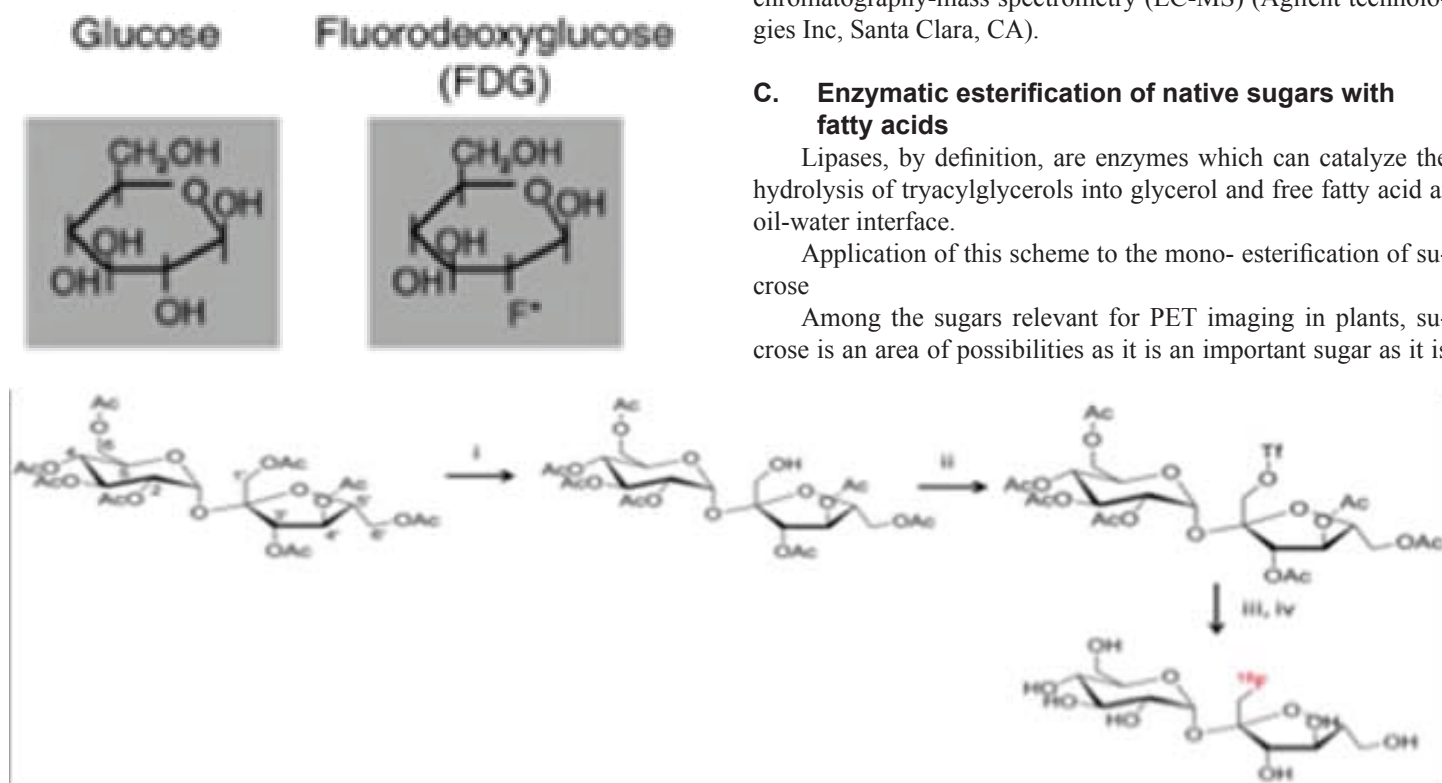
A small volume of the reaction products is pipetted into an autosampler vial, solvents are evaporated by speedvac and re-dissolved in 1mL of Acetonitrile/ distilled water (1:1). Mass spectrometry data was obtained using an Agilent 6300 Ion Trap liquid chromatography-mass spectrometry (LC-MS) (Agilent technologies Inc, Santa Clara, CA).

C. Enzymatic esterification of native sugars with fatty acids

Lipases, by definition, are enzymes which can catalyze the hydrolysis of tryacylglycerols into glycerol and free fatty acid at oil-water interface.

Application of this scheme to the mono- esterification of sucrose

Among the sugars relevant for PET imaging in plants, sucrose is an area of possibilities as it is an important sugar as it is



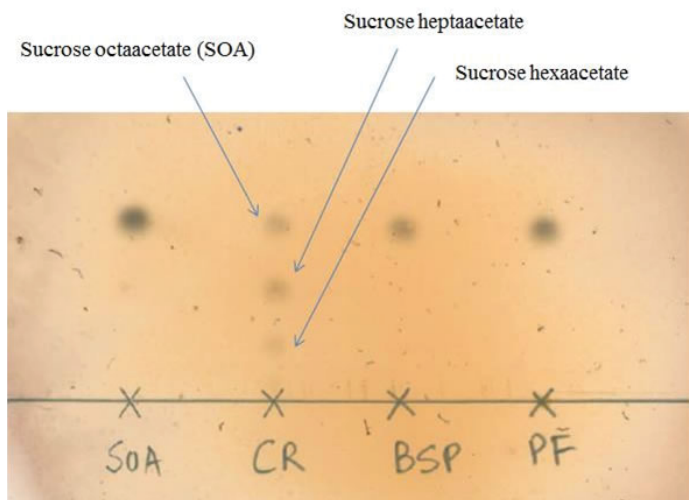
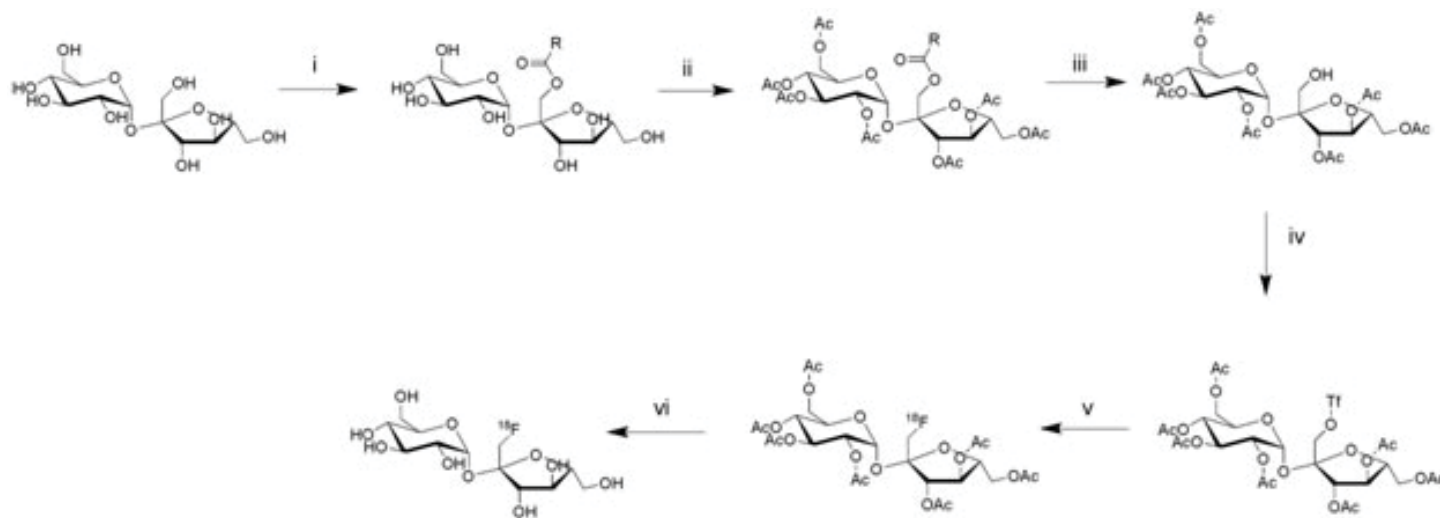
the main transported sugar in plants.

This exploratory study was meant to open up a new method of development of PET tracers, especially fructose based. One of the key factors in the success of the above reaction scheme is the maintenance of anhydrous conditions in the reaction medium. This is because the presence of even trace amount of moisture will prevent product formation by favoring the hydrolysis of the ester back into the original sugar in the reverse direction of the equilibrium. In order to prevent this, anhydrous conditions are maintained by dessicating all reagents prior to use, adding new reagents under argon and using in-situ drying agents like molecular sieves. This exploratory study can be continued with other fatty acid and sugar combination. Effectiveness of other in-situ drying agents and ingenious techniques to maintain anhydrous conditions during incubation can also be investigated in future.

VII. Results

A. Enzymatic De-acylation of Protected Sucrose Results

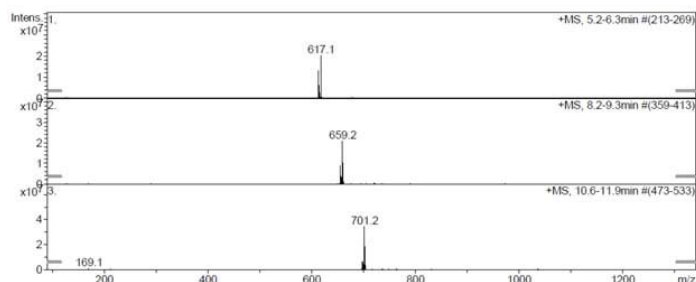
Representative Thin layer chromatography (TLC) on enzymatic deacetylation reaction



Representative HPLC-MS trace showing the corresponding m/z (mass/charge) values for the peaks in the Total Ion Chromatogram (TIC) trace above. These values help identifying the chemical composition of each chromatogram peak representing each compound produced in the enzymatic de-acylation reaction of SOA.

B. Enzymatic esterification of native sugars with fatty acids

Lipase	Solvent System	Days of Incubation	Product
Porcine Pancreatic Lipase	1	1	No
Thermomyces Lanuginosus	2	2	No
Asperigillus Niger	2	2	No
Rhizopus Arrhizus	2	2	No
Rhizopus nievus	2	2	No
Mucor javanicus	2	2	No
Burkholderia cepacia	2	2	No
Pencillin ceptacia	2	2	No
Bacillus Lichenformis	2	2	No



VIII. Discussion

This study demonstrates the development of F-18 labelled PET precursors using a chemo- enzymatic route. Sucrose octaacetate and most enzymes used here are cheaply and widely available in commercial scale, and therefore this reaction is cheap and attractive for industrial scale productions. A number of experimental factors contribute to the success and optimization of the above reactions. One of those factors is the solvent system. The solvent systems used here are mainly organic i.e. diisopropyl ether and DMF. These solvents help partially dissolve the sucrose octaacetate (a highly lipophilic molecule) so that the enzyme can act at the lipid-water interface. The enzyme system is often biphasic with aqueous buffer of pH for optimized enzyme activity. These organic solvents are known to be well tolerated by enzymes as they help in maintaining the enzyme 3D configuration and thus prevents denaturation. However, excessive quantities of DMF/DMSO are known to denature enzymes. From the data presented above, it can be observed that most enzymes work better in the presence of aqueous buffer along with the organic solvent but only up-to a certain extent. This is because optimized activity of the enzyme depends on the presence and quantity of water in the microenvironment of the enzyme in the reaction medium[6]. Other factors like pH, enzyme form and kinetics also play a role in the enzyme activity and are all closely related to the solvent system used

IX. Importance of 18F in PET imaging

Positron Emission Tomography is a medical imaging technique used for measuring the spatial and temporal distribution of positron emitters within the human body. The imaging takes place by simultaneous detection of similar energy annihilation photons generated from the same point but 180 degree phase shifted tracing back a linear path back to the detector. Advances in radiochemistry and instrumentation go hand in hand in making PET a reliable medical diagnostic tool [1]. Several important factors go into the best choice of a PET radionuclide, some which are half-life, specific activity and range along with ease and cost of its production. Below is a table illustrating these factors as compared between different available positron emitters

X. Limitations

Several reaction parameters like choice of solvent and pH, incubation time and activity of enzyme in organic solvents were optimized for the success of the chemo-enzymatic reaction scheme. One of the biggest challenges to enzyme screening experiments was the hydrophobic nature of the enzyme substrate SOA which is only soluble in organic solvents, however the enzyme itself works best in aqueous media. The reaction therefore occurs only at the aqueous and organic solvent interface within the reaction vessel which is rather small for optimized enzyme activity.

Limitations to the widespread use of PET arise from the high costs of cyclotrons needed to produce the short-lived radionuclides for PET scanning and the need for specially adapted on-site chemical synthesis apparatus to produce the radiopharmaceuticals after radioisotope preparation.

The challenges in synthesizing radiofluorinated sugars at a defined position in the sugar molecule stems mainly from the fact that native sugars like sucrose have a number of chemically identical hydroxyl groups. Additionally, for sucrose, the glycosidic bond between the glucose and fructose moieties is sensitive to

cleavage at extreme pH conditions.

One of the major limitations of the research is that it is majorly funded by the U.S. Department of Energy, this greatly changes the focus of the research to be purely focused on how it can aid the environment through biofuels. There can, however, be many other applications of this research for other aspects besides bioethanol production.

XI. Implications

Another aim of the lab is to validate [¹⁸F] fluorosucrose as a PET tracer for sucrose transport and metabolism in living plants. The labeled sucrose is used with strategies to artificially increase sink strength targeting phloem unloading could be used to promote photosynthesis in leaves, and increase yield of fermentable components, such as sugars, starch, cellulose, or overall biomass.

Once the sucrose is able to be properly ¹⁸F then it will be able to be used in P.E.T to determine the relative roles of the transported sucrose.

XII. Acknowledgements

This project was supported in part by the New York State Collegiate Science and Technology Entry Program (CSTEP) at Adelphi University under the CSTEP-Supplemental Undergraduate Research Program (SURP) at Brookhaven National Laboratory. Special thanks also goes to all the administration in the Office of Educational Programs at BNL for all of their support with the program. Also, Thank You to my research mentor Dr. Gifford for all of his guidance while in the program, and finally I want to give special thanks to Madhura Som, the graduate student who I worked along side in the lab for all of her assistance and guidance throughout the program.

XIII. References

1. Gifford AN, Bennett CV, Fowler JS. Radiosynthesis of the fluorinated sucrose analogue, 1'-[¹⁸F]fluoro-1'-deoxysucrose. *Journal of Labelled Compounds and Radiopharmaceuticals*. (2012) 55: 441-446
2. Plou FJ, Cruces MA, Ferrer M, Fuentes G, Pastor E, Bernabe M, Christensen M, Comelles F, Parra JL, Ballesteros A. Enzymatic acylation of di- and trisaccharides with fatty acids: choosing the appropriate enzymes, support and solvent. *Journal of Biotechnology*. (2002) 96: 55-66
3. Ferrer M, Cruces MA, Bernabe M, Ballesteros A, Plou FJ. Lipase-Catalyzed Regioselective Acylation of Sucrose in Two-Solvent Mixtures. *Biotechnology and Bioengineering*. (1999) 65 (1) : 1-16
4. Grochulski P, Li Y, Schrag JD, Cygler M. Two conformational states of *Candida rugosa* lipase. *Protein science*. (1994) 3: 82-91.
5. Rao KS, Rajendran S, Rajeshwara AN, Prakash V. Structural Stability of Lipase from Wheat Germ in Alkaline pH. *Journal of Protein Chemistry*. (1991) 10:291-299.

Electrical characterization of silicon photo-multipliers

J. Mwathi

Technology Department, Alabama A&M University, Normal, AL 35759

C. Woody and S. Stoll

Physics, Brookhaven National Laboratory, Upton, NY 11973

Abstract

Silicon photo-multipliers (Si-PM) are single photon sensitive, semiconductor devices built from Avalanche Photo Diodes (APDs) working in the Geiger mode. The Si-PM detectors provide an attractive solution for the detection of signals with low numbers of photons and are suitable candidates to replace Vacuum Photo-Multiplier Tubes (PMTs). They offer advantages over both PMTs and the APDs, like their compactness, insensitivity to magnetic fields, high gain (10^5), ability to be operated at moderate bias voltage (normally lower than 100 volts), and excellent timing properties. These characteristics make them suitable for applications in several fields of high energy physics and medical imaging. At Brookhaven National Laboratory, silicon photo-multipliers have been suggested as the readout device to be used in the upgraded sPHENIX electromagnetic calorimeter and future Positron Emission Tomography (PET) medical imaging systems. By characterizing the properties of these detectors which can limit the usefulness of these detectors, we were able to determine dark rate, gain, breakdown voltage, photon detection efficiency (PDE), and cross talk. Hamamatsu and SensL SiPMs of different pixel sizes were characterized in a cooling chamber to reduce the thermal noise generated from exposure to high temperatures. Other SiPM samples were irradiated and characterized to see how radiation affected their efficiency. We characterized these SiPM samples using lab instruments including a Picoameter and a digital oscilloscope. This allows us to determine the detector's response when subjected to an increase or decrease in bias voltage and different light intensity exposure in a controlled temperature below room temperature. This, in turn, helped us determine which detector designs were best suited for different applications and to design the circuits and electronics needed to operate the SiPMs. A Lab view program controlling and reading out the Keithley Picometer via an IEEE-GPIB interface was developed to automate the measurement of dark current as a function of bias voltage.

I. Introduction

Silicon Photo multipliers are made up of a matrix of avalanche photodiodes connected in parallel and operated above breakdown voltage in Geiger mode. SiPM devices provide high gain with low voltage input and a fast response time. SiPMs also known as Multi-Pixel Photon Counters have been suggested as the desired readout detectors for the proposed sPHENIX upgrades here at Brookhaven National Laboratory. These upgrades will include a Hadronic calorimeter which will consist of steel plates with scintillating tiles in between, that are readout with wave shifting fibers and an electromagnetic calorimeter which will be a tungsten scintillating fiber design with a radiation length ~ 7 mm and a Moliere radius ~ 2 cm. Both calorimeters will use SiPMs as readout sensors. These sPHENIX upgrades will enable a compre-

hensive measurement of jets in relativistic heavy ion collisions; provide enhanced physics capabilities for the studying of nucleon-nucleus collisions. As part of a sPHENIX R&D group we characterized SiPM devices of different pixel size, from different vendors mainly Hamamatsu and SensL to study their performance to help us determine which SiPM designs were best suited for application. These studies helped determine how factors such as SiPM pixel size, number of pixels, increase in bias voltage, increase in photon flux, increase in temperature and exposure to radiation, influence SiPM characteristics. Thermal annealing and high voltage forward biasing were used in an attempt to repair the irradiated SiPM. Different lab instruments were used to develop lab setups for use in different characteristic studies.

II. Characterizations

As part of an R&D team we characterized SiPMs of different pixel sizes from different vendors to see which of this SiPMs would best be suited for application, some of the SiPMs characterized are shown in the table below. This paper gives a detailed summary of all characteristic studies performed which include current as a function of voltage (dark current), optical saturation and pre and post radiation hardness we also performed thermal annealing and high voltage forward biasing in an attempt to repair the damaged irradiated SiPM.

SIPM	Pixel size	Vop
Hamamatsu S12572 #18	25 μ m	68.91v
Hamamatsu S12572 #A0002	10 μ m	70.63v
Hamamatsu S12572 #A0004	15 μ m	68.83v
Hamamatsu S12572 #A0008	50 μ m	68.06v
SensL MicroSM-60035-X13 #50	50 μ m	29.5v
SensL MicroSL-60035-X13 #39	10 μ m	30.2v
Hamamatsu S12572 #12	25 μ m	67.89v

Table 1 showing SiPMs characterized

A. Current as a function of Voltage (Dark current)

Output current produced when a SiPM device is operated in the absence of light is called the dark current, caused by diffusion of single minority carriers injected from the peripheral boundaries of the active area depletion layer and thermally emitted carriers from Shockley-Read-Hall defects. In order to better understand the effect of dark current as a function of voltage eight SiPMs as shown in the table below were characterized. A lab setup that includes a Keithley picoameter and a temperature chamber were setup as shown in Fig1 below. The temperature chamber maintains the SiPMs temperature at 25 $^{\circ}$ c and also acts as our dark chamber

since it is fully enclosed, the SiPM is mounted on a readout circuit board that we designed, assembled and placed inside the temperature chamber. The Keithley picoameter was used to gradually increase the voltage from zero to operating voltage of the SiPM and measure the output current from the SiPM manually. The output current was recorded and plotted into I-V charts in Sigma Plot to help us better understand the linear increase in reverse bias current with increase in reverse bias voltage. We later adopted a PC based approach in this setup that combines programmable software with hardware connectivity to automate measurements acquisition from a third party instrument. A lab view program was developed to help automate this process by controlling the Keithley Picoameter via an IEEE-GPIB interface bus. The IEEE-GPIB interface bus communicates with the Keithley picoameter by sending DDC commands from the lab view VI. Graphical user interface of the lab view program shown in figure 1 below allows the user to remotely control the Keithley picoameter 6847 enabling us to automate the process of increasing the reverse bias voltage from zero to operating voltage, measure output current as a function of input voltage, graphically visualize measured points on a scaled XY graph as shown in Fig3 and later the user can store the XY points as a Microsoft excel file.

B. Optical Saturation

After discharge a cell needs time to recharge back to over voltage after dropping to breakdown voltage, in order for another photon to be detected. If a cell is triggered while recharging the output charge that corresponds with the second photon will be reduced this is referred to as saturation. Saturation of the SiPM devices is a function of Photon detection efficiency, over-voltage, Light intensity and pulse frequency. The finite pixel number (m) results in the saturation of the SiPM signal with increasing light intensity. It affects device linearity at high photon flux rate, and limits the range of signals that the SiPM can be used to measure. The lab setup shown in figure 4 below including an ADC (not

shown) were setup to measure the saturation curve of SiPMs at operating voltage as we increase the LED light intensity. A Hamamatsu PMT R4598Q with a known gain of (4.6×10^4) at operating voltage of (1250v) and known quantum efficiency of (0.27) at 420nm was used to calibrate the photon flux. Since the area of the PMT window is larger than that of the SiPM a 3/8 aperture was used to normalize the active areas. An integrating sphere was used to diffuse the light from the LED evenly on to the 3/8" PMT aperture; the LED was pulsed at 114 KHz and the light intensity was gradually increased until the PMT was saturated. An oscilloscope and an ADC system were used to readout the PMT pulse peaks. The following formulas were used to calibrate the photon flux;

$$\bullet ((\text{ADC}_{\text{peak}} \text{ ch}) \times (.25\text{pC}/\text{ch}) \times (6.25 \times 10^6 \text{ e}/\text{pC})) / (4.6 \times 10^4 (\text{gain})) = \text{detected photoelectrons}$$

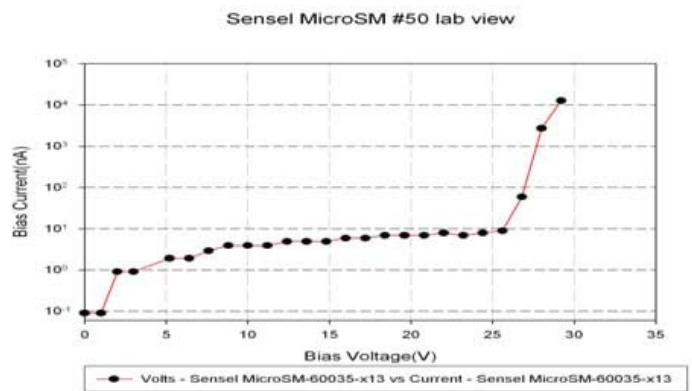


Figure 1 Lab view Graphical User Interface

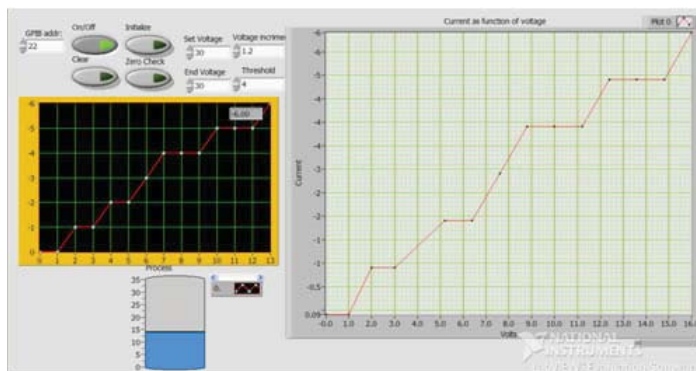
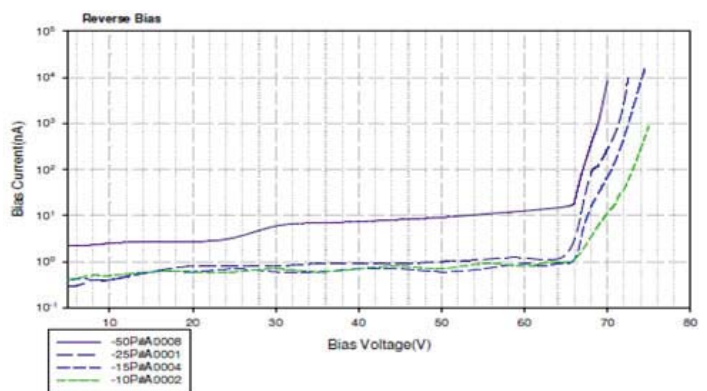
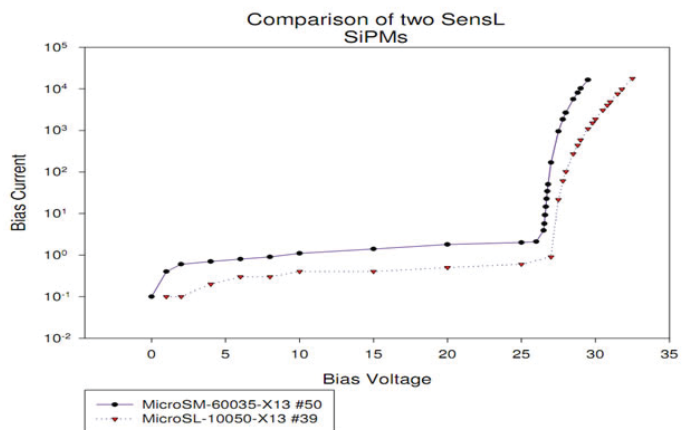


Figure 2 Lab view GUI plotting I-V measurements

Plot 1 Lab view data plotted in Sigma plot



Plot 2 Sigma plot comparison of 4 different pixel size Hamamatsu SIPMs

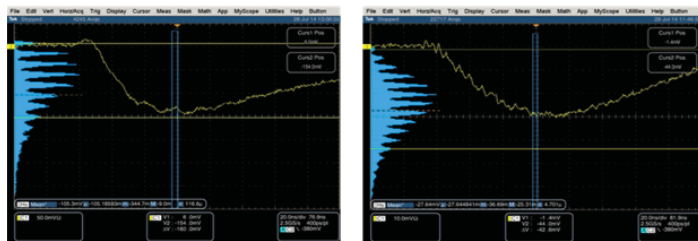
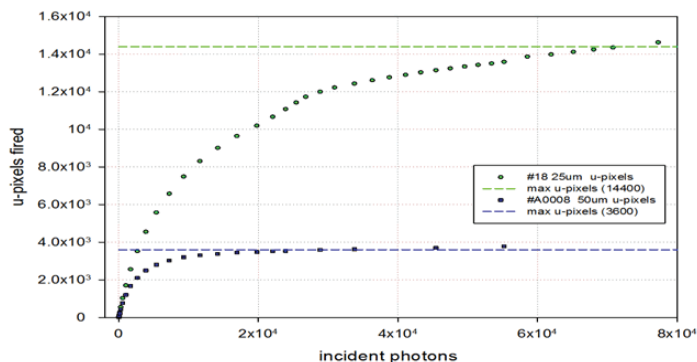


Plot 3 Sigma plot comparison of 2 different pixel size SensL SIPMs



Figure 3 (above)
Lab setup to
measure saturation
curve

Figure 4 (left) Inte-
grating sphere



Plot 4 Hamamatsu (25μm) Vs Hamamatsu (50μm) SiPM saturation
curve

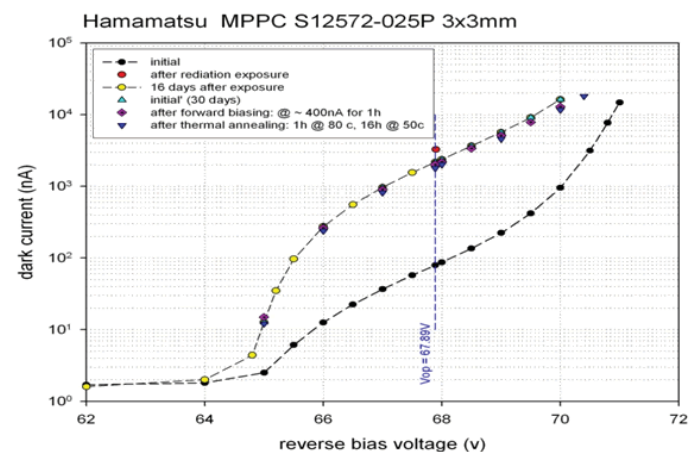
- $((\text{detected photoelectrons}) / 0.27 (\text{quantum efficiency})) = \text{Incident Photons on PMT}$
- $\text{incident photons on PMT} \times 0.602 (\text{area correction}) = \text{incident photons on SiPM}$

After calibrating the photon flux we proceeded to measure and compare the saturation curve of two different SiPM devices of different sizes and micro pixel sizes. Fig6 shows a plot of pixels fired as a function of incident photons as read out by the ADC system and plotted in Sigma plot.

Oscilloscopes was also used to readout the pulse of three different SiPMs and plot the histograms shown in the figures below, which show a peak for every incident photon counted which was equal to number of pixels fired.

C. SiPM radiation hardness

Since SiPM devices have been suggested as readout sensors for calorimetry in experiments involving nucleon-nucleus collisions, and since most of the damage to SiPM devices is expected to be caused by neutrons, the characterization of the SiPMs was necessary in order to study the effects of radiation on these de-



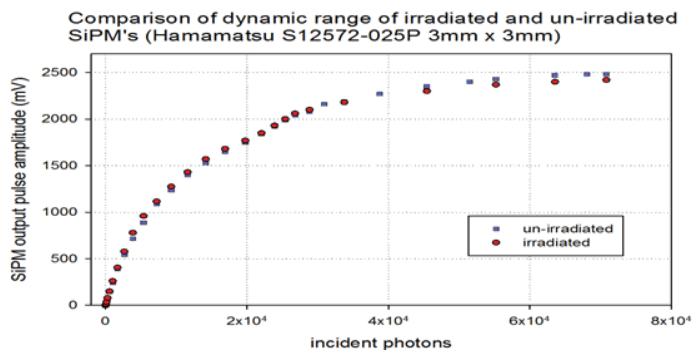
plot 5 dark current pre and post radiation

vices. A single Hamamatsu SiPM device of 25μm pixel size was exposed to radiation at the PHENIX experiment at RHIC for a number of days and later characterized to see how the exposure had affected its performance and efficiency. We measured the current as a function of reverse bias voltage right after the radiation exposure and noted a significant rise in Dark current. This was caused by defects created in the SiPM after radiation exposure. An attempt to repair the damaged SiPM was made through:

1. Forward Biasing- The exposed SiPM was forward biased at ~400nA for one hour and characterized to study any changes in current as a function of voltage, a very minimal drop in dark current was noted.
2. Thermal annealing-The exposed SIPM was later thermally annealed in a temperature chamber at 80°C for 1 hour and at 50°C for 16 hours and later characterized. Since a more distinct drop in dark current was noted we measured the saturation curve and noticed that it had decreased due to pixel damage as shown in the plot below.

III. Conclusion

In conclusion, from the characterized SiPM devices we confirmed that saturation measurements show linearity of the output



Plot 6 of number of pixel fired Vs incident photon

signal is maintained at low incident photon flux. Once the number of incident photons is more than the number of micro-cells in a SiPM, saturation occurs. Hamamatsu SiPM (25 μ m) with a higher number of pixels had a higher saturation curve than Hamamatsu (50 μ m) since more APDs are present to detect a more significant amount of photons. Single P.e. resolution of the irradiated device got much worse after irradiation. This is presumably caused partly by the increase in the dark current that affects the measurement, but given that the measurement was done with a triggered LED, it shows that the intrinsic resolution is also degraded. There is also some indication that some of the pixels may have become inoperative after irradiation, since the level of the saturation curve is slightly lower after the exposure. Forward biasing and thermal annealing after irradiation seemed to slightly decrease the dark current, although it still was higher than the initial dark current before irradiation. More SiPMs of different pixel size, from different vendors are still under characterization.

IV. References

- A Comprehensive Model of the Response of Silicon Photomultipliers IEEE TRANSACTIONS ON NUCLEAR SCIENCE, VOL. 57, NO. 4, AUGUST 2010 Herman T. van Dam, Stefan Seifert, Ruud Vinke, Peter Dendooven, Herbert Löhner, Freek J. Beekman, and Dennis R. Schaart
- The Silicon Photomultiplier - A new device for High Energy Physics, Astroparticle Physics, Industrial and Medical Applications N. Otte, Max-Planck-Institut für Physik, Föhringer Ring 6, 80805 Munich, Germany SNIC Symposium, Stanford, California -- 3-6 April 2006

V. Acknowledgement

- I would like to thank the Department of Energy for funding this research through the office of educational programs at Brookhaven National Laboratory.
- I would like to thank my Mentors Craig Woody and Sean Stoll for their help, motivation and guidance.

The careful puppet master: using continuous integration to prevent errors in Puppet Configurations

Gabriel Richman

Physics Department, Oberlin College, Oberlin, Ohio 44074

Jason Smith and Antonio Wong

Physics Department, Brookhaven National Laboratory, Upton, NY 11973

Abstract

The RHIC and ATLAS Computing Facility (RACF), BNL's main Physics computing center, uses a configuration management program called Puppet to control the software on the machines. Administrators are frequently making changes to the Puppet code in order to create the correct framework for programs to run. Occasionally, someone will make a mistake which could cause particular setups to stop working, potentially taking the entire computing facility offline. In order to minimize this possibility, I've incorporated a continuous integration system called Jenkins into the approval stage of the process. In my system, any change to the Puppet configuration gets automatically tested on a number of different virtual machines. If any fail, the change must be fixed before it can be accepted, thus preventing an error from entering the main Puppet code.

I. Introduction

A. Puppet

Puppet is a program that handles configuration management, meaning it automates the setup and management of computers. Puppet governs which files, programs, and program configurations are on each computer. Puppet is used as an alternative to keeping a master image and copying it onto other computers. It is faster and significantly more mobile because changes in configurations can be made quickly and easily. Puppet also makes it easy to have many different configurations. The style of Puppet code is different from other configuration management programs because it is declarative instead of procedural. Procedural code, which most scripts would be classified as, describes how something should be done. Declarative code, by contrast, describes the final state of the system as the coder desires it. Because of this declarative nature, the Puppet configurations additionally serve as documentation for how each program is used.

Administrators at the RACF are always making changes to the Puppet code. We use Git, the most popular version control system, to keep changes in different environments separate. Using Git, people can make a change in one branch for testing, and then merge that branch into production to implement it. The problem is that there is always the possibility for error. Even when the programmer has tested exhaustively, it is possible for errors to occur. This is because when the administrators test their Puppet code, they test it with a specific set of programs and files managed by Puppet. It is possible that everything will work fine during testing, but fail on a computer with different files on it. These kinds of failures are usually only noticed once the change has been merged into the production branch, causing something to break in the Computing Facility. The best way to ensure that nothing will fail

when introducing changes into a new environment is automated testing with continuous integration.

B. Jenkins

Jenkins is a program which provides a continuous integration system. Continuous integration means that it should be easy to make changes to code and transfer those changes from a testing environment into the main production environment. Jenkins is a popular tool among software developers which is used to ensure that their project is always working correctly. In many companies, lots of employees make changes to the same project, and it is easy for errors to occur. Whenever a change is made Jenkins immediately runs tests to ensure that the project is still compiling and running correctly. Continuous integration ensures that errors that could prevent a project from being merged into the production environment are quickly found and corrected, rather than slowly fixing errors accumulated during months of development in a testing environment. Jenkins doesn't inspect code in any way. It mainly functions to schedule tasks, check that jobs compile, and run unit tests to ensure that the code works correctly.

For the purpose of this project, we use Jenkins to manage a network of virtual machines and handle job scheduling. When someone makes a change to puppet, Jenkins connects to several virtual machines with different configurations and run a Puppet test. If Puppet fails on any of the virtual machines, the failure is reported. These virtual machines are created by RHEV (Red Hat's virtualization service), and are set up to be able to connect freely with the Jenkins server. Jenkins handles all job scheduling among the testing nodes, meaning that if multiple tests are requested, Jenkins will place them in a queue and run them as earlier ones finish.

II. Methods

This project consisted of writing many scripts, and editing others, in order to integrate automated testing into the current workflow.

The process starts when an administrator uses git to merge their change to production. This triggers a git hook to run that places the changes as a pending branch displayed on our approval website. This script already existed, but I edited it so that it would turn those changes into an environment on Puppet. This allows computers to be able to connect to that environment and perform a run of puppet. After that, I added an instruction for the script to connect to the server that hosts Jenkins, and start the testing process.

The script on the Jenkins server queues multiple jobs. The first synchronizes the newly created puppet environment with a program called Foreman, which is used to monitor computers and change their configurations in Puppet. The second job switches

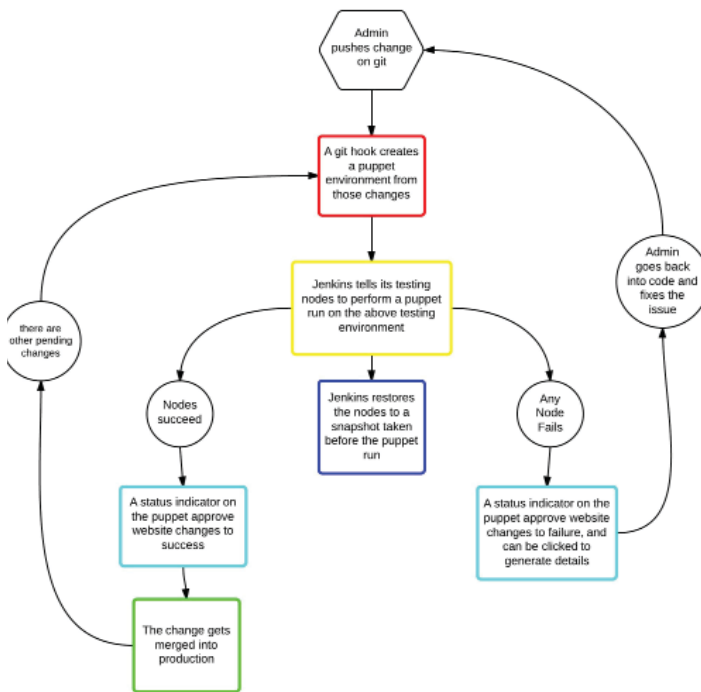


Figure 1: The workflow for automated testing with Jenkins

the virtual machines used for testing to this puppet environment. A third job performs the actual puppet run. The success or failure of this third job determines whether the changes had errors. A fourth job restores the virtual machines to the state they were in before the puppet run, guaranteeing that all puppet runs will be the same. The status of the third job (the puppet run), will be reported to the approval website.

The Puppet approval website maintains a list of changes pending approval. This existed before my project, but I've added things in order to integrate automatic testing. There's a status indicator with an image and mouseover text to report the success or failure of jobs. Some JavaScript code runs in the background every ten seconds which queries the Jenkins server for the status of each job. It then updates every image and mouseover text. If the changes did not succeed in Jenkins, it will not be allowed to be merged into production. The status indicator is also a link to get more detailed information about the status of the job.

This script is a CGI script that gives more detailed information about how the job ran. A CGI script programmatically generates HTML, creating a webpage that has state, and is more suitable for certain tasks. The CGI script queries the Jenkins server, gets the list of virtual machines that tested the job, the result of the test on each virtual machine, and links to the report in Jenkins and Puppet. This is useful because changes to Puppet code might succeed on some configurations but fail on others. This webpage

Hello Gabriel Richman, there are currently 2 changes waiting for approval:

Main Production Approvals									
Date	Age	User	Environment	Changes	Changelog	Status	Approve	Reject	
Tue Jul 29 12:35:16 2014	1 hour	Gabriel Richman	production	diff	pending-production-grichman-4abdc4-20140729T163516UTC		merge	delete	
Tue Jul 29 13:24:10 2014	22 minutes	Gabriel Richman	production	diff	pending-production-grichman-4abdc4-20140729T172410UTC		merge	delete	

Figure 2: the approval website for changes to Puppet

allows administrators to easily discover what failed, and on which machine. With this information, they can fix the error and re-submit the change.

An additional test is required whenever any change is merged. It is possible that there could be two pending changes that had both succeeded in Jenkins that would cause an error if they were both merged into production. This is because each change has been testing using the Puppet code without the changes made by the other. To account for this, whenever a change gets merged into production, all other pending changes must be retested before they can be approved.

III. Conclusion

Before Jenkins, every change to the Puppet code came with the possibility that the change would break someone's configuration – or worse, shut down the entire computing facility. These errors could occur either because of a mistake, or because the error was almost impossible to find even with extensive testing. In either case, with the old system it was impossible to ensure that mistakes would never be made. Puppet is about automation, and Jenkins adds the additional element of automatic testing. Jenkins makes it quick and easy to find hidden errors, and the automatic testing provides a greater degree of certainty that errors will be caught.

Results for pending-production-grichman-4abdc4-20140729T163516UTC

slave name	result	timestamp	link to foreman	jenkins
jenkins02.usatlas.bnl.gov		07/29/14, 13:44:23	puppet report	jenkins run
jenkins03.usatlas.bnl.gov		07/29/14, 13:44:23	puppet report	jenkins run

Figure 3: Detailed information about the status of a job in Jenkins

Designing radioanalytical methods for the characterization of Strontium-82 produced at Brookhaven Linac Isotope Producer

Valerie Sabatasso

Physics Department, Stony Brook University, Stony Brook, NY 11794

Suzanne V. Smith, Jean Odin McCabe, Maria Isabel Garza

Collider Accelerator Department, Brookhaven National Laboratory, Upton, NY 11973

Abstract:

Strontium-82 (Sr-82: $T_{1/2}$ =25.34 days) produced at Brookhaven National Laboratory (BNL) is used in a generator to produce Rubidium-82 (Rb-82: $T_{1/2}$ = 1.273 minutes) for Positron Emission Tomography (PET) imaging of the heart. This project involved the development of radioanalytical methods to determine the limit of detection and quantification of the radio- contaminant Rubidium-83 (Rb-83: $T_{1/2}$ =86.2 days) in the presence of Sr-82 on a gamma spectrometer. Pure samples of Rb-83 and Sr-82 were obtained and accurately diluted to varying known concentrations (0.0045 - 120.2 uCi) and measured on a gamma spectrometer. The measured radioactivity in each sample was analyzed using Gamma Vision software and compared with calculated values. Additional mixed radionuclide samples of Rb-83 were prepared in the presence of excess Sr-82 (to simulate typical production analytical methods) and then analyzed by gamma spectrometry. This data will be used to revise quality control procedures currently deployed and to set the limit of detection for the quality control of Rb-83. Such data is critical for establishing more accurate and precise release and expire dates for Sr-82.

I. Introduction

Gamma spectrometry is used to identify isotopes based on each isotope's characteristic peaks. It is critical for the characterization of medical radioisotopes used in diagnosing and treating cancer. Brookhaven National Laboratory (BNL) is one of two major producers in the United States of Strontium-82 to be used in the course of PET scans.

During production of Sr-82, other isotopes are coproduced that are considered radio- contaminants. They include Sr-83 ($T_{1/2}$ =32.4 hours), Sr-85 ($T_{1/2}$ =64.8 days), Rb-83 ($T_{1/2}$ =86.2 days), Rb-84 ($T_{1/2}$ =33.1 days), and Ba-131 ($T_{1/2}$ =11.5 days). Rb-83 is produced from the decay of Sr-83. It has a considerably long half-life and its presence can greatly influence the shelf life of the Sr-82. In order to assure that the patient receiving the injection is getting the lowest dose of radiation possible, it is imperative that most of these radio- contaminants are removed. Gamma spectrometry is used to identify the isotopes based on each isotope's characteristic gamma emission or 'finger print.' Table 1 displays the isotopes involved in the production of Sr-82 and their specific characteristics. By identifying the isotopes in the sample, researchers can take steps to remove the contaminants from the final, isolated product. Although gamma spectrometers are sensitive machines, they are not without limits. An isotope may be present in a sample, but in a minuscule amount and will not be identified by the device. There is a limit of detection and a limit

of quantification in identifying each isotope present. The limit of detection is the smallest amount of radioisotope in a sample that can be distinguished from background radioactivity. The limit of quantification is the amount at which a measurement is precise – i.e. a reproducible measurement. The specification for the final Sr-82 must be met before it can be released for use. This data will assist in defining the shelf life of the product by determining the lower limits of detection and quantification of Rb-83.

Radioisotope	Half-life	Gammas (keV), Intensity (%)
Rubidium-83	86.2 days	520, (44.7); 529, (29.3); 552, (15.9)
Rubidium-84	33.1 days	881, (71.7)
Strontium-83	32.4 hours	381, (14.07); 389, (1.66); 418, (4.41); 423, (1.59); 762, (30); 778, (1.97); 1147, (1.28); 1160, (1.48); 1562, (1.76)
Strontium-85	64.8 days	514, (95.7)
Barium-131	11.5 days	123, (28.97); 216, (19.66); 373, (14.04); 496, (46.8)

Table 1: Physical Characteristics of contaminating radionuclides present in Sr-82

II. Experimental Details:

Pure Sr-82 production at BNL requires removal of radio-contaminant isotopes that are coproduced during production. Data from Sr-82 batches record of 2014 were used to define a working range for gamma spectroscopy for Sr-82 and Rb-83 pure solutions (known concentration). This information was used to define samples for determining the limits of detection and quantification of the radio-contaminant Rb-83 on the gamma spectrometer. An 80uL sample of accurately measured Rb-83 solution was obtained at 6.01 ± 0.01 mCi/ml (stock). Stock solutions of 0.0045-120.2uCi were obtained by pipetting 10uL of this stock into 500uL of 0.1M HCl (working standard). From this, 115uL was pipetted into 2885uL of 0.1M HCl to obtain the 3mL volume needed for the gamma spectrometer. The calculated activity was 13.55uCi. Three samples were prepared this way and run on the gamma spectrometer for 5000s. Four other samples with different activity levels (1.5-120.2uCi) were prepared in this manner, but the activity levels proved too high and contained much more than a typical batch would.

In a usual QC analysis, the production sample of Sr-82 con-

tains a level of Sr-82 that is one thousand times more concentrated than Rb-83. Aliquots of 10, 25, 50, 100, and 500uL were taken from the sample with the lowest level of activity (1.5uCi) in the first set. The levels of activity of the Rb-83 in these pure samples (0.0045-0.225uCi) were one thousand times lower than the levels of Sr-82 in production batches. The activity levels for pure Sr-82 samples (1.39-22.91uCi) were calculated and prepared to mimic QC analysis levels and run on the gamma spectrometer using GammaVision software. Excess Sr-82 (1000 fold) was added to Rb-83 solutions to assess the effect of the presence of high concentration of Sr-82 on the accuracy of Rb-83 measurements. The Sr-82 volumes needed for this mix were prepared to match the activity levels of the Sr-82 pure solutions. The Rb-83 activity was calculated to be one thousandth of the Sr-82 activity. Each of these samples was run on the gamma spectrometer for 2500 and 5000 seconds.

III. Results and Discussion:

The lower limits of detection and quantification of Rb-83 were determined to be $4.5e-3$ and $4.5e-2$ uCi/3mL, respectively. The limits were determined based on uncertainties, the amount of activity in the samples (dead time), and the percent error.

Pure solutions of Sr-82 (1.39-29.91uCi) were then prepared

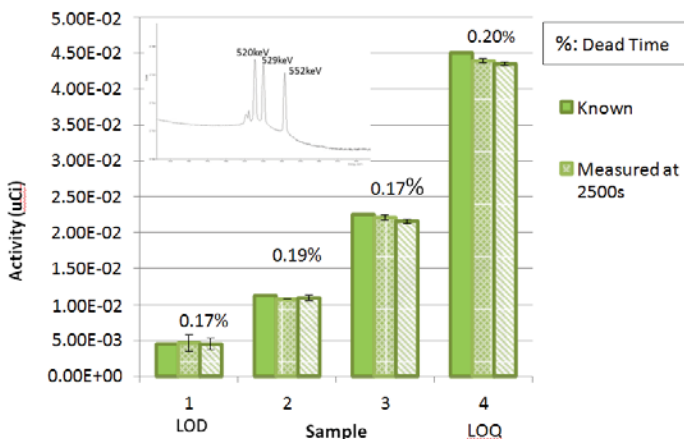


Figure 1: Selected data for Known vs Measured activity for pure Rb-83 samples after counting for 2500s and 5000s.

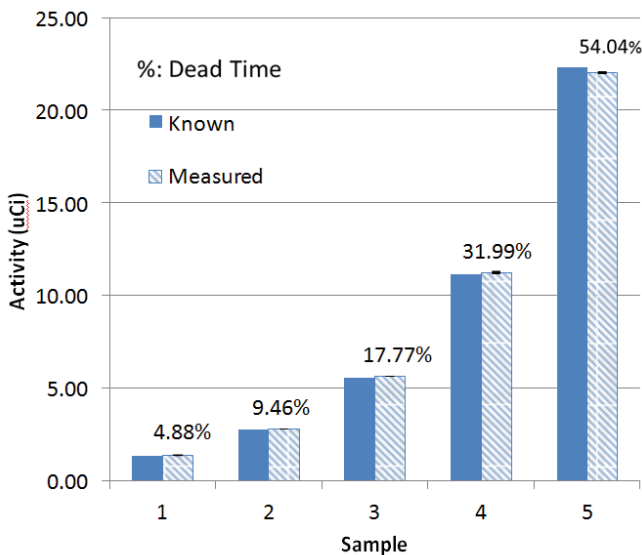


Figure 2: Known vs. Measured activity levels of pure Sr-82.

according to the activity levels of record batches from 2014.

The data (Figure 1 and 2) for both the pure Rb-83 and the pure Sr-82 samples showed the gamma spectrometer accurately counts pure radioisotope samples, even at high dead times.

Excess Sr-82 (1000 fold) was then added to the Rb-83 solutions to mimic typical production QC analysis tests.

The data (Figure 3) showed that the GammaVision software over-estimated Rb-83 activity in the presence of excess Sr-82.

The 511keV gamma emission peak seen in the presence of Strontium interfered with GammaVision's ability to accurately read Rb-83's 520, 529, and 552 gamma emission peaks. These results will be used to set the limit of detection for the quality control of commercially produced Sr-82 samples.

IV. Conclusion

The processed data obtained from the gamma spectrometer included the time of count activity and time corrected activity in uCi. The raw data consisted of the net area counts for each peak of interest. For Rb83, the peaks of interest are 520, 529, and 552 keV. For Sr82, the peak of interest is 776keV. Run time was based on typical production QC protocols. The time corrected decay from the spectrometer was calculated to chosen decay dates for each sample. The calculated decay was based upon the amount of days that had passed between receiving the sample and running each aliquot. The pure samples of Rb-83 and the mixed solutions were run on the gamma spectrometer for 5000s, but data was collected after 2500s and then after 5000s. The levels of activity used in this experiment were at the same magnitude as the levels seen in typical production batches. This allowed for the definitions of

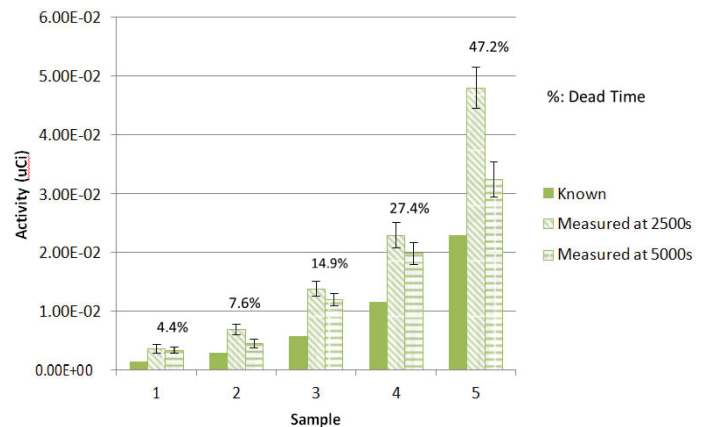


Figure 3: Known vs. Measured activity levels of Rb-83 in the mixed solutions.

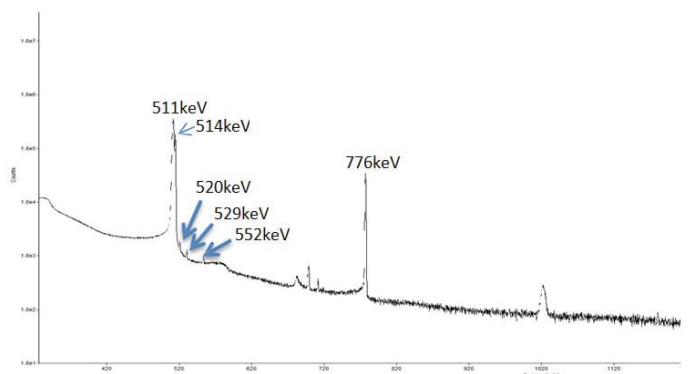


Figure 4: Gamma Spectroscopy for Rb-83/Sr-82 mix.

the limits of detection and quantification of Rb-83 on the gamma spectrometer to be set for production of commercially sold Sr-82.

The LOD and LOQ limits were determined for Rb-83; these levels were based on uncertainties, amount of activity in sample (dead time), and the percent error. The data from the mixed samples showed the 511 keV peak and the 514keV peak from the Sr-85 interfered with calculation of Rb-83's activity using 520, 529, and 552 gamma emission peaks. The GammaVision software tends to over-estimate the presence of the Rb-83 contaminant in Sr- 82 samples. Longer counter times reduced the over-estimation but did not give accurate values. These data confirm that the Sr-82 product has a longer shelf-life than previously estimated and current methods for determining alert levels for reprocessing need to be improved.

V. Acknowledgements

This research is made possible by:

Suzanne Smith as my mentor and my guide through this enriching experience.

Jean Odin, Anna Goldberg, Maria Isabel Garza, and Lisa Muench as co-mentors assisting me with work on the gamma counter and gamma spectrometer.

Brookhaven National Laboratory for serving as my host laboratory.

This project was supported in part by the U.S. Department of Energy, Office of Science, Office of Workforce Development for Teachers and Scientists (WDTS) under the Science Undergraduate Laboratory Internships Program (SULI).

VI. References

- Currie, Lloyd A. "Limits for Qualitative Detection and Quantitative Determination Application to Radiochemistry." *Analytical Chemistry* 40.3 (1968): 586-93. Web.
- "Chart of Nuclides." *Interactive Chart of Nuclides*. National Nuclear Data Center/Brookhaven National Laboratory, n.d. Web.

Evaluation of survival and DNA double-strand break repair kinetics in cells exposed to low dose charged particle irradiation and HDACi treatment

Katherine Z. Sanidad

Stony Brook University, Stony Brook, NY 11790

Alicia M. Johnson, Paula V. Bennett, Deborah J. Keszenman, and Paul F. Wilson

Biosciences Department, Brookhaven National Laboratory, Upton, NY 11973

ABSTRACT

Ionizing radiation (IR) can cause several forms of DNA damage, the most critical being DNA double-strand breaks (DSBs). If incorrectly repaired or neglected, DSBs can generate potentially carcinogenic chromosomal aberrations. During radiotherapy, cells in surrounding normal tissues are exposed to lower doses of IR, and are at risk for secondary cancer induction. We examined how histone deacetylase inhibitors (SAHA, M344, and PTACH) impact survival and DNA damage induction/repair kinetics in human apparently normal and tumor cells exposed to low doses of cesium-137 γ -rays or 290 MeV/n charged particles (carbon, oxygen, and protons) delivered at the NASA Space Radiation Laboratory (NSRL) at BNL. From the first NSRL experiment conducted in Spring 2013, we evaluated DSB levels up to 24 h post-irradiation by monitoring co-localization of two DSB markers, γ -H2AX and 53BP1, using immunocytochemistry techniques and microscopy. We showed that SAHA-treated NFF28 fibroblasts are significantly more radiosensitive than dimethyl sulfoxide (DMSO)-treated control cells following γ -irradiation, but not after carbon ion irradiation. We show that SAHA-treated cells irradiated with carbon ions had lower DSB induction levels but interestingly showed delayed but more efficient repair (below background levels) in contrast to cells irradiated with γ -rays. This fall, we conducted a second NSRL experiment very similar to the first experiment. A new tumor cell line, A549 adenocarcinoma cells, were used as well. Data analysis is ongoing and results are not finalized as of yet.

I. INTRODUCTION

During cancer radiotherapy, cells in the surrounding normal tissues can be exposed to lower doses of ionizing radiation (IR), which place them at a higher risk for secondary cancer induction. IR is a genotoxic agent that appears in different forms such as low linear energy transfer (LET) photons (X and gamma rays) and protons, and high LET "heavy" ions such as carbon ions. IR can cause several forms of DNA damage, the most critical being DNA double-strand breaks (DSBs). If DSBs are incorrectly repaired or neglected, they can generate potentially carcinogenic chromosomal aberrations. Previous studies have shown increased DSB levels observed in precancerous tissues [1]. To monitor DSBs, researchers have used the phosphorylated histone H2AX (γ -H2AX), a variant of the core histone H2A family, as a biomarker. H2AX molecules are phosphorylated by several DNA damage response protein kinases when DSBs are formed. This phosphorylation is one of the earliest events detected after exposure to a DNA damaging agent. Specific antibodies can be used against γ -H2AX molecules leading to immunochemical detection

of γ -H2AX at Ser139 through immunofluorescence [2].

Another potential contribution to carcinogenesis is the disruption of the activities of histone acetyltransferases (HATs) and histone deacetylases (HDACs), which are responsible for the acetylation and deacetylation on lysine residues and affects the regulation of gene expression. Researchers have developed histone deacetylase inhibitors (HDACi), chemotherapeutic agents used alone or as adjuvants with other cancer therapies that function to relax DNA packing around histones in cell nuclei. One particular inhibitor called vorinostat (SAHA), a hydroxamic acid multi-HDACi is currently used to treat cutaneous T-cell lymphoma. SAHA is responsible for blocking enzymatic activity by directly binding to catalytic sites of Class I and Class II HDACs and efficient at low nanomolar concentrations. When SAHA inhibits HDAC activity, it causes the activation of gene expression responsible for causing induction of differentiation or apoptosis, and may aid in the inhibition of tumor growth [3]. M344 and PTACH are HDACi that have similar molecular structures to SAHA.

We again examined how SAHA impacts survival and DNA damage induction/repair kinetics in human cells exposed to low doses of gamma rays in the BNL Biosciences Department or carbon ions from the NASA Space Radiation Laboratory (NSRL). From experiments conducted in spring 2013 and analysis done in summer 2013, we showed that NFF28 neonatal foreskin fibroblasts treated with 10 μ M SAHA are significantly more radiosensitive than cells treated with dimethyl sulfoxide (DMSO; drug vehicle control) following gamma irradiation but interestingly not carbon ion irradiation. To better understand this difference, we evaluated DSB levels in the first 24 h following irradiation by monitoring co-localization of two DSB markers, (γ -H2AX and 53BP1) which form nuclear foci at DSB sites using immunocytochemistry techniques. This fall, we repeated the experiment and are currently going through data analysis. Results are not finalized as of yet.

II. MATERIALS AND METHODS

A. Cell culture and HDACi treatments

Low-passage apparently normal primary human neonatal foreskin fibroblasts NFF28 were used. Cells were cultured in α MEM medium with 15% fetal bovine serum, 100U/ml penicillin, 100 μ g/ml streptomycin, vitamins, amino acids, and GlutaMAXTM-I (GIBCO/Invitrogen) at 37°C in an incubator supplied with 95% air/5% CO₂ mixture. They seeded in two-well microscope chamber slides at ~30% density and grown for 5 days to full confluency. On day 2, the medium was changed and replaced with α MEM medium with 0.2% fetal bovine serum, antimycofungal, and GlutaMAXTM-I, and 25 mM N-2 hydroxyethylpiperazine-N'-2

ethanesulfonic acid (HEPES). 5 μM SAHA or 0.2% DMSO were added to slides 18 h prior to gamma ray irradiation and 10 μM HDACi or 0.2% DMSO were added to the slides 18 h prior to carbon ion irradiation. Both SAHA concentrations radiosensitized cells to the same degree following gamma ray irradiation (~2-fold; see Fig. 3).

B. Carbon ion and gamma cell irradiations

290 MeV/n carbon ion irradiations (LET=13 keV/ μm) were performed at the NSRL and 137Cs 662 keV gamma ray irradiations (LET=0.8 keV/ μm) were performed using a J.L. Shepherd Mark I Model 68A irradiator in Building 490. Samples were immediately returned to the incubator and then fixed with 4% paraformaldehyde at 10, 30, 120, 360, and 1440 min and rinsed with PBS.

C. DSB-associated γ -H2AX pS139 and 53BP1 foci measurements immunofluorescence microscopy

The chamber slides were fixed with 4% formaldehyde at room temperature for 15 min, then permeabilized with 0.5% Triton X-100 on ice for 10 min. Slides were blocked with in PBS with 1% BSA, 2% fetal bovine and goat sera, 0.1% Triton X-100, and 0.05% Tween-20 for 30 min at room temperature. Slides were then incubated in a 37°C humid chamber for 30 min with primary monoclonal antibodies (anti- γ -H2AX pS139 and 53BP1) diluted 1:400 in PBS with 1% BSA. Slides were rinsed in PBS and incubated in a 37°C humid chamber for 30 min with Alexa Fluor® 488 (green) and 594 (red) secondary antibodies (Molecular Probes/Invitrogen) diluted 1:500 in PBS. Slides were rinsed in PBS, treated with 3.7% formaldehyde, and mounted with Pro-Long Gold antifade reagent with 0.2 $\mu\text{g}/\text{ml}$ 4', 6-diamidino-2-phenylindole (DAPI; Molecular Probes/Invitrogen). Images were captured at 630X magnification using a Zeiss Axio Observer Z1 microscope

equipped with the appropriate fluorescence filters and Zeiss imaging software as shown in Fig. 2B–C (150–200+ cells per treatment). Cells were scored by eye and nuclei with atypical size or morphology or those with very high foci counts (presumably S-phase cells) were not scored. Data analyses and graphs were created using Excel (Microsoft Corporation) software package.

III. RESULTS

53BP1 foci was adopted as a marker to verify the presence of γ -H2AX-associated DSBs based on the criteria that both large γ -H2AX foci and smaller γ -H2AX foci with co-localizing 53BP1 foci are scored, as shown in Fig. 1B–C. Serving as controls for NFF28 cells irradiated by gamma rays, non-irradiated DMSO-treated and SAHA-treated cells had averages of 1.65 foci/nuclei and 2.03 foci/nuclei, respectively. These averages were lower than averages of controls for cells irradiated by carbon ions that were 1.79 foci/nuclei (DMSO-treated) and 2.70 foci/nuclei (SAHA-treated).

Differences in kinetics of peak induction and repair over 24 h among the NFF28 cell strains are documented in detail in Fig. 1A. DMSO-treated gamma-irradiated NFF28 cells were only analyzed at two time points (10 min and 1440 min) so DSB repair kinetics could not be compared to other treatments in these experiments. Despite this, curves reveal that DSB foci peak 30 min post-irradiation for all other treatments as shown in Fig. 1A. They also show that the DMSO-treated and SAHA-treated NFF28 cells irradiated with gamma rays had higher DSB foci induction than cells irradiated with carbon ions. SAHA-treated carbon-irradiated NFF28 cells had the lowest foci induction of all the treatments and the slowest repair kinetics from 30 min to 120 min. Interestingly, foci levels 24 h post-irradiation were reduced below background levels only after carbon ion irradiation.

Due to these preliminary results, we expect the same results

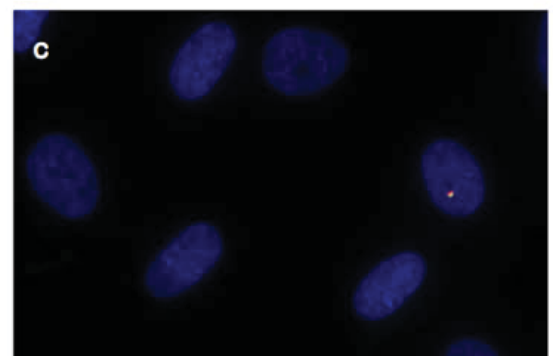
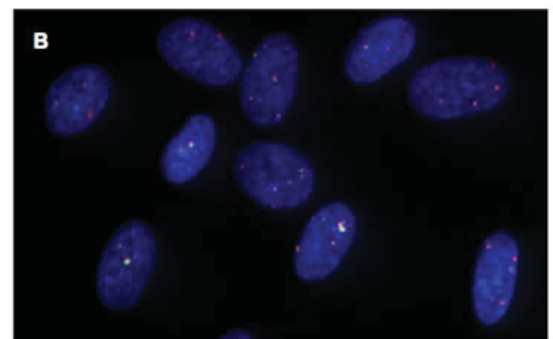
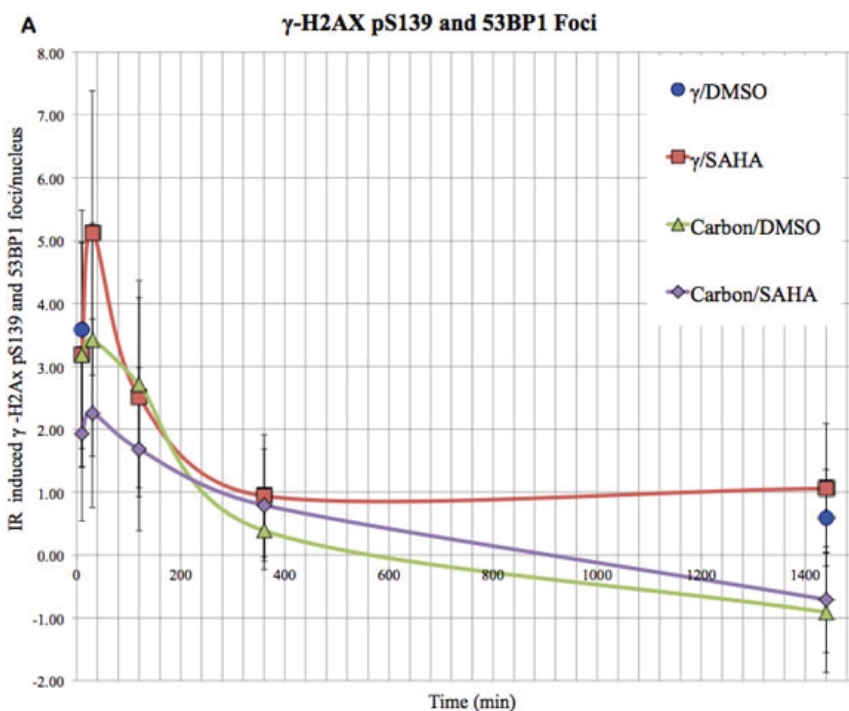


Figure 1. (A) NFF28 DSB-associated foci kinetics (mean \pm SEM) following 18 h treatment with SAHA or DMSO (drug vehicle control). Immunofluorescent images of co-localized γ -H2AX/53BP1 foci in SAHA-treated carbon-irradiated NFF28 nuclei at 30 min (B) and 1440 min (C) post-irradiation (green: γ -H2AX pS139; red: 53BP1; yellow: merge; blue: DAPI).

when analyzing the experiments that have been conducted this fall 2013 and will be conducted in spring 2014.

IV. DISCUSSION

NFF28 cells were shown to have DSB foci peaks at 30 min versus the initial 10 min time point. There is speculation that this may reflect slower damage recognition or initial repair compared to other apparently normal fibroblast strains [1]. Also, according to aforementioned averages of non-irradiated, drug-treated cells, it appears that the NFF28 control cells for carbon ion irradiation may have undergone extra stress compared to the controls for gamma irradiation. This may be due to mechanical stresses of being transferred a farther distance to NSRL compared to the distance to the Building 490.

Radiation cell survival curves of NFF28 fibroblasts treated with SAHA or DMSO after carbon ion irradiation or gamma irradiation are documented in Fig. 2. DSB induction/repair kinetics were evaluated to aid in our understanding of the patterns of these survival curves that show significantly decreased survival of SAHA-treated NFF28 cells compared to DMSO controls after gamma-irradiation as shown in Fig. 2B. Interestingly, these curves show significantly increased survival of SAHA-treated NFF28 cells (dashed line) compared to DMSO controls (solid line) after irradiation of carbon ions (Fig. 2A). The DSB induction/repair kinetics analyzed supported these survival analyses, i.e., SAHA-treated NFF28 cells after carbon irradiation had lower DSB induction levels than DMSO-treated cells. Such sparing following carbon ion irradiation was an unexpected result given the ~2-fold radiosensitization observed following gamma irradiation. These findings may limit the utility of HDACi for hadron radiotherapy.

Another interesting finding was that although SAHA-treat-

ed NFF28 cells after carbon irradiation had lower DSB induction levels, they appeared to have a delayed DSB repair compared to the other treated cells. Other researchers believe that the combination of SAHA and radiation helped prolong the expression of DNA repair proteins such as γ -H2AX [4].

To summarize, per Fig. 2 above, radiation cell survival curves show that SAHA-treated NFF28 fibroblasts are significantly more radiosensitive than DMSO-treated cells following γ -irradiation, but the opposite occurred following carbon ion irradiation. Evaluation of γ -H2AX pS139 and 53BP1 foci kinetics show that SAHA-treated cells irradiated with carbon ions had lower DSB induction levels, showed delayed repair, and repaired DSB levels to below spontaneous untreated control cultures in contrast to cells irradiated with γ -rays. These experiments are also being conducted using U2OS osteosarcoma cells and U87 glioma cells treated with SAHA and two other related HDACi with similar chemical structures to SAHA (M344 and PTACH). These cell lines, along with NFF28, have been irradiated with protons, oxygen, helium, and carbon ions during the NSRL-13A spring campaign. Further experiments have been conducted during the NSRL-13C (during fall 2013) and will be conducted in the NSRL-14A (during spring 2014) campaigns to examine the relative effectiveness of these different ions for hadron radiotherapy and the utility of adjuvant HDACi treatments.

This fall I was able to continue with the same project, but was able to practice and learn and more of the methods used in the experiment, especially in the cell staining using immunocytochemistry techniques. I was very involved in the analysis of the survival curves for the NFF28, U2OS, and new A549 cell lines that were exposed to low dose particle irradiation.

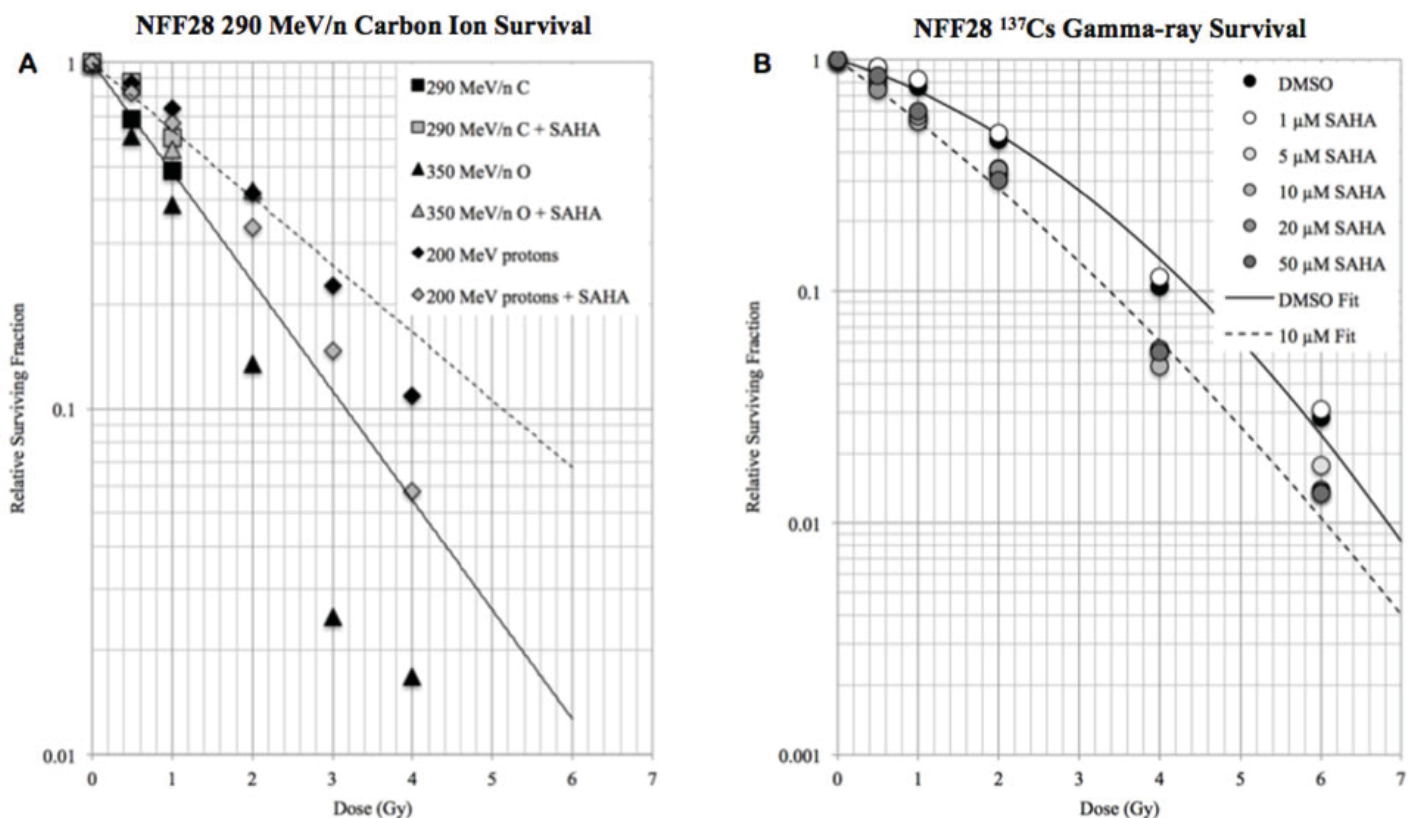


Figure 2. (A) Survival of NFF28 fibroblasts treated with SAHA (dashed line) or DMSO (solid line) after 290 MeV/n carbon ions. (B) Survival of NFF28 fibroblasts treated with SAHA or DMSO after ¹³⁷Cs gamma irradiation.

V. ACKNOWLEDGEMENTS

This project was supported by BNL LDRD 12-012 (PFW) and in part by the U.S. Department of Energy, Office of Science, Office of Workforce Development for Teachers and Scientists (WDTS) under the Science Undergraduate Laboratory Internships Program (SULI) (KZS). Thank you to the NSRL scientists for their assistance with beam delivery. I would like to also thank my mentor Dr. P. F. Wilson for all of his guidance, instruction, and encouragement during my SULI placement; A. M. Johnson for her encouragement and providing images for this project; P. Bennett, D. Keszenman, and J. Jardine for their assistance; and A. Emerick, B. Daniels, L. Kolodiuk, L. Selva, S. Tafrov, and J. Trunk for their support.

VI. REFERENCES

- [1] P.F. Wilson, P.B. Nham, S.S. Urbin, J.M. Hinz, I.M. Jones, and L.H. Thompson. "Inter-individual variation in DNA double-strand break repair in human fibroblasts before and after exposure to low doses of ionizing radiation." *Mutation Research* 683, 91–97 (2010).
- [2] A. Ivashkevich, C.E. Redon, A.J. Nakamura, R.F. Martin, and O. A. Martin. "Use of the γ -H2AX assay to monitor DNA damage and repair in translational cancer research." *Cancer Letters* 327, 123–133 (2012).
- [3] V.M. Richon, J. Garcia-Vargas, and J.S. Hardwick. "Development of vorinostat: Current applications and future perspectives for cancer therapy." *Cancer Letters* 280, 201–210 (2009).
- [4] A. Munshi, T. Tanaka, M.L. Hobbs, S.L. Tucker, V.M. Richon, R.E. Mayb. "Vorinostat, a histone deacetylase inhibitor, enhances the response of human tumor cells to ionizing radiation through prolongation of γ -H2AX foci." *Molecular Cancer Therapeutics* 5 (8), 1967–1974 (2006).

Infra-red absorptions from charges on conjugated polymers in films and solutions

Sabrina Santiago

Department of Biology, Suffolk County Community College, Selden, NY 11784

Matthew Bird and John Miller

Department of Chemistry, Brookhaven National Laboratory, Upton, NY 11973

Abstract

This experiment involved pulse radiolysis using the Brookhaven National Laboratory's Laser Electron Accelerator Facility (LEAF) measuring the absorbances of charges in regio-regular (RR) and regio-random (RRa) poly(3-hexylthiophene) (P3HT), and polyfluorene (pF) films with thickness of 100, 200, and 300 micrometers. We measured the extinction coefficients of the neutral polymer in the films. For the first time, we were able to measure the IR spectra of charges in conjugated polymers in the solid state. We also want to see what small molecule will quench electrons, holes, and triplets in the polymer solid state by adding them to polymer solutions in benzene. Finally we compared the IR spectra of P3HT anions produced by chemical reduction and pulse radiolysis where the anion is expected to be ion paired in the former and free in the latter. This will be important for understanding charge generation and transport polymer solar cells so that we can create renewable energy more efficiently. From this project, I have gained valuable experience learning and utilizing laboratory techniques including LEAF, UV Visible (UV VIS), and the Fourier Transform Infra Red (FTIR).

I. Introduction

Through pump probing of the Laser Electron Accelerator Facility (LEAF), we can observe the absorption over time in polymers films of regio-regular (RR) and regio-random (RRa) poly(3-hexylthiophene) (P3HT) along with polyfluorene (pF).

Figures 1 and 2 show the structures of P3HT and pF. The diagram to the left shows the structure of the P3HT. For the RR P3HT, the side chain is always on the right like the picture shown above. For RRa P3HT, the side chain can be on either side randomly, hence the name regio-random. The degree of regio-regularity greatly affects the packing of the polymer films. The structure to the right is polyfluorene (pF). The pF we specifically used had two hexyl side chains shown by "R" in this picture. The average lengths of the polymers were 30 repeat units. The RR P3HT has a much different absorption due to the packing order of the molecule. In the RR-P3HT, this allows for the formation of a highly ordered structure that involves interaction of the side chains and extensive pi-pi stacking of the polymers. In theory, this could account for an increased mobility of charges along the polymer as well as the differing properties between the two types of polymer films.¹

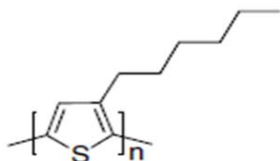


Figure 1: Structure of P3HT

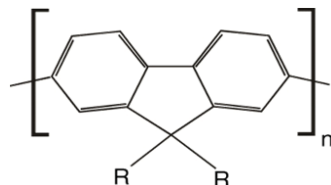


Figure 2: Structure of pF

In previous experiments, polymers were chemically doped with a counter ion, Na or NaK, where the spectra gave a different absorbance than one of the neutral polymer. When a polymer is chemically doped, a counter ion, or a cation, is next to the polymer creating a difference in absorption. These absorptions were taking because the electrons on the polymer are excited because of the laser. The laser shoots electrons at the polymer causing it to go into excited state giving us the spectra. When the electron goes into excited state, it can either be a triplet, singlet, or charge. Because of this reason, this is why we constructed the experiment with Maleic Anhydride, Ferrocene, Fumaronitrile, TMPD, and P3HT with and without oxygen to see what would kill the triplet, etc.

II. Methods

A. Solid State

In order to begin the pulse radiolysis process, we began by creating polymer films.

We measured out a certain amount of polymer to create a certain thickness of 100, 200, or 300 micrometers for the films. Once the polymer was measured we used the pellet press shown above in the picture. We heated up the polymer, the RR P3HT to about 150 degrees Celsius, the RRa P3HT to about 60 degrees Celsius, and the pF to about 100 degrees Celsius. Once the polymer was heated, we pressed the polymer down with the pressure of 10kN/cm² which is about – tons. The polymer did lose thickness due to

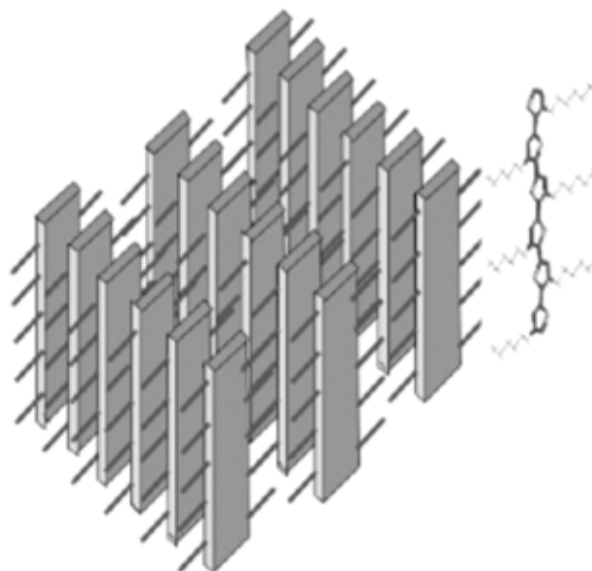


Figure 3 Example of highly ordered structures that can form in the pressed RR-P3HT films.²

either the heat being too extreme or the pressure being too strong because for the RRA and the pF, some of the polymer ran up the side of the press leaving some behind. Note that this is the first time a polymer in solid state has been tested in LEAF and was able to measure the IR spectra.

B. Ion Quenching

Not only did we create these polymer films, we also created solutions to test along with the films. For the solutions, we took the solvents of P3HT without oxygen (made in the fume hood with Ar), P3HT bubbled with oxygen, Ferrocene, Maleic Anhydride, Fumaronitrile, and TMPD. For these solutions, we made them to test which polymer would kill electrons, holes, and charges. We put these polymers in benzene and took them down to LEAF to test their absorbance. We then shot an electron beam at the solution causing the electrons in the solution to become excited and the absorbance we got would tell us whether it was a triplet, singlet, or hole.

C. Solutions

Also, we used a custom made FTIR cell in order to hold the liquid polymer pF. We tested the absorbance then compared it to Matibur's previous study that showed the effect of a counter ion.³ We also compared this spectra with the one of the solid state polymer to see if a solution form will give a different reading.

III. Results

A. Films

The figure (figure 6) above shows the spectra of the RR P3HT films in solid state. This spectra shows RR P3HT following pulse radiolysis of 205 micrometers thick. There appears to be a peak around 1240 cm^{-1} , this means that the film absorbs most of the light in this region. For the first time, we were able to get a spectra of a polymer in a solid state.

The figure (figure 7) above is the spectra of RRA P3HT following pulse radiolysis at 180 micrometers thick. What we noticed is that there is a difference of absorbance of about a factor



Figure 4: Pellet press used to make polymer films

of 10 compared to the RR P3HT even though the only difference is that the side chains are in random positions. It is hard to be exact about where the peak is for this polymer but we still get the spectra.

The figure (figure 8) above shows the spectra of pF following pulse radiolysis at 180 micrometers thick. The decay in pF is much faster than observed in the P3HT due to the electron on the polymer being trapped by oxygen. There appears to be a peak at around 1190 cm^{-1} showing the biggest absorbance.

B. Solutions

Above is the spectra taken of pF made in a solution of benzene. We were only able to take a spectra of pF because the others

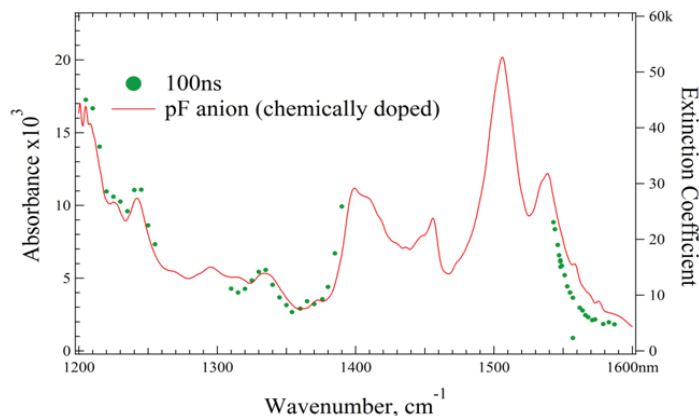


Figure 5: Comparison between a polymer that is chemically doped and one that is not.

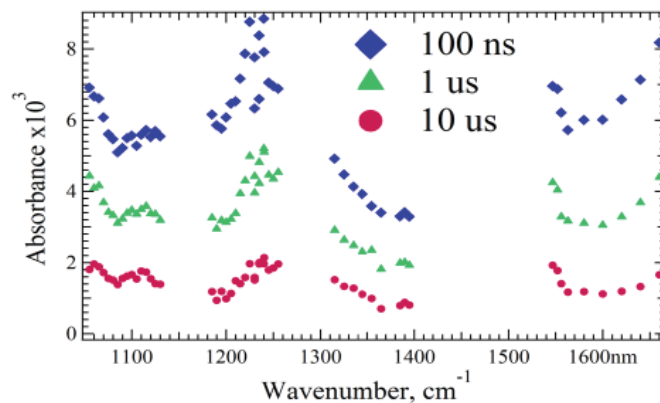


Figure 6: Spectra of RR P3HT

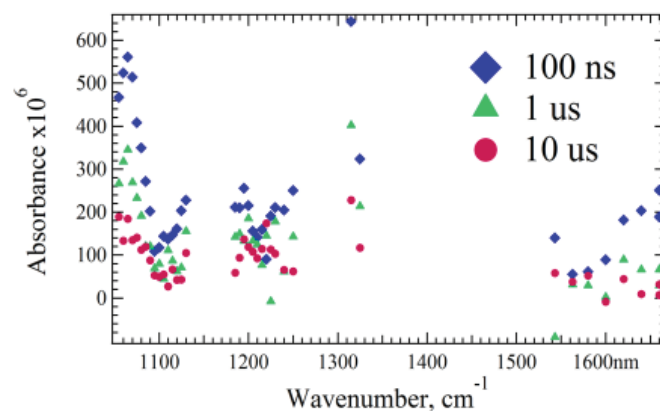


Figure 7: Spectra of RRA P3HT

did not dissolve properly. This spectra shows that the films and the solutions have very different absorbances even though it is the same polymer but just in a different state. This may be the case because a film is more compact and is solid while the solution has free moving particles and the molecules aren't packed as tightly causing more electrons to be excited creating this absorption.

C. Quenching Molecules

The Figure on the left shows the spectra in the visible/near IR region from a solution of P3HT in benzene following pulse radiolysis. We want to find small molecules to put in the films to selectively trap electrons or holes. To test these small molecules, we observed the absorption from the polymer cation and anion at 1629 nm after adding various small molecules. The figure on the right shows that they effectively captured the charges. Fumaronitrile captures the electrons, Oxygen and Maleic Anhydride capture the electrons and triplets, and TMPD and Ferrocene capture the holes.

IV. Discussion

For the first time, we were able to measure the IR spectra of charges in conjugated polymers in the solid state. We have also have discovered that Fumaronitrile captures the electrons, Oxygen and Maleic Anhydride capture the electrons and triplets, and TMPD and Ferrocene capture the holes. These polymers were

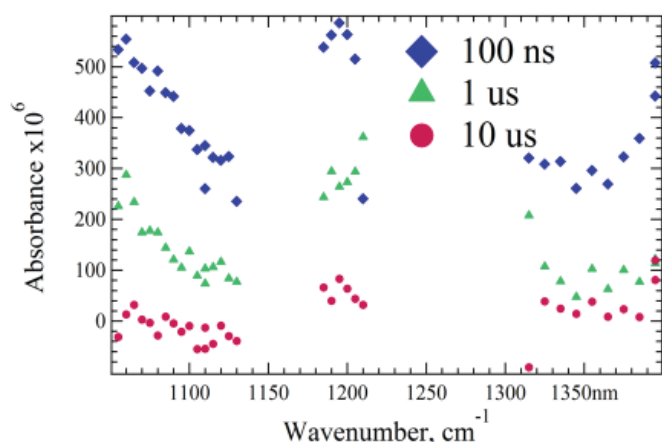


Figure 8: Spectra of pF

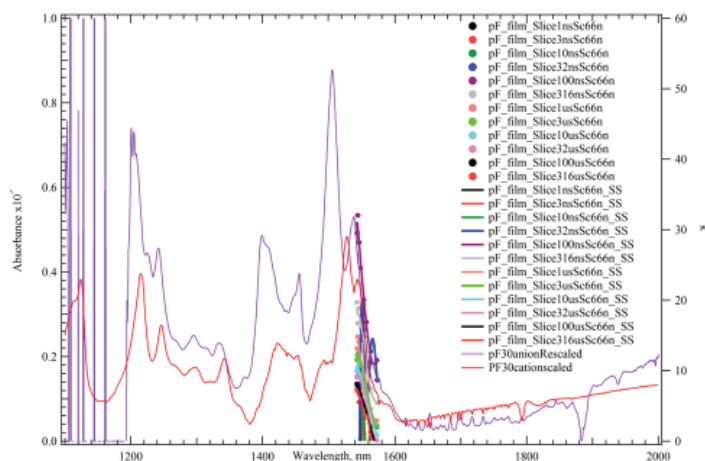


Figure 9: Spectra of pF solution

tested to see if they would be more efficient for solar cells for creating renewable energy.

V. Acknowledgements

This project was supported in part by the New York State Collegiate Science and Technology Entry Program (CSTEP) at Suffolk County Community College under the CSTEP-Supplemental Undergraduate Research Program (SURP) at Brookhaven National Laboratory.

¹Sirringhaus, H.; Brown, P. J.; Friend, R. H.; Nielsen, M. M.; Bechgaard, K.; Langeveld-Voss, B. M. W.; Splering, A.J.H.; Janssen, R. A. J.; Meijer, E. W.; Herwig, P.; de Leeuw, D. M. Two-dimensional charge transport in self-organized, high-mobility conjugated polymers. *Letters to Nature*. 1999, 401, 685-688.

²Brinkmann, M.; Rannou, P. Effect of Molecular Weight on the Structure and Morphology of Oriented Thin Films of Regio-regular Poly(3-hexylthiophene) Grown by Directional Epitaxial Solidification. *Advanced Functional Materials*. 2007, 17, 101-108.

³<http://www.nature.com/ncomms/2013/131115/ncomms3818/full/ncomms3818.html> vfgjuhfv. (4554). ukfc. cugfj, 231.

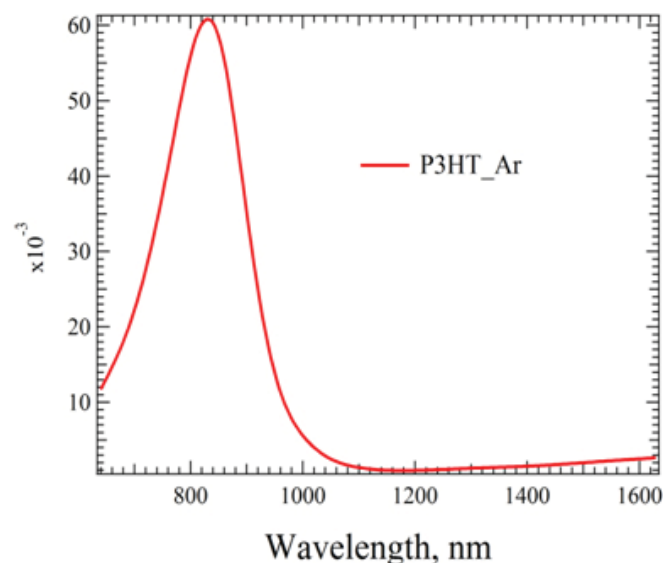


Figure 10: Absorbance of P3HT bubbled with Ar

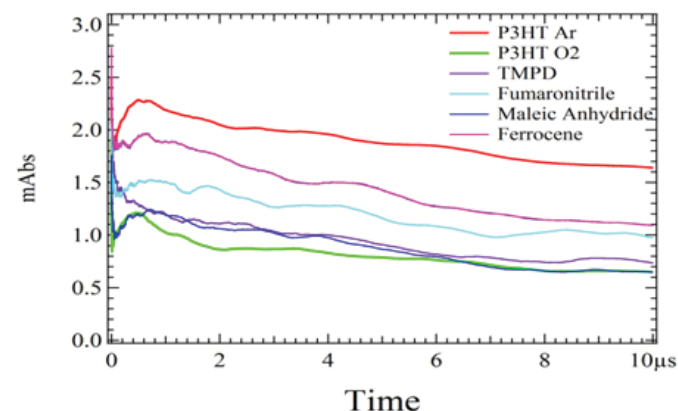


Figure 11: Zoomed in absorbance of the wavelength from 1400-1650 nm

Design and modification of a Halbach permanent quadrapole magnet

Michael Severance, Physics Department, Stony Brook University, Stony Brook, NY 11790
 Nicolaos Tsoupas, Collider-Accelerator Department, Brookhaven National Laboratory, Upton, NY 11793

Abstract

There are currently plans at Brookhaven National Laboratory to upgrade the Relativistic Heavy Ions Collider (RHIC) so that it can collide electrons and hadrons. In this upgraded facility, there will be two distinct electron energy rings: the low energy ring and the high energy ring. In order to focus the electron beams in each ring, a weaker quadrapole is needed for the low energy ring when compared to the strength of the quadrapole needed for the high energy ring. Besides focusing the beam, the synchrotron radiation produced from bending the beam, the strength of the integrated multipoles, and the price of the magnet have to be taken into account in order to have a successful magnet. After taking all of these factors into consideration, we decided that modifying a Halbach magnet by removing material for the top, bottom, and both sides could have some promise to it. The idea for removing the material arose so that we could deal with the synchrotron radiation that would be present in the horizontal plane. Up to this point, we have used OPERA software and created both 2D and 3D models and have obtained surprisingly good results, almost completely ideal in some of our studies. However, this should be taken with a grain of salt for we have not yet produced one of these magnets and are not sure of the reproducibility of this magnet. With that being said, this magnet still seems to be rather promising, not only in eRHIC, but in other user facilities and various other applications. This project has given me a deeper respect and understanding of electricity and magnetism, which may have taken much more time to develop if I had not done this research.

I. Background

These modified Halbach magnets will be used in both the low energy and the high energy electron rings of eRHIC, which is a potential upgrade to the Relativistic Heavy Ion Collider so that the collider can eventually collide hadrons with electrons in order to perform experiments that could not take place on the current RHIC. In the initial design for the electron rings, there was going to be a separate magnet designed for each of the 16 lines different energy levels of the electrons. However, this initial design for the magnets would prove to be far too expensive. The design ultimately moved towards having two different types of magnets, one model for the 11 lines of the high energy rings and one model for the 5 lines of the low energy ring. The main difference between these two magnets for the different energy level electron rings would be the gradient. The high energy magnet will need a larger gradient than the low energy version. Another requirement that these magnets need to meet is to have very small multipoles even at a given distance from the center of the magnet. If this was not the case, the electrons of certain lines would not feel the same field as the other electrons in the other lines. These magnets, for

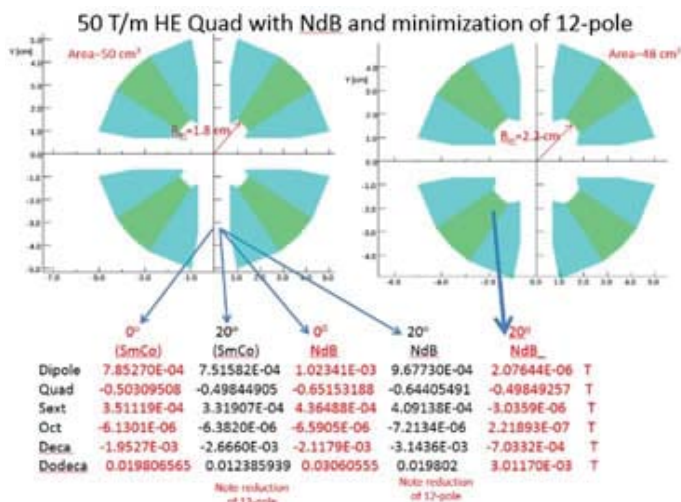
both the high and low energy models, cannot have material in a place that would be affected by the massive amounts of synchrotron radiation that is produced from the electrons.

II. High Energy Magnet

There are a few different models that have been worked out for the high energy model of this magnet.

There have been certain suggestions to go from the initial gradient of 50 T/m to 40 T/m so that it would be easier to minimize the multipoles in this model. Another suggestion was to increase the gap of the magnet from 14 mm to 16 mm in an effort to make it much easier to fit a realistic chamber that had a wall thickness of 3 mm instead of 2 mm and to have 10 mm space for the spread of the synchrotron radiation. On top of these suggestions, the idea of using NdFeB instead of SmCo as the permanent magnet material has been thrown around. NdFeB would be able to give us stronger fields, however there are some problems that might arise if we use this material such as this material having a lower Curie point than SmCo. Now, let's examine the magnet designs.

The diagram on the left shows both the models for the 50 T/m model of the high energy magnet with a 14 mm gap. The angle above the different multipoles corresponds to the difference in angle of the magnetization vectors of the pieces of magnetic material compared to what the distribution should be. By doing this, you can introduce a dodecapole to negate the initial dodecapole that the magnet gives. You can also see that there still exists a slight problem with the dodecapole in all these models, as even the lowest model has 30 G of dodecapole. That is one of the main reasons that the idea was brought up to decrease the gradient. From the diagram on the right, it is clear to see that it is much easier to produce a 40 T/m magnet with very low multipoles at .96 cm, which would be the furthest from the center of the magnet that the lines could be.



However, when we try to increase the gap size of the magnet to 16 mm to accommodate the larger chamber diameter, the model below would appear to be the best would could do at this point without adding iron in strategic locations and overcomplicating the design of the magnet.

As you can see from this model, we get a rather significant dodecapole of about 46 G. This value can be lower by adding iron as briefly mentioned before. But again, the magnet design then becomes very complicated and will most likely cost significantly more to produce. It is also reassuring to know that after performing some 3-D analysis of these magnets, the gradient appears to be very constant along the x axis.

This can easily be seen in the corresponding diagram. When looking at the plot on the right you can see how the magnetic field behaves as a function of distance from the center of the magnet. Since it is very linear to about 1 cm, this magnet should have the required constant gradient for all the different energy lines.

III. Low Energy Magnet

Not unlike the high energy model, there are also two different gradients that have been given for the low energy magnets. However, in this case, it is not as clear as to the gradient that will ultimately be used for this project. It is also important to note that for the low energy models, we were able to just use SmCo and a 16 mm gap and still obtain very good results.

As you can see, the 10 T/m model seems to be very ideal since all of the multipoles are so low even at a R=2cm. It is also important to note that in this model, the dodecapole has already been corrected for, which is why it is so low in the above model. The 15 T/m model will be shown below.

Overall this model looks very promising as well. However, you will notice the very strong decapole. This should not happen because when you have a quadrupole magnet, the next allowed state would be the dpdecapole (which has already been corrected for in this model). Some people may say that this is most likely a meshing error, but since one eighth of the model was designed and then copied, all of the mesh should be congruent. Another thing to note is that when the analysis of the multipoles is run with an inherent assumption of symmetry in the analysis, we no longer see this decapole.

I have yet to produce 3-D models for these 16 mm gap low energy magnets as this was a much more recent development in my research. However, if these magnets with the increased gap are anything like the 14 mm gap magnets, then they should also have very constant gradients.

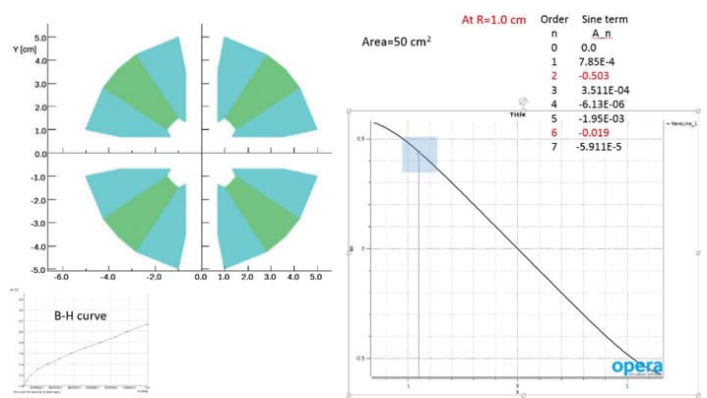
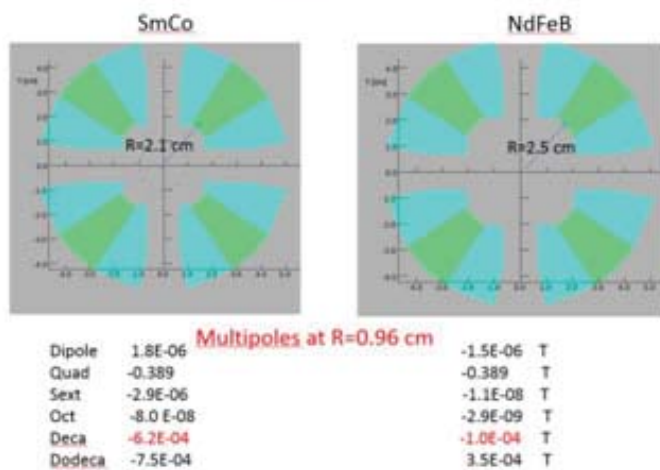
IV. Correctors and Reproducibility

Since many of the correctors for each of the magnets would be very similar, I have decided to showcase the correctors that will be used for the 10 T/m, 16 mm gap, low energy magnet.

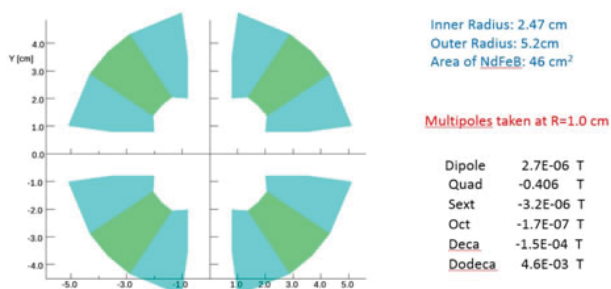
As you can see from the corresponding diagram, by distributing the correct amount of wires in the specific distributions that correspond to the normal dipole, skew dipole, and normal quadrupole, we are able to produce significant fields. It should be noted that we would only have room for two of the three listed correctors. The correctors we use in each magnet might change in different magnets as you continue down the line.

Another issue that should be addressed is the reproducibility of these magnets. That is, will this magnets be very consistent from magnet to magnet. If that is not the case, then these magnets may not be the best answer for eRHIC. I performed a small preliminary study on the reproducibility of these magnets using the errors that certain companies that might ultimately build these magnets have given us. This data was found by taking 10 trials using the 50 T/m, 14 mm gap, high energy magnet and incorpo-

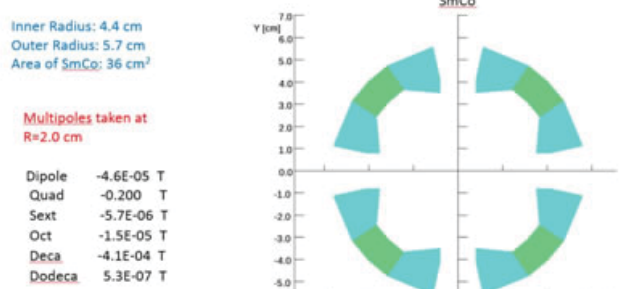
40 T/m HE Quad with NdFeB and minimization of 12-pole



16 mm gap, 40 T/m, NdFeB, High Energy Quad



16 mm gap, 10 T/m, Low Energy Quad



rating random errors into both the magnetization vectors of each piece of magnetic material and also incorporating positional errors in the magnet.

You can see from this chart that even the combined errors of the position and magnetization vectors do not have that great of an effect on the multipoles. With that being said, the error is definitely present and most of this error comes from the error in the magnetization vectors. So if that error can be minimized these magnets should be able to be reproduced more consistently.

V. Conclusion

This magnet seems to have a lot of promise to eventually be used in eRHIC. However, there are a few other magnet designs so it is no guarantee this this model will ultimately be used. With that being said, this magnet may have other uses in different user fa-

cilities and in various other applications. Even if this magnet does not end up being a part of a specific project, it is still good to learn from the surprisingly good properties that this magnet possess that many people would not expect this particular magnet to have.

VI. Acknowledgements

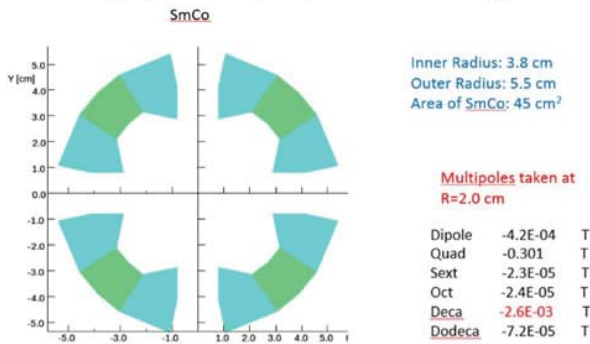
This project was supported in part by the U.S. Department of Energy, Office of Science, Office of Workforce Development for Teachers and Scientists (WDTS) under the Science Undergraduate Laboratory Internships Program (SULI). With that being said, I would really like to thank the DOE for having programs like this available and for funding this research.

I would also like to thank BNL and all of the employees that I have come into contact with as they have shown a great deal of hospitality and really have made this place feel like home.

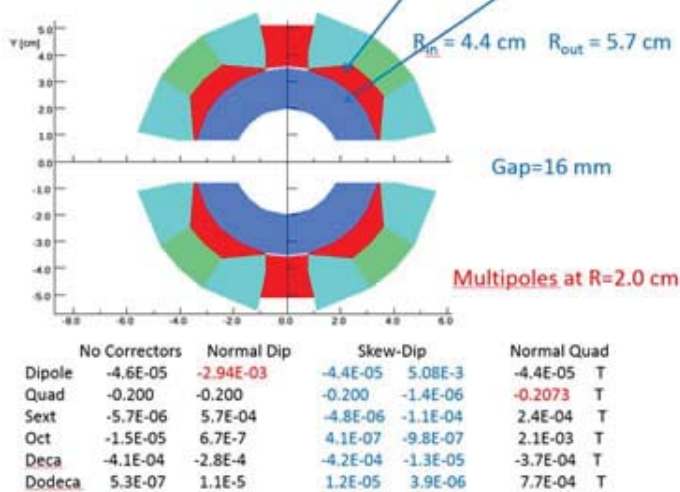
I would also like to especially thank my mentor through the SULI program, Nicholaos Tsoupas, for his constant encouragement and for his insight on all of the troubles that I ran into. Without his trust and expertise, this project would not have been possible.

Finally, I would like to thank all of my colleagues, especially those whom I encountered at the eRHIC meetings that I attended every week who did not look at me as an undergraduate, but as a peer. In particular I would like to thank Francois Meot and Dejan Trobjevic for their assistance on this project and for enhancing my experience in this program.

16 mm gap, 15 T/m, Low Energy Quad



Low Energy Quad at 10 T/m with N/S Dipole and Quad correctors



Magnitude of Multipole Fields taken at R= 1cm

(14 mm gap, 10 trials each)

	No Error	±1° M vector	±1 mm error in x and y	Error in Both
Dipole [T]	8.1x10 ⁹	± 1.1x10 ³	± 5.3x10 ⁴	± 1.5x10 ³
Quadrupole [T]	5x10 ¹	± 2x10 ⁴	± 7.5x10 ⁴	± 7.5x10 ⁴
Sextupole [T]	4.36x10 ⁷	± 1.8x10 ⁴	± 2.2x10 ⁴	± 1.8x10 ⁴
Octapole [T]	3.01x10 ⁷	± 6.1x10 ⁵	± 1.2x10 ⁴	± 1.4x10 ⁴
Decapole [T]	2.37x10 ⁴	± 2.5x10 ⁵	± 3.5x10 ⁵	± 5.4x10 ⁵
Dodecapole [T]	3.11x10 ³	± 4.7x10 ⁶	± 3.0x10 ⁵	± 3.8x10 ⁵

Standardization and optimization of training requirements in the Standards-Based Management System (SBMS)

Claire Shanklin, Political Science, State University of New York at Geneseo, NY 14454

Lauren Lavelle, English, Temple University, Philadelphia, PA 19122

Teresa Baker, Quality Management, Brookhaven National Laboratory, Upton, NY 11973

Nicole Puglin, Quality Management, Brookhaven National Laboratory, Upton, NY 11973

Abstract

The Standards-Based Management System (SBMS) provides institutional policies, procedures, and processes to staff, guests, and visitors at Brookhaven National Laboratory (BNL), including over 170 subject areas. The focus of this project was to standardize and optimize the training information within these subject areas. To complete this project, we worked with the relevant Subject Matter Experts (SMEs) to catalog, review, and update the training requirements and reporting obligations in each subject area. The primary goals were to ensure the accuracy of existing content as well as provide more specific training information (i.e., course numbers, course titles, direct hyperlinks to web-based training, points of contact, etc.). First, we documented the current training requirements and reporting obligations information in a Microsoft Excel spreadsheet. Next, we engaged the BNL Training and Qualifications Manager to receive his input on our project. After receiving his feedback, we contacted each SME via email and requested that they verify the existing training requirements and reporting obligations and provide additional details as applicable. We tracked the responses in Microsoft Outlook, created a Microsoft Excel spreadsheet to organize the responses, and scheduled follow-up meetings with SMEs as needed. This project will allow the Laboratory community to easily access training requirements and reporting obligations that are relevant to their research and/or operational work scope. Our work on this project has enhanced our ability to navigate Microsoft Office, communicate effectively with all levels of staff and management, and understand the complexities of working within a large organization.

I. Introduction

A. Background

1. Standards-Based Management System (SBMS)

The Standards-Based Management System (SBMS) provides institutional policies, procedures, and processes to staff, guests, and visitors at Brookhaven National Laboratory (BNL). The procedures and processes contained in SBMS may be driven by internal/external requirements or established by management. All documents in SBMS are organized into 30 management systems, each of which is described in a Management System Description and owned/managed by a Management System (MS) Steward and MS Executive. There are five types of documents within SBMS:

1. Management System Descriptions (30)
2. Subject Areas (172)
3. Program Descriptions (23)
4. BNL Manuals (6)
5. Interim Procedures (7).

This project focused on subject areas, each of which describes an institutional procedure or work process and is owned/managed by an assigned Subject Matter Expert (SME). In addition to describing a procedure or process, each subject area provides additional information to help staff execute the work. This includes the relevant training requirements and reporting obligations.

2. Training and Qualifications

The purpose of the Training and Qualifications program at BNL is to ensure that BNL employees, guests, users, and contractors are trained and qualified to perform their assigned tasks and job functions. The Laboratory has established training requirements in accordance with regulatory requirements for work to be performed, hazards that may be encountered, areas that will be accessed, potential for risk, and general site requirements. BNL has defined minimum training requirements for work to be performed, and monitors the completion of these requirements. In addition to ensuring that personnel receive appropriate training, the Laboratory is committed to ensuring that its workers are qualified to perform their jobs.

Staff need only meet the necessary training and qualification to perform a task regardless of whether it is linked by Job Training Assessment (JTA) or not. Supervisors/managers are responsible for ensuring that staff are trained and qualified for work before assigning tasks. Supervisors/managers are responsible for ensuring that staff do not perform tasks without having first completed initial required training or with lapsed required training or qualifications. Staff are authorized to perform tasks independently only after successful completion of the required training and when required, have demonstrated the knowledge and skills needed to perform the work unsupervised.

B. Issue

There is an opportunity to standardize and optimize the training requirements and reporting obligations contained within SBMS subject areas.

Training requirements are managed through the Brookhaven Training Management System (BTMS). The BTMS and SBMS databases are not linked. Currently, we rely upon SMEs to provide the training information that is relevant to their subject area(s). As a result, the two systems are disjointed and the level of detail in the training requirements section is inconsistent across subject areas.

Currently, some subject areas state that training requirements exist, however, many of them do not specify the details. Course numbers and titles were available in some subject areas but the level of detail provided was inconsistent. Providing the exact course names and numbers in each subject area would enable us-

ers to easily identify the applicable training. This would help to ensure that all staff, guests, and visitors understand their training requirements, which supports a safe working environment.

Additionally, reporting obligations were not well defined or understood. As such, this section was blank in many subject areas. This project provided an opportunity to clarify the definition and engage SMEs in managing and understanding the SBMS content that they own.

C. Scope

The scope of this project was to review and enhance the training requirements and reporting obligations in each subject area contained within the SBMS. Accomplishing this task requires inventorying all of the existing training information and reporting obligations contained in SBMS. It then requires the engagement of all of the relevant SMEs to verify the existing information and provide specific training course names and numbers. Responses will need to be tracked and additional follow-up meetings scheduled. The final deliverable will be a consolidated document of all training requirements and reporting obligations. This document will be used by the SBMS Office to update the training requirements and reporting obligations in each subject area.

D. Objectives

The primary objectives of this project are as follows:

- Standardize: ensure that training requirements and reporting obligations are consistent throughout SBMS
- Optimize: strengthen the link between Laboratory-wide procedures (i.e., subject areas) and applicable training requirements

To meet these objectives, we first needed to ensure the accuracy of the existing content. We then collected more specific training information relevant to each subject area, including training course numbers, course titles, direct hyperlinks to web-based training, points of contact, and other information. This will ensure that a consistent level of detail is provided across subject areas and will allow users to easily identify required training. We also clarified the definition of a reporting obligation and engaged the SMEs to ensure consistency and standardization.

The end goal is to help BNL staff, guests, and users to easily access the training requirements and reporting obligations that are relevant to their research and/or operational work scope. We hope that making training requirements easily accessible will not only make SBMS more user-friendly, but positively contribute to BNL's goal of maintaining a safe working environment for its employees. Safety is a core value at BNL.

II. Methods

First, we documented the current training requirements and reporting obligations information in a Microsoft Excel spreadsheet. We then further organized this information into categories based on the level of information currently provided.

Next, we met with the BNL Training and Qualifications Manager to receive his input on our project. We discussed the possibility of including hyperlinks to the training website in SBMS and he provided us with valuable feedback on how to best organize the training information. We learned about improvement efforts currently underway in the Training and Qualifications Office and were able to align our project with their ongoing efforts.

Once gaining feedback from the Training and Qualifications Manager, we requested each SME to update their training and reporting obligation content via email. We provided each SME with a table that contained the existing information for each of their subject areas. We requested that they review the information for accuracy, add any missing information, and specify the course numbers that applied to the training requirements in their subject area. We sent emails to 90 SMEs in total and created a Microsoft Excel spreadsheet to organize the responses that we received.

We tracked SME responses and sent out follow-up emails on a continual basis. We also scheduled meetings with some of the SMEs to discuss and resolve issues that arose during their review. These discussions proved to be very valuable and in some cases, even shed light on how the training in their subject area could be improved.

III. Results and Conclusion

This project has demonstrated the complexities of managing information within a large organization that relies on various systems. As such, one of the primary goals for this project was to strengthen the connection between Laboratory-wide procedures (SBMS) and the related training requirements (BTMS) and reporting obligations. This was achieved by inventorying existing content, engaging the right people across the Laboratory to verify accuracy, and gathering additional detailed information.

The final deliverable for this project is a consolidated document of all training requirements and reporting obligations contained in SBMS. This document will be used by the SBMS Office to update the training requirements and reporting obligations in each subject area. This will allow employees to easily access the training requirements and reporting obligations that are relevant to their research and/or operational work scope.

Ultimately, this project has laid down the groundwork for the standardizing and optimizing the training requirements and reporting obligations in SBMS subject areas.

Charge coupled device characterization techniques and analysis enhancement

Thomas Smith, Math Department, Saint Joseph's College, Patchogue NY, 11772
Ivan Kotov, Instrumentation Division, Brookhaven National Laboratory, Upton NY, 11973

The Large Synoptic Survey Telescope (LSST) under construction in Chile, a multinational effort to build a powerful telescope with unique abilities, is a wide angle telescope which will allow it to gather more data, faster, and more precisely than other telescopes. When operational, it will gather 30 TB of data per night, totaling 60 PB of raw data and 30 PB of catalog data over 10 years. The sensors used to gather this data, called Charge Coupled Devices (CCDs), are used in most cameras today. The instrumentation division at Brookhaven National Laboratory (BNL) is in the process of developing techniques for characterizing the CCDs to be used in the LSST. This summer, we have added region marking and catalog creation functionality to the C++ code that is used for x-ray analysis and pocket pumping, two techniques used for the visualization of found objects. This work speeds up data analysis by marking regions of interest on images automatically, and presenting data such as amplitudes and coordinates in a clear, easy to read, tabular format in catalogs. We have also explored the option of using an Organic Light Emitting Diode (OLED) display for CCD testing.

The purpose of this research is to develop code and systems that will aid in the characterization of charge coupled devices. Characterization is important so we can gain a better understanding of what the CCDs can and can't do, so systems can be implemented to use the sensors to gather the most detailed information and take the best images possible. The code developed this summer added region marking and catalog creation to existing C++ code that is used in x-ray analysis and pocket pumping. The Python code was developed for a different test to operate a small OLED screen that displays test images for the sensor.

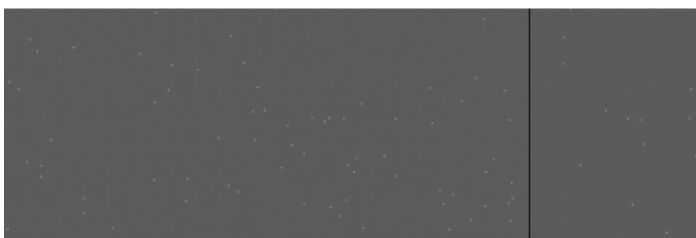


Fig. 1- X-ray cluster image without regions

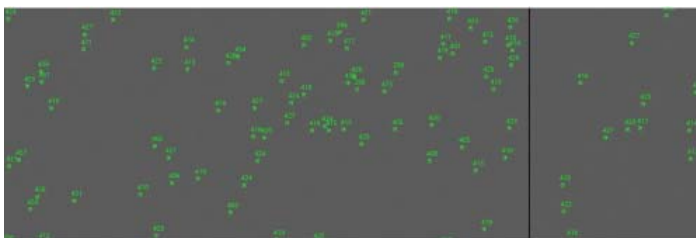


Fig. 2- The same image as Fig.1, but with regions

I. Methods and Materials

Since the project contained 2 sub-projects, they shall be discussed separately:

- Region marking and catalog creation capability
- OLED display for test images

A. Region marking/ Catalog creation

Marking a region on an image is a useful tool for being able to visualize the number of instances of what you are looking for.

This presents two challenges: finding the area of interest, and recording all of the areas. Fortunately, the code that was used in the program to analyze the image (.fits files) had already been written by Ivan Kotov, leaving only the region file creation. It is now important to understand the structure of a region file. It is a text file that has 2 lines of text for each region. One line is the CCD segment number (as it is a 16 segment CCD) and the line directly below it contains the region information such as shape, coordinates, size of region, color, and text.

First, the file needs to be created; See Fig. 4 for region file creation code.

Next, this line of code is run every time the analysis code finds a hit, to populate the file with data:

```
1 # tile 1
2 image; box 451 1947 3 3 0 # color = green text={ 428}
3 # tile 1
4 image; box 69 1423 3 3 0 # color = green text={ 460}
5 # tile 1
6 image; box 51 621 3 3 0 # color = green text={ 452}
7 # tile 1
8 image; box 70 1329 3 3 0 # color = green text={ 423}
9 # tile 1
10 image; box 279 1665 3 3 0 # color = green text={ 422}
11 # tile 1
12 image; box 505 1892 3 3 0 # color = green text={ 422}
13 # tile 1
14 image; box 456 1507 3 3 0 # color = green text={ 424}
15 # tile 1
16 image; box 138 1184 3 3 0 # color = green text={ 415}
17 # tile 1
18 image; box 212 1886 3 3 0 # color = green text={ 448}
19 # tile 1
20 image; box 454 1841 3 3 0 # color = green text={ 425}
```

Fig. 3- Text of a region (.reg) file

```
//Region File Creation
string catName = "Regions_" + *FL.FName_Iter; //prepends Regions_ to name of fits file
basic_string<char>::size_type indexF;
indexF = catName.find(".fits"); //finds .fits at end of file name
catName = catName.replace(indexF,5,".reg"); //replaces .fits with .reg
printf("Output cat File: %s \n", catName.c_str());

FILE * pFreg;
pFreg = fopen(catName.c_str(),"a+");
if(pFreg == 0){
    printf("File %s can't be open \n", catName.c_str());
    Flag = -1;
    return;
}
//End Region file creation
```

Fig. 4- C++ code used to create a region file

```
fprintf(pFreg, "# tile %i \n image; box %i
%i %i %i 0 # color = %s text={%6.0f} \n", ch_
idx+1, hit.ixb + 1 , hit.jyb + 1, Ohit::NXs-
rch, Ohit::NYSrch, colr[3], hit.sum);
```

This will append each region to the file in turn. Finally the file is closed: fclose(pFreg);

Catalog files are created in a very similar way, except they are .xml files that need a header and footer surrounding the rows of data. The code to create the file and code to populate the file are very much similar to the code mentioned above and not worth noting.

The header is put into the file after it is created, the data rows are added as the analysis finds hits, and the footer is added prior to closing the file.

One difference between regions and catalogs that made it difficult to switch between the two was the coordinate systems. The analysis code returns image coordinates which are used for region, but catalogs cannot use it. We ended up using the image's coordinate transformation matrix and vector to switch between image (logical) coordinates and physical coordinates.

- LTM1_1, LTM2_2 are scaling parameters
- LTM1_2, LTM2_1 are rotation parameters
- LTV1, LTV2 are translational vector parameters

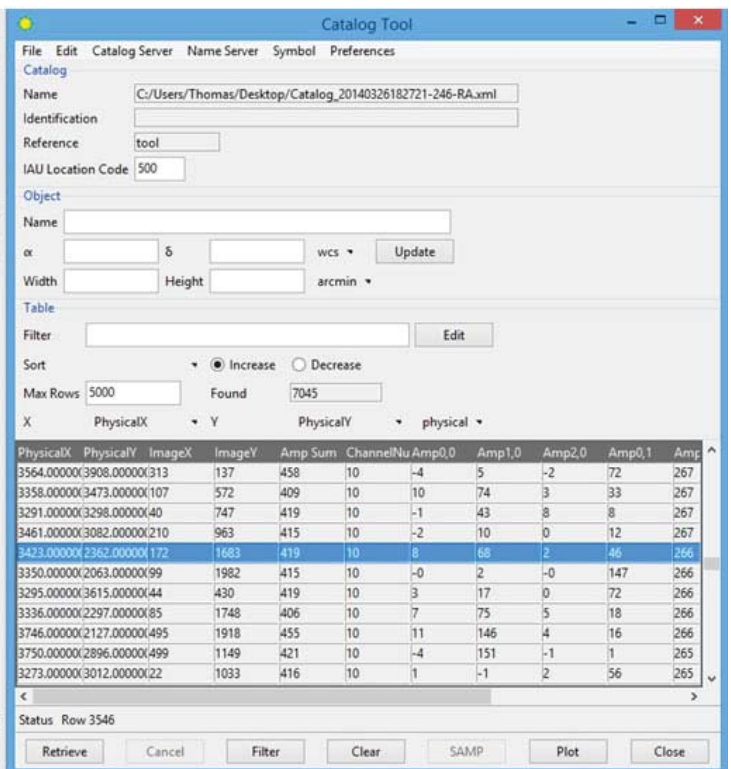
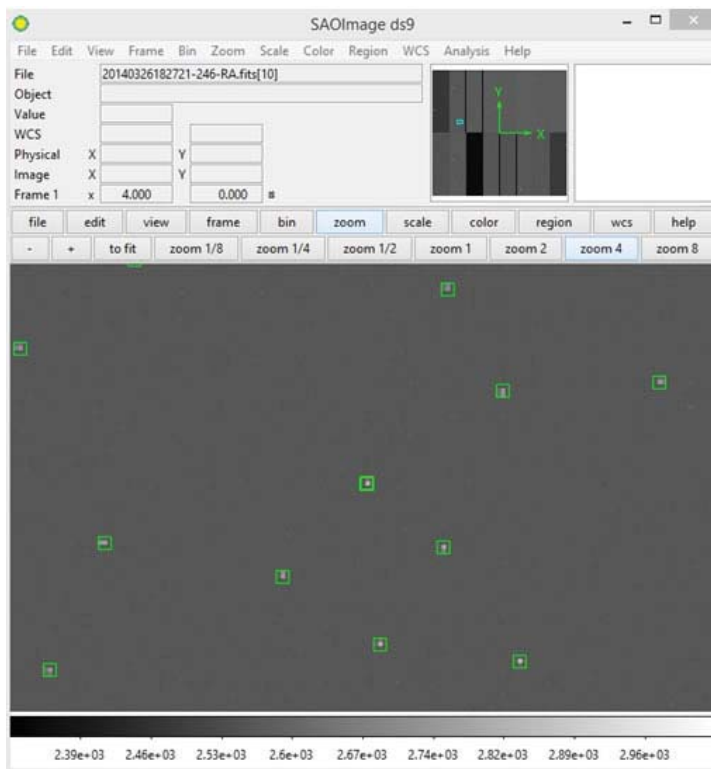


Fig. 5, Fig. 6- Ds9 displaying an image of X-ray clusters, Catalog with table of attributes about each cluster

$$\begin{bmatrix} LTM1_1 & LTM1_2 \\ LTM2_1 & LTM2_2 \end{bmatrix} \begin{bmatrix} P1 \\ P2 \end{bmatrix} + \begin{bmatrix} LTV1 \\ LTV2 \end{bmatrix} = \begin{bmatrix} L1 \\ L2 \end{bmatrix}$$

Fig.7- Coordinate transformation matrix equation from physical to logical coordinates

This transformation was inverted, to obtain the image to physical coordinate transformation.

Since there was no LTM1_2 and LTM2_1 (rotation parameters) I was able to simplify the expression using matrix operations for the inversion and solve for the x and y coordinates individually, yielding these 2 equations:

$$Px = (1 / LTM1_1) * (Ix - LTV1)$$

$$Py = (1 / LTM2_2) * (Iy - LTV2)$$

Where Px and Py represent the physical x and y; Ix and Iy represent the image x and y.

B. OLED Screen

For this project, I collaborated with another intern, Jeremy Hyde, and a student research assistant, John Kuczewski. We were given an Adafruit 1.3 inch OLED (Fig. 8) display and a serial controller called a Bus Pirate (Fig. 9) that acted as a means of communicating with the device from a PC's USB port.

We managed to find an existing python script online that displays a clock on the screen, and we used that for the backbone of our display code. After removing clock functionality, we imported the Python Imaging Library (PIL) so we could use its' powerful image manipulation tools. There is too much code to put on this poster, but it basically goes through a few steps:



Fig. 8- Adafruit 1.3" OLED display

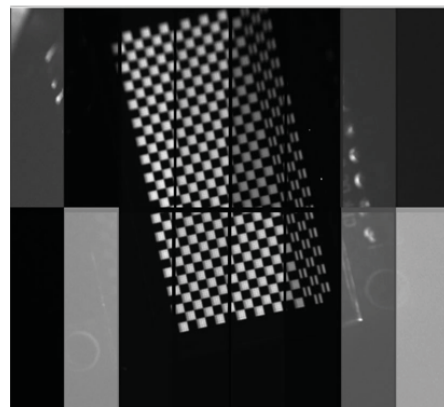
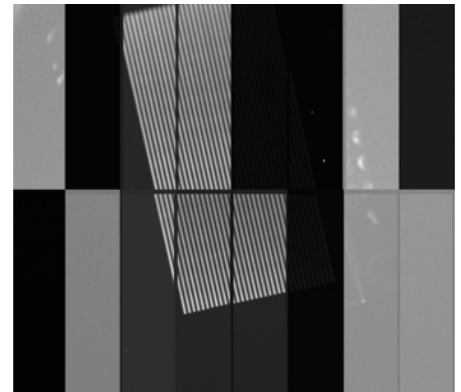
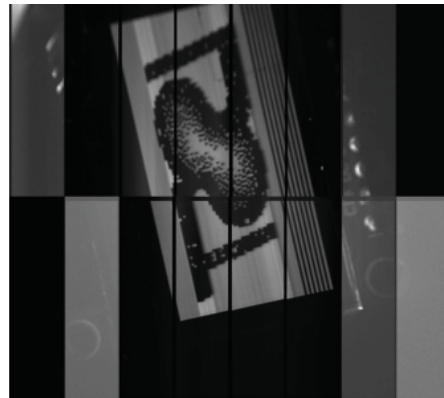
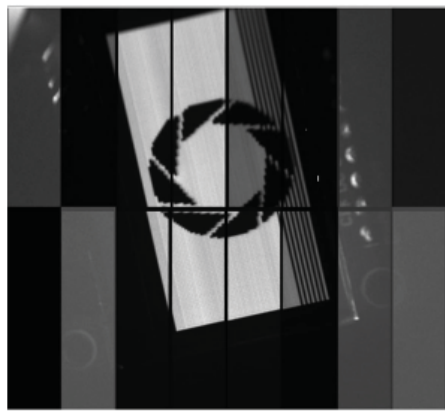


Fig. 9- Dangerous Prototypes Bus Pirate serial controller

- Bus pirate switched to Serial Peripheral Interface (SPI) mode
- OLED is initialized (Contrast set, volatile memory cleared, voltage turned on, screen turned on, test image displays)
- Black image is immediately displayed (which basically turns the screen off while still being powered up)
- Images are ready to display!

At this point, the python script will ask for the image name with full path. Thanks to the PIL, the images can be .jpg, .png, .jpeg, among many others. Also, the size of the image does not matter because the script will dynamically resize it to the 128x64 pixel size of the screen. If using a large image with great resolution, much of this data is lost and the image appears super low resolution. Most of the test images used were created with a painting program (GIMP) at 128x64 pixels to preserve the resolution. After an image is entered it will ask for an exposure time, then the image is displayed for that amount of time.

The conditions of the experiment were not ideal. Ideal operating temperature of the CCD would be -100C or lower to reduce dark current; for this experiment we were operating at about -18C (due to a supply of liquid nitrogen that ran out). Also, there was no back bias applied for this experiment which would have helped sharpen the image by reducing diffusion. These are some of the images captured using this technique:



II. Conclusions

Region marking and catalog creation functionality were explored and implemented in existing C++ code used for the analysis of x-ray cluster data and pocket pumping data. Both of these allow for quicker identification of areas of interest, and allow for storage of useful information about these areas. Manually cataloging this data would be nearly impossible, but with the use of computing it can be done in seconds with literally the push of a button.

The Python code was also written for a small OLED screen so that it can display images that can be used to test various properties of the charge coupled device quickly and easily. This display was tested successfully on the actual CCD but can still be further optimized.

III. Acknowledgements

Brookhaven National Laboratory and the Office of Educational Programs

Saint Joseph's College Math/ Computer Science Department

John Kuczewski and Jeremy Hyde for all their help with both projects

Ivan Kotov for being a great mentor and role model

Paul O'Connor for providing materials and guidance for the OLED project

This project was supported in part by the U.S. Department of Energy, Office of Science, Office of Workforce Development for Teachers and Scientists (WDTS) under the Science Undergraduate Laboratory Internships Program (SULI).

Troubleshooting, project management, and asset tracking of HVAC systems

Derek Squires

Engineering Science, Suffolk Community College, Selden NY 11784

John Biemer

Facilities Operations Center, Brookhaven National Laboratory, Upton NY 11973

Ariel Nunez

Facilities Operations Center, Brookhaven National Laboratory, Upton NY 11973

Abstract

Much of the research done at Brookhaven National Laboratory requires very specific and controlled environments. The Heating Ventilation and Air Conditioning (HVAC) systems present at BNL are the backbone of these environments and there are many resources allocated towards the maintenance of these systems. My project included accompanying Facility Project Manager, John Biemer, on various work related tasks such as inspecting mechanical rooms for faulty equipment, following up on building occupants' requests for work, and diagnosing issues related to HVAC systems. One significant issue included the testing of a fume hood in a Class 1000 clean room in the Physics building. This particular room is designed to have no more than 1,000 air particulates larger than 0.5 microns. Typically, fume hoods will not allow any air from within the hood to escape into the room to prevent any contamination of the rest of the room. One of this room's fume hoods was leaking air from the bottom right corner of its sash. To test the theory that one of this room's return air vents was causing this disturbance, we used a smoke generator to observe the air flow along the sash of the fume hood. In addition, we used a velocimeter to observe the air velocities along the front of the sash. After the testing, it was determined that there were two return air vents pulling air out of the fume hoods and the air flow of the room would need to be modified in order to alleviate this issue. This air flow issue will be rectified by placing Plexiglas over the problematic vents in order to prevent any possible contamination in the room. In addition, this summer has exposed me to the Maximo asset management software, the process of tracking assets, and many HVAC issues that require troubleshooting and resolution.

There is no substitute for hands-on, practical experience in the engineering field. As a mechanical engineering intern, I received this type of experience at Brookhaven National Laboratory (BNL) working within the Facilities and Operations department. The focus of my summer was the heating, ventilation, and air-conditioning (HVAC) systems in the East Complex (one of the four complexes on-site). Many of these systems have been active for over a decade and they require consistent preventive maintenance as well as spontaneous and instantaneous diagnosis and repair. The significance of these systems cannot be overstated; without their operation much of the research present at BNL cannot take place.

On a day to day basis much of my activities included accompanying John Biemer for various work-order related tasks. A work order occurs when there is a facility related issue in need of resolution. When an issue arises, the Facility Project Manager

(FPM) assigned to the building in question will assess the situation in-person to determine a priority level. Then the request is entered into an asset management software database called Maximo. Unless the work is a priority one (an emergency requiring immediate resolution) or two (an urgent matter requiring resolution within 24 hours), it is typically completed at a later date. Each week there is a planning meeting where work orders are assigned to the appropriate trade and scheduled for completion. All of these steps are tracked through Maximo until the task has been completed. I have learned that one of the challenges to being an effective FPM involves the proper management of priority level and the appropriate scheduling of tasks. For instance, if the maintenance of an air handler demands a full day of work, it is impractical to also schedule the completion of other task's on that same day.

Some buildings contain rooms that are more sensitive to operational changes than others. Cleanrooms, for example, are of great importance in many research areas at BNL. A clean room is a meticulously designed space that maintains a certain level of air particulates and has a specially designed air flow. Clean rooms are vital for many applications such as biological experiments, microelectronics, semiconductors, pharmaceuticals, etc. At Brookhaven National Lab, there are a large number of clean rooms of varying specifications for various applications. BNL's Instrumentation Division, for example, uses the Semiconductor Detector Development and Processing Lab (SDDPL), which is an ISO 5 cleanroom, to develop customized radiation and particle detectors (RPD) used in particle accelerators at BNL and around the globe. The SDDPL encountered high humidity concerns this summer and high humidity in combination with electronic components on the microscopic level is a major issue. If there is too much moisture in the air the electronic components can be destroyed and thousands of dollars in wages, materials, and research can be lost. This particular environment has a dedicated air handling unit that will deliberately dry the air entering the room, regardless of the outside air humidity levels. When this event occurred Ariel Nunez, the Facility Complex Engineer (FCE) for the East Complex, was called upon to determine the issue. After investigating the situation he determined that the variable frequency drive (VFD) controlling the desiccant wheel in the air handler had an over voltage error. A VFD controls how fast the desiccant wheel spins based on the humidity of the outside air. If there is very high humidity but the VFD is at maximum frequency and it calls for even greater frequency, or more voltage, the VFD will shut itself down to prevent damage. In order to mediate the situation, the VFD was reset and the dehumidification process was able to resume.

From this experience I learned the process of dehumidifi-

cation utilizing a desiccant wheel. A desiccant wheel is simply a wheel that contains materials on its surface such as silica gel and lithium chloride. These materials absorb the moisture from the outside air that is forced to travel through the wheel's surface area. The air on the other side of the wheel is now very dry and is supplied to the designated area (typically a cleanroom). As the wheel spins, the moisturized portion of the wheel eventually passes through a portion of the wheel that is isolated. Within this isolated portion there are heaters that are taking outside air and drastically raising its temperature before blowing it across the isolated portion of the wheel. The moisture from the wheel is transferred to the hot air and exhausted back into the atmosphere. This process runs continuously in order to maintain the designed levels of humidity within the designated space.

In order to achieve the design requirements of a clean room, there are many air flow and filtration considerations to identify, such as particulate count, air changes, and laminar flow. To classify as an ISO 6/Class 1000 cleanroom, for example, a room must maintain an environment with no more than 1,000 air particulates greater than 0.5 microns in size. Additionally, there are requirements for air changes each hour to maintain that same classification. A complete air change occurs when all of the air in the room is completely replenished with fresh filtered air. There must be between 150 and 240 air changes each hour to maintain the ISO 6/Class 1000 classification. Maintaining a consistent number of air changes ensures that the room's air is always fresh and minimizes the chances of contamination. In the SDDPL, if even a single particle of dust settles on an RPD it could completely ruin the device. Laminar flow is another vital component in a cleanroom. When air is supplied into a cleanroom it is ideal to have that air travel smoothly in one direction towards the floor, where it is then pulled through the return air vents. This smooth, unidirectional air flow is essential for efficiency of particulate elimination and stabilizing temperature and humidity within a cleanroom.

The opposite of laminar air flow is turbulent air flow. One particular clean room at BNL located on the second floor of the Physics building is dealing with turbulent air flow near the corner of a fume hood's face. Adjacent to this particular fume hood are two recirculation vents with enough air velocity to funnel air from the face of the fume hood. A potential crisis exists if scientists are handling hazardous materials within the fume hood and the air flow of the room allows the materials to escape the fume hood. Not only can the scientists be harmed but the materials can be recirculated through the HVAC system and sacrifice its efficacy. This cleanroom is currently certified as an ISO 6/Class 1000 clean room and will be re-certified after researchers move-in and occupy the space.

In order to alleviate the existing air turbulence, I assisted Wai-Lin Litzke, Steven Cannella, and Mary Chu with an ASHRAE 110 smoke detection test. This test involved both small volume and large volume smoke generation. We utilized the smoke to analyze the movement of air along the face of the fume hood in question. The process consisted of holding the smoke generators at evenly spaced distances (about 6 inches) within the entire face. We started in one corner and moved across the face. Then we lowered the smoke supply and observed the airflow along that elevation across the entire face. We continued this process until we were able to gauge the air flow along the entire fume hood face. During testing, it was visually obvious that the fume hoods were pulling the smoke from the lower right hand corner. To rectify

the situation, we placed two large pieces of paper with sufficient surface area to restrict airflow to the vents. This temporary solution was visually effective and re-established sufficient laminar air flow along the face of the hood. After this testing, a work order was entered to create Plexiglas covers to restrict the air flow to the two troublesome recirculation vents.

One other cleanroom issue I encountered this summer involved HEPA filtration. In order to control air particulates within a cleanroom space High Efficiency Particulate Air filters are installed. These filters are 99.97% effective at removing air particulates at least 0.3 micrometers in diameter or larger. The efficacy of HEPA filters does diminish over time and they are typically replaced every five to ten years. In the Instrumentation Division, the Printed Circuit Board Fabrication laboratory has an area requiring HEPA filtration. Similar to the particle detectors in the SDDPL, printed circuit boards must reduce particle contamination. There were a handful of HEPA filters that were no longer providing sufficient air flow and filtration to this designated area. I assisted the assessment of this issue but manually observing the air flow through these filters and indicating which filters needed replacement. The observation consisted of placing a hand directly under the filter and determining whether there was air flow or not. A total of nine filters were considered to be functioning at below standard capacity and the replacement process has begun.

Another experience I had this summer involved a different air flow concern. In the Environment, Safety, and Health building there was an office with a problematic PTAC unit. A PTAC unit is a Packaged Terminal Air Conditioner and is commonly used for office space and residential applications. These units contain all components of the HVAC cycle within one package and are generally located within a wall that allows access to the outdoors. The occupant indicated that the room was unable to achieve the desired temperature except underneath the desk where the unit was located. After consulting with one of the HVAC mechanics it was determined that the unit was performing a "short-cycle." Short-cycling occurs when the cold air supplied into the designated space does not have travel far enough to mix with the existing warmer air. Instead, the cold air travels from the supply fan almost directly back through the return portion of the unit where the evaporator coil is located. If the desired temperature is 68 degrees Fahrenheit and that same 68 degree air is pulled across the evaporator coil, there will be no heat exchange process. Since the refrigerant no longer absorbs the heat from the room's air it does not change from a cold, low pressure liquid to a cool, low pressure gas. Instead, it remains a cold liquid and travels very slowly through the coils. As the refrigerant remains cold and slows down within the coils, the moisture from the room's air begins to condense and freeze around the coils near its designated exit point. As the short-cycling continues, the freezing occurs further and further along the coils and the compressor will need to work harder and harder to generate a hot, high pressure gas for the condenser coil.

To resolve the issue, the unit was shut down to allow for the ice to thaw. Once thawed, the unit was returned to normal functioning until the short-cycling returned a few weeks later. This time the unit was replaced with a newer, unused unit from another building with the hopes of reduced short-cycling.

In addition to diagnosing HVAC issues and concerns I was involved in the management of assets in both NSLS 1 and NSLS 2. More specifically, there were pre-action sprinkler systems that

needed identification and blueprint updates in NSLS 1 as well as asset identification tags that needed placement on various other assets. My role in this process was to assist Joann Giambalvo, an FPM in the East Complex, with locating the six pre-action sprinkler systems. It is essential to know the location of these systems in the case of an emergency and in the case of false activation. The pre-action sprinkler system in NSLS 1 is considered a dry-system. When no danger is present the system contains compressed air. If danger is present the system requires two triggers to occur in order for water to be released. First, smoke and heat detectors sense a rise in temperature and charge the system with water. The system is ready for action at this point but will not release water into the designated space. Second, a sprinkler head must activate. Activation occurs when the temperature is high enough to melt the lead previously blocking water from flowing. Once the lead melts, the charged system will release water into the endangered space. For the most part, identifying these systems was simple because there are already blueprints and drawings pointing to their locations. Two of the pre-action sprinkler stations, however, were located adjacent to one another and it was not previously indicated whether they were also connected. Ms. Giambalvo and I determined they shared a common water main pipe and submitted this information to be updated in the system's AutoCAD drawings.

Every piece of mechanical equipment requires some sort of preventive maintenance. In order to track the equipment it is given an asset identification number. A new building such as NSLS 2 has a lot of newly installed equipment that is not necessarily on a preventive maintenance schedule. If the proper preventive maintenance is not performed, equipment can become damaged over time and the efficiency of the HVAC systems may suffer. In order to help Joe Stanisci, the FPM of NSLS 2, I traveled through the entire building and compiled a list of every air handler, fan coil, eye wash station, safety shower, and reduced pressure zone valve (RPZ valve). The list totaled over 60 assets. I gained a significant amount of experience by going through the process of identifying the equipment and becoming familiar with the various systems within the mechanical rooms.

In addition to the various tasks I completed this summer, I also took tours of the Central Steam Plant, the Central Chilled Water Facility, the Center for Functional Nanomaterials, and the Interdisciplinary Science building. The exposure to these various facilities revealed the real world significance and impact of the mechanical engineering discipline on the work of important research and science at the Brookhaven National Laboratory. The vital connection between the classroom and application is significantly clearer after this internship.

I. Appendix

Participants:		
Name	Institution	Function
Derek Squires	Suffolk County Community College	Intern
John Biemer	Brookhaven National Laboratory	Mentor
Ariel Nunez	Brookhaven National Laboratory	Mentor

II. Outcomes

During my summer at BNL I produced a number of spreadsheets that help track assets. I helped gather the location of assets in NSLS 1 for the preventive maintenance schedule for FPM Joann Giambalvo. In addition, I compiled separate lists for each individual air handler, fan coil, RPZ valve, safety shower, eye wash station, and hot water tank for NSLS 2. Other contributions I made include measurements for equipment replacement submittals, updating pre-action fire sprinkler system drawings, and measurements of furniture layout in the office space of building 727.

Evaluating the effect of oxygenated compounds on the long-term stability of home heating oil

Andrew Sung

Chemical and Molecular Engineering Program, Stony Brook University, Stony Brook, NY 11794

Sabrina Chasen

General Douglass MacArthur High School, Levittown, NY, 11756

Ofei D. Mante and Thomas Butcher

Department of Sustainable Technologies, Brookhaven National Laboratory, Upton, NY, 11973

ABSTRACT

High demands for energy and the increased awareness of phenomena like climate change have been the impetus for developing and utilizing sustainable technologies. Many research groups have begun investigating different forms of biofuels, such as biodiesel and upgraded pyrolysis oil (UPO), to alleviate heating oil prices and reduce greenhouse gas emissions. This drive to incorporate biofuels into traditional home heating oil (HHO) has been ongoing, with current HHOs containing up to 5wt.% biodiesel. Studies show that blending biofuels into HHOs may accelerate degradation, causing problems with the long-term stability of the oils. This project aims to understand to what degree certain oxygenated compounds found in UPOs contribute to the long-term stability of HHO blends. In these studies, HHO doped with phenols and ketones at 1wt.%, 3wt.%, and 5wt.% by weight were subjected to aging at 80 ± 2 °C for one week. The formation of insolubles was determined using a filtration setup in accordance to the American Society for Testing and Materials (ASTM) D4625. The products were analyzed through gas chromatography-mass spectroscopy (GC-MS), Fourier Transform Infrared (FTIR) spectroscopy, and total acid number (TAN) [ASTM D974] experiments. The blends were characterized before and after aging to determine changes in chemical and physical properties. Preliminary data suggests that oxygenated compounds play a significant role in the formation of insolubles. In particular, ketones were found to produce higher levels of insolubles than phenols. For the phenols mixtures, insoluble formation reached a maximum at 3wt.% and decreased at higher concentrations.

I. INTRODUCTION

High demands for energy and diminishing quantities of fossil fuels have geared our research interests toward developing renewable energy technologies, such as bioenergy. Biomass can be produced in large quantities without threatening ecosystems or the world food supplies, giving it potential as an alternative energy resource. (Florides, 2009) Biomass can also be converted into biofuels, which could be complements to the fossil fuel energy sources we use today.

A. Fast Pyrolysis and Pyrolysis Oil

The process of fast pyrolysis, which converts biomass to pyrolysis oil, has been evaluated by many researchers as a potential solution to our energy demands. (RH Venderbosch, 2010) Fast pyrolysis is the rapid thermal decomposition of organic compounds in the absence of oxygen at 450-600°C. (Brown) Pyrolysis oil is formed through the condensation of organic vapors from this process. Unfortunately, raw pyrolysis oil cannot be added to com-

mercial liquid fuels because of its high oxygen and water content. The oxygenated compounds in pyrolysis oil are responsible for its low heating value, high energy moisture content, acidic properties, limited stability, thermal instability, and formation of insolubles. (Wolff, 2010) In particular, the acidity and formation of insolubles in raw pyrolysis oil damage home heating systems by rust and clogging, respectively.

To combat this problem, raw pyrolysis oil can be processed via hydrotreating to form upgraded pyrolysis oil (UPO). (SB Jones, 2012) UPOs have lower oxygen contents than raw pyrolysis oil, making them more suitable for blending with commercial liquid fuels. However, studies regarding the addition of UPO to liquid fuels are incomplete, making it difficult to introduce them commercially. In addition, UPOs can vary in oxygen content, from 1% up to 10%. One study determined that the oxygenated compounds present in the highest oxygen content (HOx) bio-oil blends contained too many carboxylic acids, carbonyls, aryl ethers, phenols, and alcohols, making them unsuitable for fuel blendstocks. (Christensen, 2011)

B. Biofuels in Oil-Based Home Heating Systems

Within the realm of bioenergy, studies regarding the addition of biofuels to oil-driven home heating systems have recently emerged. Traditional burners consume home heating oil (HHO) with up to 5% biodiesel present, and a goal for 20% biodiesel/80% HHO blends has been set for the near future. However, studies have shown that these blends face challenges regarding stability over long periods of time. Bio-oils introduce water and other oxygenated compounds to the blends, thus lowering their fuel and combustion efficiencies, promoting the formation of substances that degrade the blends, and jeopardizing the physical structure of home heating systems. (Knothe, 2007) Researchers propose that the role of oxygenated compounds in biodiesel/HHO blends may be the similar in all liquid biofuels.

Storage stability of fuels is a concern because fuels may not be used immediately. (Peyton, 2008) In particular, backup generators in hospitals consume oil periodically, and may be stored for extended periods of time. Unstable oils can create gums and oligomers, which can clog oil pumps. Pure biodiesel (B100) blends did not produce these gums, while biodiesel-diesel blends (B5-B20) produced gums. This indicates that the formation of gums stems from interactions between the biofuels and HHOs.

C. Project Goals

This study aims to understand how phenols and ketones contribute to the long-term stability and degradation of HHO blends with UPOs. This study also aims to identify which oxygenated compounds in HHO/UPO mixtures contribute significantly to the

formation of insolubles.

II. LITERATURE REVIEW

Experiments regarding bio-oil stability have been ongoing and require standard procedures to produce comparable and reproducible data. The American Society for Testing and Materials (ASTM) creates standard test methods for stability testing, and stability parameters. The most commonly used practice for oil studies follows ASTM D4625, in which oil blends are synthesized and subject to aging in a 43°C environment. Studies have shown that oil aged for one week in a 43°C environment produce similar amounts of insoluble compounds to oil that has aged at ambient temperature for one month. (Peyton, 2008) Modified versions of this method are ASTM D2274, which studies the stability of oils at 95°C in higher concentrations of oxygen, and one-week studies at 80°C.

Despite the type of ASTM study, problems that have been associated with storage and stability are microbial contamination and the formation of bacteria and fungi (Bento, 2001), contact with air (autoxidation) (Dunn, 2002), contact with water (Knothe, 2007), and contact with peroxides (Knothe, 2007). To combat these three particular issues, research has been done in adding antioxidants to the blends to make them less prone to reactions and increase the duration of stability. For the purpose of this study, the only variable will be the exposure of samples to air and autoxidation.

Oils are analyzed after aging using analysis methods like Gas Chromatography Mass Spectroscopy (GC-MS) and Fourier Transform Infrared (FTIR) Spectroscopy to characterize their molecular structures. Additional tests for viscosity (ASTM D445), total acid number (ASTM D974), and filtration (ASTM D5304) are used in conjunction with the GC-MS and FTIR techniques. These methods can be used to determine the composition of the oils before and after aging. A comparison between the two data sets can be the basis for producing reaction mechanisms and theorizing the reaction pathways that are present in the aging reactions.

III. MATERIALS AND METHODS

A. Materials

The chemicals that were used in this study consisted of 2,4-dimethylphenol (2,4-MP) ($\geq 98\%$ purity, Sigma-Aldrich), 3-ethylphenol (3-EP) ($\geq 95\%$ purity, Sigma-Aldrich), cyclopentanone ($\geq 99\%$ purity, Sigma-Aldrich), and 3-pentanone ($\geq 99\%$ purity, Sigma-Aldrich). Ultra low sulfur (ULS) diesel with up to 5% biodiesel was used for the experiments. Nylon filter papers with pore sizes of 0.8 μm were used for the oil filtration.

The analysis equipment consisted of a FTIR spectrometer (PerkinElmer, Frontier FT-IR/FIR Spectrometers), GC-MS (Agilent 7890A GC and 5975C MS detector), glass viscometer (calibrated CFRC (9721-B50) Series), analytical balance, and software including Microsoft Office.

B. Methods

The doped HHO blends were subject to aging studies in accordance to the ASTM standards.

1. Sample Preparation

Samples were prepared in 30 mL vials. 25 mL of ULS diesel was measured through a graduated cylinder and added to the vial.

The weight of the oil was recorded and the corresponding amount of doping (1wt.%, 3wt.%, and 5wt.%) was calculated and added. The sample was capped, vortexed for 30 seconds, and labeled. The samples were left capped or uncapped before the stability studies.

2. Stability Studies at 80 °C (Du Pont F 31)

Blends of pre-filtered ULS diesel and oxygenated compounds went through accelerated storage stability tests at 80 °C for one week. The 80 °C accelerated study models after ASTM D4625, another long-term stability study. The total amount of insolubles formed in the accelerated study in one week correlates to that of ASTM D4625. The oxygenated compounds used in this study were 2,4-dimethylphenol (2,4-MP), 3-ethylphenol (3-EP), cyclopentanone, and 3-pentanone. 100 mL samples were prepared with 1wt.%, 3wt.%, and 5wt.% of each oxygenated compound. These uncapped samples were put into a 80 °C oven for one week.

3. Visual Inspection

The blends were subject to visual inspection after the one week aging studies. Before aging, the blends were the same visually (light yellow hue). However, the blends after aging were colors ranging from yellow to dark brown.

a. Filtration of ULS Diesel

The filtration process followed ASTM D4625. The oil was filtered four times (Nylon filters, 0.8 μm).

b. Filtration of Aged Oils

The filtration process followed ASTM D4625. Filter papers (Nylon filters, 0.8 μm) were annealed for 30 minutes at 90 °C pre-filtration. The filter papers were weighed using an analytical mass balance after the annealing period and the weights were recorded. A vacuum filtration setup in accordance to ASTM D4625 was used. Each filter paper collected insolubles from four 25 mL samples (total 100 mL). The vials were rinsed out with iso-octane solution and poured through the filter paper. The papers were rinsed with iso-octane solution and placed into the oven at 90 °C to dry. The dried filter papers were weighed, and the weight of the insolubles was determined via Microsoft Excel.

4. Determining the Total Weight of Insolubles

The total weight of insolubles was the sum of the filtered insolubles and the leftover insolubles in the vials. To determine the weight of the insolubles in the vials, the vials were dried at 90 °C for 30 minutes and weighed. They were washed out with tri-solvent, reheated at 90 °C for 30 minutes, and weighed again. The difference in weight was the weight of insolubles in the vials. The total weight of insolubles was determined via Microsoft Excel.

5. GC-MS Sample Preparation and Analysis

200 mg of filtrate was weighed out. Acetone was added until the total mixture was 5 mL. The 5 mL solution was vortexed for one minute and 1.5 mL aliquots were taken for the GC-MS analysis.

The injection was held constant at 1 μL for all the trials. A split ratio of 75:1 was used for the GC-MS analysis. A 60 m x 0.25 mm DB-1701 capillary column of 0.25 μm film thickness was used for the separation of products. The inlet temperature was set to 275 °C and maintained a constant flow of 1 mL/min of helium

gas. The ion source and the interface of the mass spectrometer detector were held at 230 °C and 250 °C respectively. Electron ionization of the compounds was performed at 69.9 eV and the ions were separated by their mass-to-charge (m/z) ratios in the range of 28 to 350. The temperature gradient for the diesel method is shown in Table 1.

	°C/min	°C	hold (min)	run (min)
Initial		40	1	1
Ramp	5	275	12	60

Table 1. GC-MS Diesel Method Temperature Gradient

6. FTIR Sample Preparation and Analysis

Samples were taken to Stony Brook University for FTIR analysis. A background scan was done before each sample analysis. The spectrum of samples was obtained over a range of 4000-380 cm⁻¹ using 4 scans per run.

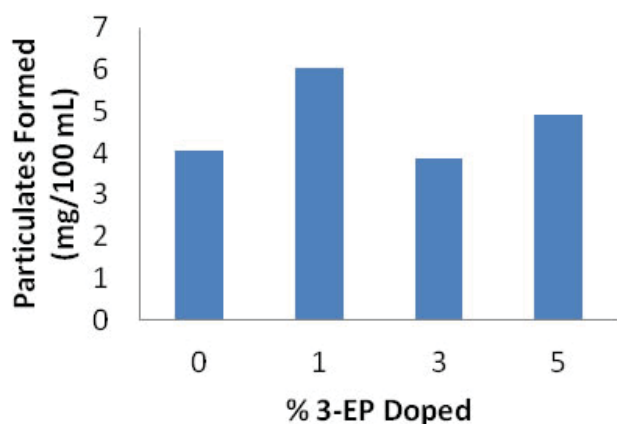


Figure 1. 3-Ethylphenol experiment with caps

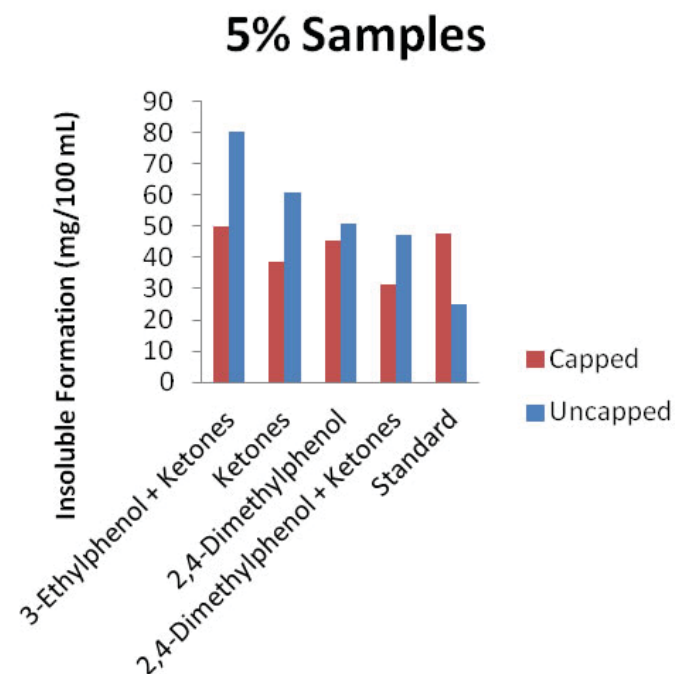


Figure 2. Preliminary data for phenol and ketone aging experiment

7. Total Acid Number (TAN)

The TAN studies were done in accordance to ASTM D974. Only the filtrates went through the TAN studies.

8. Viscosity

The kinematic viscosity of the filtrates was measured at 40°C with a 50 Cannon-Fenske upflow viscometer in accordance to ASTM D445.

IV. RESULTS AND DISCUSSION

A. Insolubles Formation

The first experiment that was conducted was to determine the insolubles formation for 3-ethylphenol after the one week study. The samples were prepared and placed into the oven, capped. Figure 1 shows the filtration results for the insolubles formed.

The data suggests that no correlation can be found between the percentage of doping and the formation of insolubles. In addition, it is unclear whether the addition of 3-EP played a role in insolubles formation.

The second experiment focused on both phenols and ketones. The types of blends were standards, phenols alone, ketones alone, and mixtures of phenols and ketones. All ketone mixtures had a 1:1 ratio of cyclopentanone and 3-pentanone. The 1% ketone mixtures consisted of 0.5% of each ketone, while the 5% ketone blends had 2.5% of each ketone. The phenol/ketone mixtures had a 2:1:1 ratio of phenol:cyclopentanone:3-pentanone. Two sets of samples were prepared for the 2:1:1 mixtures, one with 3-EP and one with 2,4-MP. Two samples of 25 mL were prepared for each blend; one was tested with the cap on and one without. The results for this experiment for samples with 5wt.% doping are shown in Figure 2.

The preliminary data suggests that capped samples did not indicate a correlation between insolubles formation and type of doping, which was observed in both Figures 1 and 2. However, the uncapped samples had increased insolubles formation with doping than the standards. This data suggests that the 1:1 ketone mixture produced more insolubles than 2,4-MP alone, and that ketones with 3-EP produced the most insolubles.

With the data shown in Figure 2, the direction of the project shifted to evaluating the effects of 3-EP, 2,4-MP, cyclopentanone,

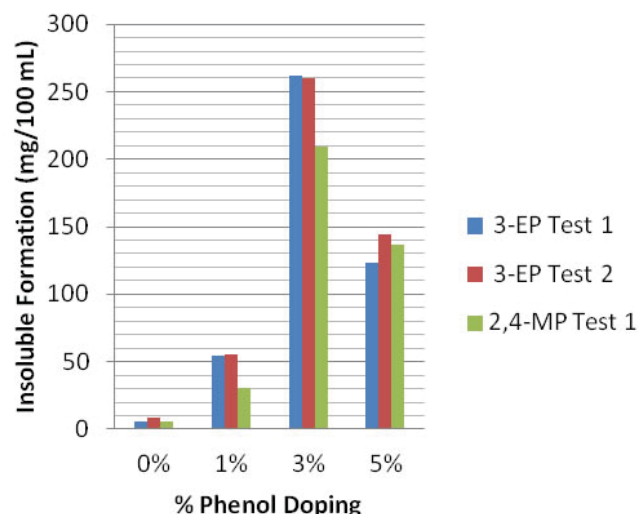


Figure 3. Phenol doped HHO experiments

and 3-pentanone blended with HHO. The next tests were the stability of oils doped with 3-EP and 2,4-MP. The results of the phenol experiments are shown in Figure 3.

Two studies have been done for the 3-EP, and one for the 2,4-MP. The 3-EP data in Figure 3 correlate very well with each other, and is similar to the 2,4-MP data. Aside from the quantitative similarity, there is a drop in insolubles formation from the 3wt.% to 5wt.% doping. This phenomenon occurs in all three phenol experiments.

B. Visual Inspection

The formation of insolubles was further supported by the visual inspection test. Although the initial blends were light yellow, the aged blends ranged from yellow to dark brown. Figure 4 and 5 illustrate the color changes that were observed for 3-EP and 2,4-MP after aging.

The color change in 3-EP is more apparent as the phenolic concentration is increased. The 5wt.% solution is the darkest, while the standard is the lightest. However, the color change in 2,4-MP correlates with Figure 3, in which the darkest sample occurred at 3wt%. The amount of filtered insolubles was the highest at 3wt%, which may explain the reason for the dark 3wt% samples. The visual tests indicate that even phenols amongst themselves can contribute to the insolubles study differently after aging.



Figure 4. Color change observed in 3-EP after aging



Figure 5. Color change observed in 2,4-MP after aging

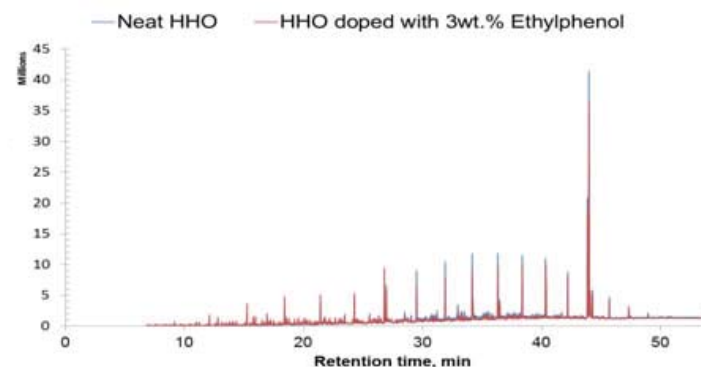


Figure 6. GC-MS chromatograph of clean HHO and HHO doped with 3-EP

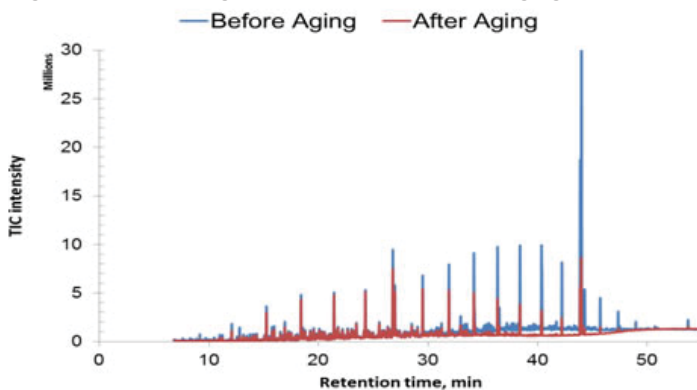


Figure 7. GC-MS data of 3wt.% 3-EP before and after aging

C. GC-MS and FTIR Analysis

The GC-MS data can be used to monitor the changes in chemical composition before and after the aging reaction. The 3-EP peak can be observed around the 24 minute mark, as shown in Figure 6.

The GC-MS data comparing the oils before and after aging are shown in Figure 7.

As shown in Figure 7, the concentration of 3-EP and other hydrocarbon peaks decrease after aging. This suggests that both phenolics and hydrocarbons are consumed during the aging process and not just the phenolics as predicted. Since there are no increasing peaks in this analysis, it can be assumed that the missing mass can be found in the insolubles that were filtered out.

Just as the GC-MS indicates what types of compounds are consumed and created, the FTIR indicates what types of functional groups are consumed and created. Figure 8 is a FTIR analysis of 5wt.% 3-EP before and after aging, and Figure 9 is that of 5wt.% 2,4-MP.

In both cases, there is a sharp decrease in the 2800-3000 cm⁻¹ range (hydrocarbons), and an increase in the 1500-1800 cm⁻¹ range (carbonyls). This supports the data shown via GC-MS, in which the hydrocarbons are being consumed in the synthesis of insolubles.

V. CONCLUSIONS

According to the GC-MS and FTIR analysis for this study, it can be concluded that the addition of oxygenated compounds to home heating oil accelerates degradation and insoluble particulate formation. Samples doped with phenols and ketones yielded higher formations of insolubles than those without, with preliminary data suggesting that ketones being more reactive than phenols. When comparing 3-EP to 2,4-MP, it seems that 3-EP is the more reactive phenol because of its higher potential for bonding.

For the phenol studies, a parabolic trend is observed as the weight percent is increased from 0% to 5%. The insoluble formation increases up to 3wt.%, and then drops off at 5wt%. Our current hypothesis is that the phenols promote the formation of antioxidants, which nullifies the increasing formation of insolubles. More in-depth analysis is being done on the GC-MS data, with hopes to finding potential antioxidant compounds to support this theory.

The GC-MS and FTIR analysis suggests that hydrocarbons contribute to insolubles formation. Given the general inactivity of hydrocarbons, this phenomenon was unexpected. Studies are being done to analyze the filtered insolubles from the samples.

Lastly, the interaction between oxygen in the air and mixtures plays a significant role for the formation of insolubles and degradation of the HHO. Preliminary experiments with oil samples exposed to air showed more insolubles formation than those without exposure to air.

VI. FUTURE STUDIES

The studies conducted in this project are being repeated with the addition of acids. The goals of these studies are to determine the role of acids in the degradation of HHO and also the degree of degradation of oils doped with oxygenates and acids. Oxygenated compounds accelerate the degradation of HHO, and it is theorized that the addition of acids will further degrade the oils. Preliminary data suggests that blends doped with acids and phenols produce more insoluble particulates than blends doped with only phenols.

Immediate future goals include: finishing the 2,4-MP studies, finishing the cyclopentanone studies, finishing the 2-pentanone studies, and producing phenol/ketone blends for studies. In addition, reaction mechanisms for the change in insolubles for the phenols and ketones will need to be proposed.

Long-term goals include: introducing anti-oxidants to phenol blends, introducing aldehydes to the experiments, and incorporating this model study to applications of UPO/HHO blends.

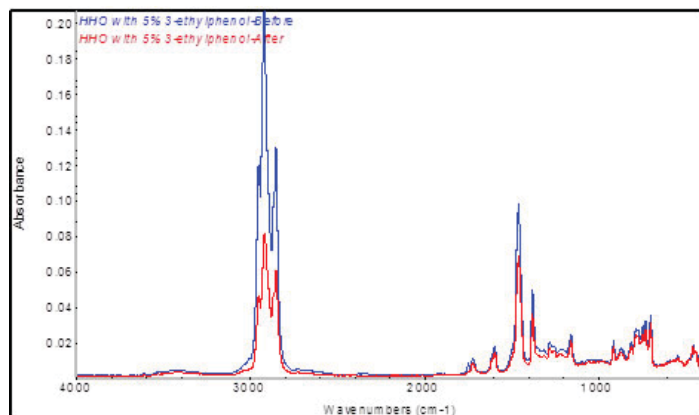


Figure 8. FTIR analysis of 3-EP before and after aging

VII. ACKNOWLEDGEMENTS

This project was supported in part by the U.S. Department of Energy, Office of Science, Office of Workforce Development for Teachers and Scientists (WDTS) under the Science Undergraduate Laboratory Internships Program (SULI). I would like to thank Dr. Ofei Mante and Dr. Thomas Butcher for their guidance and mentorship throughout the entire project. I would like to thank Dr. Taejin Kim for his assistance in operating the FTIR unit at Stony Brook University.

VIII. WORKS CITED

- Bento, F. (2001). Biodeterioration of stored diesel oil: studies in Brazil. *International Biodeterioration & Biodegradation* , 107-112.
- Brown, R. C. (n.d.). Retrieved August 6, 2014, from www.ars.usda.gov: <http://www.ars.usda.gov/sp2UserFiles/Program/307/biomastoDiesel/RobertBrown&JenniferHolmgrenpresentation-slides.pdf>
- Christensen, E. (2011). Analysis of Oxygenated Compounds in Hydrotreated Biomass Fast Pyrolysis Oil Distillate Fractions. *Energy Fuels* , 5462-5471.
- Dunn, R. (2002). Effect of Oxidation Under Accelerated Conditions on Fuel Properties of Methyl Soyate (biodiesel). *JA-OCS* , 915-920.
- Florides, G. (2009). P. Christodoulides. *Environment International* , 390-401.
- Knothe, G. (2007). Some aspects of biodiesel oxidative stability. *Fuel Processing Technology* .
- Peyton, K. (2008). Preventing Sediment Formation In Stored Biodiesel Fuel Blends. *Biodiesel Magazine*.
- RH Venderbosch, W. P. (2010). Fast pyrolysis technology development. *Biofuels, Bioprod. Bioref.* , 178-208.
- SB Jones, J. M. (2012). Production of Gasoline and Diesel from Biomass via Fast Pyrolysis, Hydrotreating, and Hydrocracking: 2011 State of Technology and Projections to 2017. Pacific Northwest National Laboratory.
- Wolff, R. (2010). Pyrolysis Oil Challenges and Solutions. *Biomass Magazine*.

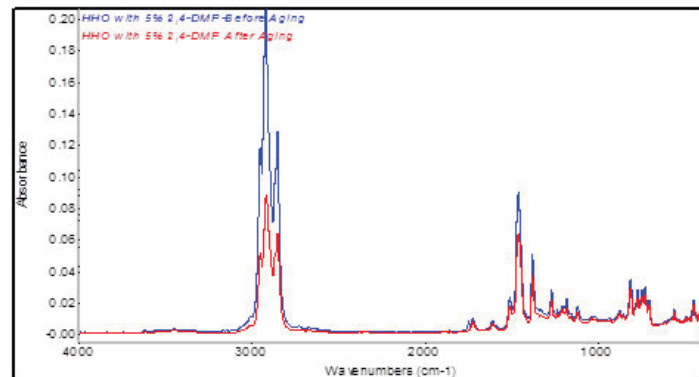


Figure 9. FTIR analysis of 2,4-MP before and after aging

High throughput screening using acoustic droplet ejection to combine protein crystals and chemical libraries on crystallization plates at high density

Ella Teplitsky

Department of Biochemistry and Cell Biology, Stony Brook University, NY, 11794-5215, USA

Karan Joshi

Department of Electronics and Electrical Communication Engineering, PEC University of Technology, Chandigarh, India

Jeffrey D. Mullen

Physics Department, University of Oregon, Eugene, OR 97403-1274, USA

Grace S. McCarthy and Alexei S. Soares

Photon Sciences Directorate, Brookhaven National Laboratory, Upton, NY, 11973-5000, USA

Abstract

We describe a method for screening up to 1728 distinct chemicals with protein crystals on a single microplate. Both co-crystallization and soaking experiments can be assembled at very high throughput (2.33 screened chemicals per second) using very small quantities of protein and chemical (2.5 nL). Each crystal and chemical is precisely co-positioned at a distinct location on a MiTeGen in situ-1 crystallization plate™ using acoustic droplet ejection (ADE). This technology builds on previously described methods for using ADE to grow protein crystals, to screen chemical libraries, and to deliver protein crystals to the X-ray beam. Acoustic ejection functions by using sound to propel a droplet of protein, a droplet of precipitant, and a droplet of each screened chemical onto a single location on the crystallization plate. Crystal growth is driven through vapor diffusion by the precipitant solution in a reservoir. The screened chemicals can be added either before crystallization (co-crystallization) or after the crystals have grown (soaking). ADE transferred droplets follow a very precise trajectory (precision is $\pm 1.3^\circ$). This accuracy allows all components to be transferred through small apertures. Consequently, the crystallization plate is at equilibrium with the reservoir before, during, and after the transfer of proteins, precipitants, and chemicals. Chemical libraries that are solvated in DMSO are sometimes intentionally allowed to evaporate, leaving only the chemical residue, because DMSO can inhibit crystallization. This strict control of the specimen environment means that crystallography experiments remain identical as working volumes are decreased from the few microliter level to the few nanoliter level. Using this system, we screened a heavy atom library with crystals of thermolysin. Each screen was performed twice, once with each chemical added before crystal growth (co-crystallization) and once with each chemical added after crystal growth (soaking). Fluorescence was used to confirm that each chemical in the heavy atom library was correctly paired with the intended protein crystal. This technology pushes towards a much faster, more automated, and more flexible strategy for high throughput screening of chemical libraries (such as fragment libraries) using as little as 2.5 nL of each major component.

I. Introduction

High throughput screening using X-ray crystallography is a powerful tool for applications such as fragment library screening

(for structure based drug discovery) and additive library screening (for improving crystal quality). For structure based drug discovery projects (Blundell et al, 2002) the screened library may consist of individual fragments (Chilingaryan et al., 2012) or pooled fragments (Nicholls et al., 2010). For crystal quality improvement projects the screened library may contain additives such as protic ionic liquids (Kennedy et al, 2011). The chemicals being screened can be added either before crystal formation (co-crystallization) or after the crystals have grown (soaking). Either way, the objective is to screen a library which may consist of several thousand chemicals using as a minimum of amount of purified protein, screened chemicals, and other consumables.

Acoustic droplet ejection (ADE) has a demonstrated utility for growing protein crystals (Villasenor et al., 2012), improving the quality of protein crystals (Villasenor et al., 2010), mounting protein crystals onto data collection media (Soares et al., 2011; Roessler et al., 2013), and high throughput screening of protein crystals (Yin et al, 2014). This method uses a sound pulse to transfer momentum to a liquid (or suspended solid) (Figure 1). The liquid is then propelled out of the source location, through a short air column, and onto an arbitrary destination (Ellson et al., 2003) with a published volumetric accuracy of 5% and a measured trajectory precision of 1.3° (data not shown; larger for some fluids). The high trajectory accuracy enables a “drop on drop” capability which supports combining distinct components from different source wells onto the same destination location. Our group has demonstrated that high “drop on drop” accuracy is sustained across a wide variety of commercially available crystallization conditions and cryo protectants (Cuttitta et al., 2014). The transferred volume of the liquid is governed by the frequency of the sound (typical working volume is 2.5 nL), and the velocity is determined by the amplitude of the sound (typical ejection velocity is 1 m/s). To eject larger volumes, the Echo 550 does not modulate the frequency of the sound, but rather emits multiple sound pulses to build up the desired volume in 2.5 nL increments. Thus the Echo 550 has the same 5% v/v precision across all volumes.

Villasenor and co-authors have suggested that acoustic methods might be used for structure based drug discovery by co-crystallizing protein and fragments using a shared reservoir on a conventional crystallization plate (Villasenor et al., 2012, 899¶6). Note that this strategy employs the same precipitant to drive crystallization in all 96 wells of the micro crystallization plate. Acoustic methods are an attractive choice for micro crystallization for several reasons. ADE is an automated technique that

is independent of operator skill. It is physically gentle with no tips or tubes that may leach chemicals, cause cross contamination between specimens (McDonald et al., 2008), or damage crystals. Transfers have high accuracy even at very low volume (2.5 nL) with zero loss of specimen since there are no tips or tubes that liquids can adhere to (zero per transfer lost volume). The inaccessible volume at the bottom of each well is very small (4 μ L dead volume; Harris et al., 2008) and can be readily reduced even further (Cuttitta et al., 2014). Specimen transfer is fast (2.33 \pm 0.04 mounts per second to multiple destinations, 500 mounts per second between fixed locations; data not shown), which reduces specimen preparation time.

As the working volume for crystallization drops below \sim 50 nL, dehydration becomes the foremost challenge. Our group made a previous attempt to develop the technology proposed by Villasenor et al. in 2012 without success (and we know of other similar attempts by other groups from personal communications). We tried several strategies for mitigating the impact of dehydration, such as working at 4°C, parsing big jobs into small pieces, or simply working faster. None of these mitigation strategies were helpful when working with 2.5 nL working volumes. Fortunately, dehydration effects can be virtually eliminated by transferring all protein, precipitant and fragment components through small apertures in a plate lid that covers the MiTeGen crystallization plate (Supplemental Figure 1). The MiTeGen plate is allowed to equilibrate with the precipitant before the crystallization fluids are added (Figure 2). The objective is to maintain the MiTeGen plate in vapor equilibrium with the precipitant before, during, and after the transfer of all fluids (except for some DMSO solvated chemicals, as described later).

Here, we describe a high throughput technique for screening protein crystals against a chemical library using acoustic droplet ejection (ADE) to prepare co-crystallization experiments or soaking experiments on MiTeGen in situ-1 crystallization plates™ (Figure 3). The Echo 550 acoustic liquid handler makes efficient use of very small volumes of each experimental building block (we used 2.5 nL of protein, precipitant, and each screened chemical). As the working volumes descend below about 100 nL, preventing dehydration becomes the dominant challenge in the experiment. When the volumes are just a few nanoliters, dehydration to room air is almost instantaneous and simple mitigation practices are not adequate. Our approach was to ensure that the crystallization plate was in vapor equilibrium with the mother liquor before, during, and after the transfer of all liquid constituents by transferring all liquids through the apertures in the plate lids.

A critical advantage of ADE is that it can deposit solutions at their intended destination with a very high positional accuracy. The capability to combine protein, precipitant, and screened chemicals at 1728 distinct locations on a crystallization microplate is one advantage of this positional accuracy that we have already mentioned. Since the precise location of each of these 1728 experiments is known, there is also the opportunity to automate the data acquisition process by programming the plate handling system (such as the G-rob system used in this work) to rapidly move between the 1728 known specimen locations. In situ data can then be obtained under computer control so that high throughput screening can occur without operator assistance. The speed and automation of this data acquisition approach could facilitate structure based fragment screening without having to group chemicals into cocktails, thus mitigating the effects of a high aggregate frag-

ment concentration on protein stability and crystallization (Boyd et al., 2010; Baurin et al., 2004), avoiding the possibility of inter fragment interactions (Drinkwater et al., 2010; Nair et al., 2012), and avoiding the need for a de-convolution strategy to differentiate between the fragments in each cocktail (Nicholls et al., 2010).

II. Methods

We used two techniques for high throughput screening of proteins against chemical libraries using X-ray crystallography as the primary screening tool:

Co-crystallization of protein with a library of chemicals: DMSO solvated libraries were screened by co-crystallization (Figure 4A). The screened chemicals were acoustically deposited on the crystallization plate before any other components were added, and the DMSO was allowed to evaporate (leaving the dry residue of the screened chemical). The reservoir was then filled with mother liquor and the crystallization plate was sealed with a custom fabricated plate lid (Figure 2). Once the crystallization plate is equilibrated to the reservoir, acoustic methods were used to separately add protein and precipitant to 18 distinct locations in each of the 96 wells of a MiTeGen crystallization plate (1728 total experiments per microplate). Acoustic transfers were made through slits in the crystallization plate cover, so that the crystallization plate was equilibrated to the mother liquor before, during, and after the addition of all components (except for DMSO solvated chemicals, which are intentionally allowed to dry).

Soaking of proteins with a library of chemicals: Soaking experiments were similar, but the screened chemicals were separately added to each of the 1728 locations on the MiTeGen plate after the crystals formed (Figure 4B). Each experiment was allowed to soak with the protein crystals for one hour before data collection. In soaking experiments, it was not possible to prevent the DMSO from contacting the protein.

Each of the 96 crystallization wells in a MiTeGen in situ thin film crystallization plates™ accommodated up to 18 co-crystallization or soaking experiments; these 1728 distinct specimens (each containing similar protein crystals and a different chemical) were then screened in situ using a plate handling system (le Maire et al., 2011). A very high density of specimens could share a single crystallization plate. This allowed the experiment to be very compact. The number of distinct experiments that can be accommodated on one MiTeGen plate is equivalent to 13½ Dewars fully loaded with 8 unit pucks each. A very high rate of sustained data acquisition was possible, using the plate handling system to rapidly move between specimen locations (see §2.3).

A plate specific definition that allows the Echo Array Maker software (Labcyte Inc., Sunnyvale, CA) to operate the Echo 550 and dispense liquids to 18 locations in each of the 96 crystallization wells on a MiTeGen plate is available on request. This plate definition was made in two stages using Echo Array Maker. First, an array definition was generated to access each of the 96 wells on the MiTeGen plate. Then, the software was used to further partition each crystallization well into 3 rows by 6 columns of accessible destination locations using 1000 μ m grid spacing.

To demonstrate the Echo 550's capability to prepare specimens in MiTeGen plates for screening chemical libraries in situ by both co-crystallization and soaking, we first used conventional manual techniques to verify reliable crystallization conditions for four test proteins (lysozyme, thermolysin, trypsin, and thaumatin) using the hanging drop vapor diffusion method (Table 1). For

each protein, the same precipitant cocktail that were identified in the manual experiments was found to be effective in the acoustic prepared experiments (with the working volume reduced 1000-fold). In our experiments the precipitant was held in place by a 1% agar solution (Whon et al., 2009). The same conditions that yielded crystals in a conventional hanging drop experiment were used to yield crystals in the MiTeGen trays.

Diffraction data were collected at the National Synchrotron Light Source (NSLS) beamlines X12b, X12c, X25, and X29. Datasets were processed with HKL2000 (Otwinowski et al., 2001) and further processed using CTRUNCATE in the CCP4i suite (Winn et al., 2011). Structures were obtained by molecular substitution from published models and refined using REFMAC (Winn et al., 2003) and ArpWarp (Perrakis et al., 2001) (starting models 1lyz-lysozyme, 4tlh-thermolysin, 4i8g-trypsin, 1thi-thaumatins)(Diamond 1974; Holmes et al., 1981; Liebschner et al., 2013; Kim et al., 1988). Binding fragments were identified in a Fo-Fc omit difference map by visual inspection using coot (Emsley et al., 2004)

A. Using a colored dye to probe for cross-contamination

Compact specimen holders such as the high density MiTeGen microplates described here can accelerate applications such as fragment screening. However, as the density of specimens is increased there is the danger that adjacent experiments will become cross-contaminated. To test the capability of the Echo liquid handler to accurately dispense building blocks to 18 distinct locations in each MiTeGen crystallization well, we alternately dispensed colored (Eosin colorant) and clear droplets to form a checkerboard pattern at nearly twice the specimen density as we used in our experiments (32 locations per well compared to 18 locations per well used in our experiments). The red dye used in this demonstration imparts a distinctive color even at 1% concentration (see Figure 5 inset), so that even very limited cross-contamination was easily detected by visual inspection.

B. Screening a heavy metal mini-library by soaking

In addition to preventing cross-contamination, compact high density formats for high throughput screening must reliably deliver each screened chemical to the desired location. To verify the fidelity of our strategy for delivering screened chemicals, we assembled a mini-library of 6 heavy metals. The soaking strategy (figure 4B) was used for this demonstration, so each heavy atom solution was added to already grown crystals. Excitation scans were then used to detect the presence of each heavy atom by recording the fluorescence peak at the expected X-ray wavelength. The excitation scans were performed using a G-rob plate screening robot to discretely target each of the 18 separate crystal containing droplets that had been soaked with six heavy metals. Each heavy metal was soaked into the crystals on the three droplets in one column of our 6 column format. This way, the MiTeGen plate well contained three similar rows, each of which contained the same sequence of heavy atoms at each of its six columns.

C. In situ X-ray data collection from microplates

Previous groups have described data collection from one or several protein crystals that reside in a micro crystallization plate well and that share a similar chemical environment (Axford et al., 2012). We obtained in situ data from 18 protein crystals that re-

side in a micro crystallization plate well and that have a dissimilar chemical environment. We used both co-crystallization and soaking approaches to combine crystals of lysozyme, thermolysin, trypsin, and thaumatin with an 18 chemical fragment mini-library in a single well of a micro crystallization plate (in total this experiment occupied eight crystallization wells). We then separately obtained in situ data from each of the four different protein crystals that were combined with each of the 18 different fragment chemicals using both the co-crystallization and the soaking strategy. Our fragment mini-library contained one known ligand for each of the four protein crystals that we tested. We identified each of the four relevant data sets, solved the structure, and verified the presence of all four of the known ligands (see Table 1).

The G-rob plate screening system at NSLS X12b was a convenient high throughput screening tool. The system includes a customizable interface for partitioning each MiTeGen crystal well into N by M discrete targets of equal size (where N and M are integers). Using the CBASS data acquisition software (Skinner et al., 2006), we could automatically move to each of the 18 locations on each of the 96 crystallization wells in the MiTeGen plates. Each target could also be automatically photographed with the in-line camera. However, the most powerful capability came from the integration of the target partitioning functionality with the data collection software. By pairing the automated data collection protocol with the programmable locations of all 1728 experiments on each MiTeGen plate, it was possible to screen our chemical libraries with an unprecedented level of automation. Since each crystal data set required about 20 minutes, the 1728 experiments in each MiTeGen microplate could hypothetically give this system an operational autonomy of 24 days. In practice, mechanical limitations restricted the achievable autonomy to just one or a few wells before the buildup of target positioning errors caused the X-ray beam to begin missing the specimen. Simple software improvements (such as coupling a short “grid scan” X-ray search protocol to a feedback loop) should prevent the buildup of positioning errors and allow fully automated screening of all 1728 experiments on each crystallization plate. Simple arithmetic demonstrates that this technology will allow the plate handling system at NSLS II to sustain a very high rate of data acquisition in high throughput screening applications.

The convenience of automated data collection with almost unlimited autonomy made the X12b setup ideal for screening. However, to obtain the best possible data required matching the low mosaic spread of our room temperature crystals with the fast readout speed of the Pilatus 6M detector at X25. In this way, we could overcome the reduced signal that is available from the low X-ray dose limits for room temperature crystals with the equally reduced background noise from aggressive fine phi slicing of the low mosaicity crystals (Owen et al., 2014). Since no plate handling system is available at x25, we mechanically cut our MiTeGen plates into fragments that were small enough to be secured onto a conventional goniometer head. All of the electron density maps in this project were obtained from X25 using these plate fragments (Soares et al., 2014).

III. Results

Our strategy was to exploit the reduced mosaicity of room temperature crystals to support an aggressive fine phi slicing data collection strategy. In this way we attempted to balance the reduced X-ray diffraction signal that is available (due to the low dose

limits of room temperature crystals) by reducing the background noise using very thin data collection wedges. In favorable cases, the low mosaicity of room temperature crystals (compared to the same crystals at 100 K) can yield a comparable signal-to-noise ratio from room temperature crystals compared the cryo cooled crystals.

A. Preventing cross contamination

Our objective was to maximize the number of specimens that can be discretely assembled on a MiTeGen plate without cross-contamination between adjacent experiments. To ensure that our proposed three-by-six specimen deposition density would adequately segregate the contents of adjacent experiments from each other, we used the Echo 550 to alternately deposit clear droplets and droplets containing a red dye (Eosin). We used a specimen density that was almost double that used in our experiments (32 versus 18 specimens per crystallization well). A representative picture of a high density field is shown in Figure 4. Visual inspection of 12 equivalent high density fields showed that cross contamination occurred in N out of the 384 repetitions that were tested. The Eosin dye used in this experiment is clearly visible even at 1% concentration (see Figure 4 inset) so we are confident that any cross-contamination would have been evident by inspection.

B. Heavy metal mini-library soaked into thermolysin crystals

To verify the fidelity of our system for screening chemical libraries, we soaked six types of heavy atoms with thermolysin crystals at each of the 18 distinct locations in one crystallization well of a MiTeGen plate. The same six heavy atoms were deposited in the same order on each of the three rows of the well (Figure 6). A picture of one row of six crystals that are soaking with six heavy atoms has been rotated by 90° for clarity (Figure 6, column 2). A close up view of the crystals in the picture is also shown (column 3). We used a G-rob plate handling system to separately probe each of the 18 soaking experiments for the presence of the expected heavy atom. In all 18 cases we positively identified that the expected heavy metal was transferred to the correct location by observing a fluorescence peak at the appropriate wavelength for each heavy atom (Figure 6, column 4). We also obtained room temperature X-ray diffraction data from one crystal was soaked with each of the six heavy metals. For each of these six data sets, one or a few representative reflections with a common resolution of ~2.3 Å were picked from the last frame of the data collection sweep to show that the cumulative X-ray dose did not excessively dim the diffraction power of the crystal (the name and signal-to-noise ratio for the reflection is shown in Figure 6 column 1, and a picture in column 5).

C. In situ ligand screening

We used both co-crystallization and soaking approaches to screen crystals of lysozyme, thermolysin, trypsin, and thaumatin with a mini library consisting of 18 chemicals (including four chemicals that are known ligands for the four protein crystals). For both the co-crystallization and the soaking strategy, the resulting electron density confirmed that our acoustic library screening system correctly paired each of the four protein crystals with its known ligand (Figure 6). For each protein, none of the other 17 screened chemicals were observed in the electron density. For

comparison, we also obtained X-ray diffraction data from cryo-cooled crystals of each of the four protein types with its known ligand. Table 1 shows that the average mosaicity for the room temperature specimens was approximately 17 times lower than the average mosaicity for the cryo cooled specimens; the average frame width for the room temperature specimens was thinner by a similar amount (0.05 vs 1). This aggressive fine phi slicing strategy yielded comparable signal-to-noise ratios for the room temperature data sets, compared to the cryo-cooled data sets. The real space r-factor for the bound ligand was also compared between the room temperature and cryo-cooled crystals. This figure was also comparable, as were the remaining data reduction and structure solving statistics.

IV. Discussion

High throughput strategies that use X-ray diffraction to screen chemical libraries will benefit from improvements in technology that make better use of resources. We outline a strategy that uses acoustic specimen preparation with an Echo 550 to assemble 1728 distinct experiments on a MiTeGen micro crystallization plate; single crystal X-ray diffraction data sets are used to screen a library of chemicals using either co-crystallization or soaking. Our strategy optimizes the use of resources such as space (1728 chemicals screened in one microplate), consumables (2.5 nL of protein, precipitant, and the screened chemical) and time (2.3 specimens prepared per second). By using the automated computer controlled data collection strategy outlined in §2.3, our method also makes optimal use of the limited availability of synchrotron X-ray diffraction end stations, and greatly minimizes the demand for scientific staff to supervise the data collection. Coupled with the brightness of 4th generation synchrotron sources such as NSLS II, our strategy will deliver unprecedented rates of data acquisition and a commensurately enhanced ability to screen large chemical libraries.

The most challenging mission for this type of high throughput screening will likely remain screening large fragment libraries for structure based drug discovery projects. Libraries of this type can contain thousands of fragments. For these projects, we anticipate that our system will support a throughput rate for fragment screening that is greater than 1 full data set per second. Using as an example the NSLS II beamline AMX used to screen room temperature crystals with low mosaicity that support a strategy with 0.1° data acquisition wedges, the maximum throughput speed will be limited by the detector readout rate (and not by the brilliance of the X-ray facility). For this example, if we optimistically project the medium term detector development outlook to a readout rate of 500 frames per second, 0.1° data wedges will sample 50° of reciprocal space per second. This is approximately equal to the mechanical data acquisition limit for most in situ crystallization plates (including the MiTeGen plate; Soliman et al., 2011), so the screening throughput rate will be approximately one screened fragment per second. This is approximately equal to the time needed for a 20µm crystal to absorb an X-ray dose equal to the Henderson limit ($D/4 = 107$ Gy, Henderson et al., 1990) at the AMX beamline (Hodgson et al., 2009). At room temperature, the dose limit will be reduced by about 50-fold, so the X-ray beam will have to be attenuated in order to obtain a full data set from one crystal (unless much faster detectors become available). The specimen screening rate would still be limited by the detector speed and would remain approximately 1 screened chemical per

second.

V. References

- Arakawa, T., Kita, Y., & Timasheff, S. N. (2007). Protein precipitation and denaturation by dimethyl sulfoxide. *Biophysical chemistry*, 131(1), 62-70.
- Axford, D., Owen, R. L., Aishima, J., Foadi, J., Morgan, A. W., Robinson, J. I., ... & Evans, G. (2012). In situ macromolecular crystallography using microbeams. *Acta Crystallographica Section D: Biological Crystallography*, 68(5), 592-600.
- Baurin, N., Aboul-Ela, F., Barril, X., Davis, B., Drysdale, M., Dymock, B., ... & Hubbard, R. E. (2004)
- Blundell, T. L., Jhoti, H., & Abell, C. (2002). High-throughput crystallography for lead discovery in drug design. *Nature Reviews Drug Discovery*, 1(1), 45-54.
- Boyd, S. M., & de Kloe, G. E. (2010). Fragment library design: efficiently hunting drugs in chemical space. *Drug Discovery Today: Technologies*, 7(3), e173-e180
- Chilingaryan, Z., Yin, Z., & Oakley, A. J. (2012). Fragment-based screening by protein crystallography: successes and pitfalls. *International journal of molecular sciences*, 13(10), 12857-12879.
- Cipriani F, Rower M, Landret C, Zander U, Felisaz F, Marquez JA (2012) CrystalDirect: a new method for automated crystal harvesting based on laser-induced photoablation of thin films. *Acta crystallographica Section D, Biological crystallography* 68:1393-1399.
- Cuttitta, C. M., Ericson, D.L., Scalia, A., Roessler, C.G., Teplitsky, E., Joshi, K., Campos, O., Agarwal, R., Allaire, M., Orville, A.M., Sweet, R.M., and Soares, A. S (2014). Acoustic transfer of protein crystals from agarose pedestals to micromeshes for high throughput screening. *Acta Crystallographica Section D: Biological Crystallography*, under review.
- Diamond, R. (1974). Real-space refinement of the structure of hen egg-white lysozyme. *Journal of molecular biology*, 82(3), 371-391.
- Drinkwater, N., Vu, H., Lovell, K., Criscione, K., Collins, B., Prisinzano, T., ... & Martin, J. (2010). Fragment-based screening by X-ray crystallography, MS and isothermal titration calorimetry to identify PNMT (phenylethanolamine N-methyltransferase) inhibitors. *Biochem. J*, 431, 51-61.
- Ellson, R., Mutz, M., Browning, B., Lee, L., Miller, M. F., & Papan, R. (2003). Transfer of low nanoliter volumes between microplates using focused acoustics—automation considerations. *Journal of the Association for Laboratory Automation*, 8(5), 29-34.
- Emsley, P., & Cowtan, K. (2004). Coot: model-building tools for molecular graphics. *Acta Crystallographica Section D: Biological Crystallography*, 60(12), 2126-2132.
- Harris, D., Mutz, M., Sonntag, M., Stearns, R., Shieh, J., Pickett, S., ... & Olechno, J. (2008). Low nanoliter acoustic transfer of aqueous fluids with high precision and accuracy of volume transfer and positional placement. *Journal of the Association for Laboratory Automation*, 13(2), 97-102.
- Henderson, R. (1990). Cryo-protection of protein crystals against radiation damage in electron and X-ray diffraction. *Proceedings of the Royal Society of London. Series B: Biological Sciences*, 241(1300), 6-8.
- Hodgson, K.O. (chairman), Anderson, W.F., Berman, L., R. Fischetti, Hendrickson, W.A., Kirz, J., Makowski, L., Phillips, G.N., Smith, J.L., Sweet, R.M., and Tsuruta, H. (2009). "Workshop of the National Institutes of Health National Center for Research Resources and the National Institute of General Medical Sciences on plans for support of future life science synchrotron research at NSLS-II, final report." June4-5, 2009, Bethesda, MD.
- Holmes, M. A., & Matthews, B. W. (1981). Binding of hydroxamic acid inhibitors to crystalline thermolysin suggests a pentacoordinate zinc intermediate in catalysis. *Biochemistry*, 20(24), 6912-6920.
- Kennedy, D. F., Drummond, C. J., Peat, T. S., & Newman, J. (2011). Evaluating protic ionic liquids as protein crystallization additives. *Crystal Growth & Design*, 11(5), 1777-1785.
- Kim, S. H., de Vos, A., & Ogata, C. (1988). Crystal structures of two intensely sweet proteins. *Trends in biochemical sciences*, 13(1), 13-15.
- le Maire, A., Gelin, M., Pochet, S., Hoh, F., Pirocchi, M., Guichou, J. F., ... & Labesse, G. (2011). In-plate protein crystallization, in situ ligand soaking and X-ray diffraction. *Acta Crystallographica Section D: Biological Crystallography*, 67(9), 747-755.
- Liebschner, D., Dauter, M., Brzuszkiewicz, A., & Dauter, Z. (2013). On the reproducibility of protein crystal structures: five atomic resolution structures of trypsin. *Acta Crystallographica Section D: Biological Crystallography*, 69(8), 1447-62.
- McDonald GR, Hudson AL, Dunn SM, You H, Baker GB, Whittall RM, Martin JW, Jha A, Edmondson DE, Holt A (2008) Bioactive contaminants leach from disposable laboratory plasticware. *Science* 322:917.
- Nair, P. C., Malde, A. K., Drinkwater, N., & Mark, A. E. (2012). Missing fragments: Detecting cooperative binding in fragment-based drug design. *ACS Medicinal Chemistry Letters*, 3(4), 322-326.
- Nicholls, A., McGaughey, G. B., Sheridan, R. P., Good, A. C., Warren, G., Mathieu, M., ... & Kelley, B. (2010). Molecular shape and medicinal chemistry: a perspective. *Journal of medicinal chemistry*, 53(10), 3862-3886.
- Otwinowski, Z., & Minor, W. (2001). *Denzo and Scalepack. Crystallography of Biological Macromolecules*, 2.
- Owen, R. L., Paterson, N., Axford, D., Aishima, J., Schulze-Briese, C., Ren, J., ... & Evans, G. (2014). Exploiting fast detectors to enter a new dimension in room-temperature crystallography. *Acta Crystallographica Section D: Biological Crystallography*, 70(5), 1248-1256.
- Perrakis, A., Harkiolaki, M., Wilson, K. S., & Lamzin, V. S. (2001). ARP/wARP and molecular replacement. *Acta Crystallographica Section D: Biological Crystallography*, 57(10), 1445-1450.
- Roessler, C. G., Kuczewski, A., Stearns, R., Ellson, R., Olechno, J., Orville, A. M., Allaire, M., Soares, A.S., & Héroux, A. (2013). Acoustic methods for high-throughput protein crystal mounting at next-generation macromolecular crystallographic beamlines. *Journal of synchrotron radiation*, 20(5), 805-808.

- Skinner, J. M., Cowan, M., Buono, R., Nolan, W., Bosshard, H., Robinson, H. H., ... & Sweet, R. M. (2006). Integrated software for macromolecular crystallography synchrotron beamlines II: revision, robots and a database. *Acta Crystallographica Section D: Biological Crystallography*, 62(11), 1340-1347.
- Soares AS, Engel MA, Stearns R, Datwani S, Olechno J, Ellson R, Skinner JM, Allaire M, Orville AM (2011) Acoustically mounted microcrystals yield high-resolution X-ray structures. *Biochemistry* 50:4399-4401.
- Soares, A.S., Mullen, J.D., Parekh, R., McCarthy, G.S., Roessler, C.G., Jackimowicz, R., Skinner, R., Orville, A.M., Allaire, M., and Sweet, R. (2014) Solvent minimization induces preferential orientation and crystal clustering in serial micro crystallography on micro-meshes, in situ plates, and on a movable crystal conveyor belt. *Journal of Synchrotron Radiation*, in press. Spurlino, J. C. (2011). Fragment screening purely with protein crystallography. *Methods Enzymol*, 493, 321-356.
- Soliman, A. S., Warkentin, M., Apher, B., & Thorne, R. E. (2011). Development of high-performance X-ray transparent crystallization plates for in situ protein crystal screening and analysis. *Acta Crystallographica Section D: Biological Crystallography*, 67(7), 646-656.
- Villasenor AG, Wong A, Shao A, Garg A, Donohue TJ, Kuglstatter A, Harris SF (2012) *Acta crystallographica Section D, Biological crystallography* 68:893-900.
- Villasenor AG, Wong A, Shao A, Garg A, Kuglstatter A, Harris SF (2010) Acoustic matrix microseeding: improving protein crystal growth with minimal chemical bias. *Acta crystallographica Section D, Biological crystallography* 66:568-576.
- Whon, T. W., Lee, Y. H., An, D. S., Song, H. K., & Kim, S. G. (2009). A simple technique to convert sitting-drop vapor diffusion into hanging-drop vapor diffusion by solidifying the reservoir solution with agarose. *Journal of Applied Crystallography*, 42(5), 975-976.
- Winn MD, Ballard CC, Cowtan KD, Dodson EJ, Emsley P, Evans PR, Keegan RM, Krissinel EB, Leslie AG, McCoy A, McNicholas SJ, Murshudov GN, Pannu NS, Potterton EA, Powell HR, Read RJ, Vagin A, Wilson KS (2011) Overview of the CCP4 suite and current developments. *Acta crystallographica Section D, Biological crystallography* 67:235-242.
- Winn, M. D., Murshudov, G. N., & Papiz, M. Z. (2003). Macromolecular TLS refinement in REFMAC at moderate resolutions. *Methods in enzymology*, 374, 300-321.
- Yin, X., Scalia, A., Leroy, L., Cuttitta, C. M., Polizzo, G. M., Ericson, D. L., ... & Soares, A. S. (2014). Hitting the target: fragment screening with acoustic in situ co-crystallization of proteins plus fragment libraries on pin-mounted data-collection micromeshes. *Acta Crystallographica Section D: Biological Crystallography*, 70(5), 1177-1189.

VI. Acknowledgments

Personnel for this study were recruited largely through the 2014 spring session of the Science Undergraduate Laboratory Internships Program (SULI), supported through the U.S. Department of Energy, Office of Science, Office of Workforce Development for Teachers and Scientists (WDTS). Major ongoing financial support for acoustic droplet ejection applications was through the Brookhaven National Laboratory/U.S. Department of Energy, Laboratory Directed Research and Development Grant 11-008 and from the Offices of Biological and Environmental Research and of Basic Energy Sciences of the US Department of Energy, and from the National Center for Research Resources (P41RR012408) and the National Institute of General Medical Sciences (P41GM103473) of the National Institutes of Health. Data for this study were measured at beamlines X12b, X12c, X25, and X29 of the National Synchrotron Light Source. Author contributions: ASS designed the experiment and wrote the paper. ET and ASS grew crystals, obtained data and analyzed data. ASS, KJ, JDM, and GSM designed and built the labware. ASS trained and supervised student interns.

Table 1: Crystallization, data collection, and model refinement statistics:

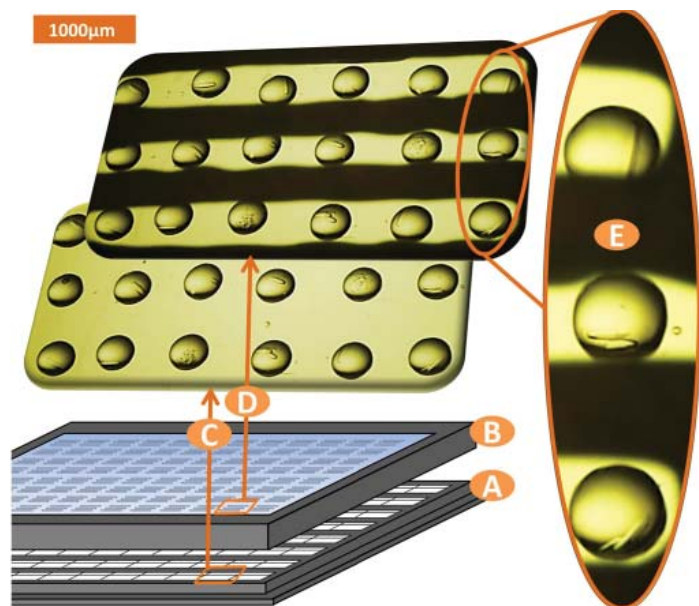
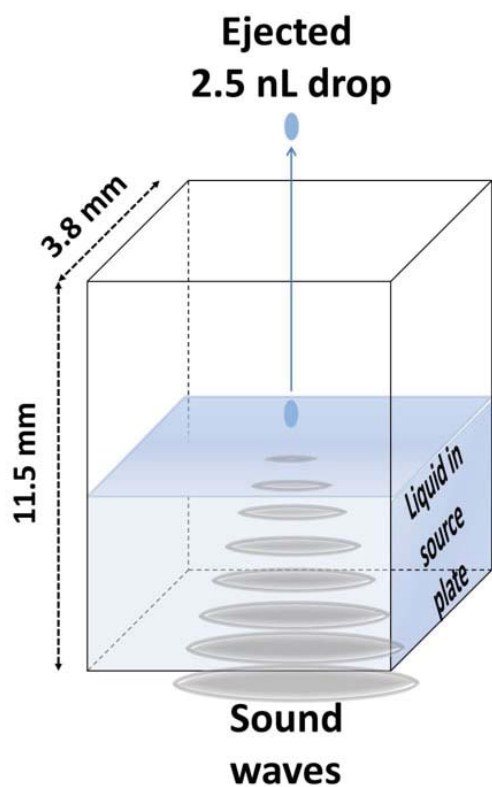


Figure 1: Acoustic droplet ejection. Acoustic droplet ejection (ADE) uses sound energy to transfer variable micro-droplets (e.g. nanoliter or picoliter) of solution (protein, precipitant, chemicals, etc.) from a well in a source plate that contains a solution, through a short air column (~1 cm) to data collection media. Sound wave energy from the transducer is channeled to the focal point (i.e. ejection zone) displacing the surface where a controlled ejection occurs. Droplet size is governed by the wavelength of the sound emitted. In this work an Echo 550 liquid handler was used to combine proteins, precipitants, and chemicals for co-crystallization and soaking experiments in 1728 distinct locations on a MiTeGen in situ crystallization plate. The Echo 550 does not use frequency changes to transfer different volumes. Instead, it uses a fixed frequency sound pulse to transfer each component in 2.5nL increments.

Figure 2: Very small volumes of protein and chemicals can be used if all components are added through apertures. Thermolysin protein and chemicals were acoustically transferred to the crystallization plate (A) through apertures in the plate lid (B) to prevent the very small volumes from drying (except for the DMSO that solvates library chemicals, which can be allowed to dry in a co-crystallization experiment). This prevents evaporation of the specimen (typically 2.5 nL of protein and chemical) while still allowing a high density of distinct experiments to share each crystallization well. MiTeGen crystallization plates, shown with the plate lid removed (C) and with the plate lid in place (D), can accommodate up to 3 rows and 6 columns of distinct co-crystallization or soaking screening experiments (18 screens per well and 96 wells make 1728 total screens per plate). Crystals can be seen through the apertures in the close up (E).

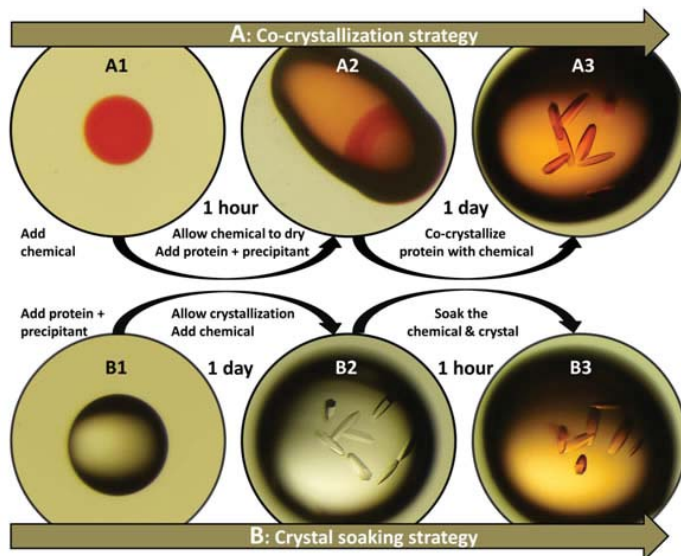
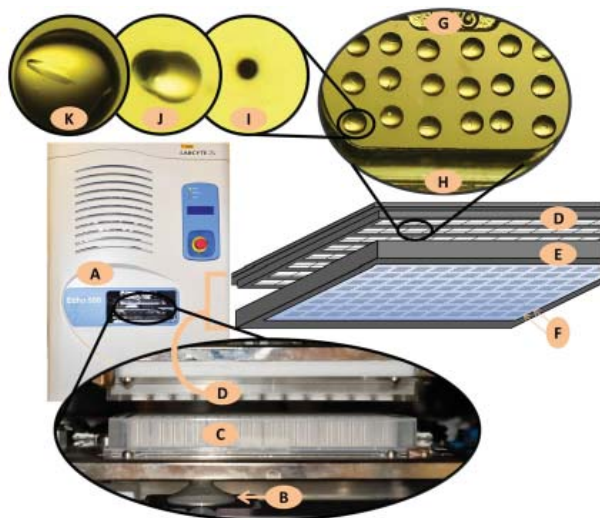


Figure 3: Using acoustic droplet ejection (ADE) to screen 1728 chemicals on one micro crystallization plate. The Echo 550 (A) uses sound energy to transfer micro-droplets of protein, precipitant, or a chemical library (typically a fragment library). A motorized transducer (B) moves under the source plate (C) to the location of each building block in the experiment and generates a sound pulse that ejects 2.5 nL onto a MiTeGen in situ crystallization plate™ (D, shown without plate lid for clarity). The crystallization plate is sealed by a plate lid (E) which contains small apertures (F) through which each component is transferred to the crystallization region (G). The precipitant in the reservoir (H) governs the humidity of the plate before, during, and after protein transfer. In a co-crystallization experiment, DMSO solvated screened chemicals are often added to the crystallization plate before the reservoir is filled (with no plate lid) and the DMSO is allowed to evaporate, leaving behind the dry chemical residue (I). The plate is then sealed by the plate lid and equilibrated with the reservoir. Protein and precipitant (J) are added through the apertures and combined with each screened chemical. Vapor diffusion drives co-crystallization (K) of the protein and each screened chemical. Soaking experiments are prepared in a similar way, but screened chemicals are added after the crystals have grown.

Figure 4: Both co-crystallization and soaking strategies are possible for high throughput screening of high density fragment libraries deposition on crystallization microplates (thermolysin crystals are shown here; pictures of similarly prepared crystals of lysozyme, trypsin, and thaumatin are in Supplemental Figure 2).

- **Co-crystallization:** High throughput screening of protein crystals and a fragment library using co-crystallization (A) uses ADE to deposit 2.5 nl of each DMSO solvated chemical fragment at each distinct location on the crystallization plate (1728 locations per MiTeGen plate)(A1). Each DMSO solvated fragment is allowed to dry for one hour. The crystallization plate is then sealed with a plate lid (figure 3) and equilibrated with the protein precipitant solution. ADE is then used to add protein and precipitant, through apertures, on top of the dry residue from each fragment in the library (A2). Vapor diffusion drives co-crystallization of each fragment and protein over 24 hours (A3). In-situ data collection is recorded from the crystals in each droplet.
- **Soaking:** High throughput screening of protein crystals and a fragment library by soaking each fragment with a crystal (B) uses ADE to deposit protein and precipitant at each distinct location in a sealed crystallization plate that is equilibrated with the protein precipitant (B1). Vapor diffusion drives crystallization over 24 hours (B2). Each chemical fragment is then soaked into a different protein crystal for 1 hour (B3) and X-ray diffraction data is obtained from each crystal plus fragment soak.

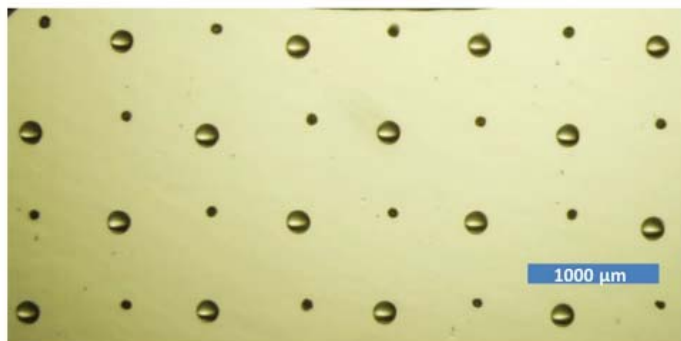


Figure 5: Highly accurate droplet transfers prevent cross-contamination. A checkerboard pattern of highly concentrated blue dye (dark spots, methylene blue) was alternated with a 50/50 mixture of water and DMSO (clear solvent). The methylene blue was solvated in water and dehydrated almost instantly (leaving the dark residue shown), while the DMSO containing drops remained hydrated (because DMSO is hygroscopic). The methylene blue is a very intense pigment that is evident at low concentration (a 100-fold dilution of the starting concentration is still very blue and easy to see), so even a modest amount of cross-contamination should be evident. The field of view shown here contains 32 equally spaced droplets at moderate magnification. We carefully examined 12 similar fields under high magnification (a total of 384 distinct droplets). None of the examined fields contained any evidence of cross-contamination. The largest positional error for all of the 384 droplets tested was less than half of the target distance between the droplets (700 μm). Given that the specimen density shown here is almost twice the specimen density that we used in our experiments, we conclude that the likelihood of cross-contamination with our high throughput screening strategy is very low.

Heavy Atom	Picture (after soak)	Magnified view	Excitation scan	Diffraction Near 2.3Å
CoCl ₂ -10 -5 -42 I/ σ =28.0				
Co(NO ₃) ₂ 12 -12 -49 I/ σ =14.3				
CuSO ₄ -32 -3 -5 I/ σ =7.0				
NaBr -5 -5 -57 I/ σ =22.9				
NiSO ₄ 31 -18 30 I/ σ =6.0				
PtCl ₂ -6 -9 -61 I/ σ =17.9				

Figure 6: Using excitation scans to confirm that crystals were successfully combined with six heavy atom compounds. Column 1 contains the name of each heavy atom compound, and information about the sample reflection indicated in column 5 (name and signal-to-noise). Column two is a single picture of six thermolysin crystals after soaking with the six heavy metal compounds. Column 3 shows a magnified view of each crystal (the insoluble platinum compound can be seen in the bottom row). Column 4 shows the excitation scan at the white line (wavelength shown) for each heavy metal compound. Column 5 is a magnified view of a few reflections from the last frame of the data collection sweep, with resolution near 2.3Å (the orange arrow indicates the reflection described in column 1).

Figure 7: In situ data collection from 18 distinct experiments in each of the 96 wells in a MiTeGen micro crystallization plate. Previous groups have described data collection from one or several protein crystals that reside in a micro crystallization plate well and that share a similar chemical environment. We obtained in situ data from 18 protein crystals that reside in a micro crystallization plate well and that have a dissimilar chemical environment. We used both co-crystallization and soaking approaches to combine crystals of lysozyme, thermolysin, trypsin, and thaumatin with an 18 chemical fragment mini-library in a single well of a micro crystallization plate (in total this experiment occupied eight crystallization wells). We then separately obtained in situ data from each of the four different protein crystals that were combined with each of the 18 different fragment chemicals using both the co-crystallization and the soaking strategy. Our fragment mini-library contained one known ligand for each of the four protein crystals that we tested. (Unavailable)

Growth of tropical cumulus congestus clouds

Katherine Towey

Department of Atmospheric and Environmental Sciences, University at Albany, Albany, NY 12222

Michael Jensen

Biological, Environmental and Climate Sciences Department, Brookhaven National Laboratory, Upton, NY 11973

The Department of Energy's Atmospheric Radiation Measurement climate research facility site at Nauru Island is one of three sites in the Tropical Western Pacific region. Vertically developed convective clouds frequently observed at these sites are forced by some of the warmest sea surface temperatures on Earth. Clouds play an important role in the local energy balance because they reflect incoming solar radiation as well as absorb and emit terrestrial infrared radiation, the net impact of which can have either a warming or cooling effect on the Earth. How deep these clouds grow is the major determining factor for their radiative impact. To determine how these clouds grow, snapshot observations from a zenith pointing cloud radar were analyzed. It is unknown at the time that the cloud passes over the radar whether it has reached its maximum height or if it will continue to grow. In order to establish whether or not these clouds continue to grow, the vertical air velocity of the cloud top is determined in order to quantify the fraction of upward or downward vertical motion that is present. From this analysis using Interactive Data Language, 39 of the 50 cases from 1999 – 2002 reveal upward vertical motion near the cloud top. This information helps us to interpret analysis of cloud growth and decay processes, most notably mixing of environmental air and cloudy air, helping us to better understand the cloud lifecycle and putting vertically pointing measurements into context.

I. Introduction

The Department of Energy's Atmospheric Radiation Measurement (ARM) climate research facility provides data of observations taken at various sites all over the world, including the Tropical Western Pacific (TWP). The TWP site was established in 1996 as the second ARM climate research facility site and consists of three facilities including Manus Island in Papua New Guinea, Nauru Island and Darwin, Australia ("Tropical Western Pacific"). These sites were chosen because this region has an important role in the interannual variability that is observed in the global climate regime ("Tropical Western Pacific"). The western Pacific Ocean, where the TWP site is located, is home to the warmest sea surface temperatures on the planet. On average, the sea surface temperatures within the TWP site are between 28°F and 30°F. These warm ocean temperatures supply heat and moisture to the atmosphere above it, causing the formation of deep convective cloud systems, including cumulus congestus clouds ("Tropical Western Pacific"). The climate research facility at Nauru Island, established in November 1998, was chosen due to its proximity to the eastern edge of the Pacific warm pool under La Niña conditions, which has a profound impact on weather patterns in the Pacific ("TWP Nauru Site").

A great variety of cloud types are often observed in the tropics, many of which can be seen in the TWP site. Shallow trade cumulus, whose cloud tops reach between 2 – 4 kilometers, and deep

convective cloud systems, whose cloud tops ascend to 12 kilometers or more, were originally believed to be the two main modes of tropical convection. A third mode of tropical convection, cumulus congestus, was found to be abundant in nature within the past 15 years (Johnson et al, 1999). Mid-level cumulus congestus cloud characterizations include cloud base heights near their lifted condensation level (LCL), cloud top heights near their freezing level, a lack of hydrometeors, and measurable precipitation reaching the ground (Jensen and Del Genio, 2006). Here we define cumulus congestus clouds as having cloud base heights below 1 kilometer and cloud top heights between 3 and 9 kilometers (Jensen and Del Genio, 2006). Cumulus congestus is a unique diabatic heat source and plays an important role in the local atmospheric balance (Luo et al, 2009). These clouds reflect incoming solar radiation as well as absorb and emit terrestrial infrared radiation, the net impact of which can have either a warming or cooling effect on the Earth. How deep these clouds grow is the major determining factor for their radiative impact.

As an important mode of tropical convection, understanding the life cycle phase of observed cumulus congestus clouds has important implications on retrieved entrainment rate estimates. Dry air entrainment, the mixing of dry environmental air with cloudy air, has a significant impact on cloud growth and decay processes. Dry air in the mid and upper levels of the atmosphere is one of the most important limiting factors of cloud growth (Jensen and Del Genio, 2006). Cloud growth can be limited by either dry air entrainment above the boundary layer or from a loss in buoyancy as air parcels encounter weak stability near the freezing level (Jensen and Del Genio, 2006). The role of dry air entrainment in the creation of cumulus congestus presents a problem for general circulation models whose cumulus parameterizations tend to underestimate the occurrence of all but deep convective clouds (Jensen and Del Genio, 2006).

One of the most notable differences between transient (clouds that continue to grow after they are observed) and terminal (clouds that have reached their maximum development when they are observed) cumulus congestus clouds is the thermodynamic structure of the cloud. Transient cumulus congestus clouds have a cloud top temperature that is warmer than the environmental temperature, which allows the cloud top to remain positively buoyant and to ascend to the level of neutral buoyancy (Luo et al, 2009). Terminal cumulus congestus clouds have a cloud top temperature equal to the environmental temperature and the parcel at the cloud top would have neutral or negative buoyancy (Luo et al, 2009). The convective updraft associated with a terminal cumulus congestus cloud if accompanied by a significant amount of dry air entrainment during ascent, which ultimately end up prohibiting further growth from occurring (Luo et al, 2009). Previous studies determined based on analysis of one year of data that approximately 30 – 40% of the cumulus congestus observed by the snapshot ob-

servations were in transient mode (Luo et al., 2009).

II. Objective

Understanding the lifecycle phase of the cumulus congestus clouds has important implications on previously retrieved entrainment rate estimates. The relationship between the life cycle phase of the cumulus congestus cloud and the amount of entrainment occurring will allow for further study in understanding the thermodynamic structure of the cumulus congestus clouds. The snapshot observations captured by the radar do not portray the full vertical growth of the cumulus congestus clouds – they only capture the height of the cloud at that precise moment in time. It is assumed that growth at the cloud top does not cease at the snapshot and as a result, a significant number of cumulus congestus cases would continue to grow after passing over the radar.

III. Methodology

The data used in this analysis was obtained from a millimeter wavelength cloud radar stationed on Nauru Island, which probes the extent and composition of the cumulus congestus clouds and whose main purpose is to determine cloud base and top heights [“Instrument: Millimeter Wavelength Cloud Radar (MMCR)”]. The millimeter wavelength cloud radar is a zenith-pointing radar that reports radar reflectivity of the atmosphere up to 20 kilometers and possesses a Doppler capability that will allow the measurement of cloud constituent vertical velocities [“Instrument: Millimeter Wavelength Cloud Radar (MMCR)”].

50 cases of cumulus congestus clouds observed at Nauru Island between 1999 and 2002 were analyzed. As a cloud passes over the radar, snapshot observations of the properties of the cloud are recorded. In order to determine whether the cloud continues to grow after passing over the radar or the cloud reached its maximum height already is unknown at the time that the snapshot observation is recorded. In order to determine if the cloud top is growing or not growing, the vertical air velocity of the cloud top must be determined. The fall velocity associated with hydrometeors, such as drizzle, that populate cloud tops need to be accounted for when calculating the vertical velocity of the cloud top. As a result, the fall velocity of the hydrometeors was subtracted from the mean Doppler velocity observed by the cloud radar in order to determine the actual vertical motion of the cloud top. Each case

was then further analyzed quantitatively through plotting profiles of the minimum, maximum and median air velocity values for a 1-kilometer deep rectangular area near cloud top, with the area’s width being determined on a case-by-case basis.

IV. Discussion & Results

50 cases of cumulus congestus clouds from 1999 – 2002 at Nauru Island were evaluated. The top kilometer of each case was analyzed in order to determine the vertical motion of the cloud top. Three criteria, shown in Fig. 1, were set in order to establish whether a cloud top could be considered growing, not growing or indeterminate. The first criterion was the percent of pixels in the top kilometer of the cloud top that portrayed upward velocities. Growing cases exhibited greater than 60% of the pixels showing upward vertical motion. The second criterion was the slope of the median vertical velocity values in the cloud top. Growing cases had slopes that became more negative with height. The third criterion was the mean of all the median values in the top kilometer of the cloud top. Negative values, which are associated with upward motion, are indicative of growing clouds. In order to be classified as growing or not growing, the case had to meet at least two out of the three criteria set forth. Indeterminate cases met one criterion in each category and thus could not be classified based solely on this information.

39 of the 50 cases analyzed met at least two of the three criteria to be classified as growing. Fig. 2 is an example of a case of a cloud that is continuing to grow. 90.9% of the pixels in the top kilometer of this cloud exhibit upward motion. The mean of the median values in the top kilometer is -1.781 m/s and the slope of the median values is -0.29598. For this case, all three criteria are met for this case to be considered growing. This upward vertical motion within the cloud top means the cloud is continuing to ascend to greater heights and is maintaining or becoming more positively buoyant.

Seven of the 50 cases analyzed met at least two of the three criteria to be classified as not growing. Fig. 3 is an example of a case of a cloud that has already reached its maximum height and is decaying. 26.9% of the pixels in the top kilometer of this cloud exhibit upward motion. The mean of the median values in the top kilometer is 0.303 m/s and the slope of the median values is 1.530492. For this case, all three criteria are met for this case to

Criteria \ Category	Not Growing	Indeterminate	Growing
Percent of upward pixels	$\leq 40\%$	41% - 59%	$\geq 60\%$
Slope of vertical velocity	Positive	Negative or Positive	Negative
Mean of median of vertical velocity	Positive	Negative or Positive	Negative

Fig 1. Criteria (vertical column) to be met for each category (horizontal column) of cloud growth.

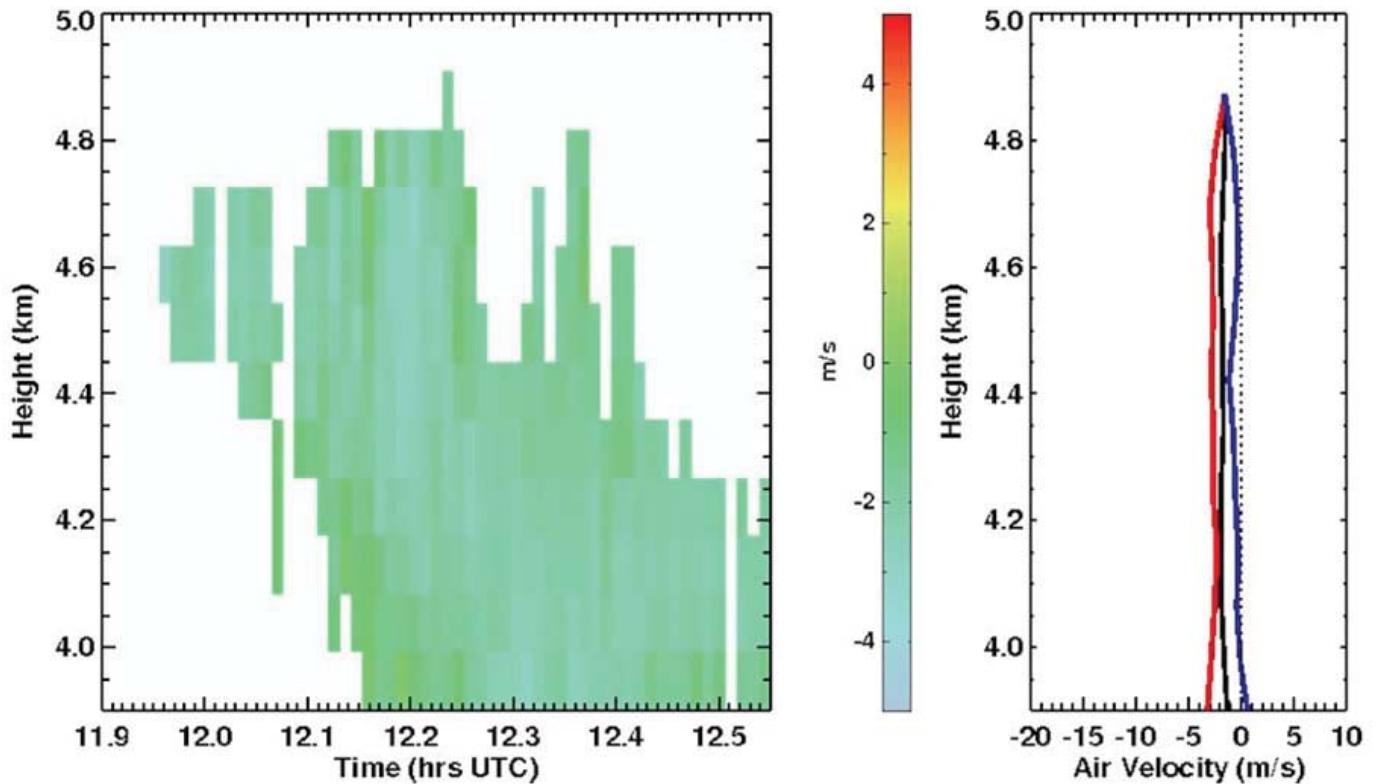


Fig. 2 Cumulus congestus cloud in transient mode on February 19, 2000 at Nauru. Left image is the vertical velocity (ms^{-1}). Right image is the minimum (red), maximum (blue) and median (black) vertical velocity (ms^{-1}).

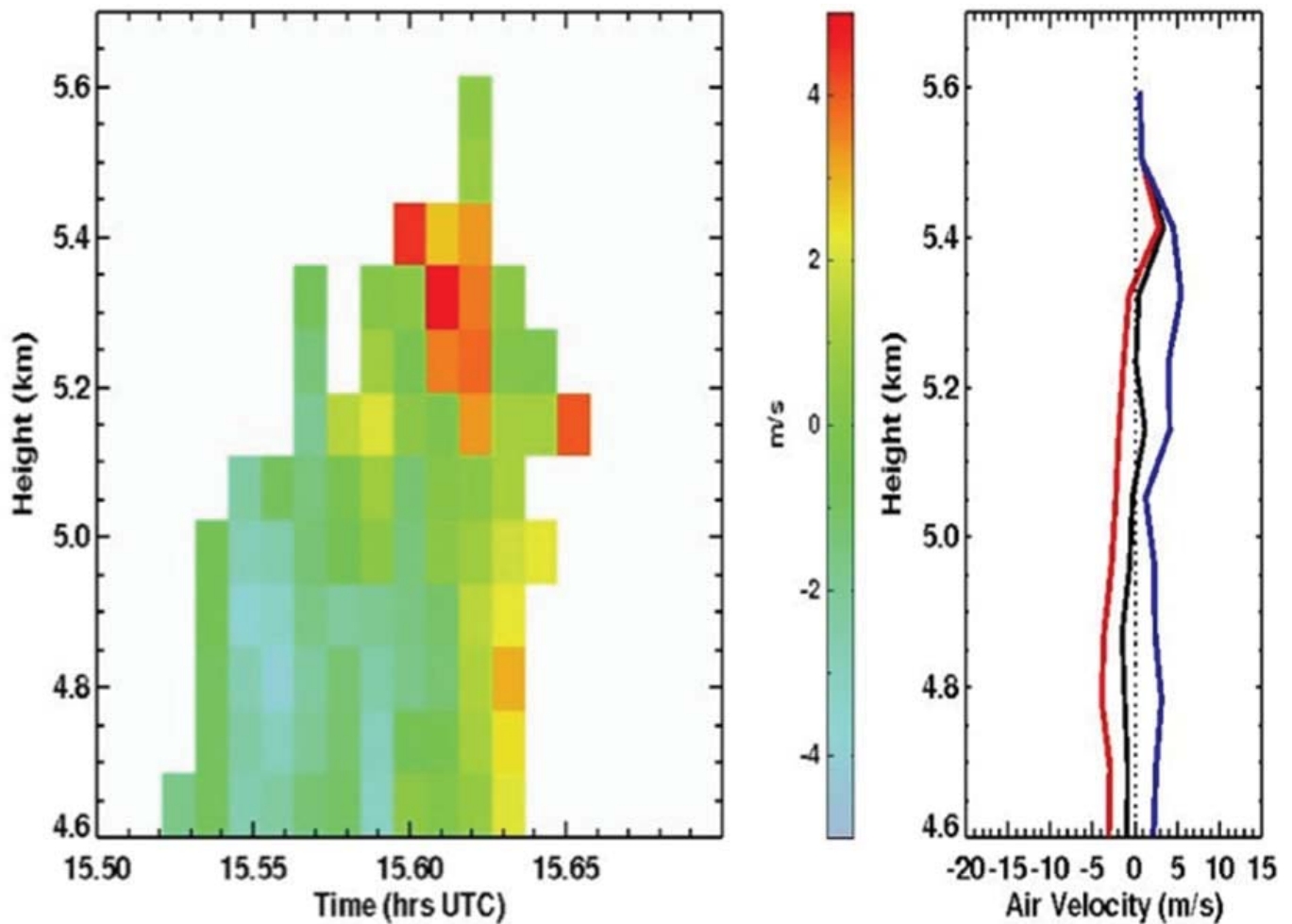


Fig. 3 Cumulus congestus cloud in terminal mode on August 2, 2000 at Nauru. Left image is the vertical velocity (ms^{-1}). Right image is the minimum (red), maximum (blue) and median (black) vertical velocity (ms^{-1}).

be considered not growing. This downward vertical motion within the cloud top means the cloud has ceased growth and has lost buoyancy, prompting the weakening of the cloud.

The four of the remaining 50 cases analyzed were classified as indeterminate because they had met one criterion for each category of growing, not growing and indeterminate. Further analysis would be needed in order to determine the category these cases could be classified under.

V. Conclusion

The fall velocity associated with the hydrometeors had a profound impact on the actual vertical velocity of the cloud top and needed to be excluded. From this analysis, over 75% of the 50 cases analyzed showed cumulus congestus clouds in transient mode. This information is useful in interpreting analysis of cloud growth and decay processes, most notably that of dry air entrainment, helping to better understand the cloud lifecycle as well as putting vertically pointing measurements into context. Further study on this topic can be done using cases at the other ARM TWP sites at Darwin, Australia and Manus Island.

VI. Acknowledgements

This project was supported in part by the U.S. Department of Energy, Office of Science, and Office of Workforce Development for Teachers and Students (WDTS) under the Science Undergraduate Laboratory Internships Program (SULI). I would also like to thank Brookhaven National Laboratory and the Office of Educational Programs.

VII. References

1. "Instrument: Millimeter Wavelength Cloud Radar (MMCR)" ARM Climate Facility <<http://www.arm.gov/instruments/mmc>>.
2. Jensen, M.P. and A.D. Del Genio, 2006: Factors limiting convective cloud top height at the ARM Nauru Island climate research facility. *J. Climate*, 19, 2105-2117
3. Johnson, R. H., T. M. Rickenbach, S. A. Rutledge, P. E. Ciesielski and W. H. Shubert, 1999: Trimodal Characteristics of Tropical Convection. *J. Climate*, 12, 2397-2418.
4. Luo, Z., Y. Liu, G.L. Stephens and R.H. Johnson, 2009: Terminal versus transient cumulus congestus; A CloudSat perspective. *Geophys. Res. Lett.*, 36, L05808, doi: 10.1029/2008GL036927
5. "Tropical Western Pacific." ARM Climate Facility <<http://www.arm.gov/sites/twp>>.
6. "TWP Nauru Site." ARM Climate Facility <<http://www.arm.gov/sites/twp/C2>>.

Analysis of laser ablation plasma formed from an anisotropic graphite target

Christine Truong

Applied Physics, New York University Polytechnic School of Engineering, Brooklyn, New York 11201, USA

Shunsuke Ikeda

Department of Energy Sciences, Tokyo Institute of Technology, Yokohama, Kanagawa, Japan

RIKEN, Wako, Saitama, Japan

Yasuhiro Fuwa

Department of Physics and Astronomy, Kyoto University, Uji, Kyoto, Japan

RIKEN, Wako, Saitama, Japan

Masahiro Okamura

Collider-Accelerator Department, Brookhaven National Lab, Upton, New York 11973, USA

Abstract

A laser with an energy density greater than its target's ablation plasma threshold can create a plasma from that target on its surface. We can subsequently measure a number of properties of the resulting plasma such as its charge state and temperature. We examined if the anisotropic properties of graphite could influence the resulting plasma. Measurements were taken with a high-power laser incident on the surface both parallel and perpendicular to the graphite layers. Results show that more plasma ions are produced when the laser struck the edge of the graphite layers (parallel) rather than the face of the layers (perpendicular), but the temperature of the plasma is unchanged. This basic provides insight into laser ion production with the same material, thus furthering our understanding of plasma generation, a field not widely understood.

I. Introduction

In laser ablation plasma, structured forms of carbon are the subject of experimental scrutiny because carbon ion production is poor despite applications in heavy ion radiotherapy. Although laser ion sources are promising, we do not know what combination of carbon structure and laser properties would maximize ion production.¹ In this experiment we studied the plasma properties of the more fragile graphite, an anisotropic and stable form of carbon, using a laser with vastly different energy outputs. The goal is to examine if the resulting plasma's properties and number of produced ions are affected by the laser's orientation with respect to the target's layers – in other words, if production is different when the target is rotated, and the laser strikes the face of a graphite layer (“perpendicular”) or the layer edges (“parallel”). See Figure 1. The interesting properties we measure in this experiment are the charge state of the ions and temperature of the plasma, described below.

If a laser has a sufficiently high energy density and strikes a target material, a plasma composed of ions from that target will form on its surface.¹ The threshold for this value is said to be on the order of 108 W/cm². Each ion in the plasma has an associated charge state equal to its number of removed electrons. For a given applied voltage, each ion's time-of-flight (TOF) corresponds to a particular charge state. The TOF is also an indicator of the plasma temperature. Because of the electric field, ions with a greater charge state have a lower TOF than ions that are of lower charge

states.

A new area on the target must be used for each measurement after it is struck by the laser because of plasma expansion dynamics: both laser power and plasma temperature would decrease.^{2,3} Additionally, the impact of the laser on the target may deform the target in the immediate vicinity (raise the edges around the strike area, create an indentation, etc) so a new area must be used. We made the assumption that measurements are consistent and the target surface is smooth; only severe surface roughness is corrected in our measurements.

II. Equipment & Setup

The graphite-target laser ablated plasma is created by a Thales Saga Nd:YAG crystal laser with a 1064 nm wavelength and 6 ns FWHM pulse width. For the parallel case, the “low” energies and corresponding power densities used are 604 ± 6 mJ and $(1.17 \pm 0.01) \times 10^{11}$ W/cm²; the “high” energies and power densities are 1851 ± 35 mJ and $(3.59 \pm 0.07) \times 10^{11}$ W/cm². For the perpendicular case, these low value sare 612 ± 7 mJ and $(1.19 \pm 0.01) \times 10^{11}$ W/cm², and the high values, 1784 ± 6 mJ and $(3.46 \pm 0.07) \times 10^{11}$ W/cm². The energies are varied with the trigger timing of a Q-switch. The laser is guided by strategically placed mirrors and the target into a near-vacuum 10⁻⁶ Torr chamber. The laser is focused by a shielded plano-convex lens with focal length 100 mm at an incident angle of 30°.

The plasma ion congregation becomes an ion current in the presence of an applied electric potential. Located 2.4 m away from the target, the plasma ion current is measured using a Faraday cup (FC) with a 10 mm diameter collimator and suppression mesh grid applied with a -3.5 kV reverse bias. The plasma ions are bent by an Electrostatic Ion Analyzer (EIA); the EIA exclusively allows particles with a given energy-to-charge state ratio to be transmitted.² The TOF of the ion is the time it takes for that ion to pass from the target to the electrodes in the EIA. The ions are then detected by a Secondary Electron Multiplier (SEM) 3.8 m away from the target; the SEM amplifies the ion current to measurable levels.³ See Figure 2.

One large graphite block (31.2 mm x 12.7 mm x 8.9 mm) was used as the target. During the experiment, the large target fractured (31.2 mm x 12.7 m x 7.2 mm); the fracture was in the 31.2 mm x 12.7 mm plane so there was no disruption in measurements, besides a re-leveling and lens re-focusing.

III. Methods

For the most consistent results, variations in the length, width and thickness of the targets should be less than 50 μm . A standard surface roughness laser displacement sensor was used to quantify this variation. If corrections were necessary, the target would be leveled using 75 μm -thick vacuum-safe tape; the process continued ad nauseam until the variation was under 50 μm .

The energy density of the laser should be maximized to maximize the number of ions produced; with a constant energy, the laser spot size on the target is at a minimum.³ The lens that focuses the laser has an optimal position determined using FC measurements, corresponding to the minimum TOF and rise time.

After the lens position is optimized, two identical voltages with opposite polarity are applied to the EIA along the elbow-shaped curve between the FC and SEM. The ions are bent according to the applied voltages, and they either reach the SEM or hit the walls of the curve. We recorded as many charge states as possible through SEM signals and then plotted the measured voltage from the SEM against the TOF of the ion. See Figure 3. The FC and integrated SEM signal are then compared to determine how greatly the SEM amplifies the signal. After accounting for this factor, the number of ions in each charge state can be extracted from the SEM composite plot.

IV. Results

For a given laser-target orientation and laser energy, measured voltage intensity of charge states C^{4+} , C^{5+} and C^{6+} occur at approximately the same TOF. See Figure 4 for a composite plot of SEM signals, displaying measured (amplified) voltage as a function of the ion's TOF. These results suggest that the temperature of the resulting plasma is unchanged by the laser-target orientation.

However the parallel case consistently produces more ions in almost all charge states than the perpendicular case. See Figure 5 for the charge state distribution. At low energy, the number of ions produced in the highest charge state (charge state 5) in the parallel case is about 1.4 times the number produced in the perpendicular case. The difference becomes less pronounced but still present at high energy. The ion current composite plot has the same shape as the SEM composite plot.

There are clear visible differences in the laser strike spots in both orientations. Figure 6 shows the spots in the perpendicular case are raised and damaged around the edges, whereas those in the parallel case are more damaged inwardly. After the fracture, laser strike streaks were visible on the side of the target where parallel measurements were taken; this suggests that more ions were produced in the parallel case because the laser has a larger surface area to ablate a plasma as it travels between layers. See Figure 7.

V. Conclusions & Further Work

The difference in the peak TOF the ions in both orientations is minimal, suggesting that the same type of plasma is created. In both the high and low power case, the number of ions present (i.e. detected by the SEM) when the laser-target orientation is parallel is larger than the case when the orientation is perpendicular.

The laser traveling between layers may explain why more ions are produced in the parallel case, but the propagation of heat may better explain the discrepancy. In the perpendicular case, heat from the laser would more easily propagate on the surface of a layer than it would penetrate the layers, whereas in the parallel

case, heat could propagate between the graphite layers, resulting in a large surface area being affected. Further experiments are necessary to determine best explain the results. Measurements can be taken in the parallel orientation with a greater variation in laser power to determine if power affects the length of the laser streaks, indirectly testing the first suggestion.

VI. Acknowledgements

I offer my thanks to the Masahiro group at the Laser Ion Source at Brookhaven National Lab: the trio of graduate students Shunsuke Ikeda, Yasuhiro Fuwa and Masafumi Kumaki; my fellow intern David Cinquegrani; my mentor, Masahiro Okamura and Takeshi Kanase.

This project was supported in part by the U.S. Department of Energy, Office of Science, Office of Workforce Development for Teachers and Scientists (WDTS) under the Science Undergraduate Laboratory Internships Program (SULI).

VII. References

- Y. Fuwa, et al., *Rev. Sci. Instrum.* 85, 02B924 (2014)
- M. Kumaki, et al., *Rev. Sci. Instrum.* 85, 02B925 (2014)
- S. Kondrashev, et al., *J. Appl. Phys.* 100, 103301 (2006)

VIII. Appendix

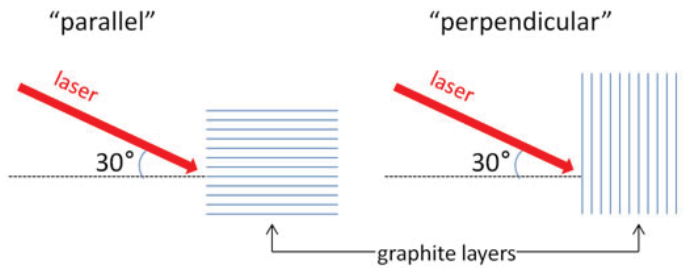


Figure 1: Naming convention for laser orientation with respect to the target's layers. The angle between the laser and the normal of the target surface is 30°.

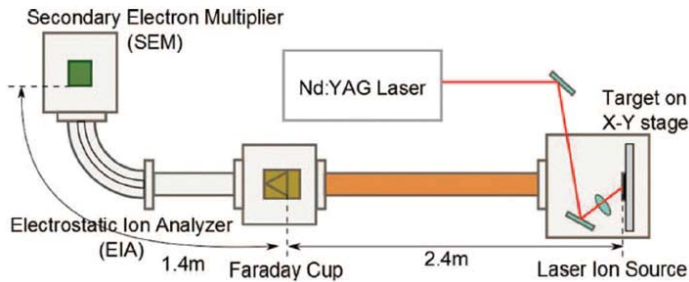


Figure 2: Experimental setup, minus the oscilloscope. Adopted from [2].

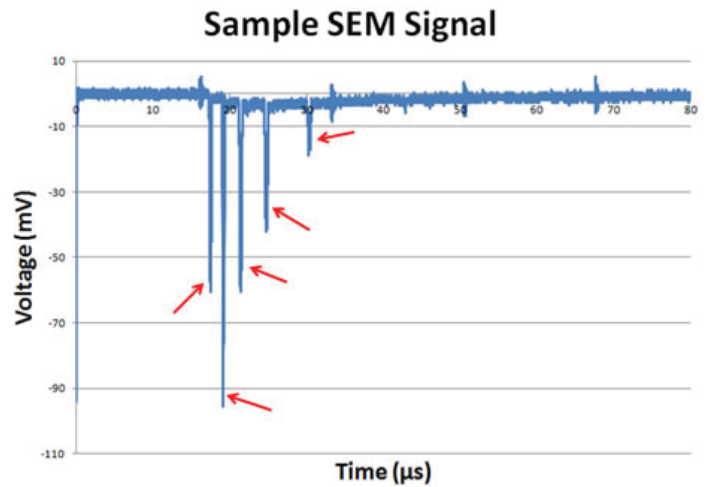


Figure 3: An SEM signal. Major dips indicated by the red arrow and indicate the presence of a carbon charge state. The consistent pulses present are caused by noise from the power supply.

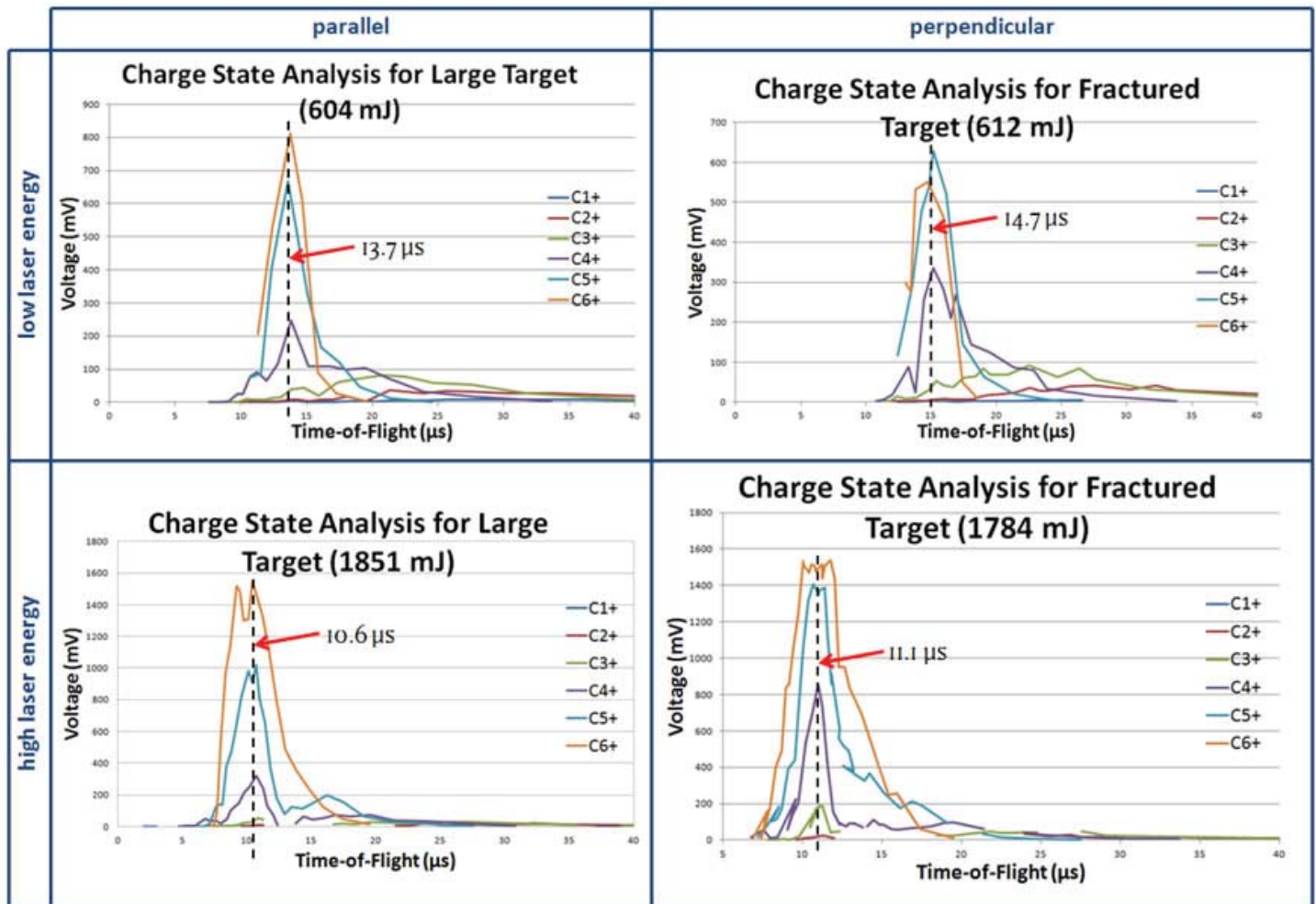


Figure 4: Charge State Analysis Composite Plot. The arrow points to the approximate TOF where the voltages for C4+, C5+ and C6+ are maximized.

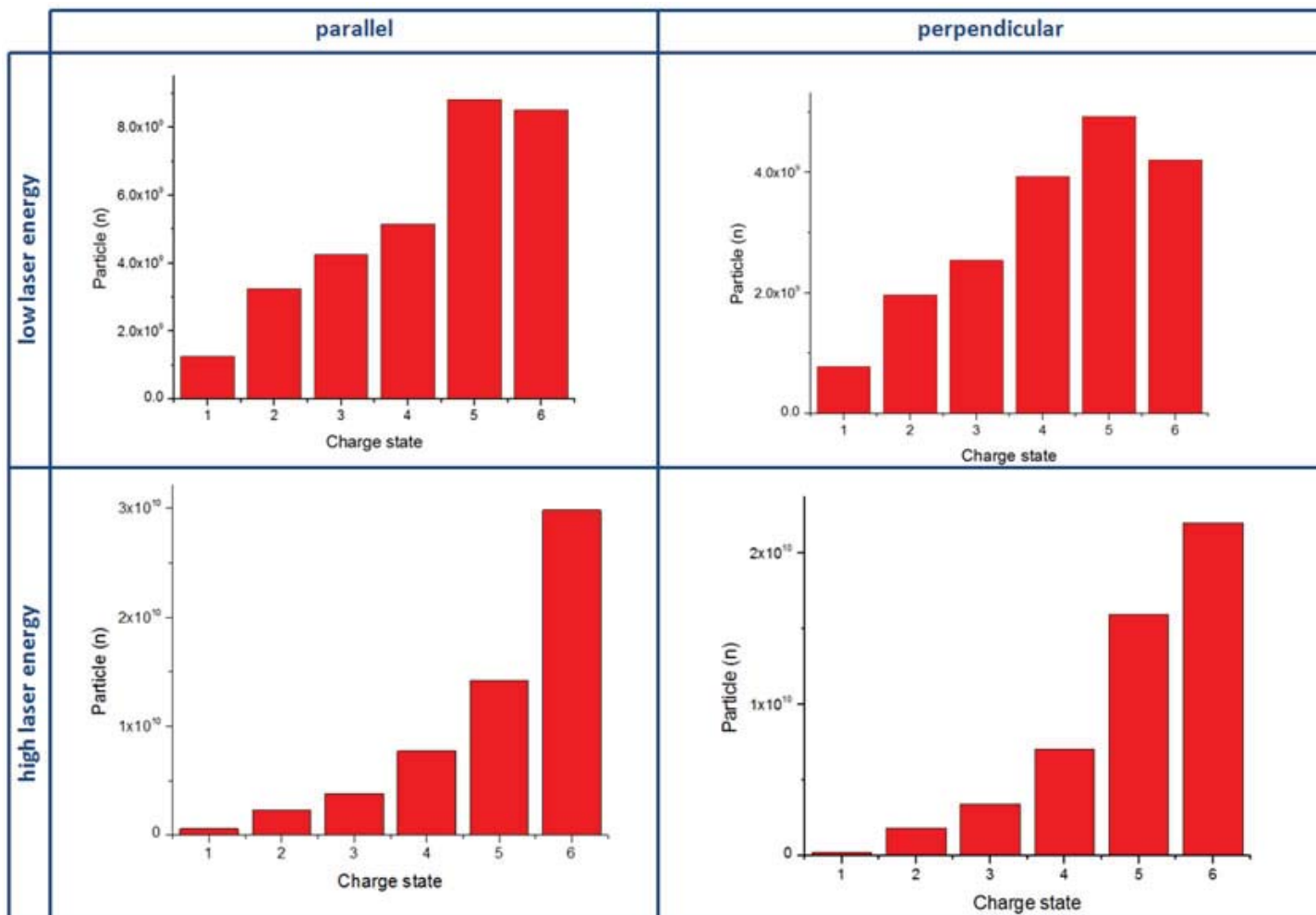


Figure 5: Charge State Intensity Plot. The y-axis represents the number of ions present.

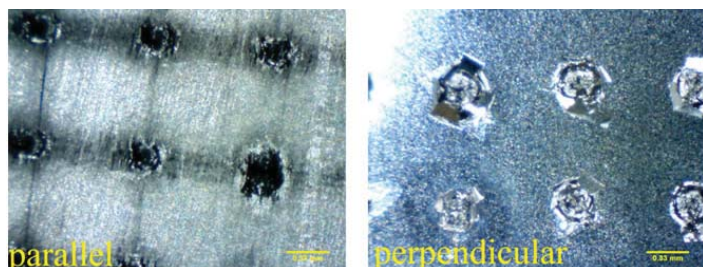


Figure 6: A zoomed-in picture of the laser strike spots in the parallel and perpendicular orientation.

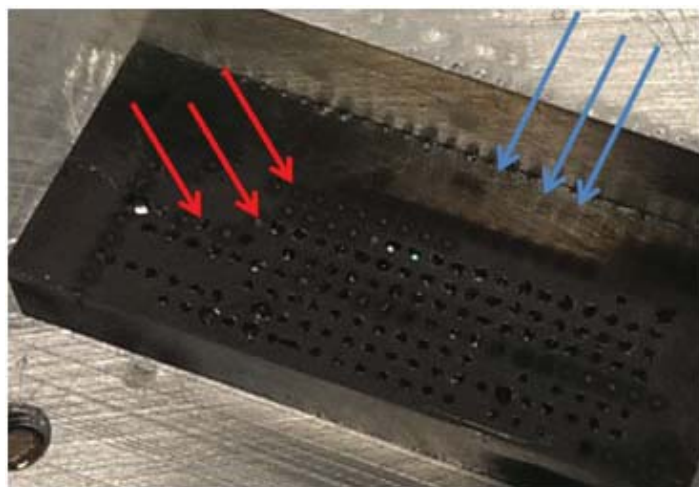


Figure 7: A picture of the fractured target after measurements. Blue arrows point to the laser streaks. Red arrows point to the laser strike spots in the perpendicular orientation.

Programmable coil winder for superconducting magnets

Nicholas Tsirakis

Watson School of Engineering, Binghamton University, Binghamton, NY 13902

Piyush Joshi

Nuclear & Particle Physics, Brookhaven National Lab, Upton, NY 11973

Abstract

A superconducting magnet can be manufactured by winding coils of wire around a cylindrical tube, which must be cooled down to cryogenically low temperatures when operated. The coils must be wrapped tightly and in precise locations to create the required magnetic field. If the winding pattern is off by a few micrometers, the entire field can change. It is, therefore, very important to pay a good deal of attention to the hardware and software that creates these patterns. At the Brookhaven National Laboratory's Superconducting Magnet Division, I was responsible for writing a program in LabVIEW that programmatically guides a highly accurate stylus around a cylinder to create a magnet. The program accepts an input of a standard text file of coordinates, extracts the necessary information, and feeds the instructions to a set of servomotors. In addition, the program has many safety features that prevent a loss of data during an emergency or a power outage. One of the most difficult aspects about this project was the obvious necessity to think in 3D coordinates rather than 2D coordinates. I had to envision the solution on three axes, which was something I had never done before. Once I felt comfortable thinking in three dimensions, I had to ensure that the whole process was synchronized; all the axes must move synchronously in order to create the appropriate pattern. After completing this project, I learned a lot about building large-scale programs and the LabVIEW programming language. All in all, I feel the experience that I have received at BNL will help me tremendously in the future when I am building my career.

I. Background

Superconducting electromagnets can be manufactured in various ways. One of the methods used by the Superconducting Magnet Division at Brookhaven National Laboratory (BNL) is the winding of superconducting wire around a cylindrical tube to create a certain pattern. When the coils are cryogenically frozen, they are able to conduct large amounts of current with no resistance, thus they can generate a powerful magnetic field with no energy lost to the environment. The coils must be wound in very specific patterns given by a set of pre-generated coordinates. The scientists at BNL use a programmable coil winder, also known as a direct wind machine, to interpret those coordinates and execute the required motion using a precision stylus that sets the wire on cylindrical substrate by using ultrasonic energy. An example of a pattern generated at the laboratory is shown in Fig. 1. A program written in the Visual Basic programming language is currently controlling the machine; BNL, however, is looking to upgrade their systems to a more modern programming language, namely LabVIEW. It was my goal, therefore, to develop an equally effective winding program in LabVIEW that had all of the features of the Visual Basic program.

II. Methods

A. Preparation and materials

Before I could write the LabVIEW program, I needed a way of testing it to make sure it worked. My mentor had a test set-up arranged for me in the laboratory; this set-up allowed me to test the program's accuracy without wasting any valuable resources, such as expensive superconducting wire and epoxy-coated cylindrical substrates. As shown in Fig. 2, the set-up consisted of a cylinder with paper wrapped around it and a pen to draw the desired coil pattern on the cylinder. Two servomotors, one linear and one rotational, were used to control the motion. Normally, the procedure uses three axes, but I used two axes to simplify the initial design process. Once the set-up was available to me, I needed to generate coordinates that the program could interpret and draw. The pattern that I chose was a spiral-like pattern that had ten loops, as shown in Fig. 3. This type of pattern was similar to those used on the actual magnets, and thus was perfect for testing. My mentor gave me various specifications that the spiral had to adhere to, such as a starting radius of ten centimeters, five millimeters of space between each loop, and a length of thirty centimeters.

Rather than derive coordinates specifically for this pattern, I decided to write a program in the Java language that could generate coordinates based on any required measurements, including the number of loops. This program simplified matters greatly because I could change the pattern at any time without needing to calculate anything else by hand. The formulas that I used to calculate the coordinates were fairly straightforward; I manipulated the Law of Sines to get these two general formulas that I used for the curved portion of the spiral:

$$X = \pm \text{radius} * \sin(180-90-\theta) \quad \text{and} \\ Y = \pm \text{radius} * \sin(\theta)$$

Of course, I had to further adjust these equations due to offsets and the like. One challenge about the spiral was that the "radius" variable was constantly changing for each point of the curve. I had to make sure to increment and update the value in my program when appropriate. After generating the coordinates, I converted them to encoder counts, the only measurement that the motors can understand, and wrote all the coordinates to a text file. Again, this was all done in Java. To verify that the pattern looked exactly as I expected, I imported the text file to Excel and viewed the coordinates graphically.

B. Programming the motion

The next step was to create the main program in LabVIEW. Before I wrote the part of the program that executed the patterned motion, I wrote a simple program that satisfied the basic needs of a motion program: "free" motion (i.e. moving a user-defined distance with a Start button), a display to see the current positions of the motors, a button to reset the positions of the motors to zero,

a method of interrupting the movement in case of a safety issue, and a button to “home” the motors, which entails moving both motors to a pre-determined location. All of these were created using functions supplied by LabVIEW that were able to interface directly with the motors. After making a base program, I was ready to write the function that handled the motion for the pattern. To start, I implemented a function that was able to read the provided coordinate text file, extract the encoder counts, and feed the values to each axis separately. Furthermore, for each point, the two axes had to start and stop at the same time. This meant that the velocity of one axis had to change for each point in order to sync up with the other axis; I accomplished this by calculating different velocities for every single point in the sequence, at runtime. After executing the movement on the motors a few times, I realized that this method would not work. As a result of interacting with the two axes separately, the axes operated asynchronously. In other words, the rotational axis would move and stop, followed by the linear axis, and so on. The result of such a motion can be found in Fig. 4. Besides being highly inaccurate, the motion was unbearably slow, and the constant acceleration and deceleration of both axes at each point was wasting too much energy from the motors. It was apparent that I needed to completely change how I operated the motion.

C. Contoured motion

I began researching the various ways that LabVIEW can perform motion. I came across many options, but only one option seemed to be a perfect solution – contoured motion. In a contoured movement, all of the coordinates are supplied at once, and a function called “Cubic Spline Interpolation” calculates all velocities and accelerations to execute that movement. In addition, perhaps the biggest advantage to contoured motion is the fact that it supports simultaneous axis movement, which means that both axes can smoothly draw the pattern without starting and stopping for each point. Implementing a contoured motion was easier said than done. I came across many issues, namely the motors jerking uncontrollably and immediately stopping. I eventually discovered that contoured movement is time-based; you must supply a time interval, between ten and thirty milliseconds, that determines how long the motors must take to move from point to point. For example, if the time interval is ten milliseconds and the first two points are ten centimeters apart, the program assumes that the motor needs to travel at one centimeter per millisecond, which is far too fast for these particular motors. This discovery explained the jerky behavior; the motors would spin very fast to try and complete the movement and then shut themselves down to prevent damage. I solved this issue by adding many more points to the coordinate file. Luckily all I needed to do was change a couple of numbers in my Java program and it would generate as many points as I needed it to. I eventually found a happy medium for these numbers and ultimately ended up with a coordinate file of over two hundred thousand points – more than fifty times the original.

Unfortunately, there was still a matter of concern. Due to the large number of points, the memory allocated to LabVIEW was not able to accommodate them all at once. I needed a way to use all of the points without inserting all of them into memory at the same time. Upon further research of the subject, I came across a buffering system that was compatible with the motors I was using. The buffers provided a way to load a few thousand points at a time; when the buffer was near empty, LabVIEW refilled it

with more points. This buffering system solved all of the issues. All two hundred thousand points could be used, but only a small chunk of them was in memory at any given time. When I tested the new version of the program for the first time, it worked perfectly. The motion was incredibly smooth, and it was able to draw the full pattern very accurately, as shown in Fig. 5.

III. Further consideration

The LabVIEW program still lacked one very important feature – the ability to pause the motion and resume it from the same location. In a real laboratory setting, these patterns can take upwards of eight hours to complete, and sometimes these hours are spread over the course of many days. This feature was a necessity if the laboratory had any intention of using the program in the future. Unfortunately, my stay at BNL ended before I could solve this problem, and I was not able to write this portion of the code. I did, however, come up with one theory that I think would work if implemented the correct way. In order to start a motion where you left off, you must capture the state of the machine during a “pause”. To do this, you could store all of the remaining points of the original data, as well as any points that are still left in the buffer, and concatenate both sets of the remaining data points into one set of coordinates. Once you have your new array, you can start the motion again by reconfiguring the buffer and recompiling a brand new contoured motion with the new set of data that was saved. This creates the illusion that you are pausing and resuming, when in reality you are executing two separate movements that happen to be part of the same pattern. Again, this is only a theory, but I am documenting my thought process to hopefully assist one of the scientists when this issue is addressed.

IV. Conclusion

All in all, I am very satisfied with my work here at BNL; the LabVIEW program works better than I expected, and I have learned a great deal. Of course, due to the fact that this is a long-term project, the program is still unfinished. A third axis needs to be added, a start-and-stop feature should be implemented, and it needs to be adjusted in order to ensure the same results with a stylus instead of a pen. Despite all that, it is in a perfectly acceptable condition to execute a movement for any pattern. I feel as though the laboratory will benefit from my research, and I am excited to see it take full effect in the near future.

V. Acknowledgements

This project was supported in part by the U.S. Department of Energy, Office of Science, Office of Workforce Development for Teachers and Scientists (WDTS) under the Science Undergraduate Laboratory Internships Program (SULI).

VI. Figures

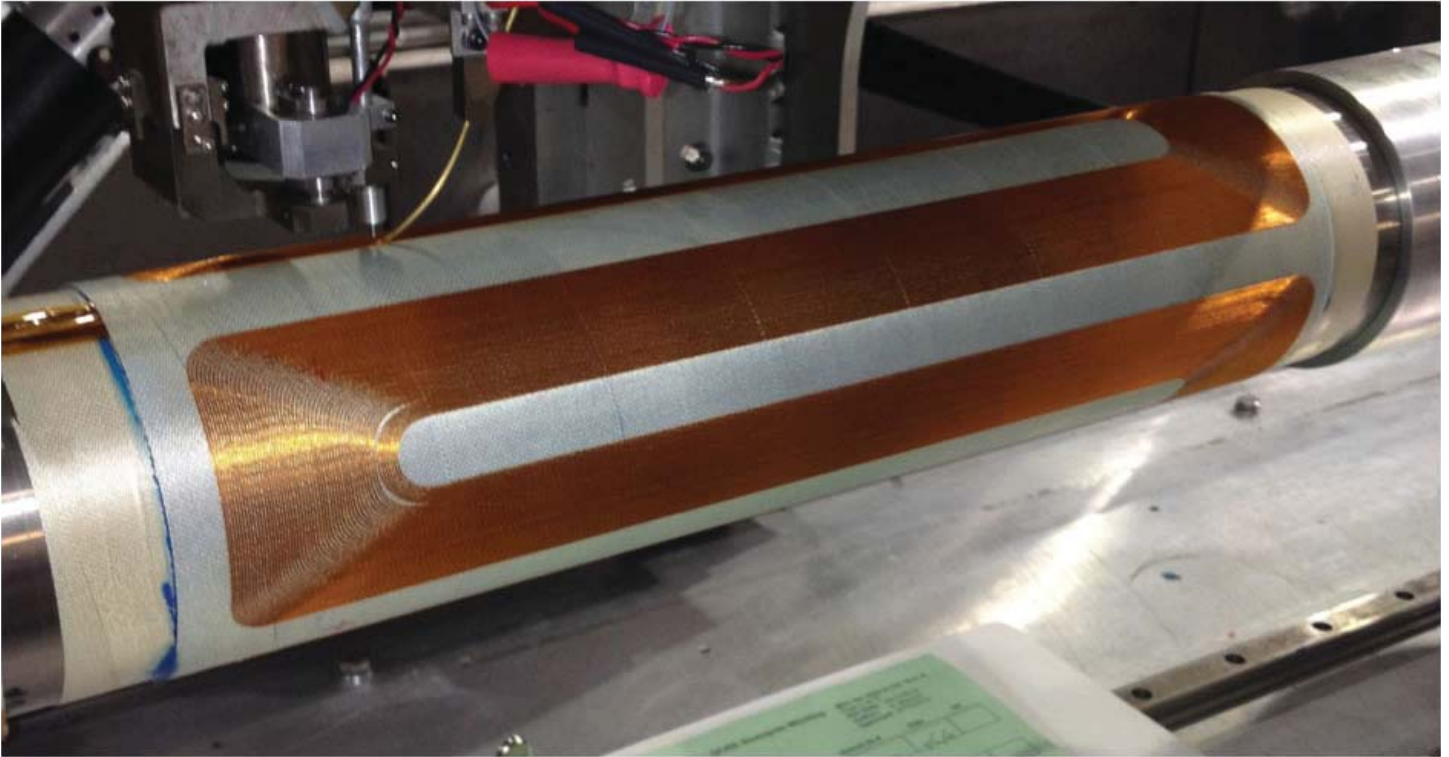


Figure 1. An example of a coil pattern generated by a direct wind machine at BNL



Figure 2. Set-up and work environment

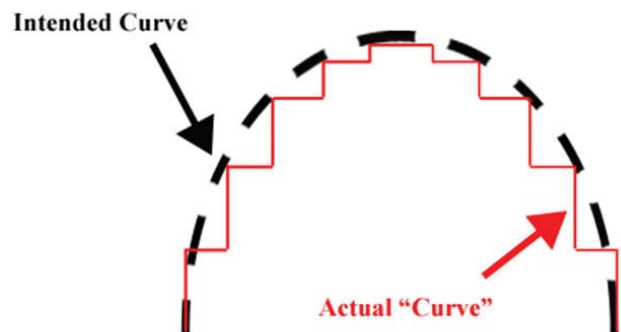


Figure 3. Sample spiral design

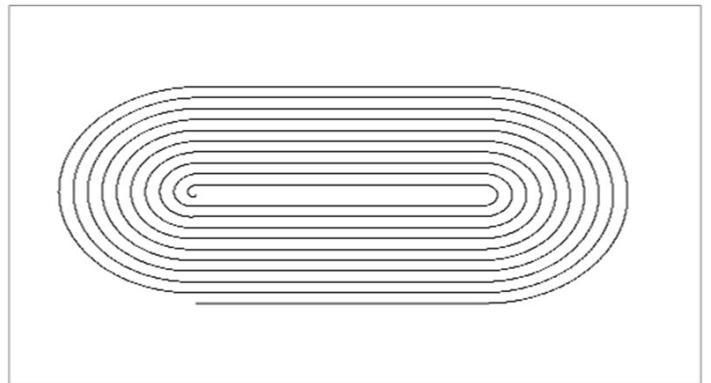


Figure 4. Illustration of asynchronous movement

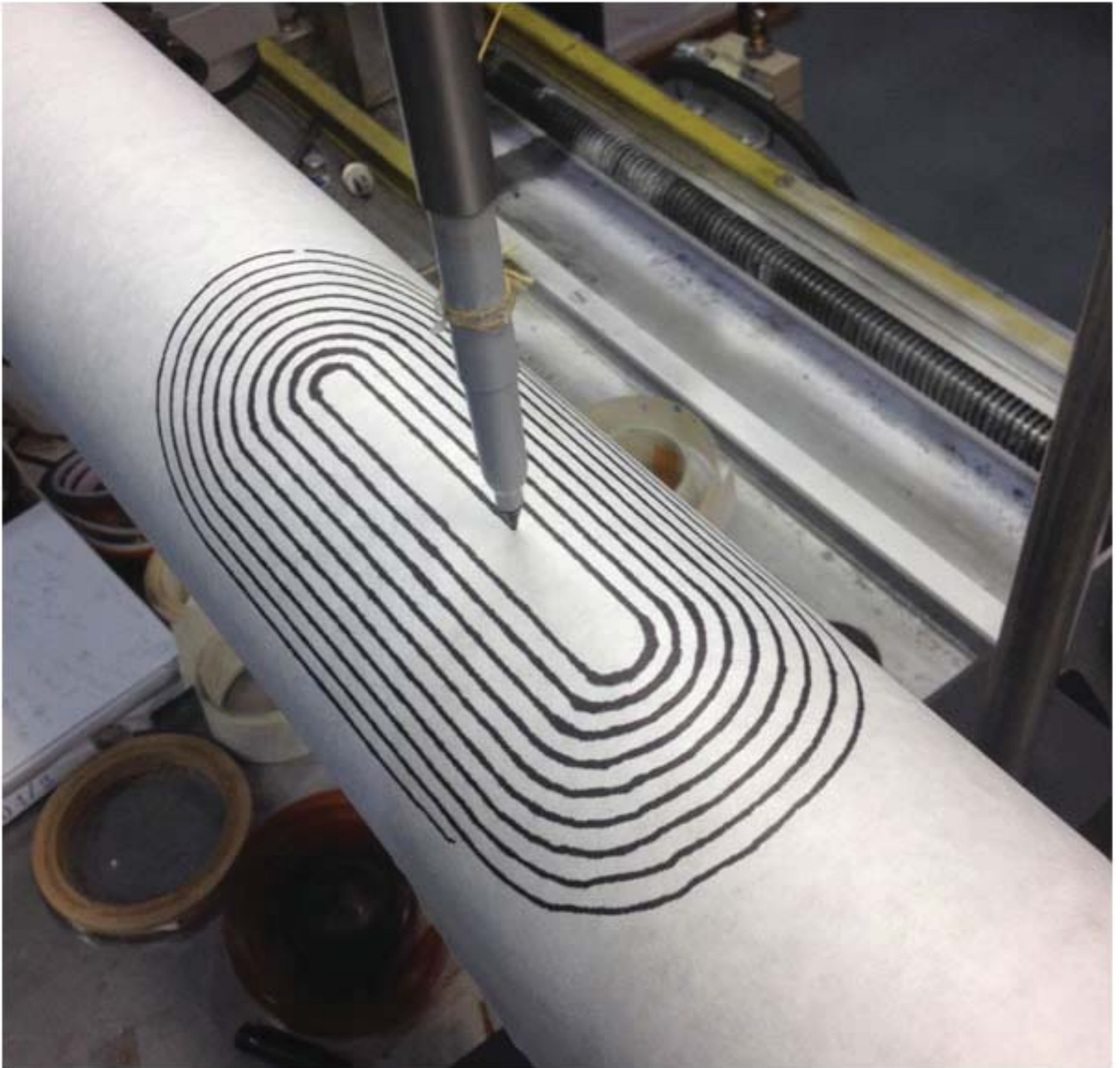


Figure 5. First successful pattern

Preliminary documentation and specifications for the infrastructure of the sPHENIX detector proposal

Nicholas Tully, Mechanical Engineering, Rose-Hulman Institute of Technology, Terre Haute, IN 47803
Don Lynch, Paul Giannotti, and Richard Ruggiero, Engineering, Brookhaven National Laboratory, Upton, NY, 11973

Abstract

The PHENIX collaboration proposes a major upgrade to the PHENIX detector at the Relativistic Heavy Ion Collider (RHIC) at Brookhaven National Laboratory (BNL). This upgrade, referred to as sPHENIX, will enable a compelling jet physics program addressing fundamental questions about the nature of the strongly coupled quark-gluon plasma (QGP), discovered experimentally at RHIC to be a perfect fluid. In order to successfully achieve the goal of implementing a more precise system, the PHENIX engineering team must upgrade the current infrastructure as well as implement new systems to allow the detector to operate flawlessly and efficiently. The engineering team must firstly, update the documentation of the infrastructure of the PHENIX detector, and secondly, create estimates for preliminary power, cooling, cryogenic, High Volume Air Conditioning (HVAC), safety and work platform access specifications. Using Autodesk, AutoCAD Electrical documents were created regarding the water cooling systems in the current detector. From the documentation of the PHENIX infrastructure, the engineering team drew rough estimations for the system specifications for the sPHENIX infra-

structure. These rough estimations were used in calculations to create more specific documentation crucial to the launch of the full scale construction of the sPHENIX detector. As a result of the work performed a familiarity with Autodesk programs, flow diagrams, electrical schematics, and documentation conventions is essential. In addition training courses were required to ensure safety at the worksite such as Lock-Out-Tag-Out procedures, radiological training, cyber security and general security clearance guidelines.

I. Introduction

With the surprising discoveries of the nature of the QGP, the PHENIX detector at RHIC is in need of a major upgrade to study and observe, in greater detail, the QGP. This requires the current detector to be completely decommissioned and a complete new construction of the sPHENIX detector. sPHENIX will use components unlike anything the PHENIX engineering team has seen before. The overall concept for how sPHENIX will sit in the existing PHENIX interaction region (IR) is shown in Figure 1. The sPHENIX team proposes an upgrade consisting of a 1.5 T superconducting magnetic solenoid with electromagnetic and ha-

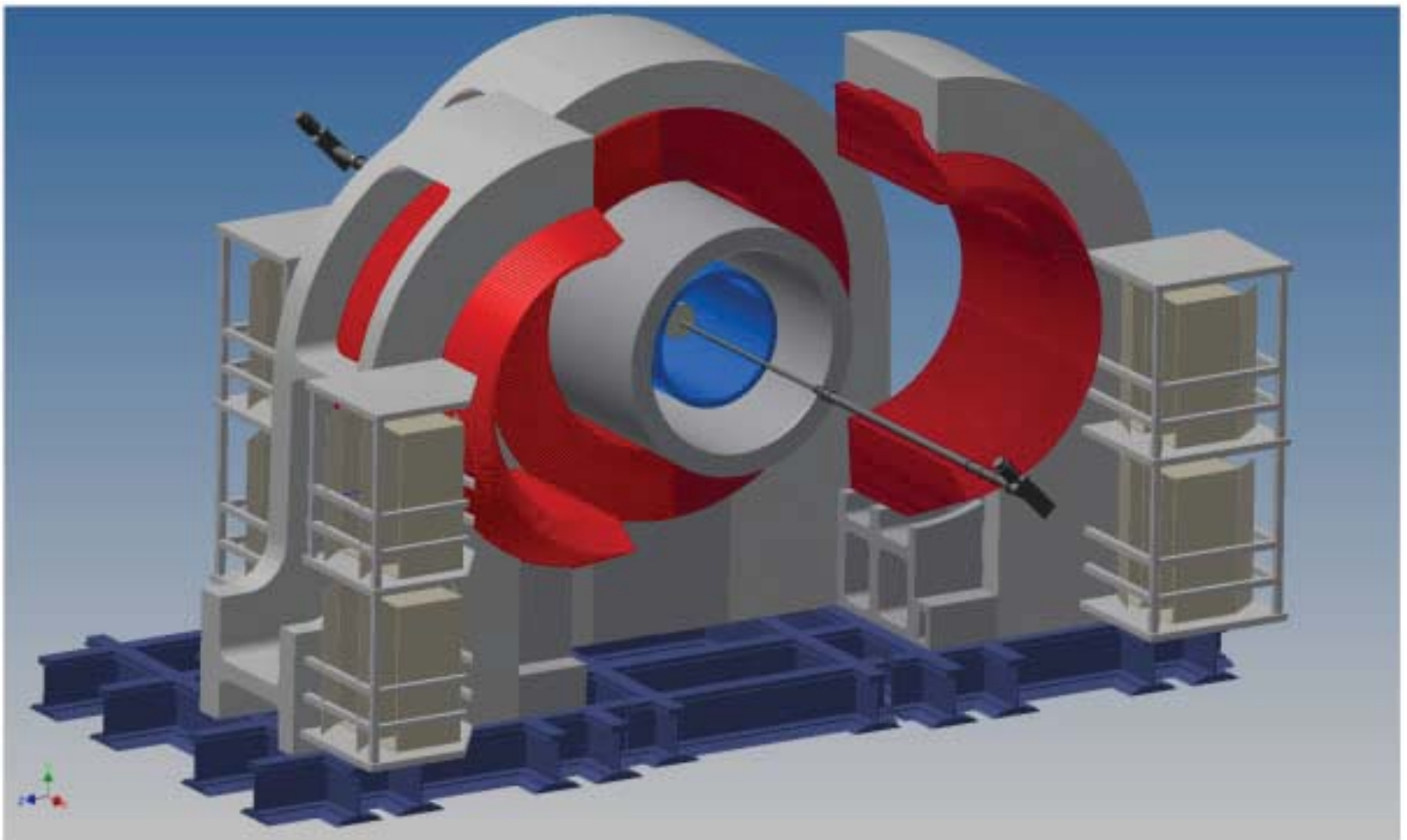


Figure 1: Illustration of sPHENIX underlying structural support, support equipment, overall assembly and maintenance concepts

dronic calorimetry. The sPHENIX solenoid is an existing magnet developed for the BABAR experiment at the Stanford Linear Accelerator Center (SLAC), and recently ownership of this key component was officially transferred to BNL. The design of sPHENIX takes advantage of a number of technological advances to enable a significantly lower cost per unit achieved by reusing significant elements of the existing PHENIX mechanical and electrical infrastructure. sPHENIX has been designed to be straightforward to manufacture and assemble, but it still requires significant and well thought out infrastructure to support and service it.

II. Methods

The sPHENIX detector relies heavily upon the existing infrastructure of the PHENIX detector. As a result nearly all the documentation for PHENIX needs to be updated and organized to depict current systems. Some current documentation is only available in a hand drawn copy and has not been electronically created. Creating electronic documentation serves a twofold purpose, the first being electronic documentation is easily transferable from person to person through a team accessible file and the second being that electronic documentation isn't easily lost or thrown away.

The Electronic Water Cooling System(EWS) uses cold water to cool the electrical components in the IR to maintain a proper operational temperature. This system was first on many different pieces of paper, was hard to read, and was not readily available to the engineering team. Using AutoCAD Electrical an accurate pipe flow diagram was electronically created. In addition to documenting the IR EWS, the source of the cooled water located in PHENIX's pump house was also documented.

Basic pipe flow diagrams documentation of the pump house was created to understand how the water is cooled and supplied to the IR. The pump house documentation records all instances of water cooling in the IR and is not specifically limited to the electronic water cooling system. This documentation shows the source for the magnet cooling water, power supply and electronic systems by use of a cooling tower/chiller system based upon

weather conditions.

In addition to updating and organizing PHENIX infrastructure new documentation based upon PHENIX infrastructure specifications and the experience of the sPHENIX engineering team to tailor preliminary specifications to support the sPHENIX detector. As a result new documentation and specifications for the sPHENIX detector were also created and focused upon the power, cryogenic, Heating Ventilation and Air Conditioning (HVAC), safety and work platform access systems. This information gathered from various individuals working on the sPHENIX engineering team was organized into tables and diagrams using Microsoft Office.

III. Results and Discussion

From a multiple page hand drawn packet for the EWS a complete electronic drawing was created. This drawing shows the pipe flow on one sheet of the EWS in the IR. Figure 2 below shows the result of the simplification from the hand drawn documentation. The figure highlights key valves for easy observation in the IR when performing maintenance and will help sPHENIX engineers in deciding what components to remove and what to leave based upon their needs.

Pump station documentation was created in a similar fashion highlighting the recognizable valves to allow for a better understanding from paper drawing to the actual system. The pump station was divided into 6 subsystems the power supply, electronics water, magnet cooling, cooling tower and the chiller water loop. These documents are shown in Figures 3-7 below.

Figures 2-7 document the existing PHENIX water cooling infrastructure. Changes from PHENIX to sPHENIX include removal of the existing magnet cooling water due to the implementation of the superconducting magnet which includes a cryogenic system to operate at temperatures of around 1-3° K.

From documentation such as the above sPHENIX engineers with the experience and collaboration with other departments are able to create preliminary specifications for the sPHENIX detec-

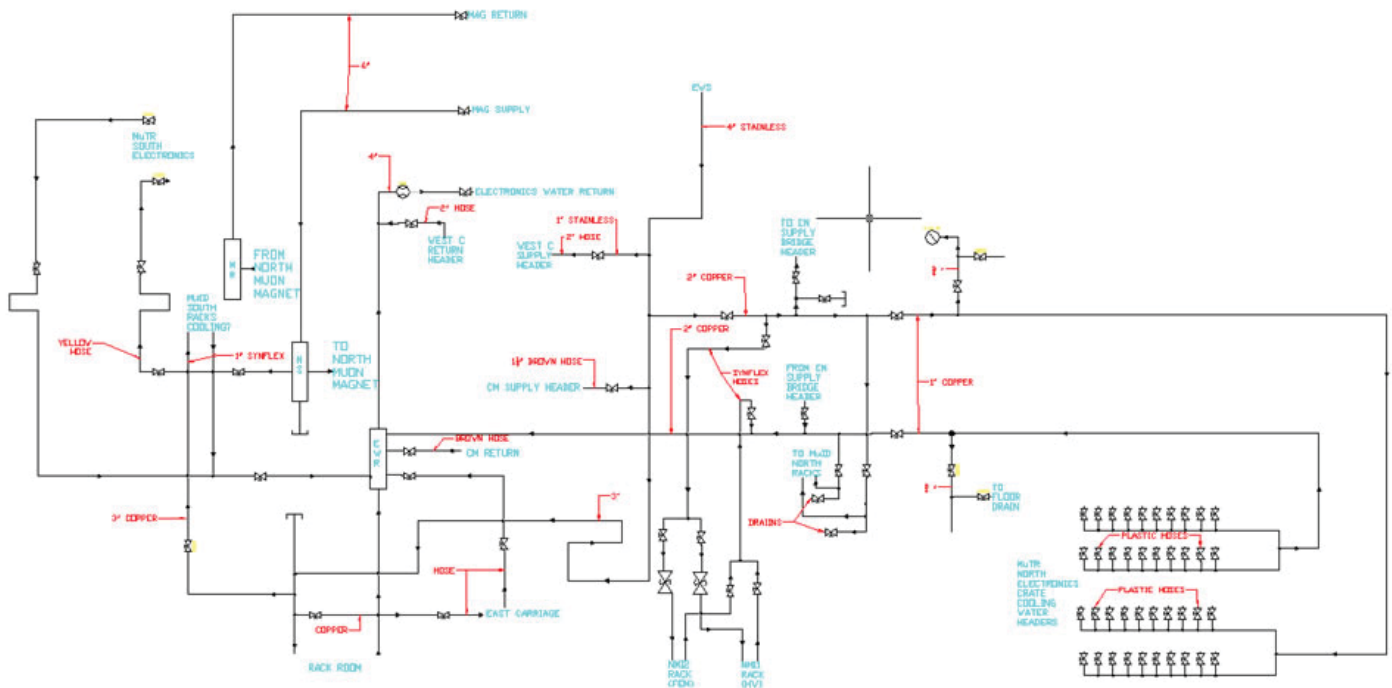


Figure 2: PHENIX electronic cooling water system

tor. These specifications are organized in tables and flowcharts and create a baseline estimate for more specific documentation for the full scale construction of the upgraded detector.

Preliminary specification documents are crucial to the design process in creating a uniform document that conveys information effectively to every individual involved with the construction of sPHENIX. Systems like power supply, safety, and HVAC all rely upon PHENIX infrastructure and serve as a spring board for the overall structure of sPHENIX infrastructure.

Preliminary documentation for the power supply system is shown in Figure 8. The terms “DP” and “DPA” refer to distribution panels already in place in the PHENIX rack room. Also the words not in boxes refer to the PHENIX experiments designation for that specific breaker.

Everything above the red line shows the existing PHENIX power supply infrastructure and everything below that line shows the proposed distribution of power to the various components of the sPHENIX detector.

With the proposal of a superconducting magnet in the sPHENIX detector there are many safety concerns that must be ad-

ressed due to the use of liquid helium. There poses a oxygen deficiency threat to the facility workers and alternate support systems for the detector if there is a liquid helium leak. The sPHENIX infrastructure must then be modified to account for the occurrence of such a helium leak. In addition to a liquid helium leak there is also a list of possible problems that could go wrong within the IR including water leaks from the cooling systems and smoke from possible electrical fires. Figure 9 shows the proposed modification to the existing safety system as well as what alarms need to be passed to department systems to ensure that the detector and workers remain safe.

Figure 9 shows that once there is an existence of a liquid helium leak or smoke three things should happen an alarm indication should appear in both the Collider Accelerator Department (CAD) office from there the CAD PASS system will be activated to shut down and purge the IR of any helium or smoke. In addition to notifying CAD of the existence of the event an alarm indicator should also appear on the sPHENIX control room panel to notify any individuals in the control room of the threat.

The sPHENIX experiment precision can be adversely affect-

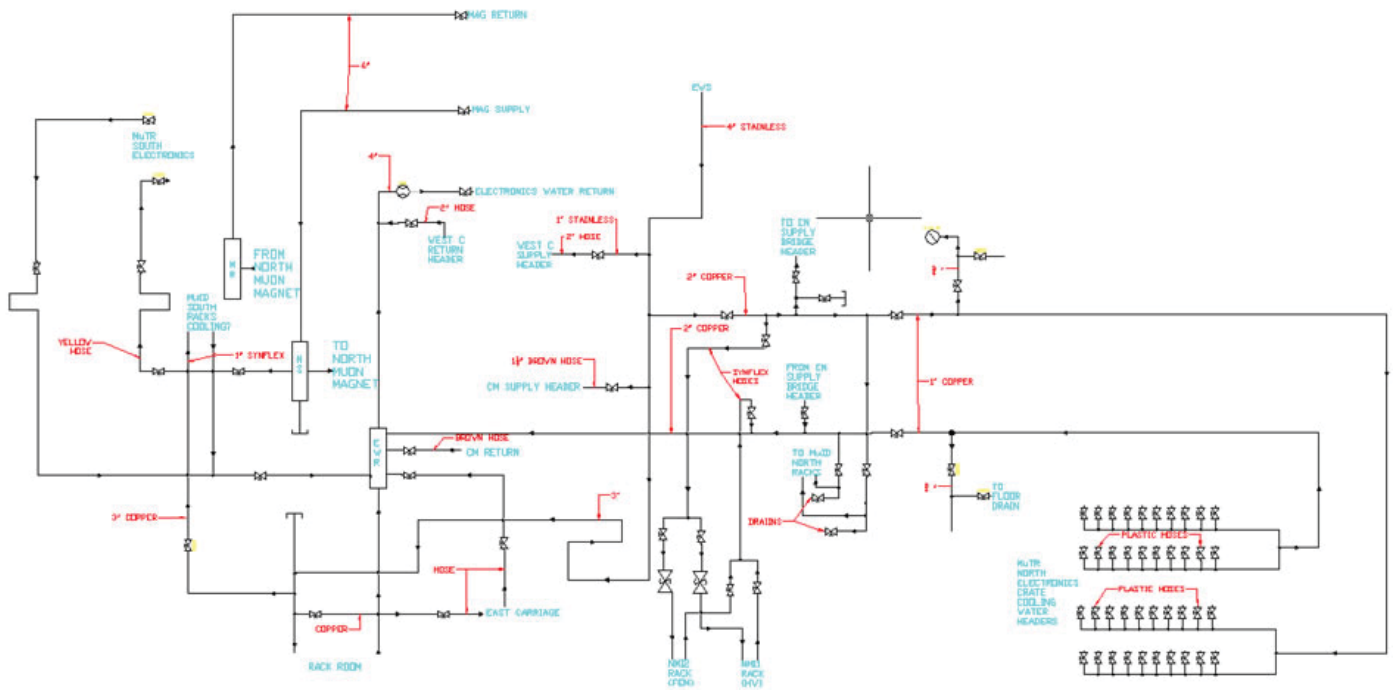


Figure 3: PHENIX pump station power supply water cooling

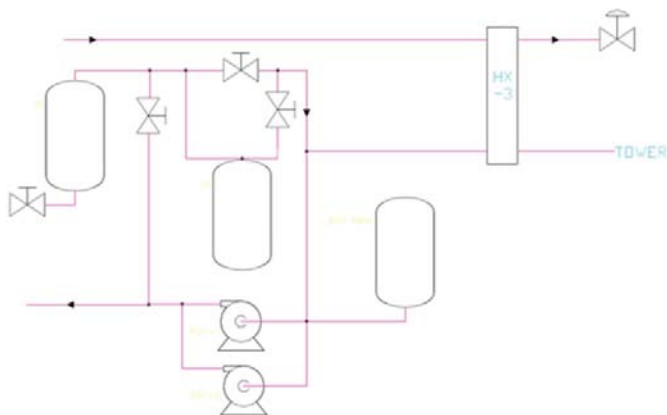


Figure 4: PHENIX pump station electronics water cooling

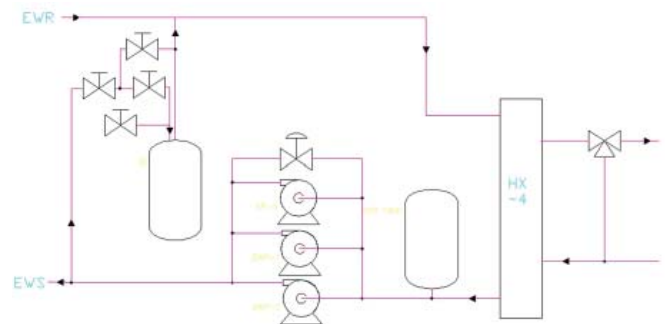


Figure 5: PHENIX pump station magnet water cooling

ed by minor changes in weather. Therefore the building in which the detector will be housed must remain at a constant temperature and humidity to reduce error within the experiment. Table 1 organizes the threshold values for the environment conditions of the sPHENIX detector building.

Upper Limit Environment Condition Specifications		
Temp	Max Humidity	Max Wind Speed
100 °F	100%	30 mph

Desired IR Condition Specifications		
Temp	Humidity	Wind Speed
68 °F	60%	N/A

Table 1: HVAC desired specifications

sPHENIX engineers have assigned a design worst case day that the building can expect is 100°F, 100% humidity and a max wind gust of 30 mph. The HVAC system must be able to create the conditions of 68°F at 60% humidity under the worst day design conditions. From these estimates, 4 units of the same capacity as the existing 3 units currently in place at the PHENIX detector are needed to maintain an optimal data collection IR environment.

Work platforms for accessing the detector subsystems are necessary to create a space for working on and maintaining the functionality of the detector. By organizing and planning the amount of platforms the engineering team would like to have offers a good estimation of how much space engineers and technicians will have. Table 2 organizes this desired information.

Location	Number of Platforms	Notes
East Carriage	2	
West Carriage	2	
Cryo Magnet Pedestal	1	Above outer HCAL
Crossover		Detachable/move-able

Table 2: Work platform access

Both the East and West carriages will require two platforms to at two different heights this will differ from the original PHENIX detector and platforms. The superconducting magnet pedestal must have a cross over to allow for easy access to the various calorimeters and various detector modules in the IR. Crossovers from the sections of the detector are necessary to be able to move above the entire detector. This provides easy transition from one section to the next. However, the crossover platform must be able to collapse or detach so the detector can be manipulated on their support rails for servicing and easier maintenance.

With the introduction of liquid helium in the design of sPHENIX, there is a requirement to allow the magnet to minimize energy loss in the coils of wire to maintain the phase of helium and not allow the helium to boil off into gas. In order to maximize the life of the liquid helium there needs to be a cryogenic system in place to supply the magnet with sufficiently cold enough liquid helium to pass the superconductivity threshold. The system must have a way of transporting the liquid via shielded transfer lines and through use of a heat exchanger gradually control the “cooldown” of the magnet to ensure no damage to the detector.

IV. Conclusion

With the recent discoveries in the nature of the QGP and the purposed implementation of the sPHENIX detector there are many preliminary specifications that need to be made to more accurately characterize the nature of the QGP. This document organizes and presents initial estimates for the support systems of the sPHENIX detector. The infrastructure documentation presents changes that need to occur in order for the detector to successfully and safely operate. By organizing the ideas and documenting existing infrastructure in the PHENIX detector this document will be a good reference to the actual full scale construction of the sPHENIX detector.

V. Acknowledgements

This project was supported in part by the U.S. Department of Energy, Office of Science, Office of Workforce Development for Teachers and Scientists (WDTS) under the Science Undergraduate Laboratory Internships Program (SULI).

Special thanks to Don Lynch, Paul Giannotti and Rich Ruggerio and both the PHENIX and sPHENIX engineering teams for their guidance and support throughout the duration of this project.

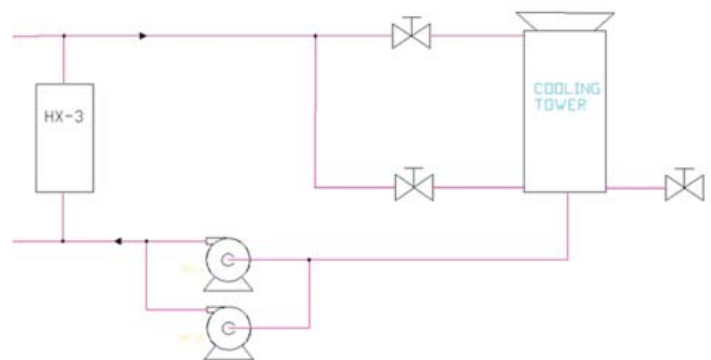


Figure 6: PHENIX pump station cooling tower

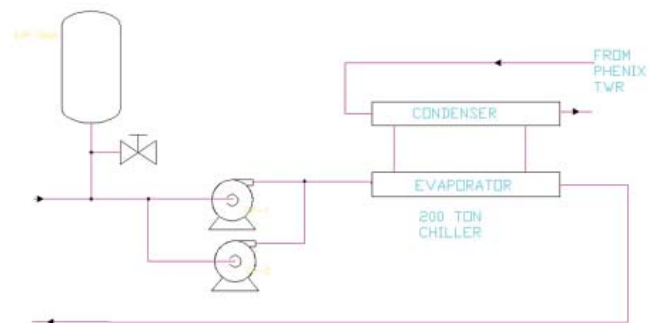


Figure 7: PHENIX pump station chiller water cooling

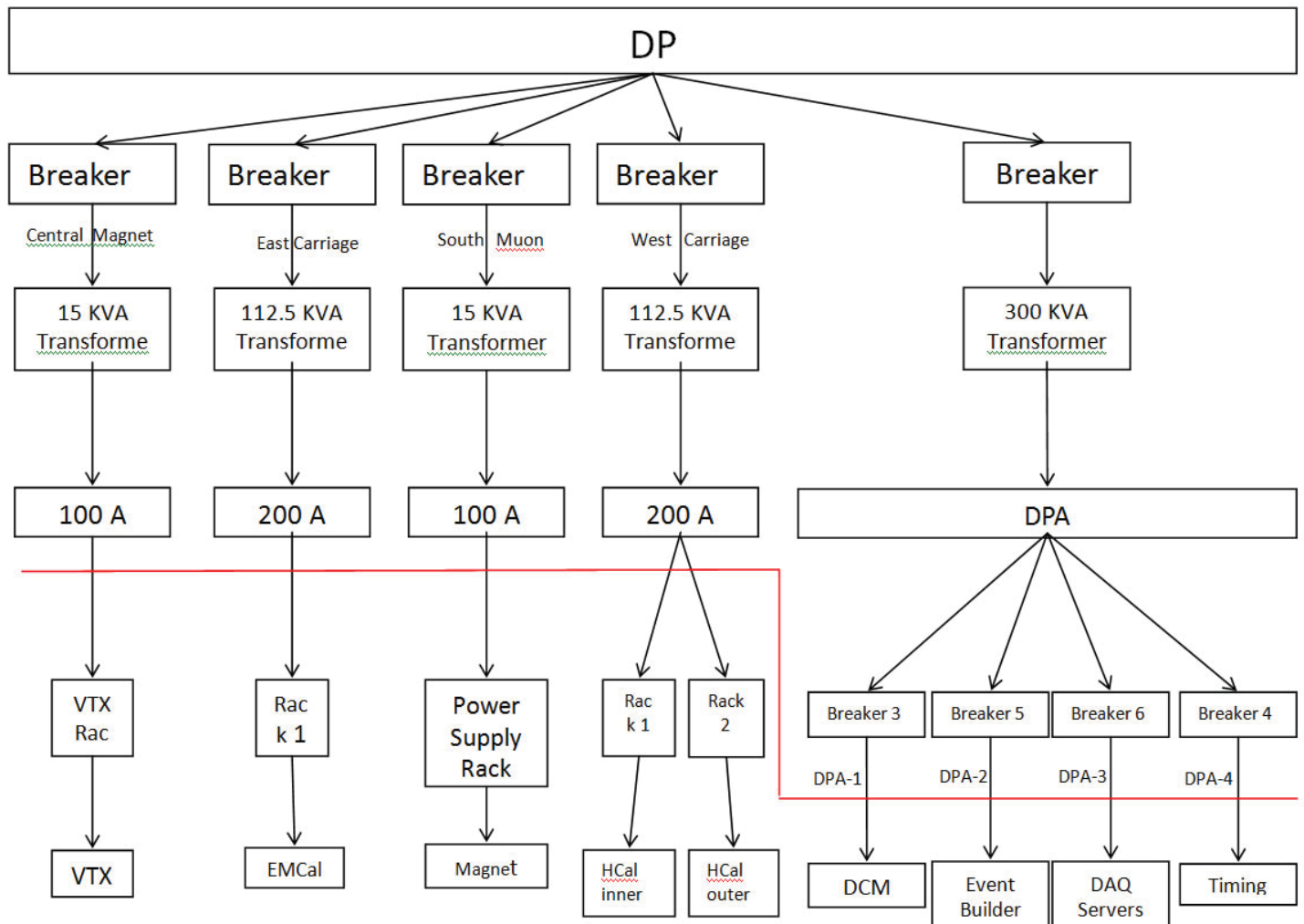


Figure 8: Power supply infrastructure

If signal trips alarm for....

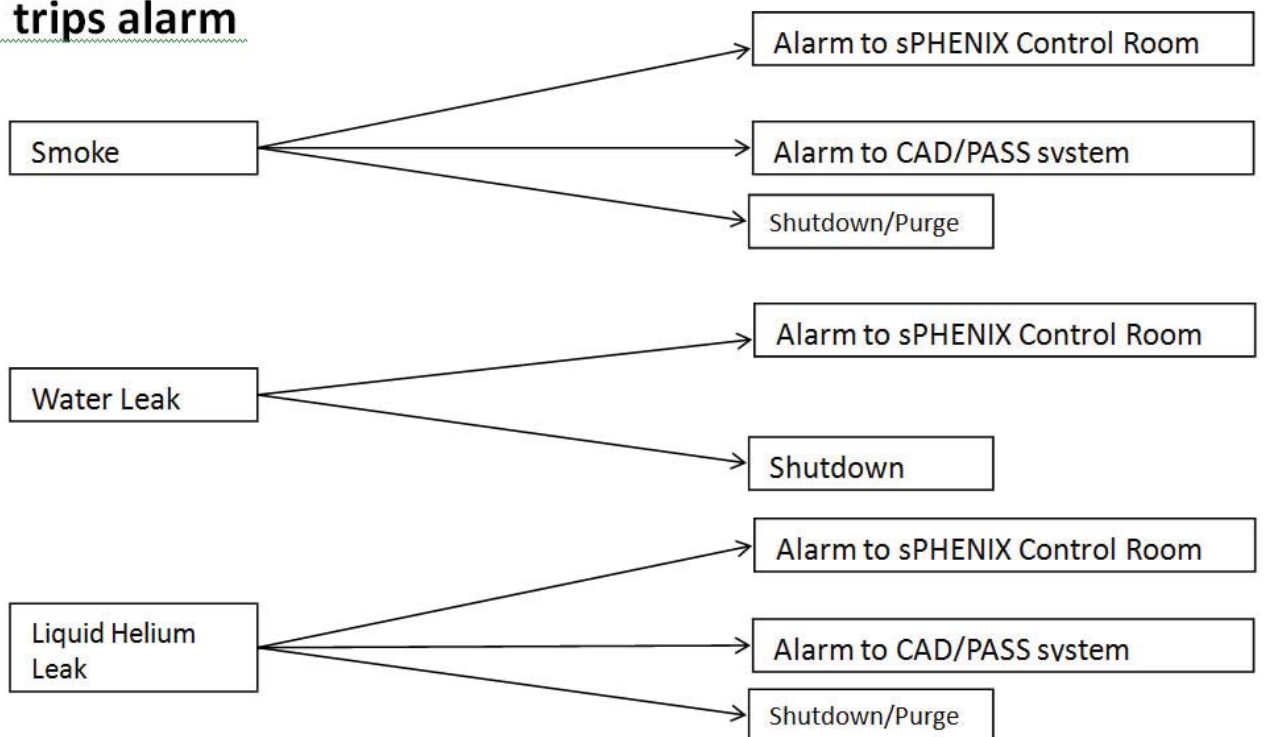


Figure 9: Safety System upgrade

Design and optimization of vacuum chambers for eRHIC

Benjamin Tuttle, Engineering Department, Cedarville University, Cedarville, Ohio 45314
Michael Mapes, Collider-Accelerator Department, Brookhaven National Laboratory, Upton NY 11973

Abstract

The Collider-Accelerator Department engineers that are designing electrion-Relativistic Heavy Ion Collider (eRHIC) have many design constraints; from the budget, to the more pressing issue of space within the RHIC tunnel itself and the space between the magnets where the vacuum chamber for this new project will reside. Working on the design of the vacuum chambers requires extensive knowledge in Finite Element Analysis (FEA) to properly analyze the chamber for stress levels well below the yield point (where the material deforms) of the aluminum. I'm looking at optimizing a single chamber to withstand the atmosphere pressure upon it by modifying critical areas in order to create a successful design. What I have found is that the constraints on the design due to the magnet gap where the chamber fits in between creates little margin for error in whether or not the chamber will deform. So, I need to add material to certain places while maintaining the proper gap between the magnet and the chamber, as well as allowing enough room for the eRHIC beam to go through the chamber which has become an increasingly tricky endeavor.

I. Background

Designing vacuum chambers for the electron beam to ride in is more of a challenge than at first glance, considering the size of the RHIC tunnel is massive and roomy. The challenge is therefore the limited room between the magnets that propel the electrons in eRHIC. When the magnets are opened up even slightly, the cost goes up significantly. So to avoid extra-unwanted expenses, the engineers working on the project must take into consideration the vacuum chamber must be optimized to fit the constraint of magnet gap size without the option of changing it much. Since my time at Brookhaven National Lab (BNL) was limited to just 10 weeks, I had to limit the scope of my research to just analyzing the stress in the chambers and making sure the dimensions were valid for the beam to ride in and for the chamber to fit into the magnets. Thus, I did not get to analyze the thermal capabilities of the chamber to make sure the aluminum extrusion was properly cooled as the beam heats up the inside by radiation. I also did not get to see any physical representation of the project since its implementation is much further down the road than just the summer I'm here. Therefore I couldn't do any physical work on the beamline and I also didn't get to physically see what designs work and which don't. Needless to say, I did fulfill the purpose of analyzing vacuum chambers to propose a working and functional design within the constraints for three different magnet designs. Therefore, my work in analyzing these three chambers will help give the engineers in the future a good head start on which magnets (and thus chambers) would work and which should be avoided.

Starting with the designing process of the chamber required a lot of consideration of chambers used in the past at BNL in or-

der to get a feel for what should and shouldn't be done for our application in designing eRHIC. So, my mentor Mike had a few cross sectional sample pieces of previously installed beamline to explain what the general requirements were, including the area the beam needs to ride through, the size and location of the cooling channel, the thickness of the wall generally required, and the tolerances by which the contracted company can extrude the vacuum chamber to. Thus, I got a clear picture of what needs to go into this design and how to approach the start of the design process.

First off, learning the 3D computer aided design (CAD) software was challenging and time consuming, but luckily I had previous experience with a similar package that I've been using for three years. Having the 2D drawings of the three magnets supplied to me by the engineers allowed for a quick chamber to be modeled based on these drawings. Essentially, I kept 1.5mm away from the magnet pole tips to allow for a slightly irregular chamber to still fit while creating a larger "evacuation" chamber on the outside of the magnet to increase the chamber's conductance (ease of which the chamber can achieve vacuum). Then, I could modify the initial chamber to include extra material where appropriate when the stress analysis gave me results that indicated a lower stress is needed. After creating a 2D sketch of the magnet chamber with the appropriate magnet gap, I imported the sketch into Creo Parametric, a 3D CAD software where I could model and edit the chamber in 3D. The next step taken was importing the newly modeled vacuum chamber into ANSYS, a finite element analysis (FEA) program that powerfully and quickly allows the user to determine stress levels, deflection, and much more by setting up the model appropriately. To set up the FEA analysis on ANSYS, I first applied real life boundary conditions such as atmospheric pressure (14.7 psi) on the outside walls of the chamber and fixed support at both ends of the chamber (zero displacement in all directions). This set-up was specified by my mentor as he explained that the chambers would be fixed on both ends and subjected to atmospheric pressure on the outside and vacuum pressure (essentially no pressure at all) on the inside. Also very important to mention is the mesh created in order to get accurate results. I had to refine the mesh in many ways, like using a sweep method along the chamber which allows the mesh to be uniform along the length because it takes the front surface mesh (source) and pulls it through the entire surface with a specified number of divisions along the length. Because the front face of the vacuum chamber was very irregular, I set a size control on how big the mesh could be in order to achieve two to three nodes thick along the thinnest part of the chamber walls. If more nodes along the thickness were desired, the only outcome would be greater computational time and not necessarily more accurate results. I also set the number of divisions along the length of the chamber to 70 (70 divisions for the sweep to follow). All of these mesh controls ended up giving me a good mesh that yielded accurate results

without an unnecessary increase in computational time, which is greatly desired especially considering I had to run around 30 independent modifications of the three proposed chambers. The same procedure was followed for the other two chambers. The results that were desired out of the ANSYS analysis was Von Mises stress, which is an equivalent stress that takes into account all the different components of shear and normal stress on a stress element. This Von Mises stress could then be compared to the yield stress of the 6063 T5 aluminum in order to see whether or not the chamber would fail. Because we also desired a safety factor of 2, the Von Mises stress needed to be below 7.5 ksi. The stress would concentrate where the material would have a sharp fillet or along the end of the chamber where the pressure from the top and pressure from the bottom would squish the chamber creating a highly stressed area. Thus, the two areas that generally needed to be thickened were around the end of the chamber and increasing the radius of the fillets. There was a trial and error process throughout the design project intended to optimize the vacuum chamber to only have a thickness of three millimeters (the minimum extrusion thickness of the chamber) and to be simple to where the cost of producing these chambers was minimal. After noticing that the stress levels were acceptable for the aluminum material (below yield point), we had to look at the deflection of the chamber to see if it was significant enough to warrant a change in design. For all three cases, the deflection was minimal and would in no way interfere with the magnets. Accordingly, the only real issue with the chambers would be whether or not they could withstand atmospheric pressure. The last thing that would have been evaluated is whether or not the heat load would be handled by the chamber. This would have been analyzed on ANSYS, but due to my lack of time and dedication towards other issues concerning the chamber, I could not evaluate this parameter in chamber design. My mentor mentioned that the chambers followed a somewhat standard water channel size of around half-an-inch, so this is what would most likely be implemented in the chamber. But I could have ran the ANSYS simulation to see if this were true after knowing the heat load per foot due to synchrotron radiation.

In summary, the three chambers analyzed were successful in withstanding atmospheric pressure, fitting within the constraints of magnet size and pole tip separation, and also allowing enough room for the beamline to fit within the chamber. The successful design of three separate chambers allows the engineers to have a head start on which magnets (and thus the vacuum chambers) would work best for the application on the stress/deflection side of the decision while the physicists designing the magnets would get a better idea of how close the magnet pole tips can be, as well as the rest of the sizing constraints allowed. I don't have many recommendations other than I believe the engineers and physicists need to collaborate closer together in order to come up with a successful magnet design, instead of the physicists giving the engineers a crude drawing that we have to interpret which could consequently be incorrect. All in all, the experience of working alongside very knowledgeable engineers that could answer my endless stream of questions provided me with a productive summer and a greater understanding of the design process, engineering computer programs, and BNL as a whole.

II. ACKNOWLEDGEMENTS

Huge thanks to Mike Mapes for answering my questions with expertise. Special thanks to Sumanta Nayak for much needed help

with ANSYS, George Mahler for teaching me TIG welding and for his extremely helpful advice in modeling and analyzing parts in Creo Parametric, Gary M for more help in Creo Parametric than I could have asked for, and The SULI program within BNL also deserves many thanks for hosting this learning experience and providing seminars to further my education. This project was supported in part by the U.S. Department of Energy, Office of Science, Office of Workforce Development for Teachers and Scientists (WDTS) under the Science Undergraduate Laboratory Internships Program (SULI).

Analysis of Temperature Gradient on Polycrystalline Silicon Cells

Ilia Vardishvili, Electrical Engineering, Stony Brook University, Stony Brook, New York 11790
John Heiser, Environmental Sciences, Brookhaven National Laboratory, Upton, New York 11930

ABSTRACT

In the summer of 2014, the Environmental Sciences Department piloted research on the effects of temperature gradients on polycrystalline silicon cells used in the photovoltaic modules based on the Long Island Solar Farm (LISF). Key scientific objectives include predicting cell degradation in photovoltaic modules and determining module performance based on individual cell temperatures. This study required thermal mapping of twenty five different panels spread throughout LISF each of which contain sixty cells. The photovoltaic modules that are being analyzed were supplied by BP Solar (Model number 3225T). These modules have a silicon substrate that is used to create a PN-junction resulting in a variation in each cell with different nominal operational cell temperature (NOCT). The variance in the NOCT may cause each cell to integrate solar irradiance into power with different efficiency, guiding the determination of performance reasoning at cell level. The data collected represent the base line for longer term aging studies. In order to be able to make conclusions on degradation of polycrystalline silicon cells, a large amount of data is required prior to analysis. The success of this research may give insight on performance based on solar irradiance integration and the ability to predict cell failure.

I. INTRODUCTION

Energy acquired from solar irradiance using photovoltaic technology is a leading interest in alternative ways to generate electricity rather than from conventional fossil fuels. Polycrystalline silicon PV modules are the most commonly used panels and are used at the Long Island Solar Farm (LISF), located at Brookhaven National Laboratory (BNL)..

Silicon cells usually consist of four layers. The top layer is

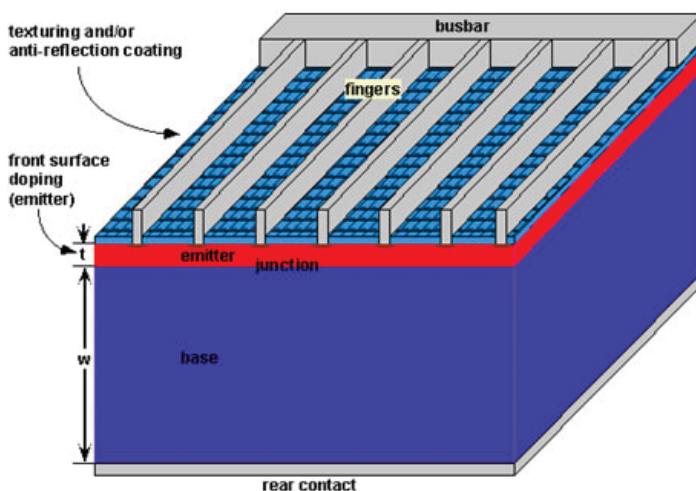


Figure 1: Layers of a polycrystalline silicon cell².

generally aluminum with an anti-reflective coating and having metallic busbars and fingers, which are used to collect and direct current. The second and third layers are n and p silicon substrates which, when put together, create a PN-junction¹. The semi conductivity of a PN-junction induced causes it to act as a diode; directing current flow one way². And, finally, the bottom layer also consists of an aluminum contact.

Now that we know how a cell is structured, the primary concern is the silicon substance. Silicon is heterogeneous as a solid causing the PN-junction to be non-uniform which leads to uncertainty in the operation of the cell³. Since the function of a cell depends on the material that it consists of, the nominal operating cell temperature has uncertainty in its operation. The standard polycrystalline silicon panels, specifically 225W Photovoltaic Module BP 3225T, used at the Long Island Solar Farm, have a nominal operation cell temperature of 47°C with an uncertainty of $\pm 2^\circ\text{C}$ at 800W/m^{2,4}. The difference between each cell greatly impacts the function of the panel while also having a possible effect on its life span. The specifications from the manufacturer show that with every one degree increase in nominal operational cell temperatures, the power and the voltage acquired from the cell decreases represented by the equations⁴:

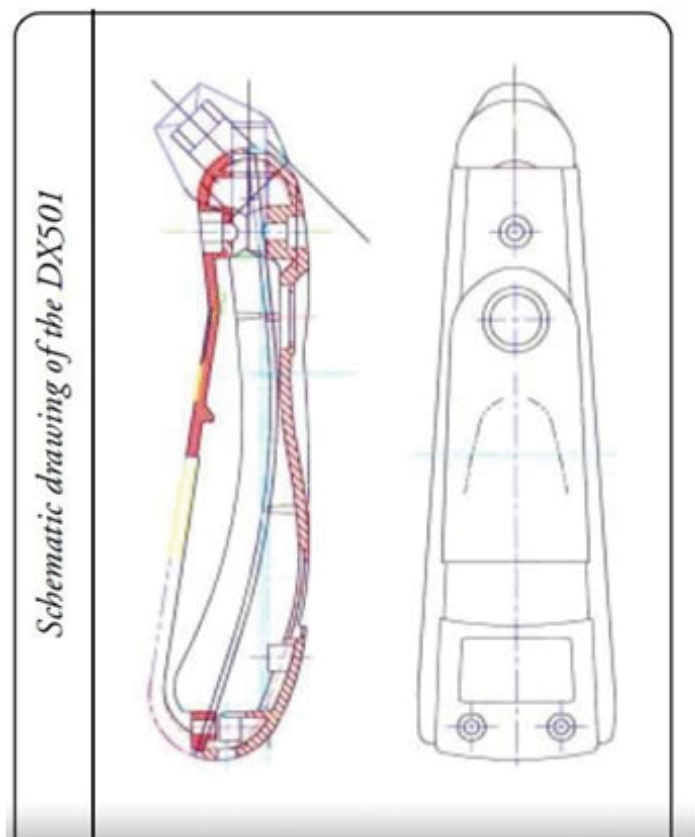


Figure 2: Exergen DX Series IR Thermometer⁵.

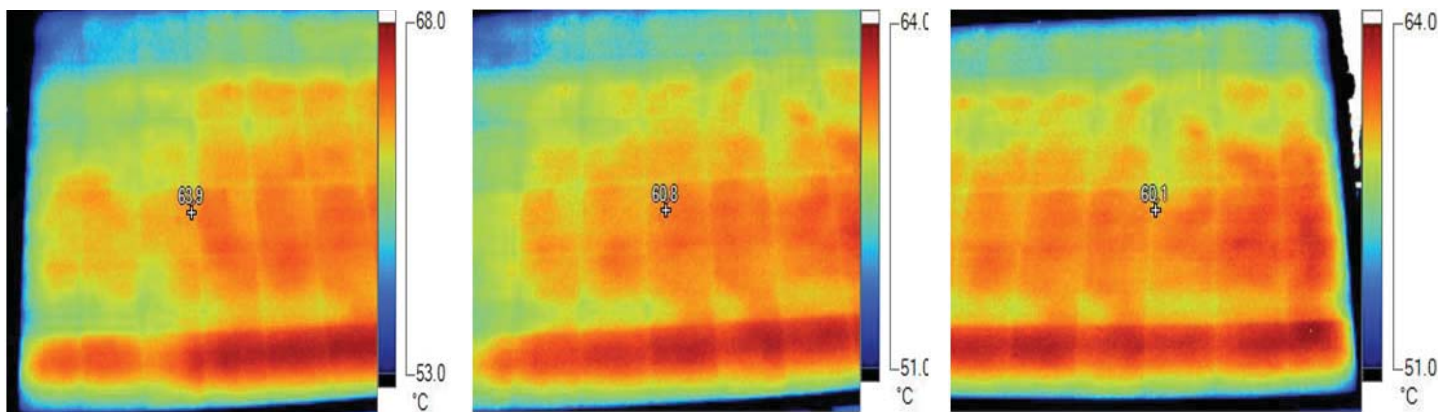


Figure 3: From left to right are sections of the BP 3225T module located on the roof of bldg. 490, BNL.

Temperature coefficient of Voc $-(0.36 \pm 0.05)\%/^{\circ}\text{C}$
 Temperature coefficient of Pmax $-(0.5 \pm 0.05)\%/^{\circ}\text{C}$

The higher the temperature of the cell, the less power and voltage are gained from solar irradiance. The power generated from each cell is summed up due to the series connection of each cell. This might negate the unsatisfactory operation of an individual cell, but the abnormal operation of a cell is what my study is targeting. The irregularity that I am examining is whether there is a large difference in temperature between cells and the effect it might have on the future of the panel overall. As a day progresses from morning into midafternoon, the change in sun's position causes an increase in solar irradiance. Thus, the temperature gradients acquired from multiple panels cannot be related to each other; however they need be correlated to the cells within the individual module. The average of each module is calculated and plotted in respect to the standard deviation. This helps to visually see the change in the temperature spread on the panel.

II. METHODS

A. Data Collection

In the field, a handheld precision IR thermometer is used to measure the temperature of a cell. Exergen Corporation has an IR thermometer model DX 501 series that is suitable for my data acquisition. A detailed procedure was necessary to obtain precise measurements. The IR thermometer has a hollow circular tip that needs to be placed flush against the surface of the cell⁵. The thermometer also has a stabilization function for when the measurement is being taken; it beeps until you can read off the tempera-

ture. Furthermore, the placement of the thermometer needs to be constant throughout the panel. The thermometer was placed in the center of each cell to rule out some possible errors.

B. Infrared Visual Imaging

To have a better visual concept of the temperature spread, an IR camera was used to acquire thermal images of the panels. The images suitably show the temperature differences with each cell outlined. When using the IR camera, reflection can result from the glass layer on top of the panels. To obtain useful images, many settings have to be adjusted. For example, the emissivity of glass was set to 0.87. The temperature level and span were adjusted due to the surrounding objects. Furthermore, the angle at which the camera is placed plays a very important role. The position at which the camera was placed ranged from thirty to sixty degrees from the panel plane and approximately three to four feet away from the surface. This ideal position provides the space for only one section of the panel resulting in multiple sectional images.

Above are infrared images of a solar panel resting on the roof of building 490 at Brookhaven National Laboratory. The outline of each cell is clearly visible as are the temperature differences. The cells on the bottom row are operating at higher temperatures than the rest of the panel. The high temperature is most likely caused by the braces on the back of the module holding it up that provide poor air circulation.

The roof of building 490 also contains a Suniva photovoltaic module, which has seventy-two cells. This model panel is used at the BNL solar research array, separate from the LISF. Figure 5 shows the cell on the right-most part of the Suniva module operates at a higher temperature than the rest. Such abnormalities will be followed over the years to come to determine what if any effects on performance result.

C. Weather Based Intensive Operational Periods

This research was conducted under clear skies to eliminate errors due to rapidly changing irradiance (as might occur on partly cloudy days). On a semi-cloudy day, the solar irradiance curve shows spikes as clouds pass over. This greatly affects the temperature of the cells and they can undergo dramatic temperature changes within a small time interval. Thus, having clouds pass over while taking measurements can introduce error. The graphs below show the difference between a cloudy and an ideal day for data collection supplied by Brookhaven National Laboratory Meteorological Services.

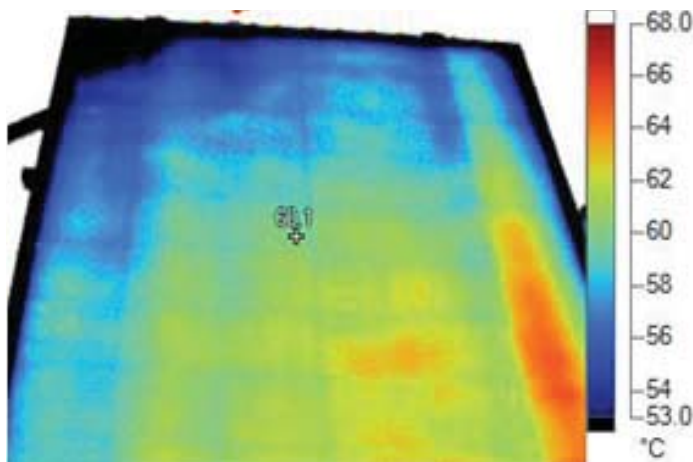


Figure 4: Side view of panel (same panel as Figure 3)

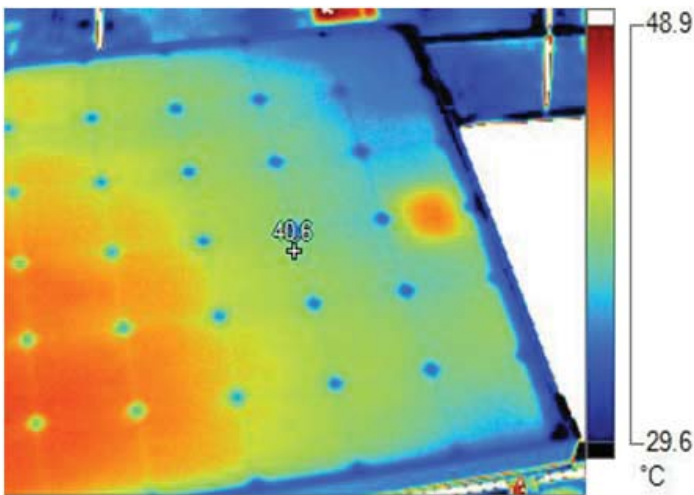


Figure 5: Suniva Module- infrared image on the left with same visible light image on the right.

III. SOURCES OF ERROR

The sensitivity of cells to their surrounding conditions needs to be accounted for. As stated in section II- iii, polycrystalline silicon cells can undergo vast temperature changes rapidly due to external forces such as wind. A gust of wind can decrease the cell's temperature by two or three degrees Celsius which could significantly affect the data. Furthermore, ambient temperature also affects the temperature of a cell as well as the module. In 2003, the Department of Renewable Energy in Madrid, Spain, published a paper on estimating photovoltaic module yearly "temperature and performance based on Nominal Operation Cell Temperature calculations", which describes the effect of ambient temperature on cell performance. Their work includes equations and graphs that demonstrate cell temperature increase relative to ambient temperature⁶:

$$T_m = T_{amb} + (NOCT - 20)$$

T_m is the module temperature, T_{amb} is the ambient temperature and E is the irradiance in W/m^2 .

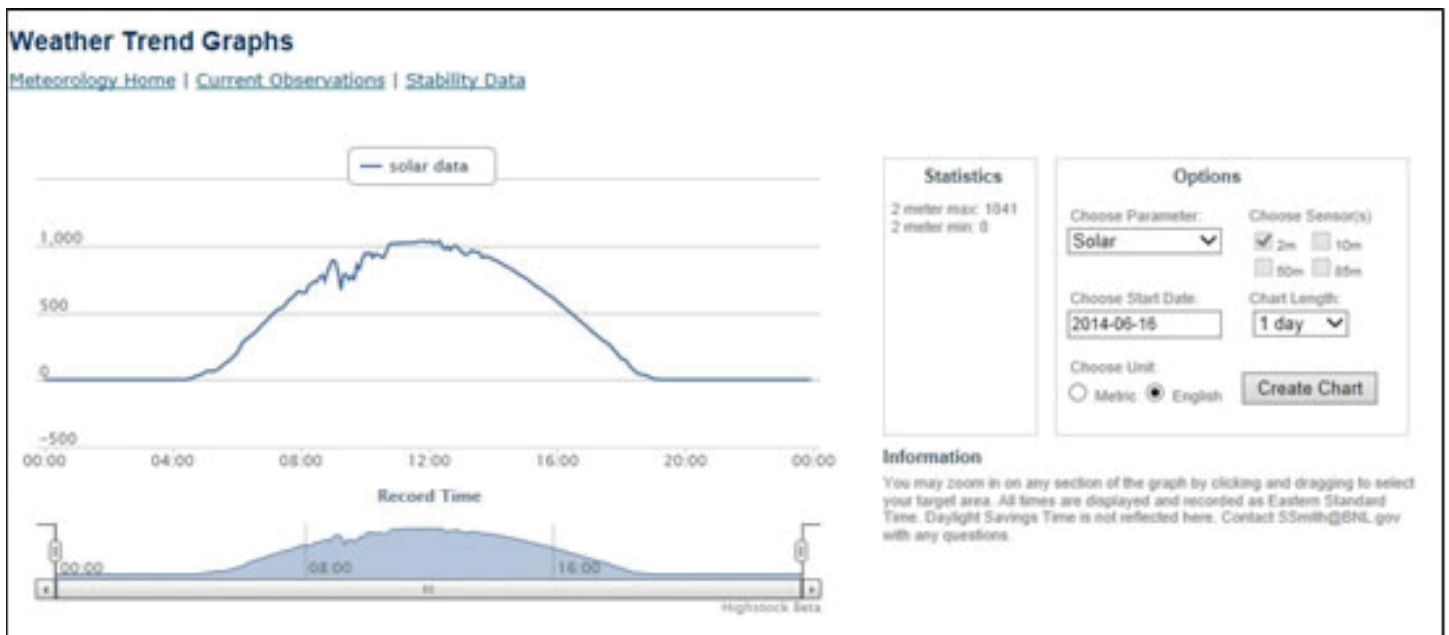
Cloud formation is also a large concern. As mentioned in section II- C, the necessary operational period is a clear day.

IV. DISCUSSION

This research lays the foundation for future studies that follow the degradation and performance of PV panels in the LISF. Data taken serves as the baseline value and identifies the temperature gradients and abnormalities for the test panels.

A. Degradation of cells

The main purpose of this research, to see if performance and/or degradation of cells can potentially be linked to temperature history of the cells. The data collected shows the average temperature of the sixty cells in each of the 25 panels and the standard deviation from the average. Since the data was collected on a purely sunny day, ruling out the potential error due to clouds, it shows specific cells operating at higher temperatures. For the goal was to provide a temperature map of cells for each of the 25 test panels. The success of this research will be able to tell whether the cells operating at higher temperatures consistently will fail first in



Graph 1: Solar irradiance on selected intensive operational periods⁷.

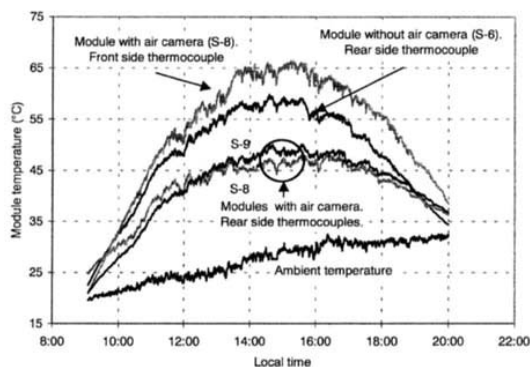


Fig. 2. Differences in module temperatures along the day depending on the position of the thermocouples.

the life time of its module. Likewise, it will show if cells operating at low temperatures have a difference in degradation. Shown in Tables 1 and 2 below are some temperature gradients acquired from LISF showing high and low operational temperatures:

B. Defining yearly module temperature variations

Typically, a module’s performance is based on the module as a whole. The yearly performance and change in temperature can be determined based on the cells of a module. Each year’s data can be compared and analyzed if the same cell’s operating parameters have changed over time. Will the operating temperature on a sunny day with 800W/s2 decrease performance? This research hopes to get in-depth insight into this newly integrated source of renewable energy.

V. CONCLUSION

The operation of polycrystalline silicon cells impacts the performance of solar modules. Knowing the degradation of a cell along with the operating temperatures through the cell’s life may give insight into failure mechanisms. The estimated period of this research is a span of approximately twenty to thirty years. These baseline measurements provide the baseline for future analysis.

-1.6	-1.8	-1.1	-2.4	-1.0	-0.6	-0.5	-0.1	-1.0	-0.8
-1.4	-0.9	-0.2	-1.3	-0.4	-0.3	0.2	0.5	0.2	-0.6
-0.4	-0.6	0.4	-0.1	0.2	0.1	0.3	0.9	0.8	-0.5
-0.6	-0.2	0.7	0.2	0.3	0.4	0.8	1.1	0.6	-0.1
-0.4	-0.1	0.5	0.3	0.5	0.5	1.2	1.1	0.7	0.3
-0.1	-0.1	0.5	0.3	0.3	0.6	1.3	0.8	1.5	0.3

Table 1: Temperature Gradient of a BP 3225T module at PB 17 showing standard deviation relative to the average.

-3.3	-2.2	-0.7	-1.7	-0.6	-0.6	0.7	1.0	1.9	1.9
-2.3	-0.7	-0.5	-1.3	-0.6	-0.3	0.6	1.1	2.0	1.2
-1.5	0.1	0.3	0.0	-0.3	0.2	1.0	0.6	2.0	1.3
-1.3	0.3	0.5	0.1	0.3	1.0	0.9	0.5	2.4	1.0
-1.5	-0.4	0.3	-0.3	-0.7	0.5	0.3	0.7	1.9	0.4
-1.6	-1.2	-1.8	-0.7	-1.0	-1.0	-0.4	-0.1	0.7	-0.4

Table 2: Temperature Gradient of a BP 3225T module at PB 2 showing standard deviation relative to the average.

VI. References and acknowledgements

[1] Skovgaard, Bech Kenneth, and Kin Thomsen. “Fabrication and Characterization of Polycrystalline Silicon Solar Cells.” Aalborg University, Department of Physics and Nanotechnology, Jun, 2011. Master thesis.
 [2] Honsberg, Christiana , and Stuart Bowden. “Nominal Operating Cell Temperature.” PVEducation. PV Education, n.d. Web. 28 July 2014.
 <<http://www.pveducation.org/pvcdrom/modules/nominal-operating-cell-temperature>>.
 [3] King, D. A.. The chemical physics of solid surfaces and heterogeneous catalysis. Amsterdam: Elsevier, 1988. Print.
 [4] BP Solar, “225W Photovoltaic Module,” BP 3225T datasheet, Jan. 2010.
 [5] Exergen Corporation, “Handheld Precision IR Thermometers,” DX501 Series datasheet, Apr. 2001 [Revised Oct. 2006].
 [6] García*, M.C. Alonso, and J.L. Balenzategui. “Estimation of photovoltaic module yearly temperature and performance based on Nominal Operation Cell Temperature calculations.” E-28040 Madrid, Spain: Elsevier, Received 10 November 2003; accepted 23 March 2004. Print.
 [7] Brookhaven National laboratory, “Weather Trend Graphs.” BNL Weather Services, Jun. 2014.

This project was supported in part by the U.S. Department of Energy, Office of Science, Office of Workforce Development for Teachers and Scientists (WDTS) under the Science Undergraduate Laboratory Internships Program (SULI).

Following people provided valuable guidance and assistance: Scott Smith, Alessandra Colli, Ricky Bhola, and LISF staff from Brookhaven National Laboratory.

Determining nanostructure quality via ultrafast emission spectroscopy for enhanced water-splitting photocatalysis

Zoey Warecki

Department of Physics, Astronomy, and Geosciences, Towson University, Towson, MD, 21286

Danhua Yan

Department of Materials Science and Engineering, Stony Brook University, Stony Brook, NY, 11790

Kannatassen Appavoo, Mingzhao Liu, and Matthew Y. Sfeir

Center for Functional Nanomaterials, Brookhaven National Laboratory, Upton, NY, 11973

Abstract

Using zinc oxide nanowires as a prototypical ultraviolet photocatalyst with potential for high-efficiency, we show how (i) doping with lithium, (ii) crystallinity of seeds that are used to grow the nanowires, and (iii) substrates on which the nanowires are grown all contribute towards losses of free carriers that are generated following light absorption. Using scanning electron microscopy (SEM) in conjunction with ultrafast transient emission spectroscopy, we compare how seed quality and lithium concentration affects the morphology and resulting photocatalytic abilities. Moreover, we find that treating the nanowires after growing them can reduce losses to carrier recombination, regardless of initial growth conditions while an optimum lithium doping is necessary to decrease recombination rates while not hindering the nanowire growth process.

I. Introduction

Water splitting using photoelectrochemical (PEC) cells has long been sought as a renewable solar energy technology because it generates chemical fuels that are more readily stored and transported than electricity. A PEC cell works by absorbing light to generate free charge carriers that are transported to the surface to participate in the redox reactions that split water into hydrogen-fuel and oxygen-byproduct. Our interest lies in studies of the size regime where the radius of the zinc oxide nanowire becomes comparable to the width of the depletion region, which is responsible for separating photoexcited charge carriers and accelerating them to the surface. Nanowires of zinc oxide have been shown to act as an efficient ultraviolet photocatalyst for the water splitting reaction. In order to increase the size of the depletion region for a given diameter of nanowires that are fabricated, we introduce lithium dopants into the growth process to produce nanowires having a lower carrier concentration. We can determine the size and uniformity of the nanowires using scanning electron microscopy (SEM). In addition, we can study the mechanism of carrier separation and recombination by measuring both the steady-state and ultrafast (sub-ps) emission. Together, these characterizations help to understand the origins of loss mechanisms in photocatalytic water-splitting materials, consequently improving incident-photon-to-current-efficiency.

II. Experimental Methods

A. Nanowire fabrication

The zinc oxide (ZnO) nanowires were grown with a seed-mediated hydrothermal method. The substrates used were indium tin oxide (ITO) and glass. To make the ZnO seeds we used two

different deposition methods, atomic layer deposition¹ and sputtering. In both cases, ~ 2.5 nm of zinc oxide was deposited onto the substrate monitored by a quartz crystal microbalance (QCM) and, rather than being in a thin film, the zinc oxide cluster into island-like features which are called seeds. This seeded substrate is then suspended upside down in the growth solution (Fig 1), an aqueous solution of zinc nitrate and hexamethylenetetramine that is heated to 75°C , for 120 min. Finally, the nanowire array is thoroughly washed with deionized water and dried in a stream of nitrogen. After realizing that nanowire growth and uniformity was worsened due to zinc oxide self-nucleation in the solution, we introduced polyethylenimine and ammonium hydroxide to the growth solution^{2,3} and were able to reproduce nanowires of a smaller and more uniform size. Once we established a reproducible method

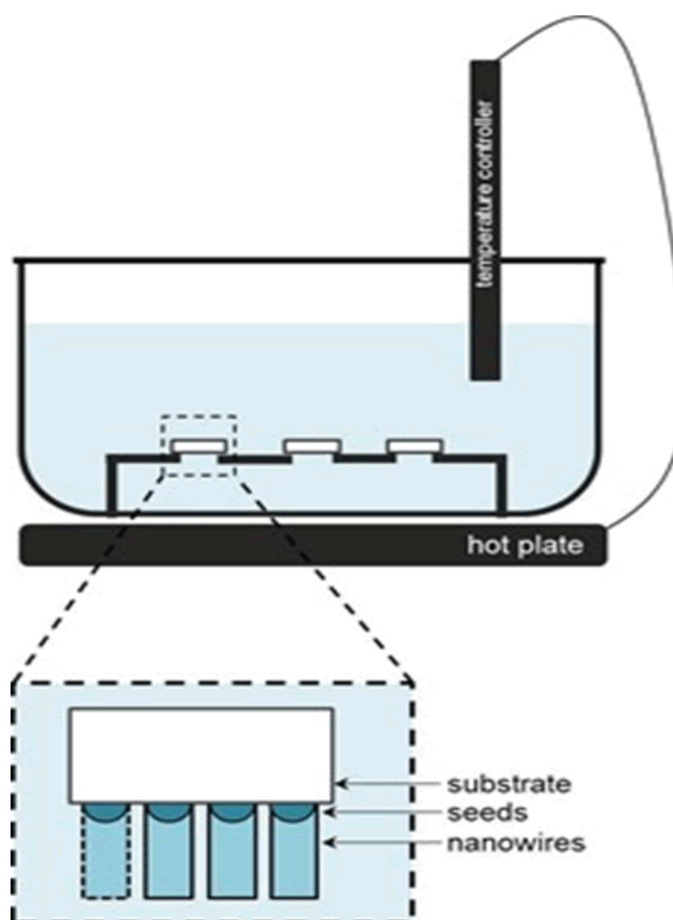


Fig 1. Schematic showing hydrothermal growth of ZnO nanowires

for growing zinc oxide nanowires, we added lithium nitrate to our solution to see if we could dope the ZnO nanowires with Li, which is a known acceptor dopant of ZnO, in order to reduce the majority charge carrier density of the zinc oxide. In a second, separate study, we grew only zinc oxide nanowires and systematically changed parameters such as substrate choice, seeding method, and seed treatment, to see how the nanowire quality was affected.

B. Ultrafast transient emission spectroscopy

Ultrafast transient emission spectra allow us to track the complex spectral evolution dynamics in ZnO and understand the role of geometry and structural imperfections⁴. We accomplish this with a high sensitivity transient emission spectrometer based on the optical Kerr effect⁵. Because we achieve very high spectral and temporal resolutions, we are able to measure the complete emission evolution profile of the ZnO nanowires. We are interested in this profile because can tell us more about the loss mechanisms than just steady-state emission spectra can. Specifically, understanding losses due to bulk recombination will allow us to characterize our photocatalysts ex situ, therefore increasing the throughput of materials that can be screened for efficient water splitting in the PEC cell. Lowering the bulk recombination rate by reducing the number of defects will increase the lifetime of the free excited charge carriers and improve the photocatalytic performance.

This technique works by exciting the sample with above bandgap 280 nm pulses and collecting and focusing the emission

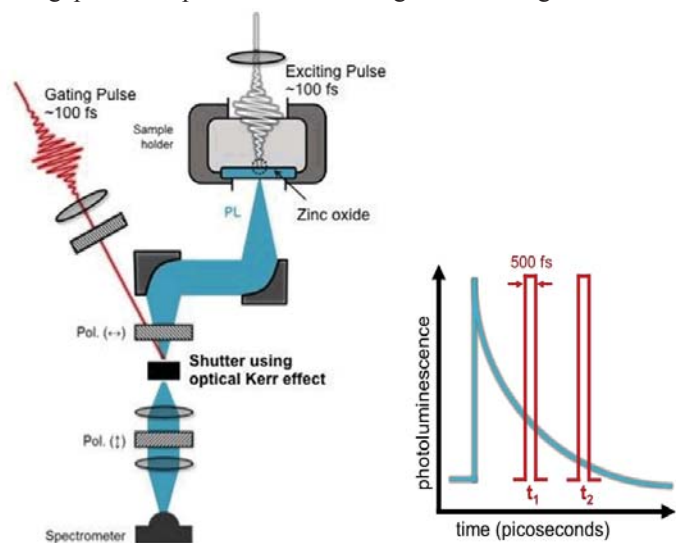


Fig 2. (a) Optics setup for ultrafast transient emission spectroscopy, (b) Illustration of a typical ZnO emission profile as well as the ultrafast gating pulse that traces the profile.

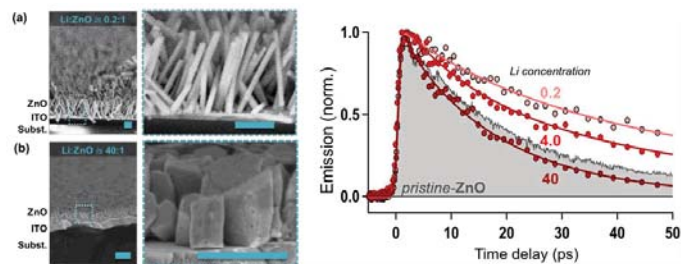


Fig 3. (a) & (b) Scanning electron microscopy images (SEM) of the lithium-doped ZnO nanowires with molar ratios of Li:ZnO of (a) 0.2:1 and (b) 40:1. (c) The emission profile of pristine and doped ZnO.

onto the Kerr medium and subsequently on the spectrometer (Fig 2a). The shutter opens when the ultrafast gating pulse switches “on” the Kerr medium’s birefringence, which slightly changes the polarization of the zinc oxide emission so that it is able to pass through the second polarizer and be detected by the spectrometer. Because the gating pulse is very short (~ 100 fs), the shutter can be actuated with similar temporal resolution (here ~ 200 -500fs). To map the broadband emission temporally, a translation stage which allows us to accurately delay the gating pulse is used, with the spectral evolution of ZnO as shown in Fig 2b.

III. Results and Discussion

A. Lithium-doping

To dope the nanowires with lithium we added lithium nitrate to the growth solution with Li:ZnO molar ratios of 0.2:1, 4:1, and 40:1. To confirm that lithium was present in the nanowires we performed electron energy loss spectroscopy (EELS) on the 0.2:1 and 40:1 and found that there was lithium at a concentration of at most 1% in both cases. We then performed scanning electron microscopy (SEM) to determine the morphology of the nanowires and also perform ultrafast emission spectroscopy on the samples. As can be seen in Fig 3a, the nanowires grown from 0.2:1 ratio were uniform, thin nanowires and also had the longest lifetime (Fig 3c), compared to pristine ZnO and the other doping ratios. It is likely that the lithium introduced in the 0.2:1 is in fact substituting for zinc sites and reducing the majority carrier concentration as expected. At 40:1, it clear that the lifetime is the lowest of all shown and that the high amount of lithium in the growth solution is also impeding the growth of the nanowires (Fig 3b). Further work to determine the exact percentage of lithium in the nanowires as well as an optimal lithium concentration to achieve the highest lifetime is necessary.

B. Seed/substrate

Additionally, we systematically studied the effects of initial seeding conditions on the lifetime of the nanowires. Here we used two different deposition methods as described previously and deposited ZnO seeds onto a dual substrate that consisted of glass and indium tin oxide (ITO) (Fig 4). Additionally, we annealed the seeds for 10 minutes at varying temperatures to see if it would improve the nanowire quality. We then took ultrafast transient emission data for the samples.

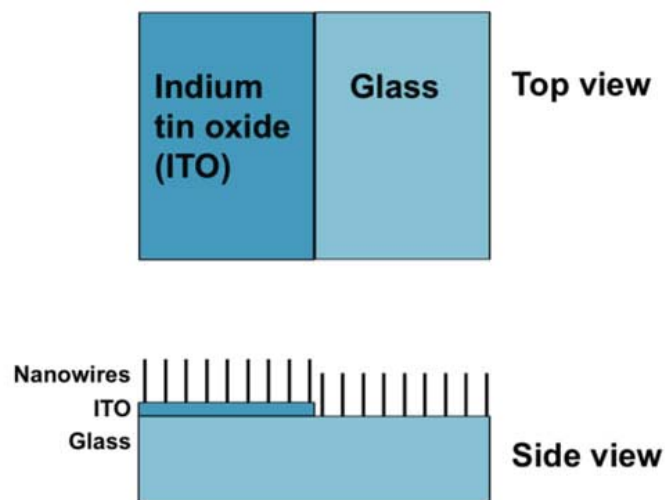


Fig 4. Schematic of substrate that ZnO nanowires were grown on

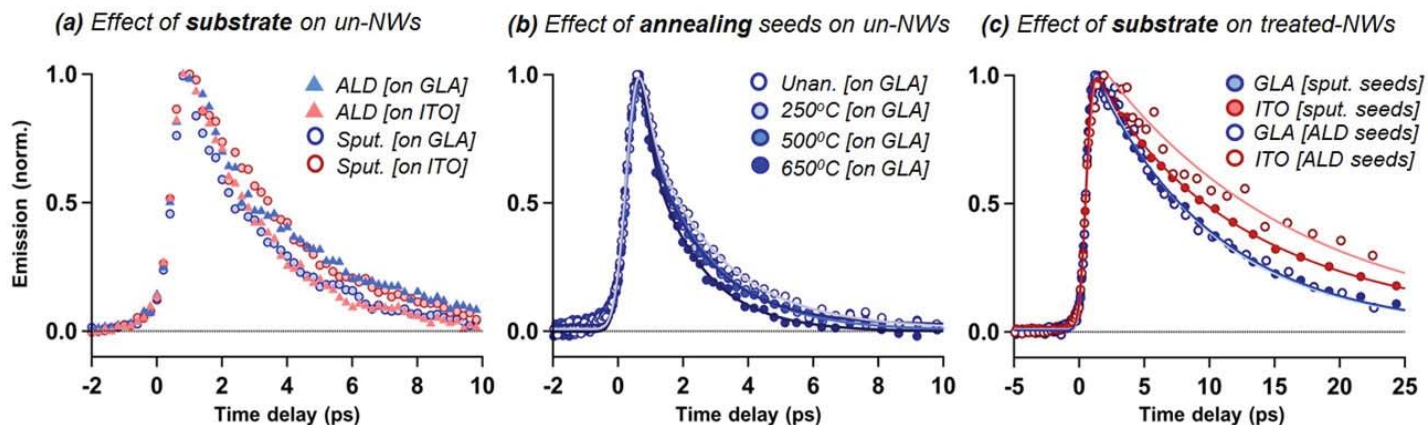


Fig 5. Time resolved emission spectroscopy of zinc oxide nanowires

As can be seen from Fig 5, nanowires grown from ITO and glass had no significant difference in lifetime. Furthermore, we saw that the nanowires grown from unannealed seeds has slightly longer lifetimes that the annealed in all cases. Lastly, we found that the seeds grown by ALD produced nanowires with slightly longer lifetimes than those from sputtered seeds.

However, we found that after treating the nanowires by annealing all the samples in O₂ at 500°C and for 10 minutes, thus ridding the nanowires of a lot of their crystal defects, the seed deposition method and seed treatment had no effect on the lifetime of the annealed nanowires. The ALD seeds and sputtered seeds performed equally well and annealing did not affect the lifetime. The nanowires on ITO had longer lifetimes than those on glass which is likely due to the larger diameter of the nanowires on ITO (Fig 6), which starts to become an important aspect once defects native to the hydrothermal fabrication protocol are removed. Further studies to be done include comparing the ex situ lifetime measurements with electrochemical impedance spectroscopy measurements to get a more complete picture as well as in situ lifetime measurements which would provide a better understanding of the charge carrier excitation and separation, both of which occur on very short time scales during photocatalysis.

IV. Acknowledgements

Research is carried out at the Center for Functional Nanomaterials, Brookhaven National Laboratory, which is supported by the U.S. Department of Energy, Office of Basic Energy Sciences, under Contract No. DE-AC02-98CH10886. This project was supported in part by the U.S. Department of Energy, Office of Science, Office of Workforce Development for Teachers and Scientists (WDTS) under the Science Undergraduate Laboratory Internships Program (SULI). We thank Xuan Shen and Dong Su for the EELS data. Additionally, I would like to thank Gwen Wright and Xiao Tung for microscopy training.

V. References

1. Liu, M., et al. "Enhancing Water Splitting and Chemical Stability of Zinc Oxide Nanowire Photoanodes with Ultrathin Titania Shells." *The Journal of Physical Chemistry C* 2013, 117 (26), 13396-13402
2. Xu, Chengkun, et al. "Preferential growth of long ZnO nanowire array and its application in dye-sensitized solar cells." *The Journal of Physical Chemistry C* 114.1 2009 125-129.

3. Rivera, Vivian Farias, et al. "Length-Dependent Charge Generation from Vertical Arrays of High-Aspect-Ratio ZnO Nanowires." *Chemistry-A European Journal* 19.43 2013 14665-14674
4. Appavoo, K., et al. "Role of size and defects in ultrafast broadband emission dynamics of ZnO nanotstructures." *Applied Physics Letters* 2014, 104 (13), 133101
5. Appavoo, K., Sfeir, M.Y., "Enhanced Broadband Ultrafast Detection of Ultraviolet Emission Using Optical Kerr Gating." *Review of Scientific Instruments* 2014 85, 055114

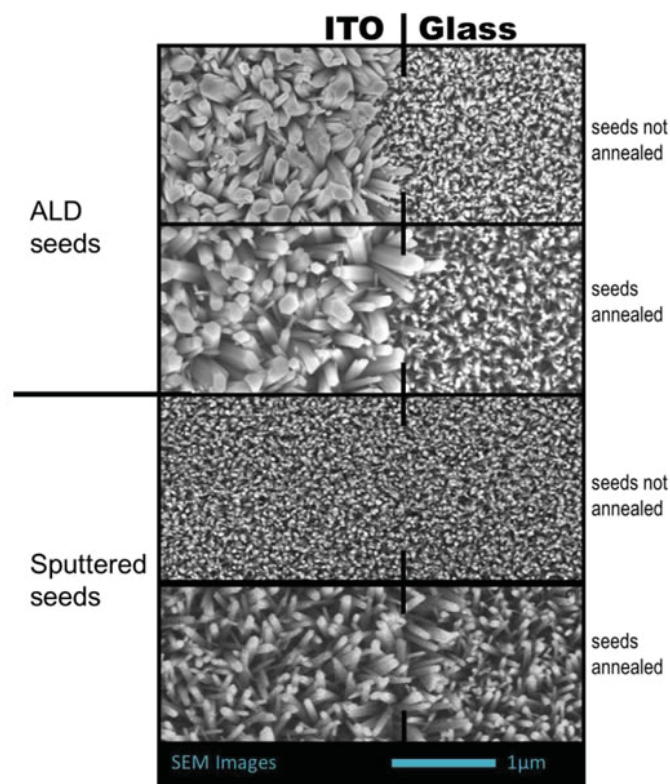


Fig 6. Top SEM image of nanowires grown from different initial conditions.

Analysis of cadmium zinc telluride crystals to determine the effects of material defects on detector response capabilities

Megan Wart

Department of Mechanical, Aeronautical and Nuclear Engineering, Rensselaer Polytechnic Institute, Troy, NY 12180

Giuseppe Camarda

Nonproliferation and National Security Department, Brookhaven National Laboratory, Upton, NY 11973

Abstract

Cadmium Zinc Telluride (CZT), a semi-conductor crystal, is an important material in radiation detection because it can be used for applications requiring room temperature detectors that are highly sensitive and have a good energy resolution. The objective of this project is to improve the quality of CZT detectors by searching for correlations between the ability of CZT to detect radiation and the structure of the crystal. Understanding these correlations would allow for refocusing the processes used to grow CZT crystals and fabricate detectors while simultaneously paying particular attention to the material properties of the crystals in order to increase the quality of the detector's resolution. To study how CZT responds to radiation, we used Beamline X27B, at the National Synchrotron Light Source to create X-ray detector response maps. The material structure of the crystal was then viewed using infrared microscopy images, X-ray topography images from Beamline X19C, and X-ray fluorescence microprobe images from Beamline X27A. Resistivity was also mapped by adding a pixelated anode electrode to the crystal and taking current-voltage (IV) curves for each pixel. Comparing these images with the response maps allowed us to identify what types of defects corresponded to areas of poor response to radiation. Identifying these defects, sets the foundation for finding methods to decrease or eliminate the occurrences of these defects in CZT. From this internship, I have gained experience at the National Synchrotron Light Source in X-ray detector response mapping and X-ray topography. I have also become familiar with detector fabrication and photolithography for depositing metal electrodes.

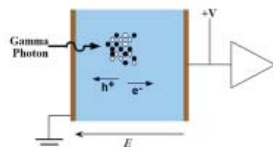
I. Background

A. Semi-conductor Detectors

Semi-conductor detectors, or solid-state detectors, are used to detect X- and gamma- rays. When radiation of a minimum energy, known as the band gap energy, passes into the semi-conductor creates by ionization electron-hole pairs in the material. If a bias voltage is applied to the semi-conductor the electrons and holes will separate and drift with the electrons moving in the opposite direction as the electrical field and the holes moving with the electrical field. The speed with which the electron and hole drift is defined by the electrical field and a material property constant, mobility (μ).

Figure 1: Semiconductor Detector

As the gamma ray enters the semiconductor, the energy is absorbed. This creates for ionization electron/hole pairs.



B. Applications

X-ray and gamma ray detection are important in many fields, such as national security, medicine, basic science and industry. CZT detectors are being targeted towards national security and medical uses, with specific applications such as mammography and nonproliferation of nuclear materials. For these applications having a good energy resolution and room temperature operation are particularly important. Many semi-conductors detectors, such as high purity germanium detectors, need to be kept at cryogenic temperatures in order to function. Though such detectors often have very good energy resolution it can be difficult to handle cryogenically cooled detectors in the field, therefore designing a detector to work at room temperature, that still give good energy resolution is important.

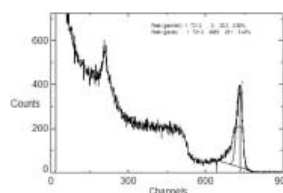


Figure 2 : ^{137}Cs spectrum

This energy spectrum was created with a bar shaped sample of CZT. The goal of this research is to improve the energy resolution of such detectors.

C. Cadmium Zinc Telluride Detectors

Cadmium Zinc Telluride (CZT) is one type of semi-conductor that can be used for X- and gamma- ray detection. So far detectors have been produced with CZT that work well at low flux; however polarization occurs at high flux. The term polarization refers to when, the effectiveness of the detector is compromised due to the electrons being recaptured before reaching and anode and creating a buildup of space charge. CZT is a good option for detectors, because it can be used at room temperature. CZT also is an advantageous choice due to its increased resistivity and therefore low leakage current, and its ability to detect high energy radiation.¹

II. Methods

A. Micron-scale X-ray Detector Mapping

Two types of X-ray response maps were generated at Beamline X27B at the National Synchrotron Light Source (NSLS): electron charge collection and hole collection maps. The X-ray response map gives a visual of how well a certain small area of the crystal detects radiation. The X-ray beam is collimated and passed through a monochromator, to create a very narrow (as small as 10 microns x 10 microns), single energy beam. This narrow beam is used to scan the detector and at each scan point the energy spectrum detected is recorded. The direction of the bias voltage determines if electrons or holes as being collected. A response map can then be compiled for the whole area of the crystal.



Figure 3. Electron Charge Collection. Darker areas indicate lower count rates of electrons, and thus lower detection abilities.

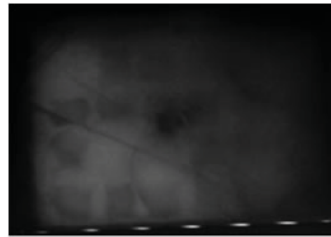


Figure 4. Hole Charge Collection. Hole collection maps give a more clear image of features in the material.

B. White Beam X-ray Diffraction Topography

White beam X-ray diffraction topography is used to view extended defects in the crystals. For these topography images the crystal was set up to be exposed in a grazing angle to an X-ray beam and a film was placed parallel to the surface of the crystal being imaged. The crystal and film were then exposed to the X-rays, and then the film was developed to show the diffraction image of the crystal. Extended defects in the crystal cause the x-rays to diffract differently from the rest of the crystal; therefore they are visible on the film, as partial images of the crystal. Previous work has shown that the fewer extended defects there are, the better the crystal will work as a detector.² This means that crystals with cleaner the X-ray diffraction topographies, and therefore fewer extended defects, the better the crystal will work as a detector.

C. Creating Pixelated Contacts

In order to break down the area of the detector being studied, new pixelated contacts were deposited for the anode electrode. A CAD file of the desired pixilation was created. The pixels were laid out in a 4x6 grid with a small non-contact gap around each, and a guard ring made of contact material lay between the non-contact borders and around the whole exterior of the crystal. A mask, of this CAD drawing was printed on a plastic film to be used with photolithography. For the photolithography the area that would contain the pixelated contact was polished and cleaned. The crystal was then coated with photoresist, using a spin coater. The crystal was then placed under the mask and exposed to ultra-violet light. The exposed photoresist was removed with developer and a gold solution was used to create the contacts, as patterned by the photoresist.

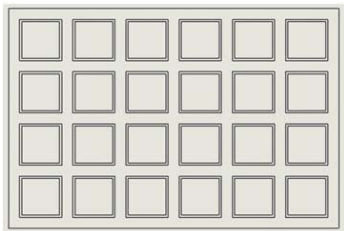


Figure 5: CAD drawing

D. IV Curves

To take current-voltage (IV) curves the sample was then placed in a circuit using the planar cathode electrode as the high voltage input, the guard-ring as the ground and one of the pixels as the output. As the voltage over the crystal was changed, measurements of the current were taken. This was done for a range of 0 to 50 volts and 0 to -50 volts. The plots of the current and voltage were linear fit to find the resistivity of the material at each

pixel. This was done for each pixel in order to see the variation of the resistivity over the whole area of the sample.

E. IR Transmission Microscopy

Infrared (IR) transmission microscopy was used to take images of tellurium inclusions inside the crystals. CZT is transparent to IR light, however tellurium is not. Therefore, by taking images on the crystal using a microscope illuminated by IR light it is possible to see the tellurium inclusions. IR images were then taken, many at a time, through the volume of the crystal and analyzed to find the distribution of the size of the Te inclusions over the volume. Tellurium inclusions are deleterious because as the charges drift through the crystal the drifting charge can be trapped by the tellurium and therefore lowering the energy resolution of the detector.

F. X-Ray Fluorescence

X-ray fluorescence images were taken at Beamline X27A at the NSLS in order to see the concentration of zinc in the crystals and its distribution throughout the crystal. X-ray fluorescence images are taken by placing the samples at a 45 degree angle to the incoming beam and exposing them to X-rays of specific energies. The energies chosen are based on the energy spectrum of the isotope being analyzed. At each scan point the spectrum given off by the sample is recorded. Since each isotope gives off its own spectrum, the recorded spectrums can be analyzed and the area density of the isotope can be determined.³

G. Experimental Determination of $\mu\tau$ (μ -tau)

The $\mu\tau$ product of the material is a description of the ability of electrons or holes to move through the material. In order to determine the $\mu\tau$, the sample of CZT was placed in a detector chamber and exposed to Americium-241, while a known voltage was applied. The signal was run through a pre-amp, and shaping amp, and a multichannel analyzer, and output as a spectrum of energies. The channel number of the main energy 60 keV peak was recorded. This process was repeated with multiple different voltages until the channel number corresponding to the photopeak stopped changing at which all of the charge was drifting to the electrode (the detector was fully depleted). This data was then analyzed using the Hecht equation (Figure 9),⁵ to find the $\mu\tau$ for electrons for each crystal. The $\mu\tau_e$ calculated for sample 10 was .0062cm²/V and for sample 11 was .0037cm²/V.

III. Data and Results

A. Analysis of the Detector Response

The X-ray maps shown in the Figures clearly show areas of good detection ability and areas of poor detection ability. The better the area of detection, the lighter the grey color show in the map. This means that the left side of sample 10 (Figure 10) is a poorer area of detection and the lower left corner of sample 11(Figure 12) is a good area of detection. The map of sample 10 also shows a bright line that corresponds to the sub-grain boundary seen in X-ray diffraction topography (Figure).

B. Analysis of Extended Defects

The tellurium (Te) inclusion distribution histograms, created by IR microscopy, show very little difference over the area of the crystal for both samples (Figure 14). This suggests that Te inclusions are not responsible for the variation in performance from

one side of the crystal to the other, seen in the X-ray response maps.

Tables of resistivity for both samples show that there is a variation in resistivity over the area of the crystal. By comparing the X-ray response maps to the resistivity maps calculated for each pixel, it can be seen that for areas of poor detection the resistivity was generally lower. However the X-ray fluorescence maps showed no pattern in the variation of Zn concentration considered the main candidate responsible for the resistivity variation) over the area of either of the crystals.

IV. Conclusions

In conclusion, the results indicate that tellurium inclusions are not responsible for the variation in performance over the area of the crystal. The results also show that the variation in resistivity and the variation in detection across the area of the crystal are directly correlated. However the variation in resistivity showed no correlation with the Zn concentration found in the crystal. The next step in this research is to determine the source of the variance in the resistivity of the crystal.

V. References

- ¹ Knoll, G. F. (2010). Radiation Detection and Measurement (Fourth ed.). Wiley.
- ² Bolotnikov, A., Camarda, G. S., Yang, G., Cui, Y., Hossain, A., Kim, K., et al. (2013). Characterization and Evaluation of Extended Defects in CZT Crystals for Gamma-ray Detectors. Journal of Crystal Growth.
- ³ Vogt, S. (n.d.). X-ray fluorescence microscopy with a nanoprobe – Opportunities and requirements from a life sciences perspective.
- ⁴ Cho, H., Lee, J. H., Kwon, Y. K., Moon, J. Y., & Lee, C. S. (n.d.). Measurement of the drift mobilities and the mobility-lifetime products of charge carriers in a CdZnTe crystal by using a transient pulse technique. IOP Publishing.

VI. Acknowledgments

This project was supported in part by the U.S. Department of Energy, Office of Science, Office of Workforce Development for Teachers and Scientists (WDTS) under the Science Undergraduate Laboratory Internships Program (SULI).

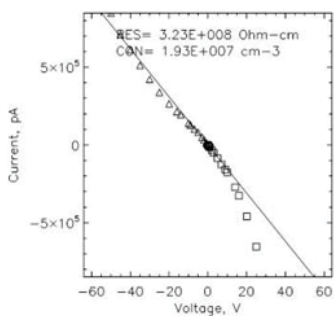


Figure 6 IV Curve . This curve is from the top left corner pixel of sample 10. The line shows the linear fit used to find the resistivity.

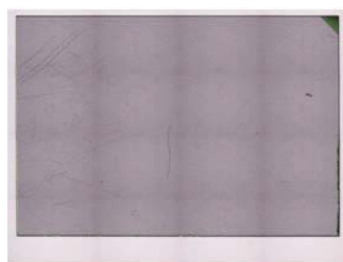


Figure 7 IR transmission image of Sample 10

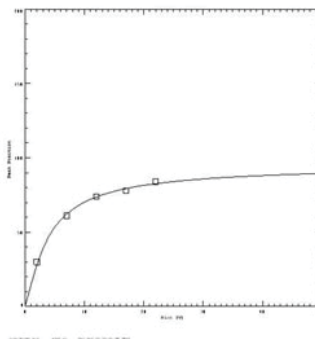


Figure 8 Hecht Equation Fit for sample 10

$$Q(V) = \frac{N_0 q V (\mu \tau) e}{d^2} \left[1 - \exp \left(- \frac{d^2}{(\mu \tau) e V} \right) \right]$$

Figure 9: Hecht Equation. N_0 is the number of charge carriers created by the incident radiation, Q the total charge collected, d the thickness of the detector, q the electronic charge, and V the applied bias voltage.

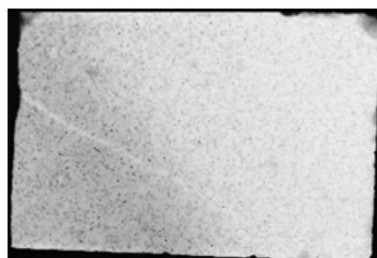


Figure 10. Electron Charge Collection Sample 10

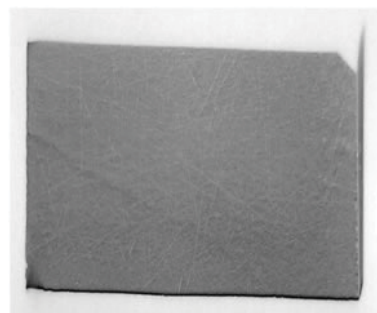


Figure 11. White Beam X-ray Diffraction Topography Image Sample 10

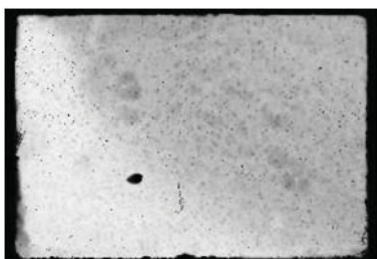


Figure 12 Electron Charge Collection Sample 11



Figure 13 White beam X-ray Diffraction Topography Image Sample 11

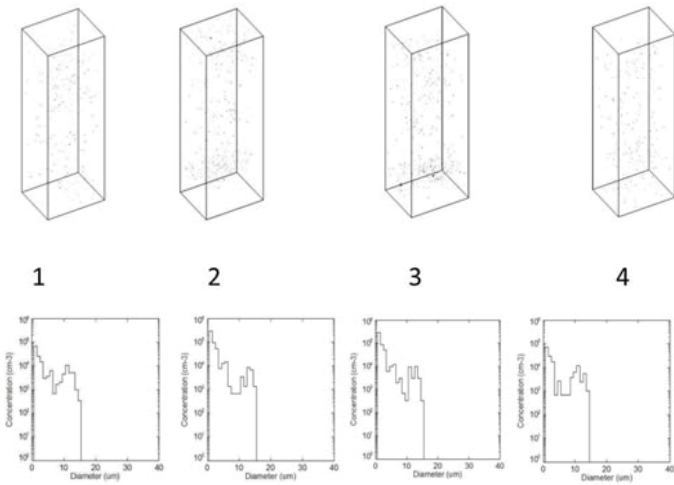


Figure 14 Tellurium Inclusion IR Data Sample 10 (above) and 11 (below)
 For the 3D images each volumetric region is 1.5mmx1mmx5mm.
 The histograms show the distribution of different size tellurium inclusions in the volume. All images are shown 1-4 respective to their placement in the crystal, left to right.

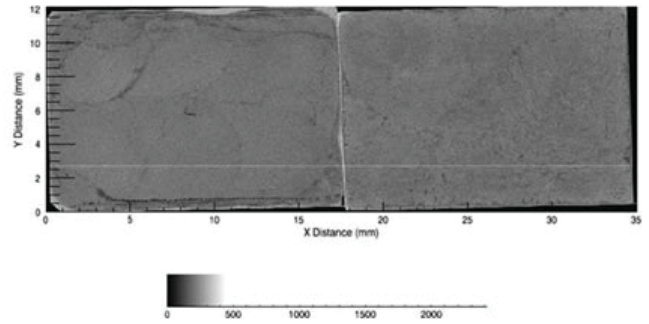


Figure 16 X-ray fluorescence microscopy
 Areas of lighter color indicate higher concentrations of Zn. Sample 10 is on the left. Sample 11 is on the right.

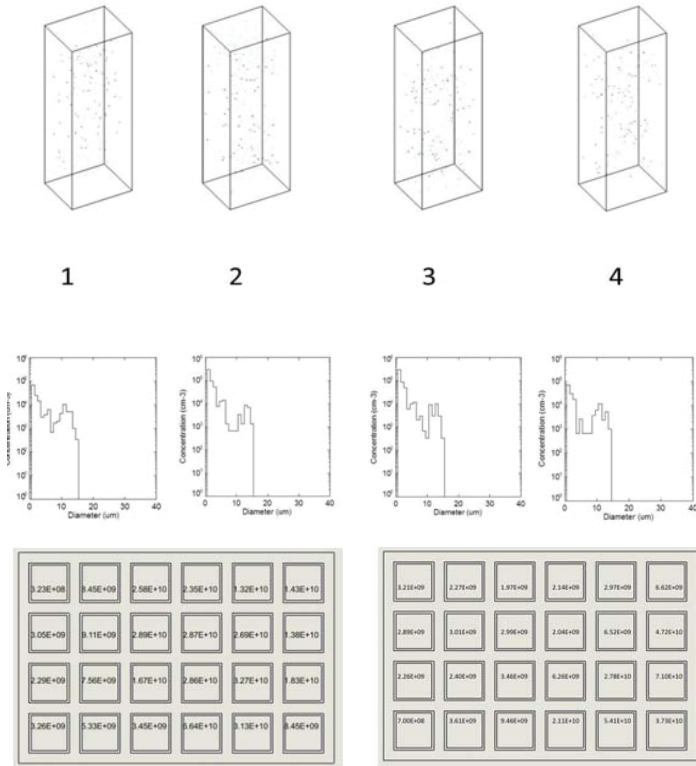


Figure 15 Resistivity Data for Sample 10(left) and 11(right)
 Each data point shows the resistivity in ohm-cm on the corresponding pixel.

Searching for high temperature superconductors

Claire Weaver

Department of Physics, Hofstra University, East Meadow, NY, 11553

Meigan Aronson, Daniel McNally, Hua He, Lucia Steinke, and Bill Gannon

Condensed Matter Physics and Material Science, Brookhaven National Laboratory, Upton, NY 11973

Abstract

Superconductors are materials that have zero electrical resistance. Zero resistivity means zero energy lost in the transport of electricity, which would greatly decrease the world's energy consumption if superconductors replaced normal conductors. Unfortunately, superconductors require expensive, bulky cryogenics to reach the transition temperature at which superconductivity occurs, limiting its application. Our research at Brookhaven National Laboratory focuses on synthesizing new, high-temperature superconductors, which we believe can be achieved by observing the link between atomic structure and magnetic moments of antiferromagnetic compounds and attempting to reproduce the physics of these known materials in new compounds.

I. Introduction

Unconventional, type II superconductors (SC), which have the potential of reaching higher transition temperatures, don't follow the Bardeen-Cooper-Schrieffer (BCS) theory of electron/phonon coupling that governs type I SC. There is no accepted theory behind type II SC, but there is a distinct relationship between anti-ferromagnetism and superconductivity. This relationship can be observed in the square-planar arrangement of the transition metal (TM) Fe in the Fe-pnictide superconductors of the ZrCu-SiAs "11 11" and the ThCr₂Si₂ "122" structure types.

We believe that the physics behind this superconductor, where Fe has d₆ valence electrons, contributes to the supercon-

ducting state, not the presence of Fe itself. For this reason, we are synthesizing materials containing neighboring transition metals, Mn and Co, combined with other elements, having ionization properties that hopefully impose d₆ valence electrons on the transition metals.

We apply similar logic to other families of superconductors and amass data on new compounds, adding volumes of information available to the Center for Emergent Superconductivity's Materials Genome initiative to enable the prediction and perfection of new high-temperature superconducting materials for use in a range of energy technologies, including applications in storage, generation and transmission.

II. Materials and Methods

The purest form of any compound is found as a single crystal, the macroscopic representation of a repeated atomic unit cell. Logically, it follows that as we seek new materials to test for superconductivity, single crystal growths will yield the most accurate data on structure and properties of new compounds. Creating these compounds proves difficult as materials for the desired compound may melt incongruently, which limits growth from a method of pure melting and mixing of the substances. Many materials also have an impractically high melting point to use this method of growth. Synthesizing compounds can also result in binaries of the elements or the compound could have a different stoichiometric ratio than the one desired. Many metals are also highly reactive with oxygen and oxidation of our material before or during the growth process is an impurity that can hinder the desired compound from forming. For these reasons, crystal synthesis requires specialized, practical growth methods that maximize crystal puri-

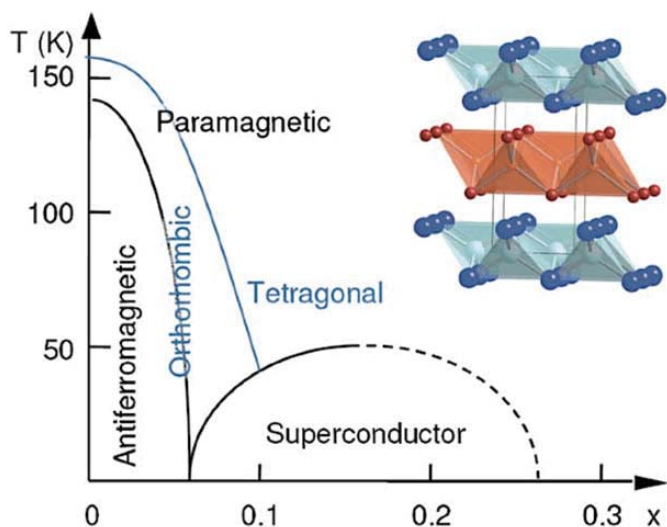


Figure 1: (above) Electronic and structural phase diagram for RFeAsO_{1-x}F_x (R=Rare Earth Metal) superconductors as a function of the electron doping with inset showing RO and FeAs layers in "11 11" crystal structure.¹

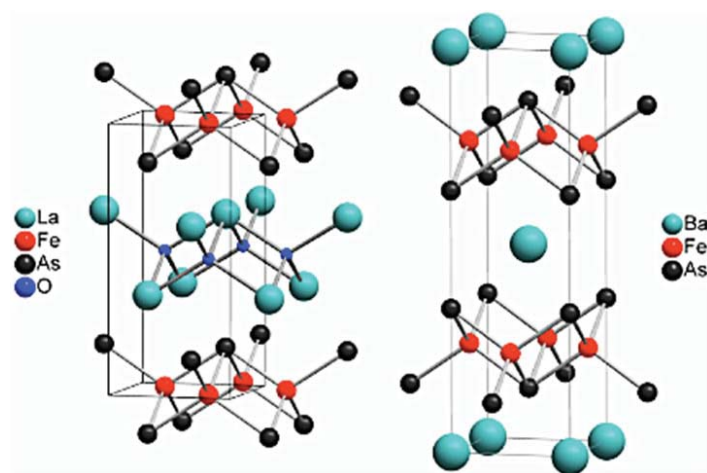


Figure 2: (above) Superconductors LaFeAsO "11 11" and BaFe₂As₂ "122" display the square net of Fe atoms (in red) tetrahedrally bound to the pnictide, As²

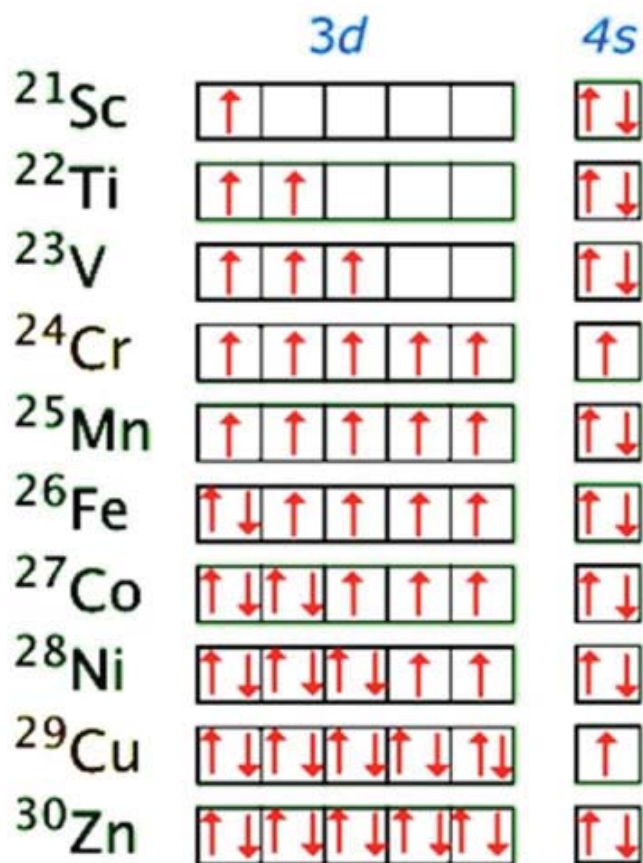
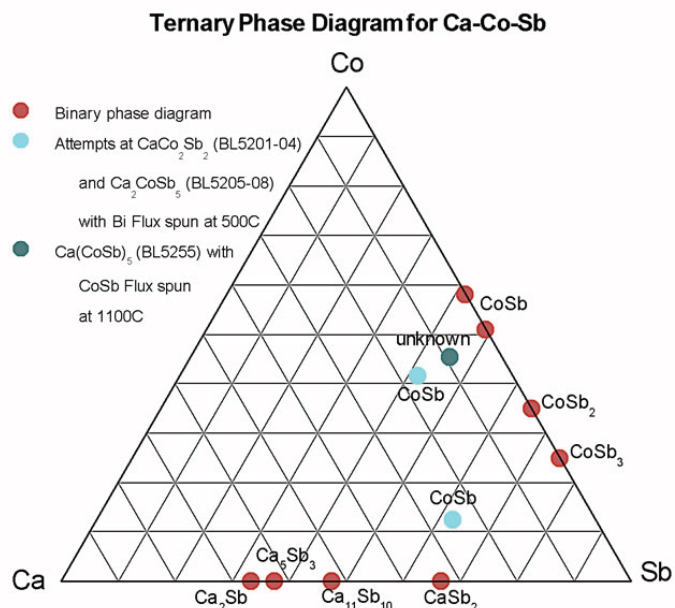


Figure 3: (above) d and s orbital electron configuration of TMs. TMs Cr-Cu are optimal for reproducing the electron configuration of known superconductors and antiferromagnetic compounds. These elements donate electrons in order to neutralize the charge designated by the other ions. We want to choose alkali earth metals and pnictogens based on the desire to exhaust the electrons in the s orbital and achieve an even number (either 4 or 6) in the d orbital.² Note: Alkali Earth Metals i.e. Ca, Sr, Ba can also be substituted with Early Transition Metals i.e. La, Yt, Sc and Pnictides i.e. P, As, Sb can be substituted with Chalcogens i.e. S, Se, Te or members of the Carbon Group i.e. Si, Ge, Sn. This will effect the number of electrons donated by the TM.

ty and single crystal production. Single crystal growths are most effectively synthesized using molten metal fluxes and salt fluxes in Al₂O₃ crucibles sealed in argon-filled quartz ampoules.³ The flux melts at a much lower melting point than the other materials allowing them to dissolve into the flux solvent, much like table salt (NaCl) dissolves in room temperature water even though its melting point is around 800 °C. The flux also getters impurities by creating a clean environment for growth, acting like a vacuum.⁴ (See Appendix 1 for examples of our single crystal growths) This method requires:

- Crucible materials Al₂O₃
- Manifold for evacuating argon-filled quartz tubes and a hydrogen/oxygen blow torch for sealing the ampoules
- Laboratory chamber furnaces that can reach 1200 °C
- Centrifuge to spin the molten metal flux off of the crystal formations⁵

(See Appendix 2 for pictures on crystal synthesis) Other methods of growths are also utilized depending on the data we anticipate collecting. In some cases, solid-state reaction growths, using pressed powder pellets from a pneumatic press, are used to synthesize nanocrystals. By pressing together a homogeneous



Formula	Notation	Tc (K)	No. of Cu-O planes in unit cell	Crystal structure
Bi ₂ Sr ₂ CuO ₆	Bi-2201	20	1	Tetragonal
Tl ₂ Ba ₂ CuO ₆	Tl-2201	80	1	Tetragonal
Bi ₂ Sr ₂ CaCu ₂ O ₈	Bi-2212	85	2	Tetragonal
YBa ₂ Cu ₃ O ₇	123	92	2	Orthorhombic
HgBa ₂ CuO ₄	Hg-1201	94	1	Tetragonal
Tl ₂ Ba ₂ CaCu ₂ O ₈	Tl-2212	108	2	Tetragonal
Bi ₂ Sr ₂ Ca ₂ Cu ₃ O ₆	Bi-2223	110	3	Tetragonal
TlBa ₂ Ca ₃ Cu ₄ O ₁₁	Tl-1234	122	4	Tetragonal
Tl ₂ Ba ₂ Ca ₂ Cu ₃ O ₁₀	Tl-2223	125	3	Tetragonal
HgBa ₂ CaCu ₂ O ₆	Hg-1212	128	2	Tetragonal
HgBa ₂ Ca ₂ Cu ₃ O ₈	Hg-1223	134	3	Tetragonal

Table 1: (above) known high-temperature cuprate superconductors and their corresponding unit cell structure

mixture of powdered materials, energy is being added to the system in addition to the heat provided by the furnace, both of which encourage crystallization restructuring into a polycrystalline lump of nanocrystals. This method has its drawbacks, which present in porosity, intergranular composition, and a higher surface to bulk ratio of its growths.⁴

It is important to mention the limitations of quartz, as all of these methods require the use of a quartz ampoule. Quartz begins to break down around 1200 °C, no longer providing the protective environment for the growths. If a temperature profile reaches higher than 1200 °C alternative measures must be taken to protect the growth from oxidation and impurities, as is shown later with my attempt to grow CaCoSb in a “122” structure.

Once we’ve synthesized the crystals, they are sorted according to purity and singularity for each measurement system.

Tier 1:

- Bruker D8 Advance Powder X-Ray Diffraction Machine
- APEX II Single Crystal X-Ray Diffraction Machine
- JEOL7600 Energy Dispersive X-Ray (Electron Microscope)

Tier 2:

- Physical Properties Measurement System (PPMS) with a 14 Tesla (T) superconducting magnet [0.1K-800K]
- PPMS with a 9 T superconducting magnet [0.4K-400K]
- Magnetic Properties Measurement System (MPMS) with a Superconducting Quantum Interface Device (SQUID) [1.8K-400K]

(See Appendix 3 for picture of measurement systems) Tier 1 measurement systems characterizes a crystal’s structure and stoichiometry. If the data from tier 1 proves that a new or relatively unexplored compound was successfully synthesized, crystals are prepared for tier 2, which characterize the crystal’s electronic and magnetic properties. Tier 2 measures the resistivity, heat capacity, thermal conductivity, and magnetization of single crystals as a function of temperature and/or magnetic field and/or pressure, which helps us to piece together what is occurring at the atomic level and how it manifests into physical properties.

III. The Hunt for CaCo₂Sb₂

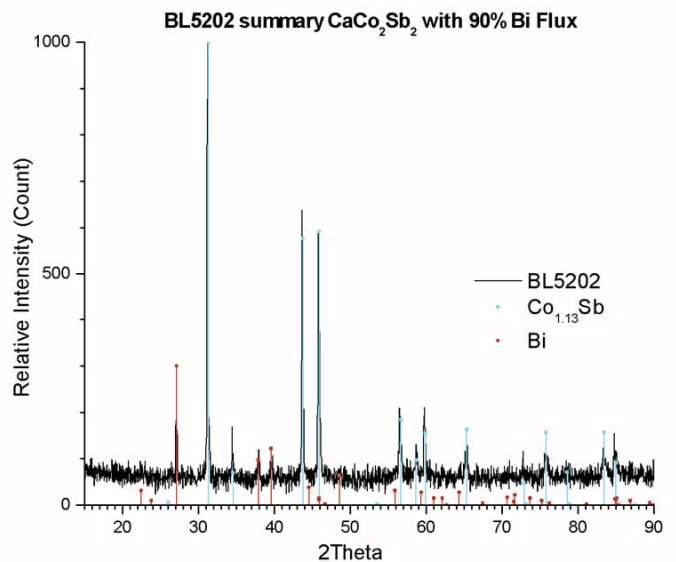
Phase diagrams are referenced before every new growth attempt to help determine the appropriate stoichiometry, temperature profile and growth method to achieve the desired compound. CaCo₂As₂ is an interesting antiferromagnetic compound to which we can apply the same principles as discussed in the introduction. CaCoSb with a “122” structure, or any other ternary compound with these three elements, has never before been grown. (See appendix 4 for binary phase diagrams of Ca, Co, and Sb)

These three binary phase diagrams give little information on how to grow a “122” structure, so from my first few growth attempts I constructed a ternary phase diagram.

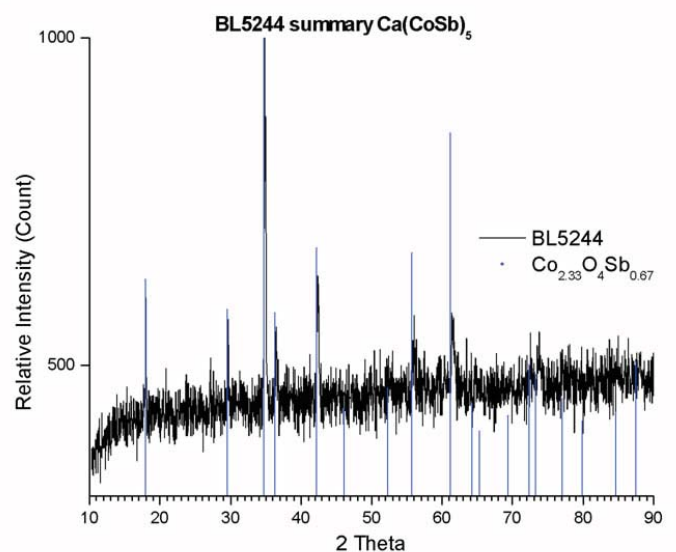
I’ve failed to grow CaCo₂Sb₂ 14 times, but through trial and error, I’ve improved on every attempt. My first 4 growths had a Sn flux, spun at 1100°C, at which temperature no crystals formed and the entire contents spun off leaving empty crucibles. My second attempt had several different elemental ratios: CaCo₂Sb₂ and Ca₂CoSb₅, both with 80% and 90% Bi flux, brought up to 1150°C and spun at 500°C and 700°C. These eight crucibles produced needles of varying purity of CoSb. My third attempt

used a ground CoSb binary, from the second attempt, as a flux: Ca(CoSb)₅ brought up to 1202°C and spun at 1100°C. Quartz weakens at 1200°C, which allowed oxygen to seep in, producing Co_{2.33}O₄Sb_{0.67}. My fourth attempt adjusted by only raising the temperature to 1180°C and spinning at 1080°C. This temperature profile didn’t introduce enough thermal energy to liquefy the polycrystalline CoSb flux, which I made from a solid state growth, resulting in no crystals growths, just an amorphous lump. My fifth attempt, coming out on 08/01/14, utilized a double ampoule with a tantalum foil layer to gether oxidation, due to the weakening of the quartz tubing.

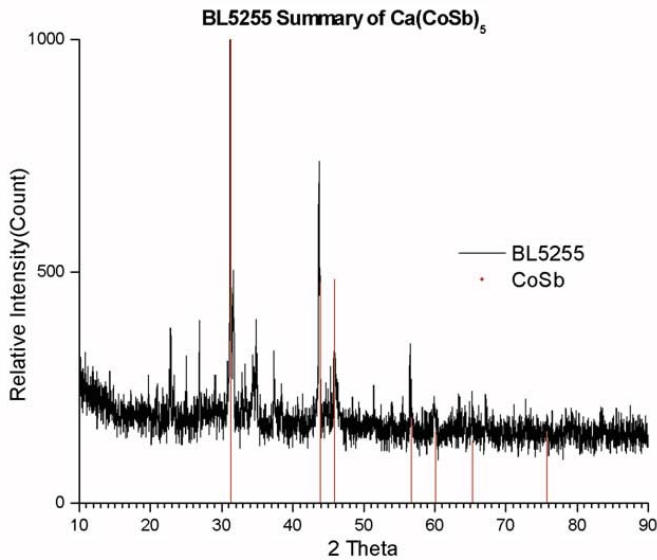
IV. Results



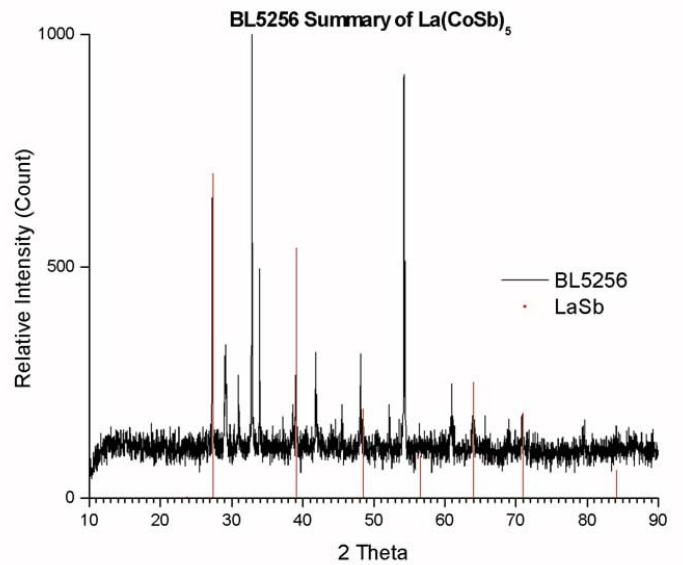
Graph 1: Powder x-ray diffraction pattern for second growth attempt produced CoSb binary with Bi impurities



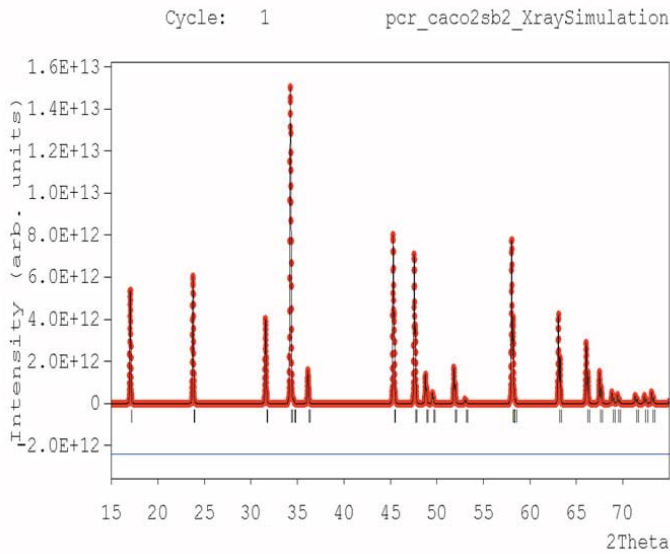
Graph 2: Powder x-ray diffraction pattern for third growth attempt produced Co_{2.33}O₄Sb_{0.67} however there are some unidentified peaks similar to BL5255 between the 20 and 30 2theta range



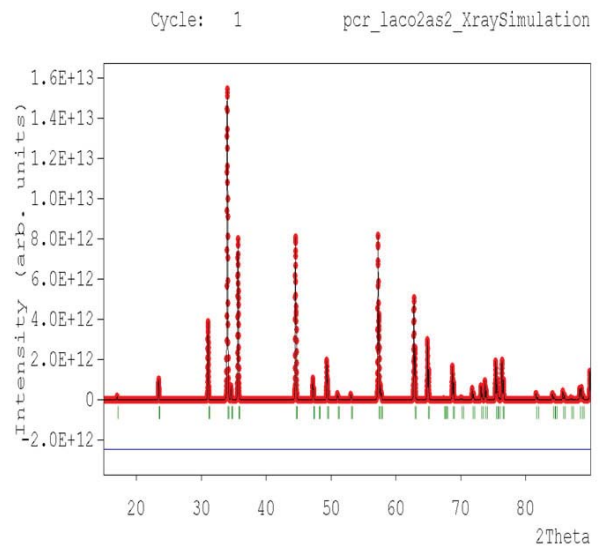
Graph 3: Powder x-ray diffraction pattern for fourth growth attempt produced CoSb binary however there are unidentified peaks



Graph 5: Powder x-ray diffraction pattern for first growth attempt for LaCo2Sb2 produced CoSb binary however there are unidentified peaks around 29-34 and 54 2theta.



Graph 4: Simulation of a powder x-ray diffraction pattern for CaCo2Sb2 from hypothesized lattice parameters based off of CaCo2As2. (To be compared to graph 3) Compliments of Daniel McNally



Graph 6: Simulation of a powder x-ray diffraction pattern for LaCo2Sb2 from hypothesized lattice parameters based off of LaCo2As2. (To be compared to graph 5) Compliments of Daniel McNally

V. Conclusions

When searching for new superconducting materials, growth methods must be adaptable to the environment, in which the desired compounds are hypothesized to form. It is difficult to predict potential setbacks; therefore persistence and educated adjustments are necessary to produce results.

BL5255 and BL5256 show promise as there are no known diffraction patterns that can account for certain peaks. Further investigation, through the production of viable crystals, single crystal x-ray diffraction and EDX, is required to confirm such hopes.

VI. Acknowledgements

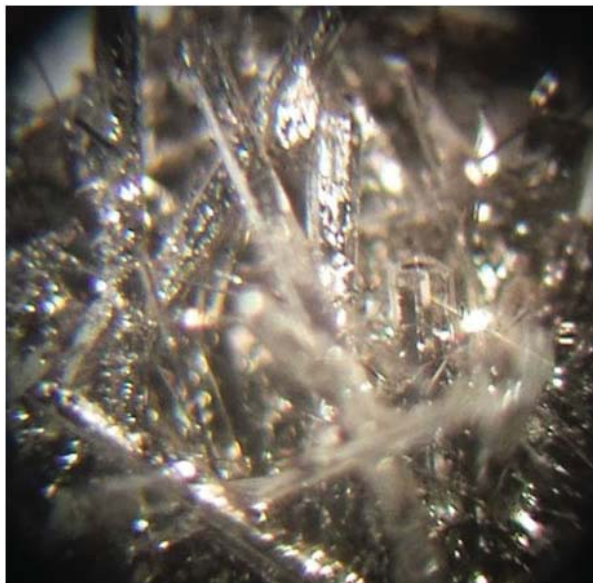
This project was supported in part by the U.S. Department of Energy, Office of Science, Office of Workforce Development for Teachers and Scientists (WDTS) under the Science Undergradu-

ate Laboratory Internships Program (SULI). Acknowledgements to the Physics department at Hofstra University. The professors' sincere desire to impart knowledge and shape the next generation of physicists has enabled me to compete with other brilliant undergraduates for such highly regarded internships. Thanks to Meigan Aronson, my research mentor, for this opportunity. Thanks to Daniel McNally, Hua He, and Lucia Steinke, postdocs and grads on my research team, for their teaching and support. Heartfelt thanks to Lynne and Richard Albrecht for educational funding, and to God for these blessings and more.

VII. References

1. Attfeld, J. P.: J. Mater. Chem. 21, 4756 (2011)
2. Tegel, M., Rotter, M., WeiB, V: J. Phys.: Condens. Matter 20 No 45 (2008)
3. Canfield, P.C., Fisk, Z.: Philosophical Magazine B 65:6, 1117-1123 (1992)
4. Fisk, Z., Remeika, J.P.: Handbook on the Physics and Chemistry of Rare Earths 12, 53-70 (1989)
5. Canfield, P., Fisher, I.: Journal of Crystal Growth 225, 155-161 (2001).
6. Springer Materials The Landolt-Bornstein Database

Appendix 1



Clockwise starting with top left:

- Sc-Co-Si-Ga needles
- Sc-Co-Si-Al rods
- Left: La-Mn-Sb-O blue plate clusters
- Right: La-Mn-Sb-O plate
- Sc-Ni-Si-Al rods and bundels
- Sc-Ni-Si-Ga rods



Appendix 2



Left: This is where the actual growth starts at the weigh station. Everything is measured to within 99% of its intended stoichiometric ratio

Below: I record the normalized measurements and the actual measurements for each sample I attempt along with its temperature profile



Below: The library of growths to date. These log books document every growth we've ever attempted in a step-by-step process

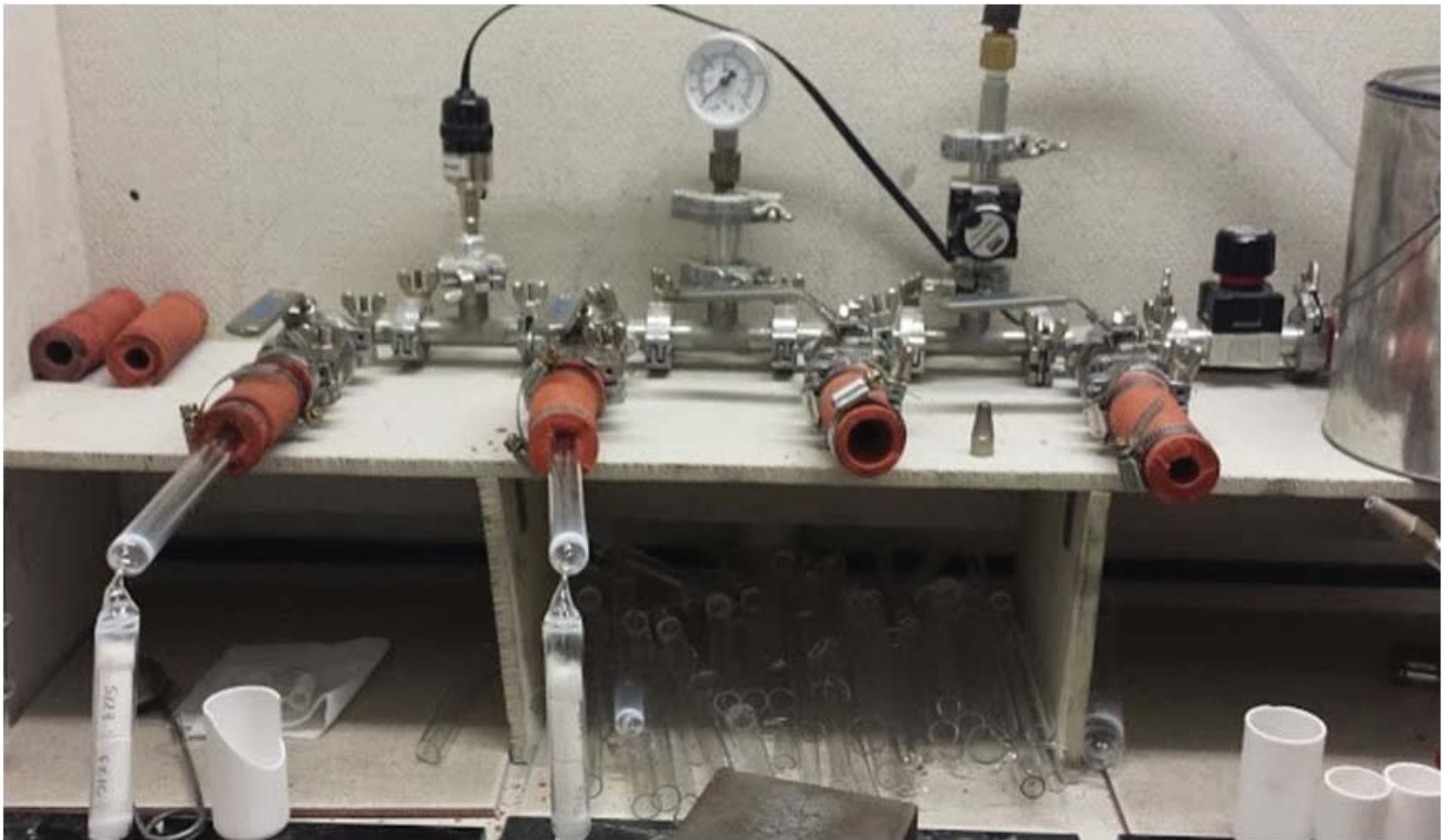




Left: The Arc Melter, which literally uses a beam of electrons, like a lighting bolt, to burn off any impurities from the raw growth materials

Below: The glove box where we store our reactive, easily oxidized, and poisonous materials, most notably As, La, Ca, and Ba₂S



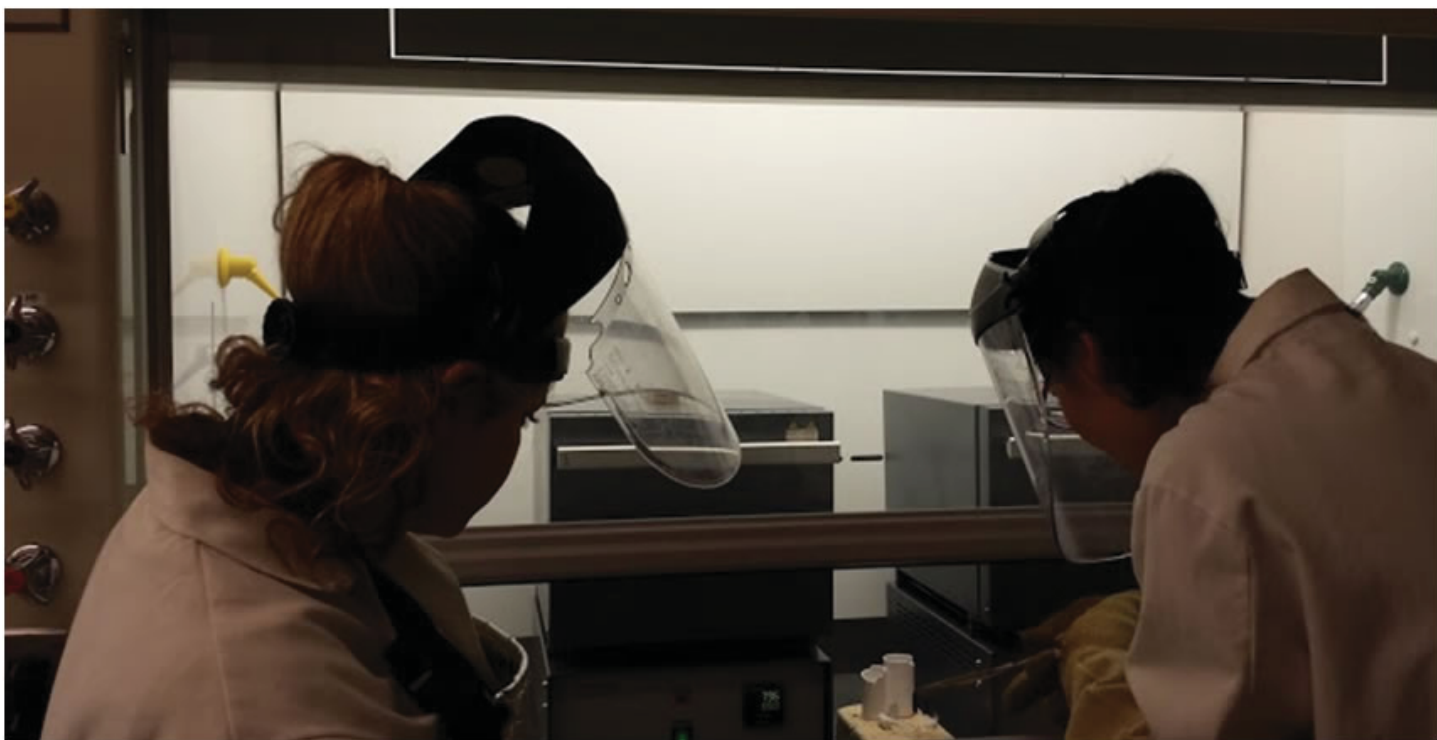


Top: Our glass box for sealing samples. Attached to our vacuum system are two necked tubes in the process of being evacuated.

Bottom left: The cord in the above picture runs to the digital vacuum monitor. Once it drops below 40 microns we cycle the system with argon (the gauge for the argon is the white dial in the middle of the system above)

Bottom right: The Hydrogen/Oxygen blowtorch, with which we seal all of our samples into quartz ampoules.

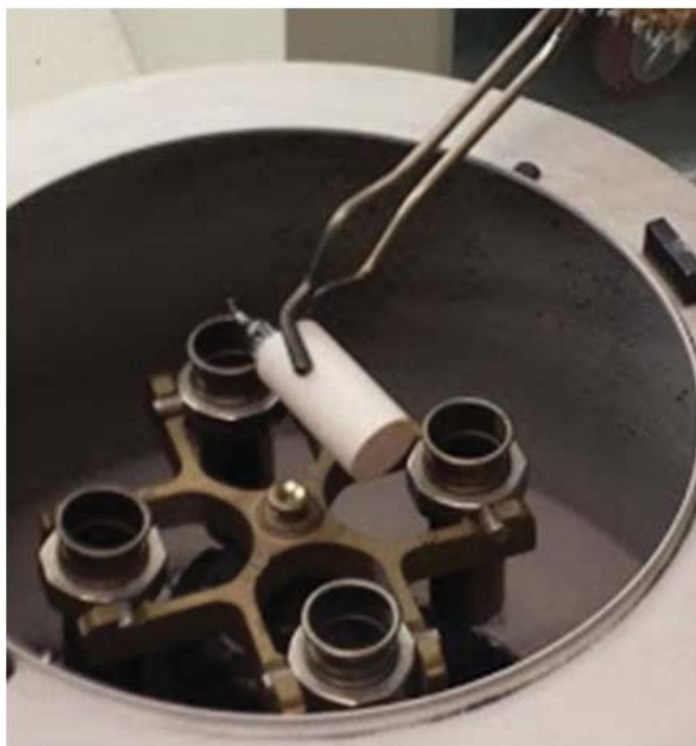
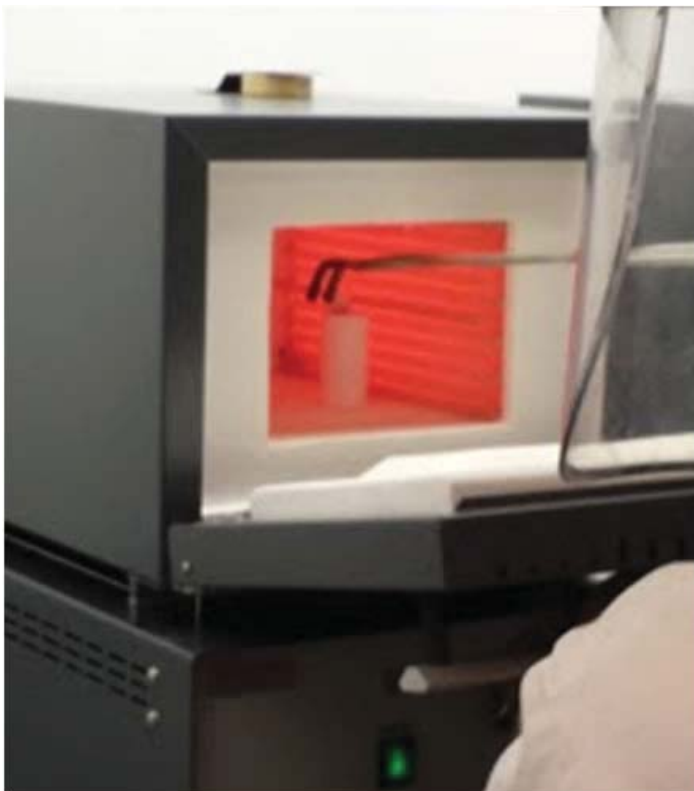


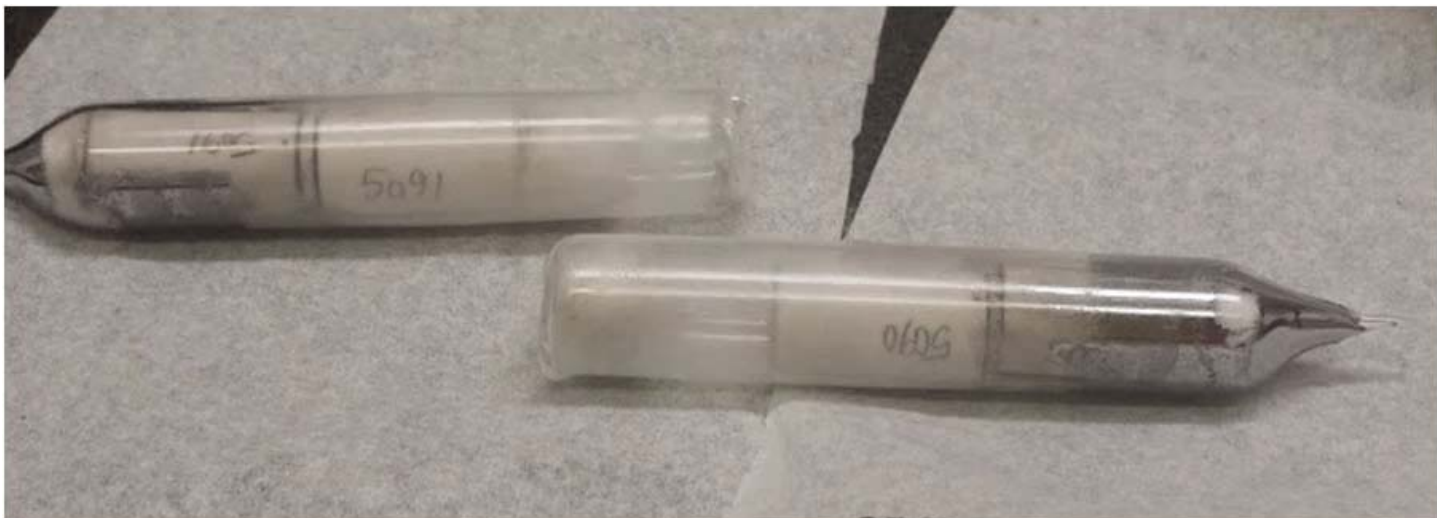


Top: 4 of our furnaces are located inside of a hood to filter away any poisonous gasses that might leak out of a cracked tube containing toxic material

Bottom left: In full protective personal protective equipment we open the ovens at temperatures as high as 900C to remove our samples

Bottom right: We then dump them quickly into the centrifuge to spin of the flux in hopes of harvesting clean crystals





Top: The ampoules after the flux has been spun off. This growth used a gallium flux, which leaked out of the catching crucible and into the tube



Middle: Salt flux growths fresh out of the furnace. They are still glowing from the extreme temperatures. The ampoule on the top right has begun to cool and the salts interaction with the quartz is noticeable as its turned white and brittle. These are my La-Mn-Sb-O salt flux growths

Bottom: The fume hood where surface impurities are chemically dissolved

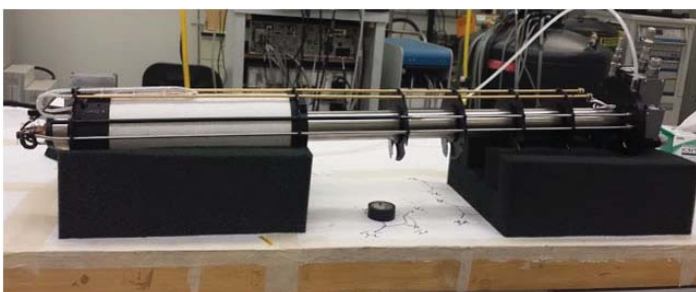


Appendix 3

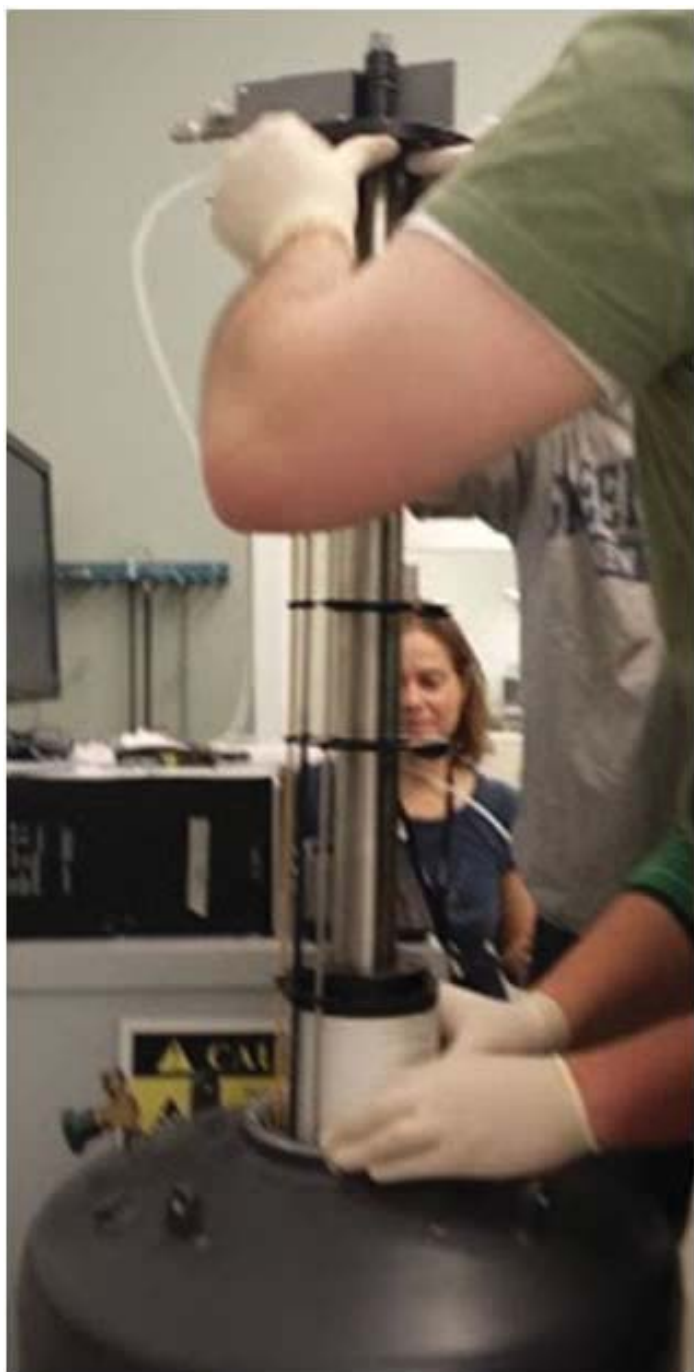


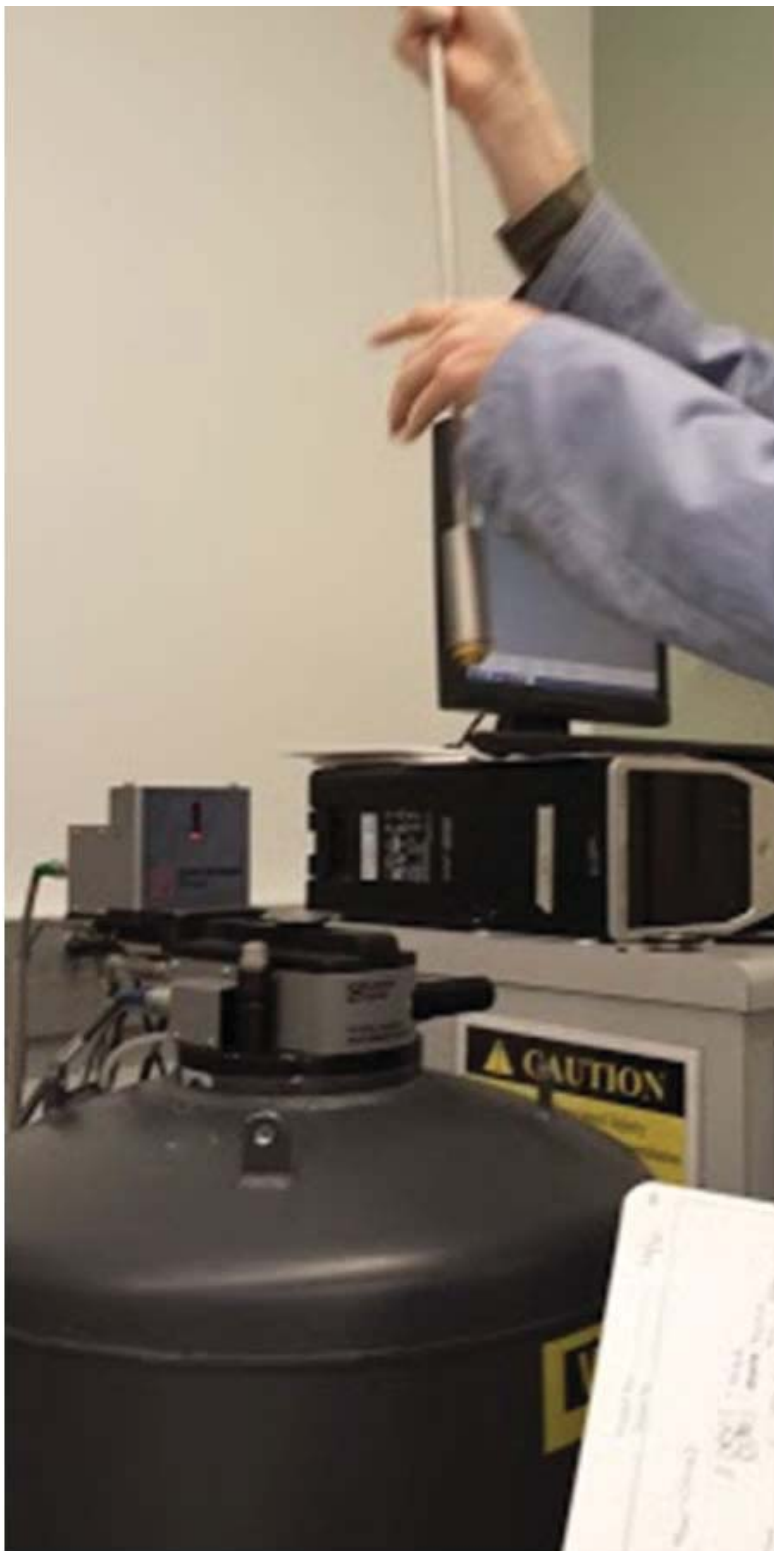
The three pictures to the left show the inner core of the 9T PPMS as its being fixed. The small hollow needle that regulates the flow of liquid helium to the chamber for temperature control was clogged and required replacement.

Below is a picture of how the core fits back into the cooling tank



Below is a picture of the core of the 14 T, which presented problems with the inductance and also required parts replacement.



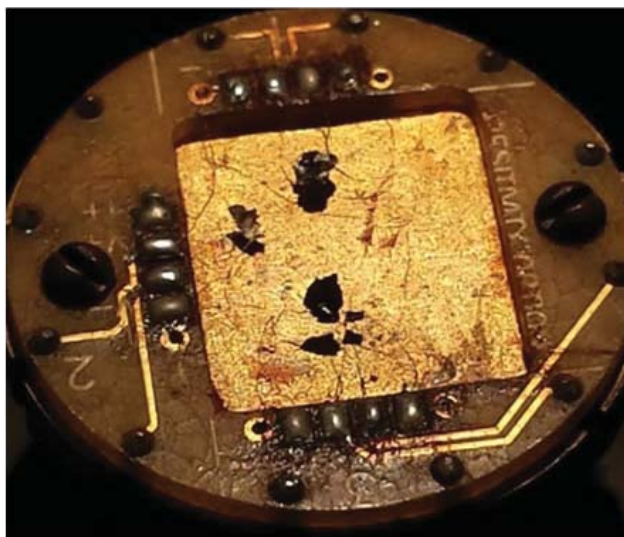
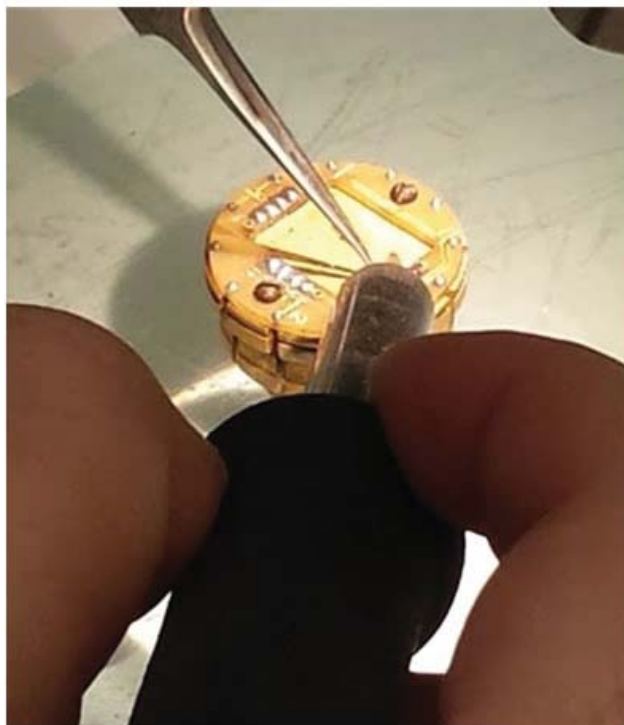


Top: The insertion rod with the puck attached to the bottom as it's about to be mounted in the core of the 9T PPMS

Right top: The puck as the platinum wires are soldered into place

Right middle: The three crystals, from various growths of La-Mn-Sb-O mounted on the puck

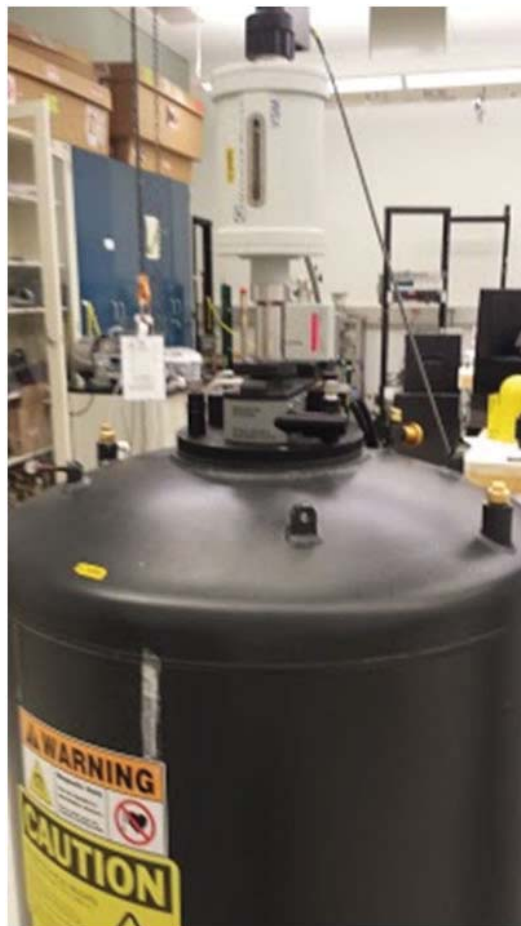
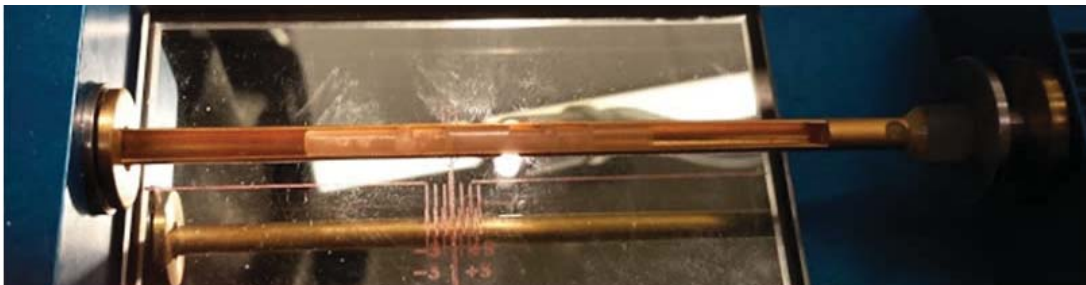
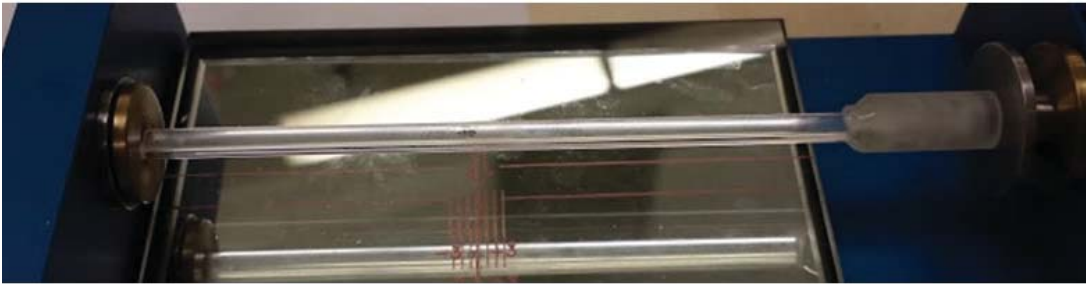
Right bottom: A close up of my crystal with the four contact wires epoxied into place

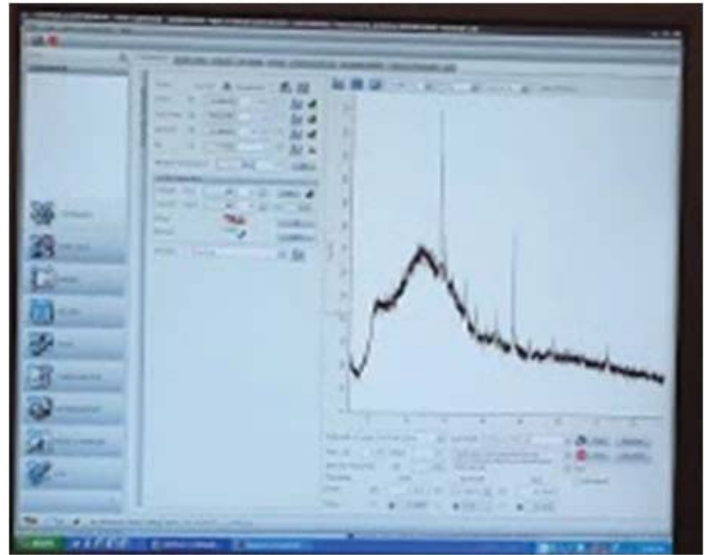


Middle: 2 types of mounting sticks to measure the growths magnetic properties.

Bottom left: A close up of the VSM attachment. The little yellow bead in the window shows the height of the rod as it oscillates the stick up and down through the magnetic field.

Bottom right: is a picture of the VSM attached to the 14T PPMS





Top Left: A close up of the powder X-Ray Diffraction Device. The arms rotate around the circular track to test varying degrees of incidence and the platform in the middle rotates to ensure measurements from every angle. The left arm emits the x-ray and the right are detects it.

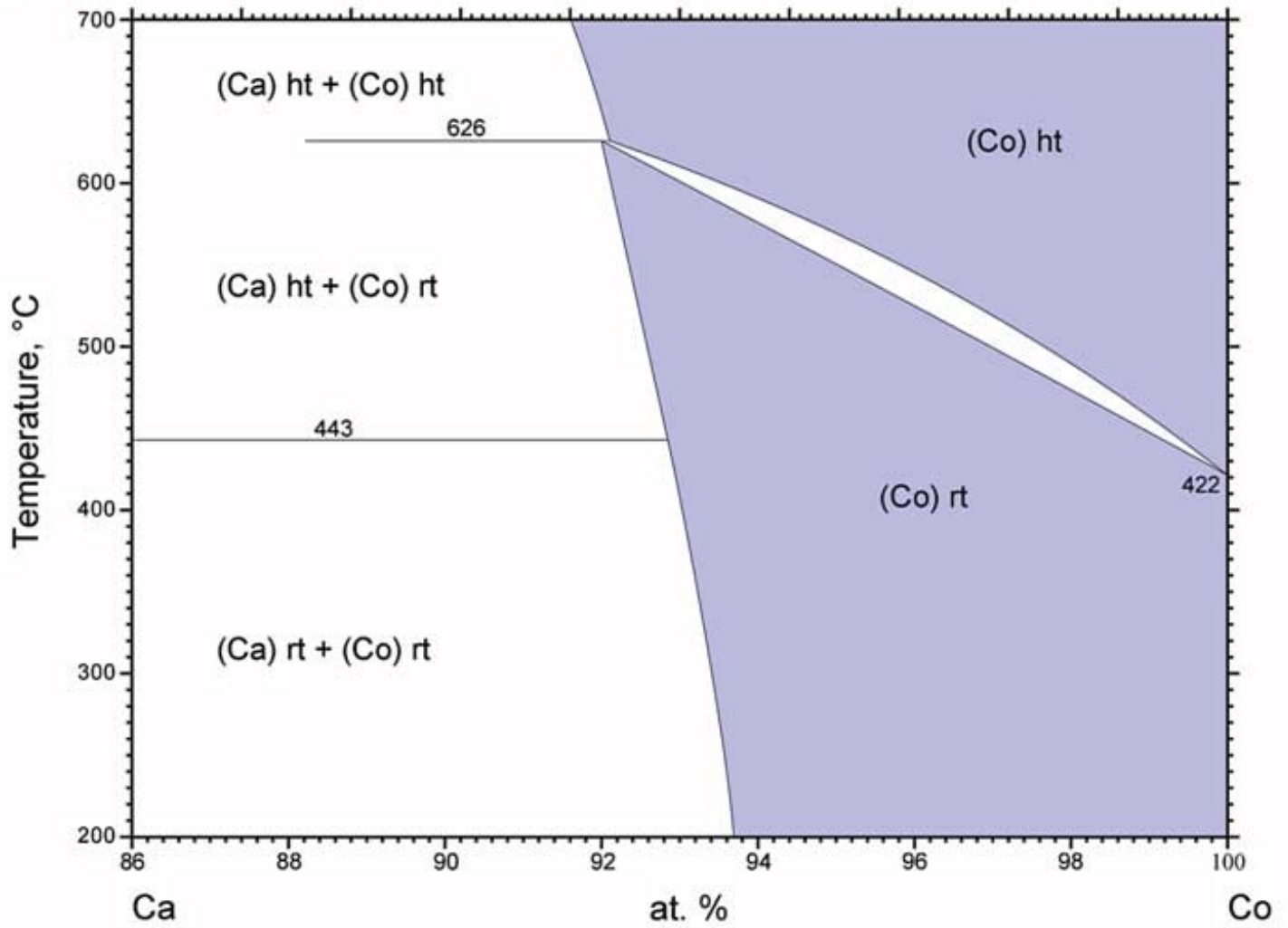
Top right: the x-ray diffraction pattern automatically calculated and graphed on the neighboring computer. This pattern is actually of un-ground plate crystals of my first La-Mn-Sb-O growth

Below: This is the microscope station I utilize to do most of my work and in the background is our X-ray Diffraction Machine

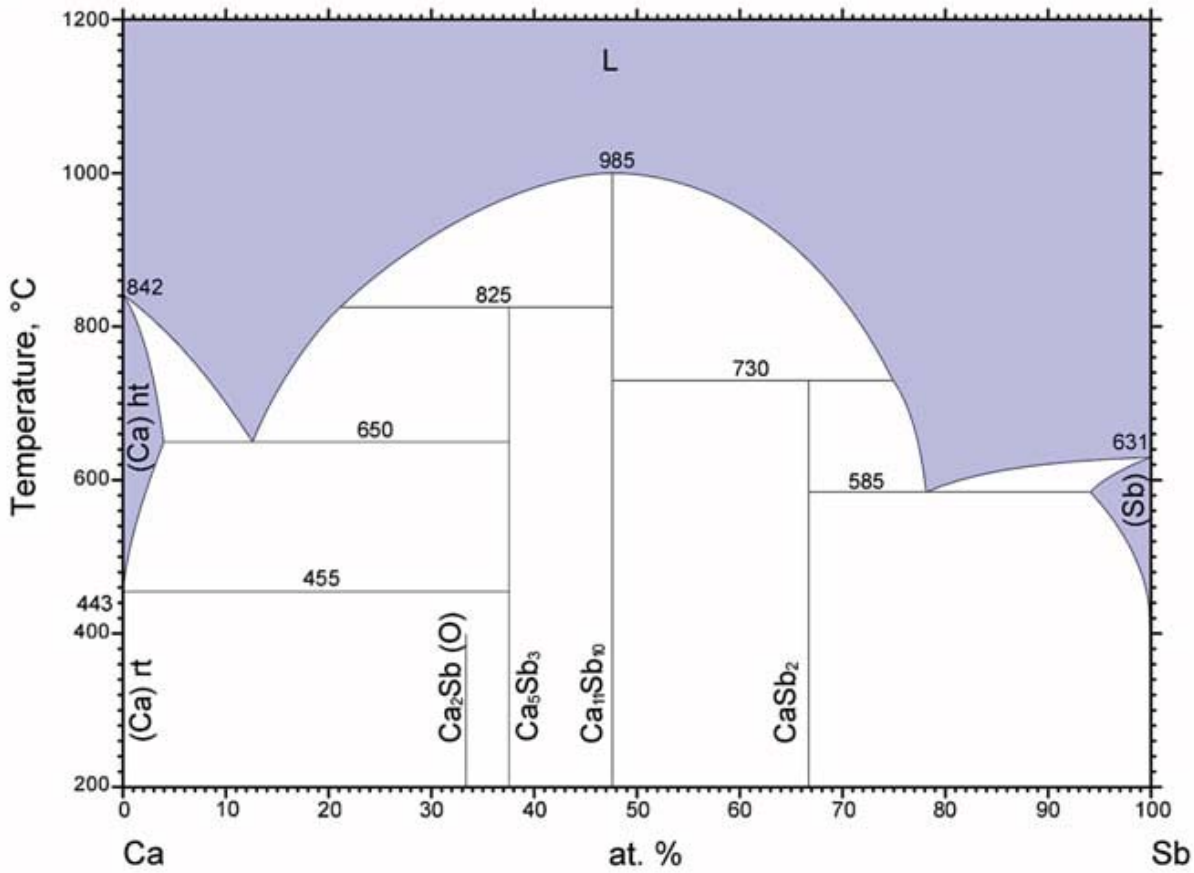


Appendix 4

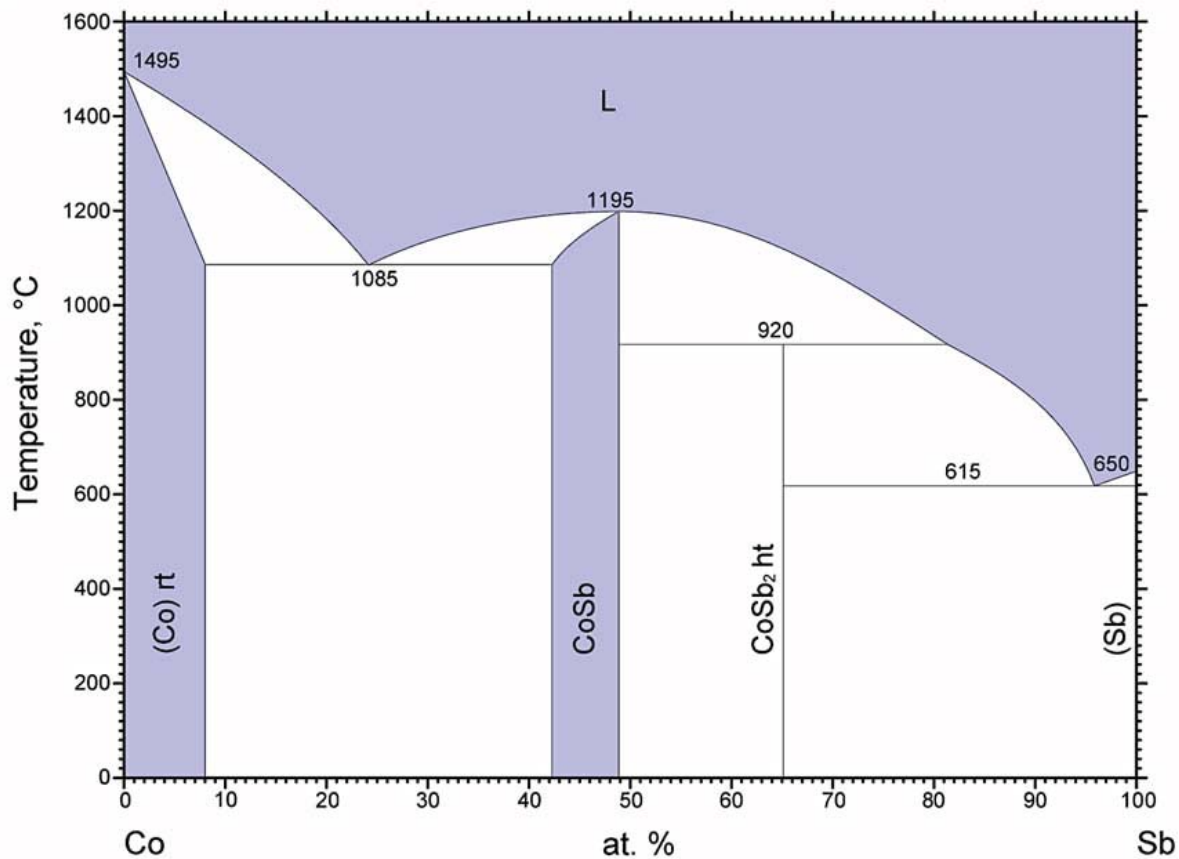
Ca-Co Binary Phase Diagram⁶



Ca-Sb Binary Phase Diagram⁶



Co-Sb Binary Phase Diagram6



Combustion analysis of upgraded pyrolysis oil with regard to efficiency and emissions

Michael Worek

Engineering Physics, University of Illinois Urbana-Champaign, Champaign, IL 61820

Thomas Butcher

Sustainable Energy Technologies, Brookhaven National Laboratory, Upton, NY 11973

Abstract

The rapidly evolving search for renewable energy increases the need for efficient and sustainable sources, mainly bio-oil. To this end, the practicability of upgraded bio-oil blends must be researched and compared with other common fuels such as No. 2 heating oil and biodiesel. For this comparison, two different upgraded pyrolysis oils blends, a high oxygen content (HOX) and a medium oxygen content (MOX), were tested with No. 2 heating oil under two overarching categories: combustion quality and material compatibility. Combustion tests included flue gas analysis, flame stability, and smoke number while material tests included swell and weight change on components that have been exposed to the bio-oil. The combustion analyses of the bio-oils show a negligible increase in oxygen and nitrogen oxides when compared with No. 2 oil and no impact in flame stability and efficiency was recorded. However material tests showed significant swell numbers and weight increases in common burner materials. From these results it can be claimed that although upgraded bio-oil blends are usable in existing systems at this time, they are detrimental to residential heating systems over time and are not ready for introduction to consumers.

I. Introduction

The United States Northeast is the largest user of heating oil in the United States relying mainly on No. 2 oil for this purpose. Of the 120 million barrels of heating oil used annually approximately 80 million of these barrels are imported.¹ This recently has become a point of concern since the price for heating oil has increased and is generally unstable due to the dependence on foreign sources. To mitigate this foreign oil dependency, the Depart-

ment of Energy has developed interest in regionally sustainable, cost effective, and functional substitute to No. 2 oil and other largely foreign home heating oils. Bio-oils, specifically upgraded pyrolysis oils fill this roll.

Pyrolysis oil, which is made from wood, is sustainable in the U.S. Northeast; what needs to be known is if it is plausible as a consumer product. The tests preformed were aimed at researching upgraded pyrolysis oil, a branch of pyrolysis oil that has been refined to a more homogeneous and usable product. The oils that will be talked about later are a high oxygen content blend (HOX) and a medium oxygen content blend (MOX), prepared by Pacific Northwest National Laboratory. The oxygen content of the oil is inversely proportional to the amount of refining that has been preformed on the oil; MOX is more highly upgraded.

The functionality of upgraded pyrolysis was based on the expectation of a residential heating apparatus, a commercial boiler, or furnace of some sort. The guidelines for this test were based on two categories, combustion quality and material compatibility. Combustion tests included flue gas analysis, flame stability, and smoke number while material tests included swell and weight change on components that have been exposed to the bio-oil using ASTM's standards.

II. Method/Experiments

In order to evaluate the functionality of the HOX and MOX bio-oil blends the tests run focused on two key aspects of home heating systems, combustion quality and material compatibility.

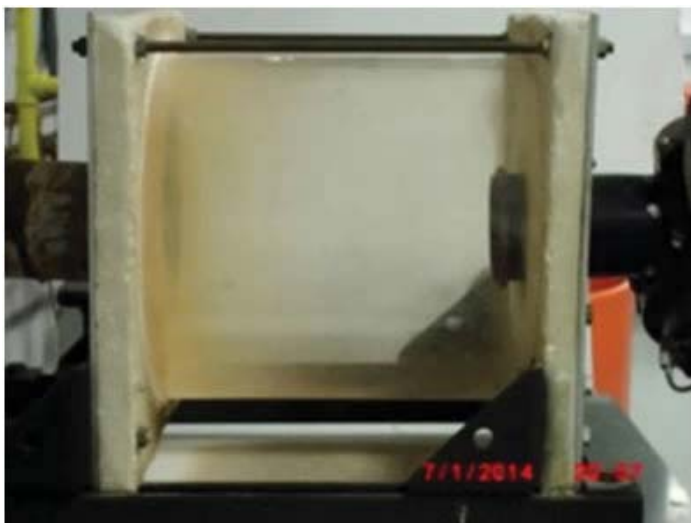


Figure 1: Quartz chamber w/ Carlin burner



Figure 2: Retention head

To test these the materials and systems used were very closely related to a commercially available home heating system with minor adjustments for measurement purposes. One system in question was a Dunkirk boiler and Carlin burner combination with a photo-resistor on the burner and a Testo 350XL flue gas analyzer mounted on the flue stack. Another system used was the same Carlin burner attached to a quartz chamber in order to physically observe the flame. With these setups flue gas, flame stability and smoke number analyses could be made to determine the combustion quality. In order to run material tests both generic nitrile seals and proprietary nitrile seals obtained from Suntec, the largest oil pump manufacture in the world, were used to preform swell test and weight changes measurements according to the ASTM 471-12A standard.²

A. Quartz Chamber

The first combustion test run was with the Carlin burner and the quartz chamber. This experiment was aimed at finding whether the bio-oils visibly differed from No. 2 oil when burned; this took into account flame brightness, flame length, and flame stability. Flame brightness and flame length were measured using a photo-resistor and inches respectively while flame stability was a qualitative measurement that dealt with how structured the flame was. When using a burner the retention head on the end shapes the flame so a well-structured flame that shows several wisps of fire is preferable to a single tongue of flame. Also an ideal burner flame is short and bright. This means the photo-resistor will show a low resistance since light incident upon a photo-resistor decreases the resistance.

In this experiment the procedure for switching fuel was done using a fuel selection valve and transitioning between the two fuels so as to conserve fuel and maintain a constant supply to the burner. The burner was started on No. 2 oil and left to achieve a stable flame at which point the overall quality, length, and brightness in terms of resistance was measured and pictures taken. Then the fuel selection valve was slowly adjusted to the HOX blend keeping air input the same. During this transition time the No. 2 oil in the burner mixed slightly with the HOX blend and was burned away. Once again in this transition state the values of the previously mentioned categories were recorded. Since there was a transition period it was clear when the transition was over; at this point qualities were measured and pictures were taken. Last, for repeatability, once we had exhausted our premeasured amount of bio-oil the burner was transitioned back to No.2 oil keeping air input the same. During this test it was decided to not use the MOX blend. The reason being it is more refined than the HOX blend so

if any irregularities showed they would be more pronounced in the HOX blend rather than the MOX blend.

B. Boiler

The second combustion test used the Carlin burner once more only this time attached to a Dunkirk boiler as would be common in a residential household. The first step in testing was to find the optimal air intake for the burner. Air intake is one of only things that can be changed on a burner to produce a better flame so as is common in a residential setting the optimal air intake and thus flame was found. To do this the burner was started using No. 2 oil and the air intake was varied from 0.87 to 0.58 gal/hr. During this time properties such as CO, NO_x, SO₂, Smoke #, and O₂ were recorded to find the setting that contained a Smoke # of 0 while having a minimal O₂ content.

Once this air setting was realized we transitioned into testing HOX and MOX blends. Once again the same selection process used above was used to transition between No. 2 oil and the bio-oil blends. First, the HOX blend was tested. During this time, using the Testo 350 XL, a continuous plot was made against time showing the change of every constituent of the flue gas. Also during this test Smoke # and photo-resistor measurements were made at regular intervals. Next, when the predetermined amount of HOX ran out the burner was transitioned back to No. 2 oil and the HOX was replaced with MOX at which point the test repeated with the same measurements being taken.

C. Nitrile Seals

The last test done focused on the material compatibility of the HOX and MOX blends with nitrile used in pumps. There were two different types of seal material used in this test. The first was standard run-of-the-mill nitrile and the second was a proprietary nitrile blend from the company Suntec that is used in their oil pumps; they are pictured in figures 3 and 4. There were two similar tests used to measure swell of the nitrile. The first test measured the swell of the nitrile by using a caliper and elementary volume calculations both before and after immersion in the HOX and MOX blends at 42°C. This assumed the pieces of nitrile were perfect rectangles or cubes. It was later realized that the volume measurements are only approximate do to the slightly irregular shapes of the nitrile. Also this first test was not run with a standard in mind; the nitrile was immersed for 9 days before a secondary measurement was taken. The ASTM standard requires 72 hours immersion before a second volume measurement. Even though this test wasn't run according to a standard and the volume measurements are approximate the results give a baseline for the second experiment that was run.

The second experiment run was done according to the ASTM 471-12A standard. This standard requires the change in volume measurement to be completed 72 hours after immersion in the



Figure 3: Generic nitrile

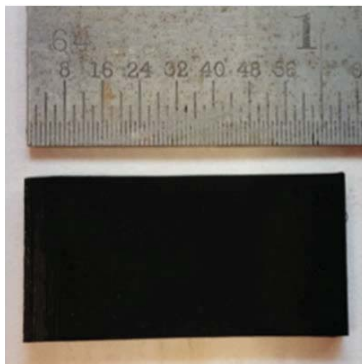


Figure 4: Suntec nitrile



Figure 5: No. 2 oil



Figure 6: HOX blend

bio-oil. This test was also run at 42°C and instead of using a caliper the volume measurements were made using water displacement at 69°F. Using this method both the volume measurements were more accurate and the results can be compared to other test performed in the same manor. The results from both tests however share the same conclusion.

III. Results

A. Quartz Chamber

During the quartz chamber test the No. 2 oil started out with a photo-resistance of 650Ω and a short well-structured flame as is visible in figure 5. This photo-resistance will be the basis for all measurements made afterwards. As steady state was achieved for the HOX blend another measurement was taken; the photo-resistance was 770Ω and once again the flame was short and well structured. These features can be seen in figure 6. Also, as mentioned above, for repeatability as the HOX blend ran out the fuel was switched back to No. 2 oil where the photo-resistance was recorded once again at 550Ω.

From the above pictures it is apparent there is no visible difference between a No. 2 oil flame and a HOX blend flame. The only difference that can be detected is the change in photo-resistance of the flame; the HOX blend is 120Ω less bright than the No. 2 oil. The comparison is however is unreliable due to the deviation of the photo-resistor. The photo-resistor can have a resistance as high as 5000Ω for a dim flame also it can obtain light from any source so a change of 120Ω is minimal compared to the range and deviation of the device.

From this observation it is clear that from visual observations HOX and No. 2 oil burn the same and it would have been unnecessary to do the same experiment with the MOX blend since it is more refined than the HOX blend. This implies that if there were any innate problems with the pyrolysis oils they would be more visible in the HOX blend.

B. Boiler

As mentioned, through the boiler test all of the flue gas quantities were measured against time. With all this information an emphasis was put on certain quantities, namely, CO, O2, and NOx. These quantities are a good indication of the quality of the gas being burned in the boiler. From figure 7 a slight rise in O2

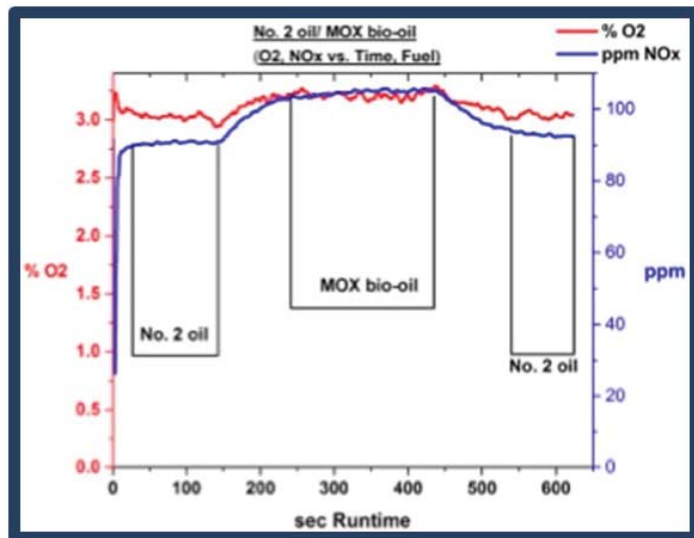


Figure 7: MOX blend

and NOx are visible when No. 2 oil was switched to HOX. The same features are almost identical in figure 8, which depicts the change from burning No. 2 oil to MOX. These increases may seem relevant however they are very small increases in ppm and percentage. Figure 9 illustrates this fact by taking an average of the O2, NOx, and photo-resistance over the running of each mentioned fuel. From this it is clear the fuels burn very similarly to No. 2. Upon closer inspection it can be seen however that the MOX blend does burn ever so slightly better than the HOX blend, meaning it produces slightly less NOx and the CAD cell resistance is lower than the HOX blend.

	No. 2 Oil	HOX bio-oil	MOX bio-oil
Ave. O2 (ppm)	3.19	3.31	3.208
Ave NOx (ppm)	90.1	114.7	104.5
CAD cell (Ω)	324.25	340.14	338.71

Figure 9: Average values

One possible explanation for the increase in O2 and NOx for these bio-oils is due to their composition. They are made from wood meaning if they haven't been refined enough they will contain more oxygen and NOx from the organics than No. 2 oil which is based in fossil fuels.

C. Nitrile Seals

Volume change after immersed in bio-oil (Caliper)

Days Exposure	Generic Nitrile %Vol Change		Pump Seal Nitrile Material %Vol Change	
	HOX	MOX	HOX	MOX
0	0	0	0	0
9	70.4	34.8	27.6	22.6
19	96.6	47.9	40	31.6

Figure 10

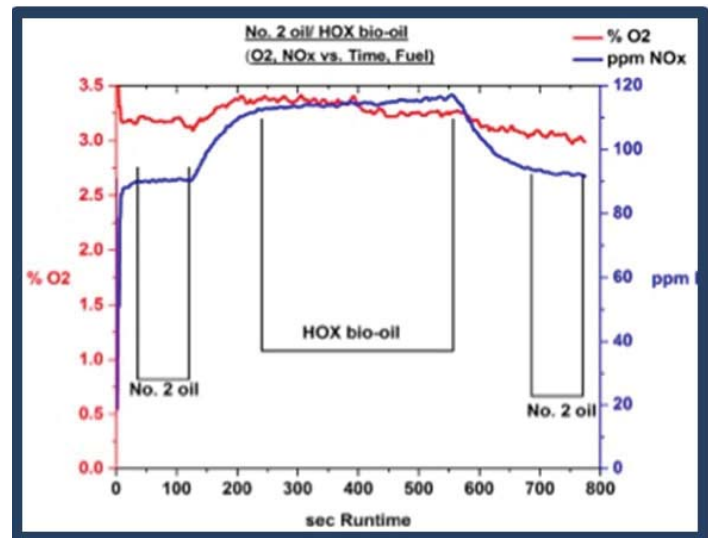


Figure 8: HOX blend

Volume change after immersed in bio-oil (ASTM)

Days Exposure	Generic Nitrile %Vol Change		Pump Seal Nitrile Material %Vol Change	
	HOX	MOX	HOX	MOX
0	0	0	0	0
3	50	50	17	25
15	90	70	33	33

Figure 11

The results for the caliper measured volume change of nitrile after being immersed in bio-oil is seen in figure 10 and the results for the ASTM method volume change after being immersed in bio-oil is seen in figure 11. According to the ASTM 471-12A standard the pass/fail threshold for a seal immersed in oil is a 25% increase in volume over the course of 72 hours. As seen in figure 11 at the end of 72 hours the volume change for the generic nitrile was 50%. This means that it fails the ASTM standard. But the Suntec nitrile volume change at the end of 72 hours is between 17-25% this means that it passes the ASTM standard. These numbers are enforced by the measurements made using a caliper.

Even though the ASTM standard ends after 72 hours it was decided to run the test longer to record further changes in the volume. Also displayed in figures 10 and 11 are changes to the volumes after 72 hours. From these numbers it is clear the seal materials do not hit their maximum volume change in 72 hours. The volume change of the seals rose well above the 25% threshold and although the seal material might pass the ASTM standard this is unacceptable to most pump manufactures. In fact, it is common practice in the pump manufacturing business to not accept seals with a volume change of over 5% which is much more stringent than the ASTM test method. By these standards none of the seal material would be compatible with the HOX and MOX bio-oil blends.

IV. Conclusion

From the tests run it is clear that the HOX and MOX bio-oils succeed and fail in the same respective categories. . More specifically, from a combustion point of view, both HOX and MOX blends exhibit flames almost identical to No. 2 oil from a visible and physical standpoint. There are minor differences such as the bio-oil blends produce a marginally higher photo-resistance meaning the flames produced are marginally dimmer. This level of accuracy is hard to justify however as the photo-resistor is not a foolproof method of measurement. Also the bio-oil blends show elevated levels of oxygen and NOx. These changes however are tiny and are directly linked to the composition of the fuels; they contain more organics than No. 2 oil.

The tests where the bio-fuels fail are the material tests. When soaked in HOX and MOX for 72 hours, rubber seal grade nitrile expanded to 17% and 25% its original size respectively. The ASTM limit for percent change in volume for seal soaked in fuel for 72 hours is 25%. This means technically the seals passed however from further observation it can be seen the seals swelled more than 25% of their original volume when immersed in bio-oil longer than the allotted 72 hours. While this may pass ASTM standards industry standards are more limiting and oil pump manufactures will generally consider a volume change over 5% a failure.

With these results the clear course of action is to not let these fuels go to market as they are. If they are allowed to do so there

will be catastrophic failures in the households that decide to use it. Instead what needs to be done is more work focused on refining pyrolysis oil further. It needs to be understood what makes these fuels so harmful to materials. With this extra refining it cannot be forgotten that these fuels need to be economical in order to be successful. This means while pyrolysis oil needs further refinement it must still be competitive with other heating oils with regard to price.

The results of these tests are not the fate of these fuels since there are many more tests that need to be done over time and many ways to refine bio-oils in order to find a perfectly competitive fuel. These are only the results for these first attempts and should be viewed in a light complimentary with the scientific method. There is always room for improvement.

V. References

- ¹ Energetics Incorporated. "Potential for a Renewable Heating Oil Substitution Fuel in New England." Technical Information Exchange on Pyrolysis Oil (2012): 1-59. Print.
- ² ASTM Standard D471, 2012, "Standard Test Method for Rubber Property - Effect of Liquids", ASTM International, West Conshohocken, PA, 2013, DOI: 10.1520/D0471-12A, www.asm.org

Processing and analysis of weather prediction model data for the Atmospheric Radiation Measurement External Data Center

James Young, Mathematics and Computer Science, St. Joseph's College, Patchogue, NY 11772

Laurie Gregory, Environmental Science, Brookhaven National Laboratory, Upton, NY 11973

Abstract

The Atmospheric Radiation Measurement (ARM) External Data Center (XDC) at Brookhaven National Laboratory (BNL) identifies external sources of weather prediction model data and acquires their data to augment the data being generated within the ARM program. When new data is to be introduced into the ARM archive, an automated process is required to reformat the data into an ARM-compatible data format. This specific data reformatting involved writing a program script in Python for converting Rapid Refresh (RAP) model data [<http://rapidrefresh.noaa.gov/>] stored in Gridded Binary (GRIB) files into Network Common Data Files (netCDF) and reformatting the data within the file to conform to the ARM Standards. After running the script on a RAP file converted from GRIB to netCDF, further analysis of the data and the layout can be conducted and the data can be plotted on a map. The plotting script utilized the composite reflectivity variable and gave a plot over the North American continent that clearly displayed cloud cover from the RAP file identical to a plot given by the National Oceanic and Atmospheric Administration (NOAA), verifying the consistency and reliability of the data. By reorganizing RAP data into a common format, the new data will be openly available to scientists who are conducting research and analysis of atmospheric weather patterns and global climate change, bringing us closer to a better understanding of the changes occurring in our atmosphere.

I. Introduction

All new data sets entered into the ARM archive must adhere to the required ARM Data Standards in order to enhance discoverability, unless an exception is granted. The benefits to adhering to the standards include: consistency across data streams, code reuse by using consistent formats, simple and consistent software able to read all standardized netCDF files, and files that are both human and machine readable to the degree possible [1]. Adherence to the standards will lead to better quality and more readily understandable netCDF files as well as a consistent format for data users who are familiar with ARM Standards. As more products adhere to the standards, fewer exceptions will be needed to be added to data product software when ingesting various input datastreams. For developers, encountering fewer exceptions results in reduced chances to introduce software errors and quicker development time. This lowers the costs for development and unintended costs to the ARM Facility through reprocessing tasks.

RAP data files that are first introduced into the ARM data system are typically stored in GRIB2 (GRIB Edition 2) format files, which are commonly used for the storage and transport of gridded meteorological data, such as Numerical Weather Prediction model output. It is designed to be self-describing, compact and portable across computer architectures. The GRIB standard was

designed and is maintained by the World Meteorological Organization and the data is used by individuals, institutions and businesses that have the means and motivation to tap into numerical data from weather models in the rawest possible form. A GRIB file is often only one step removed from the original model output and must be decoded in order for it to become readable by users. Once decoded, the data can be post-processed for visualization or used as input for numerical weather prediction applications that require gridded data [2].

Creating an automated process that converts the GRIB files into readable netCDF files will lower the amount of processing that scientists will have to do in order to access that data that they need for their research. By further reformatting the data to conform to as many of the required ARM Standards as possible and adding more global attributes to the file header we make the data more user-friendly and familiar to the other data stored in the ARM archive. On the other side of the conversion and reformatting, we have a fairly large file of highly useful weather data that spans throughout North America. The two-dimensional format of the data allows the user to see weather patterns and measurements at specific locations as well as the weather system as a whole in order to predict future weather patterns in the data. By creating a custom python script for mapping the data on a map of the target area, scientists can see the data on a full scale in order to conduct their analysis.

II. Data file conversion and reformatting

The conversion script (see Figure 1) that was written for the ARM XDC is a single input program that takes a target GRIB file path as the input and creates a new netCDF file of the same name and reformats the data within the new file to conform to the ARM Data Standards. After the initial input file path is stored, we can isolate the name of the file itself without the rest of the path in order to create the new netCDF file of the same name. After the file name is determined, we can run `wgrib2` in order to create the new netCDF file based off the data stored in the original GRIB file. The `wgrib2` function calls the program to decode GRIB files and for our own purpose export the data into a separate netCDF file by adding the netCDF option into the command line function that the python script will execute for us [3]. The command line execution will take on the following format:

```
wgrib2 -g2clib 0 <GRIB2 file path> -netcdf
<new file name (.nc)>
```

The `wgrib2` program will take some time to decode the GRIB file and export the data, but once it does the conversion script will begin reformatting the file.

The first section of the reformatting section of the program involves the updating and addition of global attributes that com-

pose the header of the netCDF file. Although the history attribute is the only one required by the ARM Data Standards, more information available about the data leads to a more discoverable data file when it is placed in the ARM Archive. The converted GRIB file comes with three attributes: Conventions, GRIB2_grid_template, and history. Since we need to reorder the header to the recommended order from the standards and also add to the history attribute to include the script conversion and reformatting, the script is going to store the current values of the global attributes in separate variables and delete all the current global attributes. This will allow the script to add both the old and new metadata to the header in the recommended order. The new global attributes that are going to be added will include the wgrib2 command as it would be executed in the command line, one from user input of the GRIB file path and five derived by the script from the file name: command_line, input_source, site_id, platform_id, facility_id, data_level, and datastream, respectively. The last five attributes that come from the file name can be derived due to the common file naming structure that is included in the standards. Even though the input file was in GRIB format in the archive, it still has to follow the naming convention since it is currently in the ARM system due to RAP data currently being listed as an exception. The script will perform string data manipulation in order to isolate the individual attributes as it adds the old and new attributes into the netCDF file in order. The history attribute is recommended to be added last and include the origin and modifications to the file, so we add the reformatting into the history making sure to include the user, the server name, and the date and time of the reformatting.

The second half of the reformatting script focuses in the reformatting of the time variable, which needs to be split into three separate time variables as specified by the ARM Data Standards: base_time, time_offset, and time. RAP data is a snapshot of the atmosphere so each variable will only contain one time value in seconds. The current time variable has the time in seconds with respect to the Unix Epoch time, January 1, 1970, and a reference date that has the date and time stored as a string. The base_time variable is created by the script and stores the data reference time in seconds with respect to the Unix Epoch time. This time variable differs from the other two since it has a metadata component for the string variation of the reference date and time, in addition to the long_name and units, which uses the letter abbreviation for the month the data was taken. The script will use the reference date from the original time variable and manipulate it in order to achieve the string metadata into the required format and then set all of the base_time metadata. The time_offset variable is the next time variable that is created and is given a value of zero since time_offset is the offset from base_time and there is only one time value for a RAP file. Although this variable may seem unnecessary, it is required by the standards for the case of data files that have a time series of data measurements rather than a single instance and is given a value and metadata.

Our final time variable is a special case to the other two since we already have a variable called time, but it is filled with other data that we have moved to the other two variables. The script will clear out the old time variable so we have a fresh variable for our own needs. The new time variable for the netCDF will be a time offset from midnight on the day the data was taken, so it will give seconds since midnight. In order to do this the script will have to do some math, where it calculated the days since the Epoch time

back during the base_time creation so it is just a subtraction of the number of days converted to seconds from the base time. After that value is stored in the variable and time is given metadata the script is done reformatting and the new netCDF file will be closed so the modified data will be written out to the disk file.

III. Model data plotting and analysis

In order to test the quality of the data that was converted from GRIB to netCDF format, we decided to analyze the data by creating a plotting script (see Figure 2) that will plot a selected data variable over a geographical map within the satellite data bounds. For the ease of determining the consistency and reliability of the data we decided to plot the composite reflectivity variable which will show cloud cover over the coordinate grid. Once the plotting script opens the netCDF file as a Dataset and retrieves the desired variable it will also retrieve the coordinate variables and determine the minimum and maximum coordinate boundaries. The script will then create the figure and axis instances and place a Basemap instance on the figure using the bounds of the latitude and longitude variables. Then the Basemap will be filled in with coastlines, state and country boundaries, the edge of the map, latitudinal parallels, and longitudinal meridians. Now the graph is set up and we need to plot the data values onto the map.

In order to match the data values in our data grid to the coordinates on the map the script creates a grid of evenly spaced data points matching the shape of the data grid and computes the map projection coordinates. Now that there are data coordinates, the Basemap instance can create filled contours for the data points and display the composite reflectivity measurements. In order to create an easier scale to follow up the measurement intervals and for easier comparison we created a custom color bar to match the measurement intervals from the NOAA website composite reflectivity maps. After the script labels the color bar with units and adds a title that includes the variable displayed and the date and time of the data the plot will be displayed. The display feature allows the user to save the picture to the current directory of they wish so it can be viewed at a future time without having to rerun the script.

We can now look at the composite reflectivity plot (see Figure 3) to see the effectiveness of the conversion from GRIB to netCDF to make sure there wasn't any data loss or corruption. At first glance we can see clearly defined contours that follow the color bar order and levels that establish the existence and continuity of the data points on the plot within the coordinate boundaries. By looking closer one can see there is apparent cloud cover that is distinguishable from clear sky. There are also apparent storm systems over the oceans as well as over land following typical storm patterns that flow over the North American continent. The data displayed by the plot appears to be consistent and supports that the data conversion and plotting was successful.

IV. Discussion and Conclusion

Initial analysis of the converted and reformatted RAP data confirmed the effectiveness of the reformatting script. It successfully created the three new time variables from the initial one time variable provided by the original GRIB file and allocated the variable metadata accordingly. The script also successfully updated the file metadata confirmed by the creation of seven new global attributes and update of three preexisting attributes. In order to test the consistency and reliability of the data I choose to plot the

composite reflectivity variable from the new file and compare the plot to an existing prediction plot developed by the NOAA. The two plots were similar in nature, although cloud placement seems to vary among the graphs for the same data time. This can be attributed to the NOAA publishing a 12-hour prediction graph, rather than actual measurements taken at the indicated time and date which would be better for direct comparison. Despite the subtle differences, the plots showed similarities in cloud placement and had distinguishable storm systems between them, showing that the data within the converted file can be used for atmospheric system study.

The success of the conversion program and analysis of the output data has concluded that GRIB files can be converted into readable netCDF files and reformatted in order to correspond with the ARM Data Standards, allowing scientists around the world easier access to RAP data in a common format. The python script currently accepts one file input at a time for conversion, but the process can be reconfigured in the future to allow groups of files to be converted when new RAP data is introduced into the system, reducing the need for the storage of GRIB files within the ARM archive. This program can also act as a basis for other types of file conversions that the ARM XDC might be in need of in the future and make the process of creating a conversion method easier. Before the script can be used in the ARM system, it must be reviewed and pass through the ARM Data Standards Committee for final approval and confirmation that the script meets the required aspects of the standards.

V. Acknowledgements

I would like to thank my mentor, Laurie Gregory, for the time she has spent with me working on this project and all of the new computer skills she has helped me develop. I would also like to thank all of the other members of the Scientific Information Systems Group for their support throughout my appointment at BNL. This project was supported in part by the U.S. Department of Energy, Office of Science, Office of Workforce Development for Teachers and Scientists (WDTS) under the Science Undergraduate Laboratory Internships Program (SULI).

VI. References

- [1] ARM Standards Committee. "ARM Data File Standards Version 1.0." Department of Energy Office of Science, 1 Apr. 2014. Web. 5 June 2014. <<http://www.arm.gov/publications/programdocs/doe-sc-arm-14-010.pdf?id=14>>.
- [2] "What is GRIB?." Environment Canada. Government of Canada, n.d. Web. 25 July 2014. <https://weather.gc.ca/grib/what_is_GRIB_e.html>.
- [3] "wgrib2: wgrib for GRIB-2." Climate Prediction Center - wgrib2: grib2 utility. NOAA / National Weather Service, 18 Aug. 2011. Web. 28 July 2014. <<http://www.cpc.noaa.gov/products/wesley/wgrib2/index.html>>

VII. Figures

Figure 1: conversion.py – conversion and reformatting script

```
# takes GRIB file, converts it to netCDF file of same name
# and reformats to ARM standards

from netCDF4 import *
import matplotlib.dates
import getpass #getpass.getuser() = username
import os #getenv for server name
import datetime

#input file path of GRIB file, convert to netCDF of same name
file_name = raw_input('Enter file path of GRIB file: ')
original_file_name = file_name.split('/')
datastream = original_file_name[len(original_file_name)-2]#second to last link
original_file_name = original_file_name[len(original_file_name)-1]
new_file_name = original_file_name.split('.')
new_file_name[len(new_file_name)-1] = 'nc'
new_file_name = '.'.join(new_file_name)
command = "wgrib2 -g2clib 0 " + file_name + " -netcdf " + new_file_name
os.system(command)
file_obj = Dataset(new_file_name, 'r+')

#store old global attributes and delete for reordering
Conventions = getattr(file_obj, 'Conventions')
GRIB2_grid_template = getattr(file_obj, 'GRIB2_grid_template')
file_obj.__delattr__('History')
file_obj.__delattr__('Conventions')
file_obj.__delattr__('GRIB2_grid_template')

#enter new global attributes in new order
#command_line
setattr(file_obj, 'command_line', command)
#Conventions reloaded into file
setattr(file_obj, 'Conventions', Conventions)
#GRIB2_grid_template reloaded into file
setattr(file_obj, 'GRIB2_grid_template', GRIB2_grid_template)
#input_source
setattr(file_obj, 'input_source', file_name)
#site_id
data_list = datastream.split('.')
info_list = list(data_list[0])
site_id = info_list[0] + info_list[1] + info_list[2]
setattr(file_obj, 'site_id', site_id)
#platform_id and facility_id
data_word = '.'.join(info_list[3:])
for l in data_word:
    if l.isupper():
        data_word = data_word.split(l)
        platform_id = data_word[0]
        facility_id = l + data_word[1]
    else:
        pass
setattr(file_obj, 'platform_id', platform_id)
setattr(file_obj, 'facility_id', facility_id)
#data_level
setattr(file_obj, 'data_level', data_list[1])
#datastream
setattr(file_obj, 'datastream', datastream)
```

```

#history
time = datetime.datetime.now()
setattr(file_obj, 'history', 'created by wgrib2 and reformatted by user ' + getpass.getuser() + ' on ' + str(os.getenv('HOSTNAME')) + ' on ' + time.strftime("%Y-%m-%d %H:%M:%S"))

#reformat time variables
months = {1 : 'Jan', 2 : 'Feb', 3 : 'Mar', 4 : 'Apr', 5 : 'May', 6 : 'June' , 7 : 'July',
8 : 'Aug', 9 : 'Sept', 10 : 'Oct', 11 : 'Nov', 12 : 'Dec'}

time_obj = file_obj.variables['time']

#base_time variable
base_time = file_obj.createVariable('base_time', 'i')
base_time[0] = time_obj.reference_time
time_standard = base_time[0]
time_standard = matplotlib.dates.epoch2num(time_standard)
days = matplotlib.dates.num2epoch(int(time_standard))
time_standard = matplotlib.dates.num2date(time_standard)

#string attribute for base_time variable
string_time = str(time_standard)
string_time = string_time.split('+')
time_standard = ' '.join(string_time)
string_time = time_standard + ' UTC'
string_time = string_time.split('-')
integer_month = int(string_time[1])
string_time[1] = months[integer_month]
string_time = '-'.join(string_time)
#base_time metadata
base_time.string = string_time
base_time.long_name = 'Base time in Epoch'
base_time.units = 'seconds since 1970-01-01 0:00:00 0:00'

#time_offset variable
time_offset = file_obj.createVariable('time_offset', 'f', ('time',))
time_offset[0] = 0 #for RAP there is only one time
#time_offset metadata
time_offset.long_name = 'Time offset from base_time'
time_offset.units = 'seconds since ' + time_standard

#clean out old time variable
for x in time_obj.ncattrs():
    time_obj.__delattr__(x)

#time variable
day_offset = base_time[0] - days
time_list = time_standard.split(' ')
date = time_list[0]
time_obj[0] = day_offset
#time metadata
time_obj.long_name = 'Time offset from midnight'
time_obj.units = 'seconds since ' + date + ' 00:00:00 0:00'

file_obj.close()

```

Figure 2: rap_plot.py – RAP data plotting script

```
from mpl_toolkits.basemap import Basemap, cm
from netCDF4 import Dataset as NetCDFFile
import numpy as np
import matplotlib.pyplot as plt
from matplotlib import colors

#load in file and variable for plotting
nc = NetCDFFile('nacrap32X1.00.20140717.160000.raw.nc')
var = nc.variables['REFC_entireatmosphere_consideredasasinglelayer_']
data = var[:]

#load coordinates and bounds
latcorners = nc.variables['latitude'][:, :]
loncorners = nc.variables['longitude'][:, :]
lon_0 = -107
lat_0 = 40
lon_min = loncorners[0][0]
lon_max = loncorners[loncorners.shape[0]-1][loncorners.shape[1]-1]
lat_min = latcorners[0][0]
lat_max = latcorners[latcorners.shape[0]-1][latcorners.shape[1]-1]

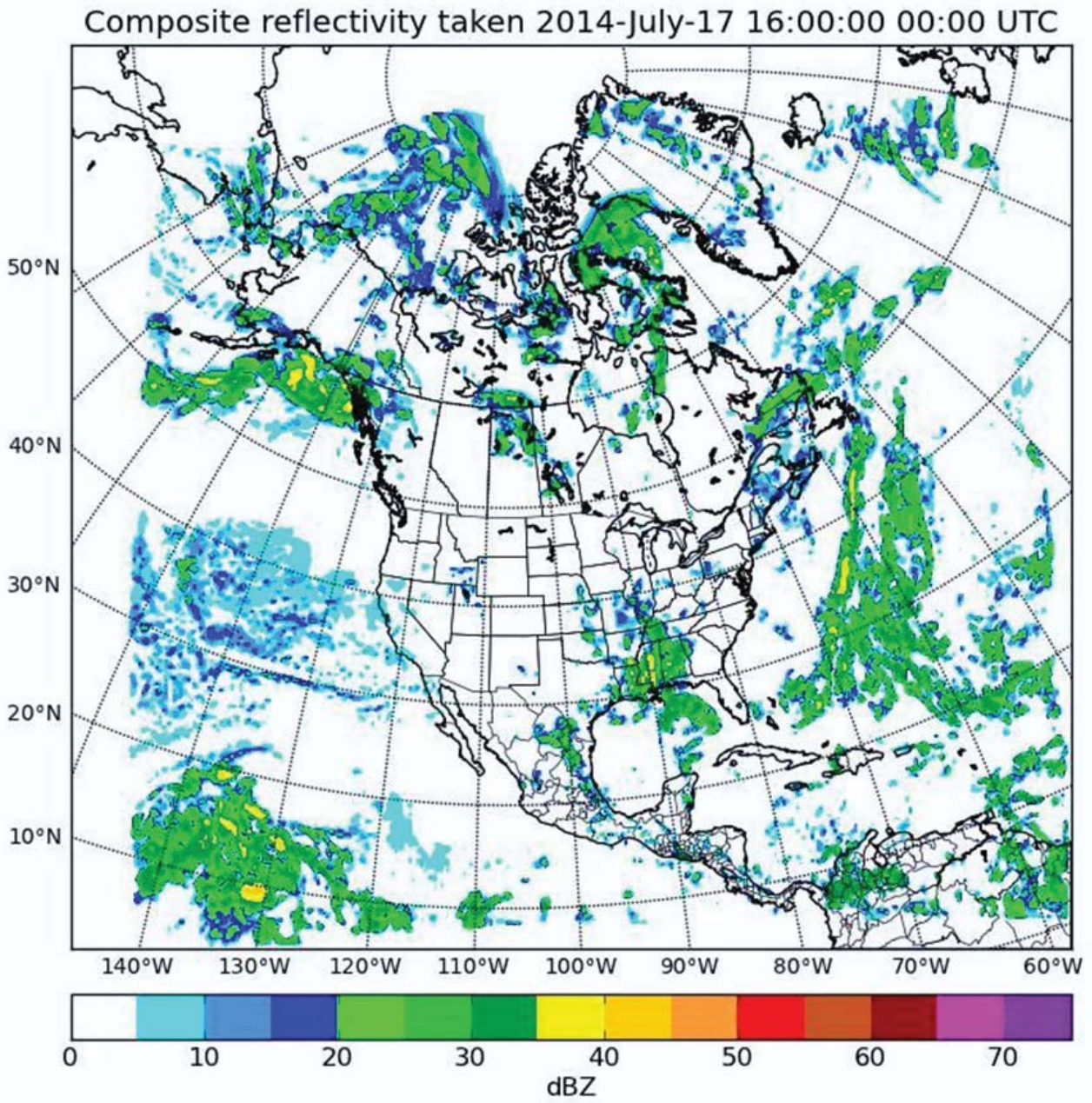
#create figure and axes instance
fig = plt.figure(figsize=(8,8))
ax = fig.add_axes([0.1,0.1,0.8,0.8])

#create polar stereographic Basemap instance
m = Basemap(projection='stere',lon_0=lon_0,lat_0=lat_0,
lat_ts=lat_0,llcrnrlat=lat_min,urcrnrlat=lat_max,
llcrnrlon=lon_min,urcrnrlon=lon_max,
rsphere=6371200.,resolution='l',area_thresh=1000)

#draw coastlines, state and country boundaries, edge of map
m.drawcoastlines()
m.drawstates()
m.drawcountries()

#draw parallels
parallels = np.arange(0.,90,10.)
m.drawparallels(parallels,labels=[1,0,0,0],fontsize=10)
#draw meridians
meridians = np.arange(180.,360.,10.)
m.drawmeridians(meridians,labels=[0,0,0,1],fontsize=10)
#match grid to coordinates
ny = data.shape[1]
nx = data.shape[2]
lons, lats = m.makegrid(nx,ny) #get lat/lons of ny by nx evenly space grid
x, y = m(lons, lats)#compute map proj. coordinates
#draw filled contours
color_list = ['#ffffff', '#00ffff', '#3399ff', '#0000ff', '#00ff00', '#00cc00', '#009933', '#f
fff00', '#ffcc00', '#ff9933', '#ff0000', '#cc5200', '#990000', '#ff00ff', '#9900cc']
cmap = colors.ListedColormap(color_list)
clevs = [0,5,10,15,20,25,30,35,40,45,50,55,60,65,70,75]
cs = m.contourf(x,y,data[0],clevs,cmap=cmap)
#add colorbar
cbar = m.colorbar(cs,location='bottom',pad="5%")
cbar.set_label('dBZ')
#add title
plt.title(var.long_name + ' taken ' + nc.variables['base_time'].string)
plt.show()
```

Figure 3: rap_plot.py output



Time lag analysis of paleoclimate data from Vostok, Antarctica

Scott Zhang

Department of Mathematics, University of North Carolina, Chapel Hill, NC 27514

Hua Song and Yangang Liu

Biological, Environmental & Climate Sciences Department, Brookhaven National Lab, Upton, NY 11973

Abstract

Ice cores collected at Vostok, Antarctica provide a 400000 year history of climate data. The data show a very strong correlation between CO₂ and δDeuterium (a proxy for surface temperature). Through time-lag and Fourier analysis of the Vostok data using MATLAB®, I attempt to empirically determine the causal- effect relationship without the incorporation of climate modeling. Also examined are probability density functions of both variables at different time lags and their relationships to improve our understanding of the processes and climate sensitivity, a key metric gauging the response of the Earth's climate system to climate forcing. Precise statistical methods are still in development and definitive results have yet to be produced.

I. Introduction

Ice cores collected at Vostok, Antarctica provide a 420 kyear climate record of various climate properties.¹ These data are rich with information about Earth's climate variability. My work aims to understand covariations of CO₂ and temperature, their possible cause-effect relationships, and climate sensitivity by using techniques of time series analysis and PDF analysis to the Vostok data. This report summarizes key results obtained, discusses problems revealed and outlines possible directions for future research.

II. Methods

Paleoclimate data were obtained from the NOAA Paleoclimatology website. All data analysis was performed using MATLAB®. All original figures displayed were produced in MATLAB. For analysis purposes, the data were interpolated at 500 year intervals using the MATLAB function *interp1*. The first analysis done was an autocorrelation and cross correlation analysis. This was achieved through use of for-loops and the function *corrcoef*. The probability density contours were created using a function *kde*, written by Zdravko Botev, which calculates the kernel density estimate with bandwidth selection by diffusion equations. This technique is more accurate in describing the multi-modal densities which occur in the data.² Frequency analysis was performed using the *fft* function, which quickly performs discrete Fourier transforms.

III. Results

It is evident from the original data (figure 1) that temperature and CO₂ correlate highly ($r = .8645$) and change with similar periods. The autocorrelation and cross correlation functions give information about how well the time series correlate when a time lag is applied. The autocorrelation functions for temperature and CO₂ are very similar in shape, which suggests that the two vary on very similar periods.(figure 2) This finding is also supported by the Fourier analysis of the data (figure 3), which displays dom-

inant periods at around 100 000, 40 000, and 23 000 years for both data sets. These results are consistent with the Milankovitch hypothesis, which states that periodic variations in the orbital inclination, axial tilt, orbital shape and other astronomical values effect climate cycles. The cross correlation functions (figure 4) show patterns and peaks similar to the autocorrelation series. The highest correlation is found when temperature leads CO₂ by 1000 years. This is relatively consistent with other studies which have looked at smaller time scales. Caillon et al. examined the Vostok data during Termination III (~240 kybp) and found a similar lag, temperature leading CO₂.³ Landais et al. found two phases in Termination II (~136 kybp), one with no lag and one with CO₂ again lagged.⁴

The probability density contours (figure 5) give interesting information about the general behavior of the time series at different time lags. Once again, we see that both temperature and CO₂ behave similarly over most time lags. The periodic nature of the data is once again visible, with the 100 000 year period being dominant. Both series show low difference values as the time lags approach the values of the major periods and the highest values at the half-periods. Interpreting the differences in the shapes of the two graphs may help decode climate sensitivity.

Cross spectral and coherence analysis (figure 6) showed phase lags found that three major peaks of coherence, each of which found values of phase lag separated by an order of magnitude from those values obtained from the other peaks. However, for the coherence analysis, the question of whether or not a peak is significant is fairly subjective in this case. Fine tuning of this technique may give further insights into the causal relationships between the two time series, although it may also be unsuitable to data of this kind.

IV. Discussion and Future Work

These results show promise for obtaining an empirical basis for determining climate sensitivity and causation. However, the problem of differentiating causation and correlation has fundamental and significant hurdles, both statistically and philosophically. In 1969, Clive Granger introduced an econometric test for causation which is applied to many different fields outside of economics. Nonetheless, Granger causality has its own problems. The test relies on the assumption that the time series tested contain all relevant causal information.⁵

The method also relies on a best linear predictor to test for causality. In the case of temperature and CO₂, this most surely over-simplifies the situation. It may be necessary to distinguish between an initial causal factor and a self-propagating feedback factor. The figures which, in my opinion, are most promising are the phase difference and difference correlation. These figures may help distinguish what parts of the time series are causally related and which are results of underlying processes, such as the Milan-

kovitch cycles.

Another area for future exploration would be finding a method of removing the externally caused variation to analyze only the relevant variables. The main problem with such an approach would be distinguishing what information in a time series is relevant and what is not. I plan to explore this further and to investigate another climate topic – aerosol effects on climate.

VI. Appendix – Figures

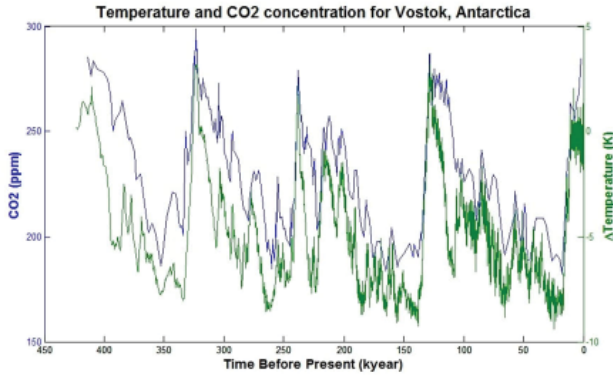


Figure 1: Time series representations of temperature and CO₂. Data obtained through the National Oceanic and Atmospheric Administration Paleoclimatology website.

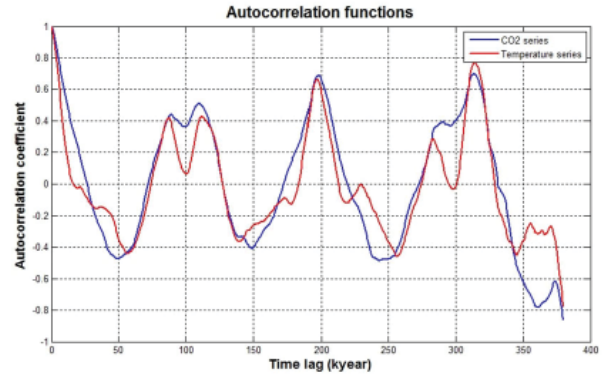


Figure 2: Autocorrelation for the CO₂ and temperature time series as functions of time lag. Autocorrelation is defined as:

$$\rho(k) = \frac{cov(y_t, y_{t+k})}{cov(y_t, y_t)}$$

where k represents time lag and yt is a time series.

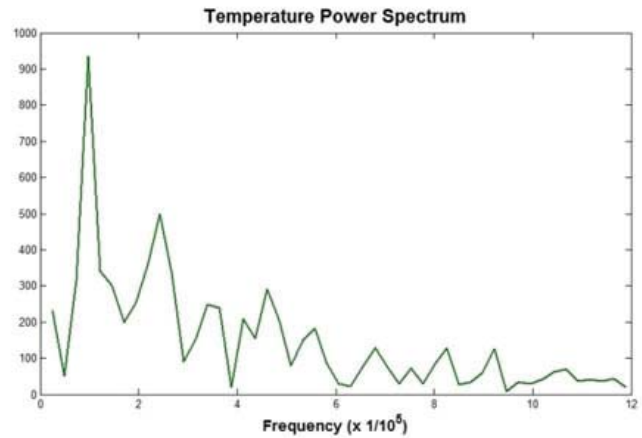
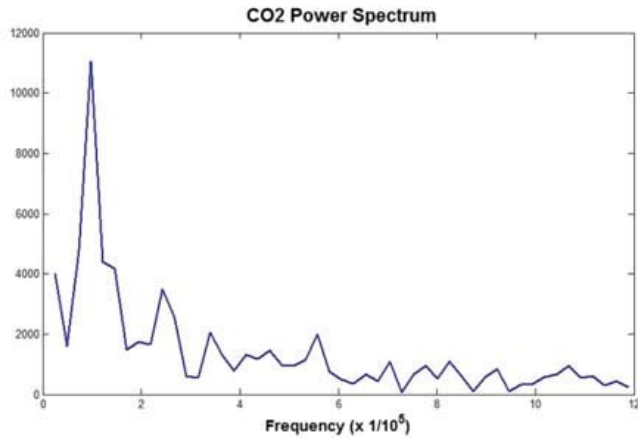


Figure 3: Fourier power spectrums for Temperature and CO₂ data with arbitrary units. Plots display the strongest periods of variance for both time series and suggest the two are highly interrelated.

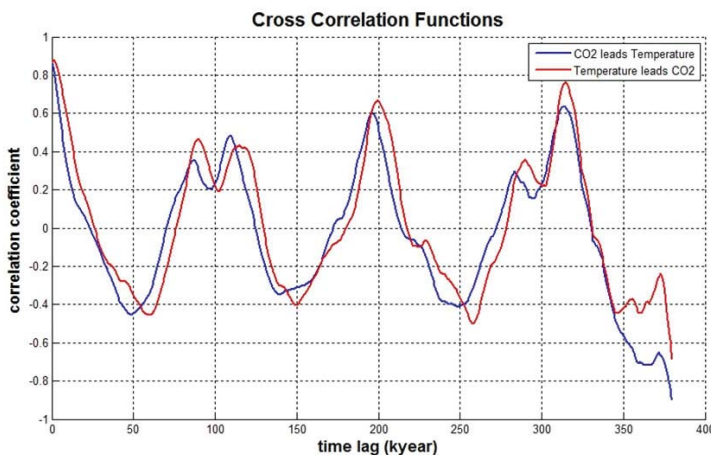


Figure 4: Cross correlation functions between temperature and CO₂. The functions are defined:

$$R_{xy}(k) = \frac{cov(x_t, y_{t+k})}{\sigma x_t \sigma y_{t+k}}$$

For the function labeled “CO₂ leads Temperature”, the time series are analyzed with the time lag applied such that the temperature series is “moved” forward in time, and has more recent values, and vice versa for the opposite function.

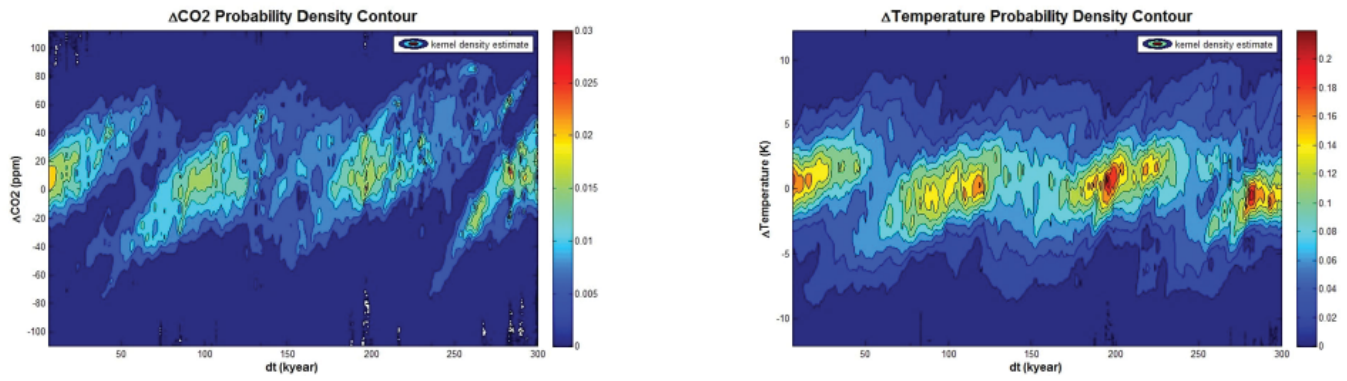


Figure 5: Probability density contours for temperature and CO₂. For each value of dt, a kernel density estimate is calculated. The multiple density estimates are concatenated and plotted to a contour. The colors of the contour represent the approximate values of the density estimate. The General behaviors of both data sets are shown to be very similar again.

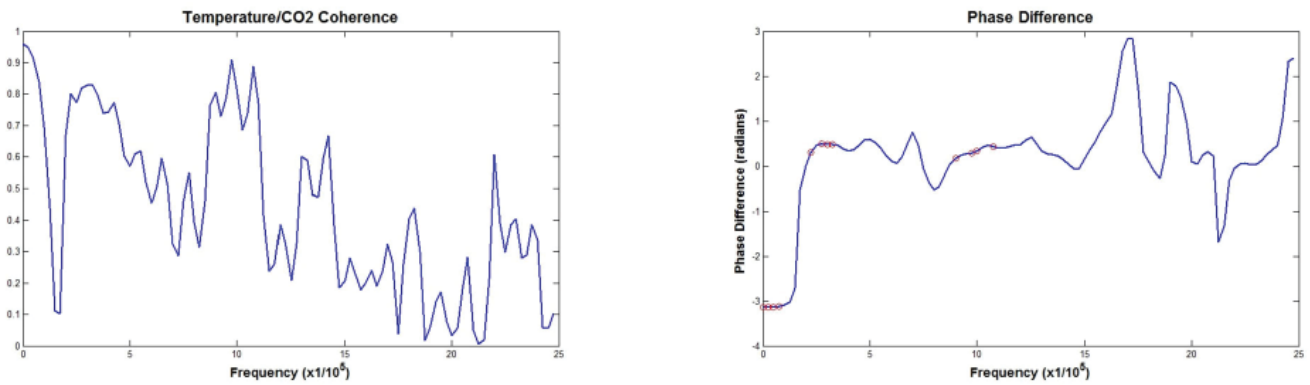


Figure 6: Coherence and phase difference figures. Calculated using functions mscohere and cpsd